

Dissertation der Fakultät für Biologie
der Ludwig Maximilians-Universität München

**Functional nuclear architecture
in normal cells and after manipulation
of the nuclear landscape**

Barbara Hübner



Eingereicht am 12.02.2020

Functional nuclear architecture in normal cells and after manipulation of the nuclear landscape.

**Dissertation der Fakultät für Biologie
der Ludwig-Maximilians-Universität München (LMU)**

zur Erlangung des akademischen Grades des Doktors der Naturwissenschaften (Dr. rer. nat.)

Angefertigt unter der Leitung von Prof. Dr. Thomas Cremer am Institut für Anthropologie und Humangenetik im Department Biologie II der Ludwig-Maximilians-Universität München

Vorgelegt von: Dipl. Biol. Barbara Hübner
aus Tutzing

Erstgutachter: Prof. Dr. Thomas Cremer

Zweitgutachter: Prof. Dr. Christof Osman

Tag der Abgabe: 12.02.2020

Tag der mündlichen Prüfung: 22.09.2020

“[...] by the help of Microscopes, there is nothing so small, as to escape our inquiry; hence there is a new visible World discovered to the understanding.”

Robert Hooke
Micrographia, 1665

Contents

DECLARATION	11
1. SUMMARY / ZUSAMMENFASSUNG	13
1.1 Summary	13
1.2 Zusammenfassung	15
2. INTRODUCTION	19
2.1 General considerations on nuclear architecture	19
2.2 Models of functional nuclear architecture	20
2.2.1 The chromosome territory – interchromatin compartment (CT-IC) model ..	21
2.2.2 The interchromosomal network (ICN) model	22
2.2.3 The lattice model.....	22
2.2.4 Other models of nuclear organization based on chromatin loops	22
2.2.5 Present view on models of functional nuclear architecture	23
2.3 Aim of this work: comparative analysis of functional nuclear architecture in normal cells and after cell manipulation	25
2.4 Hematopoiesis – a model system for studying normal nuclear architecture in primary cells during differentiation	27
2.5 Methods to manipulate the nuclear landscape and to interfere with the distribution of chromatin.....	30
2.5.1 Treatment with high or low salt concentrations.....	30
2.5.2 Microinjection	30
2.5.3 UV irradiation and caffeine posttreatment	30
2.5.4 Premature chromosome condensation (PCC).....	34
2.6 Microscopy – an indispensable tool for understanding the (dynamic) organization of the nucleus.....	35
2.6.1 Conventional wide-field (WF) microscopy	36
2.6.2 Confocal microscopy.....	37
2.6.3 Three-dimensional structured illumination microscopy (3D-SIM).....	38
2.6.4 Transmission electron microscopy (TEM)	40
2.6.5 Correlative microscopy – an approach for an increased gain of information by the sequential application of different microscopic systems	43
3. MATERIALS AND METHODS	45
3.1 Materials and technical equipment.....	45
3.1.1 Cells.....	45
3.1.2 Chemicals and reagents	45
3.1.3 Media and solutions	49
3.1.4 Equipment and devices.....	55

3.1.5	Microscopes.....	60
3.1.6	Software.....	63
3.2	Methods.....	64
3.2.1	Tissue culture.....	64
3.2.1.1	Isolation of hematopoietic cells.....	66
3.2.1.2	Thawing of cells.....	73
3.2.1.3	Splitting of cells.....	74
3.2.1.4	Seeding of cells onto coverslips.....	75
3.2.1.5	Freezing of cells.....	79
3.2.2	Treatment of living cells.....	79
3.2.2.1	Hypotonic treatment.....	80
3.2.2.2	Damage induction using UV irradiation and caffeine-posttreatment.....	80
3.2.2.3	Induction of premature chromosome condensation (PCC).....	81
3.2.2.4	Formation of hypercondensed chromatin (HCC).....	82
3.2.2.5	Incorporation of BrdU for the detection of S phase cells.....	82
3.2.3	Microinjection of adherent cells.....	83
3.2.3.1	Dialysis of the 20 nm beads.....	84
3.2.3.2	Pulling of microinjection needles.....	85
3.2.3.3	Preparation of the injection mix.....	86
3.2.3.4	Injection.....	87
3.2.4	Microscopy of living cells in 3D and 4D.....	91
3.2.4.1	Changes between normal and hypotonic conditions in granulocytes.....	94
3.2.4.2	Live cell observations after microinjection.....	95
3.2.4.3	Live cell observations after UV/caffeine treatment.....	97
3.2.4.4	Live cell observations after the induction of premature chromosome condensation (PCC).....	101
3.2.4.5	Stepwise induction of hypercondensed chromatin (HCC).....	104
3.2.5	Cell fixation.....	105
3.2.5.1	Paraformaldehyde (PFA) fixation.....	106
3.2.5.2	Methanol / acetic acid (MAA) fixation.....	107
3.2.6	Fluorescent staining of fixed samples.....	108
3.2.6.1	Immunofluorescence of specific proteins.....	108
3.2.6.2	BrdU detection.....	111
3.2.6.3	DAPI-staining.....	112
3.2.7	Fluorescence in situ hybridization (FISH).....	113
3.2.7.1	Probe generation.....	113
3.2.7.2	Preparation of metaphase spreads for 2D-FISH.....	119
3.2.7.3	2D-FISH.....	123
3.2.7.4	3D-FISH.....	125
3.2.8	Sample preparation for transmission electron microscopy (TEM).....	129
3.2.8.1	Embedding of cells in resin.....	129
3.2.8.2	Cutting ultrathin sections.....	132
3.2.8.3	Osmium ammine staining of DNA.....	135
3.2.9	Microscopy of fixed samples.....	137
3.2.9.1	Bleaching experiments to allow the sequential imaging with fluorophores with identical or similar emission spectra.....	137
3.2.9.2	Confocal laser scanning microscopy (CLSM).....	138
3.2.9.3	3D structured illumination microscopy (3D-SIM).....	139
3.2.9.4	Transmission electron microscopy (TEM).....	140
3.2.10	Notes on correlative microscopy.....	141
3.2.10.1	Requirements.....	141
3.2.10.2	Problems.....	146

3.2.11	Image processing.....	147
3.2.11.1	Correction for chromatic aberration of CLSM and 3D-SIM images.....	147
3.2.11.2	Generation of 3D-reconstructions in Amira	148
3.2.11.3	Alignment of images obtained from different microscopic systems	148
3.2.11.4	General information on image processing.....	150
3.2.12	Evaluations	151
3.2.12.1	Generation of chromatin masks	151
3.2.12.2	Determination of the number of nuclear pores and the area/pore	154
3.2.12.3	Determination of the number of RNA polymerase II signals.....	155
3.2.12.4	Determination of the amount of chromatin (CT) and interchromatin compartment (IC) and of the chromatin surface.....	157
3.2.12.5	Segmentation of chromatin stainings into classes, including the determination of the localization of additional markers in relation to chromatin.....	158
3.2.12.6	Determination of the localization of microinjected beads in relation to chromatin using line scans.....	163
3.2.12.7	Wilcoxon rank-sum test	164
4.	RESULTS.....	167
4.1	Nuclear organization of hematopoietic cells during differentiation	167
4.1.1	Variability of the general nuclear morphological features between CD34 ⁺ cells, monoblasts, myeloblasts, monocytes, and granulocytes	167
4.1.2	Consistent functional nuclear architecture during differentiation of hematopoietic cells.....	181
4.1.3	Reversible decondensation of chromatin upon hypotonic treatment.....	198
4.2	Microinjection of beads into HeLa cell nuclei – observations upon chromatin condensation.....	201
4.2.1	Localization of the beads in low-density chromatin of interphase cells	201
4.2.2	Exclusion of beads from condensing mitotic chromosomes.....	206
4.3	Characterization of nuclear phenotypes after UV irradiation and caffeine posttreatment (UV/caffeine treatment) or premature chromosome condensation (PCC) in V79 cells.....	212
4.3.1	Background analysis of the observed nuclear phenotypes reveals: UV/caffeine treatment and PCC induction represent two different phenomena with common features	212
4.3.1.1	Identification of the processes occurring during UV/caffeine treatment and PCC induction.....	215
4.3.1.2	Parachute-like chromatin conformations (PALCCs) observed after UV/caffeine treatment and PCC induced cells both represent mitotic events.....	226
4.3.2	Consistent functional nuclear architecture in selected stages of control, UV/caffeine treated and PCC induced cells.....	236
4.4	Correlative microscopy – exemplified by studies of functional nuclear architecture in HeLa cells with hypercondensed chromatin (HCC)	246
4.4.1	Two pathways of correlative microscopy	246
4.4.2	Consistent functional nuclear architecture in control and HCC induced cells	257

5. DISCUSSION	265
5.1 Functional nuclear architecture	265
5.1.1 Functional nuclear architecture is consistent in normal cells and in cells with a manipulated nuclear landscape across all different nuclear phenotypes	265
5.1.2 Evidence for a chromatin organization free of entanglements	270
5.1.3 The results of this work and the CT-IC / ANC-INC model of functional nuclear architecture.....	271
5.1.4 Side note: Correlation between general nuclear morphological features, transcriptional activity and differentiation stage in hematopoietic cell types	275
5.1.5 Conclusions on the analysis of functional nuclear architecture – the intertwined relationship of structure and function.....	279
5.2 Microscopy	280
5.2.1 Microscopy vs. chromosome conformation capture (3C) – differences and similarities	280
5.2.2 Thoughts on correlative microscopy	286
5.3 Addendum: Insights into the processes and mechanisms occurring upon UV/caffeine treatment and PCC.....	288
5.3.1 UV/caffeine treated cells and PCC: two different phenomena but both representing mitotic events	288
5.3.2 Revision of the definition of S phase PCCs	292
5.3.3 The factor depletion model as a common background for shattered chromosome complements	295
6. REFERENCES	299
7. APPENDIX.....	321
7.1 Abbreviations	321
7.2 List of figures and tables.....	323
7.2.1 List of figures.....	323
7.2.2 List of tables.....	326
7.3 Contents of the enclosed DVD / ZIP archive	326
ACKNOWLEDGEMENT / DANKSAGUNG	329
CURRICULUM VITAE.....	331
PUBLICATIONS	332
EIDESSTÄTTLICHE ERKLÄRUNG.....	333

Declaration

Substantial parts of this work are published in:

Hübner B, Strickfaden H, Müller S, Cremer M, Cremer T, Chromosome shattering: a mitotic catastrophe due to chromosome condensation failure, Eur Biophys J, 38 (6): 729-47, 2009

Hübner B, Cremer T, Neumann J, Correlative microscopy of individual cells – sequential application of microscopic systems with increasing resolution to study the nuclear landscape, Methods Mol Biol, 1042: 299-336, 2013

Hübner B, Lomiento M, Mammoli F, Illner D, Markaki Y, Ferrari S, Cremer M, Cremer T, Remodeling of nuclear landscapes during human myelopoietic cell differentiation maintains co-aligned active and inactive nuclear compartments, Epigenetics & Chromatin, 8:47, 2015

Parts of this work (text and figures) are therefore adapted from these sources.

Hübner et al. (2009) reprinted and adapted by permission from Springer Nature Customer Service Center GmbH: Springer Nature, European Biophysics Journal, copyright 2009.

Hübner et al. (2013) reprinted and adapted by permission from Springer Nature Customer Service Center GmbH: Springer Nature, Springer eBook, copyright 2013.

Hübner et al. (2015) reprinted and adapted in accordance with the Creative Commons Attribution 4.0 License (Creative Commons 4.0).

1. **Summary / Zusammenfassung**

1.1 **Summary**

The cell nucleus is known to be the carrier of hereditary information for more than 100 years now. But it was only in the last few decades that this organelle was increasingly understood as a highly compartmentalized structure and that the interest in gaining a comprehensive image of its structural and functional organization moved into the focus of science. Today evidence suggests that changes in gene expression patterns do not only depend on local epigenetic modifications of chromatin, but also on global changes of higher-order chromatin organization. However, the question of how exactly nuclear architecture in space and time is correlated with differences in gene expression is still unanswered. A key factor for this gap in knowledge is the fact that it is still controversially discussed how the 10 nm chromatin fiber folds up into a chromosome territory (CT) and where exactly functional processes take place in the nucleus.

In this context, the primary aim of this work was the comparative analysis of functional nuclear organization in various cell types under normal conditions as well as after manipulation of the nuclear landscape. 3D structured illumination microscopy (3D-SIM) in combination with computational 3D analysis tools after DAPI staining and immunofluorescence was the method of choice for this study, supported by transmission electron microscopy (TEM), live cell imaging and confocal microscopy.

Five hematopoietic cell types of different differentiation stages as well as established cell lines (Chinese hamster (V79) and HeLa cells) under normal conditions and after UV/caffeine treatment, after induction of premature chromosome condensation (PCC) or with hypercondensed chromatin (HCC) were investigated.

Across the cell types and conditions analyzed the general nuclear morphology and the chromatin patterns showed a high variability. However, the nuclear landscape was consistently built up from chromatin domains (CDs) or chromatin domain clusters (CDCs) containing a compact core and a peripheral layer of decondensed chromatin known as the perichromatin region (PR). The PR segued into the interchromatin compartment (IC) which extended throughout the entire nucleus and reached in between the CDCs with finer and thicker branches and occasional large lacunas. Similarly, also functional nuclear architecture revealed by the distribution of different markers was consistent in all cell types and conditions studied: transcriptionally competent chromatin marked by H3K4me3 was mainly located at the surface of the CDs/CDCs in the PR. RNA polymerase II was found almost exclusively in this region. SC35, a marker for splicing speckles, was almost completely restricted to the interior of larger

IC lacunas. Inactive chromatin marked by H3K9me3, in contrast, was mainly localized in more compact chromatin.

Live cell observations of granulocytes showed that both the decondensation of chromatin upon treatment with hypotonic medium as well as the (re)condensation after changing back to normal salt conditions are very rapid and reversible processes. Furthermore, small fluorescent beads microinjected into the nucleus did not get trapped in the condensing chromosomes when the cells entered mitosis but instead were expelled from the nucleus during the first cell division. Both these experiments shed light on higher-order chromatin organization and strongly argue for a nuclear architecture free of knots or entanglements, in line with the idea of chromatin being organized into fractal globules.

Taken together, these results strongly support the CT-IC model of functional nuclear architecture with its suggested organization into globular chromatin domains with a functionally distinct substructure. They also contribute to the refined version of this model, the ANC-INC network model, which is based on the interpretation that functional nuclear architecture is determined by two compartments that pervade the nucleus together as co-aligned 3D networks: an active nuclear compartment (ANC), suggested to contain decondensed chromatin and to include both the IC and the PR where functional processes take place, and an inactive nuclear compartment (INC), forming the core regions of the CDCs with the more compact chromatin.

Furthermore, the comparison of general morphological features and RNA polymerase II signals in hematopoietic cells revealed a decreasing transcriptional activity with progressing differentiation. In combination with the changing chromatin patterns of these cell types, this observation allows speculations about a functional importance of the structural appearance of the nuclear landscape. Also the fact that functional nuclear architecture was consistently the same in all cell types and conditions analyzed, despite the often substantial differences in chromatin patterns, transcription levels, and morphological features, indicates that structure and function inside the nucleus are inseparably linked to each other.

In addition, two side aspects were addressed in this work: Firstly, the thorough characterization of cells after UV/caffeine treatment and PCC induction in order to understand the phenotypes and processes involved in these treatments. These experiments revealed that the similar phenotypes observed after methanol acetic acid fixation are derived from very different, however, in both cases abnormal mitotic cells, and that the processes taking place after UV/caffeine treatment and PCC induction represent two different phenomena. Secondly, a pathway of correlative microscopy was established, spanning live cell imaging (spinning disk

laser scanning microscopy (SDLSM)), confocal (confocal laser scanning microscopy (CLSM)) and super-resolution (3D-SIM) fluorescence microscopy, and TEM.

1.2 Zusammenfassung

Der Zellkern ist nun seit mehr als 100 Jahren als Träger der Erbinformation bekannt. Jedoch erst in den letzten Jahrzehnten wurde dieses Organell zunehmend als stark gegliedertes Gefüge verstanden und rückte das Interesse, ein umfassendes Bild seiner strukturellen und funktionellen Organisation erhalten zu wollen, in den Fokus der Wissenschaft. Neuere Erkenntnisse lassen heute vermuten, dass Veränderungen in Genexpressionsmustern nicht nur von lokalen, epigenetischen Modifikationen des Chromatins abhängen, sondern auch von globalen Umgestaltungen seiner übergeordneten Organisation. Allerdings ist die Frage, wie genau die Zellkernarchitektur in Raum und Zeit mit Unterschieden in der Genexpression zusammenhängt, noch unbeantwortet. Ein Schlüsselfaktor für diese Wissenslücke ist die Tatsache, dass immer noch kontrovers diskutiert wird, wie sich der 10 nm-Chromatinfaden in ein Chromosomenterritorium (CT) auffaltet und wo genau funktionelle Prozesse im Zellkern stattfinden.

Vor diesem Hintergrund war das vorrangige Ziel dieser Arbeit die vergleichende Analyse der funktionellen Organisation des Zellkerns in verschiedenen Zelltypen sowohl unter normalen Bedingungen als auch nach experimenteller Manipulation. 3D-SIM (Structured Illumination Microscopy, d.h. Mikroskopie mit strukturierter Beleuchtung) in Kombination mit computerbasierten Werkzeugen zur dreidimensionalen Datenanalyse nach DAPI-Färbung und Immunfluoreszenz war die Methode der Wahl für diese Studie, unterstützt von Transmissionselektronenmikroskopie (TEM), Lebendzellbeobachtungen und konfokaler Mikroskopie.

Fünf hämatopoetische Zelltypen unterschiedlicher Differenzierungsstadien sowie etablierte Zelllinien (Zellen des chinesischen Hamsters (V79) und HeLa Zellen) im normalen Zustand und nach UV/Koffein-Behandlung, nach Einleitung vorzeitiger Chromosomenkondensierung (premature chromosome condensation, PCC) oder mit überkondensiertem Chromatin (hypercondensed chromatin, HCC) wurden analysiert.

Zwischen den untersuchten Zelltypen und Bedingungen zeigten die allgemeine Morphologie der Zellkerne und die Verteilung des Chromatins eine große Variabilität. Aufgebaut waren die Zellkerne jedoch immer aus Chromatindomänen (CDs) oder Clustern von Chromatindomänen (chromatin domain clusters, CDCs), die einen kompakten Kern aufwiesen und eine periphere

Schicht aus dekondensiertem Chromatin, bekannt als Perichromatin-Region (PR). Die PR ging stets über in das Interchromatin-Kompartiment (interchromatin compartment, IC), welches den gesamten Zellkern durchzog und mit feineren und größeren Verzweigungen und gelegentlichen großen Lakunen bis zwischen die CDCs reichte. Ebenso war auch die funktionelle Zellkernarchitektur, basierend auf der Verteilung verschiedener Marker, in allen untersuchten Zelltypen und Bedingungen einheitlich: transkriptionell kompetentes Chromatin, markiert durch H3K4me₃, war hauptsächlich an der Oberfläche der CDs/CDCs in der PR lokalisiert. RNA Polymerase II fand sich fast ausschließlich in dieser Region. SC35, ein Protein, das Spleißkörperchen (splicing speckles) identifiziert, war fast vollständig auf den inneren Bereich von größeren IC Lakunen beschränkt. Inaktives Chromatin dagegen, markiert durch H3K9me₃, war vor allem in kompakterem Chromatin lokalisiert.

Lebendzellbeobachtungen von Granulozyten zeigten, dass sowohl die Dekondensierung von Chromatin nach der Behandlung mit hypotoner Lösung, als auch die (Rück-)Kondensierung nach dem Wechsel zurück zu normalen Salzbedingungen sehr schnelle und reversible Prozesse sind. Des Weiteren verfielen sich kleine fluoreszierende Kügelchen, die in den Zellkern injiziert wurden, nicht in den kondensierenden Chromosomen, wenn die Zellen in die Mitose eintraten, sondern wurden während der ersten Zellteilung aus dem Zellkern ausgestoßen. Diese beiden Experimente beleuchten die übergeordnete Organisation des Chromatins und sprechen nachdrücklich für eine Zellkernarchitektur frei von Knoten und Verschlingungen, in Einklang mit der Idee, dass Chromatin in fraktale Kügelchen gegliedert ist.

Zusammengenommen unterstützen diese Ergebnisse das CT-IC-Modell der funktionellen Zellkernarchitektur mit seiner vorgeschlagenen Organisation in kugelförmige Chromatindomänen mit einer funktionell abgegrenzten Untergliederung. Sie tragen auch zur weiterentwickelten Version dieses Modells bei, dem ANC-INC-Netzwerkmodell, welches auf der Interpretation beruht, dass die funktionelle Zellkernarchitektur durch zwei Kompartimente bestimmt wird, die den Zellkern gemeinsam als miteinander verbundene dreidimensionale Netzwerke durchziehen: ein aktives Kernkompartiment (active nuclear compartment, ANC), das dekondensiertes Chromatin enthält und sowohl das IC als auch die PR umfasst, und ein inaktives Kernkompartiment (inactive nuclear compartment, INC), welches die Kernregionen der CDCs mit kompakterem Chromatin bildet.

Zusätzlich offenbarte der Vergleich von allgemeinen morphologischen Merkmalen mit der Anzahl von RNA Polymerase II Signalen in hämatopoetischen Zellen eine abnehmende transkriptionelle Aktivität bei fortschreitender Differenzierung. In Kombination mit den sich verändernden Chromatinmustern dieser Zelltypen erlaubt diese Beobachtung Spekulationen

über eine funktionelle Bedeutung des strukturellen Erscheinungsbildes des Zellkerns. Auch die Tatsache, dass die funktionelle Zellkernarchitektur in allen untersuchten Zelltypen und Bedingungen trotz der oft erheblichen Unterschiede in den Chromatinmustern, der transkriptionellen Aktivität und den morphologischen Merkmalen beständig gleich war, deutet darauf hin, dass Struktur und Funktion im Zellkern untrennbar miteinander verknüpft sind.

Darüber hinaus wurden in dieser Arbeit zwei Seitenaspekte beleuchtet: Zum einen die sorgfältige Charakterisierung von Zellen nach UV/Koffein-Behandlung und Einleitung von PCC, um die Phänotypen und Prozesse, die im Rahmen dieser Behandlungen auftreten, zu verstehen. Diese Experimente zeigten, dass die ähnlichen Phänotypen, die nach Methanol-Eisessig-Fixierung beobachtet wurden, von sehr unterschiedlichen, jedoch in beiden Fällen abnormen mitotischen Zellen abstammten, und dass die Prozesse, die nach UV/Koffein-Behandlung und nach Einleitung von PCC ablaufen, zwei unterschiedliche Phänomene repräsentieren. Zum anderen wurde ein Arbeitsablauf für korrelative Mikroskopie etabliert, welcher Lebendzellbeobachtungen (Spinning-Disk-Laser-Scanning-Mikroskopie (SDLSM)), konfokale (konfokale (confocal) Laser-Scanning-Mikroskopie (CLSM)) und super-auflösende (3D-SIM) Fluoreszenzmikroskopie sowie TEM umfasst.

2. Introduction

2.1 General considerations on nuclear architecture

The eukaryotic nucleus was first observed in the late 17th century by Antoni van Leeuwenhoek in blood cells of cod and salmon (Leeuwenhoek 1719-1730; cited after Gerlach 2009). It was given its name “nucleus of the cell” by Robert Brown based on the observations of orchid cells in a document read to the Linnean Society of London in 1831 and published/reprinted two years later (Brown 1831/1833). Already at the end of the 19th century through the discoveries of various scientists – among them Ernst Haeckel, Walther Flemming, and Theodor Boveri – it became clear that the nucleus is the carrier of the hereditary information (for review see Cremer 1985, Dahm 2005). However, it was only in the last few decades that this organelle was increasingly understood as a highly compartmentalized structure and that the interest in gaining a comprehensive image of its structural and functional organization, i.e. the functional nuclear architecture, moved into the focus of science. The importance and urgent need for such research is emphasized by the launch of the “4D Nucleome Program” in 2015, a \$120 million multidisciplinary research program initiated by the National Institute of Health (NIH) with the aim to understand nuclear organization and its underlying principles in space and time and the role it plays in normal cellular function and in various diseases (4D Nucleome website). Increasing evidence suggests that the regulation of gene expression patterns that are important for example for different cell cycle stages, cell types or differentiation stages, does not only depend on local epigenetic modifications of chromatin, i.e. histone modifications, DNA methylation or histone variants, but also on global changes of higher-order chromatin organization (e.g. Kurukuti et al. 2006, Williams et al. 2006, Meister et al. 2010, Deng et al. 2012, Zhang et al. 2013, Lupianez et al. 2015; for review see e.g. Meshorer and Misteli 2006, Joffe et al. 2010, Gaspar-Maia et al. 2011, Watanabe et al. 2013). The nucleus can therefore be seen as a hierarchical system, where information is encoded (1) at the genome level in the DNA sequence, (2) at the epigenetic 4D level through chromatin signatures in space and time that (might) change across species and cell types and (3) through the 4D nuclear architecture with universally valid as well as cell type or species-specific higher-order chromatin arrangements. However, the question of how exactly the 4D nuclear architecture is correlated with differences in gene expression patterns – that is which changes in structure precede or follow or cause changes in function – is still unanswered.

In the field only two facts are generally accepted: (1) the existence of the 10 nm fiber, i.e. the DNA strand wrapped around the core histones, as the basic organization of chromatin (Olins and Olins 1974, Kornberg 1974, Kornberg and Thomas 1974, Woodcock et al. 1976; for review see Olins and Olins 2003) and (2) the presence of chromosomes as chromosome territories

(CTs) in interphase as a basic and evolutionary conserved feature of nuclear architecture (Cremer et al. 1982b, Manuelidis 1985, Schardin et al. 1985; for review see Cremer and Cremer 2010). However, how the 10 nm fiber folds up into a CT – i.e. the questions about the 3D chromatin organization within CTs and about potential basic units that constitute CTs – is still highly controversially discussed. A hierarchy of chromatin foldings with increasingly larger fibers and/or loops has been suggested in which as the first step the 10 nm fiber coils up into a 30 nm fiber. The 30 nm fiber was studied extensively *in vitro* (for review see Bassett et al. 2009, Grigoryev and Woodcock 2012, Li and Zhu 2015), but whether it also exists *in vivo* is still unclear and highly debated (for review see Grigoryev and Woodcock 2012, Maeshima et al. 2014, Hansen et al. 2018). Even less is known about the structures beyond the scale of the 30 nm fiber (for review see Harnicarova Horakova et al. 2010, Woodcock and Ghosh 2010). The gap of knowledge between the 10 nm fiber and CTs therefore still persists and is emphasized by the lack of generally agreed models of (functional) nuclear architecture.

2.2 Models of functional nuclear architecture

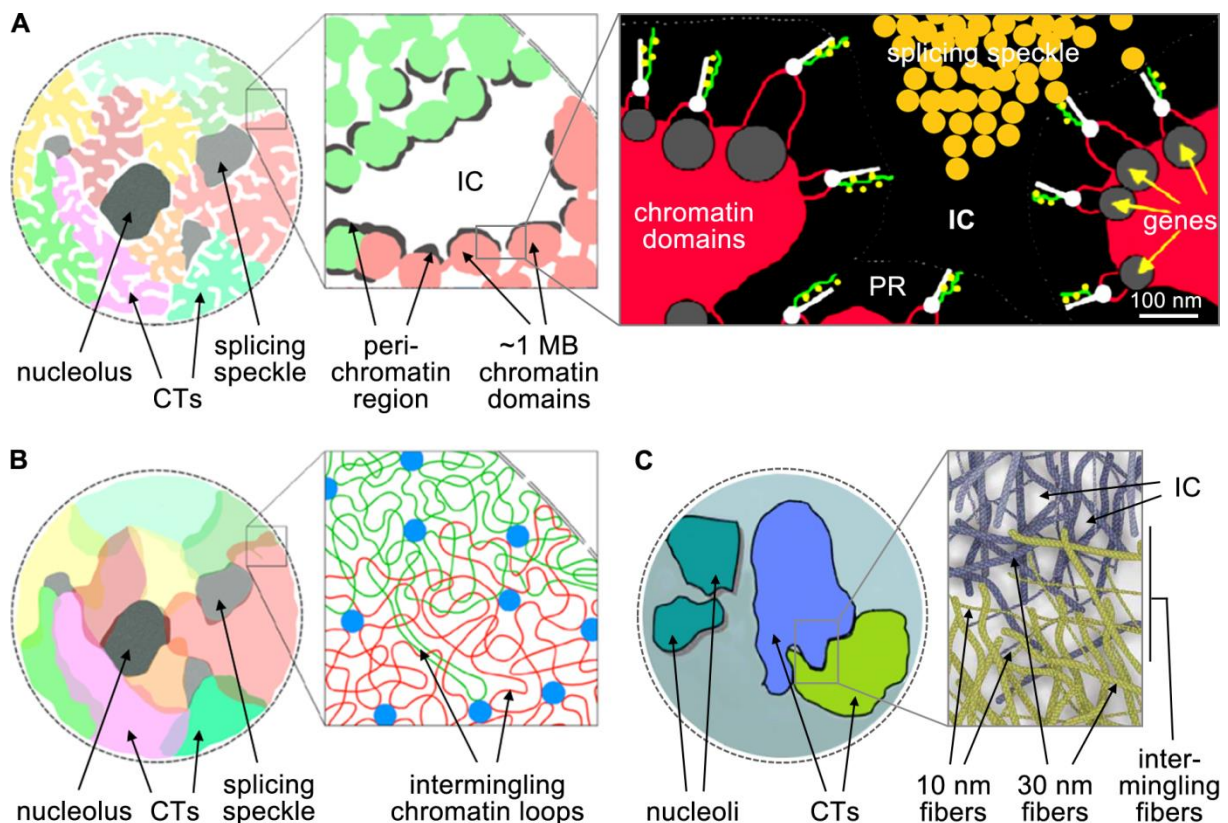


Figure 1: Models of functional nuclear architecture. (A) Chromosome territory – interchromatin compartment (CT-IC) model. For explanation see section 2.2.1. Figure adapted from Cremer and Cremer (2010). Reprinted with permission from Cold Spring Harbor Laboratory Press, copyright 2010. **(B)** Interchromosomal network (ICN) model. Blue dots represent interactions in *cis* and *trans*. For explanation see section 2.2.2. Figure adapted from Branco and Pombo (2006). Reprinted in accordance with the Creative Commons Attribution License. **(C)** Lattice model. For explanation see section 2.2.3. Figure adapted from Dehghani et al. (2005). Reprinted with permission from Elsevier.

Models of *functional* nuclear architecture try to explain not only the structure of chromatin itself but also include information about where exactly functional processes like transcription, DNA repair or DNA replication take place.

The subsequent chapters present the current models of functional nuclear architecture (see also **Figure 1**) and give an outlook into the present situation.

2.2.1 The chromosome territory – interchromatin compartment (CT-IC) model

The chromosome territory – interchromatin compartment (CT-IC) model (**Figure 1 A**) was first proposed in 2001 (Cremer and Cremer 2001; for review see also Cremer and Cremer 2006, Rouquette et al. 2010). Globally it distinguishes between a chromatin compartment (CC) – the chromosome territories (CTs) – and an interchromatin compartment (IC). CTs are supposed to be built up from interconnected chromatin domains (CDs) in the range of a few hundred kbp up to 1 Mbp in size (~1 Mbp CDs) which persist during all stages of interphase and through cell generations. CDs of neighboring CTs are often in close proximity to or even in direct contact with each other so that in most cell types CT borders cannot be recognized without staining. However extensive intermingling of chromatin from different CTs is not expected.

The ~1 Mbp CDs or clusters of ~1 Mbp CDs consist of a core of compact chromatin and a periphery of more decondensed chromatin with small-scale loops, called the perichromatin region (PR). Functionally, the PR represents the nuclear sub-compartment where transcription, pre-mRNA processing, DNA replication, and DNA repair take place (see details below). Topologically, it forms a border zone to the IC, a coherent three-dimensional network of channels and wider lacunas that pervades the entire nucleus and is both highly crowded and highly organized. Channels start at nuclear pores, traverse the peripheral layer of heterochromatin and interfuse the CC between and within the CTs with larger and smaller branches. The wider, apparently DNA-free lacunas contain splicing speckles and nuclear bodies. The IC provides factors and complexes essential for functions carried out in the PR and may also serve as a compartment for traffic of macromolecular complexes within the nucleus as well as for export out of the nucleus.

First evidence for a functionally active PR came from early transmission electron microscopic (TEM) studies which indicated that compacted CDs are lined by an approximately 100 nm wide layer of decondensed chromatin at the interface between the CC and the IC (for review see Fakan and van Driel 2007, Rouquette et al. 2010). This layer – the PR – was found to be enriched in nascent RNA (Fakan and Bernhard 1971, Nash et al. 1975, Cmarko et al. 1999, Niedojadlo et al. 2011) and RNA in general (Derenzini and Farabegoli 1990), splicing components (Fakan et al. 1984, Puvion et al. 1984, Spector et al. 1991, Cmarko et al. 1999),

nascent DNA (Liu et al. 1995, Jaunin et al. 2000) and DNA repair factors (Solimando et al. 2009, Rube et al. 2011, Lorat et al. 2015; for remarks on the latter two publications see 5.1.3 in the discussion) and was thus suggested as the nuclear subcompartment for transcription, pre-mRNA processing, DNA replication, and potentially also DNA repair.

2.2.2 The interchromosomal network (ICN) model

Fundamentally different from the CT-IC model described in the previous section, the interchromosomal network (ICN) model (Branco and Pombo 2006, **Figure 1 B**) suggests that an IC that largely separates neighboring CTs does not exist. Instead, adjacent CTs are believed to intermingle heavily at their borders with smaller and larger chromatin loops. Occasionally large loops of one territory can extend far into another territory.

Functional processes do not occur in a defined nuclear subcompartment, but at numerous sites throughout the nucleus – transcription, for example, is suggested to take place at clusters of RNA polymerases termed transcription factories – leading to or resulting from interactions of chromatin in both *cis* and *trans*. These functional associations are thought to have an influence on higher-order chromatin organization in the nucleus by determining the degree of intermingling between CTs and by establishing/maintaining local intra- and interchromosomal arrangements.

2.2.3 The lattice model

The lattice model (Dehghani et al. 2005, **Figure 1 C**) proposes a nuclear organization based on a network of fibers with diameters of 10 nm to 30 nm. This network is claimed to provide a very open chromatin configuration that is fully accessible to macromolecular complexes and thus allows transcription to occur everywhere throughout the nucleus.

Similar to the CT-IC model (see section 2.2.1) an IC pervading the nucleus as a channel system with extended interconnected inter- and intra-chromosomal DNA free spaces was described. However, here in the lattice model (extensive) intermingling of the chromatin fibers of neighboring CTs may occur, as also described by the ICN model (see previous section).

2.2.4 Other models of nuclear organization based on chromatin loops

Other models of nuclear organization are based on or include the existence of (giant) chromatin

loops, expanding up to several micrometers across the nucleus (Chubb and Bickmore 2003, Kosak and Groudine 2004, Fraser and Bickmore 2007).

Transcription is suggested to take place either (1) in so-called expression hubs (Kosak and Groudine 2004) or transcription factories (Fraser and Bickmore 2007), clusters of RNA polymerases and regulatory proteins, where genes come together irrespective of whether they are located large distances apart on the same chromosome or on different chromosomes or (2) throughout the nucleus inducing the giant chromatin loops, which condense back into the default state of chromatin as soon as transcription is stopped (Chubb and Bickmore 2003).

2.2.5 Present view on models of functional nuclear architecture

In the last years increasing evidence has accumulated in favor of the CT-IC model of nuclear architecture: (1) Fluorescence super-resolution microscopy data showed on the single-cell level in a variety of human, murine and bovine cell types that histone markers for transcriptionally competent chromatin, RNA polymerase II and also nascent DNA and nascent RNA are located on the surface of more compacted chromatin domains (Markaki et al. 2010, Markaki et al. 2012, Smeets et al. 2014, Popken et al. 2014, Hübner et al. 2015; for details see section 5.1 in the discussion). (2) Molecular data collected in high throughput approaches with chromosome conformation capture (3C) -based methods, where chromatin contacts are crosslinked, isolated, amplified and sequenced (for review see Kong and Zhang 2019), revealed that the mammalian genome consists of defined topologically associating domains (TADs) of about 100 kbp to 3 Mbp in size (**Figure 2 A**). These domains are to a large extent maintained in different cell types and are highly conserved across species. Often they are characterized by specific histone modifications or DNA binding proteins and coincide with lamin associated domains (LADs) or co-regulated gene clusters (Dixon et al. 2012, Nora et al. 2012, Rao et al. 2014, Dixon et al. 2015; for review see Tanay and Cavalli 2013, Cubenas-Potts and Corces 2015, Sexton and Cavalli 2015). (3) Computer simulations of the three-dimensional folding properties of a 4.8 Mbp long polymer chain demonstrated that the experimental data collected in the high throughput studies match the organization of chromatin into so-called fractal globules (Lieberman-Aiden et al. 2009, Mirny 2011). In contrast to equilibrium globules in which the polymer chain has no inherent organization or structure, the polymer chain in fractal globules forms a series of spatial sectors or domains (**Figure 2 B**). Only fractal globules are free of entanglements and allow the unfolding of the polymer chain as (large) loops (**Figure 2 B**). These properties are important for both the “closure” and the “opening” of chromatin: e.g. during chromosome condensation in prophase the fractal organization can help to avoid detrimental chromatin entanglements and during interphase it

can help to open up chromatin structures in order to fulfill the demands of transcription, DNA replication and potentially also DNA repair.

However, in schematic representations of the nucleus in textbooks and review articles (largely) unorganized chromatin fibers intermingling and meandering through a CT or even the entire

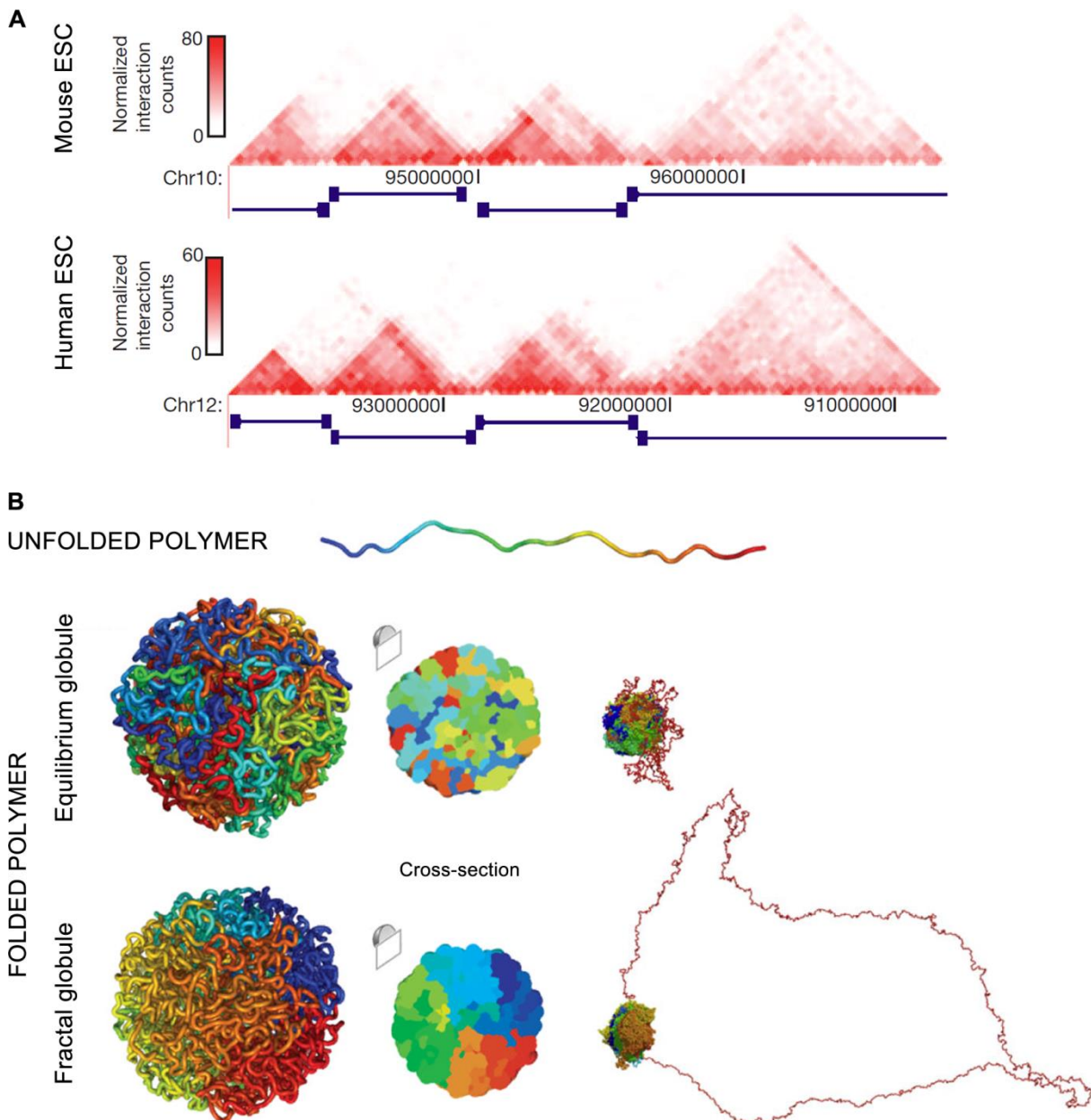


Figure 2: Evidence for a global organization of chromatin. (A) Molecular data collected in high throughput approaches revealed topologically associating domains in mammalian genomes. The corresponding chromosomal segment is shown for mouse (top) and human (bottom) embryonic stem cells (ESCs). Figure adapted from Dixon et al. (2012). Reprinted by permission from Springer Nature Customer Service Center GmbH: Springer Nature, Nature, copyright 2012. **(B)** Computer simulations of polymer folding. Top: equilibrium globule, bottom: fractal globule. The fractal globule consists of a series of domains and allows the unfolding of the polymer chain as a large loop. This is not possible in the equilibrium globule due to severe entanglements. Figure adapted from Lieberman-Aiden et al. (2009) and Mirny (2011). Reprinted with permission from AAAS / in accordance with the Creative Commons Attribution NonCommercial License (Creative Commons NC 2.0), respectively.

nucleus are still predominant (e.g. Misteli 2011, Smith and Aladjem 2014, Ulianov et al. 2015) and also the 3D visualization of 3C-based data gives this impression (Stevens et al. 2017, Tan et al. 2018, Dekker lab website). This emphasizes that the concept of a globular higher-order organization of chromatin is still far from being generally accepted and that further work is needed in this area of research.

2.3 Aim of this work: comparative analysis of functional nuclear architecture in normal cells and after cell manipulation

In this context, the aim of this work was the comparative analysis of nuclear organization in different cell types under normal conditions and after manipulation of the nuclear landscape.

It is well known that cell nuclei occur in a large range of different morphologies and chromatin patterns. Often striking differences can be observed between established cell lines that are commonly used in basic research and primary cells or tissues. While cell lines have the advantage of being well-characterized and easier to work with and certainly provide valuable findings, the analysis of primary cells is of utmost importance. Among other advantages (Kaur and Dufour 2012) they exhibit normal karyotypes, are not immortalized and do not suffer from changes in nuclear architecture or response mechanisms due to extended cultivation on hard surfaces (plastic/glass) so very different from the normal substrate in the intact organism (a topic which has gained increased attention in the recent years; for review see Janmey et al. 2009, Uhler and Shivashankar 2017).

Comparative analyses of the (functional) nuclear architecture in different primary cell types as well as in cells of established cell lines under normal conditions and after experimental manipulation will reveal to what extent nuclear organization differs between cell types, differentiation stages and/or treatments and whether there are common principles detectable in all cells. The presence of such common principles would provide strong evidence for them being basic and essential building blocks of (functional) nuclear architecture. As a consequence, they would help to provide evidence for or against the different models of nuclear architecture currently discussed in the literature (see section 2.2) and would therefore hopefully help to establish a generally accepted foundation for future research.

In this work, in a first step normal human primary cells were studied during differentiation using hematopoiesis as a model system. Five selected hematopoietic cell types were analyzed based on microscopic data acquired with 3D structured illumination microscopy (3D-SIM) after

DAPI and immunofluorescence staining and transmission electron microscopy (TEM) after specific DNA staining with osmium ammine B. After the characterization of general nuclear morphological features functional nuclear architecture was studied based on the spatial distribution of several markers: histone 3 tri-methylated on lysine 4 (H3K4me3) for transcriptionally competent chromatin, histone 3 tri-methylated on lysine 9 (H3K9me3) for inactive chromatin (for review see Izzo and Schneider 2010, Zhou et al. 2011), RNA Polymerase II phosphorylated on serine 2 (elongating form) (RNA Pol II Ser 2P) or serine 5 (located at promoters) (RNA Pol II Ser 5P) for transcription sites (Heidemann et al. 2013) and SC35 for nuclear speckles (for review see Spector and Lamond 2011).

In a second step several different methods to manipulate the normal nuclear architecture were applied (see section 2.5 for a detailed introduction of each technique): (1) Low salt conditions combined with live cell observations of hematopoietic cells were used to gain insights into higher-order chromatin organization. (2) Microinjection of small fluorescent beads into HeLa cells was performed as a method to introduce artificial landmarks into an otherwise normal nuclear environment. The analysis of the localization of the beads upon chromatin condensation – either induced by applying high salt conditions (i.e. induction of hypercondensed chromatin (HCC)) or after entry into mitosis – served to provide further understanding of higher-order chromatin organization. (3) UV irradiation and caffeine posttreatment (UV/caffeine treatment) and (4) premature chromosome condensation (PCC) in V79 Chinese hamster cells were used as examples for semi-artificial systems: mitosis or DNA damage are artificially induced but the processes that subsequently take place are the intrinsic mechanisms of the cell. In order to be able to understand the background of the observed phenotypes, the particular cells of both processes were first thoroughly characterized and compared. Live cell imaging and morphological observations using different fixation procedures were performed and several markers were analyzed: Lamin B, a component of the nuclear lamina which gets degraded in mitosis (for review see Dechat et al. 2010), histone 3 phosphorylated on serine 10 (H3S10p), a histone modification that is dramatically increased upon entry into mitosis (Hendzel et al. 1997), α -tubulin, a major component of the cytoskeleton, which undergoes dramatic reorganization when cells enter mitosis by forming the mitotic spindle (for review see Janke and Bulinski 2011), Ki67, a rather poorly characterized nucleolar protein, which, however, is well known to be a reliable marker for cycling cells (for review see Jurikova et al. 2016, in addition also Biocyclopedia 2012) and was recently shown to be essential for chromosome separation in mitosis (Cuylen et al. 2016), and SMC2 (structural maintenance of chromosomes 2), a subunit of condensin which is involved in chromosome condensation (for review see Aragon et al. 2013). In addition, centromeres were detected to gain insights into chromosome orientation. Then the actual objective was addressed:

chromatin organization and functional nuclear architecture of the observed nuclear phenotypes of both processes. The analysis was performed equivalent to the studies in hematopoietic cells using 3D-SIM and H3K4me3, H3K9me3 and RNA Pol II Ser 2P as markers for nuclear topography. (5) High salt conditions (HCC) were used in HeLa cells as an alternative way to induce chromosome condensation. Again chromatin organization and functional nuclear architecture of these particular cells were analyzed using 3D-SIM and the markers H3K4me3, H3K9me3, and RNA Pol II Ser 2P. These experiments were combined with the establishment of a pathway of correlative microscopy spanning live cell imaging (using spinning disk laser scanning microscopy (SDLSM)) for capturing dynamic processes, confocal (confocal laser scanning microscopy (CLSM)) and super-resolution (3D-SIM) fluorescence microscopy for multi-color imaging after the performance of immunofluorescence and TEM after specific staining of DNA for gaining insights into the ultrastructure of the cell.

The following sections will provide the theoretical and methodological background for these experiments.

2.4 Hematopoiesis – a model system for studying normal nuclear architecture in primary cells during differentiation

Hematopoiesis – the process that gives rise to all blood cell types in the body – is a naturally occurring somatic differentiation system. As it is very well studied and cells of specific differentiation stages can be obtained easily from blood samples, it makes a perfect model system for analyzing normal nuclear architecture and the changes the nucleus might or might not undergo during the transition from undifferentiated to terminally differentiated cells.

All blood cells originate from hematopoietic stem cells (HSCs), a small population of pluripotent cells characterized by the ability of self-renewal and of reconstituting the entire blood system of a recipient after transplantation through differentiation. HSCs generate multipotent progenitor cells which develop further and gradually increase their lineage commitment until they differentiate into lineage-restricted precursor cells. From those arise then the (terminally) differentiated mature cells (for reviews see Orkin and Zon 2008, Rieger and Schroeder 2012, Wognum and Szilvassy 2015). This process of increasing commitment is associated with tightly controlled changes in gene expression patterns (e.g. Komor et al. 2005, Manfredini et al. 2005, Gemelli et al. 2006, Ferrari et al. 2007, Liu et al. 2007, Novershtern et al. 2011, Zhang et al. 2012a). Among the differentially expressed genes are genes that code for proteins located on the cell surface, including growth factor receptors, adhesion molecules, extracellular

enzymes, and signal transduction molecules, which can be used to identify cells of certain differentiation stages. Some of these cell-surface antigens are restricted to a specific cell lineage, others are more widely expressed. Typically a combination of markers is required to identify a specific subpopulation of cells within the hematopoietic system (for reviews see Payne and Crooks 2002, Giebel and Punzel 2008, Rieger and Schroeder 2012).

In this work, the marker CD34 (cluster of differentiation 34) was used to isolate a mixed population of undifferentiated cells from umbilical cord blood. In adults, hematopoiesis takes place almost exclusively in the bone marrow – with the exception of the maturation of t-cells which occurs primarily in the thymus (Alberts et al. 2015) – and under normal conditions only a small number of stem and progenitor cells is found in peripheral blood (Bethesda 2011). Umbilical cord blood, in contrast, is rich in HSCs and other immature cell types (for review see

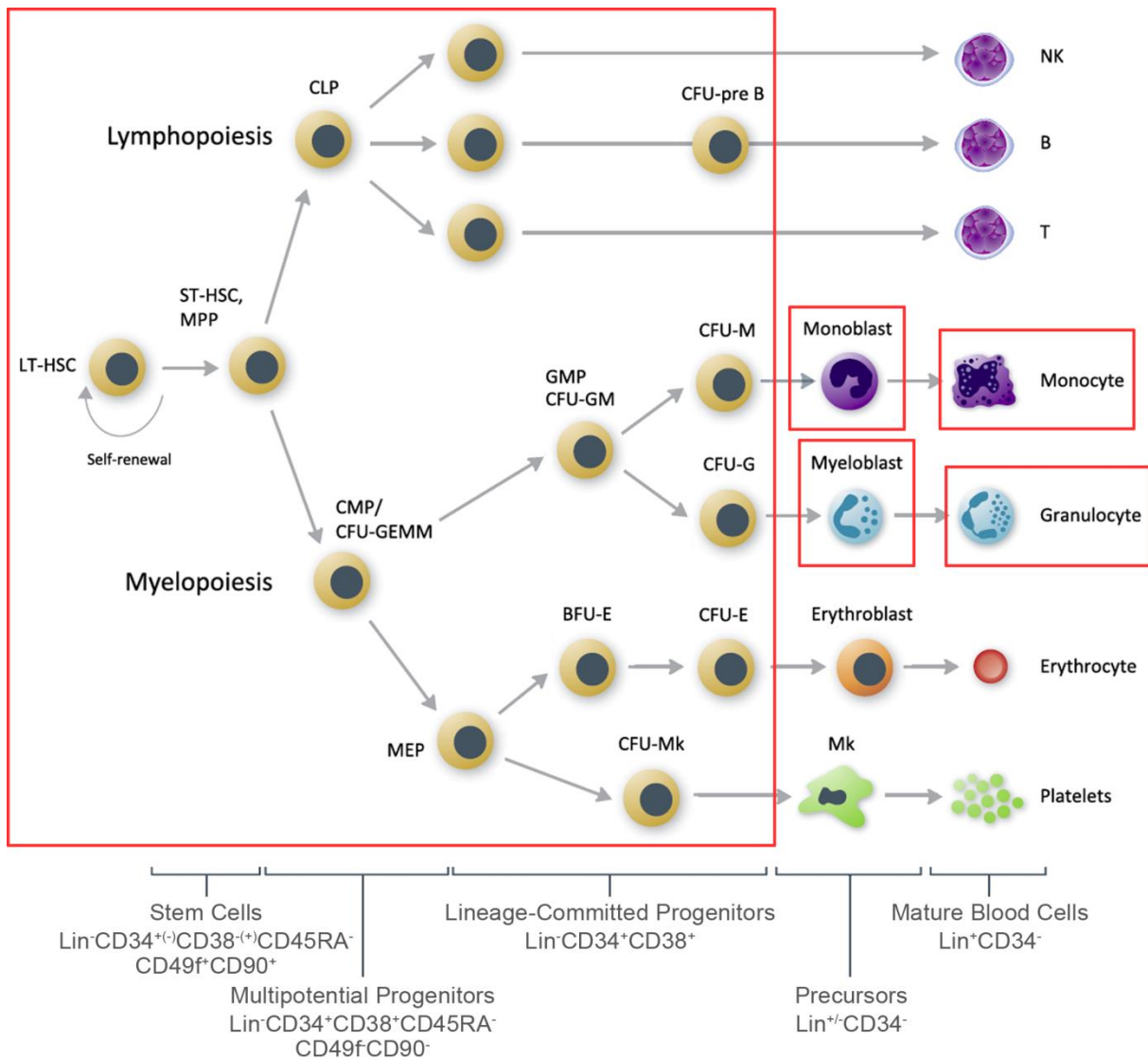


Figure 3: Hematopoietic differentiation pathways. The boxed cell types were used in this work: CD34⁺ cells, a mixed population of stem cells and progenitors – monoblasts and myeloblasts representing the precursor stage – monocytes and granulocytes representing (terminally) differentiated cells. Figure adapted from Wognum and Szilvassy (2015). Copyright of STEMCELL Technologies. Image used with permission.

Mayani and Lansdorp 1998). It can be collected from normal deliveries and is typically stored for therapeutical purposes. Blood samples with insufficient cell numbers can be released for research. The CD34 positive (CD34⁺) cell population represents about 1% of the nucleated cells in umbilical cord blood (Mayani and Lansdorp 1998) and includes HSCs (which are however rare, less than 0.05% of all cord blood cells (Hao et al. 1995, Majeti et al. 2007), i.e. only 5% of the CD34⁺ cell population) and progenitor cells (for reviews see Mayani and Lansdorp 1998, Payne and Crooks 2002, Giebel and Punzel 2008, Rieger and Schroeder 2012). From this cell population committed precursors – here monoblasts and myeloblasts – can be obtained through differentiation (Montanari et al. 2005, see also section 3.2.1.1). In addition to these three cell types (CD34⁺ cells, monoblasts, myeloblasts), monocytes and granulocytes were studied here, as examples for (terminally) differentiated cells. While granulocytes are terminally differentiated, monocytes can develop into macrophages or dendritic cells upon stimulation (for review see Imhof and Aurrand-Lions 2004). Both cell types exit from the bone marrow into the blood and can migrate into tissues in order to perform their tasks in the response to inflammations and infections (Henderson et al. 2003, Imhof and Aurrand-Lions 2004, Wantha et al. 2013). A scheme of the hematopoietic differentiation pathways is shown in **Figure 3**. The five cell types used in this work are highlighted.

The cell types of the hematopoietic system – especially the precursors and mature cells – can be well distinguished in blood smear preparations using combinations of basic and acidic stains such as Giemsa, Wright or May-Grünwald in order to visualize both, nucleic acids and alkaline granules. Since more than a century such samples are used as diagnostic tools for all types of blood cancers and other blood disorders by monitoring cell counts and especially by evaluating changes in the cellular appearance and the nuclear phenotypes (for overview see Houwen 2000, Thelml et al. 2004, Barcia 2007, Keohane et al. 2016). TEM data support and complement the observations made on these classical hematological samples (e.g. Ohwada and Eguchi 1993, Djaldetti et al. 2004, Ru et al. 2009, Jost et al. 2015; for overview see Keohane et al. 2016). However, typically these studies use classical TEM staining methods which unspecifically increase contrast by staining RNA, DNA and proteins at the same time (compare section 2.6.4).

Only little is known about the high(er) resolution chromatin organization in hematopoietic cells and even less about their functional nuclear architecture.

2.5 Methods to manipulate the nuclear landscape and to interfere with the distribution of chromatin

In the literature, numerous possibilities exist to manipulate the nuclear landscape and to interfere with the distribution of chromatin. The next few chapters briefly introduce the methods applied in this work.

2.5.1 Treatment with high or low salt concentrations

Hypotonic treatment, i.e. the incubation of cells in low salt conditions, can be used to induce chromatin decondensation in intact nuclei of living cells. Here 0.3x PBS (phosphate-buffered saline) was employed, exhibiting a salt concentration of only ~45 mM compared to the normotonic value of ~150 mM of 1x PBS. Typically such treatment is applied to avoid shrinkage during fixation, especially when working with blood cells (e.g. Cremer et al. 2007, Rauch et al. 2008, Nagel et al. 2012, Glukhov et al. 2013, Ollion et al. 2015).

Alternatively, cell nuclei can be subjected to higher than physiological salt conditions (Albiez et al. 2006). Already a brief incubation in medium with about double the osmolarity of normal cell culture medium (570 mOsm instead of 290 mOsm) leads to hypercondensed chromatin (HCC). As a result of the condensed chromatin, the interwoven interchromatin channels are wider than usual and can therefore be observed more easily. HCC can be induced either directly or stepwise through a series of media with increasing osmolarity and is fully reversible. The induction of HCC provides an easily applicable system to study nuclear architecture under artificial conditions.

2.5.2 Microinjection

Microinjection is a helpful tool to directly deliver larger particles or molecules, which normally would not cross the plasma membrane or the nuclear envelope, into cells, especially specifically into the nucleus. In this work, small fluorescent beads were microinjected into cell nuclei.

2.5.3 UV irradiation and caffeine posttreatment

Ultraviolet (UV) irradiation is well known to cause DNA damage and consequently to activate

DNA repair mechanisms as well as – depending on the severity of the DNA damage – to induce delays in cell cycle progression, chromosome aberrations or even cell death. One of the potential effects of UV irradiation is chromosome fragmentation or shattering. First observations on this phenomenon were already made in the 1940s (for overview see Chu 1965) and the term “chromosome shattering” was introduced about a decade later for multiple chromosome fragmentations of mitotic cells after UV irradiation of *Tradescantia paludosa* pollen (Lovelace 1954). The basis for the studies in this work was established in the mid-1970s to mid-1980s when comprehensive analyses were carried out in Chinese hamster (*Cricetulus griseus*) cells after UV irradiation and caffeine posttreatment (e.g. Zorn et al. 1976, Cremer et al. 1980, Cremer et al. 1981a, Cremer et al. 1981b, Cremer and Cremer 1986; for review see Cremer and Cremer 2006). Cells were irradiated with UV light, incubated in caffeine (= caffeine posttreatment) and allowed to proceed to mitosis. Subsequent chromosome preparations performed according to standard protocols including hypotonic treatment, methanol / acetic acid (MAA) fixation and air drying revealed a phenotype termed generalized chromosome shattering (GCS), i.e. mitotic figures that show fragmentation or – more frequently and therefore more characteristic for this phenomenon – pulverization of the entire chromosome complement (**Figure 4**).

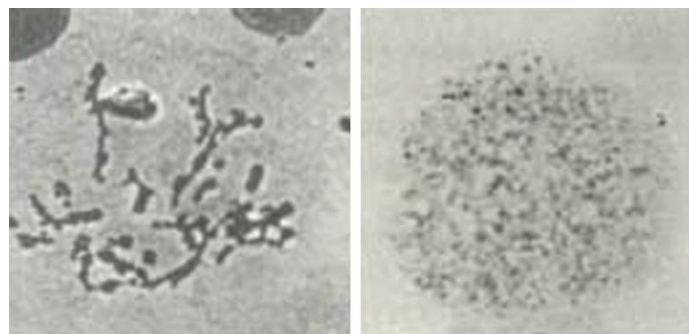


Figure 4: Morphology of generalized chromosome shattering (GCS) observed after conventional chromosome preparations of UV irradiated and caffeine posttreated Chinese hamster cells. Left: fragmentation, right: pulverization. Figure taken from Cremer et al. (1980). Reprinted with permission from John Wiley and Sons / Wiley Company, copyright 1980, Alan R. Liss Inc / Wiley-Liss Inc, A Wiley Company.

Caffeine posttreatment was critical in these experiments as the effects induced by UV irradiation did not remain visible when it was omitted (Cremer et al. 1980, Cremer et al. 1981b, Cremer and Gray 1982, Cremer et al. 1982a). Back in the time when these experiments were performed, it was unclear how caffeine – a stimulant present in many plants, most well known in coffee beans and tea leaves, but also in others such as kola nuts (Coca Cola) or cocoa beans – potentiates the effects of UV irradiation. Today it is generally believed that caffeine inhibits ATM (Ataxia telangiectasia mutated) and ATR (Ataxia telangiectasia and Rad3-related) (Blasina et al. 1999, Hall-Jackson et al. 1999, Sarkaria et al. 1999, Zhou et al. 2000), the two major kinases involved in cell cycle control (for review see Awasthi et al. 2015). Cell cycle

progression is controlled by a complex network of signaling pathways, whose complete coverage would go beyond the scope of this work. Therefore only the basics will be mentioned here (**Figure 5**) (for review see Donzelli and Draetta 2003, Hurley and Bunz 2007, Yu 2007, Morandell and Yaffe 2012, Awasthi et al. 2015). Typically, ATM is activated upon DNA double-strand breaks and ATR upon problems during replication (i.e. DNA single-strand breaks). Under certain circumstances, however, these two kinases are also reported to be able to indirectly activate each other. Activated ATM and ATR initiate two major signaling cascades that ultimately lead to cell cycle arrest: (1) ATM and ATR phosphorylate and with that activate Chk2 (Checkpoint kinase 2) and Chk1 (Checkpoint kinase 1), respectively, which then have an inhibitory effect on Cdc25 (cell division cycle 25) phosphatases: phosphorylation of Cdc25A results in its ubiquitinylation and subsequent degradation and phosphorylation of Cdc25B and C leads to their sequestration into the cytoplasm. As a consequence, the inhibitory phosphorylations on cyclin/Cdk (cyclin-dependent kinase) complexes cannot be removed and cell cycle progression cannot be promoted. The missing activation of cyclinB/Cdk1 (originally known as maturation or M-phase promoting factor (MPF)) through Cdc25A as well as Cdc25B and C leads to a halt at the G2/M boundary, the missing activation of cyclinE/Cdk2 through

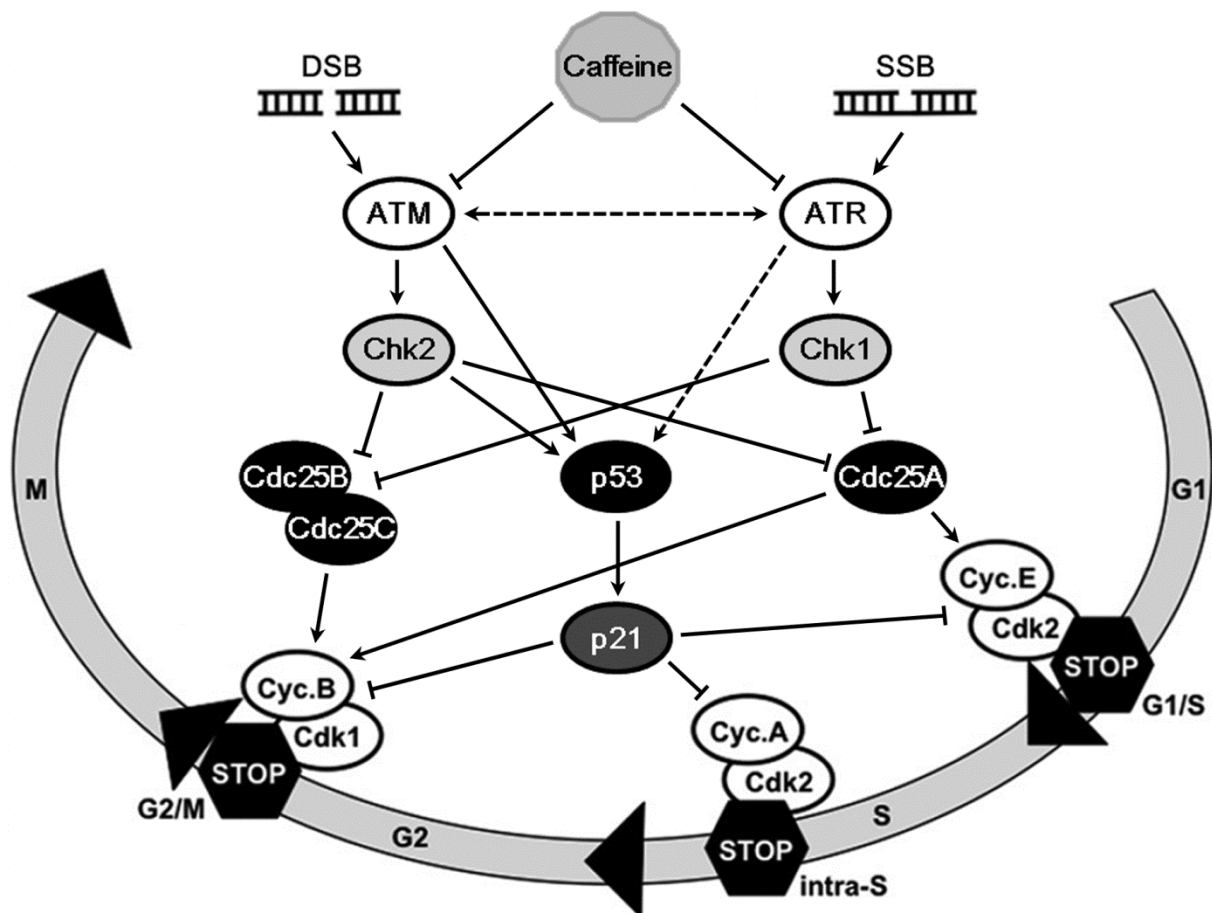


Figure 5: Cell cycle control through ATM and ATR signaling and the influence of caffeine. Arrow = promotion, bar = inhibition. Figure adapted from Morandell and Yaffe (2012). Reprinted with permission from Elsevier.

Cdc25A results in a stop at the G1/S boundary. (2) ATM, Chk2 and potentially also ATR phosphorylate and with that stabilize p53. This allows p53 to induce the transcription of p21, a checkpoint protein which inhibits Cdk1 and Cdk2 and therefore prevents the transition from G1 to S phase (mediated through cyclinE/Cdk2), the progression through the intra-S-checkpoint (cyclinA/Cdk2) as well as mitotic onset (cyclinB/Cdk1).

Upon inhibition of ATM and ATR – for example through caffeine – these signaling pathways do not get activated anymore: the Cdc25 phosphatases are not hindered from activating cyclin/Cdk complexes and due to its missing expression also the inhibitory effect of p21 on Cdk1 and 2 gets lost. As a consequence, the cell will enter mitosis or S phase despite massive DNA damage (**Figure 5**).

However, some studies doubt the influence of caffeine on ATM and ATR – at least in certain cells – and suggest that caffeine directly inhibits other components of this complex signaling network (Cortez 2003; for review see Bode and Dong 2007).

Massive DNA damage that remains unrepaired typically leads to cell death after an interval of several hours. The best-studied type of such a kind of delayed cell death is apoptosis (for review see Chowdhury et al. 2006, Galluzzi et al. 2012, Kiraz et al. 2016), but also other less well defined non-apoptotic endpoints have been described (for review see Blank and Shiloh 2007, Galluzzi et al. 2012). GCS was classified as mitotic catastrophe (Hübner et al. 2009), a term that is often used in exchange with mitotic cell death. Together mitotic catastrophe and mitotic cell death summarize a variety of cellular endpoints which typically involve the name-giving occurrence of aberrant and/or fragmented mitotic figures and are observed after DNA damage induction in the presence of inhibited or defective cell cycle checkpoints (e.g. Ianzini and Mackey 1997, Castedo et al. 2004b, Nitta et al. 2004, Blank et al. 2006, Mansilla et al. 2006, Stevens et al. 2007, Zhang et al. 2011). Until today these different phenomena are not well defined and difficult to separate, although the underlying molecular mechanisms are slowly getting revealed (for review see Castedo et al. 2004a, Eriksson and Stigbrand 2010, Caruso et al. 2011, Vitale et al. 2011, Galluzzi et al. 2012).

As mentioned above, GCS was so far only described after methanol / acetic acid (MAA) fixation (e.g. Zorn et al. 1976, Cremer et al. 1980, Cremer et al. 1981a, Cremer et al. 1981b, Cremer and Cremer 1986). Observations of this phenomenon in living cells or after paraformaldehyde (PFA) fixation are missing. Also information about the presence or absence of mitotic markers and with that about the similarity of these cells with normal mitotic cells is not available.

2.5.4 Premature chromosome condensation (PCC)

Premature chromosome condensation (PCC) describes the formation of condensed chromosomes from interphase cells upon induction, either through cell fusion using viruses (Johnson and Rao 1970) or polyethylene glycol (PEG) (Lau et al. 1977, Hanks et al. 1982, Pantelias and Maillie 1983) or through chemicals like Okadaic acid (Yamashita et al. 1990, Gotoh et al. 1995) or Calyculin A (Gotoh et al. 1995). The morphology of PCC differs depending on the cell cycle stage of the induced cell: G1 PCCs show chromosomes with one – typically more elongated – chromatid, S PCCs exhibit a shattered chromosome complement similar to GCS observed after UV/cafeine treatment (see section 2.5.3) and G2 PCCs show condensed chromosomes with two chromatids very similar to normal mitotic cells (e.g. Johnson and Rao 1970, Hanks et al. 1983, Gotoh et al. 1995; for Calyculin A-induced PCC as used in this work see Bezrookove et al. 2003, Hatzi et al. 2006) (**Figure 6 A**). Since PCC can also be induced in non-dividing cells it is frequently used as a valuable diagnostic tool in radiation studies (e.g. Lamadrid Boada et al. 2013, Hu et al. 2013, Puig et al. 2013, M'Kacher et al. 2015, Romero et al. 2015).

As mentioned above, in this work PCC was induced using Calyculin A, a chemical isolated from the marine sponge *Discodermia calyx* (Kato et al. 1986). It is a potent, cell-permeable inhibitor of type 1, type 2A and to a lesser extent type 2B phosphatases (Ishihara et al. 1989, MacKintosh and MacKintosh 1994). Canceling the inhibitory effect of protein phosphatase 2A (PP2A) on Cdc25 leads to its phosphorylation, i.e. activation, which then again promotes the activation of the cyclin B / Cdk1 complex through dephosphorylation of Cdk1 (called Cdc2 in *Schizosaccharomyces pombe*). This induces mitosis – or in interphase cells PCC – by activating mitotic events like chromosome condensation, breakdown of the nuclear envelope, formation of the mitotic spindle, etc. (for review see Gotoh 2009 and also Donzelli and Draetta 2003, Bollen et al. 2009, Fisher et al. 2012) (**Figure 6 B**). In addition, protein phosphatase 1 and 2A are also reported to be involved in the exit from mitosis (for review see Bollen et al. 2009, Rebelo et al. 2015), leading to the accumulation of mitotic or PCC cells following their inhibition.

In the literature, PCC is mainly characterized after MAA fixation (see all articles cited in the first paragraph of this chapter apart from Yamashita et al. 1990). Information on the morphology of these cells in the living state or after PFA fixation is very limited and hardly anything is known about the early stages of PCC before condensed chromosomes get apparent and about the morphological changes involved (see details in section 5.3.1 in the discussion). Also the presence or absence of mitotic markers and therefore the similarity of PCC cells to normal mitotic cells is not well studied. Observations on individual markers are

described occasionally (see details in section 5.3.1 in the discussion), but a fully comprehensive study or overview – especially for PCC induced by Calyculin A – is missing.

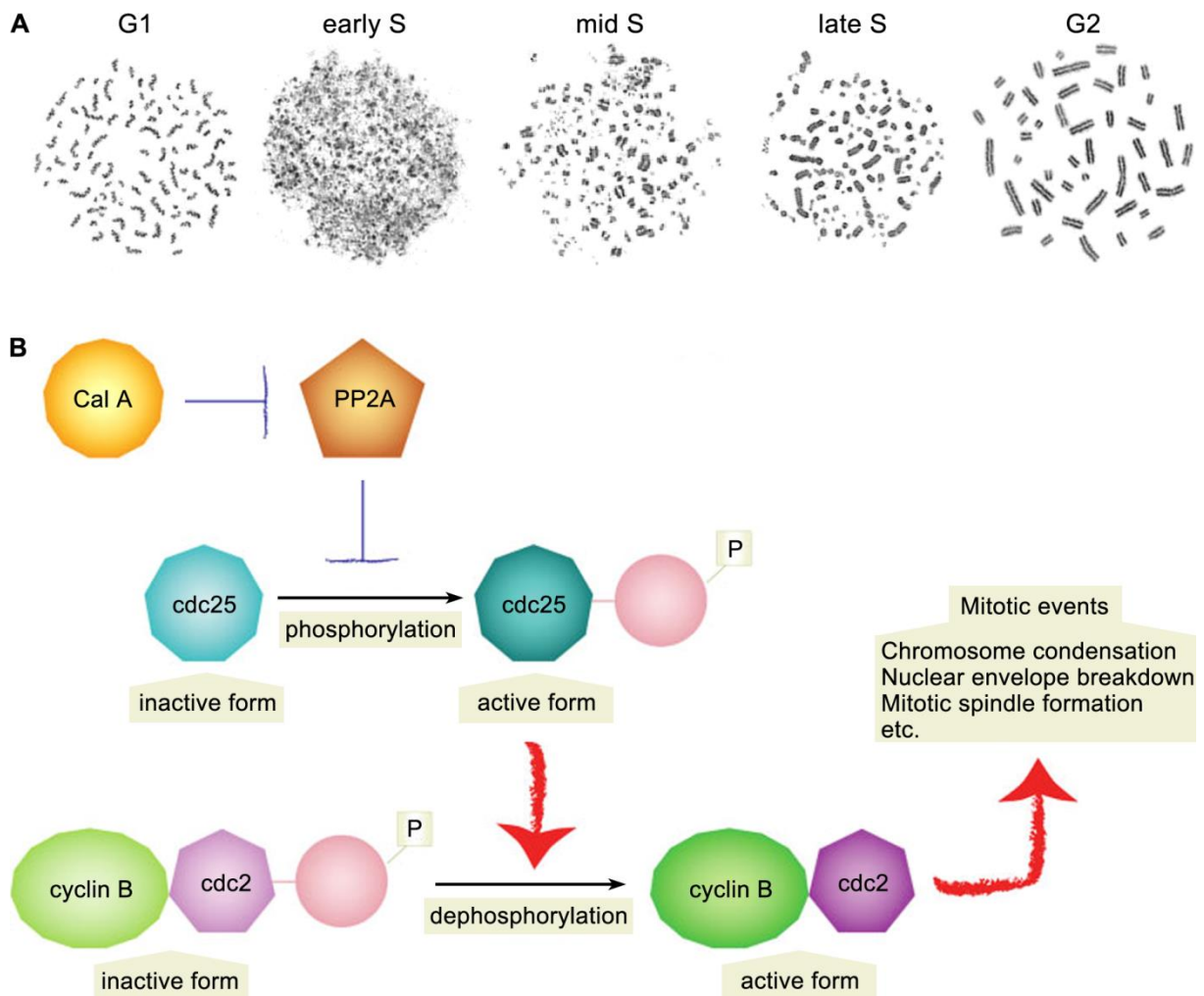


Figure 6: PCC induction using Calyculin A. (A) Typical morphologies after PCC induction: human lymphocytes were treated with colcemid and 30 min Calyculin A, fixed and prepared using standard methods and classified as G1, early S, mid S, late S and G2 PCC (from left to right). Figure adapted from Hatzi et al. (2006). Reprinted in accordance with the Creative Commons Attribution 4.0 License (Creative Commons 4.0). **(B)** Mechanism of PCC induction through Calyculin A (Cal A). Red arrow = promotion; blue bars = inhibition. Figure adapted from Gotoh and Durante (2006). Reprinted with permission from John Wiley and Sons / Wiley Company, copyright 2006, Wiley-Liss Inc, A Wiley Company.

2.6 Microscopy – an indispensable tool for understanding the (dynamic) organization of the nucleus

Light and electron microscopy belong to the most important techniques in biological sciences and have been widely used for the visualization of all kinds of structures within cells and tissues. While imaging methods were initially almost exclusively limited to the analysis of fixed specimens, fluorescence microscopy by now also provides well-established and reliable

approaches for the observation of living cells. In contrast to other frequently used techniques, like for example gene expression profiling, flow cytometry, western blotting or chromosome conformation capture methods, where data are typically acquired by averaging thousands or even millions of cells, microscopy provides an indispensable tool for the analysis of individual cells. Single-cell studies are very important (for review see Yuan et al. 2017) as only they can provide sufficiently detailed information on the heterogeneity of the cell population analyzed, reveal rare, but potentially functionally important sub-populations – as for example in the early stages of cancer where typically only one small clone of malignant cells is present (Alberts et al. 2015) – and most importantly in the case of microscopy, deliver a direct insight into the organization of the cell.

Awarding the Nobel Prize in Chemistry 2014 to Erik Betzig, Stefan W. Hell and William E. Moerner for the development of super-resolved fluorescence microscopy (The Royal Swedish Academy of Sciences 2014) brought the importance of microscopy and therefore also of single-cell analyses back into the limelight and back into the focus of interest of many researchers worldwide.

2.6.1 Conventional wide-field (WF) microscopy

For a long time, conventional wide-field (WF) microscopy was the only method available for imaging subcellular structures tagged with fluorescent dyes. These epi-fluorescence microscopes provide a resolution of about 200-300 nm laterally and in the best case 600-1000 nm axially.

Resolution is a central issue in microscopy. The resolution limit represents the smallest distance at which two point-like objects can still be observed separately and was first described by Ernst Abbe in 1873 (Abbe 1873) and – being unaware of Abbe's publication until finishing the manuscript – by Hermann von Helmholtz one year later (Helmholtz 1874). In the case of conventional light microscopy, two objects optically merge in lateral direction (xy-plane) when they get closer than approximately half of the wavelength of the illuminating light. In axial (z) direction the resolution is limited even more by a factor of 2-3. This definition is typically referred to as the classical Abbe limit. However, all optical devices including light microscopes have their own intrinsic resolution limit, which may substantially differ from the classical Abbe limit.

In the past conventional WF microscopy was eagerly used by a tremendous number of scientists. Today, however, due to the development of confocal microscopy (see section 2.6.2)

and even more of various super-resolution approaches (see section 2.6.3) which both deliver (much) higher resolution, it is often smiled at and considered insufficient. Although being certainly not the method of choice for answering every question, WF microscopy can still be a valuable tool: it can easily be equipped with (1) specialized fluorescence filter sets optimized for the fluorochromes / fluorescent proteins used and suitable for the simultaneous detection of fluorophores with different excitation and/or emission spectra, (2) halogen lamps and UV filters to minimize the exposure to harmful light of short wavelengths and (3) sensitive cameras that allow image acquisition with low light intensities. In addition, the low axial resolution contributes to the high light sensitivity of such systems, as also the out-of-focus signals are collected during acquisition (for a review on epifluorescence microscopy see Webb and Brown 2013). Especially point two and three make conventional WF microscopy very suitable for long-term observations of living cells which require the reduction of sample stress to an absolute minimum.

2.6.2 Confocal microscopy

Confocal laser scanning microscopy (CLSM) (for review see Conchello and Lichtman 2005, Claxton et al. 2005) was developed in the 1970s (for review see Cremer and Masters 2013) and has been the gold standard of fluorescence microscopy for many years. Compared to conventional WF microscopy it offers only a marginal increase in resolution (180-250 nm laterally, 500-700 nm axially), but the implementation of pinholes that greatly reduce out-of-focus light and as a result drastically increase contrast provided CLSM with substantially improved possibilities for three-dimensional (3D) imaging compared to WF microscopy. CLSM allows light optical serial sectioning and the generation of 3D reconstructions from the acquired data sets. In addition, modern CLSM systems are excellent tools for multi-color experiments – depending on the setup up to 5 or even up to 7 different colors and therefore proteins/structures can be visualized in one single experiment with comparatively little effort. Combining these features, CLSM has become the method of choice for 3D studies of all kinds of fixed cells, including tissue sections.

Although CLSM has also been successfully employed for four-dimensional (4D) studies of living cells in space and time, its suitability for such experiments is limited due to the acquisition process: images are obtained by scanning the sample with a single focused laser beam and recording the fluorescent output with a photomultiplier tube (PMT) separately at each focal point, generating the final image voxel by voxel. This point-scanning technique – although very beneficial for optical sectioning – is time-consuming and requires high illumination intensities, typically resulting in a high total light exposure of the recorded cell (Toomre et al. 2012, Graf

et al. 2005, Conchello and Lichtman 2005).

A great improvement for live cell observations was the development of spinning disk laser scanning microscopy (SDLSM). Here the laser light passes through a disk, which contains approximately 20 000 small pinholes arranged in such a way that the rotation of the disk leads to the full illumination of the sample. As the disk rotates with high speed in the range of 1500–10 000 rpm and fluorescence from all focal points is thus recorded simultaneously, image acquisition of one plane is achieved within a few milliseconds for the entire specimen. Up to 30 frames per second are possible with conventional samples, constituting a dramatically enhanced speed of image recording (for review see Graf et al. 2005, Conchello and Lichtman 2005, Toomre et al. 2012; the first two references include a comparison with CLSM). A small downside of this technique is the so-called pinhole cross-talk, i.e. that light scattered or emitted by structures outside the focal plane can reach the detector through adjacent pinholes. Consequently, the axial resolution is somewhat reduced in comparison to CLSM (Toomre et al. 2012). However, in addition to the improved imaging speed mentioned above, SDLSM also has the advantage that it uses CCD cameras instead of PMTs for signal detection, resulting in reduced light stress on the sample. Thus, the spinning disk system offers great possibilities for 4D imaging of living cells, even if the acquisition of image stacks over longer periods of time remains challenging.

2.6.3 Three-dimensional structured illumination microscopy (3D-SIM)

The concept of structured illumination microscopy (SIM) was independently proposed by Heintzmann and Cremer (1999) and Gustafsson (2000). SIM belongs to the so-called super-resolution microscopy approaches that have become available in the last two decades. Other methods include STED (stimulated emission depletion) (Hell and Wichmann 1994, Klar and Hell 1999, Klar et al. 2000; for review see Blom and Widengren 2014), STORM / PALM / FPALM (stochastic optical reconstruction microscopy / photoactivated localization microscopy / fluorescence photoactivation localization microscopy) (Rust et al. 2006 / Betzig et al. 2006 / Hess et al. 2006; for reviews see Nelson and Hess 2014, Sengupta et al. 2012, Hajj et al. 2014), and lattice light-sheet microscopy (Planchon et al. 2011, Gao et al. 2012, Chen et al. 2014) that will not be further described here (for general reviews on super-resolution microscopy see Schermelleh et al. 2010, Huang et al. 2010, Cremer and Masters 2013). Although these techniques partially differ strongly in their functional principle, they all achieve the same goal as the generic term “super-resolution microscopy” already suggests: they break the Abbe limit of resolution (see section 2.6.1) and therefore allow the visualization of

structures smaller than the diffraction limit of light. Since many subcellular structures and macromolecular complexes fall into that category, these microscopic techniques opened a multitude of new possibilities and catapulted light microscopy to an entirely new level.

In SIM the improvement in resolution is achieved by superimposing the unknown unobservable sample structure with a known illumination pattern, causing coarse and observable interference patterns (moiré fringes) from which the fine underlying details of the sample can be retrieved using mathematical algorithms. The striped illumination pattern is typically generated by a diffraction grating (Heintzmann and Cremer 1999, Gustafsson 2000), heterodynes with the structure of the object and shifts higher frequency components that represent subtle sample details from the outside into the observable region of the reciprocal space of the microscope (Gustafsson 2000). In order to reconstruct an image with double the conventional resolution, images of three or more – typically five – shifts of the illumination pattern perpendicular to the stripes have to be acquired for each image plane. For improving the resolution also in a second lateral direction, the orientation of the grating has to be rotated accordingly. The more orientations used, the better the high-resolution coverage in the xy space, an advantage which is however gained at the cost of prolonged acquisition time and additional light stress. Three to five equally spaced orientations are regarded as sufficient and typically only three orientations – i.e. a rotation of the grating by 60° and 120° – are implemented (Gustafsson 2000). In three dimensional (3D) -SIM a three-beam interference is used that includes in addition to the -1 and +1 diffraction order also the 0 order and thus results in the creation of a 3D sinusoidal illumination pattern (Gustafsson et al. 2008). This allows a doubling in resolution not only in lateral (xy) direction but also in axial (z) direction. The final reconstructed image therefore is characterized by a resolution of about 100-130 nm laterally and 250-340 nm axially, which lies beyond the classical Abbe limit and represents an eightfold increase in resolution in 3D (Schermele et al. 2010).

The generation of a final 3D-SIM image requires a massive computational effort. As described above, the typical setup results in the acquisition of 960 images per color for one 3D stack (based on 15 images per z-position (three angles with five phase shifts each) and 64 z-sections (with the standard z-spacing of 125 nm and a typical z-volume of $8 \mu\text{m}$)). Therefore, 3D-SIM requires samples with bright signal intensities, fluorochromes that are fairly resistant against bleaching and mounting in antifade medium in order to diminish bleaching during the recording of serial images. In addition, movements within the sample have to be minimized, as fluorescent particles that float around during image recording can introduce artifacts. Despite sounding challenging, these requirements can easily be met with standard sample preparation protocols and standard fluorophores. In combination with the fact that multi-color experiments

can be performed effortlessly – enabling the study of several cellular components / macromolecular complexes at the same time and therefore their spatial relationship to each other – this constitutes the huge advantage of 3D-SIM compared to other super-resolution approaches, although those reach an even higher resolution (down to the range of tens of nanometers, see reviews and articles mentioned above). This makes 3D-SIM particularly suitable for studying the functional nuclear architecture in 3D.

The conventional 3D-SIM setup used in this work can only be applied for imaging of fixed cells. In particular due to the slow acquisition time, but also due to the high light intensities needed. However, new developments helped to dramatically improve these values and made 3D-SIM also usable for the observation of fast processes in living cells (Kner et al. 2009, Shao et al. 2011, Fiolka et al. 2012, Strauss et al. 2012, for review – not only for live cell 3D-SIM but also in general – see Mennella 2016), at least for short periods of time. If these applications also allow long-term live cell imaging still remains to be investigated.

Overall, regarding the tremendous progress the field made in the last years and is still making today, it seems realistic to expect that new developments and improvements in super-resolution microscopy will allow 3D and 4D imaging of fixed and living cells with a resolution of about 10 nm.

2.6.4 Transmission electron microscopy (TEM)

Transmission electron microscopy (TEM) provides the highest possible resolution reaching low nanometer or even Angstrom values due to the small wavelength of the electron beam. However, this huge advantage comes along with a lot of downsides of TEM imaging:

(1) Electron microscopes operate in vacuum, so the sample has to be embedded in plastic or vitreous ice, which both makes live cell observations impossible.

(2) After embedding ultrathin sections – typically with a thickness of around 70-100 nm – have to be cut as the electron beam can only penetrate thin specimens. While this leads to a high resolution not only in lateral (xy) but also in axial (z) direction, it also involves the loss of 3D information. Serial sections can be collected, imaged and aligned to a 3D-stack, but this procedure is very laborious and time demanding and requires outstanding sectioning skills.

New approaches make use of the combination of scanning electron microscopy (SEM) with ultramicrotomy (serial block-face (SBF) -SEM) (Denk and Horstmann 2004, Zankel et al. 2009)

or focused ion beam (FIB) milling (Heymann et al. 2006, Knott et al. 2008): serial images of the sample surface are recorded after the sequential removal of ultrathin slices (with a thickness of down to 30 nm in case of ultramicrotomy and 3 nm in case of FIB) leading to a full 3D acquisition of the specimen (for review see Hartnell et al. 2016). Although the resolution in SEM is somewhat reduced compared to TEM and only images of the sample surface are recorded (i.e. the information within the section is not accessible), the value of the 3D information is – dependent on the question – clearly more than sufficient to compensate for this.

A great tool for retrieving the 3D information within an ultrathin section is electron tomography. The acquisition of a tilt series typically ranging from about -65° to $+65^\circ$ in one (single tilt) or two (double tilt) directions and the subsequent reconstruction of a 3D density map based on the 2D projection images helps to tremendously increase resolution, mainly in z-direction (down to about 2 nm in xy and 3 nm in z-direction) (for reviews see Baumeister 2002, Subramaniam et al. 2003).

However, both techniques, SBF/FIB-SEM and tomography, are time-consuming methods that require a significant computational effort and most notably only allow imaging of a very small part of the cell (at least at high resolution).

(3) Staining possibilities, especially for depicting several different proteins or nucleic acids simultaneously, are much more limited compared to multicolor imaging with fluorescent light microscopy, as electron microscopy depends solely on differences in electron-density.

Conventional staining procedures that are routinely employed in electron microscopy are based on heavy metals like uranium and lead. Uranyl acetate and lead citrate is the standard contrasting method that stains lipids, proteins, RNA and DNA at the same time. Aqueous uranyl acetate alone is more specific for nucleic acids, however, also other negatively charged molecules are stained (Leica 2013). In contrast to that several new methods have been developed that allow the detection of DNA or proteins in a highly specific manner. Staining of DNA can be achieved by specific uranyl acetate staining after RNA extraction and blockage of amino and carboxyl groups (NAMA-Ur, Testillano et al. 1991) or by osmium ammine B staining after RNA degradation (Vazquez-Nin et al. 1995; for a more detailed explanation see section 3.2.8.3). Only recently Ou et al. (2017) reported a less harsh method for staining DNA for EM. It is based on fluorescent DNA dyes that can generate singlet oxygen upon illumination which in turn can oxidize diaminobenzidine (DAB). This leads to the formation of an insoluble reaction product which can be made electron-dense using osmium tetroxide. This reaction is based on several preceding studies published in the last few years which made a lot of progress on the specific detection of proteins: Similar to GFP for light microscopy several tags are now available for electron microscopy (for review see Ellisman et al. 2012), the most common ones

being miniSOG (mini singlet oxygen generator) (Shu et al. 2011) and APEX/APEX2 (enhanced ascorbate peroxidase (APX)) (Martell et al. 2012, Lam et al. 2015). In the case of miniSOG, the polymerization of DAB at the site of the tag is also achieved through illumination, in the case of APEX/APEX2 through a peroxidase enzyme reaction in the presence of H₂O₂. These new techniques and the great possibilities associated with them will certainly give TEM studies a new boost and will enable scientists to gather new and detailed insights into many open questions.

Despite these great advancements, the possibilities for labeling different proteins in the same sample are still very limited. Currently, there are only two ways: One (A) is performing immunodetection with secondary antibodies coupled to differently sized gold-particles (e.g. 6, 10, 15 nm in diameter). However, either the labeling efficiency is low as antibodies cannot penetrate the sections of plastic-embedded samples (post-embedding detection) or the ultrastructure is diminished due to the necessity of permeabilization to enable access of the antibodies (pre-embedding approach) (for a detailed article on immunolabeling for EM see De Paul et al. 2012). Tokuyasu sectioning (Tokuyasu 1973), where frozen samples are sectioned under cryo-conditions and subsequently brought back to room temperature for staining, offers a solution to this problem but requires excellent sectioning skills and highly specialized and expensive equipment. And also here another substantial problem of immunodetection persists: each antibody has a size of about 12-18 nm. With two antibodies – primary and secondary – this adds up to a distance of up to 36 nm between the gold grain and the actual detection site. While this deviation is negligible for most light microscopic approaches (the resolution limit for conventional light microscopy is around 200 nm, compare sections 2.6.1-2.6.3), it has a high impact in TEM where resolution reaches the low nanometer or even the Angstrom scale. The second technique (B) for labeling different proteins in the same specimen was only developed recently. It makes use of coupling different lanthanides to DAB and reacting the different proteins of interest in a sequential approach followed by energy-filtered TEM which can distinguish between the different elements (Adams et al. 2016). Currently, this method still suffers from slightly low sensitivity and more importantly from the limited availability of genetically encoded tags that can react DAB at different wavelengths. In this paper the second “color” next to miniSOG was achieved through the application of specific fluorochrome coupled molecules or labeled antibodies, which however come with the same caveats described for method (A), i.e. requiring cell permeabilization and resulting in an increased distance between the label and the protein of interest. But given the rapid progression of this field of research, this technique has great potential for becoming a reliable method for multi“color” EM despite its current limitations.

(4) Cryo-electron microscopy in the absence of chemical fixation and dehydration promises

the best structural preservation (Dubochet and Sartori Blanc 2001). However, this advantage comes with the downside of having to abstain entirely from staining procedures (Glaeser 2008).

But advances in fluorescence light microscopy under cryo conditions (for review see Wolff et al. 2016) and new methods for sample preparation such as cryo-FIB (for review see Schaffer 2018) offer great opportunities for correlative light and electron microscopy and are about to take cryo-electron microscopy of cell samples to a whole new level.

To conclude, in light of all these new developments of possibilities for 3D imaging and specific staining of cellular substructures, TEM is often wrongly considered old-fashioned and out-of-date. Of course it struggles with certain problems – just like any other microscopic technique, too –, but with its unmatched high-resolution TEM remains a highly valuable tool for single-cell analyses.

2.6.5 Correlative microscopy – an approach for an increased gain of information by the sequential application of different microscopic systems

As described in the previous sections (section 2.6.1-2.6.4) each microscopic technique has its individual strengths and weaknesses. Therefore, correlative microscopy, i.e. the sequential visualization of one and the same cell using different microscopic systems, provides a valuable tool for single-cell analyses as it allows the combination of information that cannot be obtained with a single approach alone. It makes it possible to join the individual advantages of each microscopic technique and to compensate for the disadvantages. Furthermore, correlative microscopy also helps to detect artifacts that might be created by a given type of microscopy. The importance of this approach is stressed by the numerous publications in the last few years using and combining all kinds of microscopic approaches, including but not limited to CLSM, cryo light microscopy, two-photon microscopy, super-resolution microscopy (3D-SIM, PALM, STORM), X-ray microscopy, atomic force microscopy, TEM, SEM, and FIB/SBF-SEM.

A central challenge in correlative microscopy – next to relocalizing the region of interest on each system – are the different and partially very specific requirements that come along with every microscopic technique. They affect not only the experimental setup (for example the need of live cell chambers for live cell observations, but mounting of the sample in antifade-medium on a microscopic slide for 3D-SIM) but also the treatment of the sample (e.g. mild fixatives and permeabilization of the cells for the detection of proteins via immunofluorescence for light microscopy versus strong fixatives and avoidance of detergents for the best possible

preservation of the ultra-structure for TEM). However, with the high and still increasing interest in correlative microscopy also the ideas and techniques regarding how to overcome and/or unite the different requirements in order to allow and improve the combination of certain microscopic approaches expand constantly and are supported by the development of new probes and detection methods.

3. Materials and Methods

3.1 Materials and technical equipment

3.1.1 Cells

See **Table 1** in section 3.2.1.

3.1.2 Chemicals and reagents

Primary antibodies / Fluorochromes	Dilution	Company
Avidin-Alexa488	1:200	Molecular Probes, Eugene, OR, USA
Goat-anti-LaminB	1:100	Santa Cruz Biotechnology, Dallas, TX, USA
Human-anti-nucleolus (nucleolar positive control)	1:10 (or 1:20)	Antibodies Incorporated, Davis, CA, USA
Human-anti-centromere (centromere positive control)	1:20	Antibodies Incorporated, Davis, CA, USA
Mouse-anti-BrdU	1:200	Roche, Mannheim, Germany
Mouse-anti-Dig-Cy5	1:100	Jackson Immuno Research, Newmarket, United Kingdom
Mouse-anti-H3K9me3	1:100	Active Motif, Carlsbad, CA, USA; #39285
Mouse-anti-H3S10p	1:200	Kindly provided by Jan Postberg (University of Witten, Germany)
Mouse-anti-IdU/BrdU	1:500	Caltag, Buckingham, United Kingdom
Mouse-anti-SC35	1:2000	Sigma-Aldrich, Deisenhofen, Germany; #S4045
Mouse-anti- α -tubulin (clone DM-1A)	1:500	Sigma-Aldrich, Deisenhofen, Germany
Rabbit-anti-DNP	1:200	Sigma-Aldrich, Deisenhofen, Germany
Rabbit-anti-H3K4me3	1:100	Abcam, Cambridge, United Kingdom; #ab8580
Rabbit-anti-H3S10p	1:500 (or 1:200)	Abcam, Cambridge, United Kingdom
Rabbit-anti-Ki67	1:50	Leica Biosystems, Newcastle, United Kingdom
Rabbit-anti-SMC2	1:200	Bethyl Laboratories, Montgomery, TX, USA
Rat-anti-RNA Pol II Ser 2P	1:10	Kindly provided by Prof. Dr. Dirk Eick (Helmholtz Center, Munich, Germany)
Rat-anti-RNA Pol II Ser 5P	1:20	Kindly provided by Prof. Dr. Dirk Eick (Helmholtz Center, Munich, Germany)

Secondary antibodies	Dilution	Company
Donkey-anti-goat-Alexa488	1:400	Molecular Probes, Eugene, OR, USA
Donkey-anti-goat-Cy3	1:500	Molecular Probes, Eugene, OR, USA
Donkey-anti-human-Cy5	1:200	Jackson Immuno Research, West Grove, PA, USA

Materials and Methods

Donkey-anti-rabbit-Alexa594	1:200	Molecular Probes, Eugene, OR, USA
Donkey-anti-rabbit-Cy3	1:200	Jackson Immuno Research, West Grove, PA, USA
Donkey-anti-rabbit-DyLight488	1:400	Jackson Immuno Research, West Grove, PA, USA
Donkey-anti-rat-Alexa594	1:300	Molecular Probes, Eugene, OR, USA
Goat-anti-avidin-FITC	1:200	Vector Laboratories, Burlingame, CA, USA
Goat-anti-human-FITC	1:200 or 1:500	Jackson Immuno Research, West Grove, PA, USA
Goat-anti-mouse-Alexa488	1:400 or 1:500	Molecular Probes, Eugene, OR, USA
Goat-anti-mouse-Alexa594	1:300	Molecular Probes, Eugene, OR, USA
Goat-anti-mouse-Cy5	1:100 or 1:200	Jackson Immuno Research, West Grove, PA, USA
Goat-anti-rabbit-Cy3	1:200	Jackson Immuno Research, West Grove, PA, USA
Sheep-anti-mouse-Cy3	1:500	Jackson Immuno Research, West Grove, PA, USA
goat-anti-human-Alexa594	1:300	Molecular Probes, Eugene, OR, USA
goat-anti-rabbit-Alexa488	1:400	Molecular Probes, Eugene, OR, USA

Chemicals	Company
Acetic acid	Merck, Darmstadt, Germany
Acetone	Sigma-Aldrich, Deisenhofen, Germany
Agarose SeaKem ME	Cambrex Bio Science Rockland, Rockland, ME, USA
BrdU (5-bromo-2'-deoxyuridine)	Sigma-Aldrich, Deisenhofen, Germany
BSA (bovine serum albumin) for PBS solutions	Sigma-Aldrich, Deisenhofen, Germany
BSA (bovine serum albumin) for SSC solutions	MP Biomedicals, Solon, OH, USA
Buffer 10x	Amersham Pharmacia Biotech, Braunschweig, Germany
Caffeine	Sigma-Aldrich, Deisenhofen, Germany
Calyculin A	Wako, Neuss, Germany; #038-14453
Certipur (calibration solution for pH meter)	Merck, Darmstadt, Germany
Colcemid 10 µg/ml	Biochrom AG, Berlin, Germany
Coverslip removal fluid (glass bottom fluid DCF OS 30)	MatTek, Ashland, MA, USA
DAPI (4',6-diamidino-2-phenylindole)	Sigma-Aldrich, Deisenhofen, Germany
Dextran sulfate	Amersham Pharmacia Biotech, Braunschweig, Germany
Dextran-FITC (250 kDa, 10 mg/ml in H ₂ O)	Sigma-Aldrich, Deisenhofen, Germany
Dextran-TRITC (76 kDa, 10 mg/ml in H ₂ O)	Sigma-Aldrich, Deisenhofen, Germany
DMEM (Dulbecco's MEM)	Biochrom AG, Berlin, Germany
DMEM (Dulbecco's MEM) without phenol red	Invitrogen, Carlsbad, CA, USA; #21063-029
DMSO (dimethyl sulfoxide)	Sigma-Aldrich, Deisenhofen, Germany
EDTA (Titriplex III)	Merck, Darmstadt, Germany
EGTA (ethylene glycol bis(2-aminoethyl)-tetraacetic acid)	Roth, Karlsruhe, Germany Sigma-Aldrich, Deisenhofen, Germany

Ethanol, absolute	Merck, Darmstadt, Germany Sigma-Aldrich, Deisenhofen, Germany
Ethanol, technical	VWR, Darmstadt, Germany
Ethidium bromide	Sigma-Aldrich, Deisenhofen, Germany
FCS (fetal calf serum) (= FBS Superior)	Biochrom AG, Berlin, Germany
FBS (fetal bovine serum)	Sigma-Aldrich, Deisenhofen, Germany
Ficoll-Hypaque (Lymphoprep)	Nycomed Pharma, Oslo, Norway
Fish skin gelatine 45%	Sigma-Aldrich, Deisenhofen, Germany
FluoSpheres 20 nm	Molecular Probes, Eugene, OR, USA; #F8787
FluoSpheres 40 nm	Molecular Probes, Eugene, OR, USA; #F8792
FLT3-L (FMS-like tyrosine kinase 3 ligand) 10 µg/ml	Miltenyi Biotec, Bergisch Gladbach, Germany
Formamide	Merck, Darmstadt, Germany
Formamide, deionized	Sigma-Aldrich, Deisenhofen, Germany; #F9037
GeneAmp PCR buffer 10x	Applied Biosystems, Darmstadt, Germany
Glutamine 200 mM	Biochrom AG, Berlin, Germany EuroClone, Pero, Italy
Glycerol	Merck, Darmstadt, Germany
Glycine	Merck, Darmstadt, Germany Sigma-Aldrich, Deisenhofen, Germany
H ₂ O _{bidest}	Obtained from the Milli-Q system
H ₂ O _{dest}	
Ham's F-10	Biochrom AG, Berlin, Germany
Ham's F-10 without phenol red	Biochrom AG, Berlin, Germany; #F0723
HCl (hydrochloric acid) 1 N	Roth, Karlsruhe, Germany
HCl (hydrochloric acid) fuming 37% (= 12.5 N)	Merck, Darmstadt, Germany
Heparin (Na-heparin) 25 000 I.E. / 5 ml	Braun Melsungen AG, Melsungen, Germany
Hepes	Calbiochem, San Diego, CA, USA Sigma-Aldrich, Deisenhofen, Germany
Histopaque 1077	Sigma-Aldrich, Deisenhofen, Germany
Histopaque 1119	Sigma-Aldrich, Deisenhofen, Germany
Hoechst 33342 (bisBenzimide H 33342 trihydrochloride)	Sigma-Aldrich, Deisenhofen, Germany
Human serum	Lonza, Basel, Switzerland
IL-3 (Interleukin 3) 10 µg/ml	Miltenyi Biotec, Bergisch Gladbach, Germany
IL-6 (Interleukin 6) 10 µg/ml	Miltenyi Biotec, Bergisch Gladbach, Germany
IMEM (Iscove's Modified Dulbecco's Media)	EuroClone, Pero, Italy
Immersion oil	Zeiss, Jena, Germany
Immersion oil for the OMX 3D-SIM with refractive indices from 1.510 to 1.518 (in steps of 0.002)	Chromaphor, Oberhausen, Germany Cargille Laboratories, Cedar Grove, NJ, USA
KCl (potassium chloride)	Merck, Darmstadt, Germany Sigma-Aldrich, Deisenhofen, Germany
KH ₂ PO ₄ (potassium phosphate)	Calbiochem, San Diego, CA, USA BDH (British Drug Houses), London, United Kingdom
Liquid nitrogen	
Loading Dye 6x	Fermentas, St. Leon-Rot, Germany
LR white resin, uncatalyzed	Science Services, Munich, Germany; #LR14381
Meliseptol	Braun Melsungen, Melsungen, Germany
Methanol	Merck, Darmstadt, Germany

MgCl ₂ · 6 H ₂ O (magnesium chloride hexahydrate)	Merck, Darmstadt, Germany Sigma-Aldrich, Deisenhofen, Germany
Na ₂ HPO ₄ (di-sodium hydrogen phosphate anhydrous)	Merck, Darmstadt, Germany Sigma-Aldrich, Deisenhofen, Germany
Na ₂ S ₂ O ₅ (sodium disulfite)	Merck, Darmstadt, Germany
NaCl (sodium chloride)	Merck, Darmstadt, Germany Sigma-Aldrich, Deisenhofen, Germany
NaOH (sodium hydroxide)	Merck, Darmstadt, Germany
Osmium ammine B	Polysciences, Eppelheim, Germany; #21033
Paraformaldehyde	Merck, Darmstadt, Germany BDH (British Drug Houses), London, United Kingdom
Penicillin/Streptomycin (10 000 U / 10 000 µg/ml)	Biochrom AG, Berlin, Germany EuroClone, Pero, Italy
Poly-L-lysine-hydrobromide	Sigma-Aldrich, Deisenhofen, Germany
SCF (stem cell factor) 10 µg/ml	Miltenyi Biotec, Bergisch Gladbach, Germany
SDS (sodium dodecyl sulfate)	Sigma-Aldrich, Deisenhofen, Germany
Sodium azide (NaN ₃)	Merck, Darmstadt, Germany
Sodium citrate dihydrate (C ₆ H ₅ Na ₃ O ₇ · 2 H ₂ O)	Calbiochem, San Diego, CA, USA
TPO (Thrombopoietin) 10 µg/ml	Miltenyi Biotec, Bergisch Gladbach, Germany
Tris	Roth, Karlsruhe, Germany
Tris / HCl 1 M pH 7.8 or 8.0	Sigma-Aldrich, Deisenhofen, Germany
Triton-X-100	Sigma-Aldrich, Deisenhofen, Germany
Trolox (6-hydroxy-2,5,7,8-tetramethylchroman-2-carboxylic acid)	Sigma-Aldrich, Deisenhofen, Germany; #23,881-3
Trypan blue	Seromed, Munich, Germany Sigma-Aldrich, Deisenhofen, Germany
Trypsin/EDTA 10x	Biochrom AG, Berlin, Germany
Tween 20	Calbiochem, San Diego, CA, USA
Vectashield Antifade Medium	Vector Laboratories, Burlingame, CA, USA

Enzymes	Company
DNase I (2000 U/mg)	Roche, Mannheim, Germany
Pepsin	Sigma-Aldrich, Deisenhofen, Germany
Proteinase K 14-22 mg/ml	Roche, Mannheim, Germany
Taq-Polymerase	Amersham Pharmacia Biotech, Braunschweig, Germany

Kits	Comment	Company
EasySep cell isolation kit for the isolation of CD34 and CD14 positive cells	including EasySep positive selection cocktail, EasySep magnetic nanoparticles, and EasySep magnet	StemCell Technologies, Grenoble, France

Nucleotides / Primer / DNA	Company
6 MW primer	MWG-Biotec, Ebersberg, Germany
Biotin-16-dUTP	Roche, Mannheim, Germany
dATP 100 mM	Roche, Mannheim, Germany
dCTP 100 mM	Roche, Mannheim, Germany
dGTP 100 mM	Roche, Mannheim, Germany
Digoxigenin-11-dUTP	Roche, Mannheim, Germany

DNP-11-dUTP	NEN Life Science Products, Inc., Boston, MA, USA
dTTP 100 mM	Roche, Mannheim, Germany
Salmon sperm	Invitrogen, Carlsbad, CA, USA
λ /HindIII (Lamda DNA / HindIII) 0.5 μ g/ml / 50 μ g	Fermentas, St. Leon-Rot, Germany

3.1.3 Media and solutions

Medium / Solution	Constituents	Preparation / Comment
6 MW primer 100 μ M	100 μ M 6 MW primer 10% TE buffer H_2O_{bidest}	29.4 μ l 1700 μ M 6 MW primer + 50 μ l TE buffer + 420.6 μ l H_2O_{bidest}
6 MW primer 1700 μ M	1700 μ M 6 MW primer TE buffer	1.693 μ g 6 MW primer (= 250 nM) + 147 μ l TE buffer
ACG mix	2 mM dATP 2 mM dCTP 2 mM dGTP H_2O_{bidest}	10 μ l 100 mM dATP + 10 μ l 100 mM dCTP + 10 μ l 100 mM dGTP + 470 μ l H_2O_{bidest}
Agarose gel	1% agarose 1x TAE buffer	2 g agarose were dissolved in 200 ml 1x TAE buffer in the microwave or on a heated stirrer. Leftovers were kept and melted again when needed.
Blocking buffer	2% BSA 0.5% fish skin gelatine 1x PBS / 0.02% Tween	5 g BSA + 2.78 ml 45% fish skin gelatine \rightarrow ad 250 ml with 1x PBS / 0.02% Tween To facilitate pipetting the fish skin gelatine, it was warmed up to 37°C before use.
Blocking buffer Hepes based	150 mM NaCl 15 mM Hepes/NaOH 2 mM $MgCl_2$ 0.1 mM EGTA 0.2% Triton-X-100 0.5% fish skin gelatine 2% BSA H_2O_{bidest}	12.5 ml 3 M NaCl + 3.75 ml 1 M Hepes/NaOH pH 7.4 + 0.5 ml 1 M $MgCl_2$ + 62.5 μ l 400 mM EGTA pH 8.0 + 0.5 ml Triton-X-100 + 2.78 ml fish skin gelatine + 5 g BSA \rightarrow ad 250 ml with H_2O_{bidest} To facilitate pipetting the fish skin gelatine, it was warmed up to 37°C before use.
BrdU 50 mM	50 mM BrdU DMSO	100 mg BrdU + 6.51 ml DMSO
BSA 2% in 1x PBS / 0.01% Tween	2% BSA 1x PBS / 0.01% Tween	20 ml 4% BSA in 1x PBS / 0.01% Tween + 20 ml 1x PBS / 0.01% Tween
BSA 2% in 4x SSC / 0.2% Tween	2% BSA 4x SSC / 0.2% Tween	20 ml 4% BSA in 4x SSC / 0.2% Tween + 20 ml 4x SSC / 0.2% Tween
BSA 4% in 1x PBS / 0.01% Tween	4% BSA 1x PBS / 0.01% Tween	4 g BSA for PBS solutions \rightarrow ad 100 ml with 1x PBS / 0.01% Tween
BSA 4% in 4x SSC / 0.2% Tween	4% BSA 4x SSC / 0.2% Tween	4 g BSA for SSC solutions \rightarrow ad 100 ml with 4x SSC / 0.2% Tween
Caffeine 100 mM	100 mM caffeine H_2O_{bidest}	1 g caffeine + 50 ml H_2O_{bidest} (exact concentration = 103.9 mM) The solution was warmed up to 37°C

		and vortexed well in order to dissolve all caffeine. Subsequently, it was filtered with a 0.2 µm sterile filter.
Calyculin A 80 µM	80 µM Calyculin A DMSO	10 µg Calyculin A + 123.9 µl DMSO
DAPI stock solution 10 µg/ml	10 µg/ml DAPI 1x PBS	20 µl 500 µg/ml DAPI stock + 980 µl 1x PBS
DAPI stock solution 500 µg/ml	DAPI H ₂ O _{bidest}	10 mg DAPI + 20 ml H ₂ O _{bidest}
DNA buffer	100 mM EDTA 200 mM Tris	2 ml 0,5 M EDTA + 2 ml 1 M Tris / HCl pH 7.8 or 8.0 + 6 ml H ₂ O _{bidest}
DNase I stock solution	2000 U/ml (= 1 mg/ml) DNase I 0.15 M NaCl 50% glycerol H ₂ O _{bidest}	100 mg DNase I + 5 ml 3 M NaCl + 45 ml H ₂ O _{bidest} + 50 ml glycerol
dNTP mix	2.5 mM dATP 2.5 mM dGTP 2.5 mM dCTP 2.5 mM dTTP H ₂ O _{bidest}	20 µl 100 mM dATP + 20 µl 100 mM dGTP + 20 µl 100 mM dCTP + 20 µl 100 mM dTTP + 720 µl H ₂ O _{bidest}
dTTP 1 mM	1 mM dTTP H ₂ O _{bidest}	10 µl 100 mM dTTP + 990 µl H ₂ O _{bidest}
EDTA 0.5 M pH 8.0	0.5 M EDTA H ₂ O _{bidest}	1.86 g EDTA → ad 8 ml with H ₂ O _{bidest} The pH was adjusted to pH 8.0.
EGTA 400 mM pH 8.0	400 mM EGTA H ₂ O _{bidest}	3.8 g EGTA → ad 25 ml with H ₂ O _{bidest} The pH was adjusted to pH 8.0.
Ethanol, absolute, 30%, 50%, 70%, 80%, 90%	30%, 50%, 70%, 80%, 90% ethanol H ₂ O _{dest}	30 ml, 50 ml, 70 ml, 80 ml or 90 ml absolute ethanol → ad 100 ml with H ₂ O _{dest}
Ethanol, technical, 70%, 80%, 90%	70%, 80%, 90% ethanol H ₂ O _{dest}	70 ml, 80 ml or 90 ml technical ethanol → ad 100 ml with H ₂ O _{dest}
Ethidium bromide 1 mg/ml	Ethidium bromide H ₂ O _{bidest}	10 mg ethidium bromide + 10 ml H ₂ O _{bidest}
Ethidium bromide bath	0.5 µg/ml ethidium bromide 1x TAE	600 ml 1x TAE + 300 µl 1 mg/ml ethidium bromide
Formamide 50% in 2x SSC pH 7.0	50% formamide 50% 2x SSC	100 ml formamide + 100 ml 4x SSC The pH was adjusted to pH 7.0.
Freezing medium	10% DMSO FCS	9 ml FCS + 1 ml DMSO
Full live cell medium	10% FCS 1% Penicillin/ Streptomycine (P/S) Minimal live cell medium	45 ml minimal live cell medium + 5 ml FCS + 500 µl P/S
Full medium	<i>All adherent cell types, granulocytes, and mononuclear cells:</i> 10% FCS 1% Penicillin/ Streptomycin (P/S) Minimal medium	450 ml minimal medium + 50 ml FCS + 5 ml P/S

	<p>according to Table 1 in section 3.2.1</p> <p><i>CD34⁺ cells:</i> 20% human serum 1% Penicillin/ Streptomycine (P/S) 2 mM glutamine IMDM minimal medium 10 ng/ml IL-3 10 ng/ml IL-6 50 ng/ml FLT3-L 50 ng/ml SCF 20 ng/ml TPO</p> <p><i>Monoblasts, myeloblasts:</i> 20% FBS 1% Penicillin/ Streptomycin (P/S) 2 mM glutamine IMDM minimal medium Cytokines as for CD34⁺ cells but without TPO</p> <p><i>Monocytes:</i> Same as for CD34⁺ cells but with only 10% human serum and without cytokines</p>	<p>39 ml minimal medium + 10 ml human serum + 0.5 ml P/S + 0.5 ml 200 mM glutamine + 50 µl 10 µg/ml IL-3 + 50 µl 10 µg/ml IL-6 + 250 µl 10 µg/ml FLT3-L + 250 µl 10 µg/ml SCF + 100 µl 10 µg/ml TPO</p> <p>39 ml minimal medium + 10 ml FBS + 0.5 ml P/S + 0.5 ml 200 mM glutamine + 50 µl 10 µg/ml IL-3 + 50 µl 10 µg/ml IL-6 + 250 µl 10 µg/ml FLT3-L + 100 µl 10 µg/ml SCF</p> <p>44 ml minimal medium + 5 ml human serum + 0.5 ml P/S + 0.5 ml 200 mM glutamine</p>
Glycerol 20%	20% glycerol 1x PBS	50 ml glycerol + 200 ml 1x PBS
Glycine 20 mM	20 mM glycine 1x PBS	10 ml 200 mM glycine + 90 mM 1x PBS
Glycine 200 mM	200 mM glycine 1x PBS	0.75 g glycine → ad 50 ml 1x PBS
HCC live cell medium 340 mOsm	1% 20x PBS (1:100) Full live cell medium	100 µl 20x PBS + 9.9 ml full live cell medium
HCC live cell medium 425 mOsm	3% 20x PBS (1:33) Full live cell medium	303 µl 20x PBS + 9.7 ml full live cell medium
HCC live cell medium 570 mOsm	5% 20x PBS (1:20) Full live cell medium	500 µl 20x PBS + 9.5 ml full live cell medium
HCC medium 570 mOsm	5% 20x PBS (1:20) Full medium	500 µl 20x PBS + 9.5 ml full medium
HCl 0.01 N	0.01N HCl H ₂ O _{dest}	99 ml H ₂ O _{dest} + 1 ml 1 N HCl
HCl 0.1 N	0.1 N HCl H ₂ O _{dest}	45 ml H ₂ O _{dest} + 5 ml 1 N HCl
HCl 0.25 N	0.25 N HCl H ₂ O _{bidest}	15 ml H ₂ O _{bidest} filtered with a 0.2 µm sterile filter + 5 ml 1 N HCl
HCl 5 N	5 N HCl H ₂ O _{bidest}	4.5 ml H ₂ O _{bidest} filtered through a 0.2 µm sterile filter + 3 ml 12.5 N HCl The solution was always prepared fresh.

Hepes / NaOH 100 mM pH 7.4	100 mM Hepes / NaOH H ₂ O _{dest}	5 ml 1 M Hepes / NaOH pH 7.4 + 45 ml H ₂ O _{dest} The pH was adjusted to pH 7.4 with 1 N NaOH.
Hepes / NaOH 1 M pH 7.0 or pH 7.4	1 M Hepes H ₂ O _{bidest}	23.8 g Hepes → ad 100 ml with H ₂ O _{bidest} The pH was adjusted to pH 7.0 or pH 7.4 with 1 N NaOH.
Hepes 1 M	1 M Hepes H ₂ O _{dest}	23.8 g Hepes → ad 100 ml with H ₂ O _{bidest}
Hoechst 33342 1 mg/ml	1 mg/ml Hoechst 33342 H ₂ O _{bidest}	25 mg Hoechst 33342 + 25 ml H ₂ O _{bidest}
Hybridization mastermix	20% dextran sulfate 2x SSC	8 g dextran sulfate were solved in 40 ml 2x SSC. Subsequently, the solution was vortexed well and filtered with a 0.45 µm sterile filter.
KCl 0.56%	0.56% KCl H ₂ O _{dest}	1.4 g KCl → ad 250 ml with H ₂ O _{dest}
Mastermix for label- PCR	GeneAmp PCR buffer 2 mM MgCl ₂ 2 µM 6 MW primer 100 µM ACG mix 80 µM dTTP 20 µM dUTP-Bio / -Dig or / -DNP H ₂ O _{bidest}	100 µl 10x GeneAmp PCR buffer + 80 µl 25 mM MgCl ₂ + 20 µl 100 µM 6 MW primer + 50 µl ACG mix + 80 µl 1 mM dTTP + 20 µl dUTP- Bio / -Dig or -DNP + 620 µl H ₂ O _{bidest}
Mastermix for secondary DOP- PCR	Buffer 2 µM 6 MW-Primer 200 µM/each dNTP mix H ₂ O _{bidest}	100 µl 10x buffer + 20 µl 100 µM 6 MW primer + 80 µl 2.5 mM/each dNTP mix + 770 µl H ₂ O _{bidest}
Methanol / acetic acid	Methanol / acetic acid 3:1 (V:V)	150 ml methanol + 50 ml acetic acid
MgCl ₂ 0.05 M	0.05 M MgCl ₂ 1x PBS	10 ml 1 M MgCl ₂ + 190 ml 1x PBS
MgCl ₂ 1 M	MgCl ₂ · 6 H ₂ O H ₂ O _{bidest}	50.8 g MgCl ₂ → ad 250 ml with H ₂ O _{bidest}
MgCl ₂ 25 mM	25 mM MgCl ₂ H ₂ O _{bidest}	25 µl 1 M MgCl ₂ + 975 µl H ₂ O _{bidest}
Minimal live cell medium	25 mM freshly added Hepes Minimal medium without phenol red according to Table 1 in section 3.2.1 3.5-4 mM glutamine	The medium was aliquoted into ~50 ml. When a fresh aliquot was opened 25 mM Hepes was added in addition to the Hepes already contained (25 mM for DMEM, 10 mM for Ham's F-10): 1.25 ml 1 M Hepes + 48.75 ml medium. As Ham's F-10 medium without phenol red did not contain glutamine the 1:1 mixture of DMEM and Ham's F-10 had to be supplemented with it: 25 ml DMEM without phenol red + 25 ml Ham's F-10 without phenol red + 400 µl 200 mM glutamine.

NaCl 3 M	3 M NaCl H ₂ O _{bidest}	35 g NaCl → ad 200 ml with H ₂ O _{bidest}
NaCl 6 M	6 M NaCl H ₂ O _{bidest}	87.7 g NaCl → ad 250 ml with H ₂ O _{bidest} This amount of NaCl is higher than the solubility.
NaOH 1 N	1 N NaOH H ₂ O _{bidest}	20 g NaOH → ad 500 ml with H ₂ O _{bidest}
Osmium ammine staining solution	0.2% (= 2.8 mM) osmium ammine B 0.2 N HCl 200 mM Na ₂ S ₂ O ₅ H ₂ O _{bidest}	2.88 ml H ₂ O _{bidest} filtered with a 0.2 µm sterile filter + 6 mg osmium ammine B + 120 µl freshly prepared 5 N HCl + 114 mg Na ₂ S ₂ O ₅ First, the osmium ammine was solved, then 5 N HCl and finally Na ₂ S ₂ O ₅ were added.
PBS 0.3x	0.3x PBS H ₂ O _{bidest}	150 ml 1x PBS + 350 ml H ₂ O _{bidest} For the treatment of living cells 1x PBS without sodium azide was used.
PBS 1x	<i>For living cells:</i> 140 mM NaCl 2.7 mM KCl 6.5 mM Na ₂ HPO ₄ 1.5 mM KH ₂ PO ₄ H ₂ O _{bidest} <i>For fixed cells:</i> Add 0.02-0.04% sodium azide	25 ml 20x PBS + 475 ml H ₂ O _{bidest} 1 l 1x PBS for living cells + a generous pinch sodium azide
PBS 1x / 0.01% or 0.02% Tween	0.01% or 0.02% Tween 20 1x PBS	50 µl or 100 µl Tween 20 + 500 ml 1x PBS
PBS 20x pH 7.4	2.8 M NaCl 54 mM KCl 130 mM Na ₂ HPO ₄ 30 mM KH ₂ PO ₄ H ₂ O _{bidest}	320 g NaCl + 8 g KCl + 57.6 g Na ₂ HPO ₄ + 9.6 g KH ₂ PO ₄ → ad 2 l with H ₂ O _{bidest} The pH was adjusted to pH 7.4.
Pepsin stock solution	10% (~100 mg/ml) pepsin H ₂ O _{bidest}	1 g pepsin + 10 ml H ₂ O _{bidest}
PFA 1%	1% PFA 1x PBS	1 g PFA + 99 ml 1x PBS The solution was stirred and heated (but not boiled!) until all PFA was dissolved. After cooling down it was aliquoted and frozen at -20°C. 1x PBS without sodium azide was used.
PFA 2 %	2% PFA 1x PBS or 0.3x PBS	2 g PFA + 98 ml 1x PBS or 0.3x PBS Preparation: see 1% PFA.
PFA 4%	4% PFA 1x PBS or 0.3x PBS	4 g PFA + 96 ml 1x PBS or 0.3x PBS Preparation: see 1% PFA.
Poly-lysine stock solution	10 mg/ml poly-L-lysine-hydrobromide H ₂ O _{bidest}	100 mg poly-L-lysine-hydrobromide + 10 ml H ₂ O _{bidest}
SDS 10%	SDS H ₂ O _{bidest}	10 ml SDS + 90 ml H ₂ O _{bidest}

SSC 0.1x	15 mM NaCl 1.5 mM sodium citrate 0.02-0.04% sodium azide H ₂ O _{bidest}	5 ml 20x SSC + 995 ml H ₂ O _{bidest} + a generous pinch sodium azide
SSC 20x pH 7.0	3 M NaCl 0.3 M sodium citrate H ₂ O _{bidest}	350.6 g NaCl + 176.4 g sodium citrate → ad 2 l with H ₂ O _{bidest} The pH was adjusted to pH 7.0.
SSC 2x	300 mM NaCl 30 mM sodium citrate 0.02-0.04% sodium azide H ₂ O _{bidest}	100 ml 20x SSC + 900 ml H ₂ O _{bidest} + a generous pinch sodium azide
SSC 4x	600 mM NaCl 60 mM sodium citrate 0.2% Tween 20 H ₂ O _{bidest}	200 ml 20x SSC + 800 ml H ₂ O _{bidest} + 2 ml Tween 20
SSC 4x / 0.2% Tween	600 mM NaCl 60 mM sodium citrate 0.2% Tween 20 0.02-0.04% sodium azide H ₂ O _{bidest}	200 ml 20x SSC + 800 ml H ₂ O _{bidest} + 2 ml Tween 20 + a generous pinch sodium azide
TAE buffer 1x	40 mM Tris-acetate 1 mM EDTA H ₂ O _{bidest}	40 ml 50x TAE + 1960 ml H ₂ O _{bidest}
TAE buffer 50x pH 8.0	2 M Tris-acetate 0.05 M EDTA H ₂ O _{bidest}	242 g Tris + 18.6 g EDTA + 57.1 ml acetic acid → ad 1 l with H ₂ O _{bidest} The pH was adjusted to pH 8.0.
TE-buffer	10 mM Tris 1 mM EDTA H ₂ O _{bidest}	20 µl 1 M Tris / HCl pH 7.8 or 8.0 + 4 µl 0.5 M EDTA + 1976 µl H ₂ O _{bidest}
TE-buffer without EDTA	10 mM Tris H ₂ O _{bidest}	20 µl 1 M Tris / HCl pH 7.8 or 8.0 + 1980 µl H ₂ O _{bidest}
Triton-X-100 0.05%	0.05% Triton-X-100 1x PBS	10 ml 0.5% Triton-X-100 + 90 ml 1x PBS
Triton-X-100 0.3%	0.3% Triton-X-100 1x PBS	0.3 ml Triton-X-100 + 99.7 ml 1x PBS
Triton-X-100 0.5%	0.5% Triton-X-100 1x PBS	0.5 ml Triton-X-100 + 99.5 ml 1x PBS
Trolox 100 mM	100 mM Trolox H ₂ O _{bidest}	0.25 g Trolox → ad 9.8 ml with H ₂ O _{bidest} 100 µl 1 N NaOH were added, the solution was vortexed until all Trolox was dissolved and the solution was neutralized with 100 µl 1 N HCl.
Trolox 250 mM	250 mM Trolox Ethanol, absolute	0.25 g Trolox → ad 4 ml with absolute ethanol
Trypsin/EDTA 1x	1x Trypsin/EDTA H ₂ O _{bidest}	50 ml 10x Trypsin/EDTA + 450 ml H ₂ O _{bidest}
λ/HindIII marker	0.2 µg/ml / 20 µg λ/HindIII 2.4x Loading Dye H ₂ O _{bidest}	100 µl 0.5 µg/ml / 50 µg λ/HindIII + 100 µl 6x Loading Dye + 50 µl H ₂ O _{bidest}

3.1.4 Equipment and devices

Device	Type	Company
Autoclave steam-sterilizer	Varioklav	H+P Labortechnik, Oberschleißheim, Germany
Bunsen burner with foot pedal	GasProfi 1 ^{SCS}	WLD-Tec GmbH, Göttingen, Germany
	Pressure reducing device, gas cartridges (C 206 super) with mounting	CampingGAZ, Hungen-Inheiden, Germany
Centrifuge	Biofuge pico	Heraeus, Hanau, Germany
	C3i	Jouan Industries, Château-Goutier, France
	Rotana/S	Hettich, Tuttlingen, Germany
	GS-6r	Beckman Coulter, Brea, CA, USA
	1-14	Sigma Laborzentrifugen, Osterode am Harz, Germany
Cold room	4°C	
Electrophoresis system	Chamber including gel tray and well combs Easy Cast B1A	OWL Separation Systems, Portsmouth, NH, USA
Electrophoresis system	Voltage source E835	Consort, Turnout, Belgium
Extractor hood		
Freezer -20°C	Various types	AEG, Frankfurt a. M., Germany
		Liebherr, Ochsenhausen, Germany
		Privileg / Quelle, Fürth, Germany
		Zoppas, Porcia, Italy
Freezer -80°C	VX 380 E	Jouan Industries, Château-Goutier, France
Fridge +4°C	Various types	Bosch, Gerlingen-Schillerhöhe, Germany
Heat block	DB 2-D	Techne, Cambridge, United Kingdom
High precision balance	Analytical Plus AP250D	Ohaus, Parsippany, NJ, USA
Ice machine	AF-10	Scotsman, Bettolino, Italy
		NTF Nuove Tecnologie del Freddo, Villa Cortese, Italy
Imaging facility for gels	Foto gadget	MWG-Biotech, Ebersberg, Germany
	Printer control unit Gel Print 2000i	BioPhotonics, Ann Arbor, MI, USA
	Printer UP-D860E	Sony, Tokyo, Japan
Incubator	BB6220	Heraeus, Hanau, Germany
	Galaxy S	RS Biotech, Irvine, United Kingdom
Incubator chamber	Ceromat HK	B. Braun Biotech International, Melsungen
Laminar flow hood	Herasafe	Heraeus, Hanau, Germany
	TopSafe 1.2	BioAir, Siziano, Italy
Liquid nitrogen tank with racks and cryo boxes		Messer Griesheim, Krefeld, Germany
Microinjection system	Micromanipulator including injection arm InjectMan NI 2	Eppendorf, Hamburg, Germany
	Compressor FemptoJet	

Micropipette puller	P-97	Sutter Instrument, Novato, CA, USA
Microwave	Selection	Samsung, Schwabach, Germany
Milli-Q system	Milli-Q biocel	Millipore, Billerica, MA, USA
Oven	Heraeus	Heraeus, Hanau, Germany
	Maxi 14	Celbio, Pero, Italy
	UM 100	Memmert, Schwabach, Germany
pH meter	pH538	WTW, Weilheim, Germany
Photometer	GeneQuantII	Pharmacia Biotech, Cambridge, United Kingdom
Precision balance	2254	Sartorius, Göttingen, Germany
	KernEW	Kern&Sohn GmbH, Balingen, Germany
	Europe 500	Gibertini, Novate Milanese, Italy
Rotator	Thermomixer 5436	Eppendorf, Hamburg, Germany
Shaker	KL-2	Edmund Bühler, Hechingen, Germany
	swip KL-2	
	Unimax 2010	Heidolph, Schwabach, Germany
	711+	Asal, Cernusco, Italy
Stirrer	RCT basic	IKA Werk, Staufen, Germany
	REO	
	RH basic2	
	MR 2002	Heidolph, Schwabach, Germany
Table centrifuge	Minizentrifuge GMC-060	Neolab, Heidelberg, Germany
Thermocycler	Techne Progene	Techne, Cambridge, United Kingdom
Timer		
Ultramicrotome	Ultracut UCT	Leica Microsystems, Heidelberg, Germany
Ultrasonic bath	Sonorex RK 100	Bandelin, Berlin, Germany
UV-lamp for irradiations with black screen	Lamp NU-4 KL	Benda, Wiesloch, Germany
	Screen made of multilayered cardboard	
UV-lamp for the laminar flow hood		Kendro, Langenselbold, Germany
Vacuum centrifuge	Vacuumconcentrator	Bachhofer, Reutlingen, Germany
Vacuum pump	Bottle VacuuTrans-Container VTC including filter and tube	Vacuubrand, Wertheim, Germany
	VacuuHandControl VHC	
	Motor	
Vortex		Neolab, Heidelberg, Germany
	Reax 2000	Heidolph, Schwabach, Germany
Water bath	1003	GFL, Burgwedel, Germany
	1004	GFL, Burgwedel, Germany
	5	Julabo, Seelbach, Germany
	M12	Lauda, Lauda-Königshofen, Germany
	Thermocycler 60	Bio-med, Theres, Germany
	Tempette Junior TE-85	Techne, Cambridge, United Kingdom
Water jet pump		

Equipment	Type / comment	Company
Autoclave tape		VP GmbH, Feuchtwangen, Germany
Box for storing microinjection needles		BioMedical Instruments, Zöllnitz, Germany
Butterflies	Multifly cannula set	Sarstedt, Nümbrecht, Germany
Capsule rack		EMS (Electron Microscopy Sciences), Hatfield, PA, USA
Coplin jars		Schubert & Weiß, München, Germany
Coverslips	18x18 mm, 20x20 mm, 24x24 mm	Superior Marienfeld, Lauda-Königshofen, Germany
	8x8 mm, 12x12 mm, 15x15 mm, 18x18 mm, 22x22 mm, 24x24 mm, 24x32 mm, 24x60 mm	R. Langenbrinck, Emmendingen, Germany
	76x26 mm, 12x12 mm	Hecht, Sondheim, Germany
	8x8 mm, 15x15 mm, 24x60 mm	Menzel-Gläser, Braunschweig, Germany
	Ø 12 mm	Science Services, Munich, Germany
	Ø 42 mm	PeCon GmbH, Erbach, Germany
	Photoetched Ø 12 mm	Bellco, Vineland, NJ, USA
Coverslips, high precision	18x18 mm, thickness 170±5 µm	Carl Roth, Karlsruhe, Germany; #LH22.1
Cryo tubes	1.8 ml	Greiner bio-one, Frickenhausen, Germany
Dialysis tube	Membra-Cel MWCO 7000, Ø 16 mm	Serva, Heidelberg, Germany
Diamond knife	Diatome 45° MP281	Diatome, Biel, Switzerland
Diamond knife cleaning sticks		DDK Delaware Diamond Knives, Wilmington, DE, USA
Diamond pencils	For cutting coverslips	Kraus & Winter, Hamburg, Germany
	For gridding coverslips	Bel-Art Products, Pequannock, NJ, USA
Double edge razor blades		EMS (Electron Microscopy Sciences), Hatfield, PA, USA
Embedding capsules	BEEM size 00	EMS (Electron Microscopy Sciences), Hatfield, PA, USA
Embryo dishes with lids	Ø 30 mm	EMS (Electron Microscopy Sciences), Hatfield, PA, USA
Filter paper	Folded, Ø 125 mm	Schleicher & Schnell, Dassel, Germany
	N°111, Ø 40 mm	Durieux, Paris, France
Fixogum		Marabuwerke, Tamm, Germany
Glass bottles	Various sizes	Schott, Stafford, United Kingdom
Glass capillaries	O.D. 1.00 mm, I.D. 0.50 mm, 10 cm length	Sutter Instrument, Novato, CA, USA; #BF100-50-10
	O.D. 1.50 mm, I.D. 1.17 mm, 10 cm length, GC150-TF-10	Harvard Apparatus, Holliston, MA, USA; #30-0066
Gloves	Latex	Neolab, Heidelberg, Germany
		Starlab, Milan, Italy
	Nitrile	Neolab, Heidelberg, Germany
		Starlab, Milan, Italy

Grids for EM	Gold, mesh 300	Plano, Wetzlar, Germany
	Gold, slot 2x1 mm, formvar/carbon-coated	Science Services, Munich, Germany
Hemocytometer	Neubauer	Hecht-Assistent, Sondheim, Germany
		Precicolor HBG, Gießen-Lützellinden, Germany
Hypodermic needles	Sterican 0.60x60 mm	Braun Melsungen, Melsungen, Germany
	Sterican 0.90x40 mm	Rose GmbH, Trier, Germany
Kimwipe tissues		Kimberly-Clark, Surrey, United Kingdom
Kimtech tissues		Kimberly-Clark, Surrey, United Kingdom
Liquid waste bottle		Biochrom AG, Berlin, Germany
MatTek glass bottom dishes	Ø 35 mm with 20x20 mm coverslip attached	MatTek, Ashland, MA, USA; #P35G-1.5-14-C
	Ø 35 mm with Ø 12 mm gridded Bellco coverslip attached	MatTek, Ashland, MA, USA; #P35G-2(12 mm)-7-C-GRID (custom order)
Metal boxes with lids	Various sizes	Schubert Medizinprodukte, Wackersdorf, Germany
Microloader		Eppendorf, Hamburg, Germany
Microscope slides		R. Langenbrinck, Emmendingen, Germany
		Knittel Gläser, Braunschweig, Germany
Multiwell plates	6-well, 12-well	Greiner bio-one, Frickenhausen, Germany
		Falcon / Becton Dickinson, San Jose, CA, USA
	Quadriperm	Greiner bio-one, Frickenhausen, Germany
Nail polish, clear		Rival de Loop, Berlin, Germany
Parafilm		Pechiney Plastic Packaging, Menasha, WI, USA
Pasteur pipettes	Glass 230 mm	Poulten & Graf GmbH, Wertheim, Germany
	Plastic 3 ml	Falcon / Becton Dickinson, San Jose, CA, USA
		Neolab, Heidelberg, Germany
		LP Italiana SPA, Milan, Italy
Plastic 3 ml, sterile	Greiner bio-one, Frickenhausen, Germany	
Petri dishes	Ø 35 mm, Ø 60 mm	Falcon / Becton Dickinson, San Jose, CA, USA
	Well closing, inside diameter ~40 mm	Company not known; however, similar dishes with Ø 50 mm are available from EMS (Electron Microscopy Sciences), Hatfield, PA, USA
Pipette tips	10 µl (white)	Molecular Bio Products, San Diego, CA, USA
		Starlab, Milan, Italy
	20 µl / 200 µl (yellow), 1000 µl (blue)	Greiner bio-one, Frickenhausen, Germany
		Starlab, Milan, Italy

	With filter for PCR	Molecular Bio Products, San Diego, CA, USA
Pipettes	10 µl, 20 µl, 200 µl, 1000 µl	Gilson Inc., Middleton, WI, USA
Pipettes, serological	5 ml, 10 ml, 25 ml	Sarstedt, Nümbrecht, Germany Starlab, Milan, Italy
	1 ml, 2 ml	Falcon / Becton Dickinson, San Jose, CA, USA Starlab, Milan, Italy
	2 ml	Costar, Corning, NY, USA
Pipettor		Gilson Inc., Middleton, WI, USA
	Swiftpet	Abimed, Langenfeld, Germany
	Accu-jet	Brand, Wertheim, Germany
POC-R chamber		Visitron Systems, Puchheim, Germany
Quartz cuvette		Hellma GmbH, Müllheim, Germany
Single edge razor blades		EMS (Electron Microscopy Sciences), Hatfield, PA, USA
Soft tissue		Carl Roth, Karlsruhe, Germany
Sterile filter	0.2 µm, 0.45 µm	Sartorius, Göttingen, Germany
Syringes, sterile	1 ml, 5 ml, 10 ml, 20 ml, 50 ml, 50 ml Luer Lock	Henke Sass Wolf, Tuttlingen, Germany
Tissue culture flasks	25 cm ² , 75 cm ²	Greiner bio-one, Frickenhausen, Germany
Tubes	0.5 ml	Brand, Wertheim, Germany
	2 ml, 1.5 ml	Eppendorf, Hamburg, Germany
	15 ml	Greiner bio-one, Frickenhausen, Germany
	15 ml, 50 ml	Falcon / Becton Dickinson, San Jose, CA, USA
		EuroClone, Pero, Italy
	Polystyrene 5 ml	Falcon / Becton Dickinson, San Jose, CA, USA
Polystyrene 15 ml	Sarstedt, Nümbrecht, Germany	
Tubes with screw cap	0.5 ml	Eppendorf, Hamburg, Germany
	1.5 ml	Neolab, Heidelberg, Germany
Tweezers		Dumont, Montignez, Switzerland
Tweezers, fine	no. 2, 4, 5 as preferred, exclusively used for handling EM grids	Dumont, Montignez, Switzerland
Waste containers for sharp objects		Carl Roth, Karlsruhe, Germany

Additional equipment		
Aluminum foil	Measuring cylinders	Spoons
Beakers, various sizes	Metal loop, Ø ~3.5 mm	Stir bar retriever
Box with plain underside	Microtest plate for probe preparation for electrophoresis	Styrofoam boxes, various sizes
Brush	Pipetting aid for glass Pasteur pipettes	Tape
Colored sticker spots	Pipetting aid for serological pipettes	Tissue
Dark chamber	Safety glasses	Tourniquet

Dialysis clamps	Scalpel	Tube box
Floats	Scissors	Tube racks, various sizes
Gelatine capsules	Silicagel beads	Tweezers, large
Gloves, isolated	Slide boxes	Wash bottles
Insulated container for liquid nitrogen	Slide folders	Weighing boats, various sizes
Magnetic stir bars	Spatulas	Wooden sticks with a single eyelash attached

3.1.5 Microscopes

Microscope	Specifications (only the objectives actually used are listed)	Company
Axiovert 200 M (widefield)	<p><u>Objectives:</u> A Plan 10x / 0.25 Ph1 LD Plan NEOFLUAR 20x / 0.4 Ph2 LD Plan NEOFLUAR 40x / 0.6 Ph2 Plan NEOFLUAR 40x oil / 1.3 Ph3 Plan Apochromat 63x oil / 1.4</p> <p><u>Halogen lamp:</u> Hal 100 Bulbs: HLX 64625 100W 12V (Osram, Augsburg, Germany)</p> <p><u>Fluorescence filters:</u> DAPI (D 360/40, D 470/40, 400 dclp) FITC (HQ 470/40, HQ 522/40, Q 497 lp) YellowGFP (HQ 500/20, HQ 535/30, Q 515 lp) Cy3v1 (HQ 546/11, HQ 567/15, Q 557 lp) Cy3.5v1 (HQ 581/10, HQ 617/40, Q 593 lp) Cy5 (HQ 622/36, HQ 667/30, Q 647 lp)</p> <p><u>Camera:</u> Spot RT (Diagnostic Instruments; Sterling Heights, MI, USA)</p> <p><u>Condensers:</u> 424242 (NA 0,55; WD 26 mm) 1005-844 (Long distance condenser)</p> <p><u>Live cell setup:</u> Incubation chamber (Visitron Systems, Puchheim, Germany) Heating system: Heating unit and Tempcontrol 37-2 digital (Visitron Systems, Puchheim, Germany) UV-filter: 3RD Millenium Longpass filter LC-3RD/450LP-25 (Laser Components, Olching, Germany)</p> <p><u>Operating software:</u> MetaMorph (Universal Imaging; now part of Molecular Devices, Sunnyvale, CA, USA)</p>	Zeiss, Jena, Germany

Axiovert 25 C	<u>Objectives:</u> CP Achromat 5x / 0.12 CP Achromat 10x / 0.25 Ph1 LD Achrostigmat 20x / 0.3 Ph1 Achrostigmat 40x / 0.55 Ph2	Zeiss, Jena, Germany
Axiovert 40 C	<u>Objectives:</u> A Plan 5x / 0.12 Ph0 A Plan 10x / 0.25 Ph1 LD A Plan 20x / 0.3 Ph1 Var1	Zeiss, Jena, Germany
Axiovert 2 (widefield)	<u>Objectives:</u> Plan NEOFLUAR 40x oil / 1.3 Plan Achromat 63x oil / 1.4 <u>Mercury lamp:</u> HXP 120 C <u>Fluorescence filters:</u> DAPI (BP 365, FT 395, LP 450-490) FITC (BP 450-490, FT 510, LP 515-565) Cy3 (BP 546, FT 580, LP 590) Cy5 (BP 575-625, FT 645, BP 660-710) Triple-filter (TBP 400/495/570, FT 410/505/585, TBP460/530/610) <u>Camera:</u> Coolview (Visitron Systems, Puchheim, Germany) <u>Operating software:</u> MetaVue (Universal Imaging Group; now part of Molecular Devices, Sunnyvale, CA, USA)	Zeiss, Jena, Germany
Leica DC300f	<u>Objectives:</u> N Plan 5x / 0.12 Ph0 C Plan 10x / 0.22 Ph1 L 20x / 0.30 Ph1	Leica Microsystems, Heidelberg, Germany
Leica TCS SP5 DMI 6000 CS (CLSM)	<u>Objective:</u> HCX Plan Achromat Lambda Blue 63x oil / 1.4 <u>Laser:</u> 405 nm diode 25 mW 485, 476, 488, 496, 514 nm Ar 100 mW 561 nm DPSS 10 mW 594 nm HeNe 2.5 mW 633 nm HeNe 10 mW <u>Beam Splitter:</u> Acousto Optical Beam Splitter (AOBS) Settings for emission: DAPI (405 nm) 410-463 nm FITC (488 nm) 503-539 nm Cy3 (561 nm) 565-587 nm TexasRed (594 nm) 600-625 nm Cy5 (633 nm) 650-738 nm <u>Detection system:</u> Photomultiplier tubes (PMTs) (one for each laser) <u>Operating software:</u> Leica Application Suite	Leica Microsystems, Heidelberg, Germany

Morgagni 268 (TEM)	<p>Operated at 80 kV acceleration voltage in bright field mode</p> <p><u>Filament:</u> Tungsten</p> <p><u>Camera:</u> Megaview 3 (SIS Soft Imaging System; now Olympus Soft Imaging Solutions, Münster, Germany)</p> <p><u>Operating software:</u> Morgagni Microscope Control iTEM (Olympus Soft Imaging Solutions, Münster, Germany)</p>	FEI, Hillsboro, OR, USA
OMX Version 3 (3D-SIM)	<p><u>Objective:</u> UPlan S Apo 100x oil / 1.4 (Olympus, Tokyo, Japan)</p> <p><u>Laser:</u> 405 nm diode 600 mW (Power Technology, Alexander, AR, USA) 488 nm VECSEL 200 mW (Coherent, Santa Clara, CA, USA) 592.5 nm diode 300 mW (MPB Communications, Montréal, QC, Canada)</p> <p><u>Fluorescence filters:</u> DAPI (405 nm) 442/46 FITC (488 nm) 525/50 Alexa594 (592.5 nm) 615/24 / 629/53</p> <p><u>Cameras:</u> Cascade II (one for each channel) (Photometrics, Tucson, AZ, USA)</p> <p><u>Operating software:</u> DeltaVision OMX SoftWoRx</p>	Applied Precision, Issaquah, WA, USA
pDV	<p><u>Objective:</u> Plan Apo N 63x oil / 1.42 (Olympus, Tokyo, Japan)</p> <p><u>Xenon lamp:</u> 250 W</p> <p><u>Fluorescence filters:</u> DAPI (Ex: 350/50, Em: 455/50) FITC (Ex: 490/20, Em: 525/36) TRITC (Ex: 555/25, Em: 605/52) Cy5 (Ex: 645/30, Em: 705/72)</p> <p><u>Camera:</u> CoolSNAP HQ² (Photometrics, Tucson, AZ, USA)</p> <p><u>Operating software:</u> SoftWoRx</p>	Applied Precision, Issaquah, WA, USA
UltraView VoX (SDLMS)	UltraView VoX spinning disk confocal unit from PerkinElmer attached to a Zeiss Axio Observer D1 microscope	PerkinElmer, Waltham, MA, USA

	<p><u>Objective:</u> Plan Apochromat 63x oil / 1.4</p> <p><u>Laser:</u> 405 nm solid state 50 mW (Melles Griot, Albuquerque, NM, USA) 422 nm solid state 40 mW (Melles Griot, Albuquerque, NM, USA) 488 nm solid state 75 mW (Coherent, Santa Clara, CA, USA) 514 nm solid state 25 mW (Cobolt, Stockholm, Sweden) 561 nm solid state 75 mW (Cobolt, Stockholm, Sweden) 640 nm solid state 50 mW (Melles Griot, Albuquerque, NM, USA)</p> <p><u>Fluorescence filters:</u> DAPI / Cy3.5 (BP 445/60, BP 615/70) FITC (BP 527/55) Cyan / Cy5 (BP 485/60, BP 705/90) Cy3 (BP 587/125) FITC / TexasRed (BP 525/50, BP 640/120) Cyan / Cy3 / Cy5 (BP 477/45, BP 575/100, 705/90)</p> <p><u>Camera:</u> C9100-50 Frame transfer camera (Hamamatsu, Japan)</p> <p><u>Live cell setup:</u> Incubation chamber (PeCon, Erbach, Germany) Heating system: Heating unit and Tempcontrol 37-2 digital (Visitron Systems, Puchheim, Germany)</p> <p><u>Operating software:</u> Volocity</p>	<p>Zeiss, Jena, Germany</p>
--	--------------------------------------------------------------------------------------------------------------------------------------------------------------------------------------------------------------------------------------------------------------------------------------------------------------------------------------------------------------------------------------------------------------------------------------------------------------------------------------------------------------------------------------------------------------------------------------------------------------------------------------------------------------------------------------------------------------------------------------------------------------------------------------------------------------------------------------------------------------------------------------------------------------------------------------------------------------------------------------------------------------------------------------------------	-------------------------------------

3.1.6 Software

Note that the operating softwares for the microscopes are not listed here but under the respective microscope in section 3.1.5.

Software	Company
Adobe 3D Reviewer (part of Acrobat Pro Extended)	Adobe Systems, San Jose, CA, USA
Adobe Photoshop	Adobe Systems, San Jose, CA, USA
Amira	FEI Visualization Sciences Group, Burlington, MA, USA
Excel	Microsoft, Redmond, WA, USA
Fiji	Based on ImageJ; Schindelin et al. 2012
ImageJ	Public Domain by Wayne Rasband, USA

R	R Core Team 2013 Including the packages bioimagetools (Schmid 2013) EBImage (Pau et al. 2010, Pau et al.) And the additional software required for EBImage GTK+ (The GTK+ Team) ImageMagick (ImageMagick Studio LLC, PA, USA)
SoftWoRx	Applied Precision, Issaquah, WA, USA
Volocity	PerkinElmer, Waltham, MA, USA
Word	Microsoft, Redmond, WA, USA

3.2 Methods

Note that in the materials section of each method only specific materials are listed and general materials like e.g. tubes, pipettes, etc. are omitted.

If not otherwise mentioned, all steps were performed at room temperature (RT).

3.2.1 Tissue culture

All works were performed under a laminar flow hood to maintain sterile conditions. Solutions like 1x PBS and H₂O_{bidest} were autoclaved before being used for living cells. Only PBS without sodium azide was used for the treatment of living cells. All media and solutions for handling living cells were warmed up to 37°C before use.

Table 1 summarizes the cell types used in this work, including a short description, their origin and the corresponding growth medium for their cultivation. Detailed information on the isolation of the hematopoietic cells (CD34⁺ cells, monoblasts, myeloblasts, monocytes, granulocytes, mononuclear cells) is given in section 3.2.1.1. All cells were cultivated in an incubator at 37°C with 5% CO₂ under humid conditions.

Human hematopoietic cells were chosen as hematopoiesis provides an ideal system to study cells of different differentiation stages (see section 2.4 in the introduction for further details).

HeLa cells are commonly used since more than 60 years now. They are very easy to cultivate and are a firmly adherent cell type. These two characteristics made them ideal for establishing the procedures for microinjection and correlative microscopy.

Chinese hamster cells have a decades-long tradition in studies on DNA damage and DNA repair, including mutation assays, toxicological studies, and damage analysis after UV

Table 1: Overview of cell lines and corresponding growth media.

Cell type	Origin / description	Medium
CD34 ⁺ cells	Isolated using the EasySep system from human umbilical cord blood obtained from the Emilia Romagna Cord Blood Bank (ERCB) at the policlinic S. Orsola-Malpighi in Bologna; CD34 positive fraction	IMDM supplemented with 2 mM L-glutamine and cytokines (see full medium in section 3.1.3 for details), 20% human serum, 1% PS
Monoblasts	Isolated using the EasySep system from human umbilical cord blood obtained from the Emilia Romagna Cord Blood Bank (ERCB) at the policlinic S. Orsola-Malpighi in Bologna; CD34 positive fraction, cultivated for 7 days, purified for the CD14 positive fraction	IMDM supplemented with 2 mM L-glutamine and cytokines (see full medium in section 3.1.3 for details), 20% FBS, 1% PS
Myeloblasts	Isolated using the EasySep system from human umbilical cord blood obtained from the Emilia Romagna Cord Blood Bank (ERCB) at the policlinic S. Orsola-Malpighi in Bologna; CD34 positive fraction, cultivated for 7 days, purified for the CD14 negative fraction	IMDM supplemented with 2 mM L-glutamine and cytokines (see full medium in section 3.1.3 for details), 20% FBS, 1% PS
Monocytes	Isolated using the EasySep system from human umbilical cord blood obtained from the Emilia Romagna Cord Blood Bank (ERCB) at the policlinic S. Orsola-Malpighi in Bologna or from human peripheral blood of healthy donors – the later one turned out to give better results with regards to cell numbers and morphology and was therefore preferred; CD14 positive fraction of the mononuclear cell fraction	IMDM supplemented with 2 mM L-glutamine, 10% human serum, 1% PS
Granulocytes	Isolated using Histopaque gradients from human peripheral blood of healthy donors; lower cell fraction	DMEM supplemented with 10% FBS, 1% PS
Mononuclear cells	Isolated using Histopaque gradients from human peripheral blood of healthy donors; upper cell fraction	DMEM supplemented with 10% FBS, 1% PS
HeLa (H2B-GFP)	Cervix carcinoma cells from a female human patient, stably transfected with H2B-GFP (Kanda et al. 1998)	DMEM supplemented with 10% FBS, 1% PS
HeLa (H2B-mRFP)	Cervix carcinoma cells from a female human patient, stably transfected with H2B-mRFP; second FACS sorting (kindly provided by Dr. Manja Ziegler (GSF, Munich, Germany))	DMEM (originally RPMI was recommended) supplemented with 10% FBS, 1% PS
HeLa Kyoto	Cervix carcinoma cells from a female human patient (kindly provided by Prof. Dr. Heinrich Leonhardt (LMU, Munich, Germany))	DMEM supplemented with 10% FBS, 1% PS
V79	Male lung fibroblasts from the Chinese hamster (<i>Cricetulus griseus</i>), immortalized by spontaneous transformation (kindly provided by PD Dr. Stefan Müller (LMU, Munich, Germany))	DMEM supplemented with 10% FBS, 1% PS
V79 (H2B-mRFP, Rad51-GFP)	Male lung fibroblasts from the Chinese hamster (<i>Cricetulus griseus</i>), immortalized by spontaneous transformation, stably transfected with Rad51-GFP and H2B-mRFP (Strickfaden 2010; Rad51-GFP plasmid kindly provided by Dr. Jeroen Essers (Erasmus MC, Rotterdam, Netherlands))	DMEM or 1:1 mixture of DMEM and Ham's F-10 (always used for live cell observations) supplemented with 10% FBS, 1% PS
Diploid Chinese hamster fibroblasts	Primary male fibroblasts from the Chinese hamster (<i>Cricetulus griseus</i>) (kindly provided by PD Dr. Stefan Müller (LMU, Munich, Germany), most probably immortalized by spontaneous transformation	DMEM supplemented with 10% FBS, 1% PS

irradiation (for reviews see e.g. Bradley et al. 1981, Hartwig 1994, Marples et al. 1997, Cremer and Cremer 2006). Among other Chinese hamster cells, Thomas and Christoph Cremer and co-workers used V79 cells (Zorn et al. 1976, Cremer et al. 1980, Cremer et al. 1981a, Cremer et al. 1981b, Cremer and Cremer 1986) for their extensive irradiation studies about 30 years ago (for review see Cremer and Cremer 2006). This was the main reason for choosing V79 cells for the experiments involving UV irradiation performed in this work. In addition, they exhibit good cell division rates and are easy to cultivate. Like all rodent cells, these cells miss the global genomic repair pathway of nucleotide excision repair as they are deficient in DDB2 (p48) (DNA damage binding protein 2) (Tang et al. 2000). Furthermore, the tumor suppressor p53 is mutated and not functional in V79 cells (Chaung et al. 1997). At first glance, these two characteristics might be considered detrimental for analyzing DNA damage. However, such deficiencies can also make the cells very suitable for this kind of studies as damages are less likely to be repaired, therefore the consequences of the damage induction are more severe and can be observed more easily.

HeLa Kyoto, HeLa (H2B-GFP), HeLa (H2B-mRFP), V79, V79 (H2B-mRFP, Rad51-GFP) and diploid Chinese hamster fibroblast cells are adherent cell types and have to be split after reaching confluency (see 3.2.1.3). Hematopoietic cells grow in suspension and usually did not need splitting (exception: CD34⁺ cells during the differentiation into monoblasts and myeloblasts; see step 23 in section 3.2.1.1) as they were used within a few days after isolation and cell numbers were usually low in comparison to the amount of medium and nutrients provided.

3.2.1.1 Isolation of hematopoietic cells

Hematopoietic cells were either isolated using the EasySep system (CD34⁺ cells, monoblasts, myeloblasts, monocytes) or using Histopaque gradients (granulocytes, mononuclear cells).

Mononuclear cells isolated using Histopaque gradients and subsequently selected for cells with the typical horseshoe-shaped nuclei were used for the immunofluorescence stainings of SC35 in combination with RNA Pol II Ser 5P and H3K4me3 in combination with H3K9me3 as in these cases no qualitatively sufficient staining could be obtained in monocytes isolated in the usual way using the EasySep system. Data presented in section 4.1 of the results demonstrate that in comparison to monocytes isolated in the usual way these cells showed very similar or even identical results regarding their chromatin pattern (see **Figure 25+29 A**

and **Figure 16 A+C**), segmentation profile of the DAPI signals (see **Figure 25 B + 29 B+C** and **Figure 16 B**), staining as well as distribution into chromatin classes of SC35 (see **Figure 25** and **Figure 23+24**), RNA Pol II Ser 5P (see **Figure 25** and **Figure 21**) and H3K4me3 (see **Figure 29** and **Figure 20-23**), as well as the number of nuclear pores / nucleus (547 ± 95 ($n=10$) in mononuclear cells vs. 453 ± 91 ($n=12$) in monocytes (compare **Figure 12**)), the number of pores / $5 \mu\text{m}^2$ (9.7 ± 2.0 ($n=10$) vs. 9.8 ± 2.0 ($n=12$)), the area containing one pore ($0.539 \pm 0.126 \mu\text{m}^2$ ($n=10$) vs. $0.531 \pm 0.116 \mu\text{m}^2$ ($n=12$)) and the number of RNA Pol II Ser 5P spots ($2\,367 \pm 398$ ($n=12$) vs. $2\,370 \pm 388$ ($n=12$)) (compare **Figure 24**). Relevant differences were only observed in the appearance of nucleoli, where in the mononuclear cells 3-5 slightly larger nucleoli were noted ($n=6$) in comparison to the 2-4 nucleoli in monocytes ($n=3$) (compare **Figure 19**), and in the number of positive pixels for RNA Pol II Ser 5P, with an average of $38\,199 \pm 6\,459$ ($n=12$) in mononuclear cells in comparison to the average of $26\,995 \pm 5\,418$ ($n=12$) in monocytes (compare **Figure 24**). Consequently, mononuclear cells isolated using Histopaque gradients and subsequently selected for cells with the typical horseshoe-shaped nuclei were a valid substitute for monocytes isolated in the usual way using the EasySep system.

Isolation of CD34⁺ cells, monoblasts, myeloblasts and monocytes using the EasySep system

CD34⁺ cells, a mixed population of undifferentiated cells (for details see section 2.4 in the introduction) positive for the surface antigen CD34 (cluster of differentiation 34), were isolated from umbilical cord blood. The blood was collected from normal deliveries according to the institutional guidelines for discarded material. The samples used here were not suitable for medical treatment (transplantations) as they exhibited insufficient cell numbers. Prior to processing the samples the donor's consent for the use in basic research was obtained. To obtain monoblasts and myeloblasts, freshly isolated CD34⁺ cells were differentiated for 7 days using cytokines (50 ng/ml SCF, 50 ng/ml FLT3-L, 10 ng/ml IL-3, 10 ng/ml IL-6). Subsequently, the cell population was separated: monoblasts are positive for the surface antigen CD14 (cluster of differentiation 14), while myeloblasts are negative for CD14 (Montanari et al. 2005). Monocytes were either also isolated from umbilical cord blood or preferably from peripheral blood. They are positive for the surface antigen CD14 (for review see Ziegler-Heitbrock and Hofer 2013).

For the isolation and the separation of all cell types the EasySep system was used: The cells are first incubated with a so-called Positive Selection Cocktail containing a bispecific Tetrameric Antibody Complex (TAC). This complex carries an antibody detecting one specific

surface antigen (here either CD14 or CD34) on the one side and an antibody detecting dextran on the other side. Then, magnetic iron beads coated with dextran are added. In addition to binding to the antigen-expressing cells, the TAC now also binds to the magnetic beads, as shown in **Figure 7**. Using a magnet, cells positive and negative for the respective antigen can now be separated.

The isolation procedures are based on Montanari et al. (2005) and are published in Hübner et al. (2015).

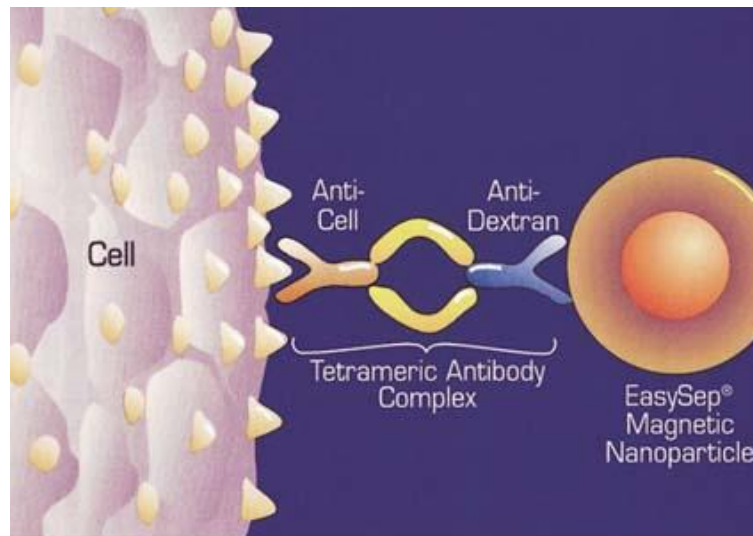


Figure 7: Schematic illustration of the working principle of the EasySep system. The bispecific Tetrameric Antibody Complex (TAC) binds to both, the antigen expressed on the cell surface and the dextran-coated magnetic bead. Figure taken from the product information sheet of the EasySep CD14 selection kit (EasySep). Copyright of STEMCELL Technologies. Image used with permission.

The cells were isolated by PhD Mariana Lomiento and the master students Fabiana Mammoli and Claudio Atene in the lab of Prof. Sergio Ferrari at the University of Modena and Reggio Emilia in Modena/Italy. I repeatedly followed the procedure very closely.

The purity of the CD34⁺ cells and monocytes after the isolation was checked using flow cytometry with antibodies against the surface antigens CD34 and CD14, respectively, and was around 95%. However, monocytes with the typical horseshoe-shaped nuclei accounted only for <10% of the total cell population. The main part of the isolated cells appeared larger (no measurements were performed) and exhibited more roundish/ellipsoid nuclei. Probably these cells are (early stages of) macrophages: monocytes can easily be activated to develop into this cell type. Their cultivation in tissue culture plates and/or in the presence of serum seems to be sufficient to lead to the attachment of the cells and with that to the initiation of the differentiation into macrophages (for overview see Saghaeian-Jazi et al. 2016).

In addition, the amount of CD14 positive and negative cells after the differentiation of monoblasts and myeloblasts from CD34⁺ cells was analyzed, again using flow cytometry with

antibodies against CD14. Around 15-20% of the entire population was positive for this surface antigen (= monoblasts) and accordingly, 80-85% of the cells were negative (= myeloblasts). These analyses were performed by the same collaborators as mentioned above, however not in my presence. Therefore no detailed protocols are included here.

The isolation or separation was done based on the manufacturer's guidelines.

Procedure:

1. When CD34⁺ cells or monocytes were isolated from blood samples, the procedure was started with step 2, when monoblasts and myeloblasts were separated it was started with step 12.
2. Umbilical cord blood or peripheral blood was diluted 1:4 with 1x PBS.
3. For each 30 ml of diluted blood one 50 ml tube with 15 ml Ficoll-Hypaque was prepared.
4. 30 ml of diluted blood were carefully loaded onto the Ficoll-Hypaque. This worked best when pipetting very slowly and holding the tube in a nearly horizontal position.
5. The samples were centrifuged for 30 min at 1800 rpm. The brake of the centrifuge was switched off in order to avoid swirls in the gradients.
6. The ring of mononuclear cells (upper cell fraction) was transferred into a new tube. The pipette was moved in circles through the cell layer to take up as many cells but as little Ficoll-Hypaque / plasma as possible.
7. The tubes were filled up with 1x PBS and gently mixed by inverting them several times. The samples were centrifuged for 10 min at 1400 rpm.
8. To wash the cells, the supernatant was carefully removed down to a few ml, the cell pellet was resuspended and step 7 was repeated.
9. Step 8 was repeated 1x or 2x.
10. Again, the supernatant was carefully removed down to a few ml and the cell pellet was resuspended.
11. The cells were counted with a hemocytometer (Neubauer): the cells were diluted 1:50 (or another appropriate ratio, dependent on cell density) in a 1:1 mixture of 1x PBS and trypan blue. After mixing well, 10 µl of this suspension were loaded onto one side of the hemocytometer. The cells in all four big squares touching the middle square were counted and the cell number per ml calculated as follows: $\frac{X}{4} \cdot 50 \cdot 10\,000 \cdot Y$ (cell number) $\cdot \frac{4}{4}$ (squares) $\cdot \frac{50}{50}$ (dilution) $\cdot \frac{10\,000}{10\,000}$ (factor between the volume of the chamber (0.1 µl) and 1 ml) $\cdot Y$ (ml cell suspension).
12. Step 7 was repeated.

When separating monoblasts and myeloblasts where the previous steps were skipped, the whole cell population was collected from the 6-well by thoroughly pipetting up and

down, especially at the periphery of the well, transferred into a tube and centrifuged according to step 7.

13. The supernatant was carefully removed completely and the cells were resuspended in EasySep medium as follows:

When isolating CD34⁺ cells:

- If the cell number was $<2 \times 10^7$ cells, the pellet was resuspended in 100 μ l medium.
- If 2×10^7 - 2×10^8 cells were obtained, the density was adjusted to 2×10^8 cells/ml.
- If the cell number accounted for 2 - 5×10^8 cells, the pellet was resuspended in 1 ml medium.

When isolating monocytes or separating monoblasts and myeloblasts:

- If the cell number was $<1 \times 10^7$ cells, the pellet was resuspended in 100 μ l medium.
- If 1×10^7 - 2.5×10^8 cells were obtained, the density was adjusted to 1×10^8 cells/ml.

14. The cells were transferred into a 5 ml polystyrene tube compatible with the EasySep magnet.
15. EasySep positive selection cocktail was added at a concentration of 100 μ l/ml cells (e.g. for 1 ml of cells 100 μ l of cocktail). The sample was mixed well and incubated for 15 min to allow binding of the TAC complex to the antigen-expressing cells.
16. Well resuspended (but not vortexed!) EasySep magnetic nanoparticles were added at a concentration of 50 μ l/ml cells (e.g. for 1 ml of cells 50 μ l nanoparticles). The sample was mixed well and incubated for 10 min to allow binding of the beads to the TAC complex.
17. EasySep medium was added to reach a total volume of 2.5 ml. The sample was gently mixed by pipetting up and down 2-3 times.
18. The tube was placed into the EasySep magnet (without cap) and was allowed to stand for 5 min.
19. The supernatant fraction was poured off by inverting the magnet with the tube in one continuous motion. The magnetically labeled cells remained in the tube. In case of isolating myeloblasts (CD14 negative!) the supernatant fraction was kept. The magnet with the tube was held in an inverted position for 2-3 sec, then it was returned to upright position. Drops that may have remained hanging at the opening of the tube were not shaken off.
20. The tube was removed from the magnet and 2.5 ml medium were added. The sample was gently mixed by pipetting up and down 2-3 times.
21. Steps 18-20 were repeated 4x (in the case of selecting for CD34⁺ cells) or 2x (in the case of selecting for CD14⁺ cells), to reach a total of 5 x 5 min or 3 x 5 min separation in the magnet.
22. The cells were counted again (see step 11) and resuspended in an appropriate amount of full medium (typically 1×10^6 cells/ml).

23. The cells were transferred into a 6-well-plate.

The isolated CD34⁺ cells and monocytes as well as the separated monoblasts and myeloblasts were allowed to recover from the isolation by incubation in the incubator overnight.

In order to differentiate CD34⁺ cells into monoblasts and myeloblasts, the cells were cultivated in the incubator for 7 days. During this time, the cells were split if their density got too high:

- An appropriate amount of fresh full medium was added to the cells in order to restore a cell density of roughly 1x10⁶ cells/ml.
- The cells were resuspended well.
- The cell suspension was distributed into several wells of the 6-well-plate.

Subsequently, the differentiated monoblasts and myeloblasts were separated according to this procedure (starting from step 12).

Materials:

6-well-plate Centrifuge (GS-6r, 1-14) EasySep cell isolation kit for the isolation of CD34- and CD14-positive cells including the EasySep positive selection cocktail, the EasySep magnetic nanoparticles, and the EasySep magnet Ficoll-Hypaque	Full medium Hemocytometer (Neubauer) Incubator PBS 1x Polystyrene tubes 5 ml Trypan blue Umbilical cord blood or peripheral blood or differentiated CD34 ⁺ cells
-----------------------------------------------------------------------------------------------------------------------------------------------------------------------------------------------------------------------------------------------------------	-----------------------------------------------------------------------------------------------------------------------------------------------------------------------------------------------

Isolation of granulocytes and mononuclear cells using Histopaque gradients

Granulocytes and mononuclear cells were isolated from peripheral blood using Histopaque gradients. The isolation was done based on the manufacturer's guidelines.

Procedure:

1. The Histopaque was taken out of the fridge at least one hour prior to use to acquire RT.
2. 1-2 drops of heparin (~1 drop of heparin for 10 ml blood) were added to a 50 ml tube. Peripheral blood was taken from a healthy donor (~10-15 ml) and immediately transferred into the prepared tube. The tube was gently mixed by inverting it several times.
3. Different from the manufacturer's guidelines the freshly isolated heparinized blood was diluted 1:3 to 1:4 with 1x PBS. The volume was brought up to multiples of 6 ml (see step 4 for explanation).
4. For each 6 ml of diluted blood one Histopaque gradient was prepared: 3 ml Histopaque 1119 was pipetted into a 15 ml polystyrene tube. It was tried to avoid drops at the walls of

the tube as these can influence the quality of the separation. Carefully 3 ml of Histopaque 1077 were layered on top. This worked best when pipetting very slowly and holding the tube in a nearly horizontal position.

- Carefully 6 ml of diluted blood were loaded onto each gradient, again pipetting very slowly and holding the tube in a nearly horizontal position.
- The samples were centrifuged at 700 g (corresponding to 2100 rpm in the centrifuge used here) for 35 min. The manufacturer indicates a centrifugation time of 30 min, however, the slightly elongated duration proved to result in a better separation. The values for acceleration and brakes on the centrifuge were set to a minimum to avoid swirls in the gradients.
- The tubes were carefully taken out. Several layers should be visible (from top to bottom): plasma, layer of mononuclear cells, Histopaque 1077, layer of granulocytes, Histopaque 1119, pellet of red cells (erythrocytes) (see **Figure 8**).

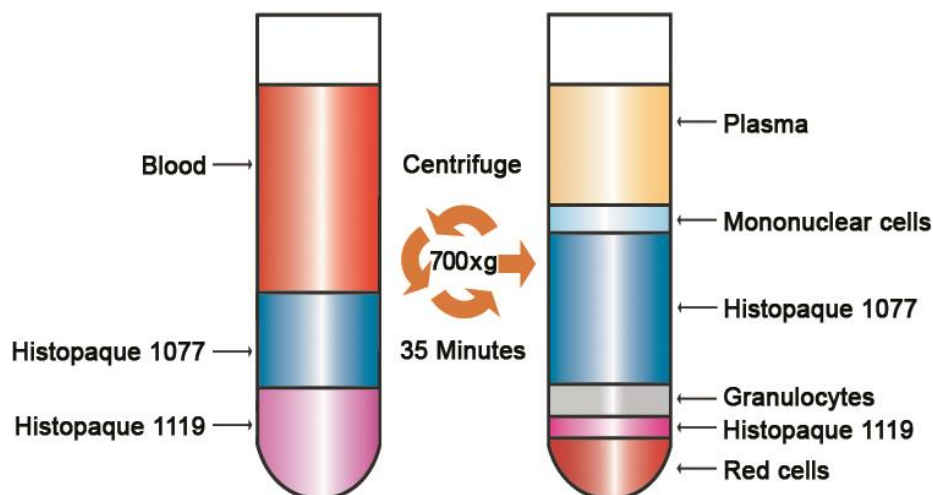


Figure 8: Scheme of the Histopaque gradient. Left: before centrifugation – 6 ml diluted blood on 3 ml Histopaque 1077 and 3 ml Histopaque 1119; right: after centrifugation – plasma, layer of mononuclear cells, Histopaque 1077, layer of granulocytes, Histopaque 1119, pellet of red cells (erythrocytes); both from top to bottom. Figure adapted from Frei (2011). Reproduced with permission from Merck KGaA, Darmstadt, Germany and/or its affiliates. Most probably due to the dilution of the blood with PBS the pattern after centrifugation was slightly different from the manufacturer.

- The plasma was aspirated down to 0.3 cm above the mononuclear cell layer (in contrast to the manufacturer's guidelines the supernatant was not aspirated until 0.5 cm within the cell layer in order not to lose any cells). The mononuclear cells were transferred into a new 15 ml polystyrene tube using a plastic Pasteur pipette. The pipette was moved in circles through the cell layer to take up as many cells but as little Histopaque or plasma as possible. Cells from two gradients were combined into one tube.
- The Histopaque 1077 was aspirated down to 0.3 cm above the granulocyte cell layer (again, as in step 8, here the supernatant was not aspirated until 0.5 cm within the cell layer as indicated by the manufacturer). The granulocytes were transferred into a new

- 15 ml polystyrene tube according to step 8.
10. The tubes were filled up with 1x PBS and gently mixed by inverting them several times. The samples were centrifuged at 200 g (corresponding to 1100 rpm in the centrifuge used here) for 10 min.
 11. The supernatant was aspirated down to about 1 ml and the cells were resuspended using plastic Pasteur pipettes. All tubes of one cell type were merged now.
 12. Steps 10 and 11 were repeated 2x.
 13. The cells were counted with a hemocytometer as described in step 11 of *Isolation of hematopoietic cells using the EasySep-system* in section 3.2.1.1. Using full medium the volume of the cell suspension was adjusted to 0.5 to 1 x 10⁶ cells/ml. The cells were incubated in the incubator and used within 3 h.

Materials:

Centrifuge (C3i, Rotana/S)	Incubator
Ethanol, absolute, 100%	PBS 1x (37°C)
Full medium (37°C)	Peripheral blood
Heparin	Plastic Pasteur pipettes, sterile
Histopaque 1119 and 1077	Polystyrene tubes 15 ml
Hypodermic needle (0.60x60)	Syringe, sterile, 20 ml, 1 ml
Hypodermic needle (0.90x40 mm) or Butterfly	Tourniquet

3.2.1.2 Thawing of cells

Different from the primary hematopoietic cells, all other cell types used in this work were kept in liquid nitrogen at -196°C and thawed a couple of days before use. As the freezing medium (see section 3.2.1.5) contains DMSO which prevents the formation of crystals damaging the cells during the freezing process but is toxic for the cells under cultivation conditions, it has to be diluted quickly upon thawing.

Procedure:

1. The cryotube with the cells was taken out of the liquid nitrogen tank and was allowed to thaw slightly.
2. About 5 ml full medium were added to a tissue culture flask (25 cm²).
3. A small amount of full medium was added to the cryotube and all liquid was transferred into the tissue culture flask. This procedure was repeated until the cell suspension was thawed completely and all cells were transferred.
4. The cells were incubated in the incubator. After the cells attached to the flask or latest after ~12 h, the medium was changed to remove all remaining DMSO.

5. The cells were incubated in the incubator for at least 2 days before using them for experiments. Occasionally the cells already had to be split the day after thawing them (see section 3.2.1.3).

Materials:

Cryo tube with cells Full medium (37°C)	Incubator Tissue culture flask (25 cm ²)
--------------------------------------------	---------------------------------------------------------

3.2.1.3 Splitting of cells

HeLa Kyoto, HeLa (H2B-GFP), HeLa (H2B-mRFP), V79, V79 (H2B-mRFP, Rad51-GFP) and diploid Chinese hamster fibroblast cells are adherent cell types and have to be split after reaching confluency using trypsin/EDTA. Trypsin is a protease that upon short incubation time only cleaves extracellular proteins. EDTA amplifies the efficiency of trypsin by complexing ions, especially Mg²⁺ and Ca²⁺, which are essential for adhesion proteins.

Split-ratios were roughly 1:12-1:20 for HeLa Kyoto, HeLa (H2B-GFP), HeLa (H2B-mRFP) and V79 cells, 1:6-1:10 for V79 (H2B-mRFP, Rad51-GFP) cells and 1:3-1:7 for diploid Chinese hamster fibroblasts. The cells were typically split every 2-3 days. Every 2-3 weeks the cell suspension was transferred into a new tissue culture flask and the old one was dismissed in order to prevent the selection for highly adherent cells.

Procedure:

1. The medium was aspirated from the tissue culture flask with the cells.
2. The cells were briefly washed with 1x PBS.
3. A small amount of trypsin/EDTA (for a 25 cm² flask 1 ml was sufficient, for a 75 cm² flask 2 ml) was added and the cells were put back into the incubator for a few minutes.
4. The cells were loosened by tapping the flask onto the bench several times. In a microscope it was checked if all cells detached. Otherwise, the cells were incubated in the incubator for some more minutes and the tapping was repeated.
5. An appropriate amount of fresh medium was added.
6. A suitable amount of cells was dismissed or transferred into a new flask. The cell suspension was brought up to an appropriate volume by adding new medium.
7. The cells were put back into the incubator.

Materials:

Full medium (37°C) Incubator Microscope (Axiovert 40 C) PBS 1x (37°C)	Tissue culture flask with cells Tissue culture flasks (25 cm ² , 75 cm ²) Trypsin/EDTA 1x (37°C)
--------------------------------------------------------------------------------	-------------------------------------------------------------------------------------------------------------------------------

3.2.1.4 Seeding of cells onto coverslips

To allow proper imaging on a microscope the cells have to be seeded onto coverslips.

Preferably number 1.5 coverslips with a thickness of 160-190 µm were used as they match the refractive index of the immersion oil best. If the samples were intended for 3D-SIM on the OMX, high precision coverslips with a thickness of 170 µm were used whenever possible, as the OMX 3D-SIM system is optimized for this thickness. As these coverslips are only available in a size of 18x18 mm, for most experiments they were cut to roughly 15x15 mm with a diamond pencil in order to save materials, especially antibodies. Note that the gridded Bellco coverslips used for correlative microscopy (see section 3.2.10) are only available in a thickness of 130-160 µm (so-called number 1.0 thickness). If the samples were intended for TEM, only Ø 12 mm round coverslips were used, as all other coverslip sized cause problems during the embedding procedure (see also section 3.2.8.1).

Hematopoietic cells grow in suspension and normally do not adhere to coverslips. However, a commonly used procedure that helps to attach cells onto glass is coating the coverslips with poly-lysine. Although even with this method still a lot of cells got lost during the subsequent experiment, usually a sufficient number remained on the coverslips. Also for experiments involving PCC-induction poly-lysine-coated coverslips were used in order to keep a higher number of PCC-cells on the glass.

For the experiments with CD34⁺ cells, monoblasts, myeloblasts and monocytes, the coating of the coverslips with poly-lysine and the seeding of the cells was done by PhD Mariana Lomiento and the master students Fabiana Mammoli and Claudio Atene in the lab of Prof. Sergio Ferrari at the University of Modena and Reggio Emilia in Modena/Italy.

Procedure:

1. When preparing samples for 3D-SIM, high precision coverslips of a thickness of 170 µm were cut to ~15x15 mm using a diamond pencil (see also above). The cut coverslips were checked for cracks to minimize the risk of them breaking during the subsequent experiment and thoroughly cleaned with 80% or 100% technical ethanol and Kimtech tissues to remove any small glass particles generated during cutting, which otherwise could later interfere with mounting or imaging.

This step was not performed under a laminar flow hood as the coverslips were sterilized in step 3.

Otherwise conventional coverslips (preferably number 1.5 with 160-190 μm thickness) were used.

2. In case specific cells had to be relocated during the experiment, either gridded Bellco coverslips were used (correlative microscopy experiments) (see pattern in **Figure 9 A**) or a grid was drawn onto the coverslips by hand (see pattern in **Figure 9 B**) using a diamond pencil (see section 3.2.10.1 for a detailed explanation):

- The grid size was kept as small as possible – 1x1 mm turned out very suitable as this still allowed freehand drawing of the grid without the need for a binocular.
- A numbering was included to allow the relocalization of the cells of interest. As with freehand drawing no exact pattern could be achieved and the numbers tended to stick out of “their” square, only every second square of the grid was numbered.
- It is important to not apply too much pressure when drawing the grid as this will result in breakage of the coverslip (in most cases not immediately when preparing it but later in the procedure) – a pressure as used when writing with a normal pencil is sufficient.

This step was not performed under a laminar flow hood as the coverslips were sterilized in step 3.

3. The coverslips were sterilized in 80% or 100% technical ethanol and individually placed in a vertical position by leaning them against the wall of an appropriate plate or Petri dish (typically 12-well-plates were used, alternatively 6-well-plates, quadriperms, 35 mm or 60 mm Petri dishes). The coverslips were laid down only after they were completely air-dried to prevent them from sticking to the well/dish.
4. For experiments with hematopoietic cells and when PCC was induced, the coverslips were coated with poly-lysine:
 - The coverslips were marked with a diamond pencil to be able to recognize the coated side later (typically the number 4 was written in one of the corners of each coverslip).
 - A 1.25 mg/ml poly-lysine solution was freshly prepared from a 10 mg/ml stock solution (1:8 dilution with $\text{H}_2\text{O}_{\text{bidest}}$). The solution was mixed well by vortexing.
 - An appropriate amount of the poly-lysine solution was distributed on each coverslip (e.g. 100-150 μl for a 15x15 mm coverslip; 50-100 μl for a \varnothing 12 mm round coverslip, 650 μl for a \varnothing 42 mm round coverslip). The very periphery of the coverslip was not covered as the cells there could not be imaged anyway, due to the mounting with nail polish in the final step of the experiment. The coverslips were let stand for (45-)50(-60) min.
 - The excess of poly-lysine was discarded or diluted by adding generous amounts of $\text{H}_2\text{O}_{\text{bidest}}$. Care was taken that the coverslips were completely covered with water and

did not float. If necessary, they were carefully pushed down using tweezers.

- The coverslips were washed 2x 5 min with H₂O_{bidest.} Again, care was taken that the coverslips were completely covered with water and did not float. If necessary, they were carefully pushed down using tweezers.

These washing steps are essential in order to remove all excessive poly-lysine as this is supposed to be toxic for the cells.

- The coverslips were air-dried in a vertical position by leaning them against the walls of the plate/dish. They were laid down only after they were completely air-dried to prevent them from sticking to the well/dish.
- On a microscope it was checked if the coated side faced up for all coverslips and they were turned if necessary.

If the coverslips were used for hematopoietic cells, the coating was not performed under a laminar flow hood, as these cells only were cultivated for maximally a few hours. For PCC experiments, however, all steps were performed under sterile conditions.

5. Adherent cells were trypsinized as described in 3.2.1.3. Cells growing in suspension (hematopoietic cells) were thoroughly resuspended using a 1000 µl pipette.
6. An appropriate amount of cell suspension was added onto each coverslip and if necessary fresh medium was added. The cells were seeded at such a density that they reached a confluency of 70-80% (30-50% for correlative microscopy experiments (see 3.2.10)) on the day they were used.

The cells were allowed to attach to the coverslips by incubating them in the incubator – adherent cells were cultivated at least overnight to achieve that they sit down properly; hematopoietic cells were incubated maximum for a couple of hours and used on the same day. The cell density and the time of attachment had to be adjusted for each hematopoietic cell type in order to maintain a reasonable number of cells on the coverslip throughout the whole experiment. Ideally 250 000 or 300 000 cells were applied to one coverslip. However, as the availability of the cells was typically limited, usually fewer cells were used, down to a minimum of 150 000. Cell numbers higher than 300 000 are not recommended as this also leads to a higher loss of cells in the course of the experiment. To shorten the time needed for the attachment and to save cells and expensive medium, the amount of medium was usually kept at a minimum and only the coverslip, not the entire well of the 12-well-plate was covered with the cell suspension. An overview of cell numbers, volumes and attachment times is given in **Table 2**.

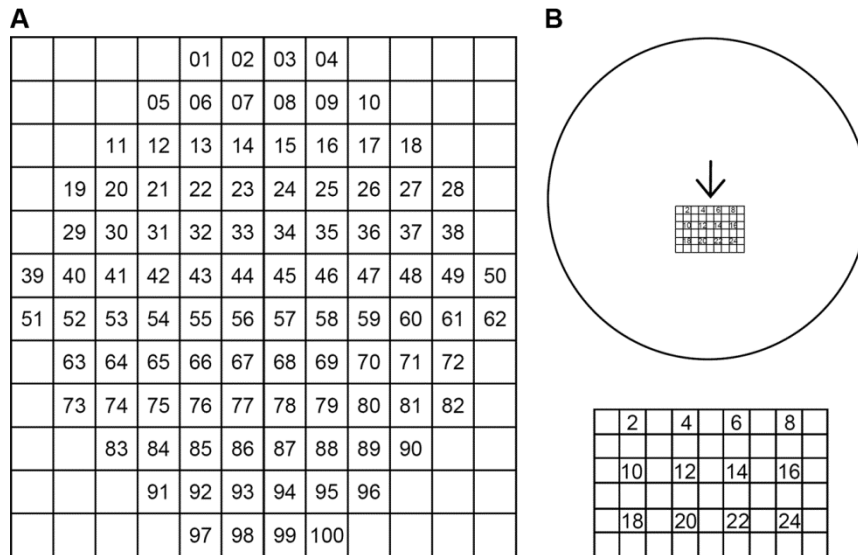


Figure 9: Patterns of the gridded coverslips. (A) Bellco coverslips (enlarged). **(B)** Handgridded coverslips. Top: Original size; positioning of the grid on a Ø 42 mm coverslip; the arrow turned out useful in finding the right orientation of the grid on the microscope. Bottom: Enlargement of the grid.

Table 2: Overview of cultivation conditions and times of attachment for the hematopoietic cell types. All cells were seeded into 12-well-plates on 15x15 mm coverslips. As the available cell number for CD34⁺ cells, monoblasts, myeloblasts, and monocytes was limited, only the coverslip was covered with the cell suspension in order to reduce the cell material needed but to maintain a consistent cell density. For granulocytes and mononuclear cells, enough cells were available to cover the whole well with the cell suspension. These culture conditions were published in Hübner et al. (2015).

Cell type	Number of cells/coverslip	Volume	Time of attachment
CD34+	150 000 - 250 000	150-250 µl	about 3 h
Monoblast	150 000 - 250 000	150-250 µl	about 2 h
Myeloblast	250 000 - 300 000	250-300 µl	about 2 h
Monocytes (from cord blood)	150 000 - 250 000	150-250 µl	1 h
Monocytes (from peripheral blood)	250 000 - 300 000	250-300 µl	1 h
Cell type	Number of cells / well	Volume	Time of attachment
Granulocytes	500 000 - 1 million	0.5-1 ml	30-60 min
Mononuclear cells	500 000 - 1 million	0.5-1 ml	45-60 min

Materials:

Coverslips (e.g. 18x18 mm high precision coverslips, 20x20 mm, 15x15 mm, 76x26 mm, Ø 12 mm, Ø 42 mm, etc.) Diamond pencil (Winter & Kraus, Bel-Art Products) Ethanol, technical, 80% or 100% Full medium (37°C) H ₂ O _{bidest} Incubator	Kimtech tissues Microscope (Axiovert 25 C, Axiovert 40 C, DC300f) Plates or Petri dishes (e.g. 12-well-plate, 6-well-plate, quadriperm, 35 mm or 60 mm Petri dishes, etc.) Poly-lysine stock solution Tissue culture flask or plate with cells Vortex
-----------------------------------------------------------------------------------------------------------------------------------------------------------------------------------------------------------------------------------------------------------------------------	----------------------------------------------------------------------------------------------------------------------------------------------------------------------------------------------------------------------------------------------------------------------

3.2.1.5 Freezing of cells

HeLa Kyoto, HeLa (H2B-GFP), HeLa (H2B-mRFP), V79, V79 (H2B-mRFP, Rad51-GFP) and diploid Chinese hamster fibroblast cells were frozen in liquid nitrogen when not needed for a longer time. Care has to be taken that the cell density is not too high when freezing the cells to ensure that the cells will grow well after re-thawing.

The freezing medium contains 10% DMSO which prevents the formation of crystals damaging the cells during the freezing process but is toxic for the cells under cultivation conditions. Therefore the freezing medium was pre-cooled and the procedure performed efficiently and on ice after adding DMSO to the cells.

Procedure:

1. The cells were trypsinized (see 3.2.1.3) and 10 ml fresh full medium was added.
2. The cell suspension was transferred into a 15 ml tube and centrifuged at 1000 rpm for 10 min at RT.
3. The supernatant was aspirated down to 0.5 ml and the cells were resuspended using a plastic Pasteur pipette.
4. Slowly 5-8 ml cold freezing medium were added.
5. The cell suspension was distributed to 3-5 cryotubes (dependent on cell density) and the tubes were immediately placed on ice.
6. The cells were frozen for 2 h at -20°C , then at least overnight (better: several days) at -80°C and finally in liquid nitrogen (-196°C). This step-wise freezing procedure should lead to the recommended drop in temperature of 1°C per minute.

Materials:

Centrifuge (C3i)	Full medium (37°C)
Cryo tubes	Liquid nitrogen tank
Freezer -20°C	Plastic Pasteur pipettes
Freezer -80°C	Styrofoam box with ice
Freezing medium (4°C)	Tissue culture flask (75 cm^2) with cells

3.2.2 Treatment of living cells

Until fixation of the cells, all procedures were performed under sterile conditions as described in section 3.2.1.

3.2.2.1 Hypotonic treatment

To induce chromatin decondensation the cells were subjected to hypotonic treatment, i.e. 0.3x PBS, prior to and during fixation. See the procedure in section 3.2.5.1 for a detailed protocol.

3.2.2.2 Damage induction using UV irradiation and caffeine-posttreatment

To induce damage using UV-light, a mercury UV-lamp mainly emitting light at a wavelength of 254 nm and a power of 500 $\mu\text{W}/\text{cm}^2$ at a working distance of 15 cm was used. With an irradiation time of 2 sec, this equaled an energy of 0.01 $\text{nJ}/\mu\text{m}^2$ ($= 10 \text{ J}/\text{m}^2$), resulting in an irradiation of about 0.5 nJ for an average nucleus with an area of 50 μm^2 . As the irradiation time was so short, it could not be stopped with a timer, but was simply counted. Therefore small deviations in the irradiation time could not be avoided.

After the irradiation the cells were incubated in 1 mM caffeine. Only with this posttreatment the effects induced by UV irradiation remained visible (Cremer et al. 1980, Cremer et al. 1981b, Cremer and Gray 1982, Cremer et al. 1982a). Typically, the cells were incubated for 16 h, as at this time point the highest number of abnormal nuclei was found.

This method is based on Cremer et al. (1980), Cremer et al. (1981a) and Cremer and Cremer (1986). The current setup described here was established by Dr. Marion Cremer (LMU, Munich, Germany) in our lab, is published in Hübner et al. (2009) and is illustrated in **Figure 10**.

Procedure:

1. A new plate or dish with full medium supplemented with 1 mM caffeine (1:100 dilution) was prepared.
2. Cells grown on coverslips were briefly washed in 1x PBS to remove the phenol red contained in the medium which possibly absorbs radiation.
3. The coverslips were placed in an empty plate or the lid of a plate under the UV-lamp (still switched off). Care was taken that the coverslips could be easily lifted again later and did not get stuck to the surface: e.g. when using a quadriperm dish the coverslips were placed in the upper part of the dish where the numbering of the wells allowed an easy lifting after irradiation; when working with 6-well- or 12-well-plates the coverslips were placed in the lid of the plate on the rim that marks the wells.

This step was performed quickly but thoroughly and not too many coverslips were handled at the same time to avoid that the cells dry out.

4. The cells were covered with a black screen and the lamp was switched on. After several

seconds when the lamp had reached full power the screen was removed and after 2 sec the lamp was switched off. It is strongly recommended to wear isolated gloves when doing this in order to protect one's skin from being irradiated.

5. The coverslips were transferred into the prepared plate with full medium supplemented with 1 mM caffeine. In case the coverslips got stuck to the surface despite the careful positioning according to step 3, 1x PBS was added to detach them.
6. The cells were typically incubated for 16 h in the incubator. Only for live cell observations incubation times deviated, see section 3.2.4.3.
7. The cells were fixed as described in section 3.2.5.

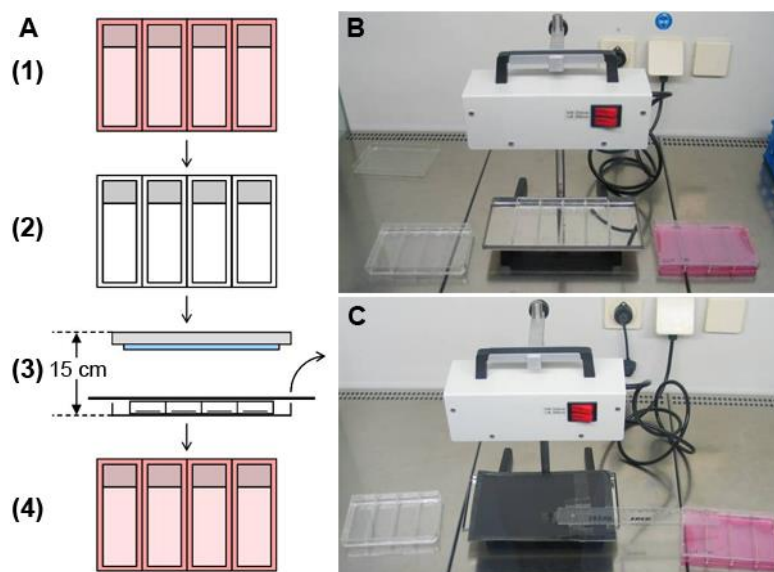


Figure 10: Illustration of the UV irradiation procedure. (A) The cells were (1) cultivated on coverslips in full medium (in the illustration 76x26 mm coverslips in quadriperms), (2) briefly washed in 1x PBS, (3) placed in an empty plate under the UV-lamp, covered with a black screen and irradiated by switching the lamp on, letting it reach full power, removing the screen and switching the lamp off after the desired irradiation time (here 2 sec). Subsequently (4) the coverslips were transferred into full medium supplemented with 1 mM caffeine. (B, C) Experimental setup without (B) and with (C) the black screen.

Materials:

Caffeine 100 mM	PBS 1x (37°C)
Cells grown on coverslips	Plates or Petri dishes (e.g. 12-well-plate, 6-well-plate, quadriperm, 35 mm or 60 mm Petri dishes, etc.)
Full medium (37°C)	UV-lamp with black screen
Incubator	
Isolated gloves	

3.2.2.3 Induction of premature chromosome condensation (PCC)

Premature chromosome condensation (PCC) was induced using calyculin A (a potent phosphatase inhibitor) as described in Bezrookove et al. (2003).

Procedure:

1. Cells grown on poly-lysine coated coverslips were washed 2x with minimal medium.
2. The cells were transferred into minimal medium supplemented with 80 nM calyculin A (1:1000 dilution).
3. The cells were incubated in the incubator for 1 h.
Calyculin A treated cells were handled with great care until fixation as the induction of PCC leads to the detachment of the cells. If the samples are shaken too much, the cells get lost.
4. The cells were fixed as described in section 3.2.5.

Materials:

Cells grown on poly-lysine coated coverslips Incubator	Minimal medium (37°) Calyculin A 80 µM
-----------------------------------------------------------	-------------------------------------------

3.2.2.4 Formation of hypercondensed chromatin (HCC)

Hypercondensed chromatin (HCC) was induced as described in Albiez et al. (2006) using medium with an osmolarity of 570 mOsm.

Procedure:

1. Cells grown on coverslips were transferred into HCC medium and incubated for 5 min.
2. The cells were fixed with PFA as described in section 3.2.5.1, but step 1 was skipped in order to avoid the reversion of the HCC effect.

Materials:

Cells grown on coverslips HCC medium (37°C)	Incubator
------------------------------------------------	-----------

3.2.2.5 Incorporation of BrdU for the detection of S phase cells

The incorporation of Bromodeoxyuridine (BrdU) is a commonly used method for the detection of S phase cells. BrdU is a thymidine analog and gets incorporated into newly synthesized DNA. The advantage of BrdU is that it is a small molecule that can penetrate the cell without permeabilization. Therefore all cells take it up. However, to make incorporated BrdU accessible for the antibodies in the detection step, the samples have to be denatured (see section 3.2.6.2).

Procedure:

1. Cells grown on coverslips were transferred into full medium supplemented with 16.7 μM (1:3000 dilution) or 25 μM (1:2000 dilution) BrdU and incubated for 30 min in the incubator. In the live cell observations occasionally BrdU concentrations and/or incubation times deviated, see section 3.2.4.3 and section 3.2.4.4.
2. Depending on the experiment, the cells were subjected to additional treatments, like e.g. PCC-induction (see section 3.2.2.3).
5. The cells were fixed as described in section 3.2.5.
6. BrdU was detected as described in section 3.2.6.2.

Materials:

BrdU 50 mM Cells grown on coverslips Full medium (37°C)	Incubator Laminar flow hood
---------------------------------------------------------------	--------------------------------

3.2.3 Microinjection of adherent cells

Microinjection is a helpful tool to directly deliver larger particles or molecules into cells, especially specifically into the nucleus. However, it is a laborious technique and only a limited number of cells can be injected in one experiment (~250 cells).

The microinjection method used here was initially developed by Dr. Hilmar Strickfaden (University of Alberta, Edmonton, Canada) (Strickfaden 2010) with basic input from other people (Dr. Marion Cremer (LMU, Munich, Germany); Dr. Christian Lanctôt (Charles University, Prague, Czech Republic); Dr. Heiner Albiez (formerly LMU, Munich, Germany)).

It was shown that the injection setup used in this work did not cause a DNA damage response with respect to single- and double-strand-breaks in microinjected nuclei (Strickfaden 2010). Also in other studies using different injections systems no increase in DNA damage after microinjection was found (Yamaizumi et al. 1986, Berneburg et al. 2000).

Here the microinjection of carboxylate-modified fluorescent beads (FluoSpheres) with a diameter of 20 and 40 nm into nuclei was established. As a positive control for the successful (nuclear) injection, fluorescently labeled dextrans were co-injected. Dextrans are glucose polymers of low toxicity and low reactivity (Pepperkok et al. 1988, Gorisch et al. 2003, Molecular Probes 2010) which are often used for cell tracing (for review see Molecular Probes 2010), as markers or controls in microinjection experiments (e.g. Featherstone et al. 2005, Derouazi et al. 2006) or for studies of the properties of the nucleus (e.g. Terasaki et al. 2001, Gorisch et al. 2003, Ihalainen et al. 2009). The dextrans used here were large enough to not

cross the nuclear envelope after nuclear injection and therefore allowed the discrimination of nuclear and cytoplasmically injected cells.

3.2.3.1 Dialysis of the 20 nm beads

While the 40 nm beads were commercially available without sodium azide as a preservative, the 20 nm beads were not and had to be subjected to dialysis prior to use.

When handling the beads all works were performed under a laminar flow hood to avoid the contamination of the beads. Only autoclaved 1x PBS was used. However, sterile conditions could not be maintained completely and therefore the procedure was repeated every few months.

Procedure:

1. A piece (about 10-15 cm) of dialysis tube was put into 1x PBS.
2. 1x PBS was filtered through a 0.2 μm filter and centrifuged for 30 min at 13 000 rpm to remove all precipitates. The upper 2/3s were transferred into a new tube, the rest was discarded.
3. The beads were diluted 1:500 in the filtered and centrifuged 1x PBS from step 2 and sonicated for 5 min.
4. A clamp was applied at the lower end of the tube, the tube was turned upside down and all PBS was drained. The bead solution was transferred into the tube and the tube was closed with a second clamp.
5. The tube was put in a large beaker filled with 1 l 1x PBS and stirred for 24 h at 4°C.
6. The PBS was exchanged and stirring was continued for 1-2 days at 4°C.
7. The tube was briefly washed in fresh 1x PBS.
8. The tube was taken out and drained well. Care was taken that especially at the ends all PBS was removed.
9. One of the clamps was opened and the bead solution was taken out with a pipette.
10. The beads were stored at 4°C.

Materials:

Fluorescent beads (FluoSpheres) Beaker, large Cold room (4°C) Dialysis clamps Dialysis tube	Laminar flow hood Magnetic stir bar PBS 1x Stirrer Ultrasonic bath
---------------------------------------------------------------------------------------------------------	--------------------------------------------------------------------------------

3.2.3.2 Pulling of microinjection needles

Needles for nuclear injections have to fulfill a decisive criterion: the tip has to be small enough to allow a gentle injection, but wide enough so that it does not get blocked immediately and allows the injection of at least 20 cells in a row. The latter point is especially problematic for the injection of beads.

Needles were pulled from borosilicate glass capillaries using a Flaming/Brown P-97 micropipette puller from Sutter with a 3x3 mm box filament. The filament heats up the glass until it gets soft and allows the capillary to be pulled to both sides, generating two microinjection needles. For setting up the puller in the right way, refer to the "Pipette Cookbook" from Sutter (Oesterle and Sutter Instrument 2011).

Despite numerous examples of specifications for pulling good microinjection needles are available in the literature (Oesterle and Sutter Instrument 2011, Zhang 2007, Wang et al. 2008, Mortusewicz 2004) and several people gave helpful advice (Dr. Alexander Kaiser (LMU, Munich, Germany), Dr. Joachim Gündel (BioMedical Instruments, Zöllnitz, Germany), Dr. Horatiu Fantana (formerly TU Dresden, Dresden, Germany)), none of those needles lead to acceptable results for the injection of fluorescent beads. However, through the combination of the knowledge gathered from these sources and extensive trial and error studies it was possible to establish parameters for the preparation of needles that give satisfying results.

Only the original Sutter glass capillaries with an outer diameter of 1.0 mm and an inner diameter of 0.5 mm turned out suitable for the injection of beads. However, the quality of the needles, i.e. their time of usability before getting blocked, was strongly dependent on factors like temperature, air pressure and most likely other factors that could not reliably be assessed. Much more stable results with regards to needle quality were obtained when using capillaries with an outer diameter of 1.5 mm and an inner diameter of 1.17 mm from Harvard Apparatus. However, those needles were only suitable for the injection of plasmids, proteins, etc., not for the injection of beads.

Procedure:

1. A ramp test was performed on the puller to determine the amount of heat required (see instructions in Oesterle and Sutter Instrument 2011). With a value of 563 the ramp value was in the recommended range of 550-650 for the 3x3 mm box filament used here.
It is not necessary to perform this test each time when preparing microinjection needles. However, it is absolutely essential after changing the filament or opening a new box of capillaries, and also after conducting other decisive changes on the machine (like alignments, adjusting position/shape of the filament, etc).
2. The settings on the puller were adjusted to the following values:

- For needles suitable for the injection of beads (Sutter capillaries):
Press = 600, Heat = ramp + 5 (here 568), Pull = 35, Vel = 45, Delay = 130.
If these settings did not produce needles of satisfying quality, it was tried to obtain better results by adjusting the Heat value to ramp (here 563), ramp -5 (here 558) or in rare cases also to ramp +10 (here 573). In rare cases, for unknown reasons, none of these parameters lead to satisfying results and microinjection was not possible on that day.
 - For needles suitable for the injection of proteins, plasmids, etc. (Harvard Apparatus capillaries):
Press = 400, Heat = ramp + 5 (here 568), Pull = 55, Vel = 90, Delay = 120.
3. A glass capillary was mounted into the puller and “PULL” was pressed.
 4. The needles were carefully demounted and kept in a closed box until use. Great care was taken that the tips did not get in contact with anything to avoid breakage. Boxes containing a strip of foam material with perpendicular cuts that safely hold the needles turned out very useful.
 5. Storage of the needles is not recommended. Even if stored in a closed box (to protect them from contamination) and only overnight, the quality of the needles clearly deteriorated.

Materials:

Box for storing the needles Glass capillaries (Sutter or Harvard Apparatus)	Micropipette puller P-97
--------------------------------------------------------------------------------	--------------------------

3.2.3.3 Preparation of the injection mix

As the needles easily get blocked, extensive care has to be taken to avoid precipitates and aggregates when preparing the injection mix.

Supplementing the injection mix with 1% BSA or using a special microinjection buffer (5 mM Hepes, 0.1 mM KCl, pH 7.0, supplemented with 1% BSA) as described in Esseling-Ozdoba (2007), did not improve the results of the microinjection of beads in our hands.

Procedure:

1. 1x PBS was filtered through a 0.2 µm filter and centrifuged for 30 min at 13 000 rpm to remove all precipitates. The upper 2/3s were transferred into a new tube, the rest was discarded.
2. An aliquot from the original stock (40 nm beads) or from the dialyzed beads (20 nm beads,

see section 3.2.3.1) was vortexed well. A 1:500 dilution of the beads was prepared using the filtered and centrifuged PBS of step 1 and sonicated for 5 min.

3. The injection mix was prepared by further diluting the beads to a final dilution of 1:5000, again using the PBS of step 1 (1:10 dilution). 1:10 dextran-FITC for the red fluorescent 40 nm beads or dextran-TRITC for the green fluorescent 20 nm beads was added. A final volume of 40 μ l turned out to be sufficient for one experiment. This means 4 μ l beads of the 1:500 pre-dilution and 4 μ l of dextran were added to 32 μ l 1x PBS.

In rare cases a higher or lower dilution of the beads was used (1:10 000 or 1:2000).

The injection mix was vortexed well.

4. The injection mix was kept on ice and used within the next few hours. It was not stored.

Materials:

Centrifuge (Biofuge pico) Dextran-FITC and -TRITC Fluorescent beads (FluoSpheres) PBS 1x Sterile filter 0.2 μ m	Styrofoam box with ice Syringe, sterile Ultrasonic bath Vortex
---------------------------------------------------------------------------------------------------------------------------------	-------------------------------------------------------------------------

3.2.3.4 Injection

Microinjection was performed on an Axiovert 200 M widefield microscope with an injection system from Eppendorf, consisting of (1) a micromanipulator (InjectMan) including a device for operating the movement of the needle and the injection arm itself and (2) a compressor (FemtoJet) providing the necessary pressure for the injection. This system allows a semi-automatic injection of the cells: the user only has to define the parameters for the injection and has to position the needle over the cells, but the system performs the actual injection in an automated way. Due to spatial reasons a long-distance condenser was used for the injections. Microinjection was performed with an angle of 45°.

Estimating the volume that is injected into the nucleus is very difficult. The amount of liquid flowing from the tip does not only depend on the settings for the injection pressure and the injection time, but also on the diameter of the needle and on the viscosity of the injection mix and inside the nucleus. Derouazi et al. (2006) determined an injected volume of ~180 fl in CHO cells. Assuming a similar nuclear volume of these cells and the HeLa Kyoto cells used here and the same level of inflation of the nuclei (see step 13 in the procedure below; also these authors observed a slight temporary inflation of the nuclei during the injection), roughly the same amount should have been injected here. Therefore, with $9 \cdot 10^{11}$ beads/ml for the 20 nm beads and $2.8 \cdot 10^{11}$ beads/ml for the 40 nm beads contained in the 1:5000 working dilution, roughly 164 and 51 beads per nucleus, respectively, would have been expected. In the

experiments conducted here, however, dramatically lower numbers of beads were observed after microinjection: on average only 8.0 beads per nucleus for the 20 nm beads (ranging between 0 and 24 beads), and 3.3 for the 40 nm beads (ranging between 0 and 11). These numbers equal an injection volume of only ~10 fl, corresponding to roughly 0.67% of the nuclear volume (estimated to be 1500 μm^3 , i.e. 1500 fl, on average). This small change in nuclear volume, however, is certainly way too small to explain the inflation of the nuclei observed during a successful injection. In contrast, the estimated injection volume of ~180 fl of Derouazi et al. (2006) equals 12% of the nuclear volume, which appears to be realistic. The small number of beads per nucleus therefore argues for an imbalanced distribution of the beads in the mix because potentially (1) the beads get stuck in the needle, (2) the compensation pressure is not high enough (although a constant flow from the tip was observed) and therefore medium gets soaked into the needle by capillary force, which then dilutes the injection mix, and/or (3) the spots detected are in fact clumped beads instead of single beads. In order to reach the number of expected beads, each clump would have to consist of 20 (20 nm) respectively 16 (40 nm) beads and therefore would have an approximate size of 60 nm for the 20 nm beads and 111 nm for the 40 nm beads (note that the packing density of beads is only about 74%). With the resolution limit of conventional light microscopy of about 200 nm laterally, it is not possible to use the fluorescent images to judge the size of the beads/aggregates. However, the protocol for the preparation of the injection mix contains several steps for vortexing and sonication (see section 3.2.3.3 above), making it more likely that the low number of beads results from the other technical difficulties than from the beads clumping together.

The use of oil immersion objectives is not recommended for the injection process itself. These objectives have a higher light yield due to their higher numerical aperture, which makes them the preferred choice for imaging, but which also causes a low depth of focus making microinjection a lot more difficult. Therefore air objectives with a larger depth of focus were used.

In order to reduce the light stress on the cells, the samples were typically incubated with 100 μM or 250 μM Trolox (this changed in the course of this thesis due to new information) and medium without phenol red was used (for detailed explanations on both see section 3.2.4). Furthermore, the microscope was equipped with a 12 V / 100 W halogen lamp and a 450 nm low-pass (LP) filter to minimize the exposure to UV light.

If the microinjection was followed by a live cell observation (see section 3.2.4.2) a microscope equipped with a well pre-heated heating chamber (37°C) was essential. For microinjection alone, this is highly recommended but not absolutely necessary.

Procedure:

1. ~20-24 h before starting the microinjection cells grown on Ø 42 mm coverslips or in MatTek dishes were transferred into full medium supplemented with 100 µM or 250 µM Trolox (1:1000 dilution). This was essential when subsequent live cell observations were performed (see also section 3.2.4). For microinjection alone, Trolox was not absolutely necessary. Preferably only cells that were seeded onto coverslips maximum 1 day prior to the microinjection were used.
2. The cells were briefly washed with 1x PBS and transferred into full live cell medium with 100 µM or 250 µM Trolox (1:1000 dilution).
3. If the cells were grown on Ø 42 mm coverslips the POC-R chamber was assembled as follows:
 - All parts were cleaned by washing them first in H₂O_{dest}, then in 80% technical ethanol. The parts were air-dried.
 - The coverslip with the cells was taken out of the medium and put in the black base plate of the POC-R chamber. A silicone seal (thick) was added on top, then a PTFE adapter (white plastic ring, ridge on the bottom side), followed by a screw ring (metal, broad groove on the upper side).
 - The chamber was screwed down tightly.
 - Full live cell medium with 100 µM or 250 µM Trolox (1:1000 dilution) was added onto the cells.
 - The lid was placed on the chamber.The procedure was performed thoroughly but efficiently to avoid that the cells dry out.
4. The underside of the dish/chamber was cleaned with 80% absolute ethanol and the sample was mounted on the microscope.
5. The lid of the chamber/dish was removed.

Contaminations of the sample were not observed when the incubation chamber of the microscope was occasionally thoroughly cleaned. As such an open system leads to evaporation of medium over time, the medium was changed about every 30 min to avoid major changes in osmolarity. Plastic Pasteur pipettes turned out to be suited best for this. It was tried to touch the dish as little as possible with the pipette to minimize the risk of moving the sample. Depending on the type of the experiment and/or the stability of the mounting, the POC-R chamber/dish was fixed on the stage using tape or Fixogum to avoid any movement and therefore loss of the stored positions.
6. The operating device (InjectMan) and the compressor (FemtoJet) were switched on. Care was taken that the tube from the injection arm was not yet attached to the compressor. The pressure was allowed to build up completely.
7. The settings shown on the display were adjusted to the following values: p_i (injection

pressure) = 150 hPa, t_i (duration of the injection) = 0.5 sec, p_c (compensation pressure; necessary for a constant flow out of the needle in order to prevent medium from entering into the needle and the tip from blocking) = 70 hPa.

8. The tube was connected to the compressor.
9. "Menu" was pressed on the compressor and a needle was prepared and inserted:
 - 3-4 μ l injection mix were loaded into the needle using a microloader. The microloader was introduced from the back and as far as it will go. In principle 1-2 μ l were easily enough, therefore the emphasis was put on avoiding air bubbles rather than on loading the whole volume.
 - It was checked if there were air bubbles in the needle. If so, it was tried to remove them by carefully tapping against the blunt end of the needle.
 - The needle was screwed into the mount of the injection arm.
 - "Menu" was pressed again.
 - After making sure that the needle was in the upmost position, the arm was brought into its working position and the needle was lowered until it dipped into the medium of the cell sample.

Care was taken not to damage the needle but to work efficiently at the same time, to prevent the formation of crystals at the tip of the needle due to evaporation, which might block the needle.

10. The 10x objective was used to check if a slight stream exited from the tip. If this was not the case "Clean" was pressed, if necessary several times. "Clean" usually also helped to remove small air bubbles at the very front of the tip. If still no stream was observed or a too strong stream, the needle was discarded and replaced by another one according to step 9.
11. The needle was brought down till short above the cell layer. It was constantly followed in the microscope and the focus was checked very carefully to avoid that the needle touches the coverslip and gets damaged. During this process the micromanipulator was switched from the course to the fine operating mode and the objective from the 10x to the 20x and then to the 40x objective.
12. The needle was moved over a cell nucleus (or over the cytoplasm, as needed) and slowly lowered further until a white spot on the nucleus got visible, i.e. where the needle touched the cell. "Limit" was pressed on the compressor and the needle was slightly moved upwards again.

This limit defines how far the needle will move down for the injection. It has to be newly set after moving larger distances on the coverslip (the coverslip is not completely plain and the sample not necessarily in an absolutely horizontal position) and after cleaning the tip (see step 14).

13. The tip was positioned over a cell nucleus and the injection button on the joystick of the operating device was pressed so that the system performed the injection with the parameters set in step 7.

The injection was successful if a gentle temporary inflation of the nucleus was visible during the injection. If this could not be observed, the needle was still set to high. In case a white spot remained on the nucleus after the injection the needle was set too low. Care was taken that the inflation was not too strong, as this typically resulted in a very short life span of the cells. The parameters for p_i and p_c (see step 7) were adjusted until good microinjection results were obtained. There are no clear rules for this as the parameters varied with each needle. Typically values of 70-250 for p_i and 30-70 for p_c turned out to be adequate.

14. The injections were continued until the needle was blocked. Typically 30-70 cells could be injected with one needle.

Sometimes the needle could be unblocked again by moving it up a bit, pressing “Home” to lift the needle entirely, pressing “Clean” to apply a higher pressure and lowering the needle again by pressing “Home” again. Subsequently, a new limit had to be set as described in step 12. However, in most cases the needle got damaged by this (recognizable by a now (very) prominent stream from the tip) and had to be replaced nevertheless.

15. Before moving to a new area on the sample the exact position of the injected cells was noted down in order to be able to relocalize them later (see also section 3.2.10.1).
16. Depending on the experiment, the cells were subjected to additional treatments like e.g. HCC-induction (see section 3.2.2.4) or a live cell observation was performed (see section 3.2.4.2).
17. The cells were fixed as described in section 3.2.5.

Materials:

Axiovert 200 M (widefield microscope)	Injection mix
Cells grown on gridded Ø 42 mm coverslips or in MatTek dishes with grid	Injection needles
Ethanol, absolute, 80%	Injection system
Ethanol, technical, 80%	PBS 1x
Microloader	Plastic Pasteur pipettes
Fixogum	POC-R chamber
Full live cell medium	Tape
	Trolox 100 mM or 250 mM

3.2.4 Microscopy of living cells in 3D and 4D

For live cell microscopy, particularly for long-term live cell observations, a microscope

equipped with an incubation chamber and a heating system is essential. Care has to be taken that the chamber is well-preheated (here to 37°C) before starting the experiment. It takes about 4 h until all components are equilibrated to the desired temperature so that shifts in focus during the acquisition are best possibly avoided. For stabilization it is important that all doors and openings of the chamber are closed. Mounting the sample on the microscope, of course, involves opening the chamber so that a certain drop in temperature is inevitable. This typically leads to a change in focus about 30 minutes after the system equilibrated again to the desired temperature. Therefore it is recommended to adjust focus and/or z-volume settings only after this time, especially when long-term observations are performed. However, despite these precautions changes in focus during the acquisition cannot be avoided entirely.

To compensate for this, a reliable contrast-based autofocus mechanism using transmission mode turned out very helpful, especially when no stacks were acquired but only single planes. Alternatively, when image stacks were acquired slight changes in focus were balanced by setting the range for the stack a bit larger than absolutely necessary. Whenever possible it is recommended to check – and if necessary to re-adjust – the focus during the experiment. However, this is of course only possible when only a limited number of time points and especially stage positions are recorded and if the time interval between the acquisitions is large enough.

Lateral shifts in xy-direction are normally not an issue, as the motorized stages of the microscopes are very precise. However, some experiments require the exchange of solutions inside the live cell chamber or dish while it is still mounted on the microscope and the subsequent acquisition of images at the same positions as before. In order to avoid any movements in lateral direction in these cases, depending on the stability of the mounting on the microscope, fixing the chamber/dish on the stage using tape or Fixogum is essential.

The cells were either seeded onto Ø 42 mm round coverslips for the POC-R chamber (for its assembly see step 3 in section 3.2.3.4) or into MatTek glass bottom dishes. These dishes are based on normal 35 mm Petri dishes but have a hole cut into the bottom and a coverslip attached from below, to allow high-resolution live cell observations with oil objectives (see section 3.2.10.1 for more details).

In case the relocalization of specific cells was necessary at some point in the experiment, gridded dishes/coverslips were used (see detailed information in section 3.2.1.4 and 3.2.10.1). Adherent cells were seeded onto coverslips 12-24 h before starting the live cell observation to allow them to attach completely. Granulocytes were seeded into poly-lysine coated MatTek glass bottom dishes only a few hours before use, as they grow in suspension and anyway only attach slightly to the slides. An overview of attachment times is given in **Table 2** in section 3.2.1.4, for a more detailed explanation of poly-lysine coated coverslips see also section 3.2.1.4.

Before starting live cell observations, especially long-term observations, the cells were treated with 100 μM or 250 μM Trolox (this changed in the course of this thesis due to new information) for minimum 12 h. Trolox is a vitamin E analog and antioxidant, providing protection against radicals and therefore reducing the effects of phototoxicity (compare Peus et al. 2001). For effective protection, Trolox should be added to the cells well before imaging as it is supposed to be incorporated only during mitosis. Medium containing Trolox was always prepared fresh. For short-term live cell observations it is not essential. However, Trolox did not entirely solve the problem of phototoxicity. Long-term observations with the acquisition of image stacks or with short intervals between time points still resulted in an increased fraction of apoptotic cells and/or impaired or even halted cell division rates.

To further reduce the effects of phototoxicity, the medium was changed from normal medium to live cell medium without phenol red 5-10 min before starting the live cell observations. Phenol red is supposed to increase the effect of phototoxicity by creating free radicals and to interfere with imaging. In addition, the live cell medium helps to maintain a stable pH outside a CO_2 -enriched atmosphere as it is not NaHCO_3^- but HEPES-buffered (Diaz et al. 1999). It is recommended to aliquot the medium into smaller amounts (e.g. 50 ml) to avoid repeated warming up and cooling down. When a new aliquot was started 25 mM HEPES was added in addition to the HEPES already contained in the medium (25 mM for DMEM, 10 mM for Ham's F-10), as this seemed to be not very stable. Cells that stop dividing during the live cell observation or are stuck in mitosis for hours are a clear indication for insufficient HEPES. However, it was also shown that HEPES generates cytotoxic products when exposed to light (Spierenburg et al. 1984), which could explain the phototoxic effects associated with intense imaging described above.

Nevertheless, with this combination of HEPES and Trolox undisturbed cell cycles were observed for up to 48 h when single images were acquired every 15 min (Hübner et al. 2009). To avoid a higher exposure to light as necessary, great care was taken that the areas chosen for imaging did not overlap, but that they were separated by minimum one field of view (the illuminated area is slightly bigger than the field of view).

Dr. Hilmar Strickfaden (University of Alberta, Edmonton, Canada) was a decisive help in conducting these live cell experiments as he established the basic requirements for live cell microscopy as it is described here in our lab (reducing phototoxicity by adding Trolox, using live cell medium, equipping the Axiovert 200 M widefield microscope with a 12 V / 100 W halogen lamp and a 450 nm LP UV-filter; setting up the contrast-based autofocus) (see also Strickfaden 2010).

The major part of these notes was adapted from Hübner et al. (2013).

3.2.4.1 Changes between normal and hypotonic conditions in granulocytes

Of all hematopoietic cell types studied in this work, granulocytes exhibit the most extreme nuclear morphology with a sharp separation of chromatin domains and interchromatin space. Therefore these cells were chosen to analyze the effects of changing from normal conditions (medium) to hypotonic conditions (0.3x PBS) and back. The experiments were performed on an UltraView VoX SDLSM or on a Leica SP5 CLSM.

This procedure was published in Hübner et al. (2015).

Procedure:

1. The medium was changed to full live cell medium. This was done very carefully in order not to lose all cells.
2. Hoechst 33342 was added at a concentration of 0.30-0.33 $\mu\text{g/ml}$ to the cells (1 mg/ml stock diluted 1:3000 or 1:3333) and the cells were stained for 30-45 min in the incubator. Subsequently, the medium was changed to fresh full live cell medium. When several samples were imaged, they were stained one after the other in order to prevent prolonged staining or washing out of the dye.
3. The underside of the dish was cleaned with 80% absolute ethanol and the sample was mounted on the microscope. Depending on the stability of the mounting, if necessary, the dish was fixed on the stage using tape or Fixogum.
4. An area was chosen where the cells appeared to be attached well, meaning where the cells shook less upon movement of the stage. One or two positions were chosen.
5. Image stacks were acquired with a z-spacing of 0.3 μm using the 405 laser for excitation and FITC filter settings for emission. The laser power was kept at a minimum to avoid bleaching and damaging the cells. If the signals were good enough, sensitivity was kept at 1 to avoid the images from getting noisy.

In order to compensate for slight changes in focus, the range for the stack was set a bit larger than absolutely necessary.

6. The medium was changed to 0.3x PBS using plastic Pasteur pipettes. Great care was taken to remove also the medium from the cavity as the exchange by diffusion seemed to be minimal. It was tried to touch the dish as little as possible with the pipette to minimize the risk of moving the sample. It could not be avoided that cells got lost during this process.
7. Immediately after the exchange was completed images were acquired equivalent to step 5. This resulted in an incubation time in 0.3x PBS of about 1 min.
8. The 0.3x PBS was changed back to full live cell medium equivalent to step 6.

9. Immediately after the exchange was completed images were acquired equivalent to step 5. After 3 min images were acquired again. This resulted in an incubation time in medium of about 1 min and 5 min, respectively.
10. Steps 6-9 were repeated as often as desired or until all cells got lost.

Materials:

Cells seeded into poly-lysine coated MatTek dishes	Incubator
Ethanol, absolute, 80%	Leica SP5 (CLSM)
Fixogum	PBS 0.3x (37°C)
Full live cell medium (37°C)	Plastic Pasteur pipettes
Hoechst 33342 1 mg/ml	Tape
	UltraView VoX (SDLSM)

3.2.4.2 Live cell observations after microinjection

After microinjection the cells were either imaged continuously for several hours (long-term observations) or soon after finishing the injections and again after several hours incubation in the incubator (short-term observations).

Long-term observations

Long-term observations of microinjected cells were either performed on an UltraView VoX SDLSM or on an Axiovert 200 M widefield microscope. In addition to an incubation chamber and a heating system available on both microscopes, the Axiovert 200 M was equipped with a 12 V / 100 W halogen lamp and a 450 nm LP filter to minimize the exposure to UV light.

While oil immersion objectives are not recommended for the injection process itself (compare section 3.2.3.4), they are essential for imaging the fluorescent beads. Due to their higher numerical aperture oil objectives collect more light and therefore provide brighter images with the same settings for exposure, laser power, etc. The dim signals of the beads are barely visible with air objectives. In addition, a higher numerical aperture also increases the resolution which also helps in imaging small objects like the 20 and 40 nm beads here.

Note that in this work for imaging with the UltraView VoX only MatTek dishes could be used, as with the available setup the POC-R chamber could not be mounted on the microscope.

Procedure:

1. The medium was replaced with fresh full live cell medium supplemented with 100 μ M or 250 μ M Trolox (1:1000 dilution).

2. The injected cells were relocalized based on the notes taken in step 15 of section 3.2.3.4 (see section 3.2.10.1 for a detailed explanation).
3. Appropriate areas for imaging were chosen (3-6 for imaging with the UltraView VOX, 2-4 for the Axiovert 200 M):
 - Using transmission mode it was made sure that the cells appeared normal: without blebs, with normal-sized nuclei, not more contrasted than non-injected cells. These characteristics are consequences of a too abrasive injection and the affected cells typically went into apoptosis within a short time.
 - With the help of the co-injected dextran it was checked if the cells were indeed injected in the nucleus (nuclear localization of the dextran).
 - Great care was taken that the areas chosen for imaging did not overlap, but that they were separated by minimum one field of view.
4. When imaging with the UltraView VoX image stacks of 6 or 8 images with a z-spacing of 2 μm were acquired every 15 min at each position with using roughly the following settings for the exposure: 200 ms at 3.0 V in transmission mode, 300 ms at 8% laser power for dextran-FITC and 1500 ms and 30% laser power for the 40 nm beads. Typically the signals were good enough to keep sensitivity at 1 to avoid the images getting noisy. In order to compensate for slight changes in focus, the range for the stack was set a bit larger than absolutely necessary.

On the Axiovert 200 M either single images or image stacks of 3 images with a z-spacing of 2 μm were acquired every 15 or 20 min at each position using roughly the following settings for the exposure: 250 ms at 3.0 V in transmission mode, 350 ms for dextran-FITC, 3000 ms for dextran-TRITC, 1500 ms for the 40 nm beads and 1000 ms for the 20 nm beads. Contrast-based autofocus in transmission mode used at each position allowed limiting the acquisitions to such a small number.

Typically the live cell observations were started within 4 h after microinjection.

Materials:

Axiovert 200 M (widefield microscope) with 40x oil immersion objective Ethanol, absolute, 80% Full live cell medium (37°C)	Microinjected cells in a MatTek dish or in the POC-R chamber Trolox 100 mM or 250 mM UltraView VoX (SDLSM)
----------------------------------------------------------------------------------------------------------------------------------	------------------------------------------------------------------------------------------------------------------

Short-term observations

Short-term observations were performed on an Axiovert 200 M widefield microscope. As described above in the section *Long-term observations*, the microscope was equipped with an incubation chamber, a heating system, a 12 V / 100 W halogen lamp and a 450 nm LP filter

and oil immersion objectives were used for imaging.

Procedure:

1. Steps 1-3 were performed as described in the section *Long-term observations* above. However, as the imaging was very limited here, Trolox was not absolutely necessary (although typically added; concentration: 100 μ M or 250 μ M (1:1000 dilution)) and also overlapping areas were imaged.
2. Either one single image or one image stack of 7 or 10 images with a z-spacing of 1 or 2 μ m was acquired at each position using roughly the following settings for the exposure: 250 ms at 3.0 V in transmission mode, 350 ms for dextran-FITC, 3000 ms for dextran-TRITC, 1500 ms for the 40 nm beads and 1000 ms for the 20 nm beads. Due to the limited number of acquisitions focus was adjusted manually.
Typically images were taken within 2 h after microinjection.
3. The cells were put back in the incubator for several hours or overnight.
4. The cells were relocalized again as described in step 2 in the section *Long-term observations* above.
5. Images were acquired again according to step 2.

Materials:

Axiovert 200 M (widefield microscope) with 40x oil immersion objective Full live cell medium (37°C)	Microinjected cells in a MatTek dish or in the POC-R chamber Trolox 100 μ M or 250 μ M
-----------------------------------------------------------------------------------------------------------	------------------------------------------------------------------------------------------------------

3.2.4.3 Live cell observations after UV/caffeine treatment

After UV/caffeine treatment (see section 3.2.2.2) both, long-term observations as well as short-term observations with a subsequent “correlative fixation” (see below) were performed on an Axiovert 200 M widefield microscope. In addition to an incubation chamber and a heating system, the microscope was equipped with a 12 V / 100 W halogen lamp and a 450 nm LP filter to minimize the exposure to UV light.

The procedures described here were published in Hübner et al. (2009).

Long-term observations

These live cell observations were done during my Diploma thesis (Hübner 2008) in the same lab. But as these data are essential for completing the overall picture of the consequences of

UV/caffeine treatment, they are included here.

Image sequences of control cells without treatment were acquired by Dr. Hilmar Strickfaden (University of Alberta, Edmonton, Canada) and Dr. Marion Cremer (LMU, Munich, Germany) in our lab.

Procedure:

1. 20-24 h before starting the live cell observation the medium was supplemented with 100 μ M Trolox (1:1000 dilution).
2. The cells were UV irradiated as described in section 3.2.2.2 and incubated for ~45 min in full medium supplemented with 1 mM caffeine (1:100 dilution) and 100 μ M Trolox (1:1000 dilution).
3. The normal medium was exchanged to full live cell medium supplemented with 1 mM caffeine (1:100 dilution) and 100 μ M Trolox (1:1000 dilution). The POC-R chamber was assembled as described in step 3 of section 3.2.3.4.
4. The underside of the chamber was cleaned with 80% absolute ethanol and the sample was mounted on the microscope.
5. 10-11 positions were chosen for the observation.
6. Starting 1 h after the irradiation images were acquired every 10 min at each position using 50-100 ms exposure at 3.0 V for transmission mode and about 300-500 ms for recording mRFP fluorescence. Contrast-based autofocus in transmission mode made it possible to record only single images (no stacks) at each position so that the light stress on the cells could be reduced to a minimum. The acquisitions were stopped 16 h 10 min to 19 h 40 min after the UV irradiation.
7. For imaging untreated control cells step 2 was skipped and the medium was not supplemented with caffeine in step 3. Images were acquired every 15 min as described in step 6 for a total duration of 48 h.

Materials:

Axiovert 200 M (widefield microscope) with 40x and 63x oil immersion objective Caffeine 100 mM Cells grown on \varnothing 42 mm coverslips Ethanol, absolute, 80%	Full live cell medium (37°C) Full medium (37°C) POC-R chamber Trolox 100 mM
------------------------------------------------------------------------------------------------------------------------------------------------------------------------------	--------------------------------------------------------------------------------------

Short-term observations with subsequent “correlative fixation”

In order to correlate the patterns of DAPI stained DNA observed after fixing the cells with paraformaldehyde (PFA), which corresponded to the phenotypes observed in the living cells,

with the deviating chromatin patterns occurring after methanol / acetic acid (MAA) fixation, a “correlative MAA fixation” – i.e. fixation under live cell conditions thus allowing imaging of the same cells before, during and after MAA fixation – was performed.

Procedure:

1. 20-24 h before starting the live cell observation the medium was supplemented with 100 μ M or 250 μ M Trolox (1:1000 dilution).
2. The cells were UV irradiated as described in section 3.2.2.2 and incubated for 16 h to 20 h 30 min in full medium supplemented with 1 mM caffeine (1:100 dilution) and 100 μ M or 250 μ M Trolox (1:1000 dilution).
3. At least 5-10 minutes prior to mounting the cells on the microscope, the normal medium was exchanged to full live cell medium supplemented with 1 mM caffeine (1:100 dilution) and 100 μ M or 250 μ M Trolox (1:1000 dilution). The POC-R chamber was assembled as described in step 3 of section 3.2.3.4.
4. The underside of the chamber was cleaned with 80% absolute ethanol and the sample was mounted on the microscope. The chamber was fixed on the stage using tape in order to avoid movements when solutions inside the chamber were changed in the subsequent steps.
5. 12-15 positions were chosen for the observation.
6. One image stack of (4 or) 5 images with a z-spacing of 3 (or 4) μ m was acquired at each position. 50-100ms at 3.0 V in transmission mode and about 300-500 ms for recording mRFP were used. Contrast-based autofocus in transmission mode used at each position allowed limiting the number of acquisitions at each position to this small number.
7. If the cells were pulsed with BrdU to detect S phase cells (compare section 3.2.2.5) the following steps were included:
 - Using plastic Pasteur pipettes the medium was changed to full live cell medium supplemented with 16.7 μ M BrdU (1:3000 dilution) and 250 μ M Trolox (1:1000 dilution). It was tried to touch the dish as little as possible with the pipette to minimize the risk of moving the sample.
 - Image stacks were acquired as described in step 6.
 - After images were recorded at all positions (with 12 positions this took about 10-12 min with the settings described here) the cells were washed with full live cell medium supplemented with 1 mM caffeine (1:100 dilution) and 250 μ M Trolox (1:1000 dilution). It is not recommended to shorten the BrdU pulse to less than 10 min as in this short time hardly enough modified nucleotides get incorporated to be visible after detection.
 - Image stacks were acquired every 15 min for a total of 45 min (= 15, 30, 45 min after

BrdU), again as described in step 6.

As BrdU had to be detected (see section 3.2.6.2) after completing the live cell observation, which required removing the sample from the microscope, it was essential to write down the positions chosen in step 5 very precisely in order to be able to relocalize the observed cells after the detection (compare also the notes on relocalizing cells in section 3.2.10.1). Gridded coverslips were absolutely essential in this case.

8. With the sample still mounted on the microscope fixing the cells with MAA (compare section 3.2.5.2) was started by changing the medium to a mixture of 1/3 0.56% KCl and 2/3 1 x PBS using plastic Pasteur pipettes. It was tried to touch the dish as little as possible with the pipette to minimize the risk of moving the sample. The solution was changed again to make sure that all medium was removed. The sample was let stand briefly.
9. The 1/3 KCl solution was changed to pure 0.56% KCl, again using a two-step-approach as described in step 8. The cells were incubated for 10-15 min, depending on how many positions were imaged – the more positions the more time is needed for imaging in step 10 and the incubation in 0.56% KCl should not exceed 25 min in total.
10. Image stacks were acquired as described in step 6.
11. Ice-cold fixative (methanol / acetic acid) was added dropwise to the KCl-solution. Repeatedly a part of the mixture was removed and fresh fixative was added until the complete replacement of the fixative was accomplished. The fixative was always kept on ice.
Fixation was completed 17 h 15 min to 21 h after UV irradiation (depending on when the experiment was started; compare step 1).
12. The fixative was removed completely and the cells were air-dried (still mounted on the microscope). Great care was taken that the sample was completely dry before continuing. To guarantee this the samples were dried for 15-25 min.
13. The cells were stained with 0.2 µg/ml DAPI (freshly diluted in 1x PBS from a 10 µg/ml solution (1:50 dilution)) for a few minutes. A generous amount of staining solution (about 4 ml) was added in order to make sure that the whole chamber was covered.
14. The cells were washed with 1x PBS.
15. Image stacks were acquired as described in step 6. As the cells were very flat after MAA fixation it could happen that the autofocus was not precise enough and all images of the stack were out of focus. In these cases the focus was adjusted manually and single images (no stacks) were acquired again at each position.
16. If the cells were labeled with BrdU it was detected as described in section 3.2.6.2.

Materials:

Axiovert 200 M (widefield microscope) with 40x oil immersion objective	KCl 0.56% (37°C)
BrdU 50 mM	Methanol / acetic acid (ice-cold = -20°C)
Caffeine 100 mM	PBS 1x (37°C)
Cells grown on Ø 42 mm coverslips	Plastic Pasteur pipettes
DAPI stock 10 µg/ml	POC-R chamber
Ethanol, absolute, 80%	Styrofoam box with ice
Full live cell medium (37°C)	Tape
Full medium (37°C)	Trolox 100 mM or 250 mM

3.2.4.4 Live cell observations after the induction of premature chromosome condensation (PCC)

After PCC induction (see section 3.2.2.3) both, long-term observations with PCC release as well as short-term and long-term observations with a subsequent “correlative fixation” (compare *Short-term observations with subsequent “correlative fixation”* in section 3.2.4.3) were performed on an Axiovert 200 M widefield microscope. In addition to an incubation chamber and a heating system, the microscope was equipped with a 12 V / 100 W halogen lamp and a 450 nm LP filter to minimize the exposure to UV light.

Long-term observations with PCC induction and release**Procedure:**

1. 20-24 h before starting the live cell observation the medium was supplemented with 250 µM Trolox (1:1000 dilution).
2. At least 5-10 minutes prior to mounting the cells on the microscope, the normal medium was exchanged to full live cell medium supplemented with 250 µM Trolox (1:1000 dilution). The POC-R chamber was assembled as described in step 3 of section 3.2.3.4.
3. The underside of the chamber was cleaned with 80% absolute ethanol and the sample was mounted on the microscope. The chamber was fixed on the stage using tape in order to avoid movements when solutions inside the chamber were changed in the subsequent steps.
4. 8 positions were chosen for the observation.
5. Images were acquired at each position using 50-100 ms exposure at 3.0 V for transmission mode and about 300-500 ms for recording mRFP fluorescence. Contrast-based autofocus in transmission mode made it possible to record only single images (no stacks) at each position so that the light stress on the cells could be reduced to a minimum.

6. The cells were labeled with BrdU to allow the detection of S phase cells (compare section 3.2.2.5):
 - Using plastic Pasteur pipettes the medium was changed to full live cell medium containing 16.7 μM BrdU (1:3000 dilution) and 250 μM Trolox (1:1000 dilution). It was tried to touch the dish as little as possible with the pipette to minimize the risk of moving the sample.
 - The cells were incubated for 30 min with BrdU. During this time images were acquired every 15 min as described in step 5.
7. BrdU was removed by washing 2x with minimal live cell medium supplemented with 250 μM Trolox (1:1000 dilution). Again, it was tried to touch the dish as little as possible with the pipette to minimize the risk of moving the sample.
8. PCC was induced as described in section 3.2.2.3 by changing the medium to minimal live cell medium supplemented with 80 nM Calyculin A (1:1000 dilution) and 250 μM Trolox (1:1000 dilution) equivalent to step 7 (but one exchange was sufficient). The cells were incubated for 1 h. During this time images were acquired every 5 min as described in step 5.
9. The cells were washed 3x with full live cell medium supplemented with 250 μM Trolox (1:1000 dilution) equivalent to step 7.
10. Images were acquired every 15 min as described in step 5 for 22 h, i.e. up to 23 h 35 min total duration of the experiment.
11. For imaging untreated control cells only 3 positions were chosen. In step 7 the cells were washed 2x with full live cell medium instead of minimal live cell medium and steps 8-10 were skipped.

Instead, images were acquired every 5 min for 1 h (equivalent to the imaging during PCC induction in step 8) as described in step 5, then the rate was decreased to one acquisition every 15 min (equivalent to step 10). In total, the cells were imaged up to 40 h 15 min.
12. Due to the outcome of the experiment, i.e. the PCC induction being not reversible (see section 4.3.1.1), other than planned the cells were not fixed after the completion of the live cell acquisitions and consequently also the BrdU detection was omitted.

Materials:

Axiovert 200 M (widefield microscope) with 40x oil immersion objective	Full live cell medium (37°C)
BrdU 50 mM	Minimal live cell medium (37°C)
Calyculin A 80 μM	Plastic Pasteur pipettes
Cells grown on poly-lysine coated \varnothing 42 mm coverslips	POC-R chamber
Ethanol, absolute, 80%	Tape
	Trolox 250 mM

Short- and long-term observations with subsequent “correlative fixation”

Partially these experiments were performed by Korbinian von Heckel, Stephanie Peklo and Mareike Fitschen during their “Forschungspraktikum” (research internship) respectively bachelor thesis (Fitschen 2009) under my instruction and supervision.

Procedure:

1. 20-24 h before starting the live cell observation the medium was supplemented with 250 μ M Trolox (1:1000 dilution).
2. At least 5-10 minutes prior to mounting the cells on the microscope, the normal medium was exchanged to full live cell medium supplemented with 250 μ M Trolox (1:1000 dilution). The POC-R chamber was assembled as described in step 3 of section 3.2.3.4.
3. The underside of the chamber was cleaned with 80% absolute ethanol and the sample was mounted on the microscope. The dish was fixed on the stage using tape in order to avoid movements when solutions inside the chamber were changed in the subsequent steps.
4. 6-20 positions were chosen for the observation.
5. If a long-term observation was included (ranging between 17 h 45 min and 23 h), images were acquired every 15 min at each position using 150-200 ms exposure at 3.0 V for transmission mode and 500-600 ms for recording mRFP fluorescence. Contrast-based autofocus in transmission mode made it possible to record only single images (no stacks) at each position so that the light stress on the cells could be reduced to a minimum. If no long-term observation was performed, images were either acquired as described above (one time point) or one image stack of 7 images with a z-spacing of 3 μ m was acquired at each position.
6. The cells were labeled with BrdU to allow the detection of S phase cells (compare section 3.2.2.5):
 - Using plastic Pasteur pipettes the medium was changed to full live cell medium supplemented with 16.7 μ M (1:3000 dilution), 25 μ M (1:2000 dilution) or 33.3 μ M (1:1500 dilution) BrdU and 250 μ M Trolox (1:1000 dilution). It was tried to touch the dish as little as possible with the pipette to minimize the risk of moving the sample.
 - The cells were incubated for 30 min with BrdU. During this time images were acquired every 15 min or once after 20 min incubation as described in step 5.
7. BrdU was removed by washing with minimal live cell medium supplemented with 250 μ M Trolox (1:1000 dilution). Again, it was tried to touch the dish as little as possible with the pipette to minimize the risk of moving the sample.
8. PCC was induced as described in section 3.2.2.3 by changing the medium to minimal

medium supplemented with 80 nM Calyculin A (1:1000 dilution) and 250 μ M Trolox (1:1000 dilution) equivalent to step 7. The cells were incubated for 1 h. During this time images were acquired every 5 (or 10) min as described in step 5.

9. With the sample still mounted on the microscope fixing the cells with MAA (compare section 3.2.5.2) was started by changing the medium to a mixture of 1/3 0.56% KCl and 2/3 1 x PBS using plastic Pasteur pipettes. It was tried to touch the dish as little as possible with the pipette to minimize the risk of moving the sample. The sample was let stand briefly.
10. The 1/3 KCl solution was changed to pure 0.56% KCl as described in step 9 and the cells were incubated for 20-25 min. During this time images were acquired every 5-10(-20) min as described in step 5.
11. The cells were fixed and stained with DAPI as described in steps 11-14 of *Short-term observations with subsequent "correlative fixation"* in section 3.2.4.3.
12. Images were acquired as described in step 5. As the cells were very flat after MAA fixation it could happen that the autofocus was not precise enough and all images of the stack were out of focus. In these cases the focus was adjusted manually and single images (no stacks) were acquired again at each position.
13. BrdU was detected as described in section 3.2.6.2.

Materials:

Axiovert 200 M (widefield microscope) with 40x oil immersion objective	KCl 0.56% (37°C)
BrdU 50 mM	Minimal live cell medium (37°C)
Calyculin A 80 μ M	PBS 1x (37°C)
Cells grown on poly-lysine coated \varnothing 42 mm coverslips	Plastic Pasteur pipettes
Ethanol, absolute, 80%	POC-R chamber
Full live cell medium (37°C)	Tape
	Trolox 250 mM

3.2.4.5 Stepwise induction of hypercondensed chromatin (HCC)

As the formation of hypercondensed chromatin (HCC) is a very rapid process a stepwise induction can be performed in order to facilitate imaging (Albiez et al. 2006). After imaging in normal medium (290 mOsm), the cells were incubated in media with osmolaric concentrations of 340 mOsm, 425 mOsm and 570 mOsm for 5 min each. For control cells, images were taken every 5 min for 15 min total duration. The images were acquired on an UltraView VoX SDLMS. The procedure described here was published in Hübner et al. (2013).

Procedure:

1. 12-24 h before starting the live cell observation the medium was supplemented with 250 μ M Trolox (1:1000 dilution).
2. At least 5-10 minutes prior to mounting the cells on the microscope, the normal medium was exchanged to full live cell medium.
11. The underside of the dish was cleaned with 80% absolute ethanol and the sample was mounted on the microscope. Depending on the stability of the mounting, if necessary, the dish was fixed on the stage using tape or Fixogum.
3. A stack with a z-spacing of 0.2 μ m was acquired using 20% laser power and 250 ms exposure in normal medium (= stack 1). If the signals were good enough, sensitivity was kept at 1 to avoid the images from getting noisy. In order to compensate for slight changes in focus, the range for the stack was set a bit larger than absolutely necessary.
4. The normal medium was changed to HCC live cell medium with an osmolarity of 340 mOsm using plastic Pasteur pipettes. Great care was taken to remove also the medium from the cavity as the exchange by diffusion seemed to be minimal. It was tried to touch the dish as little as possible with the pipette to minimize the risk of moving the sample.
5. After 4 min a stack (= stack 2) was acquired as described in step 11. This lead to a total incubation time of 5 min. During the 4 min incubation, position and focus of the sample were checked and if necessary readjusted.
6. Steps 4 and 5 were repeated with HCC live cell media of an osmolarity of 425 mOsm and 570 mOsm (= stacks 3 and 4, respectively).
7. For control cells, steps 4-6 were skipped and images were acquired every 5 min in normal full live cell medium for a total duration of 15 minutes (= 4 stacks) instead.
8. The cells were fixed as described in section 3.2.5.1.

Materials:

Cells grown in MatTek dishes	Plastic Pasteur pipettes
Ethanol, absolute, 80%	Tape
Fixogum	Trolox 250 mM
Full live cell medium (37°C)	UltraView VoX (SDLMS)
HCC live cell media (340, 425, 570 mOsm) (37°C)	

3.2.5 Cell fixation

For the use after cell fixation, PBS-based solutions were supplemented with 0.02-0.04% sodium azide to avoid bacterial growth.

3.2.5.1 Paraformaldehyde (PFA) fixation

Paraformaldehyde (PFA) fixes the cells by crosslinking proteins, nucleic acids, and lipids via different reactive groups, especially NH₂-groups, and maintains the 3D-morphology of the cell. PFA should always be prepared fresh or kept at -20°C and thawed shortly before use. Once an aliquot is thawed the leftovers should not be frozen again, as reusing this fixative typically leads to high autofluorescence background levels.

Drying out of the samples has to be avoided by all means. Plastic Pasteur pipettes turned out to be most suitable for exchanging buffers and solutions. The next solution needed was already taken up with the pipette before the old one was removed from the sample and the samples were processed one after the other. For timed incubation steps, the timer was started when the solution of the first sample was changed.

Typically, the cells were fixed with 4% PFA. For 3D-SIM, however, Markaki et al. (2012) showed that fixation with 2% PFA yields an even better structural conservation of chromatin. Therefore all hematopoietic cell samples intended for 3D-SIM and all samples for correlative microscopy were fixed with 2% PFA.

PFA-fixed cells intended for widefield microscopy or CLSM can be kept a few weeks in 1x PBS at 4°C. Cells intended for 3D-SIM, however, should be used within maximally a few days. Samples for TEM should preferably be processed the same day, at the latest the following day. If keeping cells at 4°C, make sure that the plates/dishes are sealed well with Parafilm to avoid evaporation.

PhD Mariana Lomiento and the master students Fabiana Mammoli and Claudio Atene from the group of Prof. Sergio Ferrari at the University of Modena and Reggio Emilia in Modena/Italy helped with fixing CD34⁺ cells, monoblasts, myeloblasts, and monocytes.

Procedure:

1. The cells were briefly washed with 1x PBS.

This step was skipped for HCC treated cells to avoid the reversion of the HCC effect.

For studying chromatin structure under hypotonic conditions the cells were incubated for 1 min in 0.3x PBS instead.

2. The cells were fixed for 8 min with 2% PFA or 10 min with 4% PFA. Typically fixative based on 1x PBS was used; only for studying chromatin structure under hypotonic conditions the fixative was prepared in 0.3x PBS.
3. The cells were washed 2x 5 min with 1x PBS.

In the experiments of correlative microscopy, the fixative was replaced with 1x PBS / 0.02% Tween in a stepwise manner: first roughly the same amount of 1x PBS / 0.02%

Tween was added to the fixative, then repeatedly a part of the mixture was removed and new 1x PBS / 0.02% Tween was added. This helps to avoid that the cells dry out and that artifacts are created. Subsequently, the samples were washed 2x with 1x PBS / 0.02% Tween instead of 1x PBS.

Materials:

Cells grown on coverslips PBS 1x (37°C) PBS 0.3x (37°C)	PBS 1x / 0.02% Tween PFA 2% or 4% in PBS 1x or 0.3x (37°C)
---------------------------------------------------------------	---------------------------------------------------------------

3.2.5.2 Methanol / acetic acid (MAA) fixation

In contrast to PFA, methanol / acetic acid (MAA) fixes the cells not by crosslinking but by dehydration and therefore by precipitation of proteins and nucleic acids. Due to that MAA fixation results in poor conservation of the 3D morphology and the samples are not suitable for the immunodetection of specific proteins. In order to counteract the shrinking effects of the fixative, the cells are subjected to hypotonic treatment with 0.56% KCl prior to fixation. The ascending ethanol series serves to clean the samples and leads to complete dehydration. After that, the samples can be kept at RT for a long time.

Procedure:

1. The cells were briefly incubated in a mixture of 1/3 0.56% KCl and 2/3 1x PBS.
2. The 1/3 KCl solution was changed to pure 0.56% KCl and the cells were incubated for 20-25 min in the incubator.
3. Ice-cold fixative (methanol / acetic acid) was added drop by drop to the KCl solution. Repeatedly a part of the mixture was removed and fresh fixative was added until the complete replacement of the fixative was accomplished. The fixative was always kept on ice.
4. The samples were air-dried.
5. An ascending ethanol series was performed by incubating the cells in 70%, 90%, 100% technical ethanol for 3 min each.
6. The samples were air-dried again.

Materials:

Cells grown on coverslips Ethanol, technical, 70%, 90%, 100% Incubator KCl 0.56% (37°C)	Methanol / acetic acid (ice-cold = -20°C) PBS 1x (37°C) Styrofoam box with ice
--------------------------------------------------------------------------------------------------	--------------------------------------------------------------------------------------

3.2.6 Fluorescent staining of fixed samples

Drying out of the samples has to be avoided by all means. Plastic Pasteur pipettes turned out to be most suitable for exchanging buffers and solutions. The next solution needed was already taken up with the pipette before the old one was removed from the sample and the samples were processed one after the other. For timed incubation steps, the timer was started when the solution of the first sample was changed.

3.2.6.1 Immunofluorescence of specific proteins

For the detection of specific proteins with immunofluorescence, only PFA fixed samples were used (compare section 3.2.5).

Depending on at which microscope the samples should be imaged two slightly different procedures were applied. However, both follow the same common principle: blocking of unspecific binding sites, incubation with the primary antibody, incubation with the secondary fluorescently labeled antibody, DNA counterstaining using DAPI.

For imaging with 3D-SIM, procedure A was followed. Dr. Yolanda Markaki (University of California (UCLA), Los Angeles, USA) introduced this protocol in our lab and it was published in Hübner et al. (2013). The procedure includes a quenching and a postfixation step because 3D-SIM requires very clean samples as background fluorescence or moving particles can create artifacts in the images. Of course also samples intended for widefield microscopy or for CLSM can be prepared according to this protocol, but as the above-mentioned problems do not play a (big) role here, it was sufficient to prepare these samples according to the shortened protocol described in procedure B.

Which blocking buffer is used best in procedure A, strongly depends on the cells to be stained. There are no rules, it has to be tested which buffer gives better results. Here in the experiments with the hematopoietic cells which apparently have a dense cytoplasm, the use of a HEPES based blocking buffer resulted in cleaner samples with less unspecific signals. Such buffers actually are commonly used in microtubule stainings, but were adapted by Dr. Yolanda Markaki (University of California (UCLA), Los Angeles, USA) for the use in immunofluorescence experiments for chromatin related proteins (Markaki 2008). The adapted protocol for performing immunofluorescence for 3D-SIM using this buffer was published in Hübner et al. (2015).

PhD Mariana Lomiento and the master students Fabiana Mammoli and Claudio Atene from the group of Prof. Sergio Ferrari at the University of Modena and Reggio Emilia in Modena/Italy

helped with performing the immunofluorescence experiments with CD34⁺ cells, monoblasts, myeloblasts, and monocytes.

Slides of control and UV/caffeine treated V79 cells stained with Lamin B and H3S10p were kindly provided by Fritzi Beck. Partially these data are already included in my Diploma thesis (Hübner 2008) done in the same lab. But as they are essential for the overall characterization of the consequences of UV/caffeine treatment and for the comparison with PCC induced cells they are included here.

Stainings of PCC induced V79 (H2B-mRFP, Rad51-GFP) cells with Lamin B or H3S10p were partially performed and in the case of H3S10p also imaged by Stephanie Peklo and Mareike Fitschen during their "Forschungspraktikum" (research internship) respectively bachelor thesis (Fitschen 2009) under my instruction and supervision.

The samples of control and UV/caffeine treated HeLa (H2B-GFP) cells stained with SMC2 were already done during my Diploma thesis (Hübner 2008) in the same lab. But as they are essential for the overall characterization of the consequences of UV/caffeine treatment and for the comparison with PCC induced cells they are included here.

Procedure A – for 3D-SIM:

1. The samples were quenched with 20 mM glycine in 1x PBS for 10 min to minimize background auto-fluorescence.
2. The samples were washed 2x with 1x PBS / 0.02% Tween.
In case of working with hematopoietic cells where the Hepes based blocking buffer was used, the samples were washed with 1x PBS instead.
3. The cells were permeabilized for 10 min with 0.3% Triton in 1x PBS.
4. The samples were incubated in blocking buffer for 1 h to 1 h 30 min.
In case of working with hematopoietic cells where the Hepes based blocking buffer was used the blocking was extended to 1 h 30 min to 2 h.
5. A dark humidified chamber was prepared using 1x PBS or blocking buffer and a strip of Parafilm well attached to a plain surface (e.g. plastic plate) was placed inside. The primary antibodies were diluted in blocking buffer on ice and the samples were incubated for 1 h to 1 h 30 min on drops of antibody solution (typically 30-60 µl per coverslip) on the Parafilm in the chamber. The coverslips were briefly blot dried before they were placed with the cells facing down on the drop to avoid further dilution of the antibodies.
When using the Hepes based blocking buffer (hematopoietic cells) the incubation with the primary antibody was extended to 1 h 30 min to 2 h.
6. The samples were washed 4x with blocking buffer.
7. The coverslips were incubated for 45-60 minutes with the secondary antibodies equivalent to step 5.

8. The samples were washed 6x with blocking buffer.
9. The samples were washed 2x with 1x PBS / 0.02% Tween.
When using the Hepes based blocking buffer (hematopoietic cells) the samples were washed with 1x PBS instead.
10. The samples were postfixed for 10 min with 4% PFA in 1x PBS. The fixative was exchanged to 1x PBS / 0.02% Tween in a stepwise manner as described in step 3 of section 3.2.5.1. In order not to lose too many cells this stepwise exchange was omitted for the hematopoietic cells.
11. The cells were washed 2x with 1x PBS / 0.02% Tween. Again, when using the Hepes based blocking buffer (hematopoietic cells) the samples were washed with 1x PBS instead.
12. The cells were stained with 2.5 µg/ml DAPI (freshly diluted in 1x PBS / 0.02% Tween or 1x PBS from a 500 µg/ml solution (1:200 dilution)) for 7-8 min equivalent to step 5.
13. The samples were washed 5x with 1x PBS.
14. The samples were mounted in Vectashield: a generous amount of Vectashield was applied onto a slide cleaned with 80% technical ethanol. The coverslips were blot dried and placed onto the Vectashield with the cells facing down. This procedure was performed thoroughly but efficiently to avoid sample drying. Only one sample was processed at a time.
All excess of Vectashield was removed with soft tissue, but care was taken not to squeeze the cells. The coverslips were sealed with clear nail polish.

Procedure B – for widefield microscopy and CLSM:

1. The cells were permeabilized for 10 min with 0.5% Triton in 1x PBS.
2. The samples were washed 2x 5 min in 1x PBS.
3. The samples were blocked for 10-20 min with 4% BSA / 1x PBS / 0.01% Tween.
4. A dark humidified chamber was prepared and the cells were incubated with the antibodies as described in step 5 of procedure A. But here the primary antibodies were diluted in 2% BSA / 1x PBS / 0.01% Tween and the samples were incubated for 1 h at RT or 45 min at 37°C.
5. The samples were washed 3x 5 min in 1x PBS / 0.01% Tween.
6. The coverslips were incubated with the secondary antibodies equivalent to step 4.
7. Step 5 was repeated.
8. The cells were stained with 0.2 µg/ml DAPI (freshly diluted in 1x PBS / 0.01% Tween or 1x PBS from a 10 µg/ml solution (1:50 dilution)) for 5-10 min equivalent to step 4.
9. The samples were briefly washed with 1x PBS.
10. The samples were mounted as described in step 14 of procedure A.

Materials:

Antibodies	Microscope slides
Blocking buffer	Parafilm
Blocking buffer Hepes based	PBS 1x
BSA 2% in PBS 1x / 0.01% Tween	PBS 1x / 0.01% Tween
BSA 4% in PBS 1x / 0.01% Tween	PBS 1x / 0.02% Tween
Clear nail polish	PBS 1x / 0.3% Triton-X-100
DAPI stock solution (10 µg/ml, 500 µg/ml)	PBS 1x / 0.5% Triton-X-100
Dark chamber	PFA 4% in 1x PBS
Ethanol, technical, 80%	Soft tissue
Fixed cells on coverslips	Styrofoam box with ice
Glycine 20 mM in 1x PBS	Vectashield
Incubator chamber (37°C)	

3.2.6.2 BrdU detection

Incorporated BrdU (see section 3.2.2.5) is detected based on a normal immunofluorescence protocol (procedure B in section 3.2.6.1) after the modified nucleotides were made accessible for the antibodies. This can be achieved either by adding DNase I to the primary antibody solution (1:200 dilution and in addition 5 mM MgCl₂) or by using heat denaturation. The latter one turned out to be more reliable in our hands and therefore was used for the experiments in this work. To achieve good results, the incubation in 50% formamide in 2x SSC analogous to fluorescence in situ hybridization (FISH) (see section 3.2.7.4) was essential.

Procedure:

1. The cells were equilibrated for minimum 30 min in 50% formamide in 2x SSC.
2. An appropriate amount of 50% formamide in 2x SSC (e.g. for a 15x15 mm coverslip ~5 µl) was applied on a microscope slide cleaned with 80 % technical ethanol. The coverslips were briefly blot dried and placed onto the drop with the cells facing down. Excessive liquid was removed using soft tissue, but care was taken not to squeeze the cells. The coverslips were sealed with Fixogum.
3. After the Fixogum dried completely the slide was denatured for 2 min 30 sec at 76°C on a well pre-heated heat block. The samples were let cool down.
4. The Fixogum was removed, the slides were briefly dipped into 1x PBS and the coverslips were carefully removed. Only one sample was processed at a time.
5. The samples were washed 2x with 1x PBS.

BrdU was detected using mouse-anti-BrdU and goat-anti-mouse-Cy5 or goat-anti-mouse-Alexa488 antibodies following procedure B in section 3.2.6.1. For PFA-fixed samples only the mouse-anti-IdU/BrdU antibody from Caltag worked fine (1:500 dilution), while for MAA-fixed samples the mouse-anti-BrdU antibody from Roche (1:200) gave better results.

Materials:

Antibodies Ethanol, technical, 80% Fixed cells treated with BrdU on coverslips Fixogum Formamide 50% in 2x SSC	Heat block (76°C) Microscope slides PBS 1x Soft tissue
----------------------------------------------------------------------------------------------------------------------------	-----------------------------------------------------------------

3.2.6.3 DAPI-staining

Equivalent to the immunofluorescence of specific proteins (see section 3.2.6.1) two slightly different protocols were used for DAPI-staining: procedure A for samples intended for 3D-SIM and if DAPI-fluorescence should be imaged in ultrathin sections after embedding and cutting of the sample (when strong signal intensities were crucial), procedure B for imaging with widefield microscopy or CLSM.

The steps for permeabilization and DAPI-staining are the same as the corresponding steps in the respective immunofluorescence procedures. However, the permeabilization time can be shortened as DAPI is a small molecule in contrast to an antibody. Furthermore, the dark chamber does not need to be humidified here as the coverslips are only incubated for a very limited time period.

PhD Mariana Lomiento and the master students Fabiana Mammoli and Claudio Atene from the group of Prof. Sergio Ferrari at the University of Modena and Reggio Emilia in Modena/Italy helped with the DAPI-stainings of CD34⁺ cells, monoblasts, myeloblasts, and monocytes.

Procedure A – for 3D-SIM and ultrathin sections:

1. The cells were permeabilized for 5-10 min with 0.3% Triton in 1x PBS.
2. The samples were washed 2x with 1x PBS.
3. A dark chamber containing a strip of Parafilm well attached to a plain surface (e.g. plastic plate) was prepared. The cells were stained with 2.5 µg/ml DAPI (freshly diluted in 1x PBS from a 500 µg/ml solution (1:200 dilution)) for 7-8 min by incubating them on drops of DAPI solution (typically 30-60 µl per coverslip) on the Parafilm in the chamber. The coverslips were briefly blot dried before placing them with the cells facing down on the drops to avoid further dilution of the DAPI.
4. The samples were washed 5x with 1x PBS.
5. The cells were mounted in Vectashield: a generous amount of Vectashield was applied onto a slide cleaned with 80% technical ethanol. The coverslips were blot dried and placed onto the Vectashield with the cells facing down. This procedure was performed thoroughly but efficiently to avoid sample drying. Only one sample was processed at a time.

All excess of Vectashield was removed with soft tissue, but care was taken not to squeeze the cells. The coverslips were sealed with clear nail polish.

If the cells were intended for embedding and cutting ultrathin sections the coverslips were not mounted, but the procedure was continued with the embedding of the cells as described in section 3.2.8.1.

Procedure B – for widefield microscopy and CLSM:

1. The cells were permeabilized for 5-10 min with 0.5% Triton in 1x PBS.
2. The samples were washed 2x 5 min in 1x PBS.
3. A dark chamber was prepared and the cells were stained with DAPI as described in step 3 of procedure A. But the cells were stained with 0.2 µg/ml DAPI (freshly diluted in 1x PBS from a 10 µg/ml solution (1:50 dilution)) for 5-10 min instead.
4. The samples were briefly washed with 1x PBS.
5. The cells were mounted in Vectashield as described in step 5 of procedure A.

Materials:

Clear nail polish	Parafilm
DAPI stock solution (10 µg/ml, 500 µg/ml)	PBS 1x
Dark chamber	Soft tissue
Ethanol, technical, 80%	Triton-X-100 0.3% in 1x PBS
Fixed cells on coverslips	Triton-X-100 0.5% in 1x PBS
Microscope slides	Vectashield

3.2.7 Fluorescence in situ hybridization (FISH)

Using fluorescently labeled probes fluorescence in situ hybridization (FISH) allows the detection of specific DNA-sequences in cell nuclei.

If not otherwise mentioned, the experiments were performed as described in Cremer et al. (2008) and were published in Hübner et al. (2009).

3.2.7.1 Probe generation

The DNA material, chromosome painting probes for the Chinese hamster (*Cricetulus griseus*) chromosomes #1, #2, #5 obtained by flow sorting of CHO derived cell lines (Chinese hamster ovarian cancer) (kindly provided by PD Dr. Stefan Müller (LMU, Munich, Germany)), was first amplified using DOP-PCR, then labeled using Label-PCR and finally hyb-mixes were generated.

Typically the hyb-mix contains Cot-1-DNA to saturate repetitive sequences. However, this is not commercially available for the hamster used here. Therefore fragmented genomic DNA was generated and used as a substitute.

Reamplification of probe material by secondary DOP-PCR

DOP-PCR is a polymerase chain reaction (PCR) with degenerated oligonucleotide primers (DOP) to ensure a (relatively) equal amplification of the entire probe. Here 6-MW-primers were used (Telenius et al. 1992).

Typically the DNA sequences to be detected in the cells are amplified in a primary and for reasons of efficiency in a subsequent secondary DOP-PCR. As the primary DOP-PCR product was already available in the lab, immediately the secondary DOP-PCR was performed here. The secondary DOP-PCR was performed during my Diploma thesis (Hübner 2008) in the same lab, but as the PCR-product was also used in this work, the procedure is included here.

Procedure:

1. 1 μ l DNA (from original DNA material or primary DOP-PCR) and 0.5 μ l Taq-polymerase were added to 24 μ l mastermix on ice (different from Cremer et al. 2008, where 48.5 μ l mastermix are added). The mix was shortly vortexed and spun down.
2. The PCR was run with the following settings:
 - initial denaturation: 96°C, 3 min
 - denaturation: 94°C, 1 min
 - annealing: 56°C, 1 min
 - extension: 72°C, 2 min } 35 cycles
- final extension: 72°C, 5 min
3. The efficiency of the amplification was checked on a 1% agarose gel:
 - The agarose was melted in a microwave and let cool down slightly.
 - A 4-5 mm thick gel was poured on a gel tray with a well comb. If necessary, air bubbles were removed. After the gel solidified the comb was carefully removed.
 - The gel on the gel tray was placed into the chamber and was covered with TAE buffer.
 - The probes were prepared by mixing 1 μ l PCR-product with 4 μ l H₂O_{dest} and 1 μ l 6x loading dye and were then loaded on the gel. Also a size standard (e.g. 3 μ l of λ /HindIII) was included.
 - The gel was run for 20-30 min at 130 V.
 - The gel was removed from the chamber, stained for (10-)15 min in an ethidium-bromide bath and subsequently washed for (5-)10 min in H₂O_{dest} to remove excessive

ethidium-bromide.

- A picture of the gel was taken.
4. The PCR-product was stored at -20°C or probe preparation was continued with the label-PCR described below.

Materials:

Agarose 1%	Microwave
DNA (primary DOP-PCR-product)	Styrofoam box with ice
Electrophoresis chamber including a gel tray, a well comb, and a voltage source	Table centrifuge
Ethidium-bromide bath	TAE buffer 1x
H ₂ O _{dest}	Taq-polymerase
Imaging facility for gels	Thermocycler
Loading dye 6x	Vortex
Mastermix for secondary DOP-PCR	λ/HindIII marker

Label-PCR

In this step, the amplified DNA-sequences obtained by DOP-PCR (see section *Reamplification of probe material by secondary DOP-PCR* above) are labeled using modified dUTPs in the reaction mix. In this work, the labeling was done indirectly using the haptens biotin (bio) for chromosome #1, digoxigenin (dig) for chromosome #2 and dinitrophenol (DNP) for chromosome #5.

The label-PCR was performed during my Diploma thesis (Hübner 2008) in the same lab, but as the PCR-product was also used in this work, the procedure is included here.

Procedure:

1. (1-)1.2 µl DNA (from secondary DOP-PCR) and 0.5 µl Taq-polymerase were added to 48 µl mastermix on ice. The mix was shortly vortexed and spun down.
2. The PCR was run with the following settings:
 - initial denaturation: 94°C, 3 min
 - denaturation: 94°C, 1 min
 - annealing: 56°C, 1 min
 - extension: 72°C, 30 sec
 } 30 cycles (instead of 20-25 as in Cremer et al. 2008)
 - final extension: 72°C, 5 min
5. The length of the fragments was checked on a 1% agarose gel as described in step 3 of the section *DOP-PCR* above.

The fragments should be 300-800 bp long. If they were too long (>2000 bp) they were digested using DNase I:

- A 1:10 (instead of a 1:250 as in Cremer et al. 2008) pre-dilution of DNase I was prepared in H₂O_{bidest} on ice.
 - 1 µl of the 1:10 dilution was added to the label PCR product (~50 µl) (final dilution of the DNase I was 1:500) and the sample was incubated for 1 min at RT (in contrast to Cremer et al. 2008 where a final dilution of 1:12 500 and an incubation time of 5-10 min was used).
 - The tube was placed on ice to halt the activity of the DNase I.
 - The length of the fragments was checked again on a 1% agarose gel.
 - If the fragments now had the right length, DNase I was inactivated by adding 0.8 µl 0.5 M EDTA (the amount of EDTA added was slightly reduced in comparison to Cremer et al. 2008 where 1 µl was used). Otherwise, the incubation at RT was repeated and again a gel was run until the fragments were short enough.
6. The PCR-product was stored at -20°C or probe preparation was continued with the preparation of the hyb-mix described below.

Materials:

DNA (secondary DOP-PCR-product)	Styrofoam box with ice
DNase I stock solution	Table centrifuge
EDTA 0.5 M	Taq-polymerase
H ₂ O _{bidest}	Thermocycler
Mastermix for Label-PCR	Vortex

Preparation of the hybridization solution (hyb-mix)

After amplification and labeling the DNA-sequences are combined with each other and finalized for the use on the sample by generating a hybridization-mixture (hyb-mix).

Typically, Cot-1-DNA consisting of repetitive sequences is added to the hyb-mix to avoid cross-hybridizations of the probes. However, this is not available for hamster. As a supplement fragmented genomic DNA was used as competitor DNA (for its preparation, see section *Generation of fragmented genomic DNA* below). Salmon sperm serves as a carrier. It is important to use maximally 1 µl of salmon sperm as it can agglutinate in higher amounts, causing background in the sample.

Procedure:

1. Approximately 150 ng of each labeled probe and 500 ng of fragmented genomic DNA per µl final hyb-mix should be used. Here this corresponded to 2.5 µl probe and 1 µl fragmented DNA for 1 µl final hyb-mix. This is about the same as the recommendation in Cremer et al. (2008) which suggests using 2 µl label-PCR-product for 1 µl hyb-mix.

Typically hyb-mixes with a final volume of 6 or 12 μl (i.e. containing 15 or 30 μl probe and 6 or 12 μl fragmented DNA) were prepared. Irrespective of the volume 1 μl salmon sperm was added to the mix.

2. The 2.5-fold volume of 100% absolute ethanol (ice-cold) was added to the DNA. The sample was briefly mixed by pipetting up and down.
3. The DNA was precipitated for at least 2 h at -20°C .
4. The sample was centrifuged for 25 min at 13 000 rpm. The supernatant was removed immediately.
5. The pellet was dried in a vacuum centrifuge for 5-10 min.
6. An appropriate amount of deionized formamide (half the volume of the final hyb-mix, compare step 1; here typically 3 or 6 μl) was added and the pellet was resuspended by shaking overnight on a rotator at $38-40^{\circ}\text{C}$.
7. The same amount of hybridization-mastermix as formamide in step 6 (here therefore again typically 3 or 6 μl) was added. The hyb-mix was mixed well by vortexing.
8. The hyb-mix was stored at -20°C .

Materials:

Centrifuge (Biofuge pico)	Hybridization-mastermix
DNA (label-PCR-product)	Rotator
Ethanol, absolute, 100% (ice-cold = -20°C)	Salmon sperm
Formamide, deionized	Table centrifuge
Fragmented genomic hamster DNA	Vacuum centrifuge
Freezer -20°C	Vortex

Generation of fragmented genomic DNA

As mentioned above, for the Chinese hamster Cot-1 DNA is not commercially available and therefore fragmented genomic DNA was used as competitor DNA. The procedure for its isolation as it is described here was provided by PD Dr. Stefan Müller (LMU, Munich, Germany).

The fragmented genomic DNA was generated during my Diploma thesis (Hübner 2008) in the same lab, but as it was also used in this work, the procedure is included here.

Procedure:

1. At least 1 large (75 cm^2) tissue culture flask with diploid Chinese hamster fibroblasts was trypsinized as described in 3.2.1.3. After trypsinization fresh full medium was added.
2. The cell suspension was transferred into a tube and centrifuged for 10 min at 1000 rpm.
3. The supernatant was removed and the pellet was resuspended in 4.5 ml DNA buffer using

plastic Pasteur pipettes.

4. Proteinase K with a final concentration of $\sim 440 \mu\text{g/ml}$ ($\sim 1:40$ dilution = $126 \mu\text{l}$) and SDS with a final concentration of 1% ($1:10$ dilution = $500 \mu\text{l}$) was added to fracture the cells, degrade the proteins and therefore isolate the DNA. The sample was incubated for several hours on a shaker at $(38-40(-45))^\circ\text{C}$ until the solution got completely clear. Potentially this could take overnight.
5. 2 ml 6 M NaCl was added to extract all proteins. The sample was vortexed for 15 sec on the highest setting.
6. The sample was centrifuged for 15 min at 3800 rpm.
If the supernatant was not clear, it was centrifuged again for 10 min at 3800 rpm.
If the supernatant still was not clear, it was filtered using filter paper.
7. The supernatant or the filtrate was transferred into a new tube.
8. The 2.5-fold volume of 100% absolute ethanol (ice-cold) (here 11.25 ml) was added to precipitate the DNA. The sample was mixed by turning the tube over several times. The DNA should be visible as a white cloud.
If the DNA was not visible or only faintly, the sample was let rest for 30 min at -20°C and if necessary centrifuged for 10 min at 3800 rpm.
9. The DNA cloud was taken out of the tube using a glass Pasteur pipette bent over a Bunsen burner. The DNA was washed in 70% absolute ethanol, the excess of ethanol was slightly squeezed out and the DNA was transferred into $250 \mu\text{l}$ TE-buffer without EDTA.
10. The sample was put on a rotator for several hours until the DNA was completely dissolved.
11. The DNA was fragmented by incubating it in a water bath at $92-94^\circ\text{C}$ for about 1.5 h. Every 15 min it was vortexed for 1-2 min on the highest setting.
12. The size of the DNA fragments was checked on a 1% agarose gel as described in step 3 of the section *Reamplification of probe material by secondary DOP-PCR* above. The fragments should be 100-800 bp in size.
If this was not the case, the sample was incubated and vortexed again as described in step 11 for an appropriate time and subsequently the size of the fragments was checked again.
13. The DNA-concentration was determined in a photometer. Here it accounted for $\sim 500 \mu\text{g/ml}$.
14. The DNA was stored at -20°C .

Materials:

Bunsen burner	Plastic Pasteur pipettes
Centrifuge (C3i, Rotana/S)	Proteinase K
DNA buffer	Quartz cuvette
Ethanol, absolute, 100% (ice-cold = -20°C)	Rotator
Ethanol, absolute, 70%	SDS 10%
Filter paper, folded	Shaker
Freezer -20°C	TE-buffer without EDTA
Glass Pasteur pipettes	Tissue culture flask (75 cm ²) with cells
NaCl 6 M	Vortex
Photometer	Water bath (Thermocycler 60) 92-94°C

3.2.7.2 Preparation of metaphase spreads for 2D-FISH

Metaphase spreads are needed for testing the quality of the probes before applying them onto 3D-samples. To prepare them, first a cell suspension has to be generated which is then dropped onto microscope slides. Before the samples are ready to use they have to be posttreated using pepsin.

Preparation of the cell suspension

In order to obtain a higher yield of mitotic cells, the cells are treated with colcemid prior to fixation. Colcemid causes depolymerization of the microtubules and also impairs their formation. This leads to an inactivation of the mitotic spindle apparatus and therefore arrests the cell in mitosis (Rieder and Palazzo 1992). However, as a prolonged incubation with colcemid also results in a shortening of the chromosomes (Rieder and Palazzo 1992), it is highly recommended to follow the given incubation times.

The same applies to the incubation in 0.56% KCl: this hypotonic treatment leads to a swelling of the cells so that they burst when they are dropped onto microscope slides and that the chromosomes spread well. Too long incubation, however, results in bursting of the cells already before dropping, which makes the cell suspension useless.

The cell suspension was prepared according to Beatty and Scherer (2002). As in this work, adherent cells were used instead of cells growing in suspension, the cell harvesting procedure (steps 1-3 in the procedure below) was adjusted accordingly.

Procedure:

1. Colcemid was added at a final concentration of 80 ng/ml (1:125 dilution) to a large (75cm²) tissue culture flask with 70-80% confluency. The cells were incubated for 30 min in the incubator.

2. The cells were trypsinized as described in section 3.2.1.3. However, all removed medium and PBS was collected and used for stopping the trypsin reaction instead of adding fresh medium (in order not to lose mitotic cells that easily detach).
3. The cell suspension was transferred into a 50 ml tube and centrifuged for 10 min at 1000 rpm.
4. The supernatant was aspirated down to a few ml and the cells were resuspended using plastic Pasteur pipettes.
5. Carefully and with gentle mixing 0.56% KCl was added up to 20 ml. The cells were incubated for 20 min in the incubator. Different from Beatty and Scherer (2002) the cells were not washed in PBS prior to this hypotonic treatment. As here adherent cells were processed, the incubation was prolonged to 20 min (instead of 10 min) in order to achieve a sufficient degree of swelling.
6. Carefully 1 ml of ice-cold fixative (methanol / acetic acid) was added by letting it run down the walls of the tube. The sample was gently mixed by turning the tube upside down and centrifuged for 10 min at 1000 rpm.
7. Step 4 was repeated.
8. Equivalent to step 5 fixative was added up to 20 ml. In contrast to Beatty and Scherer (2002), the cell suspension was not incubated at RT and washed several times in fixative, but the sample was directly incubated for minimum 30 min at -20°C, preferably overnight.
9. The sample was centrifuged for 10 min at 1000 rpm.
10. The supernatant was aspirated down to 2-2.5 ml and the cells were resuspended using plastic Pasteur pipettes.
11. The cell suspension was transferred into a 15 ml tube.
12. The quality of the cell suspension was checked by dropping it onto a microscope slide (see section *Dropping of the cell suspension onto microscope slides to obtain metaphase spreads* below).
13. The cell suspension was stored at -20°C.

Materials:

Centrifuge (Rotana/S)	Methanol / acetic acid (ice-cold = -20°C)
Colcemid 10 µg/ml	Plastic Pasteur pipettes
Incubator	Styrofoam box with ice
KCl 0.56% (37°C)	Tissue culture flask (75 cm ²) with cells

Dropping of the cell suspension onto microscope slides to obtain metaphase spreads

For the dropping, two slightly different procedures exist. Which of the two is more suitable depends on the cell suspension. If the cells burst very easily procedure A is recommended.

For the dropping, either a plastic Pasteur pipette or a 200 µl pipette with a yellow tip can be used.

Both procedures were developed previously in our lab. Procedure A was loosely influenced by Henegariu et al. (2001) and Deng et al. (2003), procedure B is roughly based on the protocol provided by Deng et al. (2003).

Procedure A:

1. During the whole procedure the cell suspension was kept on ice.
2. Microscope slides were cleaned with 80% technical ethanol and cooled well in ice-cold H₂O_{dest.}
3. One slide was drained briefly, put on a wet tissue on the lid of the well pre-heated water bath (55°C), one or two drops of the cell suspension were dropped onto the slide and the slide was let air dry.
4. The result was checked on the microscope:
 - If the nuclei were still surrounded by too many remnants of the cytoplasm up to 10 washing steps were performed based on Beatty and Scherer (2002): Carefully and with gentle mixing, fixative was added up to 10 ml. The sample was centrifuged for 10 min at 1000 rpm. The supernatant was aspirated down to 2-2.5 ml and the cells were resuspended using plastic Pasteur pipettes. The quality was checked again by dropping.
 - If the cell density was too high, the cell suspension was diluted with methanol / acetic acid.
 - If the cell density was too low, the sample was centrifuged for 10 min at 1000 rpm and the cells were resuspended in a smaller volume.
 - If the chromosomes were not spread well, the slide was slightly tapped on the hand directly after dropping the cells onto it in order to increase the spreading or procedure B was tried.
5. The slides were stored at RT and the *Posttreatment of metaphase spreads* described below was performed within a few days.

Procedure B:

1. During the whole procedure the cell suspension was kept on ice.
2. A metal box was put into the well pre-heated water bath (55°C). It was attached to the wall so that it did not move later.
3. Microscope slides were cleaned with 80% technical ethanol and let dry.
4. 2 slides were put into the metal box, the lid of the water bath was closed for minimum 30 sec, one or two drops of cell suspension were dropped onto each slide, immediately

the lid was closed again and the samples were let dry briefly.

5. The result was checked on the microscope as described in step 4 of *Procedure A* above.
6. The slides were stored at RT and the *Posttreatment of metaphase spreads* described below was performed within a few days.

Materials:

Cell suspension Centrifuge (Rotana/S) Ethanol, technical, 80% H ₂ O _{dest} Metal box Methanol / acetic acid (ice-cold = -20°C) Microscope (Axiovert 25 C)	Microscope slides Pipette (200 µl) with yellow tip Plastic Pasteur pipettes Styrofoam box with ice Tissue Water bath (M12) (55°C)
-------------------------------------------------------------------------------------------------------------------------------------------------------------------------------------------------	--------------------------------------------------------------------------------------------------------------------------------------------------

Posttreatment of metaphase spreads

The posttreatment of the slides consists of two parts: first, remnants of the cytoplasm are removed using pepsin (a protease), then the samples are completely dehydrated using an ascending ethanol series and baking at 60°C.

Due to their different fixation, the metaphase spreads do not have to be treated with liquid nitrogen and HCl as it is obligatory for samples for 3D-FISH (see section 3.2.7.4)

After complete dehydration the slides can be stored almost unlimited at -20°C.

Procedure:

1. After dropping (see above) the slides were aged at RT overnight (or up to a few days) (based on Beatty and Scherer 2002).
2. 0.005% pepsin was added to warm 0.01 N HCl (1:2000 dilution; e.g. 50 ml 0.01 N HCl + 25 µl 10% pepsin stock). The solution was mixed well.
3. The slides were incubated in this pepsin-solution for ~5 min. The exact duration of the incubation depended on how clean the slides were. The process was checked on a microscope to avoid overpepsinization of the slides, as this results in “fringy” chromosomes with poor quality. Potentially, for very clean slides, this step can be skipped.
4. The slides were washed 3x 5 min in 1x PBS.
5. The slides were dehydrated in an ice-cold ethanol series of 70%, 90, 100% technical ethanol for 5 min each and subsequently air-dried (Beatty and Scherer 2002).
6. The slides were baked in an oven at 60°C for 2-3 h (expanded aging).
7. After the slides cooled down completely (up to several days at RT are possible) the slides were frozen at -20°C in a slide box containing a package of silica gel beads and well sealed with tape (Beatty and Scherer 2002).

Materials:

Ethanol, technical, 70%, 90%, 100% (ice-cold = -20°C) HCl 0.01 N (37°C) Metaphase spreads Microscope (Axiovert 25 C) Oven (60°C)	PBS 1x Pepsin stock solution Silicagel beads Slide box Tape
----------------------------------------------------------------------------------------------------------------------------------------------	-------------------------------------------------------------------------

3.2.7.3 2D-FISH

FISH on metaphase spreads as generated in section 3.2.7.2 is called 2D-FISH.

It is highly recommended to always first test the probes (generated as described in section 3.2.7.1) with 2D-FISH before moving on to 3D-FISH – 2D-FISH reveals if the quality of the probes is good enough and if they indeed label what they are supposed to label.

The procedures for 2D-FISH are equivalent to 3D-FISH (see section 3.2.7.4), just that here the cells are located on the microscope slide instead of the coverslip and that they are fixed differently (compare section 3.2.7.2 and section 3.2.5), which both leads to small differences in the protocols.

The procedure consists of two parts: hybridization of the probe onto the cells and detection of the specific signals (including washing off all unspecifically bound and all excessive probe).

Hybridization

In this step probe and sample get denatured, so that the two DNA-strands open up and the probe can anneal to the corresponding sequences in the cells.

Procedure:

1. The box with the posttreated metaphase spreads was taken out of the freezer well ahead of time (minimum 30 min). It was made sure that the slides were completely thawed before the tape of the box was removed in order to avoid that the samples absorb moisture again.
2. Areas of about 10x10 mm with good metaphases (well spread, clean) were marked on the slides using a diamond pencil. Up to 6 areas were marked on one slide. However, be aware, that all areas on this one slide have to follow the same detection scheme later (see section *Washing and detection* below).
3. The probe (= hyp-mix) was denatured for 2 min at 85°C in a water bath and was subsequently immediately put on ice. Other than in Cremer et al. (2008), this step was included here to make sure that the probe was completely denatured.

4. 1 µl probe was applied to each area and was covered with an 8x8 mm coverslip.
5. After the probe spread completely under the coverslip, it was sealed well with Fixogum.
6. After the Fixogum dried completely, probe and sample were denatured simultaneously for 1 min 50 sec to 2 min at 76°C (instead of 75°C as in Cremer et al. 2008) on a well pre-heated heat block. The slides were immediately transferred into a metal box with lid.
7. The samples were incubated for 1-3 days at 37°C.

Materials:

Coverslips 8x8 mm	Microscope (Axiovert 25 C)
Diamond pencil (Kraus & Winter)	Posttreated metaphase spreads
Fixogum	Probe (= hyb-mix)
Heat block (76°C)	Styrofoam box with ice
Metal box with lid	Water bath (Thermocycler 60) (85°C)

Washing and detection

After hybridization, all excessive and all unspecifically bound probe has to be washed away and the specific signals have to be detected by immunolabeling.

In this work, the probes were always detected according to **Table 3**.

The detection steps follow the same principles as in an immunofluorescence experiment (see section 3.2.6.1).

Table 3: Detection scheme for FISH.

Hapten	Probe	Antibodies 1 st layer	Antibodies 2 nd layer
Bio	Chr. #1	Avidin-Alexa488	Goat-anti-avidin-FITC
Dig	Chr. #2	Mouse-anti-Dig-Cy5	Goat-anti-mouse-Cy5
DNP	Chr. #5	Rabbit-anti-DNP	Goat-anti-rabbit-Cy3

Procedure:

1. The Fixogum was removed, the slides briefly dipped into 2x SSC and the coverslips carefully removed.
2. The samples were washed 2x 3 min (instead of 3x 5 min as in Cremer et al. 2008) at 37°C in 2x SSC on a shaker.
3. The sample was washed 3x 5 min at 60°C in 0.1x SSC. Preferably this step was performed directly inside the water bath to maintain the high temperature (but great care was taken that the water did not dilute the 0.1x SSC). Otherwise, these washing steps were performed on a shaker as in Cremer et al. (2008).
4. The samples were briefly equilibrated in 4x SSC/0.2% Tween.
5. The samples were blocked for 20-30 min in 4% BSA/4x SSC/0.2% Tween at RT (in Cremer et al. 2008 10-15 min).

6. The antibodies for the first layer were diluted in 2% BSA/4x SSC/0.2% Tween on ice (in Cremer et al. 2008 1% BSA only was used). Depending on the coverslip size 30-150 μ l were needed.
A suitable amount of antibody dilution was applied onto the hybridization area(s), then the areas were covered with a coverslip. If there was more than one area on the slide, all were covered with one large coverslip.
7. The samples were incubated for 45 min at 37°C in a dark humidified chamber prepared using 4x SSC/0.2% Tween. It turned out useful to place the slides on elevated bars in the chamber to avoid that the antibody solution gets diluted by the liquid in the chamber.
8. The samples were washed 3x 5 min in 4x SSC/0.2% Tween at 37°C on a shaker (instead of 3x 3 min as in Cremer et al. 2008).
9. Steps 6 and 7 were repeated with the secondary antibodies.
10. Step 8 was repeated.
11. The cells were stained with 0.2 μ g/ml DAPI (freshly diluted in 4x SSC / 0.2% Tween from a 10 μ g/ml solution (1:50 dilution)) for 5-10 min equivalent to steps 6 and 7.
12. The samples were washed with H₂O_{dest} in a Coplin jar by vigorously rinsing them from the back.
13. The slides were air-dried.
14. The samples were mounted in Vectashield by applying a generous amount of Vectashield onto the marked area(s) and covering it/them with a suitable coverslip. All excess of Vectashield was removed with soft tissue by carefully pressing onto the sample. The coverslip(s) were sealed with clear nail polish.

Materials:

2% BSA in 4x SSC/0.2% Tween	Hybridized metaphase spreads
4% BSA in 4x SSC/0.2% Tween	Shaker
Antibodies	SSC 0.1% (60°C)
Clear nail polish	SSC 2x (37°C)
Coplin jar	SSC 4x /0.2% Tween (37°C)
Coverslips	Soft tissue
DAPI stock solution 10 μ g/ml	Styrofoam box with ice
Dark chamber	Vectashield
Incubator chamber (37°C)	Water bath (5) (60°C)
H ₂ O _{dest}	

3.2.7.4 3D-FISH

Also for 3D-FISH a pretreatment of the cells is necessary. Due to a completely different fixation procedure in contrast to the metaphase spreads used for 2D-FISH (see section 3.2.7.2) – especially when fixing with PFA, but also when fixing with MAA (see section 3.2.5) – the

structure of the cell is maintained much better. However, while this is highly appreciated for the nucleus, the accompanying good preservation of the cytoplasm creates problems for probe penetration. To overcome this, the pretreatment for 3D-FISH includes an extended permeabilization step, repeated freezing and thawing cycles in liquid nitrogen, a – in contrast to metaphase spreads (see *Posttreatment of metaphase spreads* in section 3.2.7.2) obligatory but more gentle – treatment with pepsin and a pre-denaturation with HCl.

The staining procedure following these pretreatment steps is equivalent to 2D-FISH (see section 3.2.7.3) and again consists of two parts: hybridization of the probe onto the cells and detection of the specific signals (including washing off all unspecifically bound and all excessive probe). Be aware that now the cells are always situated on the coverslip, not on the slide and that – as mentioned above – the fixation of the cells for 3D-FISH is different, which both leads to small differences in the protocols.

Especially with PFA-fixed samples drying out has to be avoided by all means. Plastic Pasteur pipettes turned out to be most suitable for exchanging buffers and solutions. The next solution needed was already taken up with the pipette before the old one was removed from the sample and the samples were processed one after the other. For timed incubation steps, the timer was started when the solution of the first sample was changed.

Pretreatment of the cells

Procedure:

1. The cells were washed for 5 min in 0.05% Triton in 1x PBS (instead of 3x 3 min in 0.01% Triton in 1x PBS in Cremer et al. 2008).
2. The cells were permeabilized for 20 min in 0.5% Triton in 1x PBS at RT. With this prolonged permeabilization in comparison to Cremer et al. (2008), where only 5-15 min are done, better results were obtained with the V79 cells used here.
3. The cells were transferred to 20% glycerol and incubated for minimum 1 h at RT, better overnight at 4°C.
4. One coverslip was drained briefly, the remaining glycerol was distributed evenly over it by holding it in a horizontal position and it was deep-frozen by dipping it into liquid nitrogen for several seconds. The coverslip was put on a tissue and was let thaw. It was made sure that the cells did not dry out – therefore the coverslip was put back into 20% glycerol when a small remnant of ice was still left on the sample.
5. Step 4 was repeated 2x (instead of 4x as in Cremer et al. 2008).
6. The cells were washed 3x 5 min in 0.05% Triton in 1x PBS. Due to the addition of Triton, the washing steps could be reduced to 3x 5 min instead of 3x 10 min as in Cremer et al. (2008).

7. The cells were denatured in 0.1 N HCl for exactly 5 min.
8. The samples were washed 2x with 2x SSC.
9. The samples were incubated in 50% formamide in 2x SSC for minimum 1 h at RT, better several days at 4°C (up to weeks/months is possible).
10. The cells were equilibrated first in 2x SSC, then in 1x PBS.
11. The samples were pepsinized:
 - 0.002% pepsin (instead of 0.005% in Cremer et al. 2008) were added to warm 0.01 N HCl (1:5000 dilution; e.g. 50 ml 0.01 N HCl + 10 µl 10% pepsin stock) and the solution was mixed well.
 - The coverslips were incubated in this pepsin-solution for 3-5 min. The process was followed under the microscope to avoid overpepsination of the cells.
 - The cells were washed 2x 5 min in 0.05 M MgCl₂ in 1x PBS to inactivate the pepsin.
12. The cells were postfixed for 10 min in 1% PFA.
13. The samples were washed 5 min in 1x PBS, then 2x 5 min in 2x SSC.
14. The cells were stored in 50% formamide in 2x SSC at 4°C or – if the hybridization was performed on the same day – they were incubated for minimum 1 h at RT.

Materials:

Fixed cells on coverslips	Microscope (Axiovert 25 C)
Fridge 4°C	PBS 1x
Formamide 50% in 2x SSC	PBS 1x / 0.05% Triton-X-100
Glycerol 20%	PBS 1x / 0.5% Triton-X-100
HCl 0.01 N (37°C)	Pepsin stock solution
HCl 0.1 N	PFA 1% in 1x PBS
Liquid nitrogen	SSC 2x
MgCl ₂ 0.05 M in 1x PBS	

Hybridization

Procedure

1. In case the cells were grown on large coverslips (e.g. 76x26 mm), small pieces of about 10x10-15x15 mm were cut from these using a diamond pencil:
 - The coverslips were transferred into 2x SSC.
 - As many samples as needed were cut from the large coverslip.
 - The coverslips were transferred back into 50% formamide in 2x SSC and equilibrated very well (minimum 30 min).
2. The probe (= hyp-mix) was denatured for 2 min at 85°C in a water bath and was subsequently immediately put on ice. Other than in Cremer et al. (2008), this step was included here to make sure that the probe was completely denatured.

3. For each coverslip 3-3.5 μ l probe were applied on a microscope slide. The coverslips were briefly blot dried and placed with the cells facing down onto the probe. It was tried to avoid air bubbles. Excessive liquid was removed using soft tissue, but care was taken not to squeeze the cells. The coverslips were sealed with Fixogum.
4. After the Fixogum dried completely, probe and sample were denatured simultaneously for (2 min to) 2 min 30 sec (to 3 min) at 76°C (compare: 2 min at 75°C in Cremer et al. 2008) on a well pre-heated heat block. The slides were immediately transferred into a metal box with lid.
5. The samples were incubated for 2-3 days at 37°C.

Materials

Diamond pencil (Kraus & Winter)	Posttreated cells on coverslips
Fixogum	Probe (= hyp-mix)
Formamide 50% in 2x SSC	Soft tissue
Heat block (76°C)	SSC 2x
Metal box with lid	Styrofoam box with ice
Microscope slides	Water bath (Thermocycler 60) (85°C)

Washing and detection

In this work, the probes were always detected according to **Table 3** in section 3.2.7.3.

Procedure:

1. Steps 1-11 were performed as described for 2D-FISH (see section 3.2.7.3, *Washing and detection*).
Be aware that the cells now were situated on the coverslip, not on the slide. Therefore the dark humidified chamber in step 7 contained a strip of Parafilm well attached to a plain surface (e.g. plastic plate) and the cells were incubated on drops of antibody solution on the Parafilm. The coverslips were briefly blot dried before they were placed with the cells facing down on the drop to avoid further dilution of the antibodies.
2. Instead of washing in 0.2% Tween in 4x SSC as in Cremer et al. (2008), the cells were briefly washed in 2x SSC to wash away all Tween.
3. The samples were mounted in Vectashield: a generous amount of Vectashield was applied onto a slide cleaned with 80% technical ethanol. The coverslips were blot dried and placed with the cells facing down onto the Vectashield. This procedure was performed thoroughly but efficiently to avoid sample drying. Only one sample was processed at a time.
All excess of Vectashield was removed with soft tissue, but care was taken not to squeeze the cells. The coverslips were sealed with clear nail polish.

Materials:

Clear nail polish Ethanol, technical, 80% Hybridized cells on coverslips Microscope slides	SSC 2x (37°C) Soft tissue Vectashield
-----------------------------------------------------------------------------------------------------	---------------------------------------------

3.2.8 Sample preparation for transmission electron microscopy (TEM)

Processing samples for TEM involves several steps: first, the cells have to be embedded in resin. After the polymerization of the resin, the obtained blocks have to be cut on an ultramicrotome and subsequently the sections have to be stained.

Dr. Jacques Rouquette (ITAV, Toulouse, France) introduced TEM in our lab. The notes and procedures described in this section were published in Hübner et al. (2013) and Hübner et al. (2015).

The main part of the materials needed for sample preparation for TEM (especially the ultramicrotome and the diamond knife are to be mentioned), were kindly provided by Prof. Dr. Stan Fakan (formerly LMU, Munich, Germany and University of Lausanne, Lausanne, Switzerland).

3.2.8.1 Embedding of cells in resin

If possible, it is recommended to embed more than one sample of the same kind, as the procedure includes several critical steps where the sample can get lost or damaged (steps 14 and 17).

For embedding the cells were always seeded onto Ø 12 mm round coverslips or into MatTek dishes with a Ø 12 mm round coverslip attached, as only this coverslip size allowed the unproblematic embedding of the cells: in order to polymerize the samples, the coverslips were put on an embedding capsule filled with resin and turned upside down (see step 14 in the procedure below). Coverslips larger than 12 mm or square coverslips would not have been kept in place by the adhesive power during this process. If square coverslips have to be used for a certain reason, they have to be cut to at least octagons using a diamond pencil prior to embedding (however, this is not recommended as it can generate cracks in the coverslip and small, disturbing glass particles (see also step 1 in section 3.2.1.4)).

The incubation times indicated here are minimum times – longer incubations are not problematic. As ethanol evaporates very quickly great care has to be taken to replace the liquid immediately. It is better to leave a small amount of liquid on the sample than letting the cells dry out. Plastic Pasteur pipettes turned out to be most suitable for exchanging solutions. The

next solution needed, was already taken up with the pipette before the old one was removed from the sample and the samples were processed one after the other. For timed incubation steps, the timer was started when the solution of the first sample was changed.

PhD Mariana Lomiento and the master students Fabiana Mammoli and Claudio Atene from the group of Prof. Sergio Ferrari at the University of Modena and Reggio Emilia in Modena/Italy helped with embedding CD34⁺ cells, monoblasts, myeloblasts, and monocytes.

Procedure:

1. When a new bottle of resin was started it was catalyzed according to the manufacturer's guidelines:
 - The resin was allowed to acquire RT.
 - The catalyst (benzoyl peroxide) was added to the resin (9.9 g for 500 g resin).
 - First, the bottle was thoroughly shaken by hand, then it was put on a shaker for 9-10 h. During this time the bottle was shaken again thoroughly by hand, first every 5 min, with progressing time every 10, 20 and 30 min.
 - The resin was let stand overnight.
 - The resin was again put on a shaker for 2 h and shaken by hand every 30 min.
 - The quality of the resin was tested by filling a gelatin capsule with the freshly catalyzed resin and polymerizing it at 60°C for 24 h. The resin should be completely solid after this time.
 - The catalyzed resin was stored at 4°C.
2. The LR white resin was taken out of the fridge at least 1 h prior to use.
3. Samples of correlative microscopy experiments involving 3D-SIM (see explanations in section 3.2.10.1) were demounted from the microscope slide as follows:
 - The sample was incubated in 1x PBS for about 20 min until the nail polish became grayish and could be peeled off.
 - The coverslip with the cells was removed from the slide. Great care was taken not to apply shearing forces to avoid damaging the cells.
 - The cells were washed extensively by incubating them in fresh 1x PBS for minimum 1 h. During that time the PBS was changed every 10 min.
4. The samples were incubated 2x 5 min in cold (4°C) 30% absolute ethanol on ice.
5. The samples were incubated 2x 5 min in cold (4°C) 50% absolute ethanol on ice.
6. The samples were incubated 2x 10 min in cold (4°C) 70% absolute ethanol on ice.
7. The samples were incubated 2x 10 min in 90% absolute ethanol (now at RT).
8. The samples were incubated 3x 10 min in 100% absolute ethanol.
9. Embryo dishes were labeled adequately if there was more than one sample – using

colored sticker spots and labeling with pencil proved to be a safe method.

Each sample was transferred into a separate embryo dish for the last or one additional step in 100% absolute ethanol since the resin corrodes plastic.

10. The ethanol was changed to LR white resin. To remove the remaining ethanol the coverslips were moved around in the embryo dishes using tweezers until no “clouds” of ethanol were observed anymore. The samples were incubated for a minimum of 30 min.
11. The resin was changed and the coverslips were moved around again (although typically no “clouds” were observed anymore). The embryo dishes were sealed with Parafilm and incubated overnight at 4°C.
12. The samples and fresh LR white resin was taken out of the fridge and allowed to warm up to RT for at least 1 h.
13. A small box with a plain underside was turned upside down and covered with aluminum foil. It was labeled well if there was more than one sample (preferably on the surface and on the sides since the resin can destroy the label).
14. The lid of an embedding capsule was removed and it was made sure that the capsule had a clear rim without protruding pieces of plastic on the inner side (if so, small protrusions were removed by running the fingernail over it – but great care was taken not to overdo it and create groovings). The capsule was placed into a capsule-rack (stably but not too firmly) and was overfilled with resin (a convex surface is needed). Most of the resin from one embryo dish was removed, the coverslip was taken out and placed with the cells facing down onto the capsule with the resin. If necessary, it was centered over the capsule. The capsule (with the coverslip on top) was taken out of the rack using large tweezers and was turned upside down. This turning was performed without interruptions, not too slow and not too fast, to keep the coverslip in place. The capsule with the coverslip was placed on the aluminum foil. To facilitate this, a better angle was obtained by slightly turning the capsule in the tweezers before putting it down (without touching the coverslip). The capsule was carefully centered on the coverslip.

Only one sample was processed at a time.

15. The samples were polymerized for 48 h at 60°C.
16. The samples were let cool down for a minimum of 1 h (a few days are also possible).
17. The samples were taken off from the aluminum foil and the coverslips were removed by dipping the samples as short as possible (about 2 sec) into liquid nitrogen: the sample was held with large tweezers and also the coverslip was already grabbed with tweezers before dipping the sample into the nitrogen, so that the coverslip could be pulled away immediately. Too long exposures to liquid nitrogen and repeated cycles of freezing and thawing were avoided as this creates cracks on the block that can make the sample useless. Only one sample was processed at a time.

If the surface of the blocks was very small after polymerization, for the next experiments a beaker with water was placed in the 60°C oven during polymerization (step 15). Occasionally this helped to retain bigger surfaces.

18. The blocks are very stable and can be kept for extended periods (up to years) at RT. However, samples with fluorescent signals were preferably processed within 1-2 months.

Materials:

Aluminum foil	Liquid nitrogen
Box with plain underside	LR white resin
Colored sticker spots	Oven (60°C)
Embedding capsules	Parafilm
Embryo dishes with lids	Rack for capsules
Ethanol, absolute, 30%, 50%, 70% (4°C)	Styrofoam box with ice
Ethanol, absolute, 90%, 100%	Tweezers
Fixed cells on Ø 12 mm coverslips	Tweezers, large
Gelatine capsules	

3.2.8.2 Cutting ultrathin sections

Ultrathin sections (~100 nm) were cut on a Leica Ultracut UCT ultramicrotome at a speed of 1 mm/s.

Two grid types were used in this work, both have advantages and disadvantages: mesh grids are very stable but all parts of the sections located on the bars of the grid cannot be imaged with TEM. In contrast, slot grids with a formvar/carbon membrane allow imaging of the whole section but they are very fragile and the membrane can easily tear. In addition, on slot grids DAPI-signals maintained in the section were typically lower than on mesh grids, most probably due to the membrane absorbing light. Based on this, for correlative microscopy experiments or experiments with limited cell numbers both grid types were combined in a ratio of about 2:1 or 3:1 mesh:slot grids. For experiments with high cell numbers only mesh grids were used. As all samples were subjected to osmium ammine staining (see section 3.2.8.3) only gold grids were used in this work. Nickel or copper grids are not resistant to the HCl treatment involved in the staining procedure.

Procedure:

1. The capsule was removed from the polymerized block by making two cuts separated by a few mm on the long side of the capsule and using the piece in between as a zipper to peel of the capsule. Care was taken not to touch the surface of the block.
2. For the correlative microscopy experiments, the cells of interest were relocalized using the ultramicrotome. The contrast on the block can be enhanced by casting a shadow on it with

a razor blade. Care was taken not to touch and therefore cut the block.

3. A pyramid of maximum 1x1 mm in size was cut using razor blades: first, an area a little larger than the surface of the final pyramid was marked. This allowed quick and rough removal of most of the surrounding material, left some space for small adjustments and made it easier to precisely prepare the pyramid in the second step. It is important that the pyramid is as close to a perfect rectangle or square as possible. Especially the longer sides of the rectangle should be parallel – this longer side will be aligned to the knife later and therefore sectioning will take place perpendicular to it.

For easier orientation in the later steps, one corner of the pyramid was cut off.

After finishing the pyramid all resin particles were carefully removed from the ultramicrotome using a brush to prevent that pieces end up in the mechanics of the instrument.

4. A dish with filter paper was prepared and the filter paper was labeled (the grids were numbered from 1-X).
5. To clean the mesh grids they were briefly washed in 0.25 N HCl, put on filter paper to remove most of the liquid, briefly washed in acetone and let air dry on filter paper. Slot grids are very fragile, therefore they were not included in these washing steps. Both, mesh and slot grids were incubated for 20-40(-60) minutes in $\text{H}_2\text{O}_{\text{bidest}}$ filtered through a 0.2 μm sterile filter to reduce the charge of the grids. Only grids to be used within the next 30-60 min were prepared.

Care was taken that the side of the grids on which the sections were located in the end faced up on the filter paper and down on the water; for the mesh grids this is the rough side, for the slot grids this is the side where also the membrane is located (darker side).

6. The sample was mounted on the ultramicrotome and 100 nm sections (golden color) were cut using a diamond knife:
 - The boat of the diamond knife was filled with $\text{H}_2\text{O}_{\text{bidest}}$ filtered through a 0.2 μm sterile filter. Care was taken that the knife was completely in contact with water. If necessary contact was established by running a single eyelash attached to a wooden stick along the knife. Great care was taken that the knife was never touched from the top but only from the bottom in order to prevent it from getting damaged.
 - The water level was reduced until it was horizontal (even gray color).
 - The sample block was aligned to the knife with its longer side. While approaching the block with the knife the shadow of the knife on the block was always followed in order to prevent the diamond knife from getting damaged by being run into the block. As soon as the knife was reasonably close to the block the angle of the knife and the position of the block were adjusted until the knife, the shadow of the knife on the block and the block itself were parallel to each other. Great care was taken that the distance

of the knife from the block was the same at the top and at the bottom of the block. Slowly the knife was moved closer to the block while the alignment was continuously checked and if necessary readjusted.

- An upper and a lower limit for the movement of the microtome arm was set. Within this window, the arm moves with 1 mm/s to guarantee good sectioning. Outside this window, the arm moves faster to make the cutting process time-efficient. It is recommended to set the window not too small to allow the arm to stabilize prior to cutting.
- The water level in the boat of the knife was reduced so that a fine bright line was observed at a small distance from the knife.
- The ultramicrotome was set on automatic mode and sections were cut.

Occasionally it was necessary to stop the ultramicrotome again and remove incomplete sections or section fragments using an eyelash attached to a wooden stick and/or a small metal loop in order to prevent the successive sections from crumpling. In case the sections did not slide onto the water but got stuck on the knife the water level was slightly adjusted.

In case the ultramicrotome cut too thin (silver color, 70-80 nm) or too thick (purple/violet color, 150 nm; or even blue color, >150 nm) sections despite being set at 100 nm the section thickness was adjusted on the microtome until golden sections were obtained. However, usually there was no or only very little deviation.

The ultramicrotome used in this work displayed the number of the sections cut and the total thickness of the cut segment – this information was used to cut only as many sections as needed for the prepared amount of grids and to adjust the cut volume to the thickness of the cells.

7. The slot grids were taken out of the water and air-dried while they were still held with fine tweezers; they were not put down to prevent damage to the membrane. For mesh grids it was sufficient to take them out immediately before use and drain the remaining water on filter paper.
8. The sections were arranged in groups of 2-4 (depending on section size) using wooden sticks with a single eyelash attached and were taken up with the grids by approaching the sections from the top (this was facilitated when the water level was slightly increased before). Care was taken that the sections ended up on the right side of the grid (see step 5). It was tried to keep the correct order of the sections – this provided the advantage of giving a rough idea about the relative position of the section in the cell.

The mesh grids were placed on filter paper inside Petri dishes (with the sections facing up) and let air dry. As in step 7, the slot grids were dried in the tweezers before putting them onto filter paper.

Always one group of sections was arranged, taken up with a grid and placed on filter paper or put aside to dry in the tweezers before the next group of sections was arranged.

9. When enough sections were cut and all of them were taken up with grids, the sample was demounted from the microtome and all remaining section fragments still floating on the water in the boat of the knife were removed using a small metal loop.

If more samples were to be cut, the procedure was repeated from the beginning.

10. After finishing the diamond knife was cleaned by running H_2O_{dest} over it (the knife was always positioned in such a way that the water did not hit the knife directly).

In case sections got stuck on the knife during the cutting process it was cleaned using diamond knife cleaning sticks:

- A thin tip was prepared on the cleaning stick by cutting off pieces from both sides with an angle of about 30° using a fresh double edge razor blade.
- The thin tip of the cleaning stick was moved over the diamond knife in lateral direction. This was repeated until all debris was removed from the knife. Great care was taken that always a fresh area of the cleaning stick was used (the knife should not enter into one of the previous cuts).

Materials:

Acetone	Metal loop
Diamond knife cleaning sticks	Polymerized blocks
Double edge razor blades	Single edge razor blades
Filter paper (\varnothing 40 mm)	Sterile filter 0.2 μ m
Fine tweezers	Syringe, sterile
Gold grids (slot and mesh)	Ultramicrotome
HCl 0.25 N	Well closing Petri dishes
H_2O_{bidest}	Wooden sticks with eyelash
H_2O_{dest}	

3.2.8.3 Osmium ammine staining of DNA

Staining with osmium ammine – to be precise with osmium ammine B, a modified osmium ammine complex which is more stable and easier to obtain (Olins et al. 1989) – of ultrathin sections was performed as described in Vazquez-Nin et al. (1995). After being activated by SO_2 -generating reagents (here $Na_2S_2O_5$) osmium ammine represents a Schiff-type reagent that stains DNA in a Feulgen-like reaction (Vazquez-Nin et al. 1995): an incubation step with HCl removes purine bases from the DNA and thus leads to the creation of aldehyde groups which are then detected by osmium ammine (for a detailed review of the Feulgen reaction, Schiff-like reagents and osmium ammine staining see Chieco and Derenzini 1999). Therefore this staining is – in contrast to DAPI – not sequence-specific. The HCl treatment furthermore

degrades RNA which otherwise is also stained by osmium ammine (Derenzini and Farabegoli 1990) and so makes the staining highly DNA specific. A good measure for the efficiency of RNA degradation is the staining intensity in the nucleoli: their color should only be slightly darker than the cytoplasm. Be aware that small magnifications at the microscope tend to give a wrong impression of the staining quality: here the efficiency of the RNA degradation often seems poor, while it typically is fine at higher magnifications. In contrast to other staining methods, like e.g. post-embedding immunodetection with antibodies coupled to gold grains, osmium ammine has the big advantage that it can penetrate the whole section so that the staining is not only restricted to the surface of the section.

There should be a minimum of one night between cutting (see section 3.2.8.2) and staining of the sections to make sure that they are completely dry. All steps were carried out in embryo dishes. Care has to be taken that the grids are not mixed during staining – this means that only 1 or 2 grids can be stained in one embryo dish (either one mesh grid or one slot grid or one mesh and one slot grid).

Procedure:

1. 1.5 ml 5 N HCl per embryo dish were freshly prepared.
2. 0.75 ml of osmium ammine staining solution per embryo dish were freshly prepared. The solution was let stand for 30-40 min.
3. The grids were incubated for 40 min floating on 5 N HCl to degrade RNA. In comparison to Vazquez-Nin et al. (1995) this elongated incubation – 40 min instead of 30 min – was necessary to efficiently degrade RNA in the cells used here.

It was made sure that the sections were facing down and that the grids were floating in the middle of the dish, not at the periphery (if necessary surface tension was removed by moving along the periphery of the dish with tweezers).

4. The mesh grids were drained on soft tissue by carefully touching the tissue with the outer edge of the grid and immediately transferred onto the osmium ammine staining solution (in contrast to the procedure described in Vazquez-Nin et al. (1995), where a washing step with H_2O_{dest} is interposed here). Only one grid was transferred at a time. The draining step was skipped for slot grids.

The grids were incubated for 30 min in the osmium ammine staining solution according to step 3.

5. The grids were transferred onto H_2O_{bidest} filtered through a 0.2 μm sterile filter equivalent to step 4 and were washed for 5-10 minutes according to step 3.
6. Mesh grids were placed on filter paper inside Petri dishes (with the sections facing up) and let air dry. Slot grids were first air-dried while they were still held with fine tweezers; they were not put down onto filter paper immediately to prevent damage to the membrane.

Materials:

Embryo dishes with lids Filter paper (Ø 40 mm) Fine tweezers H ₂ O _{bidest} HCl 5 N Osmium ammine staining solution	Sections on gold grids Soft tissue Sterile filter 0.2 µm Syringe, sterile Well closing Petri dishes
--------------------------------------------------------------------------------------------------------------------------------------------------------	-----------------------------------------------------------------------------------------------------------------

3.2.9 Microscopy of fixed samples**3.2.9.1 Bleaching experiments to allow the sequential imaging with fluorophores with identical or similar emission spectra**

It can happen that in consecutive steps of a correlative microscopy experiment target structures have to be detected using the same fluorophores or fluorophores with a similar emission spectrum, which cannot be discriminated with the help of proper filter sets. Bleaching experiments can provide a solution to this problem.

In this work, this was the case in the correlative microscopy experiments. First H2B-mRFP fluorescence was recorded in living cells, after fixation the cells were relocalized on the UltraView VoX SDLSM where fluorescence was entirely bleached and an Alexa594-coupled secondary antibody was used in the subsequent immunofluorescence experiment.

The procedure described here was published in Hübner et al. (2013).

Procedure:

1. The underside of the dish/chamber was cleaned with 80% absolute ethanol and the sample was mounted on the microscope.
2. The cells were relocalized (see section 3.2.10.1 for a detailed explanation).
3. The observed areas were bleached using FRAP settings (20% of laser power for 488 and 561, 2 ROI intervals, 10 ms spot bleach time, 1 spot interval). Using these settings bleaching in the mid focal plane was enough to bleach the whole nucleus.
4. Step 3 was repeated 2-3 times (= overall number of cycles 3-4) until all fluorescence had vanished.
5. In case the samples should only be further processed on the next day, they were washed 2x with 1x PBS and kept well sealed with Parafilm at 4°C.

Materials:

Ethanol, absolute, 80% Fixed cells on coverslips Parafilm	PBS 1x UltraView VoX (SDLSM)
-----------------------------------------------------------------	---------------------------------

3.2.9.2 Confocal laser scanning microscopy (CLSM)

Multicolor imaging of 3D-samples as well as DAPI imaging of ultrathin sections obtained after embedding the samples in resin and cutting them on an ultramicrotome (see sections 3.2.8.1 and 3.2.8.2) was done on a Leica SP5 CLSM.

Imaging as it is described here was published in Hübner et al. (2013).

Procedure A – Imaging of 3D-samples:

1. The coverslip and the microscope slide of the sample were cleaned with 80% absolute ethanol and the sample was mounted on the microscope.
2. If necessary, the cells of interest were relocalized (see section 3.2.10.1 for a detailed explanation).
3. The cells were scanned using standard settings, typically with 700-1000 Hz, Line average 2, 50x50x210 nm voxel size. For microinjected samples a z-spacing of 100 nm was chosen due to the small size of the beads (increasing the probability that a bead was imaged directly in or at least close to its focal plane). The laser power was kept at a minimum to avoid bleaching. This was especially important for correlative microscopy samples which were scanned directly in 1x PBS instead of being mounted in Vectashield (for explanation see section 3.2.10.1).

Procedure B – Imaging of ultrathin sections:

1. Microscope slides were cleaned with 80% technical ethanol.
2. On each slide one grid was put with the sections facing up and it was covered with a big coverslip (e.g. 24x32 mm). To keep the coverslip in place small drops of Fixogum were applied on each corner (if too much Fixogum is used it can spread below the coverslip and make the grid useless when it touches it) and let dry completely. It was tried to move the coverslip as little as possible to avoid damage to the sections.
3. After the Fixogum dried completely the sample was mounted on the microscope.
4. If necessary, the cells of interest were relocalized (see section 3.2.10.1 for a detailed explanation).
5. Images (only 1 plane, no z-stacks) were acquired using 400 Hz, the maximum gain setting and as little laser power as possible (clearly higher settings were needed than for procedure A, typically 20-40%). For overview images (e.g. 480x480 nm pixel size) a line average of 8 was used, for scans of individual cells/nuclei (50x50 nm or 30x30 nm pixel size) a line average of 16. The “right” focal plane typically showed the brightest signal and the best signal-to-background ratio.
6. The exact positions of the imaged cells on the grid in relation to the center of the grid were

recorded.

- The grids were unmounted by carefully removing first the Fixogum with tweezers and then the coverslip with a scalpel. Great care was taken that the immersion oil from the microscope did not get into contact with the grid. The sections were put back on filter paper.

Materials:

Coverslips (e.g. 24x32 mm)	Leica SP5 (CLSM)
Ethanol, absolute, 80%	Microscope slides
Ethanol, technical, 80%	Samples
Fine tweezers	Scalpel
Fixogum	

3.2.9.3 3D structured illumination microscopy (3D-SIM)

Super-resolution fluorescence images were acquired on an OMX 3D-SIM.

Bright samples with low background intensities are crucial for 3D-SIM. This can be achieved by following the protocol given in procedure A of section 3.2.6.1.

The OMX 3D-SIM system is optimized for using coverslips with a thickness of 170 μm (see also section 3.2.1.4 and 3.2.10.1). Whenever possible such coverslips were used for sample preparation.

Imaging with the OMX as it is described here was published in Hübner et al. (2013) and Hübner et al. (2015).

Procedure:

- The coverslip and the microscope slide of the sample were thoroughly cleaned with 80% absolute ethanol. As this occasionally dissolved the nail polish, if necessary, the samples were resealed with clear nail polish after cleaning to prevent the coverslips from moving.
- The immersion oil with the best-matching refractive index was chosen. This depends on the sample, e.g. the thickness of the coverslip, the embedding media used, the thickness of the sample and the temperature during acquisition. Here, usually oil with a refractive index of 1.514 was used.

Clear signs for a suboptimal oil are if the reconstructions of the images are grainy and/or have a halo around the nucleus.

- For correlative experiments, relocalization of the cells of interest (see section 3.2.10.1 for a detailed explanation) and recording their positions on the pdV microscope prior to scanning with the OMX was essential. The positioning of the slide on the pdV and on the OMX is aligned with each other. Due to the 100x lens and the missing binocular on the

OMX, relocalization of cells on the OMX alone is nearly impossible.

In case the samples were not scanned on the OMX within a few hours, the oil was removed and the coverslips were cleaned again according to step 1 before scanning them, otherwise the same oil was used.

4. The samples were scanned on the OMX.

Here EMCCD 5 MHz mode was used for the red and green channel and Conv 5 MHz mode for DAPI. Care was taken that the settings for the gain (in case of EMCCD mode) and laser transmission rates were set in such a way that exposure times ranged between 25 and 100 ms and that the maximum intensities showed values between 15 000 and 20 000. Z-spacing was always 125 nm.

5. Super-resolution images were reconstructed using channel-specific OTFs in SoftWorx.

Materials:

Clear nail polish Ethanol, absolute, 80% Immersion oil of different refractive indices (ranging from 1.510 to 1.518, usually 1.514)	OMX (3D-SIM) pdV microscope Samples SoftWoRx
-------------------------------------------------------------------------------------------------------------------------------------------------	-------------------------------------------------------

3.2.9.4 Transmission electron microscopy (TEM)

TEM images were acquired on a Morgagni 268 TEM.

There should be a minimum of one night between staining (see section 3.2.8.3) and observation of the sections to make sure that they are completely dry.

TEM, as it is described here, was published in Hübner et al. (2013).

Procedure:

1. If necessary, the cells of interest were relocalized (see section 3.2.10.1 for a detailed explanation).
2. Images were acquired using different levels of magnifications to obtain both, overview images and high-resolution details. In addition to images including the whole nucleus, usually images were taken at a magnification of 11 000x, 22 000x and 44 000x. Be aware that the sample rotates with each step of magnification. Typically, images were acquired with an average gray value of 50-60% and great care was taken not to cut off signals on both sides of the spectrum (high and low values).

Materials:

Morgagni 268 (TEM)	Samples
--------------------	---------

3.2.10 Notes on correlative microscopy

For correlative microscopy, meaning the imaging of one and the same cell with different microscopic systems, certain requirements have to be fulfilled in order to allow the relocalization of the cells of interest on all microscopes. In addition, due to the fact that the different microscopes have different needs and due to the method itself, a number of problems are associated with correlative microscopy.

The major part of these notes was adapted from Hübner et al. (2013).

3.2.10.1 Requirements

In order to relocalize specific cells, the use of gridded coverslips is absolutely essential. Depending on which microscopic systems are involved in the experiment, either coverslips gridded by hand as described in step 2 of section 3.2.1.4 can be used or commercially available gridded coverslips are recommended. Hand gridded coverslips have the advantage that they are cheap and that the grid can be applied to any coverslip or glass bottom dish available. However, the grid is much rougher and exhibits a larger square size than commercially available gridded coverslips (~1x1 mm vs. 0.6x0.6 mm) and only leaves a very slight imprint in the resin after embedding the samples for TEM. Both of these points make the relocalization of the cells of interest on the polymerized block extremely difficult. Therefore, when TEM is involved in the experiment, commercially available gridded coverslips, like the Bellco coverslips used here, are preferred due to their smaller square size, the continuous numbering of the squares (with hand gridding typically only every second square is numbered) and the good imprint in the resin (the grid is carved into the glass by laser-etching). However, these coverslips have the disadvantage that they are only available as number 1.0 coverslips, meaning in a thickness of 130-160 μm , which can cause problems with imaging on the OMX 3D-SIM. This system is optimized for a coverslip thickness of 170 μm and although the reduced thickness of the number 1.0 coverslips typically can be compensated by using an immersion oil with a different refractive index, the results are not always optimal. Therefore in this work commercially available coverslips from Bellco were used only when the samples were intended also for TEM (correlative microscopy experiments). Otherwise hand gridded coverslips were used, either on high-precision coverslips with a thickness of 170 ± 5 μm (when 3D-SIM was involved) or on number 1.5 coverslips (160-190 μm).

For correlative microscopy experiments involving live cell imaging, MatTek glass bottom dishes are perfectly suitable as they combine several essential features: (1) A hole is cut into a normal plastic Petri dish and a coverslip is attached from below, which allows high-resolution live cell observations with oil immersion objectives. (2) A whole variety of predefined dishes is available, including dishes with gridded coverslips from Bellco. In this work in addition to predefined dishes with 20x20 mm square coverslips also custom made dishes with Ø 12 mm round gridded Bellco coverslips were used. (3) In contrast to other live cell systems the coverslip can easily be detached from the dish using coverslip removal fluid (see procedure below) and thus can be mounted on a microscope slide or can be embedded for TEM.

Procedure:

1. 1 ml of coverslip removal fluid was put into the lid of a 35 mm dish and the MatTek dish with the sample was placed inside. Any air bubbles were removed by carefully lifting the sample again on one side.
2. The sample was incubated for 45 min. During this time the liquid inside the dish could be changed according to the needs of the protocol (e.g. if an immunofluorescence experiment or the embedding procedure was performed in parallel). However, care was taken not to dilute the coverslip removal fluid with any other liquid as this might reduce its effectivity.
3. The sample was taken out of the lid and the coverslip removal fluid was thoroughly wiped off using soft tissue in order to avoid that the cells get into contact with it.

To avoid that the cells dry out, a larger dish (e.g. a 60 mm Petri dish) was filled with the same solution the cells were currently incubated in, the MatTek dish with the sample was held over this dish and slight pressure was applied on the coverslip from the inside so that the coverslip was detached and transferred to the 60 mm dish. Great care was taken that only the periphery of the sample was touched with the tweezers in order to avoid damaging the cells of interest.

Occasionally the detachment was not possible after 45 min of incubation, e.g. at low room temperature or if the coverslip removal fluid potentially got diluted by some other liquid. In these cases, the dish was again wiped well from below and placed into fresh coverslip removal fluid. After some time, removing the coverslip was tried again.

4. For proper mounting of the sample on a microscope slide the remnants of the glue had to be removed from the coverslip. The glue was carefully scratched off using tweezers, working from the inner rim towards the periphery of the coverslip. Great care was taken that the inner part of the coverslip was not touched in order to avoid damaging the cells of interest. The removal of the glue was done very thoroughly as even tiny remnants could cause the invasion of nail polish under the coverslip when mounting the sample, which typically destroyed it. Care was taken not to break the coverslip as even after very

thorough removal of the glue typically a small difference in height remained between the rim and the observation area. This did not play a role as long as the coverslip was intact but became a problem when a part of the rim was missing, as this typically caused the invasion of nail polish during mounting.

For embedding the sample for TEM the remaining glue on the sample after the detachment was not removed as it did not interfere with the embedding process.

Materials:

Coverslip removal fluid Petri dishes (35 mm, 60 mm) Sample in a MatTek dish	Soft tissue Tweezers
-----------------------------------------------------------------------------------	-------------------------

In this work, depending on the type of the correlative microscopy experiment, the coverslips of the MatTek dishes were detached at different time points during the procedure: if 3D-SIM was not included in the experiment (pathway I in **Figure 11**), all steps of the immunofluorescence experiment and also imaging on the Leica SP5 CLSM were performed with the coverslip still attached to the dish, without mounting it on a microscope slide but scanning the cells in 1x PBS instead. The coverslip was only detached after imaging was completed, here – in order to save time – during embedding for TEM (steps 7 and 8 of section 3.2.8.1 – if necessary, the incubation in 100% absolute ethanol was prolonged in order to reach 45 min incubation in the coverslip removal fluid). On the other hand, if imaging on the OMX 3D-SIM was involved (pathway II in **Figure 11**), the coverslip was detached from the MatTek dish already during the blocking step of the immunofluorescence staining (step 4 of procedure A in section 3.2.6.1) and was later mounted on a microscope slide. Prior to embedding in resin the coverslip was demounted again and extensively washed (see step 3 in section 3.2.8.1). These two different procedures were performed because without mounting (pathway I) subsequently the quality of the TEM images used to be better (see also section 3.2.10.2 and compare results in section 4.4.1, page 248 (**Figure 65+66 D** respectively **Figure 67+68 E**)), but the harsh imaging conditions of OMX 3D-SIM require mounting to avoid bleaching.

When choosing areas for imaging, several points are important: (1) For easier relocalization of the cells of interest it is recommended to turn the grid always into such a position that the numbers can be read in the normal way (not upside down, etc.). (2) The position of the chosen area has to be easily identifiable later. For the smaller square size of the Bellco grid and the constant numbering on these coverslips, this is basically always the case (but cell density should be taken into account, see point (4) below). When using hand gridded coverslips, however, choosing the right position is essential for the efficient relocalization of the cells of

interest. It turned out very useful to only choose positions that include a specific part of a number of the grid or that are in a corner of a square. (3) In case TEM is included in the

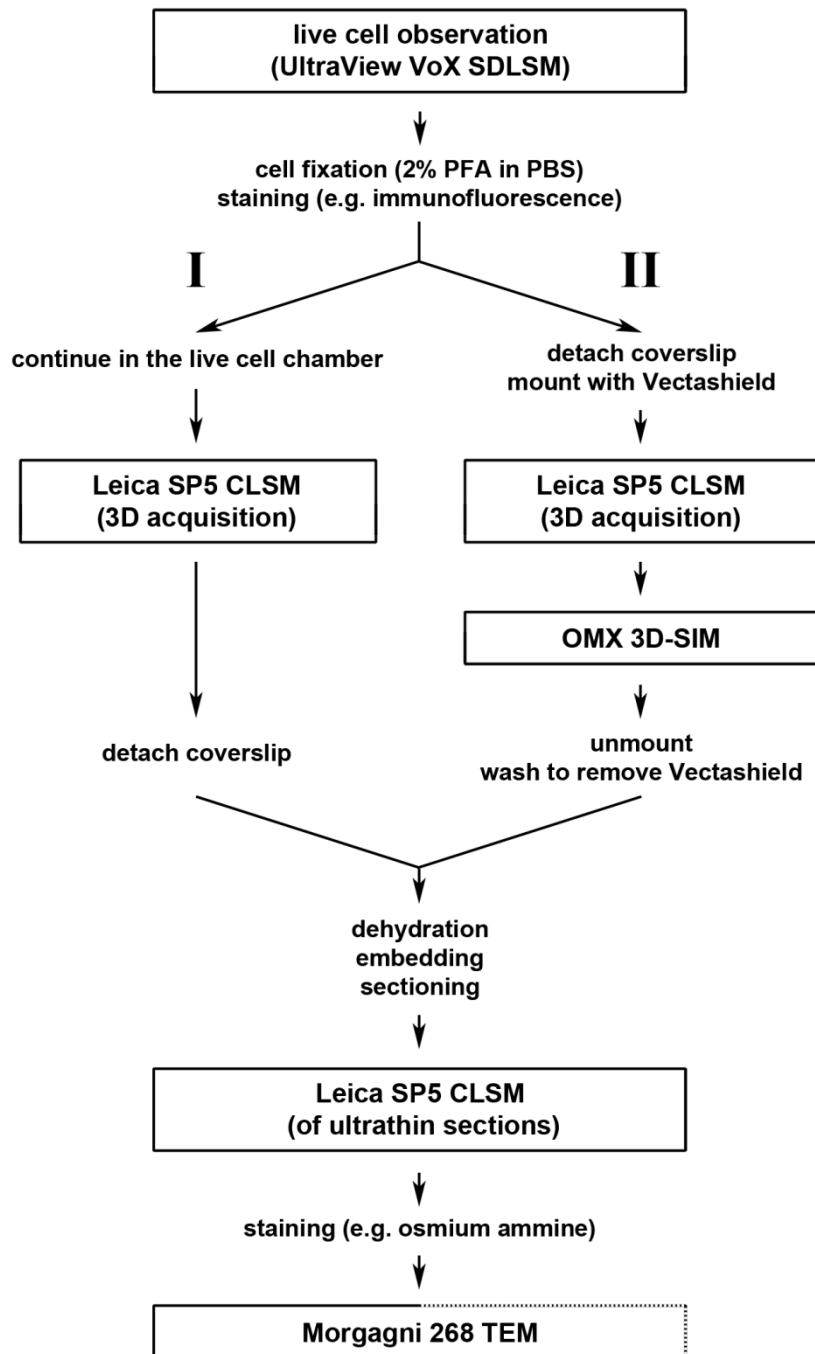


Figure 11: Flow chart for the setup of correlative microscopy. Live cell observations were performed on an UltraView VoX SDLSM. After the cells were fixed and stained, two different pathways were followed: (I) Images were acquired on a Leica SP5 CLSM with the coverslip still attached to the MatTek dish (live cell chamber). The coverslip was only detached before or during the dehydration steps. (II) Imaging on the OMX 3D-SIM is included, therefore the coverslip was detached from the live cell chamber already during the immunofluorescence staining and was mounted in Vectashield on a microscope slide. After imaging the cells on the Leica SP5 CLSM and the OMX 3D-SIM, the coverslip was unmounted again and extensively washed. From this point on both pathways were continued in the same way: first, the samples were dehydrated, embedded and ultrathin sections were cut, then the cells were imaged again on the Leica SP5 CLSM before finally the samples were stained for TEM and imaged on a Morgagni 268 TEM. Note that the TEM image quality of samples processed by pathway I used to be better than of samples that underwent pathway II. Figure adapted from Hübner et al. (2013).

experiment great care has to be taken to choose only areas in the central part of the grid, as the embedding procedure only allows a small part of the coverslip being conserved on the block. For the Bellco grid, this typically limits the usable area to the following numbers of the grid: 33-34, 43-46, 55-58 and 67-68 (see grid pattern in **Figure 9 A**). (4) Areas exhibiting a reasonable cell density should be chosen. A too high density makes it difficult to see the grid and therefore hinders effective relocalization or makes it even impossible. Therefore, for correlative microscopy, the cells were typically only seeded at a cell density of 30-50%. A too low density, on the other hand, increases the risk that none of the cells can be followed through all steps and on all microscopic systems. Due to the many steps and the various requirements involved in correlative microscopy, a number of cells inevitably get corrupted during the process (especially at the TEM level). Starting with as many cells as possible counteracts this problem. For the same reasons it is strongly recommended to record all available cells from the initial field of view with all successive microscopes.

In addition to choosing the right areas, their positions also have to be precisely registered in order to enable the relocalization of the cells of interest in the later steps. Typically a scheme of the grid was printed and the exact position of the area of interest was drawn into this. This was also done when imaging ultrathin sections on the Leica SP5 CLSM. Here the exact position of the cells on the grid was recorded in relation to the asymmetrical center of the grid. Typically positions more than 10 squares away from the center of the 300 mesh grid were not taken into account as these could not be observed on the electron microscope later.

For relocalizing the cells on a light microscope (here the Axiovert 200 M widefield microscope, the Leica SP5 CLSM, the UltraView VoX SDLMS, and the pdV widefield microscope), in a first step transmission light was used and any number on the grid was identified. Defocusing usually resulted in a better contrast of the grid. Once a number was recognized it was used as a reference point to navigate to the area of interest – it was not necessary to identify all numbers as long as track of the squares could be kept. For this reason it is recommended to have a printout of the grid at hand, in order not to lose orientation. In a second step, the microscope was switched to fluorescent mode and the cells of interest were identified. For reliable relocalization it was absolutely necessary to have a printout of the field of view in the very first experiment at hand (i.e. e.g. from the live cell experiment) in order to make sure not to miss any cells and not to waste time and effort on cells that were not included initially.

For TEM the cells of interest had to be relocalized on the block after embedding and prior to preparing the pyramid. Due to the embedding process from this step on all images were mirrored in comparison to the images acquired before. During the preparation of the pyramid all cuts were registered one by one in a drawing to ensure that the orientation on the sample

was kept (most of the numbers of the grid are cut off during this process!) and that the cells of interest were not accidentally removed. In order to facilitate the identification of the cells of interest in the microscope later, it is recommended to keep the size of the pyramid as small as possible. Nevertheless, some space should be left around the region of interest as cells on the very border of the section are difficult to image with TEM (due to deformations of the section in the electron beam if it does not cover one complete square of the mesh grid).

To relocalize the cells of interest on the TEM grids on the Leica SP5 CLSM, again transmission light was used. As the first step, the sections were searched by starting from the center of the grid and moving towards the periphery. Once a section was found, the stage was centered on it, the microscope was switched to fluorescent mode and the cells of interest were identified. Again it is recommended to have a printout of the field of view in the very first experiment at hand. It always has to be kept in mind that now only a 2D section of the 3D volume of the cell is being viewed. This means that some cells might be cut in a midsection while others might be cut quite peripherally, which makes the identification of cells difficult. Therefore it is better to focus more on comparing angles and distances of cells to each other rather than on the morphology of the cells.

On the Morgagni 268 TEM the cells of interest were relocalized by navigating to the center of a section and searching the cells from there. This process was tremendously facilitated when the cells had been imaged at the Leica SP5 CLSM and the positions of the cells of interest had been registered before (see above). Although the grid was rotated arbitrarily in comparison to its orientation on the Leica SP5 CLSM, now the cells easily could be relocalized by simply counting the squares from the center of the grid.

3.2.10.2 Problems

After embedding the cells in LR white resin only DAPI fluorescence is maintained in the polymerized block. If also other fluorochromes should be imaged on ultrathin sections, a different embedding medium is recommended (Quetol 651 kit; Polysciences, Eppelheim, Germany). Osmium ammine staining on such samples was never tried in our lab, but it is reported to be possible (Vazquez-Nin et al. 1995).

Another problem is that with the current setup, it was not possible to visualize DAPI fluorescence in the physical sections on the grids with 3D-SIM. In contrast to imaging ultrathin sections on the Leica SP5 CLSM, for 3D-SIM the grids had to be mounted with Vectashield, otherwise the image reconstruction process caused tremendous artifacts. However, as the grid and especially the sections are flexible, it was not possible to mount them in a plane way. Therefore imaging ultrathin sections with 3D-SIM was omitted in this work.

Furthermore, as already briefly mentioned in section 3.2.10.1, 3D-SIM and TEM are partially exclusive and perfectly matched images obtained with the different microscopic systems are nearly impossible to achieve. For a more detailed discussion of these two topics see section 5.2.2 in the discussion.

3.2.11 Image processing

3.2.11.1 Correction for chromatic aberration of CLSM and 3D-SIM images

A huge problem in fluorescence microscopy, especially in high- or super-resolution microscopy, is chromatic aberration, i.e. the unequal refraction of light of different wavelengths. These differences can result in a shift of focus of up to several sections between the different color channels of one acquisition. As this would influence both, observations done by eye as well as automated evaluations, this shift has to be eliminated or at least minimized in post-processing.

The correction of the Leica SP5 CLSM images was done in ImageJ using a plugin originally developed by Dr. Boris Joffe (*StackGroom*) (formerly LMU, Munich, Germany) and further adapted by Dr. Katrin Schneider (*StackGroom2*) (formerly LMU, Munich, Germany). The plugin converts the image sequence of single images obtained from the microscope into stacks (one stack for each color channel) and deletes a certain number of sections from the beginning or the end of the individual stacks, through which the shift correction is achieved. The number of sections to be deleted for each channel is defined by the user based upon recent shift measurements. These shift measurements were regularly done by Dr. Irina Solovei (LMU, Munich, Germany) using multicolored fluorescent beads.

Corrections for the chromatic shift of OMX 3D-SIM images were done in SoftWoRx. The parameters for the alignment were regularly determined by Dr. Jürgen Neumann (formerly head of the Center of Advanced Light Microscopy (CALM), LMU, Munich, Germany) or Andreas Maiser (LMU, Munich, Germany). However, depending on the sample specifications (like e.g. sample thickness and/or coverslip thickness) the common settings for the shift correction were not always sufficient to achieve a good alignment. In these cases, the images were realigned by adjusting the parameters in Softworx until the alignment seemed right by eye. The shift correction with SoftWoRx is not limited to deleting whole sections, but also sub-pixel-values can be chosen.

3.2.11.2 Generation of 3D-reconstructions in Amira

Amira is a powerful software for the 3D visualization of microscopic data, including the generation of 3D surface and volume renderings.

Procedure:

1. In ImageJ the image stacks to be reconstructed were cropped to a reasonable size. If necessary, brightness and contrast were adjusted.
2. In Amira the background was changed to black via the “view” tab.
3. The image stack to be reconstructed was opened in Amira. In the pop-up window the respective voxel size was specified (for the OMX 3D-SIM images this means 0,0395 – 0,0395 – 0,125 (note that the software required the German punctuation, i.e. commas instead of dots)).
4. The processing menu was opened with a right-click on the green bar of the dataset and in the menu item “display” the function “isosurface” was selected.
5. In the properties field the box for auto-refresh was activated and an appropriate threshold was applied.
6. For the colormap the profile “volrenRed.col” was chosen.
7. Using the snapshot function xy, xz, and yz views were exported as TIFs.
8. In the pool field the function “VRML-export” was chosen (the yellow bar of the isosurface has to be selected for that). In the properties field a filename was specified and .wrl was chosen as data format. With “apply” the document was saved.
9. Adobe 3D Reviewer was opened and a new document was created. The background was changed to black via the “view” tab.
10. Using the import function the .wrl file created in step 8 was imported and subsequently saved as PDF via “file” and “export”.
11. The Amira network was saved as “Amira Script and data files”.

3.2.11.3 Alignment of images obtained from different microscopic systems

Procedure:

1. Corresponding sections of all imaging steps were identified. This worked best when starting with the TEM image as a reference, as here typically only a limited number of z-sections (often only one) was available for each cell.
2. If necessary, single images were flipped. E.g. TEM and 3D-SIM images were always mirrored in comparison to SDLSM or CLSM images.

3. The images were manually aligned to each other using Photoshop:
- Overlays of pairs of images with chromatin staining were created by putting the two images into a two-layered image.
For fluorescent images (e.g. obtained with SDLSM, CLSM, 3D-SIM) at least one of the two images was pseudocolored, resulting in one gray-scale and one red image or one green and one red image.
For the alignment of one fluorescent image and a TEM image, the fluorescent image was pseudocolored in turquoise (merge of green and blue) and inverted (resulting in all signal being red), while the TEM image remained in grayscale.
 - The opacity of the upper layer (typically colored in red) was reduced to 50-60% and rotations and size differences between the two images were corrected by eye using the rotate and resize functions. It is recommended to increase the canvas size prior to that.
For the alignment of images obtained with SDLSM, CLSM, and 3D-SIM the factor for resizing typically could be calculated from the pixel sizes. For TEM images, however, this was not possible, as embedding typically caused some shrinkage, with the degree varying from experiment to experiment or even from sample to sample. Therefore, for images of cells on ultrathin sections (i.e. both, the CLSM image of the section and the TEM images) the image size calculated from the pixel size was smaller than required. Due to the increased resolution of TEM, the images are much bigger in size in comparison to the CLSM or 3D-SIM images. In order not to lose the advantage of the higher resolution, the alignments were done as described before, but the scale of the TEM image was set back to 100% before applying the transformations. This maintained the option to generate high-quality blow-ups of the image. If necessary the image size was reduced in a later step.
Occasionally the alignment of size and especially rotation could not be fully achieved in one step. In these cases the right parameters were figured out in as many steps as necessary, all transformations done were summed up and the alignment was repeated in one step using the unprocessed images. The reason behind this is that applying transformations practically always includes interpolation, which results in blurry images when repeated several times.
In case also other channels should be aligned in addition to chromatin, these channels were put into separate layers of the same image, their layer visibility was switched off and they were linked with the chromatin image. Like this, all transformations applied to the chromatin image were also applied to these additional channels.
 - The alignment was further improved by using the distort and warp functions equivalent to the application of the rotate and resize functions described above.
-

- The opacity was set back to 100% for all channels, if necessary the visibility of additional channels was switched on again, and all layers were exported into single tiff images using an automatic function in Photoshop (file – scripts – export layers to files).
 - If necessary pseudocolored images were converted back into gray-scales.
4. Overlay images were created in the conventional way for fluorescent images (RGB or RGB plus gray images) or according to the first two paragraphs of step 3 for merges of fluorescent and TEM images (TEM image as a gray-scale, fluorescent image inverted and with 50-60% opacity in a second layer on top).

3.2.11.4 General information on image processing

After the image stacks obtained with the Leica SP5 CLSM were corrected for chromatic aberrations (see section 3.2.11.1), a Gaussian blur with a radius of 1 was applied prior to further processing and/or evaluation. The same filter was also applied to UltraView VoX SDLSM images. The Gaussian blur removes noise and the images therefore look cleaner and less pixelated than the raw images. Furthermore, the borders are smoothed, so that the processed images also appear more contrasted.

Also OMX 3D-SIM images were corrected for chromatic aberrations (see section 3.2.11.1) and then further processed using a macro for ImageJ developed by Dr. Katrin Schneider (formerly LMU, Munich, Germany). This macro converts the original 32-bit images in such a way to 16-bit color composites that all signals in the images are maintained, in particular also signals with low intensities (negative values in the original images). To achieve this, the macro first shifts the intensities of the whole image stack, so that the lowest value or a user-chosen offset becomes 0. Meaning, if the lowest value is -200, this will become 0 and a value of 200 is added to all other pixel intensities. Then the images are converted to 16-bit. Note that the highest pixel intensity possible is now 65535. In case a pixel has a higher intensity than that, it will be reduced to this value. Therefore the macro should not be used if the signals are almost saturated, which is however rarely the case with OMX 3D-SIM images. For the creation of DAPI masks, the determination of the number of nuclear pores and for the segmentation of image stacks (see sections 3.2.12.1, 3.2.12.2 and 3.2.12.5) no offset was chosen and these 16-bit images were used for the DAPI channel. Otherwise – including the red and green channel for the determination of the localization of additional markers in relation to chromatin (see section 3.2.12.5, *Segmentation including the determination of the localization of additional markers*) – the offset was set to 0 for all channels and the images were further converted into

8-bit images (RGB color merge as well as single stacks for each channel) using standard methods implemented into a refined version of the macro. Occasionally it was necessary to go back to the 16-bit or even the 32-bit original images as the automatic conversion with the macro sometimes led to oversaturated signals (compare above).

As mentioned in step 2 of section 3.2.9.4, images at the Morgagni 268 TEM usually are taken at several magnifications and the sample rotates with each step of magnification. In addition, the electron beam typically introduces distortions in the sample. To allow a proper comparison of the images of different magnifications, these rotations and distortions have to be corrected. This was done using Adobe Photoshop. The gray-scale images were put in pairs into a two-layered image, the opacity of the upper one was reduced to 50-60% and the images were aligned by eye using the rotate and resize and potentially also warp and distort functions. Great care was taken to reset the size of the image with the higher magnification (and therefore larger dimensions) to 100% or proportional values before applying the transformations in order to avoid losing resolution. Subsequently, each layer was saved as an individual image with 100% opacity.

All further image processing, such as adjustments of brightness, contrast, color, size or splitting/merging of different color channels was done using ImageJ or Fiji and Adobe Photoshop. Note that only ImageJ and Fiji can handle image stacks.

Figures were prepared with Adobe Photoshop.

3.2.12 Evaluations

Note that for basic evaluations, like the determination of e.g. the number of positive cells, the duration of cell cycle phases or the frequencies of certain morphologies, detailed descriptions are omitted as they are assumed to be generally known.

3.2.12.1 Generation of chromatin masks

For most of the evaluations described in the following sections, masks of the chromatin staining were needed in order to define the nuclei and to eliminate potential dirt/background signals outside the nuclei. As thresholding the original gray-value images by eye is very subjective, the image stacks were segmented into seven density classes (see section 3.2.12.5) and these

segmented images were then used as a basis for the mask. This approach did not exclude, but significantly reduced the subjective influence on the generation of the mask. Although this procedure facilitated the generation of chromatin masks significantly, depending on which cells were processed several problems remained: (1) The hematopoietic cells typically are highly invaginated resulting frequently in thin “channels” pervading the nucleus which easily can get lost when generating the mask. Keeping all those “channels” is very tedious and laborious. Therefore so-called “precise masks” were only generated for the determination of the number of nuclear pores (see section 3.2.12.2). For all other evaluations so-called “rough masks” were used, which were generated with somewhat less care (i.e. partially the small invaginations got lost in the mask) and therefore needed less time. Comparisons of segmentations using precise or rough masks revealed only minor differences (data not shown). (2) Granulocytes, cells where hypercondensed chromatin (HCC) was induced and partially cells where premature chromosome condensation (PCC) was induced exhibit relatively large channels leading to the nuclear surface, which are of course part of the nucleus. But as the channels contain no or only very little chromatin, they typically do not close at the nuclear surface when the mask is generated. Therefore most of these channels had to be closed by hand. (3) Partially the image quality was not perfect although the scanning process was optimized as good as possible (compare section 3.2.9.3). This problem appeared e.g. in very thick cells (>8 µm in z-direction) or in cells with condensed chromatin (e.g. after HCC or PCC induction) and became apparent by a glow or shadow, especially in the last quarter of the image stack. In order to generate reasonable chromatin masks in these sections, chromatin was marked by hand. This procedure was described in Hübner et al. (2015).

Procedure:

1. In ImageJ the images were cropped to the smallest size possible, leaving only a small rim around the nucleus. This saves time and reduces the necessary computing power in step 2. Merely for the 2D TEM images the cropping could be omitted here.
For CLSM images all color channels were cropped simultaneously to ensure that exactly the same part of the image was chosen. For the same reason for 3D-SIM images not only all color channels but also the 16-bit and the 8-bit versions of one and the same cell were cropped at the same time.
2. In R the images were segmented into seven chromatin classes – see section 3.2.12.5 for detailed explanations –, but now no mask was implemented (commands are written in italics and underlined, comments in normal style):
 - *library(bioimager)*
 - *library(EBImage)*
 - In the tab “Datei”/“File“ the option “Verzeichnis wechseln”/“Change dir” was chosen

and the folder containing the images to be analyzed was selected.

- `bild=readImage("xxx.tif")`
 - `seg=segment(bild, 7, 0, 1/3, inforce.nclust=TRUE)`
 - `writelImage(seg$class/7, file="xxx.tif")`
 - The commands `bild=readImage("xxx.tif")`, `seg=segment(bild, 7, 0, 1/3, inforce.nclust=TRUE)` and `writelImage(seg$class/7, file="xxx.tif")` mentioned above were summarized into a script in order to facilitate the analysis of additional cells.
 - The script created in the previous step was used to analyze the next cell: (1) The command `list.files()` was executed in order to obtain a list of all files in the selected directory. (2) The file name for the chromatin image was copied from the list into the respective command of the script. (3) The name under which the segmented image was saved was updated. (4) All commands of the script were executed one after the other by repeatedly pressing STRG + R.
 - One by one all cells were segmented according to the previous step.
3. For each cell, the image with the chromatin staining was opened once and the corresponding segmented image of step 2 was opened twice (process only one cell at a time).
 4. The segmented images were thresholded so that the mask for the chromatin staining was black and the background white. Depending on which images were processed, typically the following thresholds were used: the two brightest classes were included for the 3D-SIM images of the hematopoietic cells; the three brightest classes were included for all other 3D-SIM images and for the TEM images of the hematopoietic cells; the four brightest classes were included for CLSM images. Which threshold fitted best was tested for each cell individually by comparing the thresholded image with the chromatin staining. As a result, occasionally a threshold one class higher or lower as mentioned above was used.
 5. One of the thresholded images of step 4 was further processed and used as the basis for the mask:
 - The function “dilate” was used 1-3 times in order to close as many channels at the nuclear surface as possible. As few dilation steps as possible were applied.
For precise masks this step was omitted, so that small invaginations, “channels” etc. did not get lost.
 - Using the function “fill holes” all areas inside the nucleus were filled.
 - The function “erode” was applied as often as “dilate” was used.
 6. Section for section the mask was compared with the chromatin staining and inaccurate areas were corrected by copying appropriate fractions from the image with the chromatin staining and applying a new threshold or by copying from the thresholded but not further processed segmented image. Occasionally – especially for generating masks of the
-

hematopoietic cells – it was helpful to generate another thresholded version of the segmented image including one class more respectively less (again with the mask, i.e. chromatin, being black and the background being white) and using this for complementing the mask. If necessary, areas were corrected by hand (compare explanation above).

Care was taken that invaginations, especially larger ones at the top and the bottom of the cells, were not closed/lost during the generation of the mask.

7. All signals that were not part of the nucleus (i.e. dirt, background staining, etc.) were deleted.

3.2.12.2 Determination of the number of nuclear pores and the area/pore

Due to the lack of qualitatively sufficient immunofluorescence stainings for Nup153, a component of the nuclear pore complex, the number of nuclear pores was estimated based on the number of “holes” in the chromatin on the nuclear surface. These holes represent the exit points of interchromatin channels which typically underly each nuclear pore (Smeets et al. 2014). In the following procedure for reasons of simplicity these holes are called pores.

In the few available images with a reasonably good Nup153 staining, counting the number of Nup153 spots resulted in roughly the same number of nuclear pores as calculated by the procedure described here (data not shown).

For the determination of the number of nuclear pores only cells of which precise masks (compare section 3.2.12.1) were available were used.

Procedure:

1. The 16-bit DAPI image was opened twice in ImageJ.
2. In the function “set scale” the right image properties were specified (here with the OMX 3D-SIM images 1000 pixels equal to 39.5 μm (pixel size in xy-direction is 39.5 nm)).
3. In one of the images the upper section of the stack showing the pores best was chosen. For granulocytes this was partially very difficult due to the low number of pores in these cells. Therefore often sections located somewhat more towards the nuclear interior had to be used for the evaluation.
4. In the other image, for the same section chosen in step 3 a threshold was set (with the signal being black and the background being white) so that all chromatin was included. The holes of the pores were filled with the function “fill holes”. If necessary areas were corrected by hand.
5. In the “set measurements” function the boxes “area” and “limit to threshold” were clicked on.

6. The area of the chromatin in the section was measured by marking the chromatin mask with a threshold (but without applying it!) and executing the function “measure”. Alternatively, also STRG + M can be pressed. The area in μm^2 was read from the table.
7. In the non-thresholded DAPI image the number of pores was counted inside the area of the chromatin marked in step 4.
8. Steps 3-7 were repeated with the lower section of the stack showing the pores best.
9. All other cells were analyzed according to steps 1-8.
10. For each cell the overall surface area was determined:
 - Precise masks of the DAPI-staining were generated as described in section 3.2.12.1.
 - The image stacks of the masks were loaded into Volocity.
 - “Make volumes” was used to convert the single images of each cell into one image stack.
 - In the properties of the image stacks the pixel size was adjusted to the right values (here for the OMX 3D-SIM images 0.0395 μm , 0.0395 μm , 0.125 μm for the x-, y- and z-direction, respectively).
 - The first cell was selected, in the measurements tab the function “Find objects” was chosen, “Measure” was clicked and the boxes for “Intensity and volume measurements” and “Surface area” were selected.
 - The function “Invert” was added to the protocol in order to select the nucleus instead of the surrounding.
 - The sum for the surface area was read from the summary.
 - The protocol starting with the “Find objects function” and closing with the “Invert” function was saved and one by one applied to all other cells.
11. From the area of the chromatin and the number of pores in the same area (obtained in steps 1-9), the area for one pore was calculated and from that the overall number of pores per nucleus as well as the number of pores / 5 μm^2 using the overall surface area of the cell (obtained in step 10). The values obtained from the upper and the lower section were averaged in order to achieve the final result.

3.2.12.3 Determination of the number of RNA polymerase II signals

In order to determine the number of RNA polymerase II signals, two different approaches were pursued: on the one hand, the number of positive pixels above a certain threshold was counted, on the other hand, the number of spots was determined.

It has to be stressed that these numbers should not be taken as absolute – they are rather a relative measure that allows the comparison of cells stained, imaged and analyzed under

roughly the same conditions.

These procedures were described in Hübner et al. (2015).

Based on the number of positive pixels

The total number of positive pixels for each cell was determined by summing up the number of pixels in the seven classes that were obtained in the segmentation performed according to section 3.2.12.5

Based on the number of spots

Procedure:

1. Masks of the DAPI-staining were generated as described in section 3.2.12.1.
2. The image stacks of the masks and the corresponding image stacks for the RNA polymerase II channel (8-bit images) were loaded into Volocity.
3. “Make volumes” was used to convert the single images into image stacks.
4. In the properties of the image stacks the pixel size was adjusted to the right values (here for the OMX 3D-SIM images 0.0395 μm , 0.0395 μm , 0.125 μm for the x-, y- and z-direction, respectively).
5. The RNA polymerase II channel of the first cell was selected, in the measurements tab the function “Find spots” was chosen and an appropriate offset for spot intensity was set by changing the view to “Extended focus” and adjusting the offset until all spots to be included were selected. The value for “Brightest spot within a radius of” was set to 0 μm in order not to lose spots that are located close to each other.
6. The corresponding mask was selected and a ROI was generated from it:
 - The function “Find objects” was chosen in the measurements tab.
 - The function “Invert” was dragged into the “Find objects” function in order to select the nucleus instead of the surrounding.
 - The function “Make ROIs from population” was added to the protocol.
7. With the selection of the ROI of step 6 still active, the corresponding RNA polymerase II channel was selected again and the function “Clip to ROIs” was dragged into the “Find spots” function. Like this, all spots outside the nucleus were excluded from the analysis.
8. “Population 1” was selected in the drop-down menu of the summary and the number of spots was read from there.

9. The selection of the ROI was removed and the protocol comprising steps 5-8 was one by one applied to all other cells.

3.2.12.4 Determination of the amount of chromatin (CT) and interchromatin compartment (IC) and of the chromatin surface

This procedure was published in Hübner et al. (2015).

Procedure:

1. Masks of the osmium ammine-staining were generated as described in section 3.2.12.1.
2. The masks and the corresponding images with the osmium ammine staining were loaded into Volocity.
3. In the properties of the images the pixel size was adjusted to the right values.
4. The mask of the first cell was selected and a ROI was generated from it:
 - In the measurements tab the function “Find objects” was chosen.
 - The function “Invert” was dragged into the “Find objects” function in order to select the nucleus instead of the surrounding.
 - The function “Make ROIs from population” was dragged into the “Find objects” function.
5. “Measure” was clicked and the boxes for “Intensity and volume measurements” and “Surface area” were selected.
6. The sum for the area and the perimeter was read from the summary. These two values represent the overall area of the cell and its cell surface.
7. The corresponding image with the osmium ammine staining was opened in ImageJ or Fiji, serving as a reference for thresholding the chromatin in the next step.
8. In Volocity the corresponding image with the osmium ammine staining was selected, again with the selection of the ROI of step 4 still active.
9. Chromatin was selected as follows:
 - In the measurements tab the function “Find objects” was chosen.
 - The functions “Invert” and “Clip to ROIs” were dragged into the “Find objects” function in order to select the nucleus instead of the surrounding and to exclude all signals outside the nucleus from the analysis.
 - “Population 1” was selected in the drop-down menu of the summary.
 - In the function “Find objects” the threshold was adjusted, so that chromatin was selected as good as possible.
10. “Measure” was clicked and the boxes for “Intensity and volume measurements” and

“Surface area” were selected.

11. The sum for the area and the perimeter was read from the summary. These values represent the area of the chromatin and the chromatin surface including the cell surface. In order to obtain the value for the chromatin surface inside the nucleus, the amount of cell surface (determined in steps 4-6) was subtracted from the result. Subsequently, the obtained numbers for the chromatin surface were normalized for the area of the cell. The amount of the interchromatin compartment was calculated by subtracting the area of the chromatin from the overall area of the cell (also determined in steps 4-6).
12. Both protocols, the one applied to the mask and the one applied to the image of the osmium ammine staining, were saved, the selection of the ROI was removed and the protocols comprising steps 4-11 were one by one applied to all other cells. For each cell an individual threshold had to be adjusted in step 9.

3.2.12.5 Segmentation of chromatin stainings into classes, including the determination of the localization of additional markers in relation to chromatin

The analyses were done in R, an open-source software for statistical computing and graphics, supplemented by two packages, EBImage (Pau et al. 2010, Pau et al.) and bioimagerools (Schmid 2013). The bioimagerools package contains the algorithms for the segmentation. It was developed by Prof. Dr. Volker Schmid (LMU, Munich, Germany) in consultation with Dr. Yolanda Markaki (University of California (UCLA), Los Angeles, USA) and Dr. Lothar Schermelleh (University of Oxford, Oxford, UK) and is based on Zhang et al. (2001). It is described in Markaki et al. (2012). The stained chromatin is segmented into seven density classes with equal intensity variance using a hidden Markov random field model classification which combines a finite Gaussian mixture model with a spatial model (Potts model). This allows the classification of the signal intensities at the level of individual voxels, but at the same time also considers the classification of surrounding voxels. However, in this work the influence of the neighboring voxels was set to 0 as in this case the segmented images corresponded better with the original images (both, with the 16-bit images where no offset was chosen and also with the 8-bit images after the application of an offset and, where required, of further adjustments regarding brightness and contrast). Thus, the spatial model (Potts model) was taken out of the algorithm here.

Intensity class 1 represents voxels close to background values. The classes 2-7 contain voxels with increasing intensity and therefore increasing density, with class 7 comprising the highest values.

Once the segmented image of the chromatin staining is obtained, the localization of additional

markers in the same cell can be determined in relation to chromatin: each pixel that shows a positive staining for the additional marker is correlated with the corresponding pixel in the chromatin channel and is assigned to the respective chromatin class.

The procedures as performed here were published in Hübner et al. (2015).

Installation of the required software

Procedure:

1. R was downloaded from <http://www.r-project.org/> using the CRAN mirror <http://ftp5.gwdg.de/pub/misc/cran/> and installed. Typically the 64-bit version of the program was used for the analyses.
2. The bioimagetools package was obtained from Prof. Dr. Volker Schmid (LMU, Munich, Germany). In this work, version 0.02.2 was used.
3. The EBImage package was downloaded from the following link: <http://www.bioconductor.org/packages/release/bioc/html/EBImage.html>.
4. GTK+ and ImageMagick, two additional programs required for EBImage, were downloaded and installed according to the instructions of the developers of EBImage:
 - For GTK+ the recommended all-in-one bundle of version 2.16 was downloaded from <http://www.gtk.org>. The program was installed in “C:\gtk” and the “C:\gtk\bin” path was added to the system environment PATH variable by editing the environment variables in the advanced settings of the system control panel.
 - For Image Magick the Q16 dll version was downloaded from <http://www.imagemagick.org/>. During the installation the checkboxes “Update executable search path” and “Install development headers and libraries” were checked on.
5. R was started and the two packages EBImage and bioimagetools, were installed:
 - In the tab “Pakete”/“Packages” the option “Wähle Repositories”/“Select repositories” was chosen and “BioC software” was selected from the list.
 - In the tab “Pakete”/“Packages” the option “Installiere Paket”/“Install package(s)” was chosen and EBImage was selected from the list.
 - In the tab “Pakete”/“Packages” the option “Installiere Paket aus lokaler zip Datei”/“Install package(s) from local zip files” was chosen and the bioimagetools package of step 2 was selected.
6. The commands *library(bioimagetools)* and *library(EBImage)* were executed in R in order to test the functionality of both packages.

In case additional packages were lacking, they were downloaded from appropriate sources on the internet and installed from local zip files as described in step 5. Required packages might be e.g. `abind`, `tiff`, `png`, `locfit`, and `jpeg`.

Segmentation including the determination of the localization of additional markers

Procedure:

1. Chromatin masks were generated as described in section 3.2.12.1.
2. If TEM images were to be analyzed and they were not yet cropped during the preparation of the mask, they were processed now as described in step 1 of section 3.2.12.1. The image with the chromatin staining and the image with the mask was cropped simultaneously to ensure that exactly the same part of the image was chosen.
3. In case TEM images were to be analyzed, their colors were inverted so that the chromatin was displayed in light colors (analogous to DAPI stained nuclei).
4. If 3D-SIM or CLSM images were to be analyzed and the localization of additional markers was to be determined, these additional channels were thresholded appropriately in ImageJ, so that all signals were white and the background black. For 3D-SIM images the 8-bit versions (where already an offset was applied) were used, as thresholding was much easier here than in the 16-bit versions.
5. In case 3D-SIM or CLSM image stacks were to be analyzed, all sections that did not contain signals of the mask ("empty" sections) were deleted at the beginning and the end of the stacks, as R cannot handle such sections correctly. All channels needed for the analysis, i.e. the DAPI channel (16-bit version for the 3D-SIM images), if necessary the thresholded additional marker channel(s) red and/or green and the mask, were processed simultaneously to ensure that exactly the same sections were deleted from the stacks.
6. R was prepared for the segmentation:
 - With the commands `library(bioimager)` and `library(EBImage)` the `bioimager` and `EBImage` packages were activated.
 - In the tab "Datei"/"File" the option "Verzeichnis wechseln"/"Change dir" was chosen and the folder containing the images to be analyzed was selected.
7. The segmentation was done in R with the following commands (commands are written in italics and underlined, comments in normal style):
 - `bild=readImage("xxx.tif")`
This reads in the chromatin channel; for `xxx` the respective file name was filled in.
 - `maske=readImage("xxx.tif")`
This reads in the mask; for `xxx` the respective file name was filled in.

- `seg=segment(bild, 7, 0, 1/3, inforce.nclust=TRUE, mask=(maske==1))`

This is the actual command for the segmentation: *bild* refers to the chromatin channel that was read in earlier; 7 defines the seven classes; 0 is the value for the influence of the neighboring voxels; 1/3 represents the relation of the pixel size in xy- and z-direction (for the OMX 3D-SIM images the pixel size is 0.0395 µm in xy- and 0.125 µm in z-direction; for the Leica SP5 CLSM images instead of 1/3 the value 1/4 was used as here the pixel size was 0.050 or 0.060 µm in xy- and 0.210 nm in z-direction; for 2D images, like the Morgagni 268 TEM images, this parameter can be set to any value, here also 1/3 was used); *inforce.nclust=TRUE* makes sure that indeed seven classes are generated and not less; *mask=(maske==1)* refers to the mask that was read in earlier and defines that all pixels with a value of 1 in the mask go into the analysis (for the segmentation of TEM images this value was set to 0; actually a value of 0 was also be expected for the analysis of 3D-SIM and CLSM images, as also here the pixels of the mask were black (compare step 4 in section 3.2.12.1) – but apparently the software inverted these images so that a value of 1 had to be used in the segmentation command).

Apart from rare exceptions the algorithm ran for 30 iterations with 3D-SIM images. With TEM and CLSM images the algorithm occasionally, respectively often, stopped earlier, partly with only as little as seven iterations. In these cases the segmentation was repeated and only results with at least 20 iterations were used for the analysis (apart from very rare cases, where 20 iterations could not be achieved despite many repeats).

In addition, the segmentation algorithm seemed slightly unstable when 8-bit image stacks were segmented: with repeated segmentations often different results for one and the same cell were obtained with CLSM images. Therefore these images were segmented at least three times and the average values were used for the analysis. With the 16-bit 3D-SIM images as well as with the 8-bit TEM images such variations were not observed.

- `writelImage(seg$class/7, file="xxx.tif")`

This saves the segmented image; for xxx the respective file name was filled in.

- In cases where only the chromatin staining was analyzed (i.e. for the TEM images) the data were extracted with the following commands:

`tabelle=table(seg$class)`

`tabelle`

This table shows the absolute numbers of pixels in each class. Class 0 contains all pixels outside the mask and is therefore not included in the further analysis.

The data were copied to Excel and converted into relative values.

- In cases where in addition to chromatin also the localization of additional markers was determined (i.e. for the 3D-SIM and CLSM images), these commands were executed:

```
green<-readImage("xxx.tif")
```

```
red<-readImage("xxx.tif")
```

These commands read in the green and red channel; for xxx the respective file names were filled in.

Either the original gray-value images or already thresholded binary images (with all signals being white, the background being black) can be used. When reading in gray-value images, an appropriate threshold is calculated in the subsequent command (`cc<-colors.in.classes(...)`). However, as it is not possible to monitor which thresholds are used with this function, in this work the images were thresholded by eye prior to implementing them into the analysis (see step 4). Like this, the threshold-search of the subsequent command ends up setting the threshold to 1, i.e. to all white pixels.

```
cc<-colors.in.classes(seg$class,green,red,col1="green",col2="red",test=TRUE,mask  
=maske)
```

Here the positive pixels for the additional markers are correlated with the corresponding pixel in the chromatin channel and get assigned to the respective chromatin class. In addition, a pairwise Wilcoxon rank-sum test with continuity correction is performed (DAPI vs. green, DAPI vs. red, green vs. red) in order to test for significant differences between the curves.

In case only one additional color channel was analyzed, only that one was read in and `cc<-colors.in.classes(seg$class,green,col1="green",test=TRUE,mask=maske)` or `cc<-colors.in.classes(seg$class,red,col1="red",test=TRUE,mask=maske)` was used instead.

Occasionally, especially with CSLM images, the threshold-search failed in setting a threshold and therefore the images could not be analyzed. In such cases the command given above was complemented with `sd1=0,sd2=0`, resulting in `cc<-colors.in.classes(seg$class,green,red,col1="green",col2="red",test=TRUE,mask=maske,sd1=0,sd2=0)`. This sets the threshold to the mean value, i.e. to 1 in the already thresholded image.

cc

This extracts all data, including the absolute and the relative numbers of pixels in each class for each channel and the results of the Wilcoxon rank-sum test. All data were copied to Excel.

8. All commands of step 7 were summarized into a script in order to facilitate the analysis of additional cells.
9. The script created in step 8 was used to analyze the next cell:

- The command *list.files()* was executed in order to obtain a list of all files in the selected directory.
 - The file names for the chromatin channel, the mask and if necessary the additional channels (red and green) were copied from the list into the respective commands of the script.
 - The name under which the segmented image was saved was updated.
 - All commands of step 7 were executed one after the other by repeatedly pressing STRG + R.
10. The data were transferred to Excel (compare step 7).
11. One by one all cells were analyzed according to steps 9 and 10.

Calculation of the over- and underrepresentation of additional marker signals

In addition to plotting the relative amounts of the signals in each class directly, also over-/underrepresentation curves were calculated. These demonstrate the increased or decreased amount of marker signal in comparison to the amount of chromatin (i.e. DAPI signal) in the respective class.

Procedure:

1. For each class, the relative amount of signals in the DAPI channel was subtracted from the relative amount of signals in the additional marker channel (i.e. green or red).
2. Again for each class, the difference obtained in step 1 was set in relation to the relative amount of signals in the DAPI channel by dividing the former value by the latter. This provides the relative amount of over- or underrepresentation.

3.2.12.6 Determination of the localization of microinjected beads in relation to chromatin using line scans

In order to determine the localization of microinjected beads in relation to chromatin, horizontal line scans through the brightest spot (both in xy and in z-direction) of individual beads and through the corresponding DAPI stained DNA of the cell were performed. Subsequently, the brightest pixel of the bead with its left and right neighbor was selected and the intensities of the corresponding pixels of the DAPI-channel were averaged. This value represents the localization of the bead in relation to chromatin.

Procedure:

1. An image stack of the beads and the corresponding DAPI-channel was opened in ImageJ.
2. Using the function “Stack normalizer” (in the menu item “plugins” under “stacks”) the signal intensities for both channels were normalized to an intensity of 0-255. This allowed the comparison of the determined values in the later steps.
3. A rectangular selection was created, covering the whole width of the image and one pixel in height. The selection was moved over the brightest spot of a bead and was then transferred to the DAPI-channel.
4. Line scans were performed in both images by executing the command “plot profile” from the menu item “analyze”.
5. The lists with the individual values were transferred to Excel.
6. In ImageJ the selected lines were marked white.
7. One by one each bead was processed according to steps 3-6.
8. The steps 1-7 were repeated with all other cells.
9. In Excel for each bead the brightest pixel and its left and right neighbor (i.e. three pixels in total) were selected and the intensities of the corresponding pixels of the DAPI-channel were averaged.

3.2.12.7 Wilcoxon rank-sum test

In order to test results for their statistical significance, a Wilcoxon rank-sum test with continuity correction (equivalent to the Mann-Whitney U test) was performed. In contrast to other tests like e.g. the t-test, the Wilcoxon rank-sum test has the advantage that it does not require a normal distribution of the data. Results with a p-value <0.05 are considered to be significant, <0.01 very significant and <0.001 highly significant. Only two groups can be compared at the same time. For more groups (like in this work e.g. for the five hematopoietic cell types) pairwise tests in all possible combinations have to be performed.

Two slightly different procedures were used depending on what was tested: individual values like e.g. the number of RNA polymerase II signals (obtained according to section 3.2.12.3) or distributions like e.g. the segmentation curves (obtained according to section 3.2.12.5).

Testing individual values

The test was performed in R. In the procedure below commands are written in italics and underlined, comments in normal style.

Procedure:

1. *Var1<-c(xxx, xxx, xxx, xxx)*

Var2<-c(xxx, xxx, xxx, xxx)

Var3<-c(xxx, xxx, xxx, xxx)

Var1, *Var2* and *Var3* label the groups to be tested. This designation can be renamed if desired (e.g. into CD34, monoblast, etc.). For xxx the individual values were put in.

2. *wilcox.test(Var1,Var2)*

wilcox.test(Var1,Var3)

wilcox.test(Var2,Var3)

Var1, *Var2* and *Var3* have to be designated according to step 1. As mentioned above, only two groups can be compared at the same time.

3. In order to facilitate the evaluation of additional cells, the commands in step 1 and 2 were summarized into a script.

4. The script created in step 3 was used to analyze the next cell:

– If desired the designations were updated.

– The individual values were updated.

– All commands of the script were executed one after the other by repeatedly pressing STRG + R.

5. One by one all cells were analyzed according to step 4.

Testing distributions

The test was performed in R. In the procedure below commands are written in italics and underlined, comments in normal style.

Procedure:

1. *Var1<-c(xxx, xxx, xxx, xxx)*

Var2<-c(xxx, xxx, xxx, xxx)

Var3<-c(xxx, xxx, xxx, xxx)

Var1, *Var2* and *Var3* label the groups to be tested. This designation can be renamed if desired (e.g. into CD34, DAPI, green, etc.). For xxx the individual values were put in.

In this work, percentages were used for the evaluation. In contrast to using the absolute values, where due to the large numbers (i.e. many data) already extremely small differences were detected as being highly significantly different, this reduction of the number of data allowed the detection of only reasonably large differences.

2. *Var1.all <- rep(1:7,Var1)*
Var2.all <- rep(1:7,Var2)
Var3.all <- rep(1:7,Var3)

This function determines the class of the individual voxels based on the number of voxels per class read in in step 1. *Var1*, *Var2* and *Var3* have to be designated according to step 1.

3. *wilcox.test(Var1.all,Var2.all)*
wilcox.test(Var1.all,Var3.all)
wilcox.test(Var2.all,Var3.all)

Var1, *Var2* and *Var3* have to be designated according to step 1. As mentioned above, only two groups can be compared at the same time.

Note that the Wilcoxon rank-sum test can only check for differences in the mean value, not in the actual distribution.

4. In order to facilitate the evaluation of additional cells, the commands in steps 1-3 were summarized into a script.
5. The script created in step 4 was used to analyze the next cell:
 - If desired the designations were updated.
 - The individual values were updated.
 - All commands of the script were executed one after the other by repeatedly pressing STRG + R.
6. One by one all cells were analyzed according to step 5.

4. Results

4.1 Nuclear organization of hematopoietic cells during differentiation

For the comparative analysis of nuclear architecture in primary cells five hematopoietic cell types of defined differentiation stages were compared: CD34⁺ cells (hematopoietic stem cells / progenitor cells), monoblasts and myeloblasts (precursor cells) and monocytes and granulocytes (differentiated cells). Monocytes derive from monoblasts, granulocytes from myeloblasts. While monocytes can further differentiate into macrophages upon activation, granulocytes are terminally differentiated (see details in section 2.4 in the introduction).

The experiments described in this section were performed in collaboration with the group of Prof. Sergio Ferrari at the University of Modena and Reggio Emilia in Modena/Italy. PhD Mariana Lomiento and the master students Fabiana Mammoli and Claudio Atene isolated CD34⁺ cells, monoblasts, myeloblasts, and monocytes, seeded them onto coverslips and helped with sample preparations for 3D-SIM and TEM.

The results in this chapter were published in Hübner et al. (2015). Therefore text and figures were adapted from there.

4.1.1 Variability of the general nuclear morphological features between CD34⁺ cells, monoblasts, myeloblasts, monocytes, and granulocytes

In a first step, the nuclei of the five cell types were compared with regard to their general 3D morphology, including the number of nuclear pores, the chromatin pattern and the appearance of the nucleoli (**Figure 12-19**). The cells were analyzed with both 3D structured illumination microscopy (3D-SIM) and transmission electron microscopy (TEM) in order to gain a comprehensive and complementary insight into the nuclear architecture of the cells.

DAPI staining in 3D-SIM acquisitions displayed as serial optical sections (**Figure 12 A**) and as corresponding Amira 3D reconstructions (**Figure 12 B**), revealed a distinct morphology for each cell type: nuclei of CD34⁺ cells exhibited an overall roundish shape with an invaginated surface. Monoblast nuclei were ellipsoid and usually showed more pronounced and more complex invaginations than CD34⁺ cells. Nuclei of myeloblasts appeared similar to those of monoblasts with invaginations often pervading the entire nucleus. Typical monocytes (compare section 3.2.1.1) were characterized by horseshoe-shaped nuclei with an irregular

surface. The nuclei of granulocytes were divided into several interconnected lobes. The 3D reconstructions (**Figure 12 B**) furthermore show “holes” in the nuclear surface, representing the exit points of interchromatin channels which were previously shown to lead to nuclear pores (Schermele et al. 2008, Smeets et al. 2014). These “holes” of the exit points were counted in order to compare the number and density of nuclear pores in the five cell types (**Figure 12 C**). The number of pores / nucleus increased from CD34⁺ cells over monoblasts to myeloblasts. Monocytes exhibited a significantly lower number of pores than CD34⁺ cells and granulocytes again much lower numbers. The number of pores / 5 μm^2 showed a very similar distribution, however, here the values for monoblasts and myeloblasts were the same and the difference between CD34⁺ cells and monocytes was smaller. The strongly reduced number of pores in granulocytes was clearly demonstrated by the increase in the area containing one pore.

More detailed insights into the chromatin pattern of the cells are shown in **Figure 13-17**. Within each cell type, both 3D-SIM images of DAPI stained nuclei (**Figure 13-17 A**, upper row) and TEM acquisitions after DNA specific osmium ammine staining (**Figure 13-17 C**, upper row) revealed small variations in the chromatin patterns, ranging from slightly more homogenous to slightly more heterogeneous chromatin distributions (CD34⁺ cells, monoblasts, myeloblasts) or slightly less or slightly more compacted chromatin (monocytes, granulocytes). These variations were less pronounced in CD34⁺ cells, monocytes and granulocytes than in monoblasts and myeloblasts and smaller in the TEM images than in the 3D-SIM images. However, the overall appearance of the chromatin distribution was consistent for each cell type (see also **Figure 18 A and B**): CD34⁺ cells showed a fine network of chromatin domain clusters (CDCs). CDCs were dispersed throughout the nucleus and were pervaded by finely branched IC channels with occasional enlargements into wider IC lacunas. The chromatin patterns in monoblasts and myeloblasts were very similar with only marginally larger CDCs and lacunas as observed in CD34⁺ cells. In monocytes and granulocytes, however, changes of the global nuclear landscape became very apparent: nuclei of monocytes were characterized by aggregations of CDCs into compacted chromatin islets, especially towards the periphery of the nucleus, surrounded by wide interchromatin channels and lacunas. The compaction was even stronger in granulocytes, where chromatin appeared mostly as a rather uniformly arranged, dense layer at the nuclear periphery. The interior of each lobe of the multilobulated nuclei was filled by one large contiguous IC lacuna. The increased packing density of chromatin was associated with a hard transition from chromatin to IC space, especially in granulocytes, where only a few decondensed loops seemed to expand from the compact chromatin layer towards the interior of the nuclear lobes.

A previously described segmentation algorithm (see section 3.2.12.5) was used to convert the intensities of the chromatin stainings into chromatin density maps with seven classes of equal intensity variance. For 3D-SIM acquisitions (DAPI signal) evaluations were performed using the entire 3D volume of the nucleus, TEM images (osmium ammine staining) were analyzed only in 2D. The lower rows of **Figure 13-17 A** and **C** show the segmented images, **Figure 13-17 B** and **D** the corresponding profiles. Chromatin density increases from class 1 to class 7, i.e. from blue to white.

In the 3D-SIM images of CD34⁺ cells, monoblasts and myeloblasts (**Figure 13-15 A**, lower row) the compact cores of the CDCs are represented by aggregations of pixels of the high-density classes with high signal intensities, i.e. pixels of the classes 5-7. These CDC cores are lined by a – sometimes extended – layer of decondensed chromatin of low staining intensity comprising pixels of the classes 2-4, representing the perichromatin region. Largely DNA free regions with signal values close to background intensities fall into class 1 and represent the IC system. It expands between the CDCs and includes also the larger lacunas. Also nucleoli are part of this class. In the multilobulated granulocyte nuclei (**Figure 17 A**, lower row) a single large IC lacuna (here the IC includes class 1 and 2, see explanation below), fills the interior of each lobe. It is lined by a small rim of decondensed chromatin (classes 2-4). The broad layer of chromatin at the periphery of the lobe is highly compacted (classes 5-7). Monocytes (**Figure 16 A**, lower row) represent an intermediate state between CD34⁺ cells / monoblasts / myeloblasts and granulocytes. Despite the slight differences observed in the chromatin pattern (compare above) all nuclei of each cell type show a very similar distribution of the DAPI signals into chromatin classes (**Figure 13-17 B**).

In contrast, the segmentations of the TEM images and the corresponding profiles of the chromatin distributions exhibited great variations (**Figure 13-17 C**, lower row, and **D**). This suggests that TEM images are not suitable for the segmentation algorithm used here. These images rather have a black-and-white appearance where – in contrast to the DAPI staining in the 3D-SIM images – the osmium ammine staining shows only little variation in its intensity, even with higher chromatin density. Therefore the algorithm – in order to achieve the requested seven classes – is assumed to create artificial subclasses which then leads to a wrong classification of pixels with very similar intensity and consequently to the observed variations in the segmentations. Possibly more consistent segmentation results of the TEM images would have been obtained if the number of classes was reduced, e.g. to five chromatin classes (not tested here). In addition to this problem, also other points argue against the use of TEM images for segmentation: (1) the evaluation can only be performed in 2D, therefore the presence or absence of a nucleolus in the image has a huge impact; (2) the nucleoli typically show a slightly darker color than other DNA free regions in the nucleus and are consequently classified to a higher density class as they actually should be; (3) occasionally in low magnification TEM

images the contrast of the staining is not optimal, which might distort the result of the segmentation (images taken with higher magnification in the same cells showed good contrast, however, these cannot depict the whole nucleus).

Most likely due to a combination of the factors described above, the segmentation profiles obtained from the TEM images (**Figure 13-17 D**) and the profiles obtained from the 3D-SIM images (**Figure 13-17 B**) showed different distributions of chromatin into the seven classes in monoblasts, myeloblasts, and monocytes and to a lesser extent also in CD34⁺ cells, although the chromatin patterns observed with both microscopic approaches were the same. Only in granulocytes the profiles were largely consistent between both types of images. Due to the strong condensation of chromatin in these cells, the 3D-SIM images of granulocytes are in fact also rather black-and-white and so the same problem of the artificially created subclasses described above for TEM images might apply here. This would explain why the IC was expanded to class 2 in granulocytes.

Average profiles of multiple evaluated cells (**Figure 18 C and E**) demonstrated a clear shift towards higher DAPI intensity classes in differentiated cells (monocytes and even more granulocytes), corresponding to the observed increased compaction of chromatin in the images.

The black-and-white appearance of the osmium ammine staining was exploited to apply a threshold for chromatin and determine the amount of chromatin in comparison to the IC and the length of the IC surface (i.e. the lateral expansion of the interface between chromatin and the IC) (**Figure 18 D**). The fraction of the IC (orange) increased and accordingly the fraction of chromatin (red) decreased from CD34⁺ cells over monoblasts to myeloblasts. Monocytes exhibited a similar ratio as CD34⁺ cells, granulocytes were characterized by decreased amounts of the IC and respectively increased amounts of chromatin in comparison to the other cell types. The length of the IC surface was significantly reduced in monocytes and even more in granulocytes compared to CD34⁺ cells, monoblasts, and myeloblasts.

As a last feature of general nuclear morphology, the appearance of the nucleoli was compared in the five cell types (**Figure 19**). While all cell types contained similar numbers of nucleoli (typically 2-4 in CD34⁺ cells, 1-3 in monoblasts, 2-3 in myeloblasts, 2-4 in monocytes and 1 or occasionally 2 in granulocytes; data not shown), their size decreased with differentiation: On average CD34⁺ cells contained the biggest nucleoli, followed by monoblasts and myeloblasts with only slightly smaller ones. In monocytes nucleoli were distinctly shrunk compared to the more undifferentiated cells and in granulocytes they were further reduced and appeared only as small spots.

Figure 12: 3D characteristics of hematopoietic cell types. (A, B) DAPI stained DNA of PFA-fixed cells in light optical serial sections of whole 3D-SIM 3D acquisitions (A) with the respective 3D reconstructions (B). From top to bottom a CD34⁺ cell, monoblast, myeloblast, monocyte, and granulocyte is shown. For the CD34⁺ cell every fifth image of the serial sections is included, for the monoblast every second image, for myeloblasts, monocytes, and granulocytes every third image. Of the 3D reconstructions xy- (left), xz- (upper right) and yz-views (lower right) are shown. Rotatable PDFs of the 3D-reconstructions are included in the enclosed DVD / ZIP archive (File S1-5). Scale bars: 2 μm . **(C)** Evaluations of the number of nuclear pores / nucleus (left graph), the number of nuclear pores / 5 μm^2 (middle graph) and the area containing one pore (right graph), all based on DAPI stained DNA of PFA-fixed cells in whole 3D-SIM 3D acquisitions. n=22, 28, 20, 12, 11 cells were evaluated for CD34⁺ cells, monoblasts, myeloblasts, monocytes, and granulocytes, respectively. For the number of pores / nucleus all results were highly significantly ($p \leq 0.001$) different from each other, apart from monoblasts vs. myeloblasts ($p=0.216$). For the number of pores / 5 μm^2 as well as the area containing one pore highly significant ($p \leq 0.001$) differences were found for all values, apart from monoblasts vs. myeloblasts ($p=0.893$) and CD34⁺ cells vs. monocytes ($p=0.068$). Error bars: standard deviation. Figure adapted from Hübner et al. (2015).

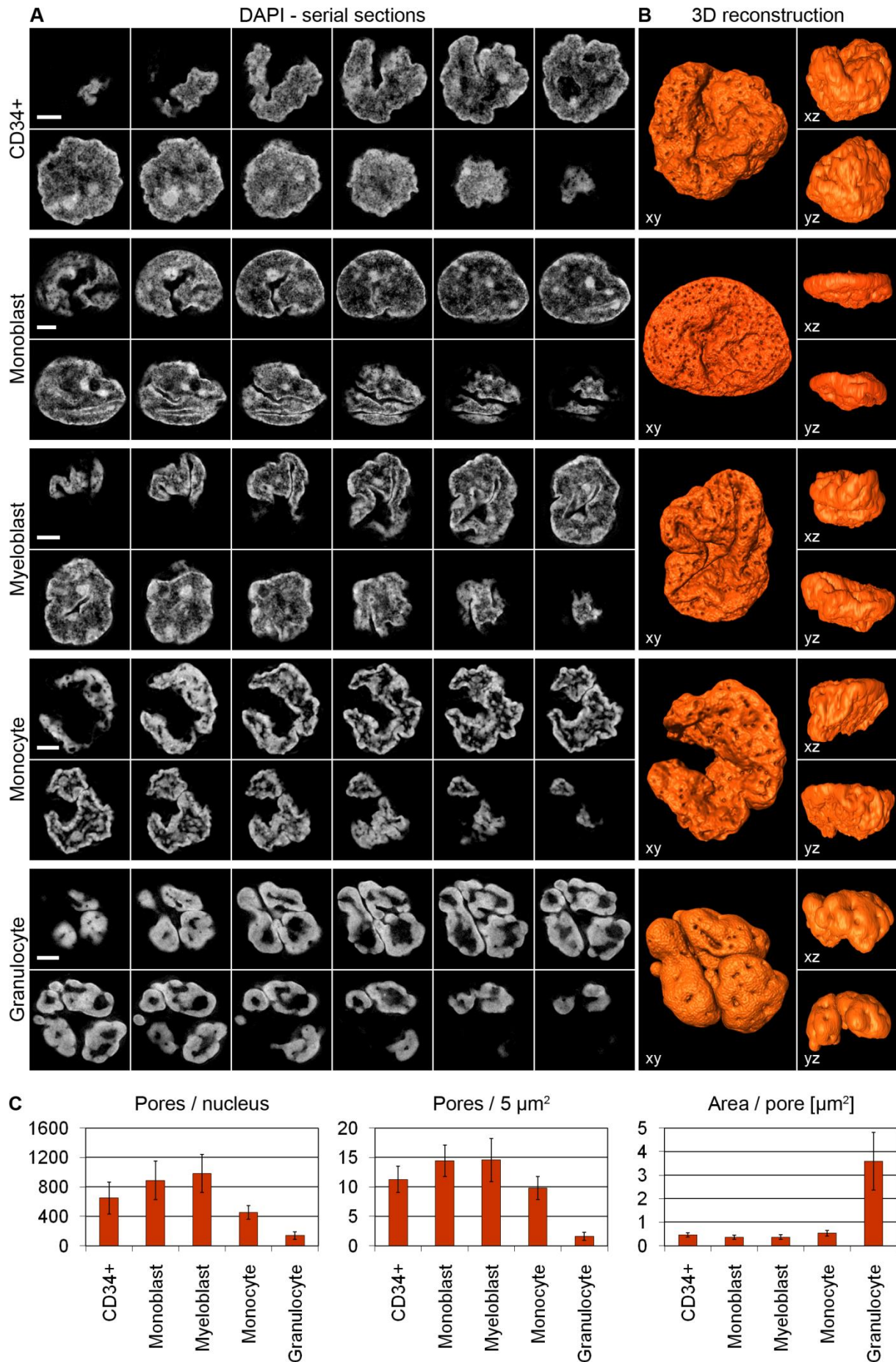


Figure 12: 3D characteristics of hematopoietic cell types (see legend on previous page).

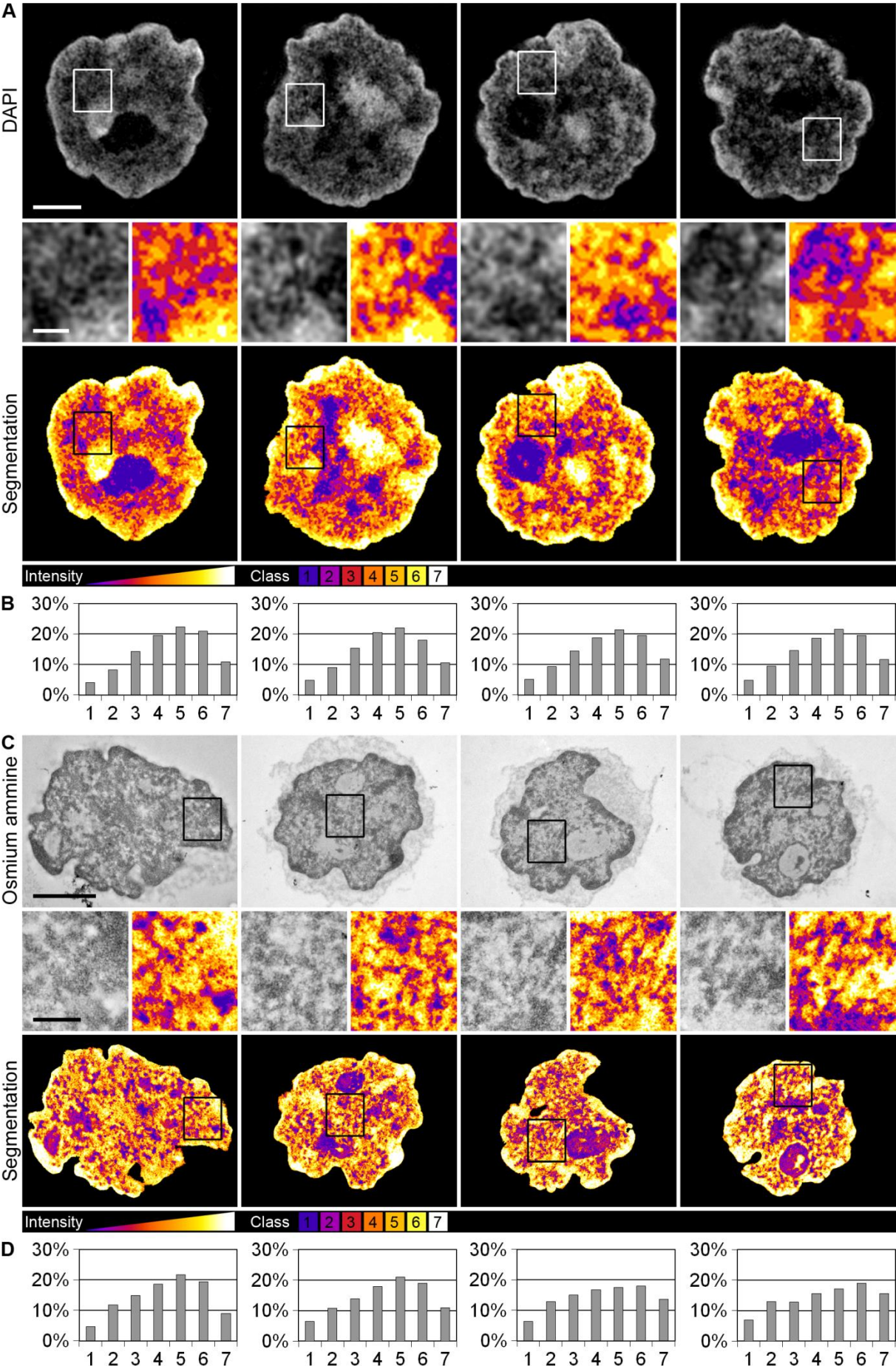


Figure 13: Variability of the chromatin pattern in CD34+ cells (see legend on page 178).

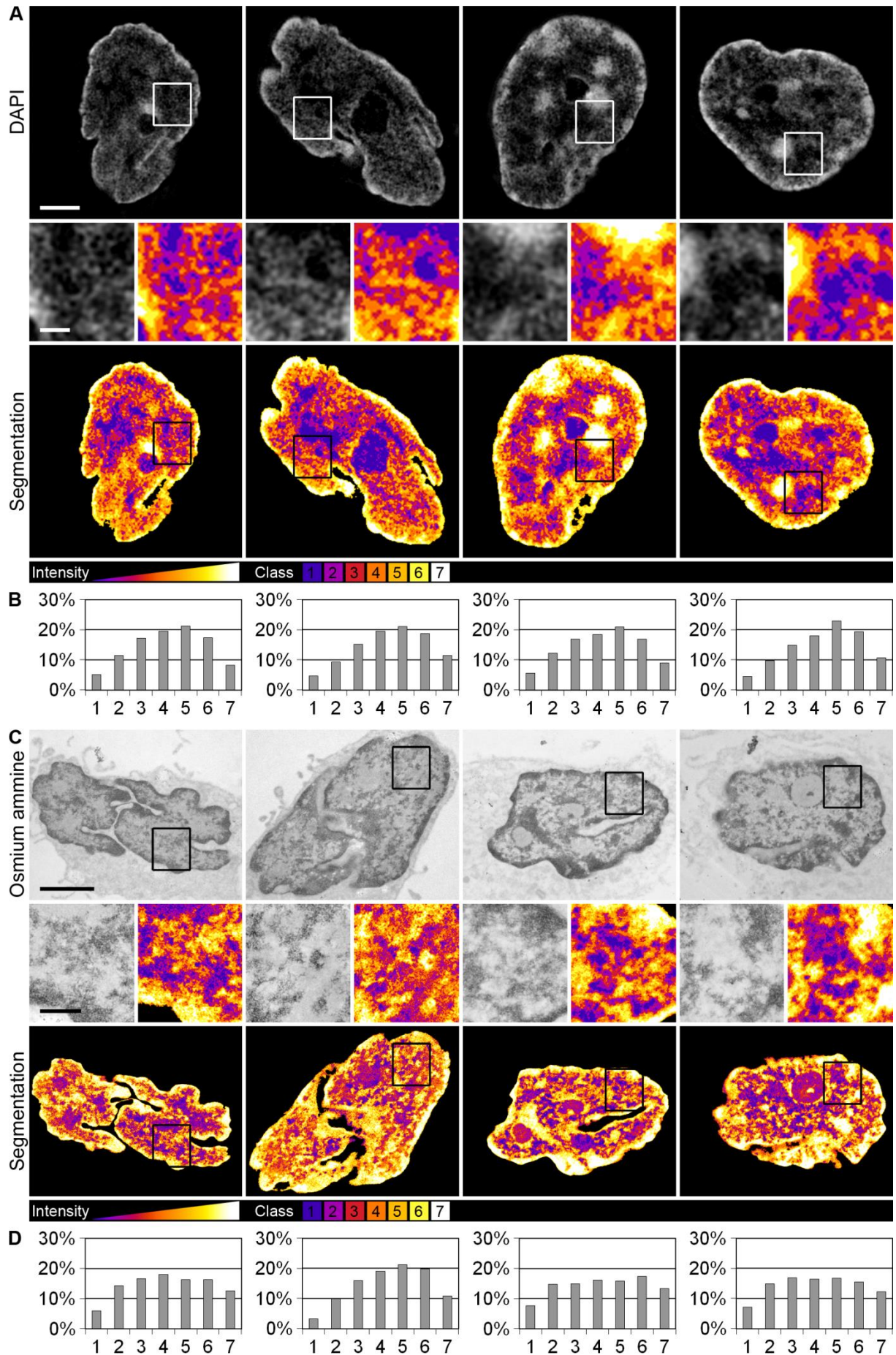


Figure 14: Variability of the chromatin pattern in monoblasts (see legend on page 178).

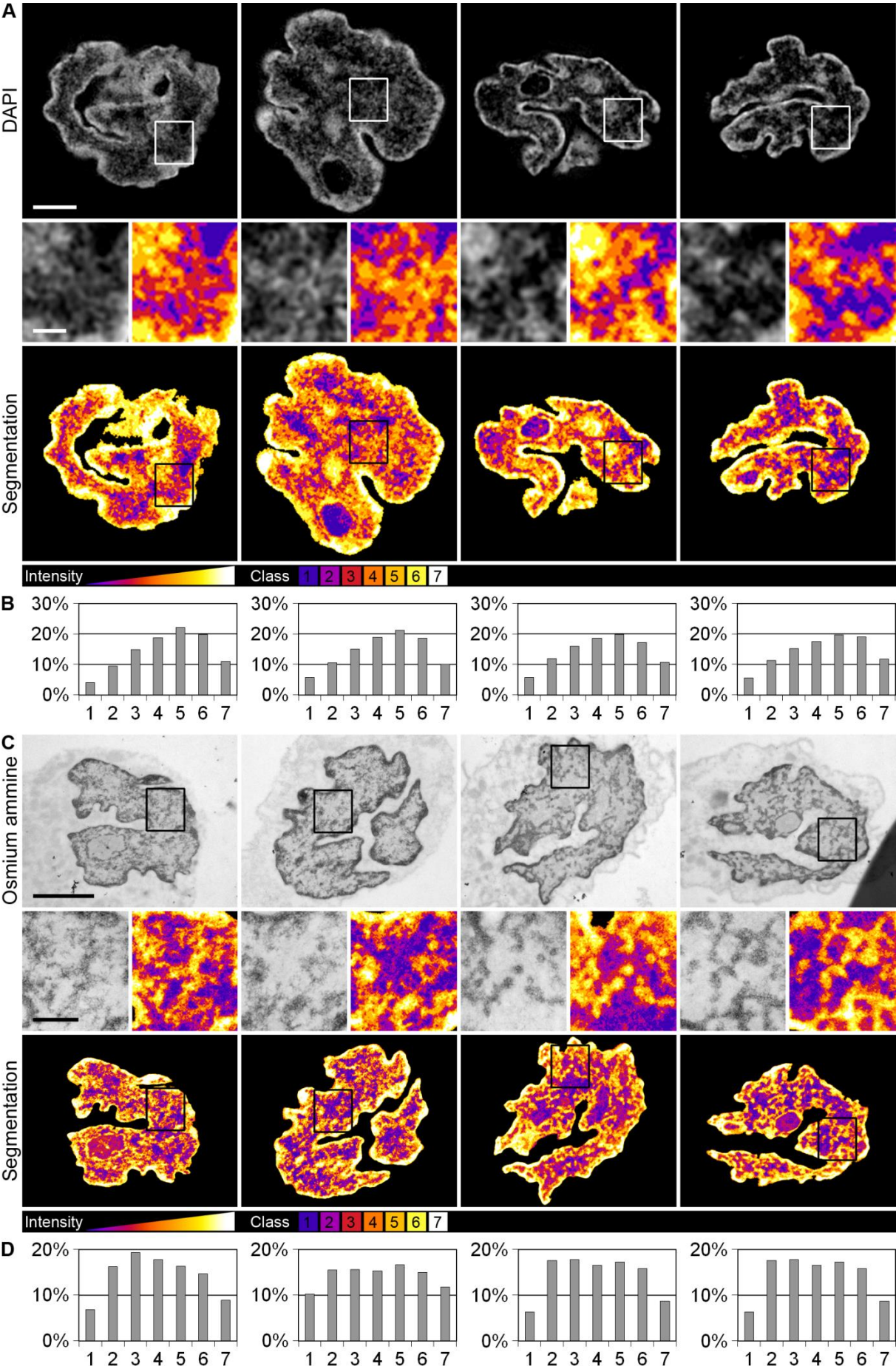


Figure 15: Variability of the chromatin pattern in myeloblasts (see legend on page 178).

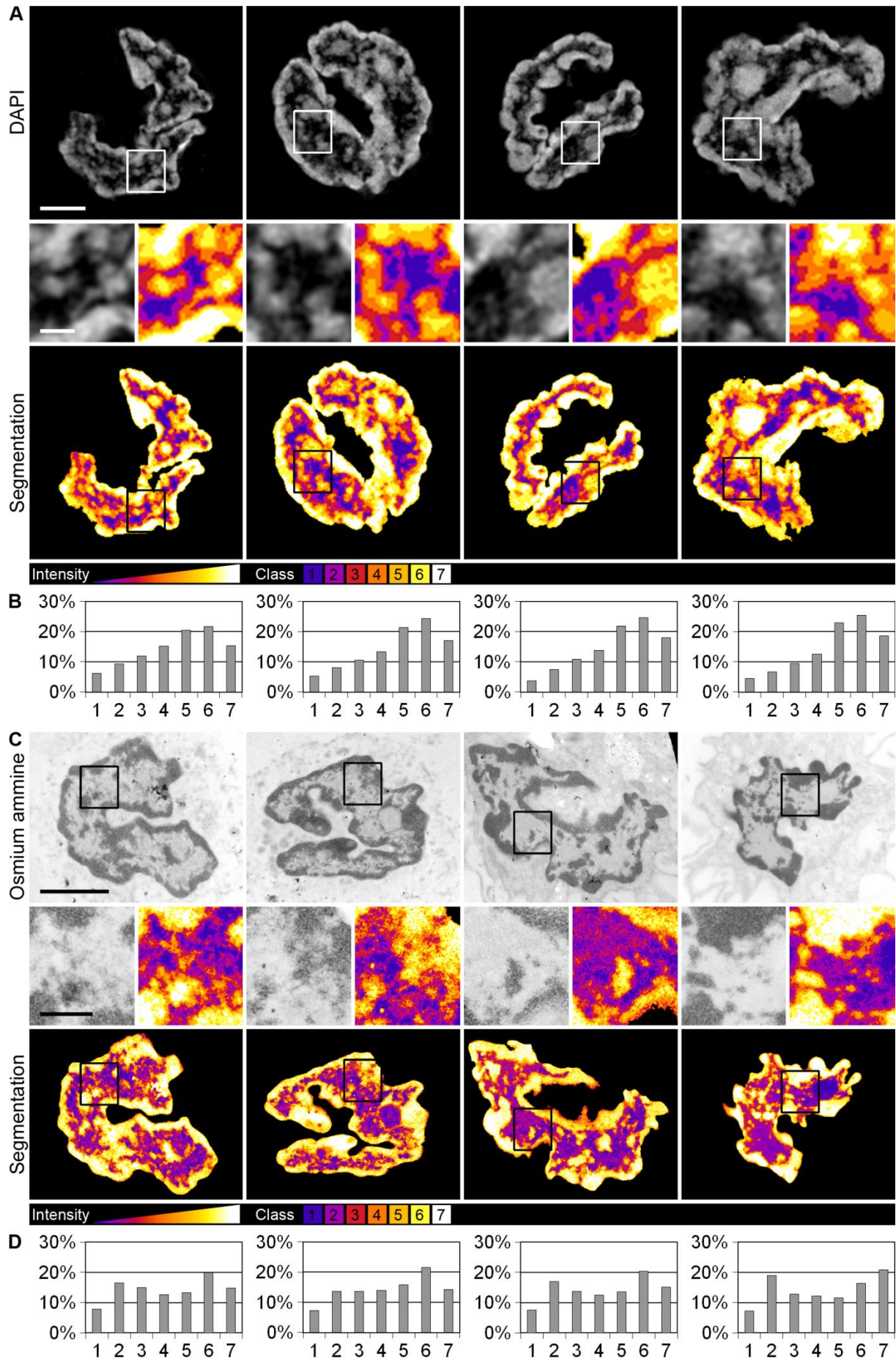


Figure 16: Variability of the chromatin pattern in monocytes (see legend on page 178).

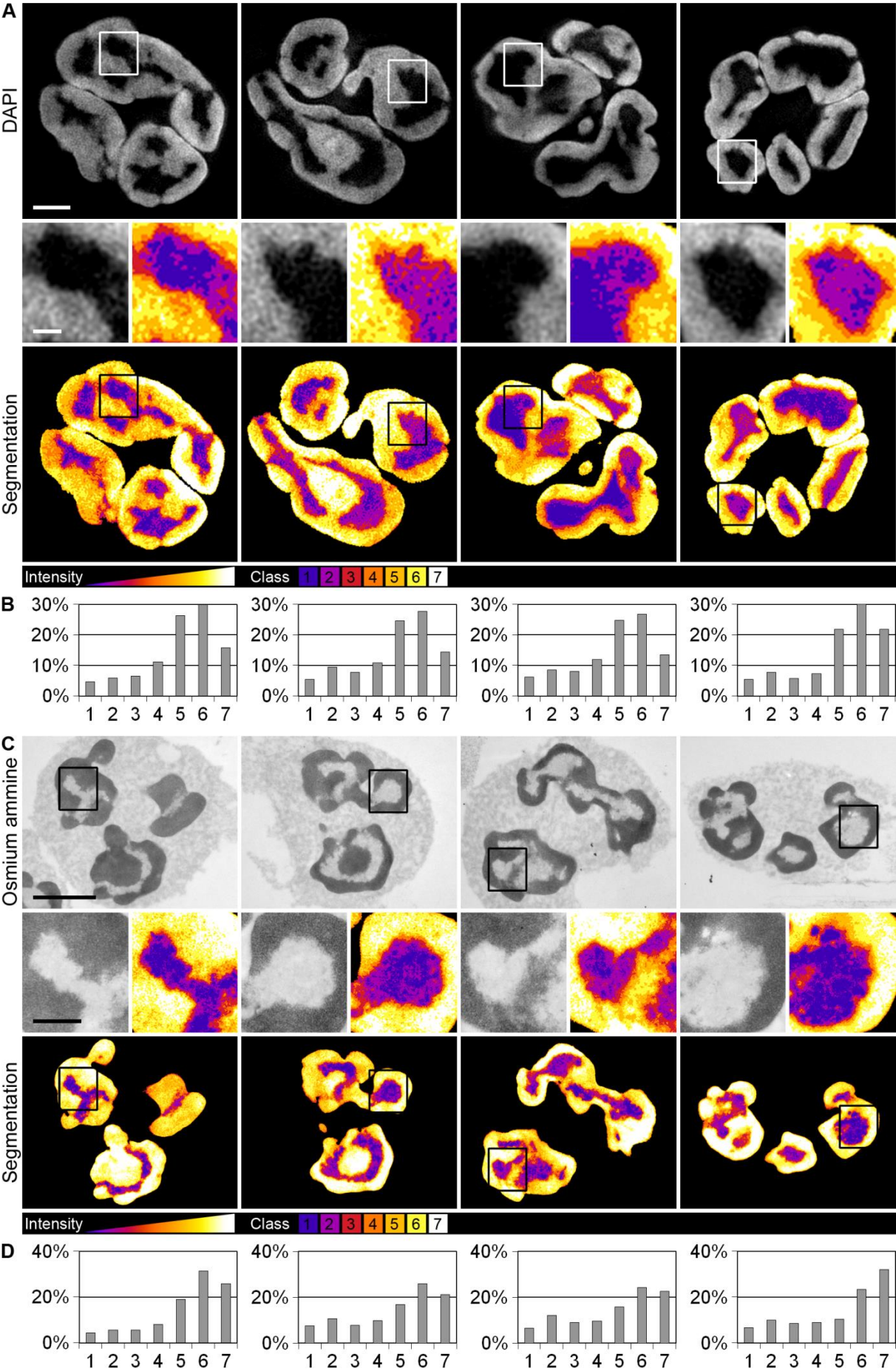


Figure 17: Variability of the chromatin pattern in granulocytes (see legend on next page).

Figure 13: Variability of the chromatin pattern in CD34⁺ cells. (A) Upper row: DAPI stained DNA of PFA-fixed cells; light optical mid-sections of four different whole 3D-SIM 3D acquisitions are shown. Lower row: corresponding segmented image. Middle row: respective magnifications of the upper and lower row. The segmentation algorithm converted the DAPI-intensities into seven classes with increasing density from class 1 to 7, i.e. from blue to white. Very minor differences in the chromatin pattern were observed, ranging from a slightly more homogenous distribution (two left images) to a slightly more heterogeneous one (two right images). (B) Profiles of the segmentations of the whole 3D acquisitions corresponding to the images shown in (A). (C) Analogous to (A), except that the upper row shows osmium ammine stained DNA of PFA-fixed cells in TEM images of physical sections. Again some nuclei showed a slightly more homogenous (left image), others a slightly more heterogeneous distribution (three right images). (D) Profiles of the segmented images shown in (C). In contrast to (B) unexpected variations were observed: while the profiles for the two left images with slightly different chromatin patterns are the same, the profiles of the three right images with equivalent chromatin patterns are different from each other. Scale bars: 2 μm in images of whole nuclei, 0.5 μm in magnifications. This data is included in Hübner et al. (2015).

Figure 14: Variability of the chromatin pattern in monoblasts. Equivalent to **Figure 13**, therefore the legend is shortened here. (A) Differences in the DAPI-stained chromatin pattern were observed, ranging from a more homogenous distribution (two left images) to a more heterogeneous one (two right images). (B) Profiles of the segmentations of the whole 3D acquisitions corresponding to the images shown in (A). (C) Again some nuclei showed a slightly more homogenous (three left images), others a slightly more heterogeneous chromatin distribution (right image). (D) In contrast to (B) unexpected variations were observed: while the profiles for the left and the right image with slightly different chromatin patterns are the same, the profiles of the three left images with equivalent chromatin patterns are different from each other. Scale bars: 2 μm in images of whole nuclei, 0.5 μm in magnifications. This data is included in Hübner et al. (2015).

Figure 15: Variability of the chromatin pattern in myeloblasts. Equivalent to **Figure 13**, therefore the legend is shortened here. (A) Differences in the DAPI-stained chromatin pattern were observed, ranging from a more homogenous distribution (two left images) to a more heterogeneous one (two right images). (B) Profiles of the segmentations of the whole 3D acquisitions corresponding to the images shown in (A). (C) Again some nuclei showed a slightly more homogenous (two left images), others a slightly more heterogeneous chromatin distribution (two right images). (D) In contrast to (B) unexpected variations were observed: while the profile for the second from left image is very similar to the profiles of the two right images despite slightly different chromatin patterns, the profiles of the two left images with equivalent chromatin patterns are different. Scale bars: 2 μm in images of whole nuclei, 0.5 μm in magnifications. This data is included in Hübner et al. (2015).

Figure 16: Variability of the chromatin pattern in monocytes. Equivalent to **Figure 13**, therefore the legend is shortened here. (A) Minor differences in the DAPI-stained chromatin pattern were observed, with some nuclei showing less strongly compacted chromatin (left image) than others (three right images). (B) Profiles of the segmentations of the whole 3D acquisitions corresponding to the images shown in (A). (C) Again some nuclei showed less strongly compacted chromatin (two left images), others stronger compacted chromatin (two right images). (D) In contrast to (B) unexpected variations were observed (although much smaller than in CD34⁺ cells, monoblasts and myeloblasts (**Figure 13-15**)): while the profile for the second from right image is the same as profiles of the two left images despite slightly different chromatin patterns, the profiles of the two right images with equivalent chromatin patterns are different. Scale bars: 2 μm in images of whole nuclei, 0.5 μm in magnifications. This data is included in Hübner et al. (2015).

Figure 17: Variability of the chromatin pattern in granulocytes. Equivalent to **Figure 13**, therefore the legend is shortened here. (A) Only very minor differences in the chromatin pattern were observed, with some nuclei showing even stronger compaction at the nuclear periphery (two right images) than others (two left images). (B) Profiles of the segmentations of the whole 3D acquisitions corresponding to the images shown in (A). (C) Again some nuclei showed even stronger compaction at the nuclear periphery (two right images) than others (two left images). (D) In contrast to (B) unexpected variations were observed (although much smaller than in CD34⁺ cells, monoblasts and myeloblasts (**Figure 13-15**)): while the profile for the second from right image is the same as the profiles of the two left images despite slightly different chromatin patterns, the profiles of the two right images with equivalent chromatin patterns are different. Scale bars: 2 μm in images of whole nuclei, 0.5 μm in magnifications. This data is included in Hübner et al. (2015).

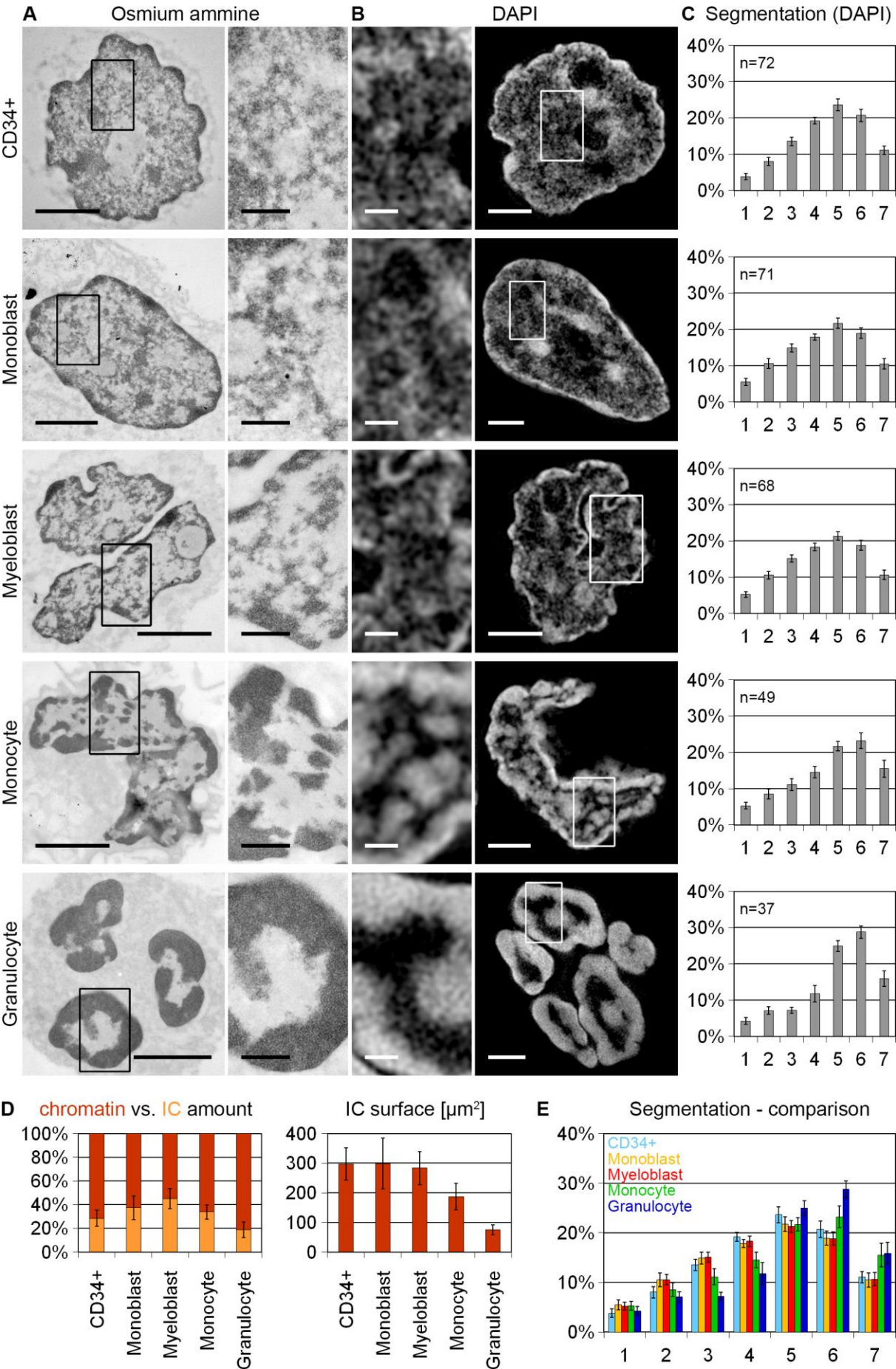


Figure 18: Chromatin pattern of hematopoietic cell types (see legend on next page).

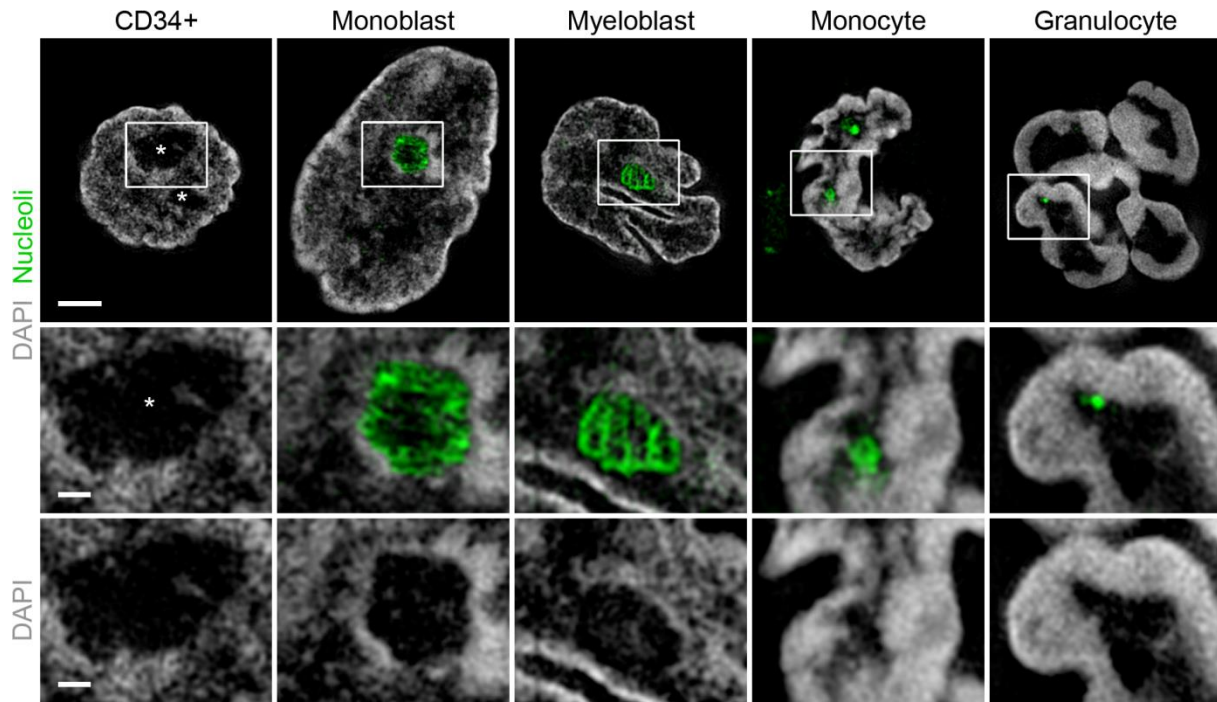


Figure 19: Nucleoli in hematopoietic cell types. DAPI stained DNA (gray) and nucleoli (green) of PFA-fixed cells in light optical mid-sections of whole 3D-SIM 3D acquisitions. Immunofluorescence for the detection of nucleoli was performed using human-anti-nucleolus, followed by goat-anti-human-FITC or goat-anti-human-Alexa594 antibodies. Upper row: whole nuclei. Middle row: magnifications of the images in the upper row. Lower row: magnifications of the DAPI staining alone. From left to right a CD34⁺ cell, monoblast, myeloblast, monocyte, and granulocyte is shown. Unfortunately for CD34⁺ cells no qualitatively sufficient staining of nucleoli could be achieved. However, the nucleoli usually could be clearly identified from the DAPI staining alone. In the image they are marked with an asterisk. Typically CD34⁺ cells contained 2-4 nucleoli (estimated from DAPI stained nuclei, n=15), monoblasts 1-3 (n=12), myeloblasts 2-3 (n=13), monocytes 2-4 (n=3) and granulocytes usually 1, occasionally 2 (n=11). Scale bars: 2 μm in images of whole nuclei, 0.5 μm in magnifications. Figure adapted from Hübner et al. (2015).

Figure 18: Chromatin pattern of hematopoietic cell types. (A) Osmium ammine stained DNA of PFA-fixed cells in TEM images of physical sections. From top to bottom a CD34⁺ cell, monoblast, myeloblast, monocyte, and granulocyte is shown. Left column: whole nuclei. Right column: magnifications. **(B)** Analogous to (A), but here DAPI stained DNA of PFA-fixed cells in light optical mid-sections of whole 3D-SIM 3D acquisitions is shown. Right column: whole nuclei. Left column: magnifications. **(C)** Profiles of the chromatin distribution after the segmentation of the DAPI intensities into seven classes with increasing density from class 1 to 7, i.e. from blue to white. From top to bottom the average curves of multiple whole 3D-SIM 3D acquisitions of CD34⁺ cells, monoblasts, myeloblasts, monocytes, and granulocytes are shown. A direct comparison of the chromatin distributions shown here is displayed in **(E)**. Statistical tests revealed significant differences only between monoblasts and granulocytes ($p=0.014$) and myeloblasts and granulocytes ($p=0.010$). Note that the Wilcoxon rank-sum test used here can only check for differences in the mean value, not in the actual distribution. **(D)** Evaluations of the amount of chromatin in comparison to the IC (left graph) and of the length of the IC surface (right graph), both based on osmium ammine stained DNA of PFA-fixed cells in TEM images of physical sections. Only images of sections from the central part of the nuclei were evaluated. In both cases, n=12, 25, 22, 13, 14 cells were analyzed for CD34⁺ cells, monoblasts, myeloblasts, monocytes, and granulocytes, respectively. For the chromatin vs. IC amount all values were highly significantly ($p\leq 0.001$) or very significantly ($p<0.01$) (CD34⁺ cells vs. monoblasts, CD34⁺ cells vs. granulocytes, monoblasts vs. myeloblasts) different from each other, apart from CD34⁺ cells vs. monocytes ($p=0.098$) and monoblasts vs. monocytes ($p=0.361$). The length of the IC surface was normalized for the area of the nucleus. All values were highly significantly ($p\leq 0.001$) different from each other, apart from CD34⁺ cells, monoblasts and myeloblasts among each other ($p=0.962$ for CD34⁺ cells vs. monoblasts, $p=0.488$ for CD34⁺ cells vs. myeloblasts, $p=0.620$). Error bars: standard deviation. Scale bars: 2 μm in images of whole nuclei, 0.5 μm in magnifications. Figure adapted from Hübner et al. (2015).

4.1.2 Consistent functional nuclear architecture during differentiation of hematopoietic cells

The next step was the analysis of the functional nuclear architecture in the five cell types. The following markers were used in pairwise immunofluorescence stainings: histone 3 trimethylated on lysine 4 (H3K4me3) for transcriptionally competent chromatin, histone 3 trimethylated on lysine 9 (H3K9me3) for inactive chromatin, RNA Polymerase II phosphorylated on serine 2 (elongating form) (RNA Pol II Ser 2P) or serine 5 (promoters) (RNA Pol II Ser 5P) for transcription sites and SC35 for nuclear speckles (for literature see section 2.3 in the introduction).

In addition to visual inspection, the spatial distribution of the markers was quantitatively analyzed by mapping the signals to the chromatin classes determined by the segmentation of the DAPI signals.

The “active” marks, H3K4me3 (**Figure 20+21+23 A** and **26-29 A**), RNA Pol II Ser 2P (**Figure 20+24 A**) and RNA Pol II Ser 5P (**Figure 21+25 A**) were mainly (for H3K4me3) or almost exclusively (for RNA Pol II) located at the surface of the chromatin domain clusters (CDCs), showing basically no staining in the interior of the IC lacunas (characterized by no or extremely low DAPI signal). The corresponding profiles of the marker signals mapped to the segmented DAPI intensity classes (**Figure 20+21+23 B** and **26-29 B+C** for H3K4me3, **Figure 20+24 B** for RNA Pol II Ser 2P, **Figure 21+25 B** for RNA Pol II Ser 5P) confirmed the observation from the images: all three markers showed a consistent overrepresentation (relative signal enrichment) in the IC (class 1) and in decondensed chromatin regions (classes 2-4) and a corresponding underrepresentation (relative signal depletion) in the high-intensity classes of more compact chromatin (classes 5-7). Compared to H3K4me3 both modifications of RNA Pol II were more enriched in regions of low chromatin density and in the IC, demonstrated by a shift towards lower chromatin classes, most noticeable by the higher overrepresentation in class 1 (the IC).

While the localization of RNA Pol II Ser 2P and 5P in relation to chromatin was the same in all cell types, quantifications of the abundance of these markers revealed clear differences (**Figure 22**). The number of RNA Pol II signals was evaluated either based on the number of positive pixels (left graph) or the number of spots (right graph). While the former procedure includes all signals and therefore can compensate for differences in the size of the detected spots (taking into account that a cell with a few large spots can have the same number of positive pixels as a cell with many small spots), the latter gives an idea of the number of potential “transcription factories” or “expression hubs”, clusters of RNA polymerases (for details see sections 2.2.2 and 2.2.4 in the introduction). Both methods and both modifications

of RNA Pol II showed the same tendency: the values were very similar in CD34⁺ cells and monoblasts and decreased over myeloblasts and monocytes to very low numbers in granulocytes. However, when counting the number of spots, the differences between CD34⁺ cells, monoblasts, myeloblasts, and monocytes were smaller than in the evaluation based on the number of positive pixels. Based on the number of positive pixels RNA Pol II Ser 2P was more abundant than RNA Pol II Ser 5P in all cell types.

It has to be noted that these values are not to be taken as absolute – they are rather a relative measure that allows the comparison of cells stained, imaged and analyzed under the same conditions. But nevertheless, with an average number of 3950/3200 spots in CD34⁺ cells for RNA Pol II Ser 2P and Ser 5P, respectively, 3750/3300 in monoblasts, 2500/2700 in myeloblasts, 2100/2350 in monocytes and 450/1000 in granulocytes, the number of potential transcription factories or “expression hubs” (for details see sections 2.2.2 and 2.2.4 in the introduction) observed here corresponds well with previously published results: Using high-resolution methods (tetraploid) HeLa cells were reported to contain 7900 RNA Pol II sites (~9700 sites for RNA Pol II and RNA Pol III; ~1800 sites for RNA polymerase III (RNA Pol III), equivalent to ~18.55% of the total number of extranucleolar transcription sites) (Pombo et al. 1999). Faro-Trindade and Cook (2006) found ~6400/~5700 BrUTP foci in undifferentiated mouse F9 and embryonic stem cells, respectively, which under the assumption of a similar ratio of RNA Pol II vs RNA Pol III sites as in HeLa cells (Pombo et al. 1999, compare above) correspond to ~5200/4650 RNA Pol II transcription factories. In more differentiated cells (Faro-Trindade and Cook 2006) the numbers dropped to ~3900 BrUTP sites, i.e. ~3200 RNA Pol II foci. In erythroblasts – one of the last nucleated cell stages in the differentiation pathway of red blood cells (Theml et al. 2004, Wognum and Szilvassy 2015) and therefore more differentiated cells than the cell types mentioned before – lower numbers of transcription factories were reported: roughly 1500 BrUTP foci, i.e. ~1250 RNA Pol II sites in human intermediate erythroblasts (Brown et al. 2008) and ~550 RNA Pol II S5P transcription factories in mouse erythroblasts (Eskiw and Fraser 2011) of a seemingly later differentiation stage than in the previous study, judging from the nuclear morphology of the analyzed cells (compare Theml et al. 2004).

SC35, a marker for nuclear speckles, (**Figure 23-25 A**) was found almost exclusively in the interior of the larger IC lacunas in all five cell types. The corresponding profiles of the marker signals mapped to the segmented DAPI intensity classes (**Figure 23-25 B**) confirmed the observation from the images: SC35 was largely restricted to the IC in all five cell types, as demonstrated by the high overrepresentation (relative signal enrichment) in intensity class 1 (and class 2 in granulocytes due to the segmentation problem described in the previous section (section 4.1.1)). An additional minor fraction of SC35 signals was found in the next higher

chromatin class, representing (very) decondensed chromatin regions. A corresponding underrepresentation (relative signal depletion) was found in all other intensity classes. Compared to H3K4me3, RNA Pol II Ser 2P, and RNA Pol II Ser 5P, SC35 was clearly shifted towards lower chromatin classes.

The “inactive” chromatin marker H3K9me3 showed a preferential localization in condensed chromatin in CD34⁺ cells, monoblasts, myeloblasts and monocytes (**Figure 26-29 A**). However, not all compacted chromatin was stained (especially in monocytes) and H3K9me3 was also detected in regions of lower density. The corresponding profiles of the marker signals mapped to the segmented DAPI intensity classes (**Figure 26-29 B+C**) showed consistent results in the classical representations (upper graphs) with a clear shift towards higher chromatin classes compared to H3K4me3. The over- and underrepresentations, representing the relative signal enrichment and depletion (lower graphs), however, revealed a broad variability within the cell types. A potential explanation for these unexpected results lacking a clear overrepresentation (relative signal enrichment) in the higher chromatin classes is provided by the close similarity of the distributions of the DAPI and H3K9me3 signals in the classical profiles. As a result, already small differences in the amount of signal can cause a change from an overrepresentation to an underrepresentation or vice versa. The fact that for H3K9me3 the degree of over-/underrepresentation (relative signal enrichment/depletion) was typically less pronounced as for the other markers (see **Figure 30**, right graphs) supports this. At the same time, these observations also demonstrate that the staining of H3K9me3 is not as strongly restricted to compacted chromatin as widely assumed (see also section 5.1.1 in the discussion).

In granulocytes, H3K9me3 could not be detected despite several repetitions of the experiment and the application of different fixation procedures (2% and 4% PFA), permeabilization methods (0.1%, 0.3% and 0.6% Triton) and antibody dilutions (1:100 and 1:50). The presence of H3K9me3 in these cells is controversially discussed in the literature: while Lukasova et al. (2005) also found granulocytes to be negative for H3K9me3, Olins and Olins (2005) and Merz (2008) – the later however under hypotonic conditions – detected several large spots with intense signals.

Figure 30 summarizes the observations described above by showing a comparison between all cell types for each marker in both the classical profiles (left) and the over- and underrepresentations (relative signal enrichment and depletion) (right) of the segmentation profiles. For each marker protein all available data from the different pairwise immunofluorescence stainings were combined. The profiles demonstrate that despite their distinctly different nuclear phenotypes on a global level, nuclei from all cell types showed a

consistent distribution of the marker signals, especially for H3K4me3, RNA Pol II Ser 2P, RNA Pol II Ser 5P, and SC35. Only for H3K9me3 the over-/underrepresentations (relative signal enrichment/depletion) revealed larger variations. In relation to H3K4me3, RNA Pol II was shifted towards lower chromatin classes and SC35 was localized in even lower density classes than RNA Pol II. In contrast, H4K9me3 was shifted towards higher chromatin classes compared to H3K4me3.

Figure 20: H3K4me3 and RNA Pol II Ser 2P in hematopoietic cell types. (A) DAPI stained DNA (gray), Histone 3 tri-methylated on lysine 4 (H3K4me3) (green) and RNA Polymerase II phosphorylated on serine 2 (RNA Pol II Ser 2P) (red) of PFA-fixed cells in light optical mid-sections of whole 3D-SIM 3D acquisitions. Immunofluorescence for the detection of H3K4me3 and RNA Pol II Ser 2P was performed using rabbit-anti-H3K4me3 and rat-anti-RNA Pol II Ser 2P antibodies, followed by donkey-anti-rabbit-DyLight488 and donkey-anti-rat-Alexa594 antibodies, respectively. Left column: whole nuclei. Middle column: magnifications of the images in the left column. Right column: magnifications of the DAPI staining alone; same area as in the middle column. From top to bottom a CD34⁺ cell, monoblast, myeloblast, monocyte, and granulocyte is shown. **(B)** Profiles of the chromatin distributions (gray) of whole 3D acquisitions after the segmentation of the DAPI signals into seven classes with increasing density from class 1 to 7, together with H3K4me3 (green) and RNA Pol II Ser 2P (red) assigned to the respective chromatin classes. For each cell type (top to bottom: CD34⁺ cell, monoblast, myeloblast, monocyte, granulocyte) both the classical profile (upper graph) as well as the calculated over- and underrepresentation of H3K4me3 and RNA Pol II Ser 2P in comparison to DAPI (lower graph) is included. Average curves of multiple whole 3D acquisitions are shown. Significant statistical differences ($p < 0.05$) between the distributions of H3K4me3 and RNA Pol II Ser 2P were only determined for monoblasts and granulocytes, but not for CD34⁺ cells ($p = 0.622$), myeloblasts ($p = 0.091$) and monocytes ($p = 0.149$). Note that the Wilcoxon rank-sum test used here can only check for differences in the mean value, not in the actual distribution. Error bars: standard deviation. Scale bars: 2 μm in images of whole nuclei, 0.5 μm in magnifications. Figure adapted from Hübner et al. (2015).

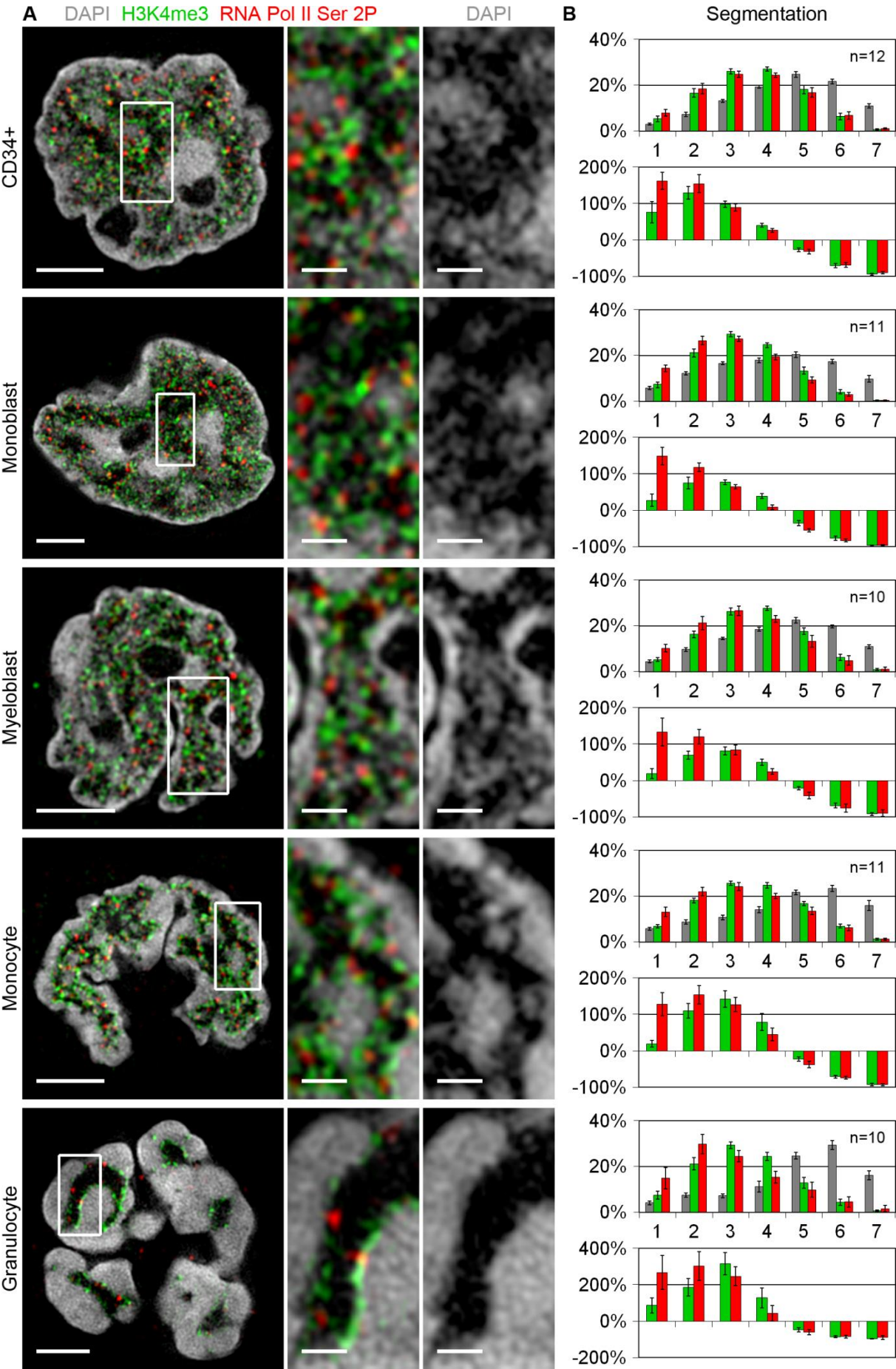


Figure 20: H3K4me3 and RNA Pol II Ser 2P in hematopoietic cell types (see legend on previous page).

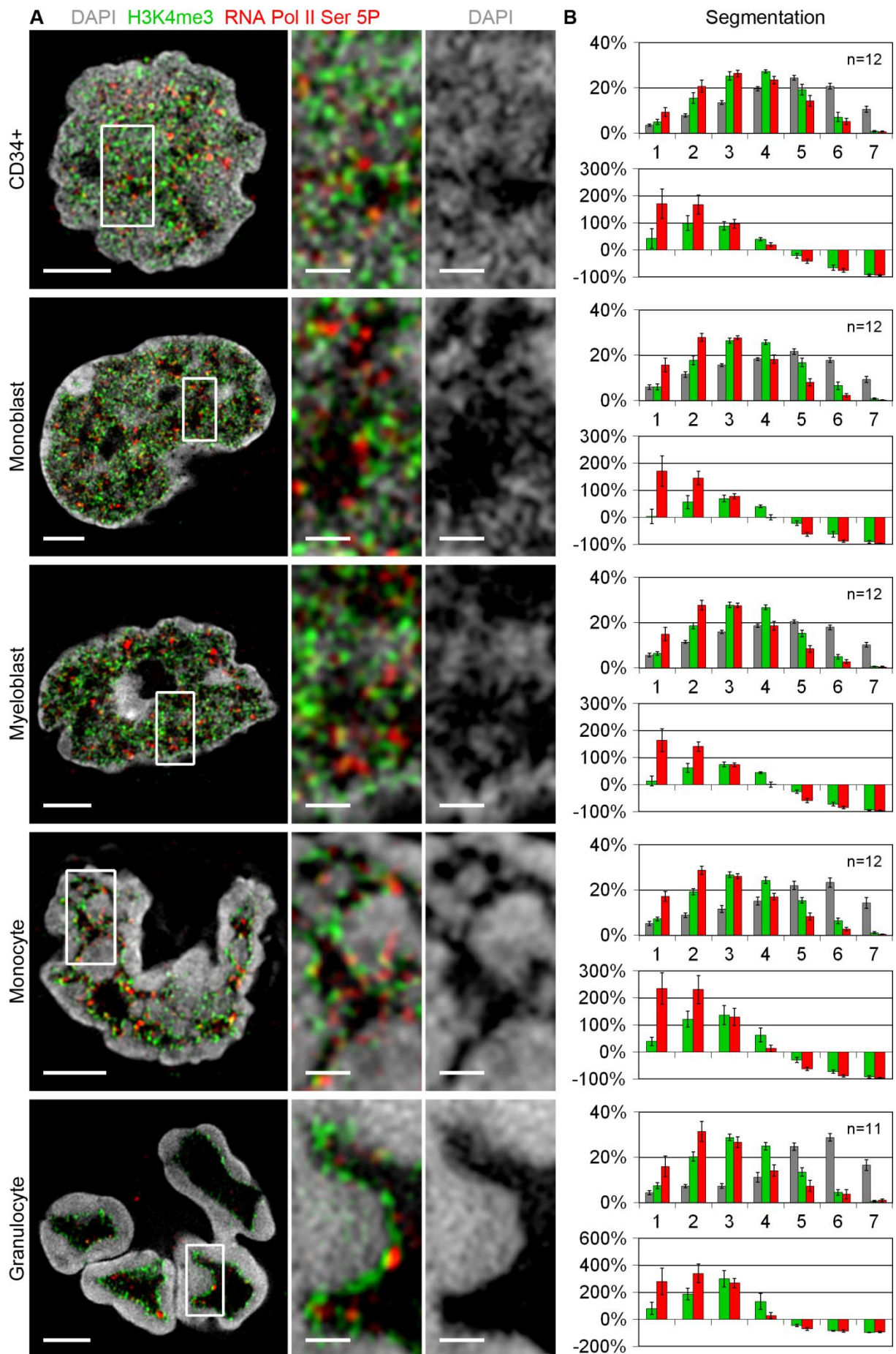


Figure 21: H3K4me3 and RNA Pol II Ser 5P in hematopoietic cell types (see legend on next page).

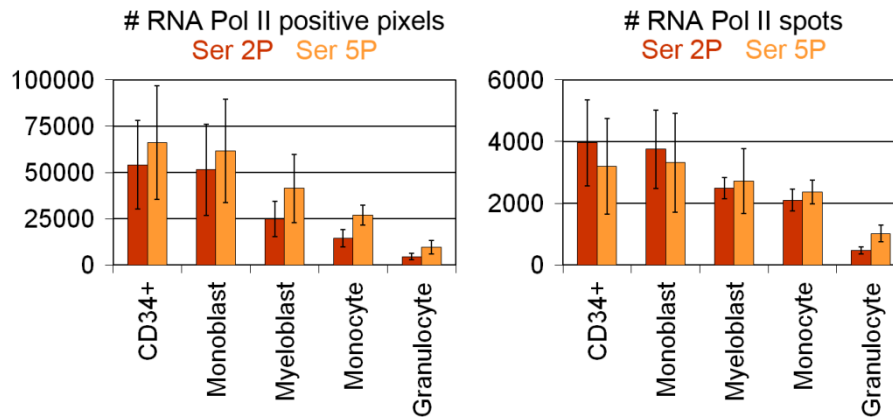


Figure 22: Number of RNA Pol II signals in hematopoietic cell types. The number of RNA Polymerase II (RNA Pol II) signals in whole 3D-SIM 3D acquisitions of immunofluorescence stainings was determined either by adding up the number of positive pixels for the staining (left) or by counting the number of spots (right). In both cases RNA Pol II phosphorylated on serine 2 (Ser 2P; red) ($n=24, 23, 19, 24, 13$ for CD34⁺ cells, monoblasts, myeloblasts, monocytes, and granulocytes, respectively) as well as RNA Pol II phosphorylated on serine 5 (Ser 5P; orange) ($n=24, 24, 24, 12, 17$ for CD34⁺ cells, monoblasts, myeloblasts, monocytes, and granulocytes, respectively) was analyzed. For RNA Pol II Ser 2P in both cases all observed differences were highly significant ($p<0.001$), with the exception of CD34⁺ vs. monoblasts ($p=0.456$ for the number of positive pixels and $p=0.620$ for the number of spots). For RNA Pol II Ser 5P the number of positive pixels varied highly significantly ($p<0.001$) apart from myeloblasts vs. monocytes, which however still varied very significantly ($p<0.01$), and CD34⁺ cells vs. monoblasts ($p=0.579$). For the number of spots, however, highly significant ($p<0.001$) differences could only be observed between granulocytes and the other four cell types and significant differences ($p<0.05$) between monoblasts and monocytes. All other values did not show significant variations ($p=0.660$ for CD34⁺ cells vs. monoblasts, $p=0.797$ for CD34⁺ cells vs. myeloblasts, $p=0.497$ for CD34⁺ cells vs. monocytes, $p=0.158$ for monoblasts vs. myeloblasts, $p=0.513$ for myeloblasts vs. monocytes). Error bars: standard deviation. Figure adapted from Hübner et al. (2015).

Figure 21: H3K4me3 and RNA Pol II Ser 5P in hematopoietic cell types. Equivalent to **Figure 20**, therefore the legend is shortened here. **(A)** DAPI stained DNA (gray), Histone 3 tri-methylated on lysine 4 (H3K4me3) (green) and RNA Polymerase II phosphorylated on serine 5 (RNA Pol II Ser 5P) (red). Immunofluorescence for the detection of H3K4me3 and RNA Pol II Ser 5P was performed using rabbit-anti-H3K4me3 and rat-anti-RNA Pol II Ser 5P antibodies, followed by donkey-anti-rabbit-DyLight488 and donkey-anti-rat-Alexa594 antibodies, respectively. **(B)** Profiles of the chromatin distributions (gray) of whole 3D acquisitions with H3K4me3 (green) and RNA Pol II Ser 5P (red) assigned to the respective chromatin classes. The differences between the distributions of H3K4me3 and RNA Pol II Ser 5P were very significant ($p<0.01$) in myeloblasts and granulocytes, and highly significant ($p<0.001$) in monoblasts and monocytes. Only in CD34⁺ cells no significant difference could be observed ($p=0.059$). Error bars: standard deviation. Scale bars: 2 μm in images of whole nuclei, 0.5 μm in magnifications. Figure adapted from Hübner et al. (2015).

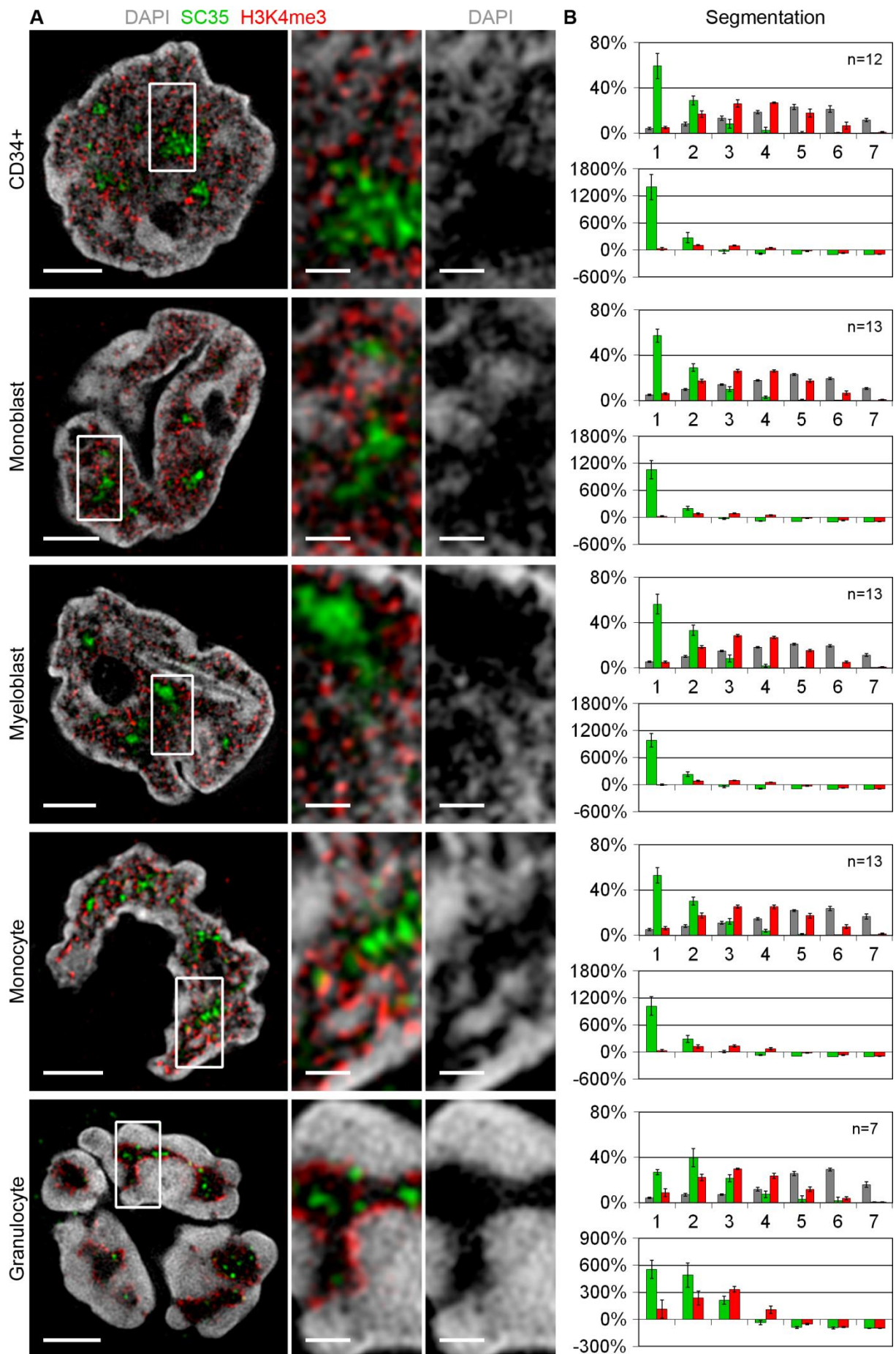


Figure 23: SC35 and H3K4me3 in hematopoietic cell types (see legend on page 192).

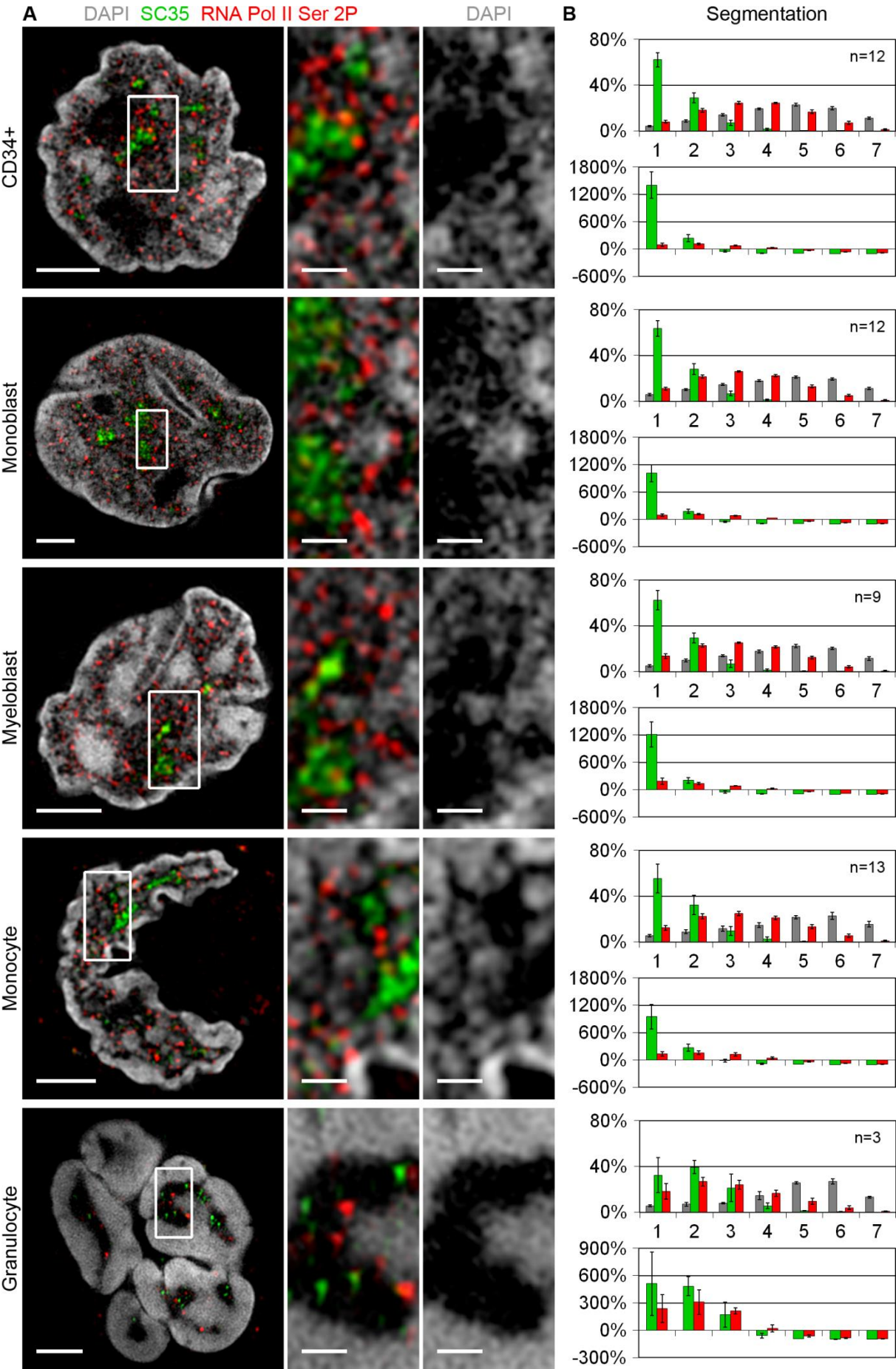


Figure 24: SC35 and RNA Pol II Ser 2P in hematopoietic cell types (see legend on page 192).

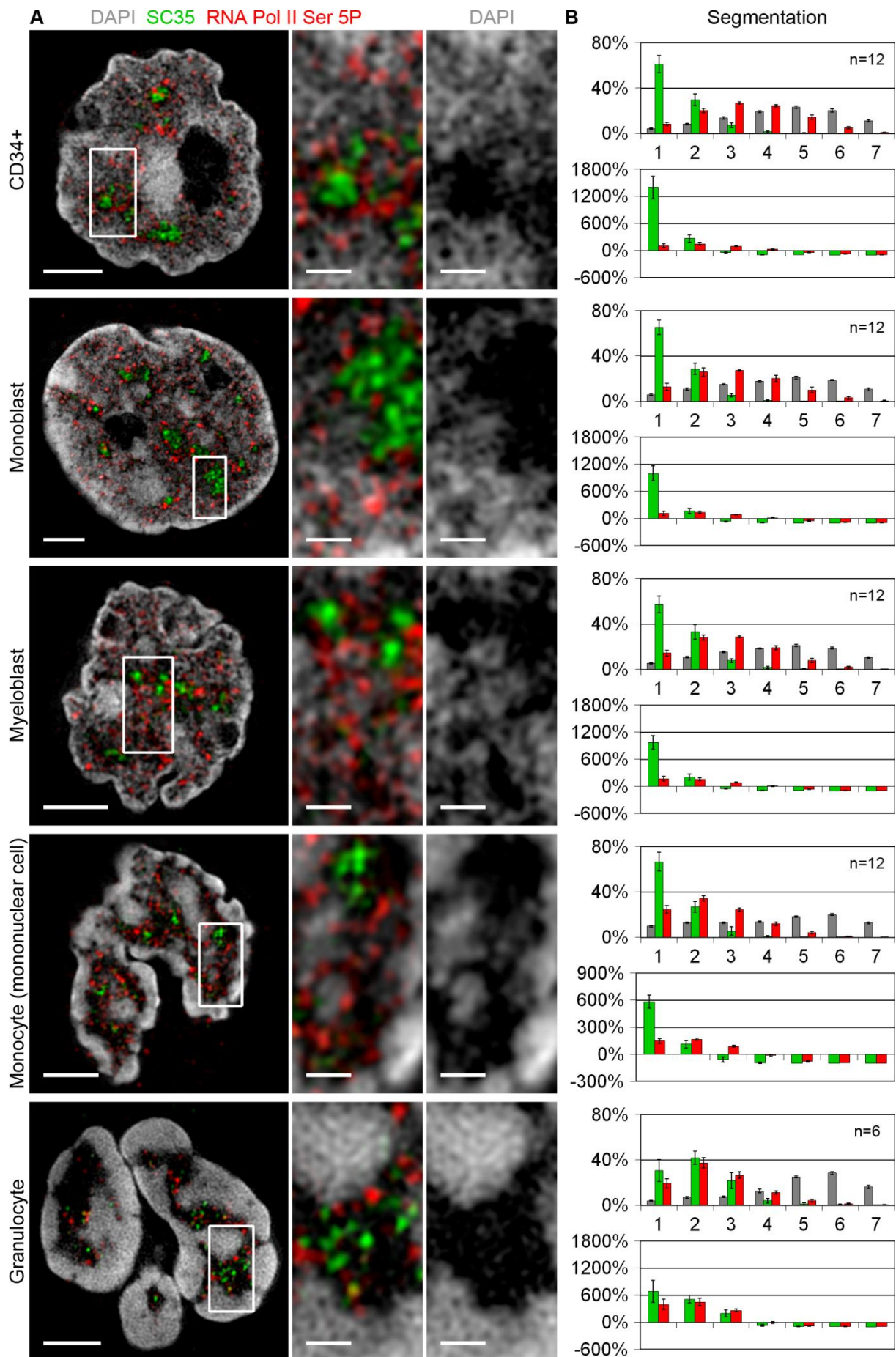


Figure 25: SC35 and RNA Pol II Ser 5P in hematopoietic cell types (see legend on page 192).

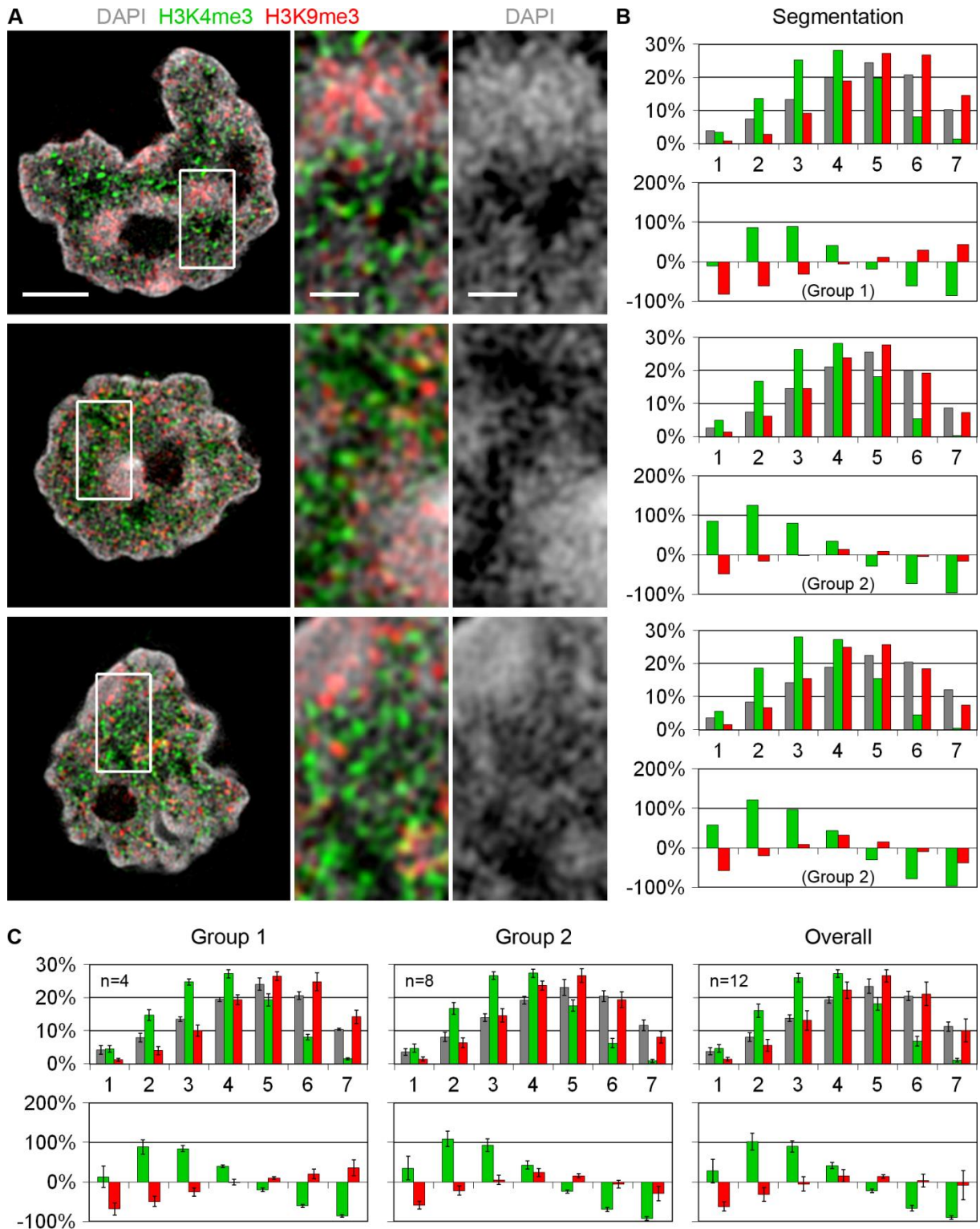


Figure 26: H3K4me3 and H3K9me3 in CD34⁺ cells. (A) DAPI stained DNA (gray), Histone 3 tri-methylated on lysine 4 (H3K4me3) (green) and Histone 3 tri-methylated on lysine 9 (H3K9me3) (red) of PFA-fixed cells in light optical mid-sections of whole 3D-SIM 3D acquisitions. Immunofluorescence for the detection of H3K4me3 and H3K9me3 was performed using rabbit-anti-H3K4me3 and mouse-anti-H3K9me3 antibodies, followed by donkey-anti-rabbit-DyLight488 and goat-anti-mouse-Alexa594 antibodies, respectively. Left column: whole nuclei. Middle column: magnifications of the images in the left column. Right column: magnifications of the DAPI staining alone; same area as in the middle column. Three different cells are shown. (B) Profiles of the chromatin distributions (gray) of whole 3D acquisitions after the segmentation of the DAPI signals into seven classes with increasing density from class 1 to 7, together with H3K4me3 (green) and H3K9me3 (red) assigned to the respective chromatin classes. For each example both the classical profile (upper graph) as well as the calculated (*legend continued on next page*)

Figure 23: SC35 and H3K4me3 in hematopoietic cell types. Equivalent to **Figure 20**, therefore the legend is shortened here. **(A)** DAPI stained DNA (gray), SC35 (green) and Histone 3 tri-methylated on lysine 4 (H3K4me3) (red). Immunofluorescence for the detection of SC35 and H3K4me3 was performed using mouse-anti-SC35 and rabbit-anti-H3K4me3 antibodies, followed by goat-anti-mouse-Alexa594 and donkey-anti-rabbit-DyLight488 antibodies, respectively. Note that the colors of the two markers were exchanged in the images compared to the detection scheme. **(B)** Profiles of the chromatin distributions (gray) of whole 3D acquisitions with SC35 (green) and H3K4me3 (red) assigned to the respective chromatin classes. In all cell types the distributions of SC35 and H3K4me3 differed highly significantly ($p < 0.001$). Due to the strong overrepresentation of SC35, the results for H3K4me3 are difficult to recognize in these graphs. Please refer to **Figure 20+21** for a better representation of the distribution of H3K4me3. Note that in this figure H3K4me3 is depicted in red and not in green as in the previous figures. Error bars: standard deviation. Scale bars: 2 μm in images of whole nuclei, 0.5 μm in magnifications. Figure adapted from Hübner et al. (2015).

Figure 24: SC35 and RNA Pol II Ser 2P in hematopoietic cell types. Equivalent to **Figure 20**, therefore the legend is shortened here. **(A)** DAPI stained DNA (gray), SC35 (green) and RNA Polymerase II phosphorylated on serine 2 (RNA Pol II Ser 2P) (red). Immunofluorescence for the detection of SC35 and RNA Pol II Ser 2P was performed using mouse-anti-SC35 and rat-anti-RNA Pol II Ser 2P antibodies, followed by goat-anti-mouse-Alexa488 and donkey-anti-rat-Alexa594 antibodies, respectively. **(B)** Profiles of the chromatin distributions (gray) of whole 3D acquisitions with SC35 (green) and RNA Pol II Ser 2P (red) assigned to the respective chromatin classes. In all cell types the distributions of SC35 and RNA Pol II Ser 2P differed highly significantly ($p < 0.001$). Due to the strong overrepresentation of SC35, the results of RNA Pol II Ser 2P are difficult to recognize in these graphs. Please refer to **Figure 20** for a better representation of the distribution of RNA Pol II Ser 2P. Error bars: standard deviation. Scale bars: 2 μm in images of whole nuclei, 0.5 μm in magnifications. Figure adapted from Hübner et al. (2015).

Figure 25: SC35 and RNA Pol II Ser5P in hematopoietic cell types. Equivalent to **Figure 20**, therefore the legend is shortened here. For this experiment monocytes selected from mononuclear cells were used (see details in section 3.2.1.1 in the Methods). **(A)** DAPI stained DNA (gray), SC35 (green) and RNA Polymerase II phosphorylated on serine 5 (RNA Pol II Ser 5P) (red). Immunofluorescence for the detection of SC35 and RNA Pol II Ser 5P was performed using mouse-anti-SC35 and rat-anti-RNA Pol II Ser 5P antibodies, followed by goat-anti-mouse-Alexa488 and donkey-anti-rat-Alexa594 antibodies, respectively. **(B)** Profiles of the chromatin distributions (gray) of whole 3D acquisitions with SC35 (green) and RNA Pol II Ser 5P (red) assigned to the respective chromatin classes. The distributions of SC35 and RNA Pol II Ser 5P differed highly significantly ($p < 0.001$) (CD34⁺ cells, monoblasts, myeloblasts, monocytes) or very significantly ($p < 0.01$) (granulocytes). Due to the strong overrepresentation of SC35, the results of RNA Pol II Ser 5P are difficult to recognize in these graphs. Please refer to **Figure 21** for a better representation of the distribution of RNA Pol II Ser 5P. Error bars: standard deviation. Scale bars: 2 μm in images of whole nuclei, 0.5 μm in magnifications. Figure adapted from Hübner et al. (2015).

Figure 26: (*legend continued from previous page*) over- and underrepresentation of H3K4me3 and H3K9me3 in comparison to DAPI (lower graph) is included. The corresponding profiles to the cells shown in (A) are depicted. In all three cells the distributions of H3K4me3 and H3K9me3 differed highly significantly ($p < 0.001$). The over- and underrepresentations revealed two subgroups of cells, exemplified by the top cell / the two bottom cells, respectively. **(C)** Average curves of the profiles of multiple whole 3D acquisitions are shown for group 1 (left) and 2 (middle) and the overall distribution including all cells (right). In all three cases the distributions of H3K4me3 and H3K9me3 differed highly significantly ($p < 0.001$). Error bars: standard deviation. Scale bars: 2 μm in images of whole nuclei, 0.5 μm in magnifications. This data is included in Hübner et al. (2015).

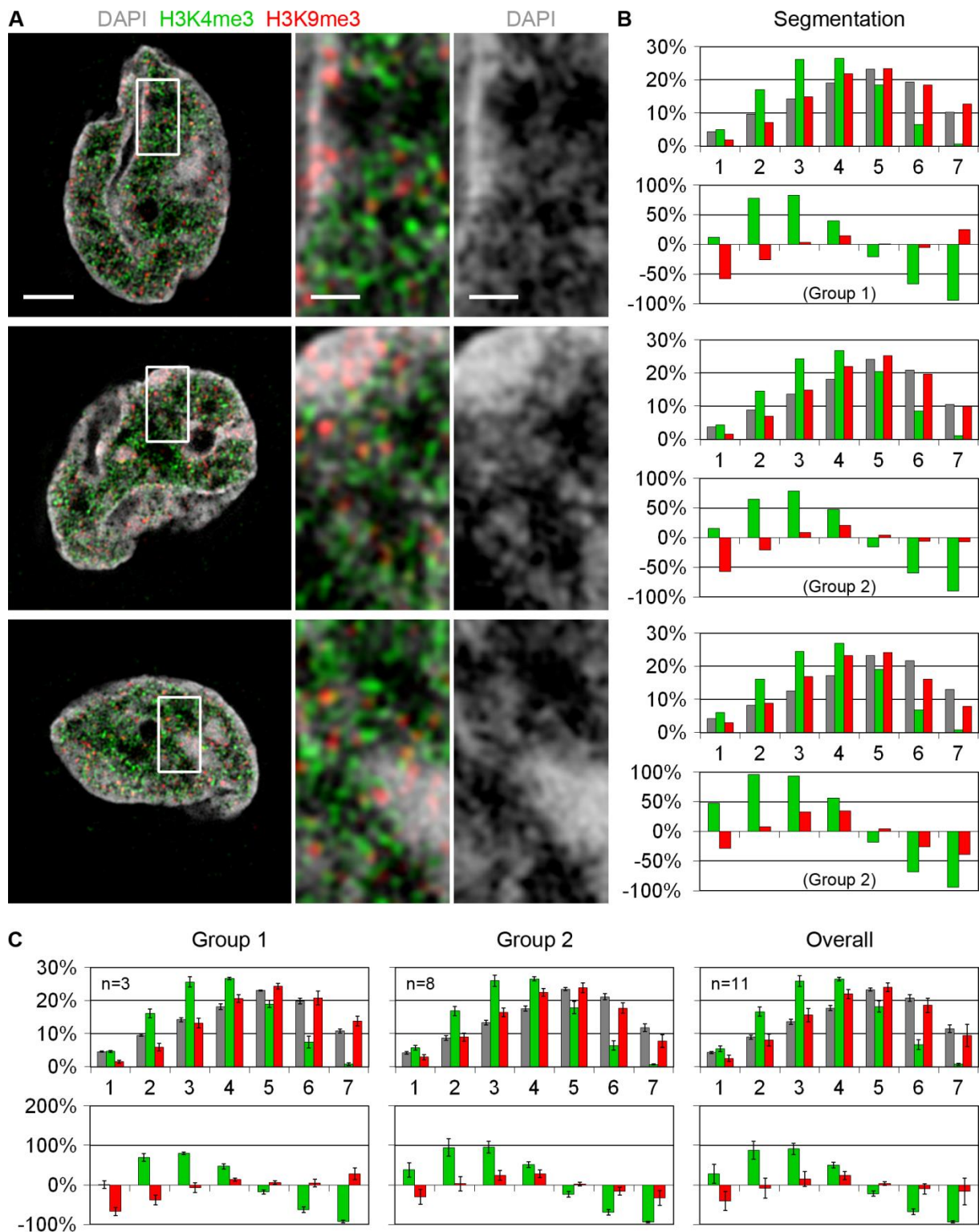


Figure 27: H3K4me3 and H3K9me3 in monoblasts. Equivalent to **Figure 26**, therefore the legend is shortened here. **(A)** DAPI stained DNA (gray), Histone 3 tri-methylated on lysine 4 (H3K4me3) (green) and Histone 3 tri-methylated on lysine 9 (H3K9me3) (red). **(B)** Profiles of the chromatin distributions (gray) of whole 3D acquisitions with H3K4me3 (green) and H3K9me3 (red) assigned to the respective chromatin classes. In all three cells the distributions of H3K4me3 and H3K9me3 differed highly significantly ($p < 0.001$). The over- and underrepresentations revealed two subgroups of cells, exemplified by the top cell / the two bottom cells, respectively. **(C)** In all three cases (group 1 (left), group 2 (middle) and the overall distribution (right)) the distributions of H3K4me3 and H3K9me3 differed highly significantly ($p < 0.001$). Error bars: standard deviation. Scale bars: 2 μm in images of whole nuclei, 0.5 μm in magnifications. This data is included in Hübner et al. (2015).

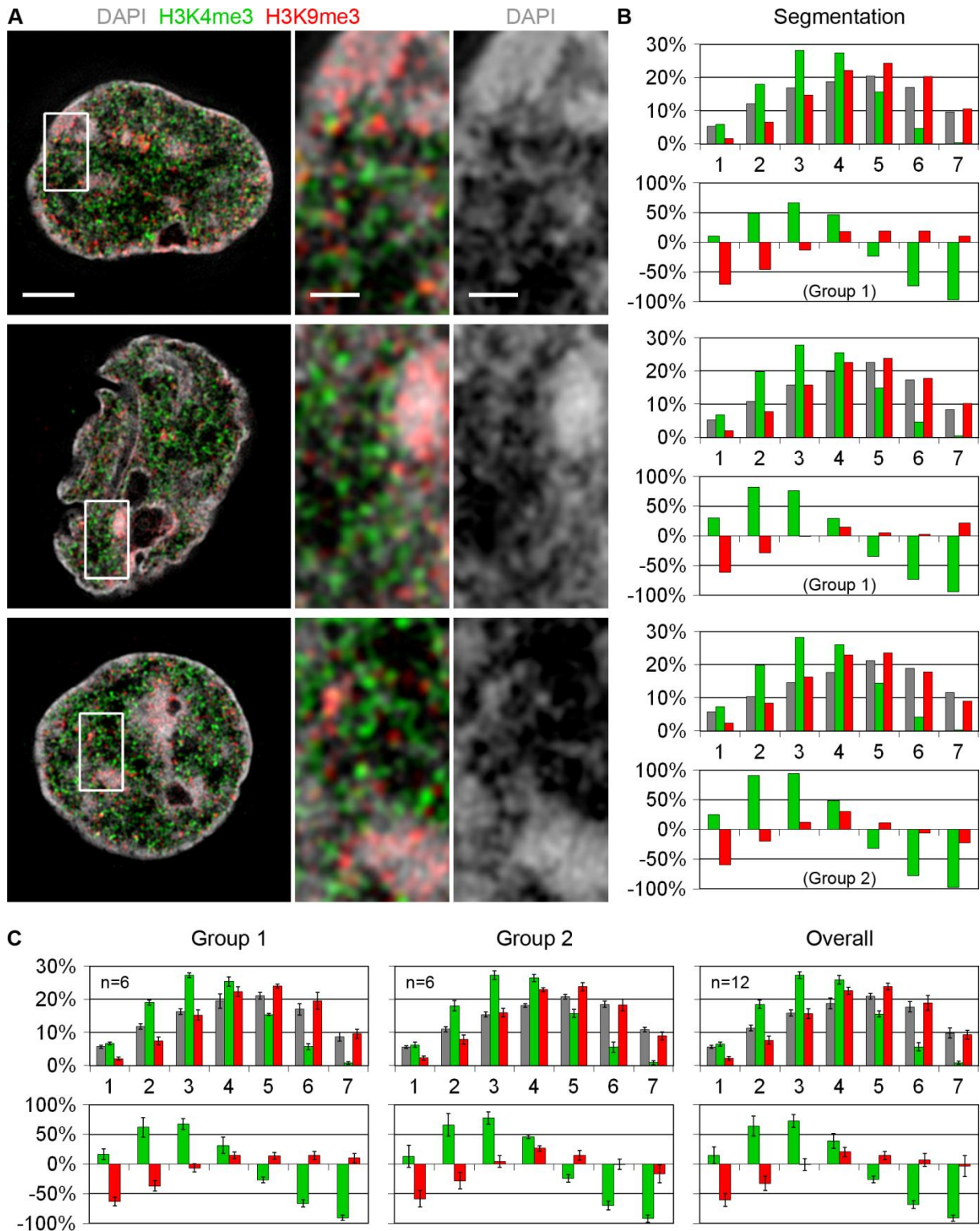


Figure 28: H3K4me3 and H3K9me3 in myeloblasts. Equivalent to **Figure 26**, therefore the legend is shortened here. **(A)** DAPI stained DNA (gray), Histone 3 tri-methylated on lysine 4 (H3K4me3) (green) and Histone 3 tri-methylated on lysine 9 (H3K9me3) (red). **(B)** Profiles of the chromatin distributions (gray) of whole 3D acquisitions with H3K4me3 (green) and H3K9me3 (red) assigned to the respective chromatin classes. In all three cells the distributions of H3K4me3 and H3K9me3 differed highly significantly ($p < 0.001$). The over- and underrepresentations revealed two subgroups of cells, exemplified by the top two cells / the bottom cell, respectively. **(C)** In all three cases (group 1 (left), group 2 (middle) and the overall distribution (right)) the distributions of H3K4me3 and H3K9me3 differed highly significantly ($p < 0.001$). Error bars: standard deviation. Scale bars: 2 μm in images of whole nuclei, 0.5 μm in magnifications. This data is included in Hübner et al. (2015).

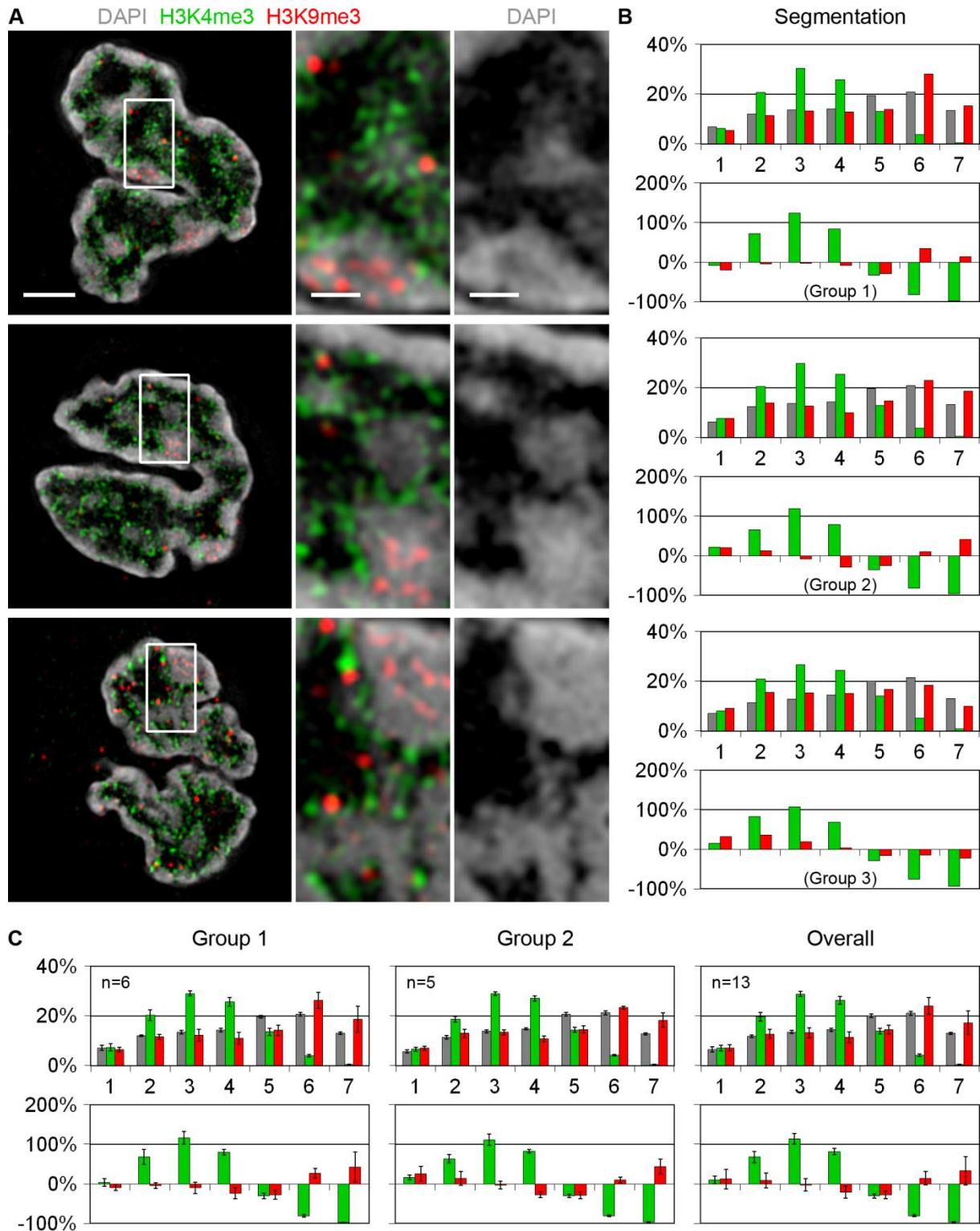


Figure 29: H3K4me3 and H3K9me3 in monocytes (mononuclear cells). Equivalent to **Figure 26**, therefore the legend is shortened here. For this experiment monocytes selected from mononuclear cells were used (see details in section 3.2.1.1 in the Methods). **(A)** DAPI stained DNA (gray), Histone 3 trimethylated on lysine 4 (H3K4me3) (green) and Histone 3 tri-methylated on lysine 9 (H3K9me3) (red). **(B)** Profiles of the chromatin distributions (gray) of whole 3D acquisitions with H3K4me3 (green) and H3K9me3 (red) assigned to the respective chromatin classes. In all three cells the distributions of H3K4me3 and H3K9me3 differed either highly significantly ($p < 0.001$) (upper and middle cell) or very significantly ($p < 0.01$) (lower cell). The over- and underrepresentations revealed three subgroups of cells, exemplified by the top/middle/bottom cell, respectively. **(C)** In group 1 (left), group 2 (middle) and the overall distribution (right) the distributions of H3K4me3 and H3K9me3 differed highly significantly ($p < 0.001$), in group 3 ($n=2$, average profile not shown) very significantly (*legend continued on page 197*)

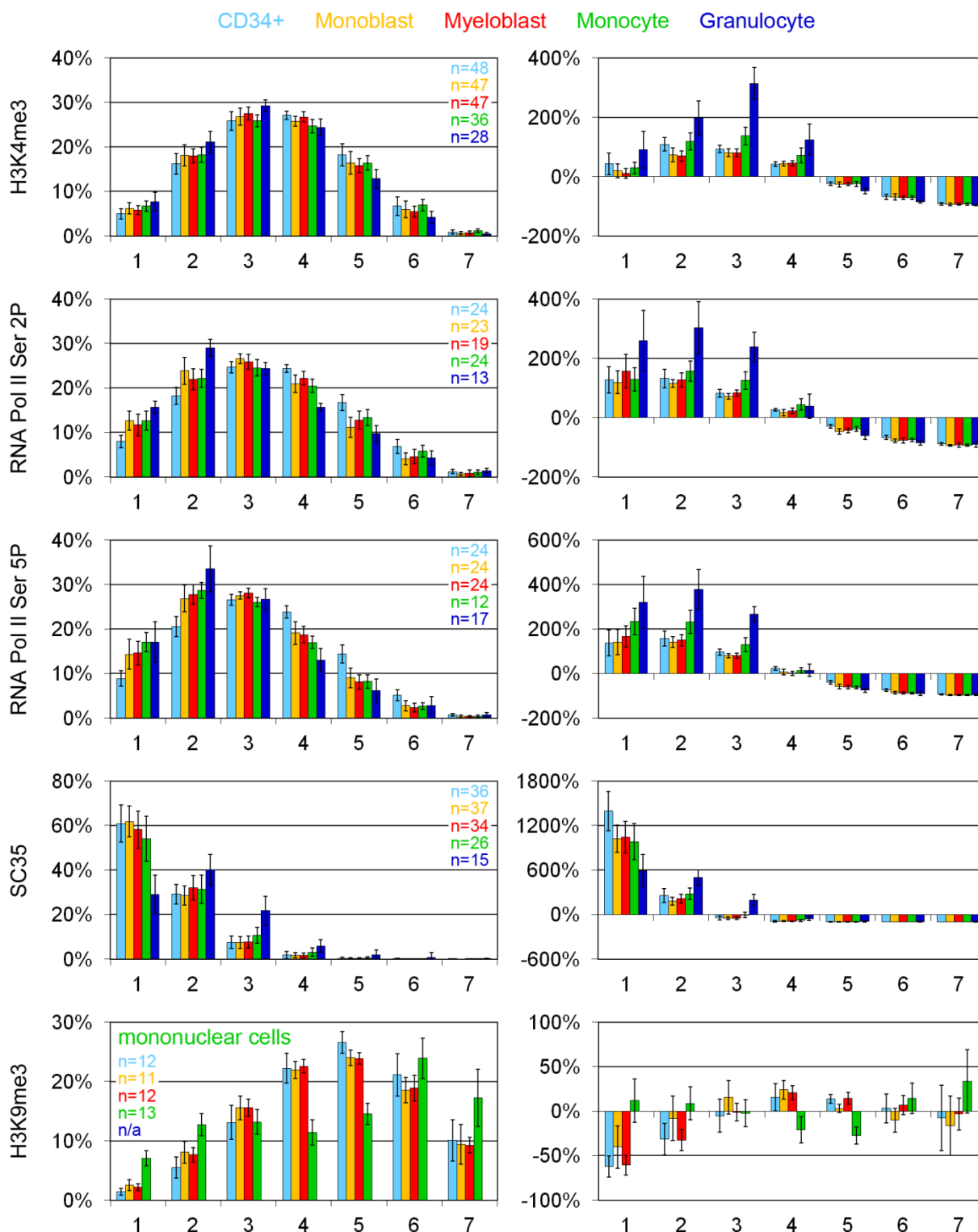


Figure 30: Comparison of markers in hematopoietic cell types. Profiles of Histone 3 tri-methylated on lysine 4 (H3K4me3), RNA Polymerase II phosphorylated on serine 2 or 5 (RNA Pol II Ser 2P or 5P), SC35 and Histone 3 tri-methylated on lysine 9 (H3K9me3) (from top to bottom) after assigning them to the respective chromatin classes of the corresponding segmentations of the DAPI signals into seven classes with increasing intensity from 1 to 7. Average curves of multiple whole 3D acquisitions are depicted. For each marker both the classical profile (left) as well as the calculated over- and underrepresentation in comparison to DAPI (right) is shown. In each graph all five cell types are included: CD34⁺ cells (light blue), monoblasts (yellow), myeloblasts (red), monocytes (green) and granulocytes (dark blue). For H3K4me3 no statistical differences were found between cell types in the classical profiles. Likewise for RNA Pol II Ser 2P, with the exception of CD34⁺ cells vs. granulocytes, which differed very significantly ($p < 0.01$). For RNA Pol II Ser 5P statistical differences were only found between other cell types: the differences were significant ($p < 0.05$) CD34⁺ (legend continued on next page)

Figure 30: (*legend continued from previous page*) cells and the for CD34⁺ cells vs. monoblasts and myeloblasts, very significant ($p < 0.01$) for CD34⁺ cells vs. monocytes and highly significant ($p < 0.001$) for CD34⁺ cells vs. granulocytes. Apart from granulocytes, which differed highly significantly ($p < 0.001$) from all other cell types, no statistical differences were found for SC35 between cell types in the classical profiles. For the staining of H3K9me3 (bottom row) monocytes selected from mononuclear cells were used (see details in section 3.2.1.1 in the Methods). For H3K9me3 no statistical differences were found between cell types. Between the marker distributions statistic tests revealed the following results: RNA Pol II Ser 2P and H3K4me3 were not significantly different ($p = 0.517, 0.053, 0.111, 0.124$ in CD34⁺ cells, monoblasts, myeloblasts, and monocytes), except in granulocytes ($p < 0.05$). For RNA Pol II Ser 5P only in CD34⁺ cells no significant difference to H3K4me3 could be detected ($p = 0.135$), while monoblasts showed a very significant difference ($p < 0.01$) and myeloblasts, monocytes and granulocytes highly significant differences ($p < 0.001$) for the two markers. RNA Pol II Ser 2P and RNA Pol II Ser 5P differed only in monocytes ($p < 0.05$); the other cell types did not show significant differences ($p = 0.425, 0.356, 0.102, 0.215$ in CD34⁺ cells, monoblasts, myeloblasts, and granulocytes). SC35 and H3K9me3 were highly significantly different ($p < 0.001$) from H3K4me3 in all cell types. The distributions of SC35, H3K9me3 and RNA Pol II Ser 2P / 5P were all highly significantly ($p < 0.001$) different among each other, apart from SC35 vs. RNA Pol II Ser 5P in granulocytes, which were however still very significantly different ($p < 0.01$). Note that the Wilcoxon rank-sum test used here can only check for differences in the mean value, not in the actual distribution. Error bars: standard deviation. Figure adapted from Hübner et al. (2015).

Figure 29: (*legend continued from page 195*) ($p < 0.01$). Error bars: standard deviation. Scale bars: 2 μm in images of whole nuclei, 0.5 μm in magnifications. This data is included in Hübner et al. (2015).

4.1.3 Reversible decondensation of chromatin upon hypotonic treatment

In order to gain insight into higher-order chromatin organization the normal nuclear architecture of CD34⁺ cells, monoblasts, myeloblasts, monocytes, and granulocytes was disrupted by subjecting the cells to hypotonic treatment.

The cells were incubated in 0.3x PBS for 1 min prior to fixation with PFA prepared in 0.3x PBS. **Figure 31** shows that under these low salt conditions (~90 mOsm compared to normotonic conditions of ~290 mOsm) the cell-type-specific chromatin patterns (compare **Figure 18**) were lost – chromatin had decondensed and filled up the IC lacunas. As a result now all five cell types displayed the same uniform distribution of chromatin.

Granulocytes were chosen to study the dynamics of this decondensation in nuclei of living cells as they exhibited the most extreme chromatin organization of the five cell types analyzed here (compare **Figure 18**). Repeated cycles of changes between normal (medium) and hypotonic (0.3x PBS) conditions were performed (**Figure 32**). Already after 1 min under hypotonic conditions, the normal phenotype with all chromatin being condensed at the periphery of the nucleus was lost and chromatin had decondensed into the IC lacunas in the interior of the lobes. After changing back to normal conditions, again within 1 min the original morphology was completely restored, including nuclear substructures (arrows). This showed that the expansion and contraction of chromatin was a very rapid and reversible process in these cells.

The lighter stain in the center of the lobes under hypotonic conditions is a consequence of Hoechst33342 binding preferentially to AT-rich regions. GC-rich DNA, which is present in the

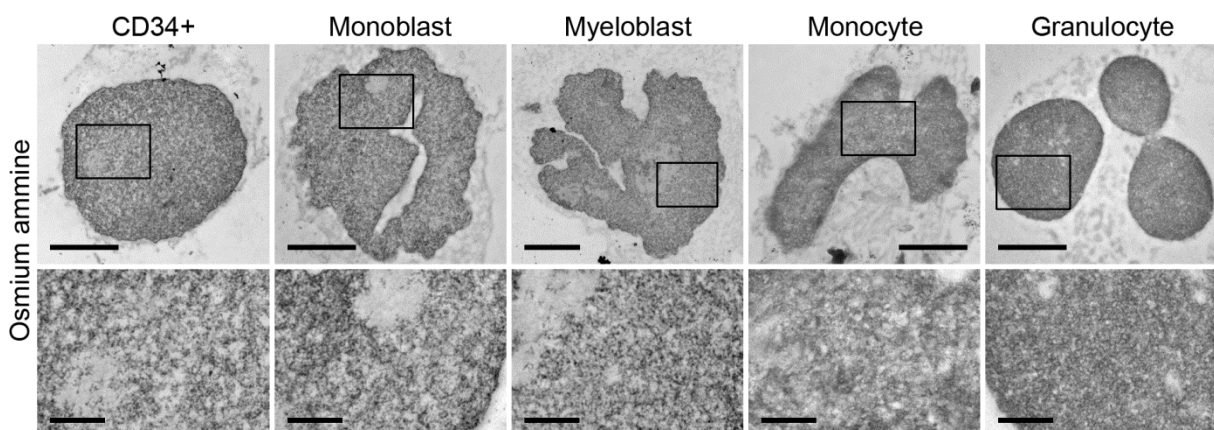


Figure 31: Chromatin pattern of hematopoietic cell types after hypotonic treatment. Osmium ammine stained DNA of cells incubated in 0.3x PBS for 1 min and subsequently fixed with PFA prepared in 0.3x PBS in TEM images of physical sections. From left to right a CD34⁺ cell, monoblast, myeloblast, myeloblast, monocyte, and granulocyte is shown. Upper row: whole nuclei. Lower row: magnifications. Scale bars = 2 μ m in images of whole nuclei, 0.5 μ m in magnifications. Figure taken from Hübner et al. (2015).

interior of the lobes under low salt conditions (Illner 2012, Hübner et al. 2015) is much less efficiently stained by this compound. The TEM images (**Figure 31**) demonstrated that indeed the entire big lacuna of each lobe was evenly filled with decondensed chromatin.

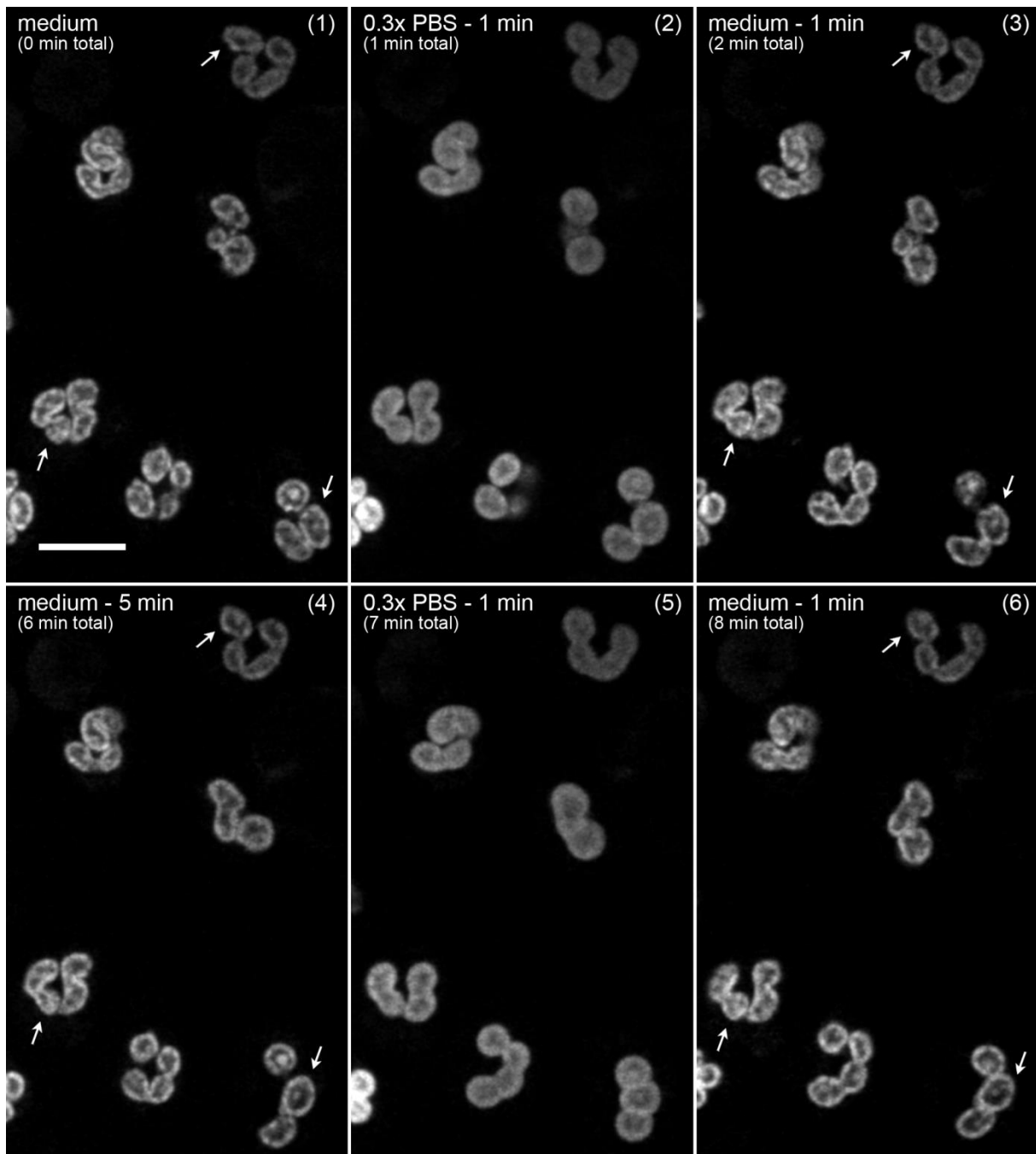


Figure 32: Changes between normal and hypotonic conditions in granulocytes. DNA stained with Hoechst33342 in light optical mid-sections of whole SDLSM 3D acquisitions of living granulocytes. Repeated cycles of changes between normal (medium) and hypotonic (0.3x PBS) conditions were performed. After one cycle was completed, the cells were allowed to recover for additional 3 min in medium, were imaged again (image (4)) and then the next change was started. Arrows point at nuclear substructures that were restored over several cycles of changes. Note that the focal plane is slightly different between images. Scale bar = 10 μ m. Figure adapted from Hübner et al. (2015).

Summary of section 4.1

Nuclear organization of hematopoietic cells during differentiation

CD34⁺ cells, monoblasts, myeloblasts, monocytes and granulocytes, representing various stages of hematopoietic cell differentiation, showed distinct differences in their general 3D morphology: the chromatin patterns (both in 3D-SIM images of DAPI stained DNA and TEM images of osmium ammine stained DNA), the number of nuclear pores, the length of the IC surface, the appearance of the nucleoli and the number of RNA Pol II signals differed in the five cell types.

But despite these differences, all five cell types exhibited a common functional nuclear architecture. 3D-SIM images and segmentation profiles demonstrated a consistent localization of H3K4me3, RNA Pol II Ser 2P, RNA Pol II Ser 5P, SC35 and H3K9me3 in CD34⁺ cells, monoblasts, myeloblasts, monocytes and granulocytes. H3K4me3 was mainly located at the surface of the chromatin domain clusters, RNA Pol II Ser 2P and RNA Pol II Ser 5P were found almost exclusively in this region. SC35 was detected in the interior of the larger IC lacunas and H3K9me3 was preferentially located on compacted chromatin.

Upon hypotonic treatment the cell type specific chromatin patterns got lost and all cell types were characterized by a uniform distribution of chromatin. This decondensation was a rapid and reversible process.

4.2 Microinjection of beads into HeLa cell nuclei – observations upon chromatin condensation

Small fluorescent beads with a diameter of 20 or 40 nm were microinjected into HeLa cell nuclei and their localization in relation to chromatin was analyzed. Of particular interest was the question of how the beads behave when chromatin condenses – Do they get trapped into chromatin or not? –, as this will give an insight into higher-order chromatin organization.

4.2.1 Localization of the beads in low-density chromatin of interphase cells

First, the localization of the beads was investigated in interphase nuclei after the induction of hypercondensed chromatin (HCC) in comparison to cells under normal conditions. In addition to visual inspections (**Figure 33**) intensity profiles of line scans through individual beads and the corresponding DAPI signals were analyzed (**Figure 34+35** for 20 nm respectively 40 nm beads; for evaluation see **Figure 36**).

In both conditions, in control cells and in HCC induced cells, the 20 nm and the 40 nm beads were typically found in chromatin of low density, represented by low DAPI intensities. Only occasionally in control cells, they were localized in chromatin with a more intense DAPI staining (**Figure 33**, bottom few examples of **Figure 34-35 A**). However, even in these cases the DAPI signals were still in the lower half of the intensity spectrum (compare also **Figure 36**). In control cells (**Figure 36 A**) the beads of both sizes showed the same distribution, while in HCC induced cells (**Figure 36 B**) 40 nm beads localized to higher DAPI intensities than 20 nm beads. However, both 20 nm and 40 nm beads were found in chromatin with lower DNA density in HCC induced cells than in control cells.

Figure 33: Localization of beads in control and HCC induced HeLa cells. HeLa Kyoto cells were microinjected with fluorescent beads, fixed with PFA – either without treatment (control) or after HCC induction – and their DNA was counterstained with DAPI (gray). **(A)** 20 nm (green) (top) or 40 nm (red) (bottom) beads in control cells. For each cell three different light optical sections of the same whole CLSM 3D acquisition are shown. The sections with the brightest signals of the beads magnified below were selected. In the magnifications (lower rows) both the merged image (left) as well as the DAPI staining alone (right) is shown. **(B)** Equivalent to (A) but depicting HCC induced cells. Scale bars: 4 μm in images of whole nuclei, 1 μm in magnifications.

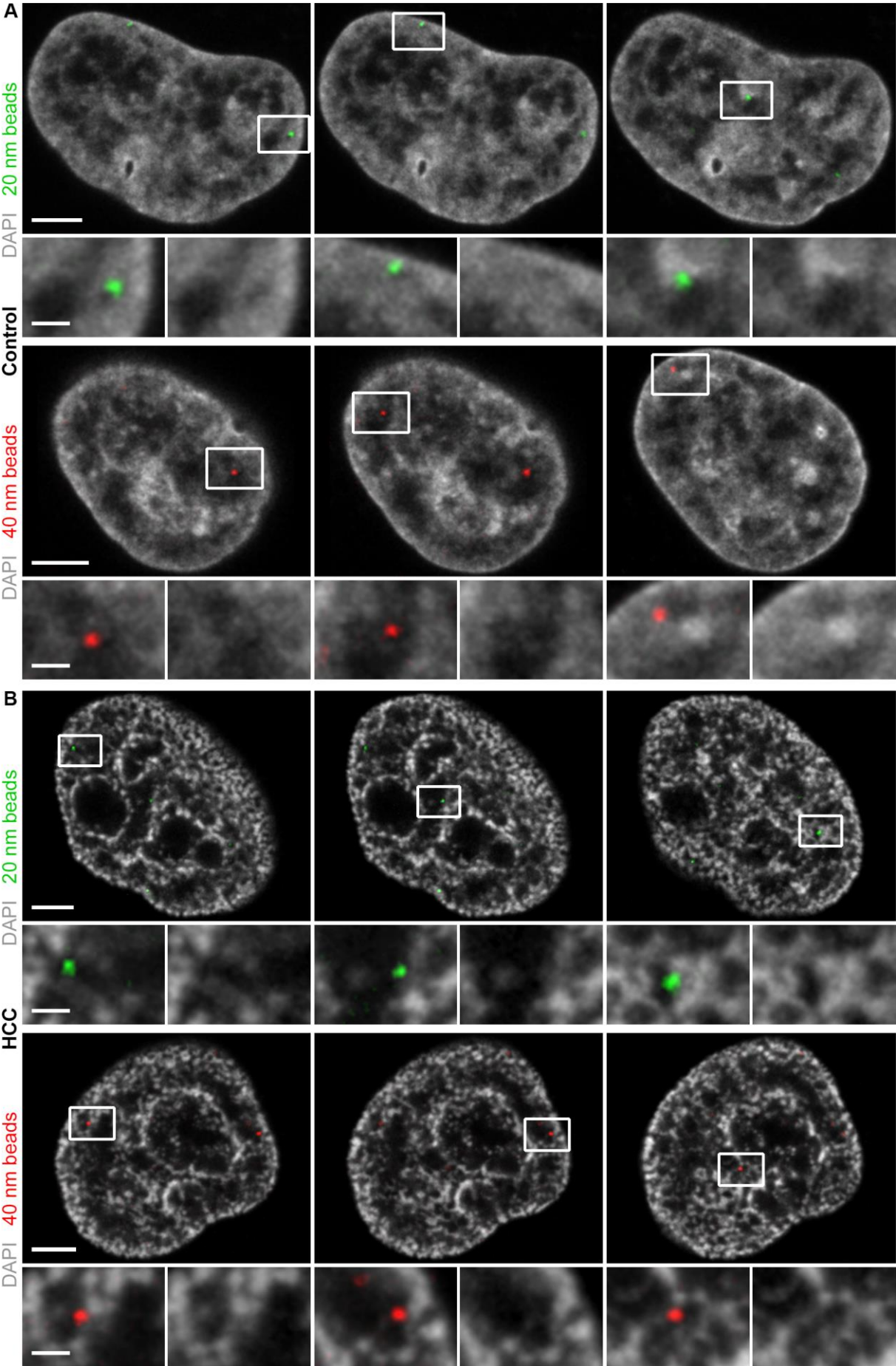


Figure 33: Localization of beads in control and HCC induced HeLa cells (see legend on previous page).

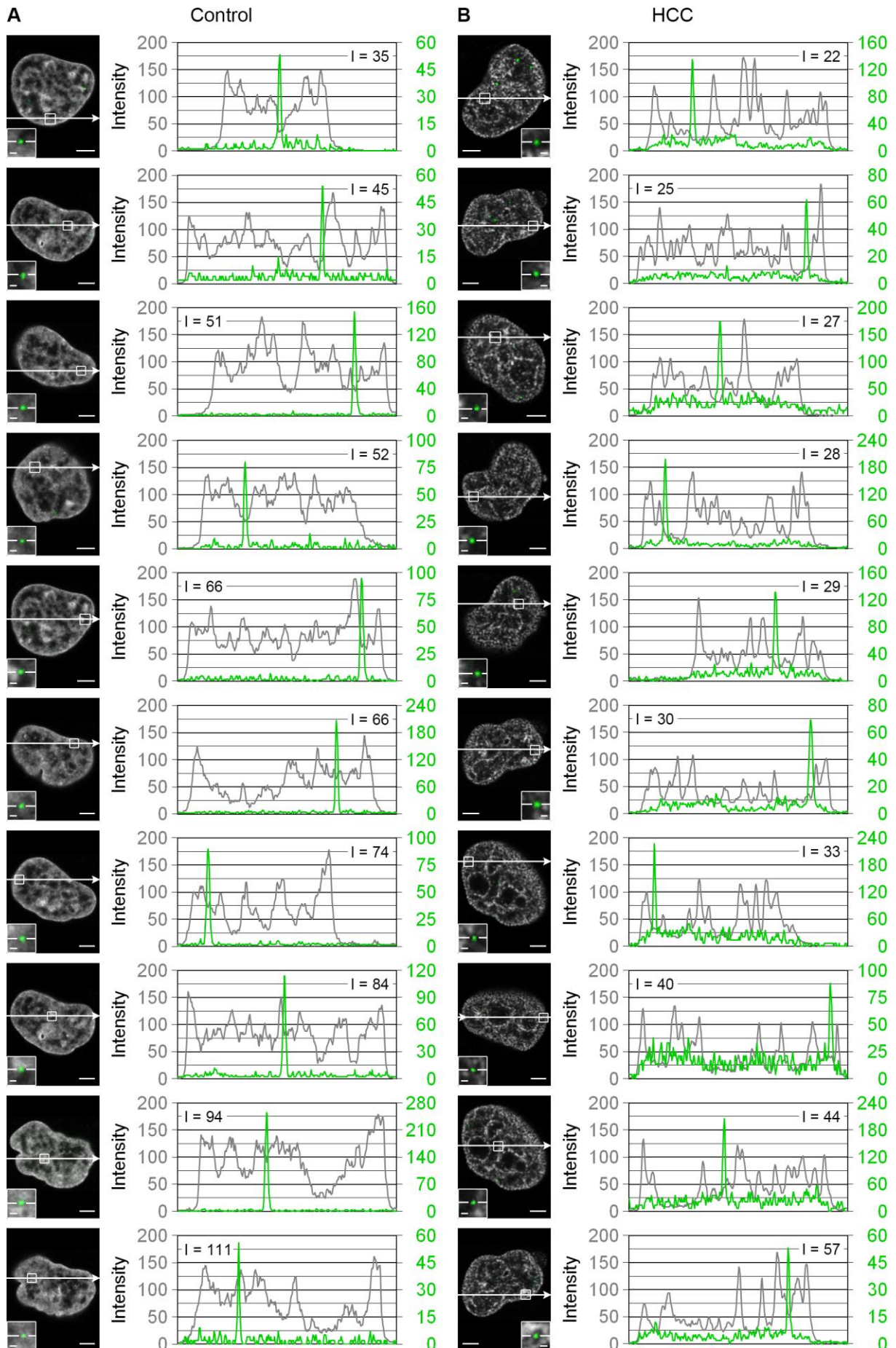


Figure 34: Localization of 20 nm beads in control and HCC induced HeLa cells (see legend on page 205).

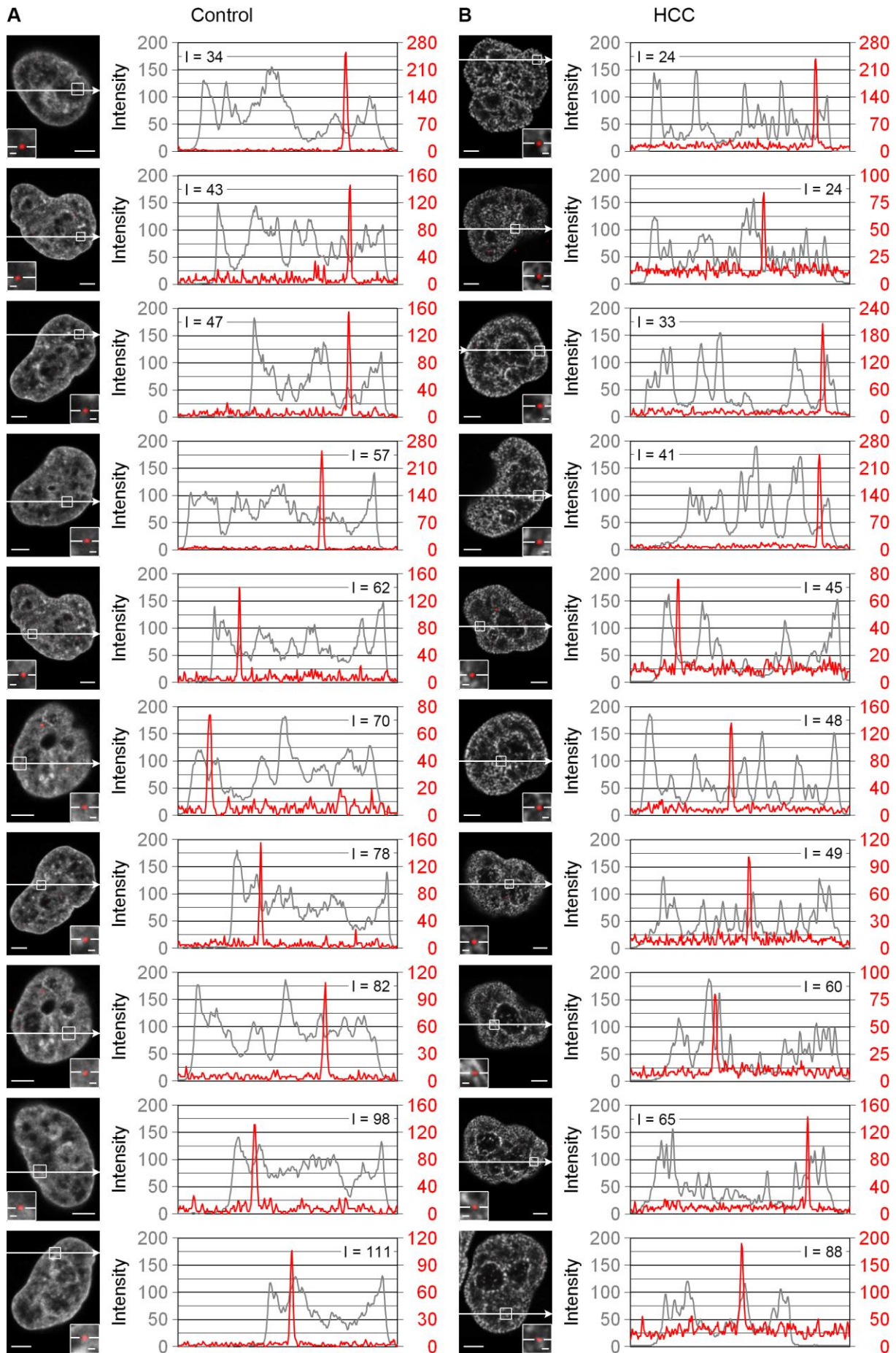


Figure 35: Localization of 40 nm beads in control and HCC induced HeLa cells (see legend on next page).

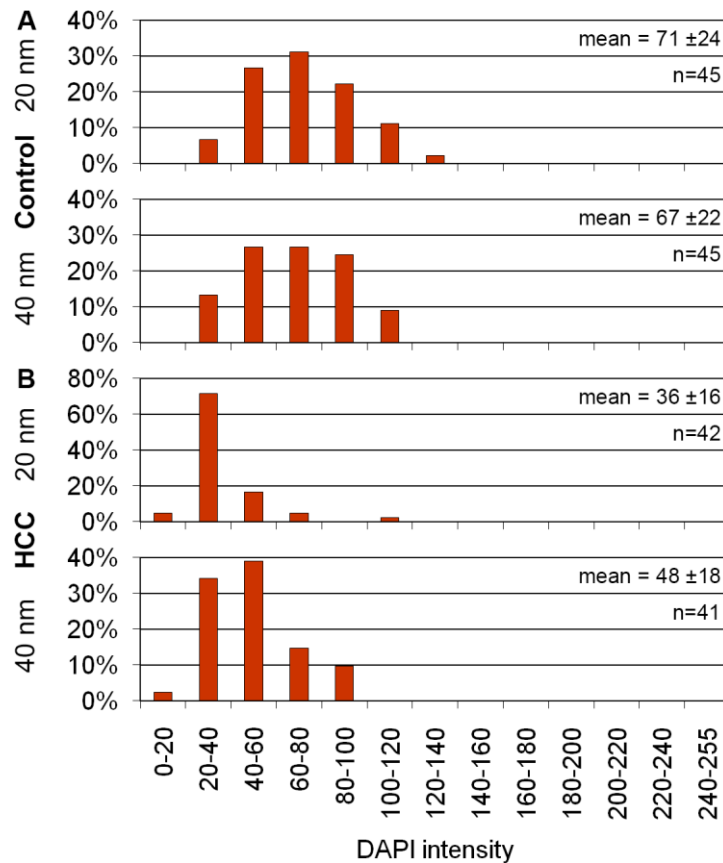


Figure 36: Summary of the localization of beads in control and HCC induced HeLa cells. The localization of microinjected fluorescent beads in relation to DAPI stained chromatin was determined in HeLa Kyoto cells fixed with PFA either without treatment (normal) (A) or after HCC induction (B) using line scans (equivalent to Figure 34+35). The graphs for the 20 nm beads are depicted in the upper rows, the graphs for the 40 nm beads in the lower rows. In control cells the DAPI intensities at the bead positions ranged between 27.3 and 125.0 with a mean value of 71.4 in the 20 nm beads and between 26.3 and 111.3 with a mean value of 67.4 in the 40 nm beads. In HCC induced cells the DAPI intensities at the bead positions ranged from 17.7 to 104.0 with a mean value of 35.9 in the 20 nm beads and from 18.7 to 89.7 with a mean value of 48.4 in the 40 nm beads. In control cells (A) no statistically significant difference ($p=0.434$) was found between the distributions of the 20 nm and 40 nm beads, in HCC induced cells (B) they differed highly significantly ($p<0.001$). For both the 20 nm and the 40 nm beads the distributions differed highly significantly ($p<0.001$) between control and HCC induced cells. For reasons of better visualization, the values were summarized into groups of 20 intensity values for the graphs. Error: standard deviation.

Figure 34: Localization of 20 nm beads in control and HCC induced HeLa cells. HeLa Kyoto cells were microinjected with fluorescent 20 nm beads (green), fixed with PFA – either without treatment (control) (A) or after HCC induction (B) – and their DNA was counterstained with DAPI (gray). In whole CLSM 3D acquisitions horizontal line scans were performed through the brightest spot of individual beads and the corresponding normalized DAPI images. The line scans with the DAPI intensity in gray and the bead intensity in green are depicted in the right column, the corresponding merged images in the left column. The intensity (I) of the DAPI signal at the bead position is indicated in the graphs. The images show the position of the line, the arrow denotes the scanning direction. The area of the bead is magnified in the inset. For reasons of better visualization, the line is interrupted at the position of the bead. Scale bars: 4 μm in images of whole nuclei, 0.5 μm in magnifications.

Figure 35: Localization of 40 nm beads in control and HCC induced HeLa cells. Equivalent to Figure 34, therefore the legend is shortened here. Line scans were performed through microinjected fluorescent 40 nm beads (red) and the corresponding DAPI signals (gray) in control cells (A) or cells after HCC induction (B). Scale bars: 4 μm in images of whole nuclei, 0.5 μm in magnifications.

4.2.2 Exclusion of beads from condensing mitotic chromosomes

In order to be able to study the behavior of nuclear-injected beads upon chromatin condensation better than in the HCC induced cells live cell observations were performed.

Movies acquired after the injection of 40 nm beads (**Figure 37**) showed that the nuclear-injected cells on average exhibited a longer duration of the cell cycle (25.6 h) than the internal uninjected control cells (21.8 h) (**Figure 38**), but that they typically divided without apparent difficulties. Within the observation period of 64 h, most cells divided at least once (primary mitoses; arrows in **Figure 37**) with the majority of the daughter cells going through mitosis again (secondary mitoses; arrowheads in **Figure 37**). Occasionally reunions of daughter cells and/or abnormal mitoses were observed (marked with an asterisk in **Figure 37**) that typically resulted in the cells going into apoptosis within several hours. In general, however, nuclei revealed inconspicuous phenotypes over the entire duration of the observation. Cells injected with 20 nm beads were monitored over a time period of 18 h (**Figure 39**). The co-injected dextran got excluded from the nucleus during the first cell division (**Figure 37+39**).

Figure 40+41 demonstrate that while the beads were still localized inside the nucleus in undivided interphase cells even many hours after the injection (first row) as well as in prophase cells (second row of **Figure 40**), they spread into the cytoplasm during metaphase (third row of **Figure 40**) and remained there also after mitosis was completed (last row) (see also evaluation in **Figure 42**). Only few beads were still found inside the nucleus after cell division of nuclear injected cells (**Figure 42**). In prophase and metaphase cells (second respectively third row of **Figure 40**) the beads were clearly excluded from the condensing chromosomes.

Figure 37: Live cell observation of HeLa cells after the microinjection of 40 nm beads. After the microinjection of HeLa Kyoto cells with fluorescent 40 nm beads, a live cell observation was performed on a widefield microscope. Images of the beads, the co-injected dextran-FITC and the cells (transmission mode) were acquired every 15 min over a total time period of 64 h. Here only the co-injected dextran is shown. Only every eighth image is shown. The complete movies (each of the three channels separately and a merge of the dextran and the beads) are included in the enclosed DVD / ZIP archive (File S6-9). Arrows and arrowheads point at dividing nuclear-injected cells, with arrows marking primary mitoses and arrowheads marking secondary mitoses. Occasionally observed reunions of daughter cells and/or abnormal mitoses are marked with an asterisk. Scale bar: 10 μ m.

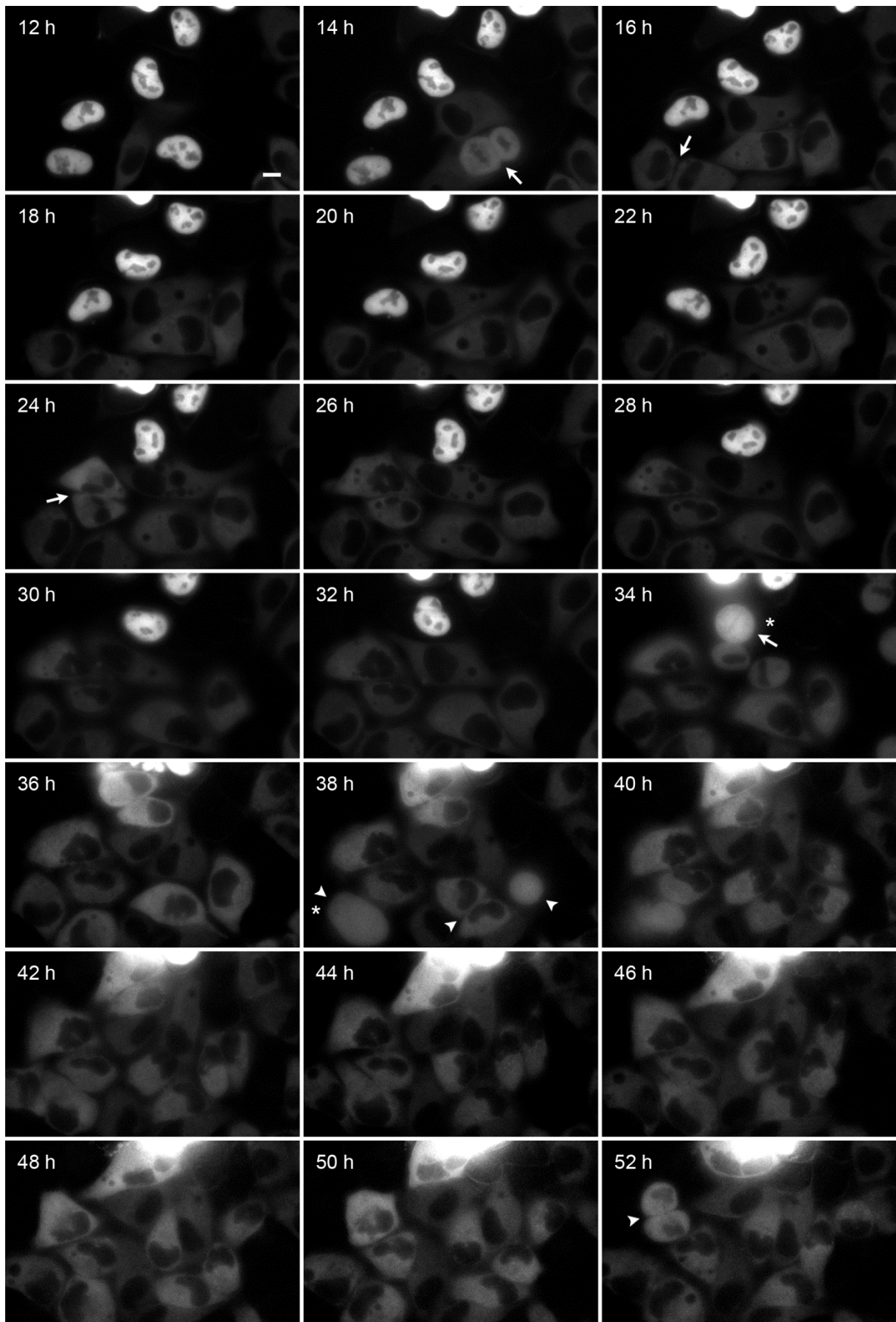


Figure 37: Live cell observation of HeLa cells after the microinjection of 40 nm beads. Only the co-injected dextran is shown (see full legend on previous page).

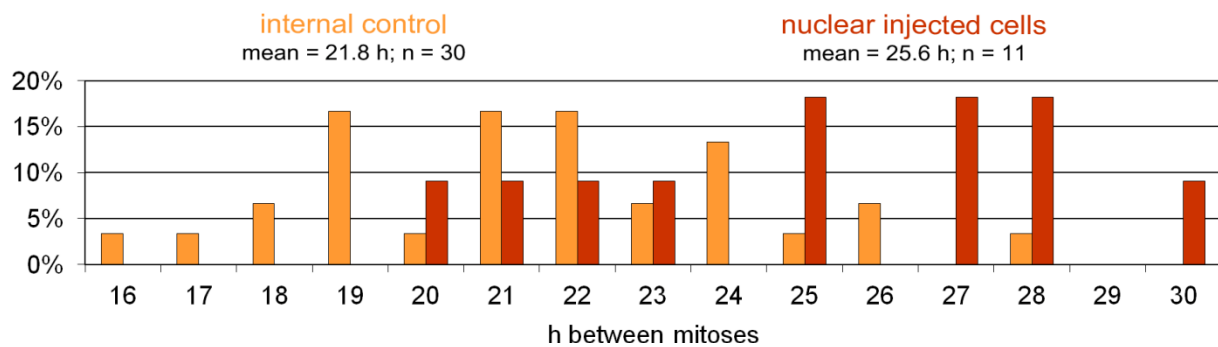


Figure 38: Duration of the cell cycle in HeLa control cells and cells microinjected with 40 nm beads. The cell cycle duration was evaluated from live cell observations by calculating the time from the entry into the primary mitosis until the entry into the secondary mitosis based on transmission light images. Both, internal control cells (orange) and cells after nuclear injection of 40 nm beads (red) were analyzed. While internal control cells exhibited a cell cycle duration of 15.5-28.0 h with a mean value of 21.8 h, nuclear-injected cells showed highly significantly ($p < 0.001$) longer cell cycle times with 20.0-30.3 h and a mean value of 25.6 h.

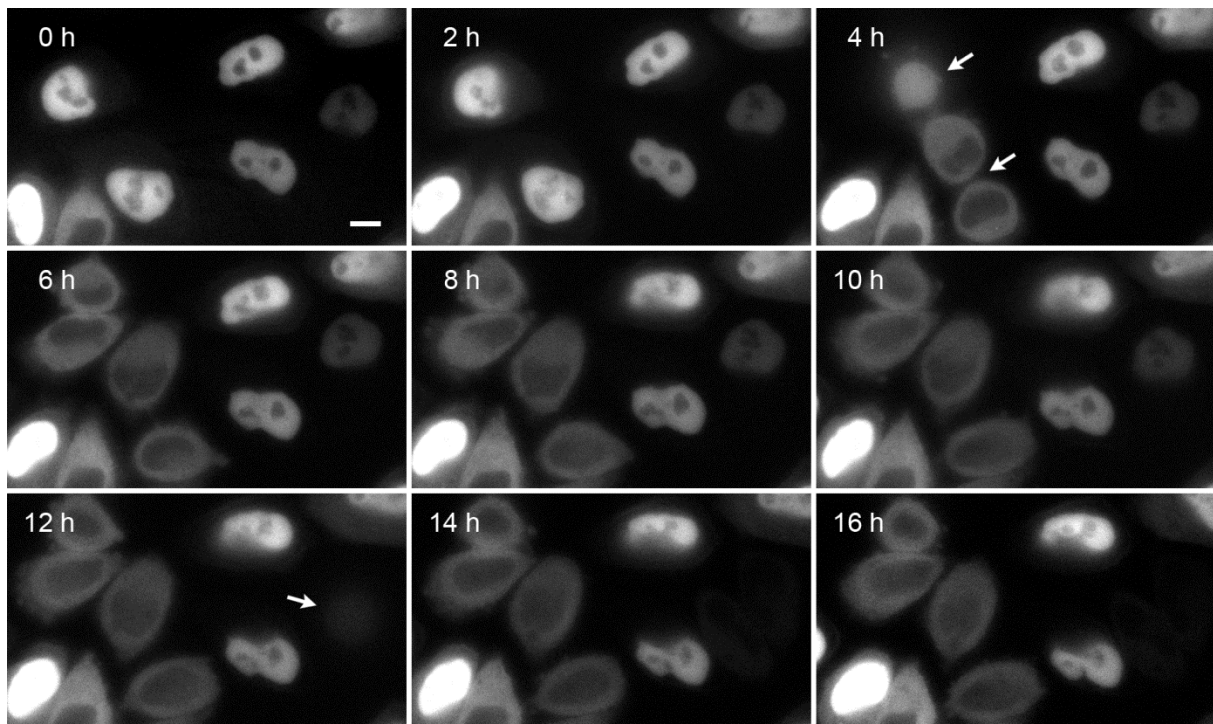


Figure 39: Live cell observation of HeLa cells after the microinjection of 20 nm beads. After the microinjection of HeLa Kyoto cells with fluorescent 20 nm beads, a live cell observation was performed on a widefield microscope. Image stacks of the beads and the co-injected dextran-TRITC and single images of the cells (transmission mode) were acquired every 15 min over a total time period of 18 h. From the image stacks for each time point, the most central section was selected. Here only the co-injected dextran is shown. Only every eighth image is shown. The complete movies (each of the three channels separately and a merge of the dextran and the beads) are included in the enclosed DVD / ZIP archive (File S10-13). Arrows mark dividing nuclear-injected cells. Scale bar: 10 μ m.

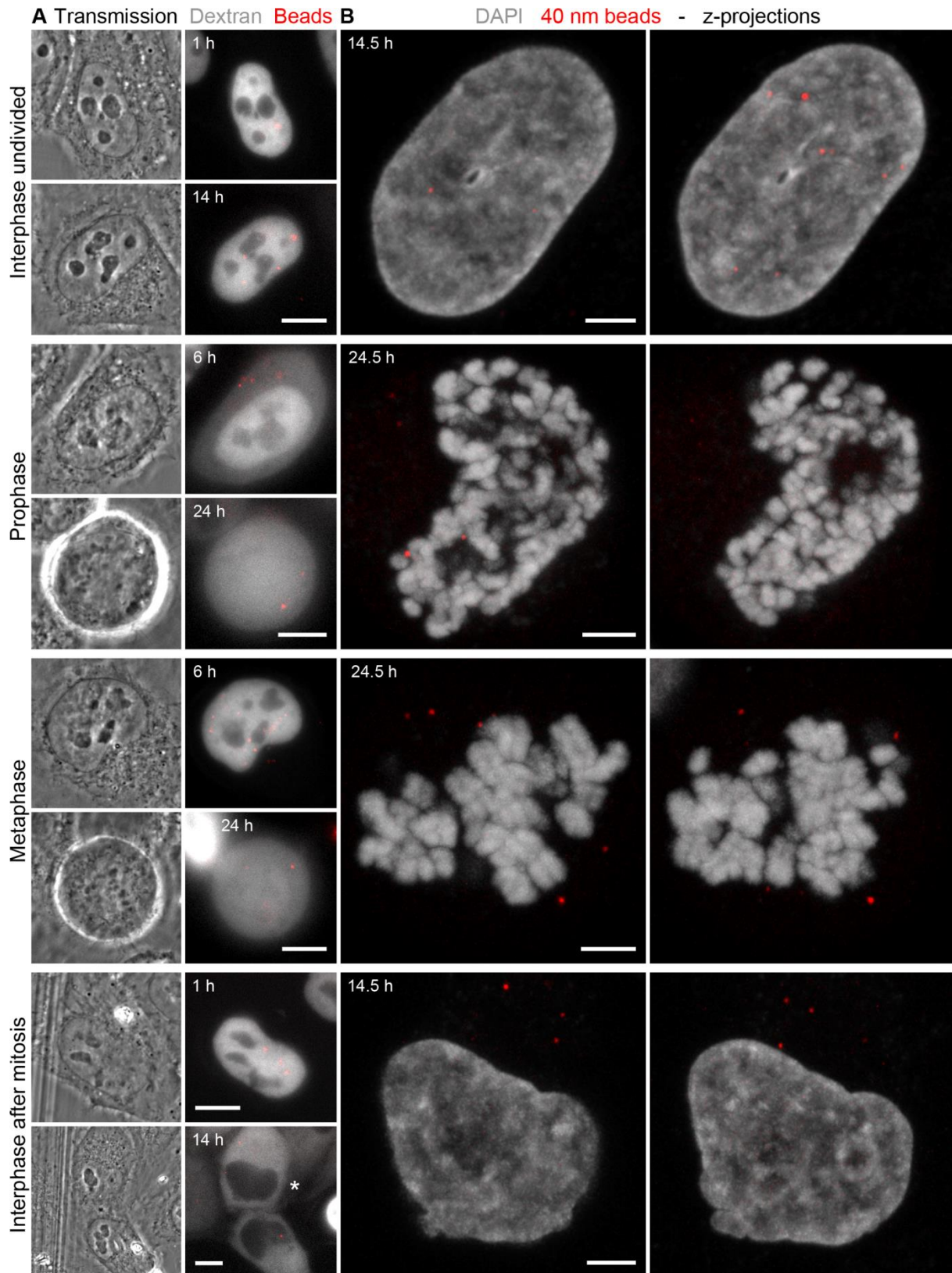


Figure 40: Localization of 40 nm beads in HeLa cells before, during and after mitosis. HeLa Kyoto cells were microinjected with fluorescent 40 nm beads and dextran-FITC and were imaged in the living cell state (A) and after fixation (B). The approximate time intervals between the microinjection and the acquisitions are indicated on the images. From top to bottom nuclear-injected cells which at the time of fixation still had not divided, were in prophase respectively metaphase or had divided during the observation period, are shown. (A) Image stacks of the beads, the co-injected dextran and the cells (transmission mode) were acquired of living cells on a widefield microscope short after the completion of the microinjection (top) and again several hours later (bottom) short before (*legend continued on next page*)

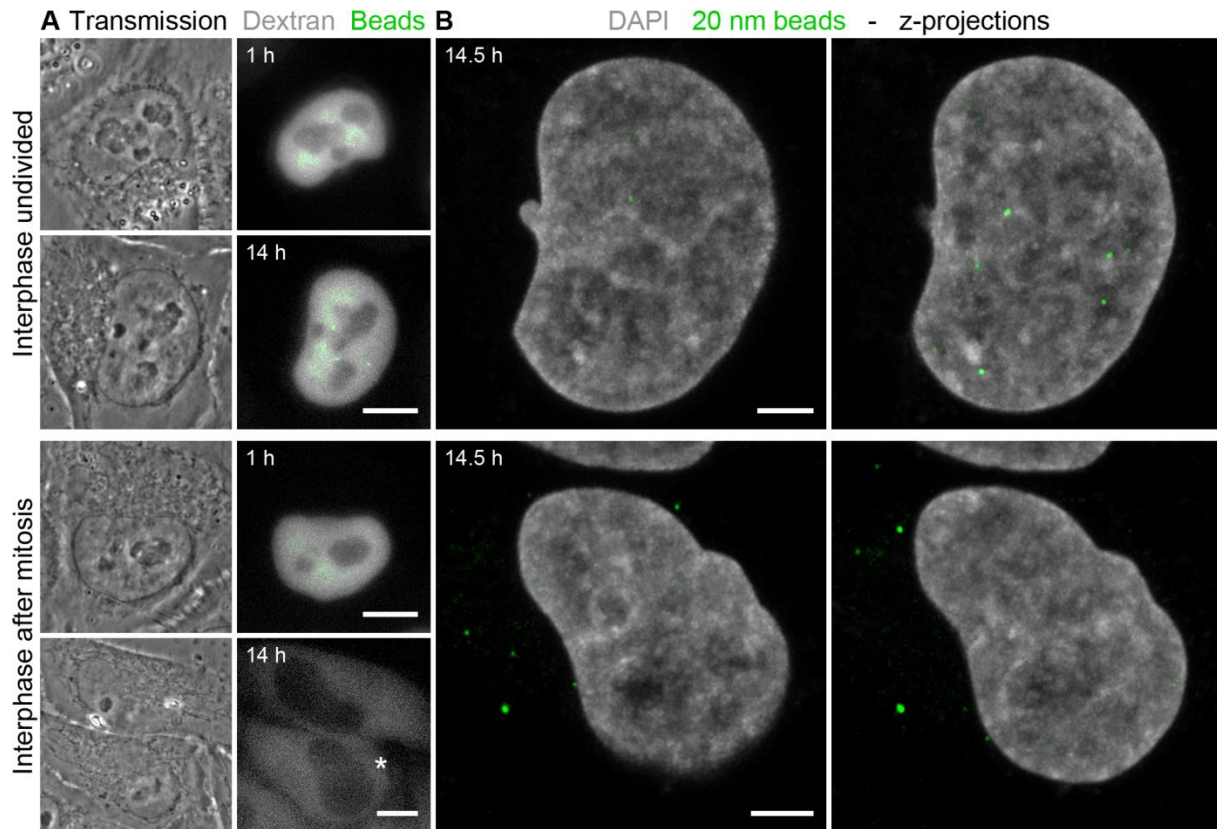


Figure 41: Localization of 20 nm beads in HeLa cells before and after mitosis. Equivalent to **Figure 40**, therefore the legend is shortened here. The cells were microinjected with fluorescent 20 nm beads and dextran-TRITC. A cell which at the time of the fixation still had not divided (top) and a cell that had divided (bottom) during the observation period is shown. **(A)** The dextran proved that both nuclei were injected into the nucleus. Note that the filters available on the microscope were not optimal for the spectral separation of the dextran-TRITC and the green fluorescent beads. Of the interphase cells after mitosis (last row) the cell that is shown in **(B)** is marked with an asterisk. **(B)** Z-projections of 15 light optical sections (corresponding to 1.5 μm) from the center of the nucleus towards both sides of the image stack (merged images; DAPI = gray, beads = green) are shown. Scale bars: 10 μm in **(A)**, 4 μm in **(B)**.

Figure 40: (*legend continued from previous page*) fixation. Light optical mid-sections of the cells in transmission mode (left), as well as a merged image of the co-injected dextran (gray) and the beads (red) (right), are shown. The dextran proved that all four nuclei were injected in the nucleus. Of the interphase cells after mitosis (last row) the cell that is shown in **(B)** is marked with an asterisk. **(B)** Whole CLSM 3D acquisitions of the same cells shown in **(A)** were recorded after PFA fixation and DNA counterstaining with DAPI (gray). Z-projections of 15 light optical sections (corresponding to 1.5 μm) in interphase cells respectively 40 light optical sections (4 μm) in pro- and metaphase from the center of the nucleus towards both sides of the image stack are shown (merged images; DAPI = gray, beads = red). Note that the prophase cell was not only injected into the nucleus but partly also into the cytoplasm (compare with **(A)**), which explains the beads located outside the nucleus at the top left of the left image. Scale bars: 10 μm in **(A)**, 4 μm in **(B)**.

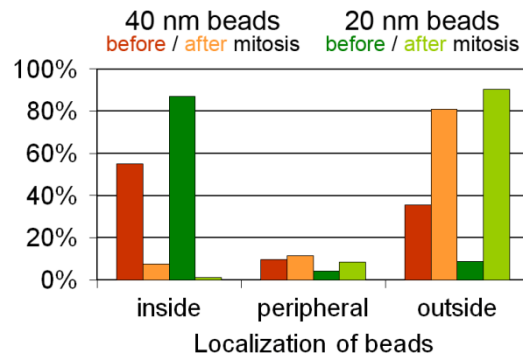


Figure 42: Evaluation of the localization of beads in HeLa cells before and after mitosis. The evaluations were performed on whole CLSM 3D acquisitions as presented in **Figure 40+41 B**. Both cells that had not divided during the observation period (= before mitosis) and cells that did divide (= after mitosis) were analyzed. Only cells with nuclear injection were included. For the 40 nm beads $n=144$ beads / $n=27$ cells before mitosis were evaluated (red), $n=105/33$ after mitosis (orange). For the 20 nm beads $n=93/19$ (dark green), respectively $n=83/20$ (light green) beads/cells. Beads whose position could not be determined clearly were counted as peripherally located. For both bead types the distributions before and after mitosis were highly significantly ($p<0.001$) different from each other.

Summary of section 4.2

Microinjection of beads into HeLa cell nuclei – observations upon chromatin condensation

Nuclear injected beads of a size of 20 nm or 40 nm were both typically localized in chromatin of low density, represented by low DAPI intensities. In HCC induced cells both bead types were shifted towards lower DAPI intensities compared to their localization in control cell nuclei.

Live cell observations demonstrated that, apart from an elongated cell cycle duration, microinjected cells typically continued the cell cycle and divided without apparent difficulties. Occasionally, however, abnormalities were observed that usually led to apoptosis.

During the first cell division the beads and the co-injected dextran got expelled from the nucleus and the beads were clearly excluded from condensing mitotic chromosomes.

4.3 Characterization of nuclear phenotypes after UV irradiation and caffeine posttreatment (UV/caffeine treatment) or premature chromosome condensation (PCC) in V79 cells

UV irradiation with subsequent caffeine posttreatment (UV/caffeine treatment) and premature chromosome condensation (PCC) provide the possibility to manipulate the nuclear landscape in a semi-artificial way: mitosis or DNA damage are artificially induced but the processes that subsequently take place are the intrinsic mechanisms of the cell (see sections 2.5.3 and 2.5.4 in the introduction). Using V79 Chinese hamster cells it was interesting to investigate whether the functional nuclear architecture of cells after both types of treatments was different from control nuclei and from each other or not. In the case of UV irradiated cells also because evidence suggests that DNA damage – or rather its repair – results in the rearrangement of chromatin towards a more open chromatin organization (for review see Sulli et al. 2012, Chiolo et al. 2013, Feng et al. 2016). Supporting this suggestion, DNA repair factors were found to preferentially locate in the perichromatin region (Solimando et al. 2009, Rube et al. 2011, Lorat et al. 2015 (for remarks on these publications see 5.1.3 in the discussion)).

Before analyzing these questions of functional nuclear architecture in selected stages of both systems (see section 4.3.2) the processes occurring after UV/caffeine treatment and PCC were thoroughly characterized in order to be able to fully understand what the respective phenotypes represent and to be able to judge potential differences compared to control cells.

Some of the data shown in this section were already collected during my Diploma thesis (Hübner 2008) in the same lab. But as they are essential for the overall characterization of the consequences of UV/caffeine treatment and for the comparison with PCC induced cells they are included here.

Furthermore, some of the results presented here were published in Hübner et al. (2009). Therefore, parts of text and figures were adapted from there.

4.3.1 Background analysis of the observed nuclear phenotypes reveals: UV/caffeine treatment and PCC induction represent two different phenomena with common features

The crucial observation that let it appear necessary to thoroughly characterize and compare the cell types and processes occurring during and after UV/caffeine treatment and PCC induction was the occurrence of very similar nuclear phenotypes with shattered chromatin after

methanol/acetic acid (MAA) fixation following both treatments (**Figure 43**, cell 4 / 8). For historical reasons (compare section 2.5.3 and 2.5.4 in the introduction) these cells are termed generalized chromosome shattering (GCS) after UV/caffeine treatment and S phase PCCs (short S PCCs) after PCC induction. After PFA fixation these shattered chromosome complements were not observed, which raised the question where these phenotypes derive from, i.e. how the corresponding cells look like in the living cell state. The same applies also to the hardly visible and structureless “shadow nuclei” occurring in UV/caffeine treated cells and to S - G1/G2 PCCs (an intermediate form of S and G1/G2 PCCs (compare below) characterized by a shattered appearance but containing larger pieces of chromosomes) observed in PCC induced cells (**Figure 43**, cell 5 / 9). Also these phenotypes were only observed after MAA fixation. After PFA fixation other nuclear morphologies were found instead: after UV/caffeine treatment cells with a parachute-like chromatin configuration (PALCC) consisting of a bulky chromatin mass and extended chromatin fibers on one side as well as apoptotic cells (**Figure 43**, cell 6 / 7) and after PCC induction cells with a grainy appearance or with peripherally condensed chromatin as well as some undefined phenotypes (**Figure 43**, cell 11 / 12 / 13).

Additional phenotypes that occurred after both fixation methods were interphase cells, cells with micronuclei and multilobulated cells (**Figure 43**, cell 1 / 2 / 3) in UV/caffeine treated samples and interphase cells and cells with fully condensed chromosomes very similar to normal mitotic chromosomes (for historical reasons termed G1/G2 PCCs (compare section 2.5.3 and 2.5.4 in the introduction)) (**Figure 43**, cell 1 / 8) in PCC induced samples.

Note that PALCCs after UV/caffeine treatment were only observed in Chinese hamster cells – in the V79 cell used in this work as well as in diploid fibroblasts – but not in other species including human (HeLa cells), mouse (C2C12 and C127 cells) and rat (NRK cells) (data not shown).

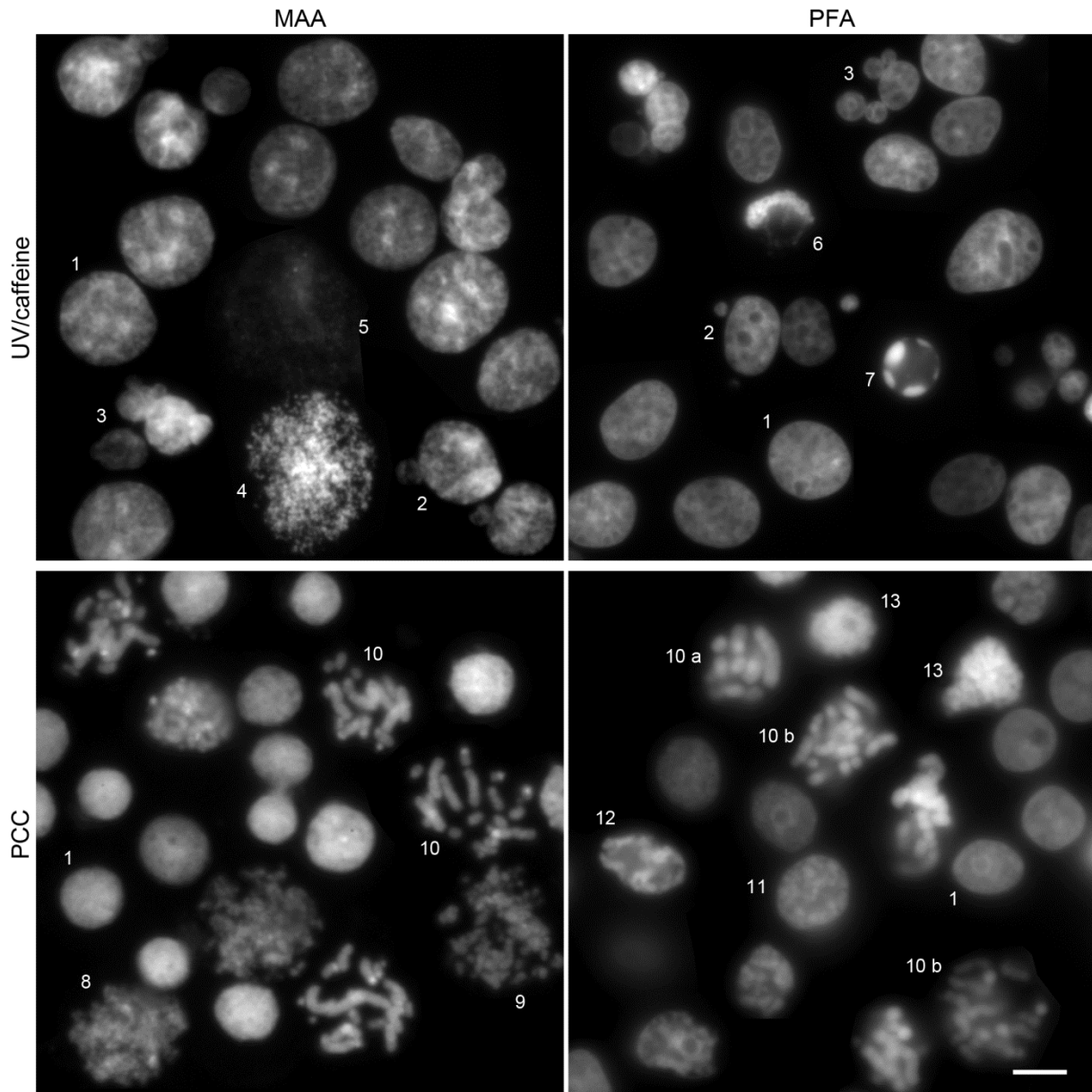


Figure 43: Nuclear phenotypes in UV/caffeine treated and PCC induced V79 cells after fixation with MAA or PFA. Widefield images of DAPI stained V79 (H2B-mRFP) cells are shown. Upper row: after UV irradiation and subsequent caffeine posttreatment (UV/caffeine); lower row: after PCC induction (PCC). (1) interphase cell, (2) cell with micronuclei, (3) multilobulated cell, (4) GCS, (5) shadow nucleus, (6) PALCC, (7) apoptotic cell, (8) S PCC, (9) S - G1/G2 PCC, (10) G1/G2 PCC (10a more compact, 10b more spread), (11) nucleus with grainy appearance, (12) nucleus with peripherally condensed chromatin, (13) undefined phenotype. For a better overview, all images shown here were composed from several images. The images of UV/caffeine treated cells are adapted from Hübner et al. (2009). Scale bar: 10 μ m.

4.3.1.1 Identification of the processes occurring during UV/caffeine treatment and PCC induction

In order to be able to correlate the different nuclear phenotypes observed after MAA and PFA fixation live cell observations combined with “correlative MAA fixation” – i.e. fixation under live cell conditions thus allowing imaging of the same cells before, during and after MAA fixation – were performed. As GCS cells observed after UV/caffeine treatment exhibited such a similar phenotype to S PCCs and those were, as their name already indicates, reported to represent S phase cells (see section 2.5.4 in the introduction), the question arose whether also GCS cells are linked to S phase. Therefore BrdU staining for the detection of S phase cells was included in these experiments.

Correlative MAA fixation showed that GCS cells were the fixation outcome of PALCCs (**Figure 44**). These cells were always BrdU negative, no matter whether the PALCC occurred before, during or after the BrdU pulse (**Figure 44 B**). These experiments also demonstrated that shadow nuclei occurred from apoptotic cells (data not shown, see Hübner et al. 2009). PALCCs were negative for the TUNEL assay and for cleaved Caspase 3 (data not shown, see Hübner et al. 2009) and are thus not apoptotic cells. Long-term live cell observations revealed that PALCCs became visible at the earliest 6 h after UV irradiation (data not shown, see Hübner et al. 2009) and that they represent abnormal mitoses (**Figure 45**): they emerged from morphologically inconspicuous prophase cells and developed into multilobulated cells about 1 h later, confirming multilobulated cells as abnormal interphase cells. The lack of distinct mitotic chromosomes hints at a condensation failure in these cells. **Figure 46** schematically summarizes the processes occurring upon UV/caffeine treatment.

Also PCC induction always occurred according to a fixed pattern of morphological changes (**Figure 47+48**): first the chromatin got grainy (early PCC cells), then the individual chromosomes became visible and were retracted to the nuclear periphery, leaving the interior of the nucleus apparently DNA free (middle PCC cells). The chromosomes condensed further and distributed throughout the nucleus again (late I PCC cells) until finally the compact conformation dissolved and the chromosomes spread more widely (late II PCC cells). Not all cells entered PCC at the same time and some also retained an interphase morphology – characterized by a smaller size of the nucleus than observed during interphase of control cells but with a non-grainy chromatin organization – throughout the entire period of PCC induction. **Figure 48** furthermore shows that only large or medium-sized cells that had not divided for several hours or cells that were in mitosis at the same time of PCC induction entered PCC (for a detailed evaluation see **Figure 51 B** and the corresponding description below). In contrast

to UV/caffeine treated cells, however, PCC induced cells did not proceed to interphase even after release from the inducing drug (**Figure 47**). Transferred back into normal medium typically first the morphological development of the PCC induction still continued, then the chromatin slightly decondensed, formed undefined clumps, and the cells seemed to go into apoptosis after several hours. This showed that PCC induction is not reversible. Correlative MAA fixation revealed that S PCCs typically are the fixation outcome of early or middle PCC cells and were mainly – but not exclusively – BrdU positive (**Figure 49**) while G1/G2 PCCs normally resulted from late I or late II PCC cells and were typically – but again not exclusively – BrdU negative (**Figure 50**) (for a detailed evaluation see **Figure 51 C** and the corresponding description below).

Detailed evaluations of the fraction of BrdU positive cells (**Figure 51 A**, upper graph) confirmed that S PCCs are typically BrdU positive, G1/G2 PCCs BrdU negative. S - G1/G2 PCCs represent an intermediate state with regard to both, morphology and BrdU staining. With increasing induction time for PCC, the percentage of BrdU positive cells increased in all three morphologies. However, the number of positive cells was always larger in S and S - G1/G2 PCCs than in G1/G2 PCCs and even after 2 h incubation time the main fraction of G1/G2 PCCs was still BrdU negative. Compared to the total number of cells (**Figure 51 A**, lower graph) a significant amount of S PCCs was only observed after 1 h, 1 h 30 min and 2 h of PCC induction, with similar frequencies at each of these time points. 10 min or 30 min of PCC induction were therefore apparently too short to give rise to this phenotype. After all applied incubation times the fraction of G1/G2 PCCs was higher than of S and S - G1/G2 PCCs and increased with prolonged incubation (as expected, given G1/G2 PCCs being the final PCC stage). Only after 2 h of PCC induction a slight decrease compared to 1 h 30 min was observed, most likely resulting from cell loss due to detachment. **Figure 51 B** shows that PCC cells either resulted from cells that were already in mitosis at the start of the PCC induction – thus explaining the fraction of G1/G2 PCCs observed already after 10 min or 30 min – or from interphase cells that had not divided for minimum 16.5 h. While the former ones mainly exhibited a G1/G2-morphology after MAA fixation and were all BrdU negative, the later ones were very heterogeneous with regards to both, their morphology after MAA fixation and BrdU staining. A more detailed correlation of the morphology in the living cell state before PCC induction and after MAA fixation after PCC induction (**Figure 51 C**) clearly demonstrated that S - G1/G2 PCCs and even more G1/G2 PCCs were the fixation outcome of later PCC stages than S PCCs.

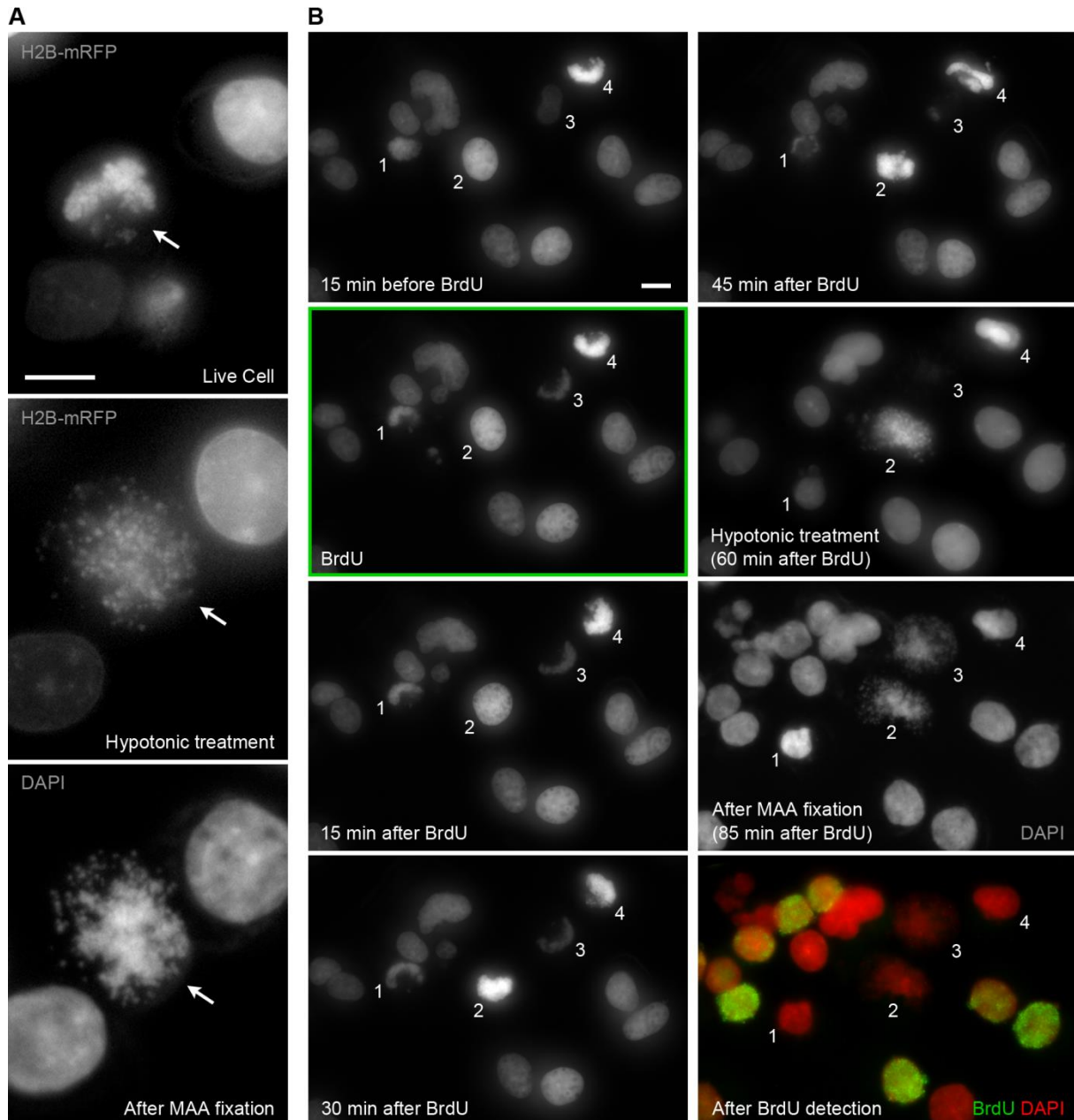


Figure 44: Correlation of living and MAA fixed UV/caffeine treated V79 cells and subsequent BrdU staining. Widefield image stacks of living V79 (H2B-mRFP) cells were acquired using H2B-mRFP stably expressed by these cells. After fixation chromatin was stained with DAPI as the fluorescence of mRFP got lost during the fixation process. **(A)** One and the same cell (arrows) during the live cell observation (top), hypotonic treatment (part of the fixation procedure) (middle) and after MAA fixation (bottom). Light optical mid-sections are shown. **(B)** Live cell observation including a BrdU pulse (about 12 min) for the detection of S phase cells, started 16 h after UV irradiation. Before, during and after the BrdU pulse images were acquired every 15 min for a total duration of 1 h. Subsequently the cells were fixed with MAA and imaged again during hypotonic treatment and after completed fixation. The images represent z-projections of 2-4 light optical sections. PALCCs appeared before (cell 1 and 4), during (cell 3) or after (cell 4) the BrdU pulse (left column, second image). Finally, BrdU was detected using mouse-anti-BrdU followed by goat-anti-mouse-Alexa488 antibodies and the cells were imaged again (DAPI is displayed in red, BrdU in green). All cells with PALCC formation during ($n=14$) or after ($n=2$) the BrdU pulse were negative for BrdU. Panel (B) is adapted from Hübner et al. (2009). Scale bar: 10 μm .

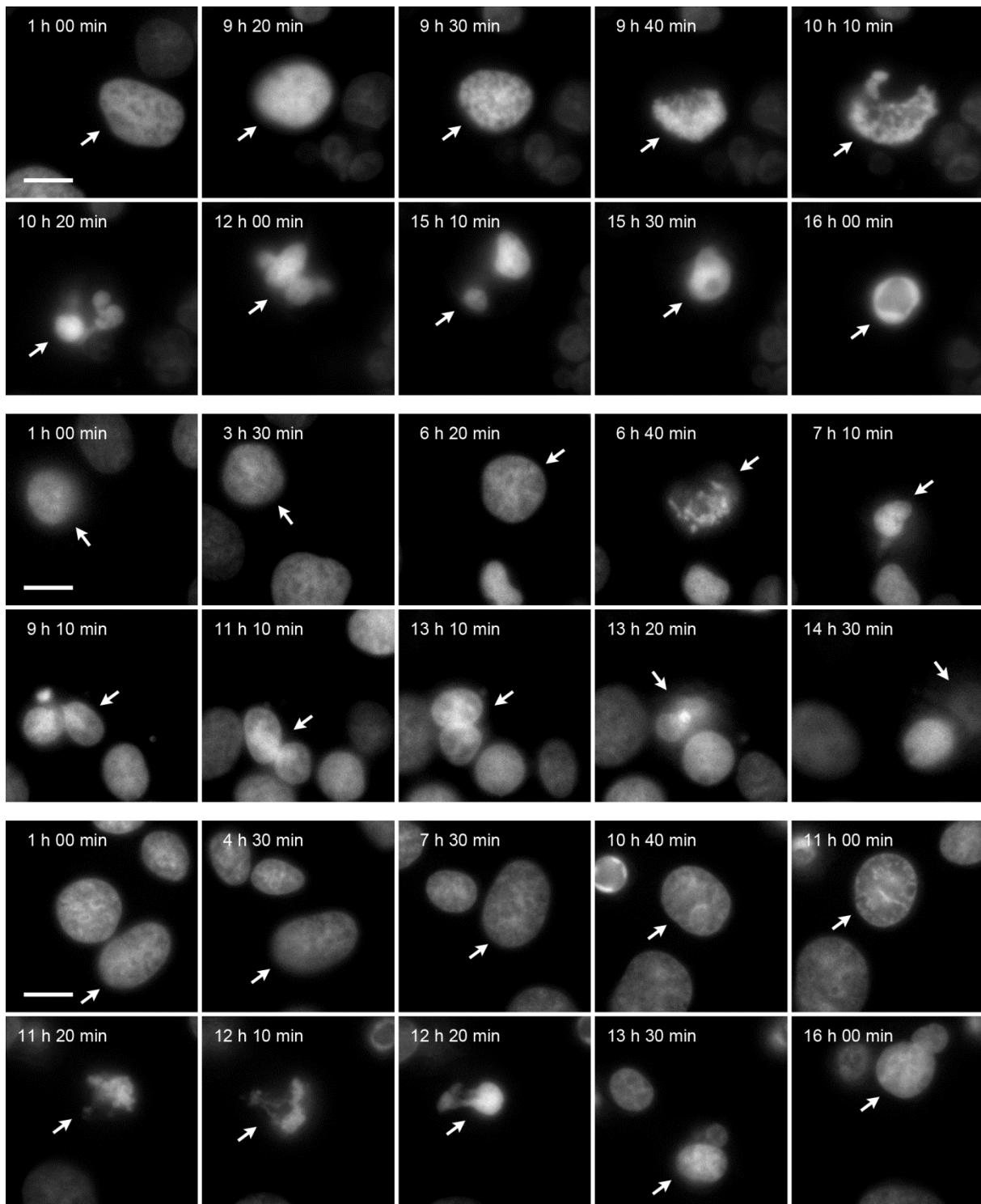


Figure 45: Long-term live cell observation of UV/caffeine treated V79 cells. Widefield images of living V79 (H2B-mRFP) cells were acquired every 10 min starting 1 h after UV irradiation for up to 16 h 10 min or 19 h 40 min after UV irradiation using H2B-mRFP stably expressed by these cells. Only selected time points are shown here. The complete movies of all three examples are included in the enclosed DVD / ZIP archive (File S14-16). Development of PALCCs (arrows): several hours after UV irradiation (here 9 h 30 min, 6 h 20 min, 11 h respectively) morphologically inconspicuous interphase cells entered prophase; 10 or maximum 20 min later a PALCC had formed; after another 30 or 40 min, a multilobulated cell had developed. Typically these cells went into apoptosis several hours later (here in the first two examples starting after ~5 h at 15 h 30 min and 13 h 20 min, respectively). Control cells without treatment divided normally throughout the entire observation period of 48 h (data not shown, but the complete movie is included in the enclosed DVD / ZIP archive (File S17)) These data are also included in my Diploma thesis (Hübner 2008) and in Hübner et al. (2009). The image of the first example for PALCC development (upper two rows) is adapted from there. Scale bar: 10 μ m.

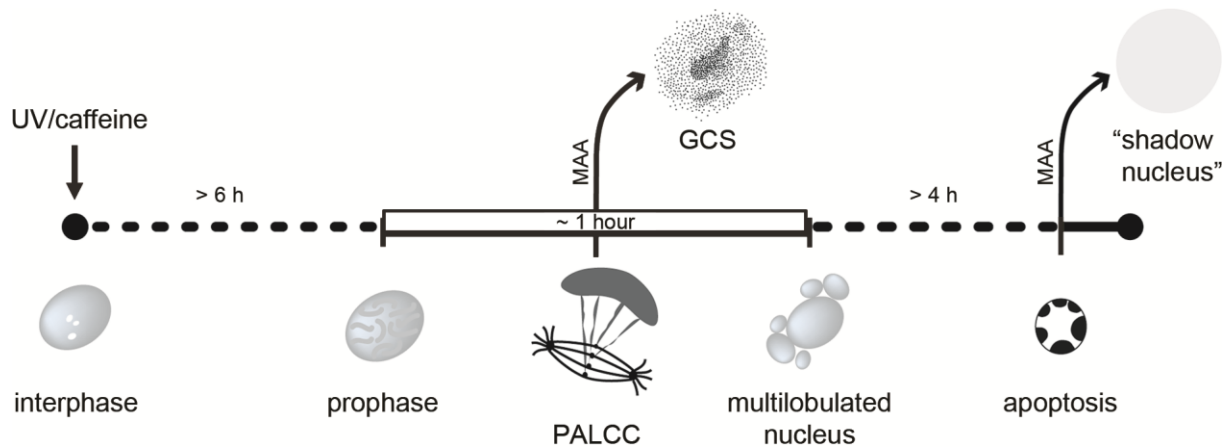


Figure 46: Schematic representation of the processes occurring upon UV/caffeine treatment of V79 cells. PALCCs became visible at the earliest 6 h after UV irradiation and emerged from morphologically inconspicuous prophase cells. They developed into multilobulated cells about 1 h after entering prophase, which then typically went into apoptosis after several hours. After MAA fixation PALCCs appeared as GCS, apoptotic cells as "shadow nuclei". Figure adapted from Hübner et al. (2009).

Figure 47: Long-term live cell observation of PCC induction and subsequent release in V79 cells. (A) Widefield images of living V79 (H2B-mRFP) cells were acquired every 5 min during PCC induction and every 15 min during the subsequent cultivation in normal medium (i.e. after release of the PCC inducing drug Calyculin A) using H2B-mRFP stably expressed by these cells. The cells were observed up to a total duration of 22 h. Only selected time points are depicted (see (B) for a typical example including all time points of PCC induction). The complete movie (covering a larger field of view as shown here) is included in the enclosed DVD / ZIP archive (File S18). Early PCC (grainy chromatin): cell 1 and 4 at 30 min PCC induction. Middle PCC (individual chromosomes retracted to the nuclear periphery): cell 4 at 60 min PCC induction. Late I PCC (chromosomes further condensed and dispersed throughout the nucleus): cell 1 and 5 at 60 min PCC induction. Late II PCC (chromosomes spread more widely): cell 2 at 30 and 60 min PCC induction. Cell 2 appeared already slightly grainy in the medium at 0 min, indicating that this cell was just about to enter mitosis, explaining the very rapid PCC progression in this cell. A few hours after drug release the cells appeared to be hardly attached and specific cells could not be tracked anymore. After several hours most cells had entered apoptosis and/or had disappeared. In the enclosed DVD / ZIP archive also the complete movie of a second example is included (File S19), which shows even better that PCC development continued after release. (B) Magnifications of cell 5 shown in (A) during PCC induction. All time points are included here. This cell did not develop into the late II PCC stage during the 1 h of PCC induction. Control cells without treatment divided normally throughout the entire observation period of 39.5 h (data not shown, but the complete movie is included in the enclosed DVD / ZIP archive (File S20)). Scale bar: 10 μ m in (A), 5 μ m in (B).

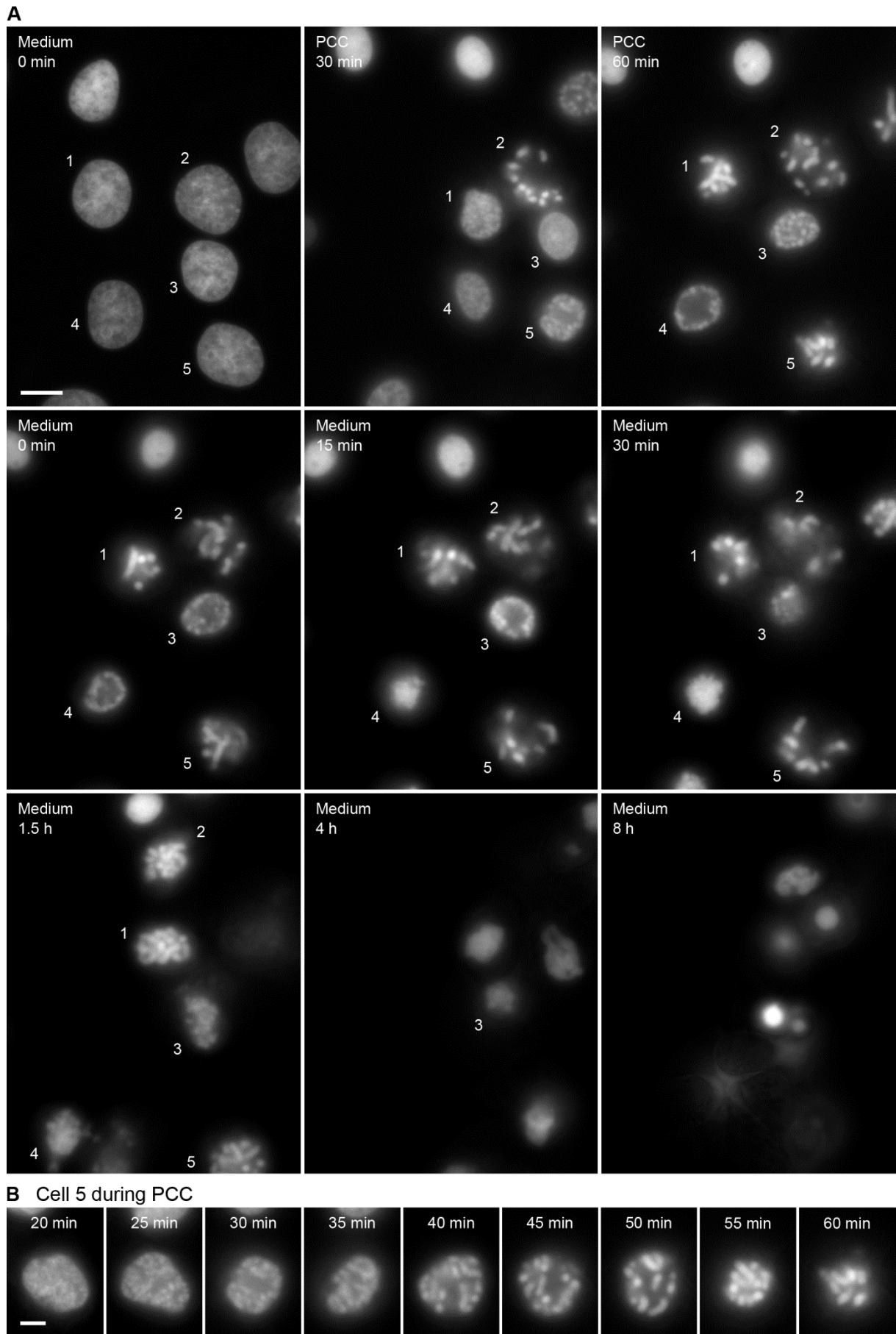


Figure 47: Long-term live cell observation of PCC induction and subsequent release in V79 cells (see legend on previous page).

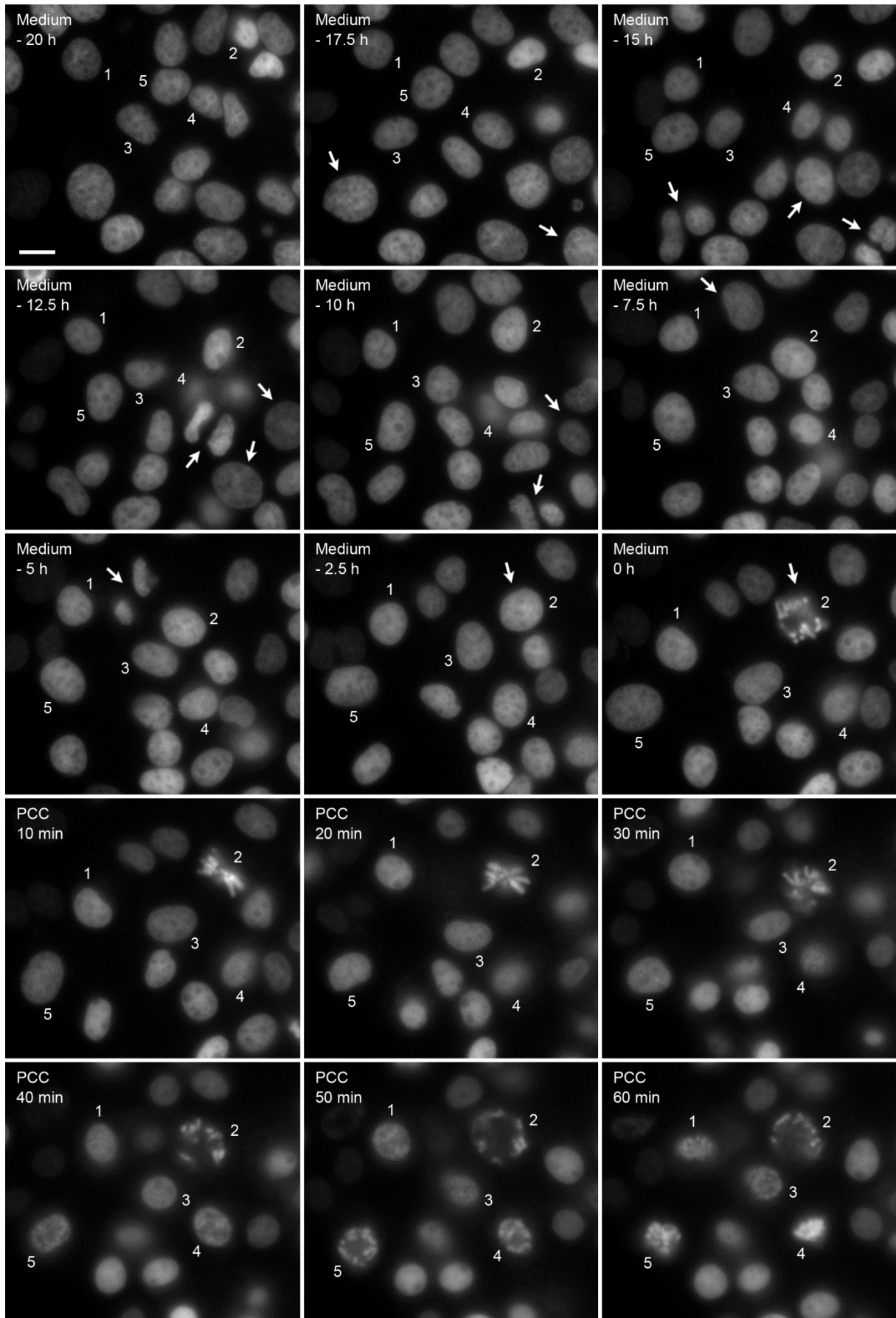


Figure 48: Long-term live cell observation with subsequent PCC induction in V79 cells. Widefield images of living V79 (H2B-mRFP) cells were acquired every 15 min for a total period of 20 h 45 min in normal medium and every 5 min during subsequent PCC induction using *(legend continued on page 225)*

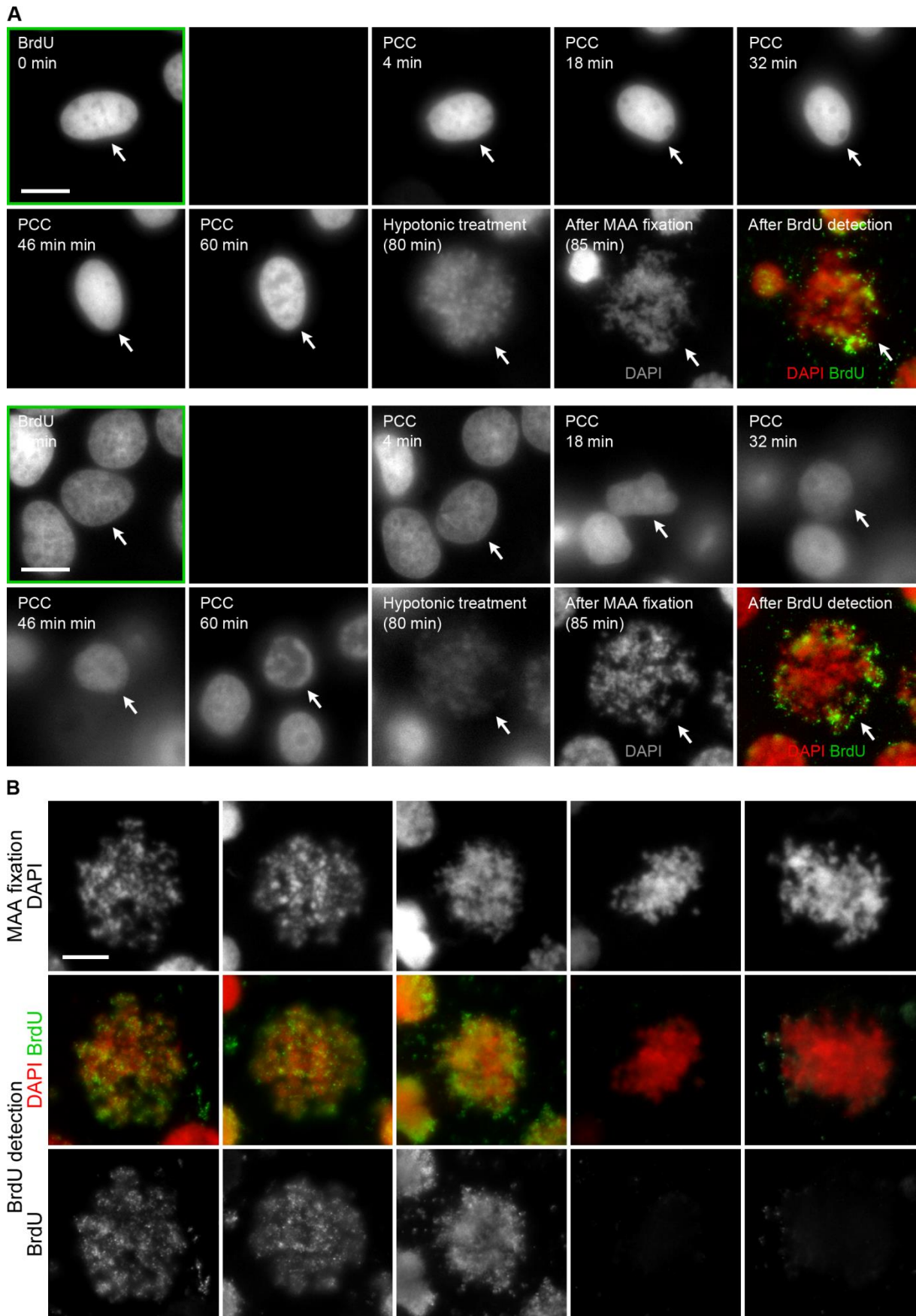


Figure 49: Correlation of living and MAA fixed PCC induced V79 cells and subsequent BrdU staining of S PCCs. (A) Widefield images of living V79 (H2B-mRFP) cells were acquired using H2B-mRFP stably expressed by these cells. Images were taken after a 30 min BrdU pulse before PCC induction, during PCC induction (roughly every 14 min), during hypotonic (*legend continued on page 225*)

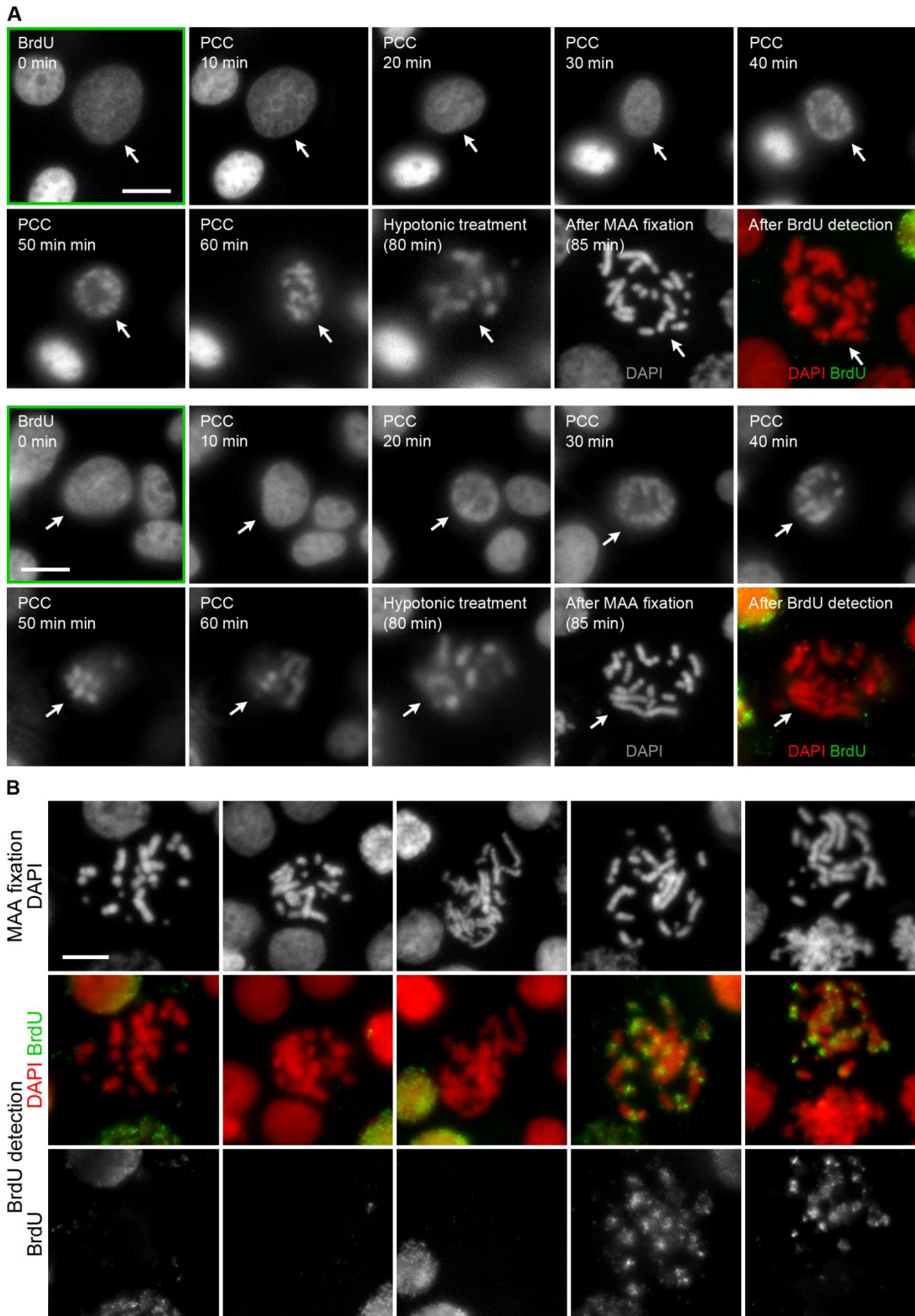


Figure 50: Correlation of living and MAA fixed PCC induced V79 cells and subsequent BrdU staining of G1/G2 PCCs. Equivalent to **Figure 49**, therefore the legend is shortened here. **(A)** During PCC induction images were taken every 10 min. G1/G2 PCCs resulted from middle/late I (upper two rows) or late II (lower two rows) PCC cells (arrows). **(B)** Further examples (*legend continued on page 225*)

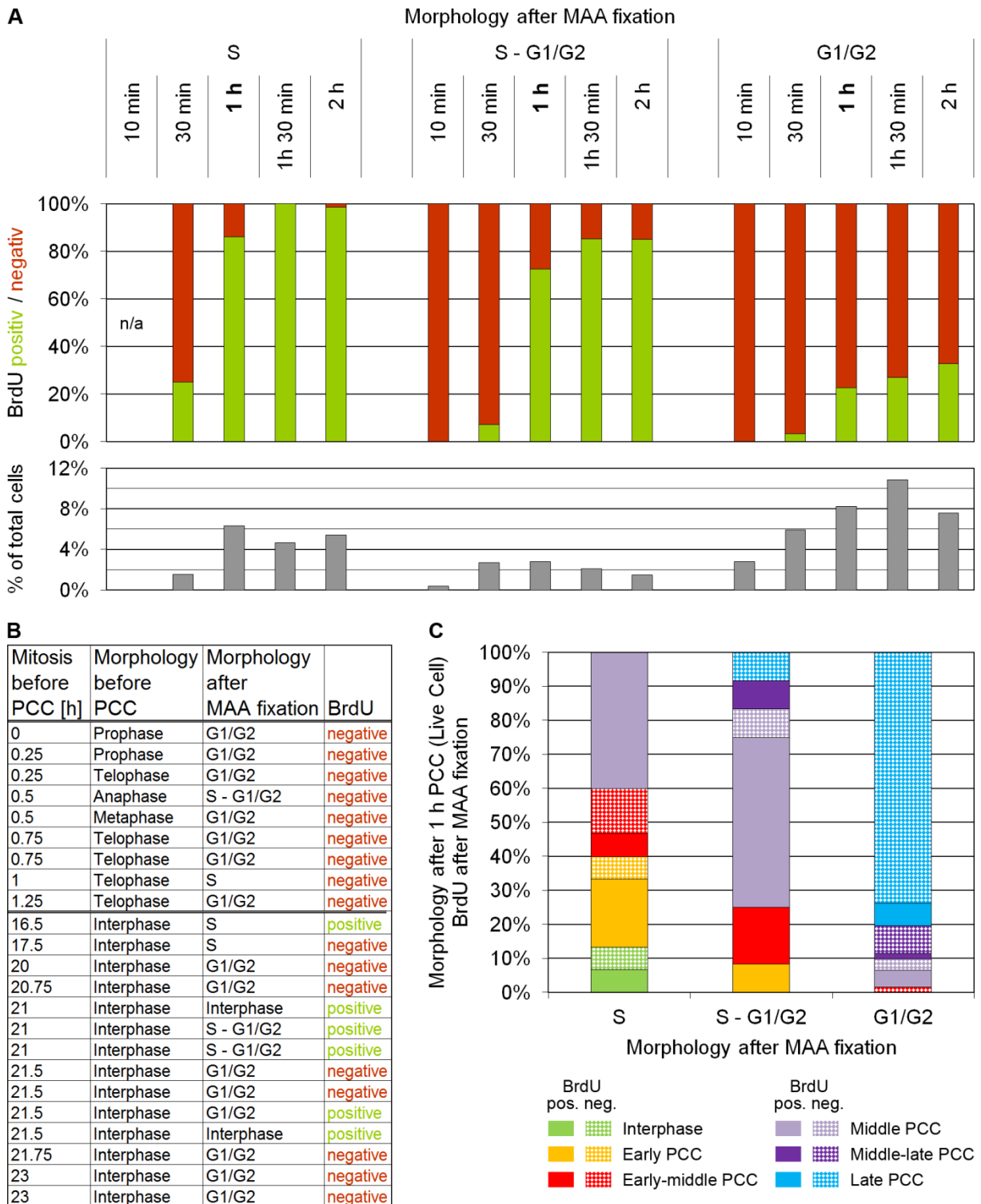


Figure 51: Evaluation of PCC induced V79 cells. (A) Upper graph: correlation between the morphology after MAA fixation after different PCC induction times (x-axis) and BrdU staining for the detection of S phase cells (y-axis). n=0, 8, 165, 61, 72 S PCCs were evaluated for 10 min, 30 min, 1 h, 1 h 30 min, 2h of PCC induction, n=2, 14, 73, 27, 20 for S - G1/G2 PCCs and n=14, 31, 216, 141, 101 for G1/G2 PCCs. Lower graph: relative amount of the respective morphological phenotypes. **(B)** Correlation between the time point of the last mitosis before PCC induction (first column), the morphology of the cells in the living state directly before PCC induction (second column), the morphology after MAA fixation (third column) and BrdU staining (last column). **(C)** Correlation between the morphology after MAA fixation (x-axis) and the morphology in the living cell state as well as BrdU staining (y-axis). As most of these data were only acquired in 2D the determination of the exact PCC stage was often difficult. Therefore late I and late II PCCs were summarized into late PCCs and the intermediate categories early-middle and middle-late were created. All three distributions (*legend continued on next page*)

Figure 48: (*legend continued from page 221*) H2B-mRFP stably expressed by these cells. Only selected time points are depicted. The complete movie is included in the enclosed DVD / ZIP archive (File S21). Dividing cells are marked by an arrow. Cell 2 was in mitosis at the time of PCC induction. Partially these experiments were performed by Korbinian von Heckel, Stephanie Peklo and Mareike Fitschen during their “Forschungspraktikum” (research internship) respectively bachelor thesis (Fitschen 2009) under my instruction and supervision. Scale bar: 10 μm .

Figure 49: (*legend continued from page 222*) treatment (part of the fixation procedure) and after MAA fixation. The fluorescence of mRFP got lost during the fixation process and was substituted by DAPI staining. Subsequently, BrdU was detected using mouse-anti-BrdU followed by goat-anti-mouse-Cy5 or goat-anti-mouse-Alexa488 antibodies and the cells were imaged again (DAPI is displayed in red, BrdU in green). S PCCs resulted from early (upper two rows) or middle (lower two rows) PCC cells (arrows). **(B)** Further examples of BrdU staining in S PCCs. Images of the DAPI pattern after MAA fixation (upper row), the merged image of DAPI (red) and BrdU (green) after BrdU detection (middle row) as well as the BrdU signal alone (lower row) are shown. Typically S PCCs were BrdU positive (column 1-3), occasionally also BrdU negative (column 4-5). Partially these experiments were performed by Korbinian von Heckel, Stephanie Peklo and Mareike Fitschen during their “Forschungspraktikum” (research internship) respectively bachelor thesis (Fitschen 2009) under my instruction and supervision. Scale bar: 10 μm .

Figure 50: (*legend continued from page 223*) of BrdU staining in G1/G2 PCCs. Typically these cells were BrdU negative (column 1-3), occasionally also BrdU positive (column 4-5). Partially these experiments were performed by Korbinian von Heckel, Stephanie Peklo and Mareike Fitschen during their “Forschungspraktikum” (research internship) respectively bachelor thesis (Fitschen 2009) under my instruction and supervision. Scale bar: 10 μm .

Figure 51: (*legend continued from previous page*) differed highly significantly ($p < 0.001$). For all evaluations BrdU was detected using mouse-anti-BrdU followed by goat-anti-mouse-Cy5 or goat-anti-mouse-Alexa488 antibodies. The data used for the evaluations presented in (B) and (C) and partially for 1 h PCC induction of (A) were collected by Korbinian von Heckel, Stephanie Peklo and Mareike Fitschen during their “Forschungspraktikum” (research internship) respectively bachelor thesis (Fitschen 2009) under my instruction and supervision.

4.3.1.2 Parachute-like chromatin conformations (PALCCs) observed after UV/caffeine treatment and PCC induced cells both represent mitotic events

The next step was then to test to which extent PALCCs and the different PCC stages represent indeed mitotic cell stages and to which degree multilobulated cells emerging from PALCCs as well as interphase cells observed after PCC induction resemble control interphase cells. In order to do that the following markers were used for immunofluorescence stainings: lamin B and H3S10p (**Figure 52**), centromeres or Ki67 and α -tubulin (**Figure 53+54**), SMC2 (**Figure 55**) and H3K4me3 and RNA Pol II Ser 2P or H3K9me3 (**Figure 56+57**) (for a more detailed explanation of these markers see section 2.3 of the introduction).

All stainings demonstrated that PALCCs were mitotic cells despite the absence of distinct, condensed mitotic chromosomes: as in control metaphase cells the lamina was degraded (**Figure 52**), chromatin was intensely stained with H3S10p (**Figure 52**), a normal mitotic spindle with centromeres located at their usual position was present, however shifted to one side of the bulky chromatin mass, resulting in the centromeres being pulled out several μ m from the chromatin mass (**Figure 54**), and chromatin lacked RNA Pol II Ser 2P (**Figure 56**) and H3K9me3 (**Figure 57**). Slight differences were only observed for the localization of H3K4me3 (**Figure 56+57**). While in control metaphase signals were clearly found inside the condensed chromosomes, they seemed to be more restricted to the surface of the chromatin domains in PALCCs.

Note that the distribution of SMC2 could not be analyzed in PALCCs as the primary antibody used here did not detect the epitope in V79 cells (data not shown).

The lack of H3K9me3 even in normal metaphase cells was surprising, as this histone modification is typically maintained or even enriched during mitosis (Fischle et al. 2005, McManus et al. 2006, Jeong et al. 2010). The reasons for this observation are unclear. Possible explanations might be the special genetic background in the hamster cells used for these experiments (see section 3.2.1 and compare: only in hamster cells the formation of PALCCs was observed) or the antibody used here rather detects H3K9me2, reported to decrease in mitosis (Duan et al. 2008, Jeong et al. 2010), instead of H3K9me3.

The different markers also revealed that after UV/caffeine treatment interphase cells as well as multilobulated cells exhibited staining patterns typical for control interphase nuclei: their lamina was intact, they were negative for H3S10p (not shown for UV/caffeine treated interphase cells) (**Figure 52**), had typically a normal and extensive cytoskeleton (**Figure 54**) and normal localization patterns of H3K4me3, RNA Pol II Ser 2P and H3K9me3

(**Figure 56+57**). As in control interphase nuclei, centromeres were distributed throughout the nucleus in UV/caffeine treated interphase cells. In multilobulated cells, however, they typically clustered in one or two lobes (**Figure 54**).

In addition, chromosome painting (**Figure 58**) of UV/caffeine treated cells revealed that chromosomes of both multilobulated cells and PALCCs exhibited a predominantly territorial organization as observed in morphologically inconspicuous interphase nuclei. This underlined that multilobulated cells were indeed interphase cells and clearly demonstrated that PALCCs suffered from a condensation failure.

In PCC induced cells the immunofluorescence stainings showed that the different PCC stages represented indeed mitotic cell stages although they deviated in some respects from the normal mitotic patterns. Similar to normal prophase the lamina (**Figure 52**) was still intact in the early and middle PCC cells and also in late I PCC cells, despite their condensed mitotic chromosomes. In late II PCC cells it was degraded, equivalent to normal metaphase. An intense H3S10p staining (**Figure 52**) was found in all PCC stages and Ki67 (**Figure 53**) started to relocate from the nucleoli to the surface of the chromatin in early PCC cells, fully covering the condensed chromosomes in late I and late II PCC cells, equivalent to the staining patterns in normal pro- and metaphase cells, respectively. SMC2 (**Figure 55**) started to associate with the chromosomes in early PCC cells, equivalent to normal prophase, and delineated the axis of the chromosomes in the later PCC stages as in normal metaphase. In the majority of cases, two strands of SMC2 staining were observed. Only very rarely (1 out of 17 cells) only one broadened chromatid was detected. Note that this SMC2 staining could only be performed in HeLa cells as the primary antibody used here did not detect the epitope in V79 cells (data not shown). PCC cells also showed normal levels and localization patterns for H3K4me3 (**Figure 56+57**) and a reduction of both RNA Pol II Ser 2P (**Figure 56**) as well as H3K9me3 (**Figure 57**) with progressing PCC induction, similar to the progression from prophase to metaphase in normal cells. Different from normal mitotic cells centromeres were found distributed throughout the nucleus in all PCC stages, even in late I and late II PCC cells (**Figure 53**), supporting the impression from the images that no proper metaphase plate was formed in these cells. Typically centromeres appeared as doublets, representing one signal from each of the two sister chromatids. Staining with α -tubulin (**Figure 53**) revealed that these cells lacked a proper spindle, explaining the abnormal localization of the centromeres: early PCC cells showed no cytoskeleton and/or spindle at all and in late II PCC cells only a very loose network of only a few microtubules was observed. In middle and late I PCC cells a rudimentary spindle was present, however, consisting of only one pole.

Interphase cells occurring after PCC induction exhibited staining patterns typical for control interphase cells: they showed an intact lamina and were negative for H3S10p (**Figure 52**), had centromeres distributed throughout the nucleus and Ki67 located in the nucleoli (**Figure 53**), a dispersed distribution of SMC2 (**Figure 55**) and normal localization patterns of H3K4me3, RNA Pol II Ser 2P and H3K9me3 (**Figure 56+57**). However, no microtubules were formed in these cells (**Figure 53**).

For a detailed analysis of the localization of H3K4me3, RNA Pol II Ser 2P and H3K9me3 in selected stages of control, UV/caffeine treated and PCC induced cells in relation to chromatin see section 4.3.2.

Figure 52: Lamin B and H3S10p in control, PCC induced and UV/caffeine treated V79 cells. DAPI stained DNA (gray), Lamin B (green) and Histone 3 phosphorylated on serine 10 (H3S10p) in PFA-fixed V79 cells without treatment (control cells) (A) or after UV/caffeine treatment (C) or V79 (H2B-mRFP) cells after the induction of PCC (B). Immunofluorescence for the detection of Lamin B and H3S10p in control and UV/caffeine treated cells was performed using goat-anti-LaminB and rabbit-anti-H3S10p antibodies followed by donkey-anti-goat-Alexa488 and donkey-anti-rabbit-Cy3 antibodies, in PCC induced cells Lamin B was detected using goat-anti-LaminB followed by donkey-anti-goat-Cy3 antibodies and H3S10p by using mouse-anti-H3S10p followed by goat-anti-mouse-Cy5 antibodies or rabbit-anti-H3S10p followed by goat-anti-rabbit-Cy3 antibodies. Light optical mid-sections of whole CLSM 3D acquisitions are shown. Left column: Merged image of DAPI staining, Lamin B and/or H3S10p. Middle column: DAPI staining alone. Right column: Merged image of the markers alone, i.e. Lamin B and/or H3S10p. **(A)** Control cells. From top to bottom an interphase, prophase, metaphase, anaphase, and telophase is shown. **(B)** PCC induced cells. From top to bottom for each staining (upper row: Lamin B, lower row: H3S10p) an interphase, (very) early, middle, late I, and late II PCC cell is shown. **(C)** UV/caffeine treated cells. From top to bottom a prophase, PALCC, and multilobulated cell is shown. Slides of control and UV/caffeine treated cells were kindly provided by Fritzi Beck. Most of these data are also included in my Diploma thesis (Hübner 2008) and partially also in Hübner et al. (2009). Stainings of PCC induced cells were partially performed and in case of H3S10p also imaged by Stephanie Peklo and Mareike Fitschen during their “Forschungspraktikum” (research internship) respectively bachelor thesis (Fitschen 2009) under my instruction and supervision. Scale bars: 4 µm.

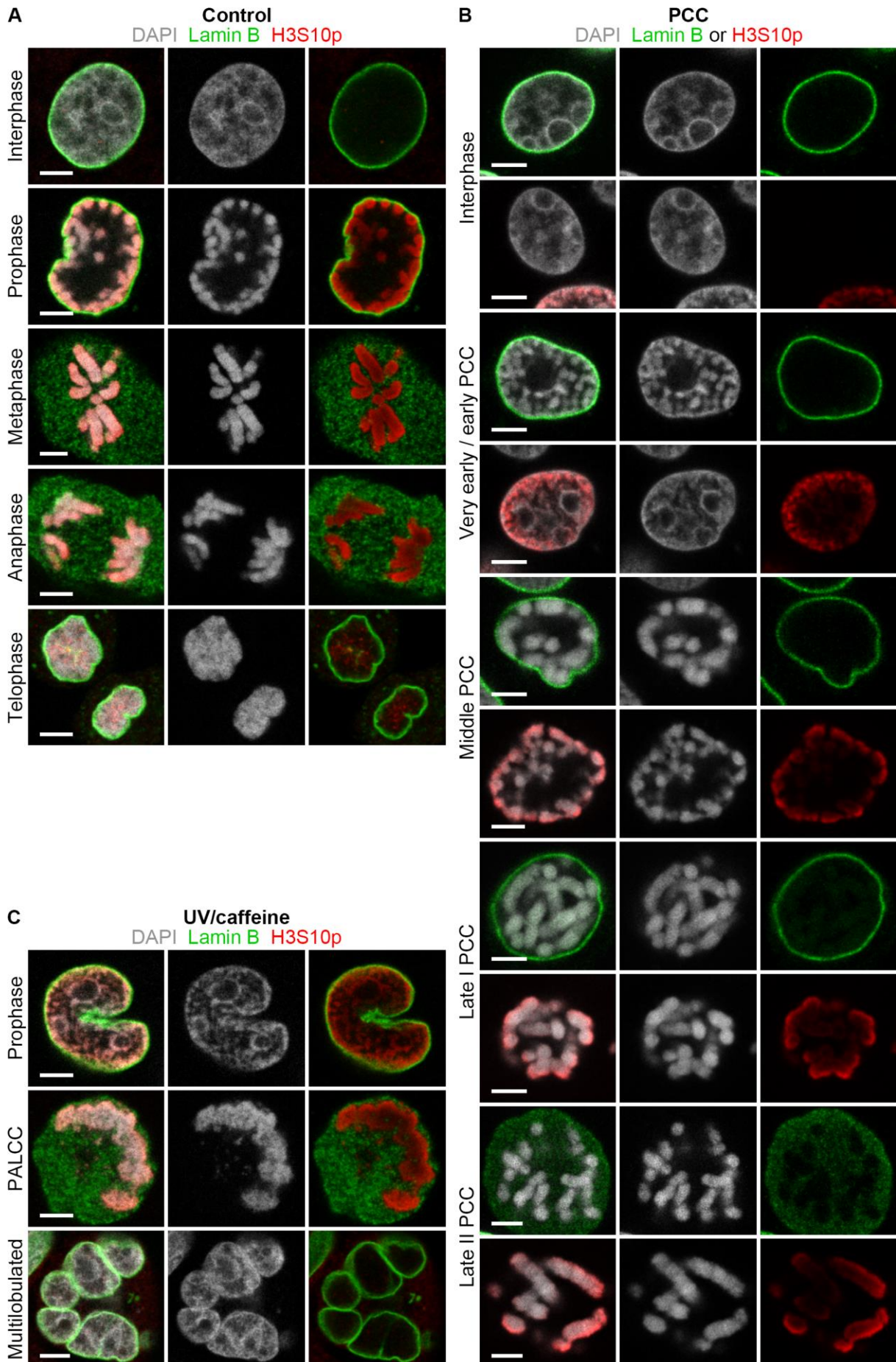


Figure 52: Lamin B and H3S10p in control and treated V79 cells (see legend on previous page).

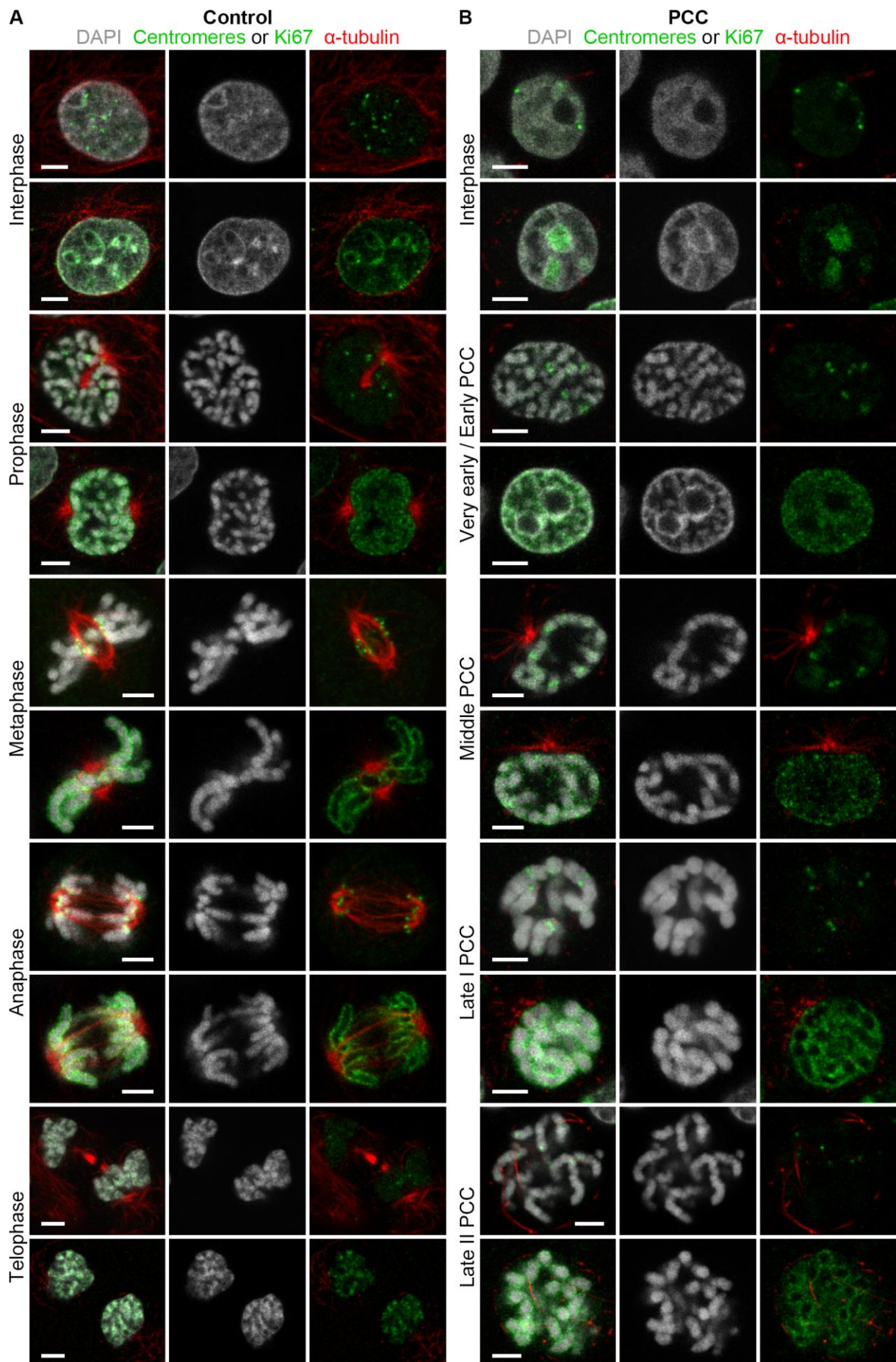


Figure 53: Centromeres, Ki67, and α -tubulin in control and PCC induced V79 cells (see legend on next page).

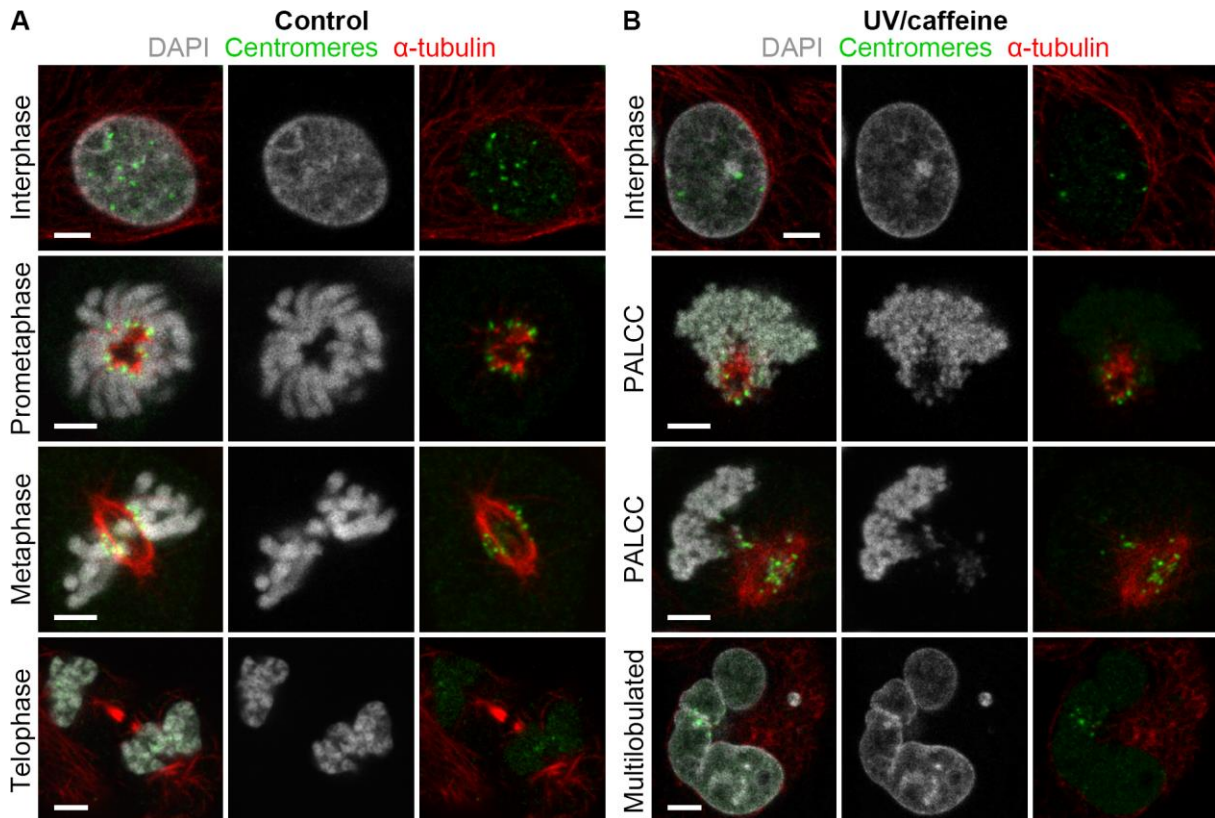


Figure 54: Centromeres and α -tubulin in control and UV/caffeine treated V79 cells. DAPI stained DNA (gray), centromeres (green) and α -tubulin in PFA-fixed V79 (H2B-mRFP) cells without treatment (control cells) (A) or after UV/caffeine treatment (B). Immunofluorescence for the detection of centromeres and α -tubulin was performed using human-anti-centromere and mouse-anti- α -tubulin antibodies followed by goat-anti-human-FITC or donkey-anti-human-Cy5 and sheep-anti-mouse-Cy3 antibodies. Light optical mid-sections of whole CLSM 3D acquisitions are shown. Left column: Merged image of DAPI staining, centromeres and α -tubulin. Middle column: DAPI staining alone. Right column: Merged image of the markers alone, i.e. centromeres and α -tubulin. **(A)** Control cells. From top to bottom an interphase, prometaphase, metaphase, and telophase is shown. Apart from prometaphase, the images are repeated from **Figure 53** in order to facilitate the comparison with the UV/caffeine treated cells. **(B)** UV/caffeine treated cells. From top to bottom an interphase, two PALCCs, and a multilobulated cell is shown. Most of these data are also included in Hübner et al. (2009). Scale bars: 4 μ m.

Figure 53: Centromeres, Ki67, and α -tubulin in control and PCC induced V79 cells. DAPI stained DNA (gray), centromeres or Ki67 (green) and α -tubulin in PFA-fixed V79 (H2B-mRFP) cells without treatment (control cells) (A) or after the induction of PCC (B). Immunofluorescence for the detection of centromeres and α -tubulin was performed using human-anti-centromere and mouse-anti- α -tubulin antibodies followed by goat-anti-human-FITC or donkey-anti-human-Cy5 and sheep-anti-mouse-Cy3 antibodies, for the detection of Ki67 and α -tubulin using rabbit-anti-Ki67 and mouse-anti- α -tubulin antibodies followed by goat-anti-rabbit-Cy3 and goat-anti-mouse-Cy5 antibodies. Light optical mid-sections of whole CLSM 3D acquisitions are shown. Left column: Merged image of DAPI staining, centromeres or Ki67 and α -tubulin. Middle column: DAPI staining alone. Right column: Merged image of the markers alone, i.e. centromeres or Ki67 and α -tubulin. **(A)** Control cells. From top to bottom for each staining (upper row: centromeres and α -tubulin, lower row: Ki67 and α -tubulin) an interphase, prophase, metaphase, anaphase, and telophase is shown. Slightly unexpected, in interphase cells Ki67 was mainly found surrounding the nucleoli. Typically this protein is well known for its location inside the nucleoli (see for example Kill 1996, Endl and Gerdes 2000, Biocyclopedia 2012 and own unpublished data). **(B)** PCC induced cells. From top to bottom for each staining (upper row: centromeres and α -tubulin, lower row: Ki67 and α -tubulin) an interphase, (very) early, middle, late I, and late II PCC cell is shown. Partially the data of control cells stained with centromeres and α -tubulin are also included in Hübner et al. (2009). Scale bars: 4 μ m.

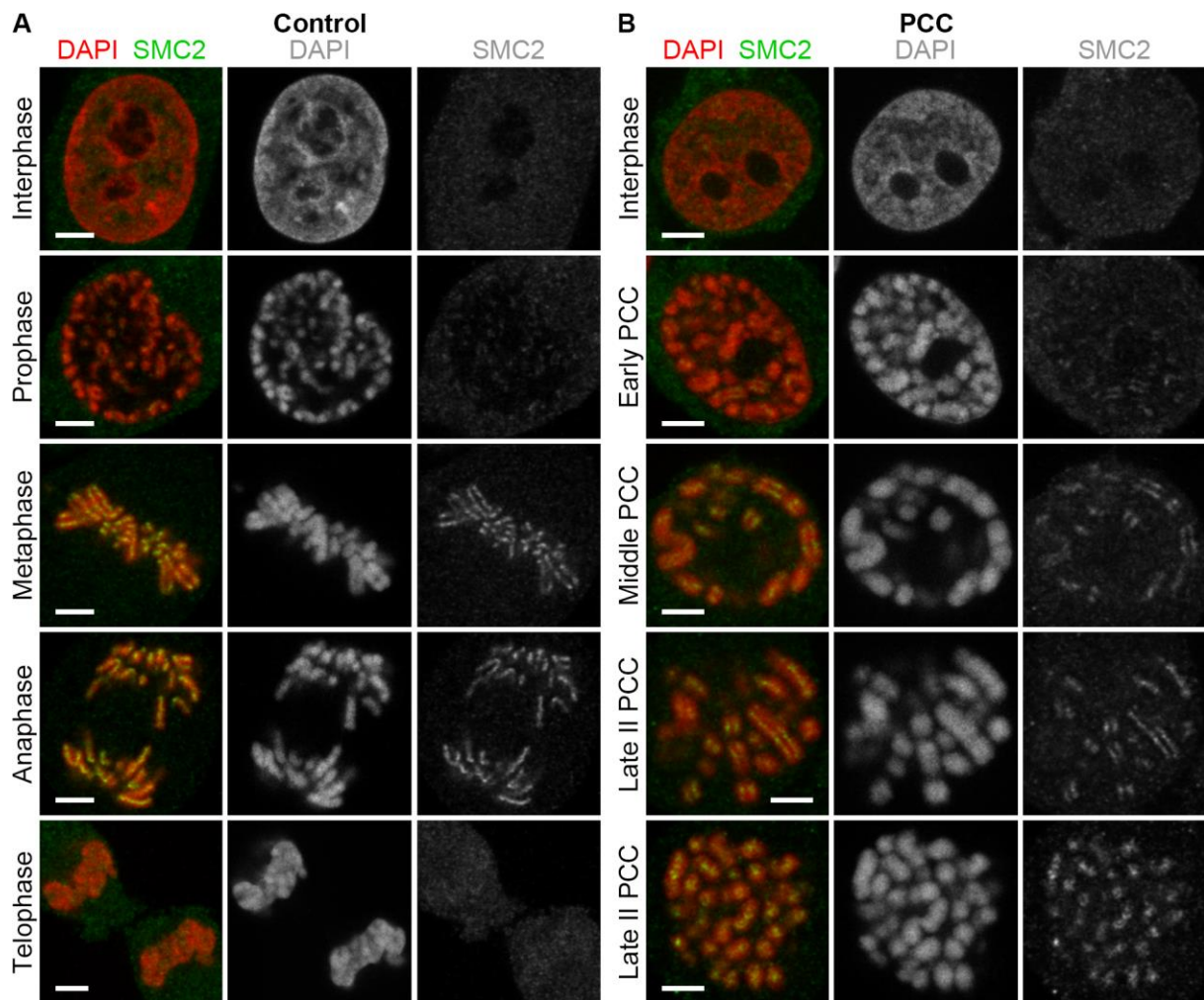


Figure 55: SMC2 in control and PCC induced HeLa cells. DAPI stained DNA (red) and SMC2 (green) in PFA-fixed HeLa (H2B-GFP) cells without treatment (control cells) (A) or after PCC induction. Immunofluorescence for the detection of SMC2 was performed using rabbit-anti-SMC2 antibodies followed by goat-anti-rabbit-Cy3 antibodies. Light optical mid-sections of whole CLSM 3D acquisitions are shown. Left column: Merged image of DAPI staining and SMC2. Middle column: DAPI staining alone. Right column: SMC2. **(A)** Control cells. From top to bottom an interphase, prophase, metaphase, anaphase, and telophase is shown. **(B)** PCC induced cells. From top to bottom an interphase, early, middle, and late II PCC is shown. In most cases (94.1%, 16 of 17 cells, all PCC stages included) two strands of SMC2 staining, representing the two sister chromatids, were observed. Only in one case (5.9%, late II PCC cell) only one broadened chromatid was detected (last row). Partially the data of control cells are also included in my Diploma thesis (Hübner 2008). Scale bar: 4 μ m.

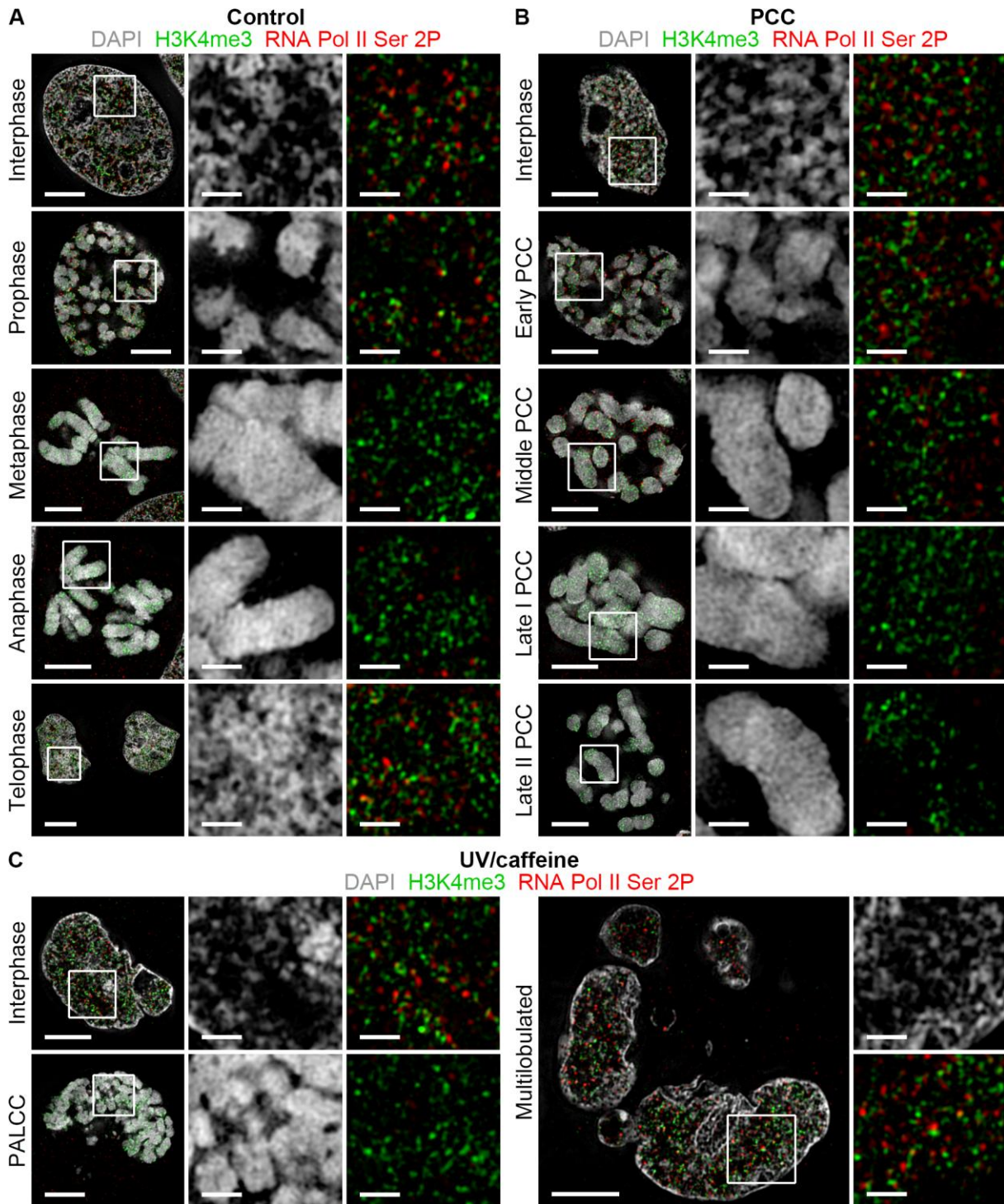


Figure 56: H3K4me3 and RNA Pol II Ser 2P in control, PCC induced and UV/caffeine treated V79 cells. DAPI stained DNA (gray), Histone 3 tri-methylated on lysine 4 (H3K4me3) (green) and RNA Polymerase II phosphorylated on serine 2 (RNA Pol II Ser 2P) (red) of PFA-fixed V79 cells either without treatment (control cells) (A), after PCC induction (B) or after UV/caffeine treatment (C). Immunofluorescence for the detection of H3K4me3 and RNA Pol II Ser 2P was performed using rabbit-anti-H3K4me3 and rat-anti-RNA Pol II Ser 2P antibodies, followed by goat-anti-rabbit-Alexa488 and donkey-anti-rat-Alexa594 antibodies, respectively. Light optical mid-sections of whole 3D-SIM 3D acquisitions are shown. Left column: Merged image of DAPI staining, H3K4me3 and RNA Pol II Ser 2P. Middle column: magnifications of the DAPI staining alone. Right column: magnifications of the merged image of the markers alone, i.e. H3K4me3 and RNA Pol II Ser 2P, same area as in the middle column. **(A)** Control cells. From top to bottom an interphase, prophase, metaphase, anaphase, and telophase is shown. **(B)** PCC induced cells. From top to bottom an interphase, early, middle, late I, and late II PCC cell is shown. **(C)** UV/caffeine treated cells. On the left, an interphase (upper row) and a PALCC (lower row) is shown, on the right a multilobulated cell (here the magnification of the *legend continued on next page*)

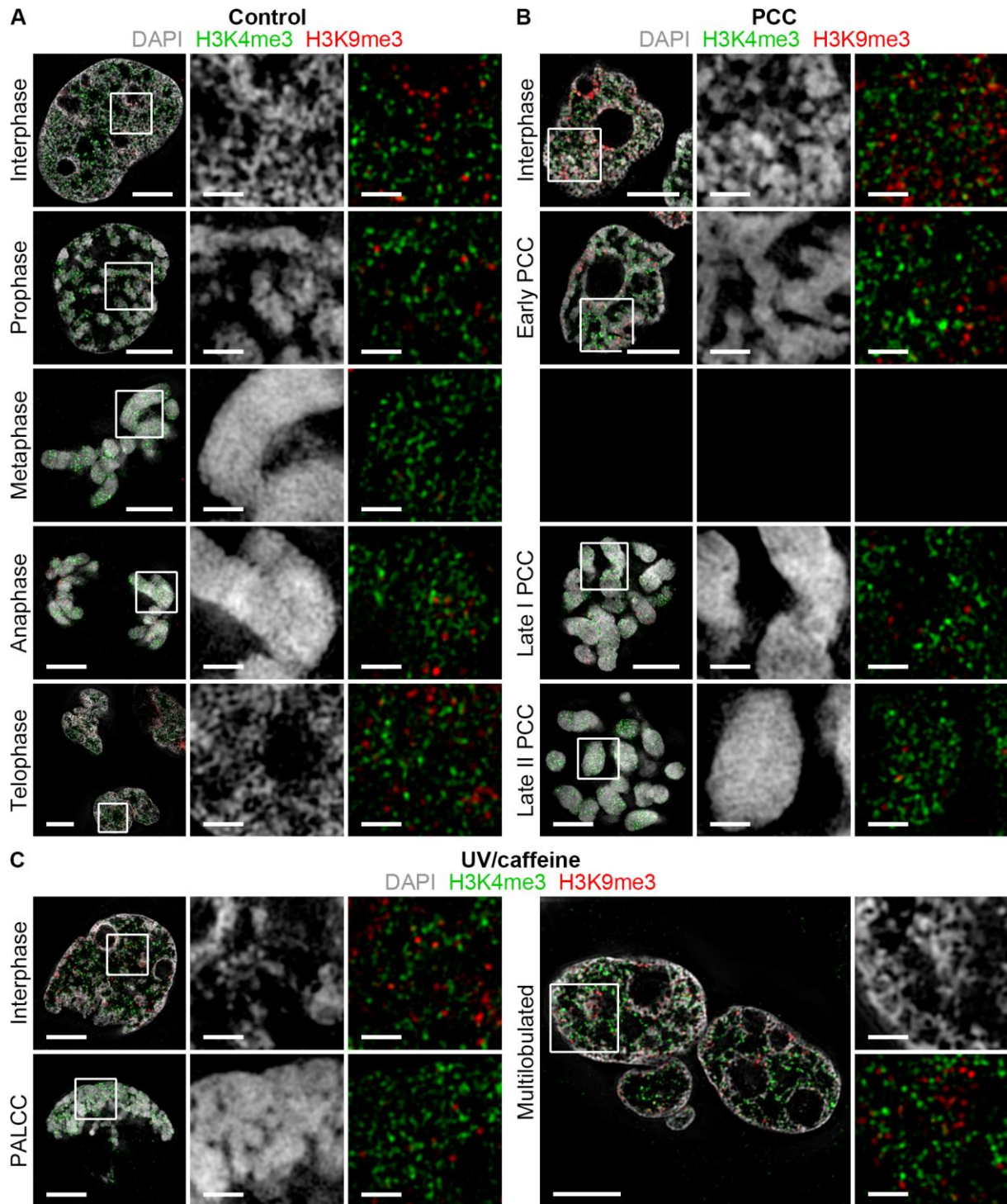


Figure 57: H3K4me3 and H3K9me3 in control, PCC induced and UV/caffeine treated V79 cells. Equivalent to **Figure 56**, therefore the legend is shortened here. DAPI stained DNA (gray), Histone 3 tri-methylated on lysine 4 (H3K4me3) (green) and Histone 3 tri-methylated on lysine 9 (H3K9me3) (red). Immunofluorescence for the detection of H3K4me3 and H3K9me3 was performed using rabbit-anti-H3K4me3 and mouse-anti-H3K9me3 antibodies, followed by goat-anti-rabbit-Alexa488 and goat-anti-mouse-Alexa594 antibodies, respectively. **(A)** Control cells. **(B)** PCC induced cells. **(C)** UV/caffeine treated cells. Scale bars: 4 μm in images of whole nuclei, 1 μm in magnifications.

Figure 56: (*legend continued from previous page*) DAPI signal is located at the top right, the magnification of the markers at the bottom right). Scale bars: 4 μm in images of whole nuclei, 1 μm in magnifications.

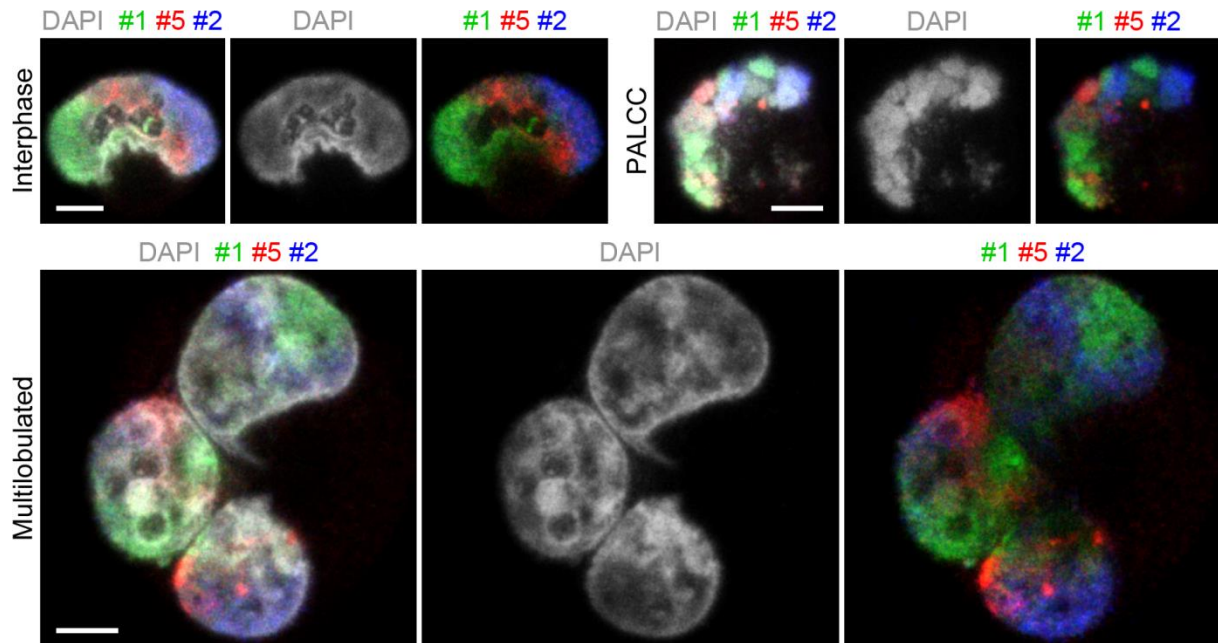


Figure 58: Chromosome painting (FISH) of whole chromosomes in V79 nuclei. DAPI stained DNA (gray) and chromosomes 1 (green), 5 (red) and 2 (blue) in PFA-fixed V79 cells after UV/caffeine treatment. 3D-FISH was performed according to the detection scheme in **Table 3** in section 3.2.7.3, *Washing and detection*. Light optical mid-sections of whole CLSM 3D acquisitions are shown. Left column: Merged image of DAPI staining and chromosomes 1, 5, 2. Middle column: DAPI staining alone. Right column: Merged image of the chromosome paints alone. An interphase cell (upper row, left), PALCC (upper row, right), and multilobulated cell (lower row) is shown. Note that the later typically contained four copies of each chromosome. These data are also included in Hübner et al. (2009). There it is furthermore shown that 2D-FISH confirmed two homologs of each chromosome and that the probe for chromosome 5 painted an additional fragment on an unidentified chromosome. Scale bars: 4 μm .

4.3.2 Consistent functional nuclear architecture in selected stages of control, UV/caffeine treated and PCC induced cells

Now that there was clarity about what the different phenotypes occurring after UV/caffeine treatment and PCC represent and how they relate to each other and to control cells, the main objective behind these experiments was addressed: the functional nuclear architecture of these manipulated cells in comparison to control cells. Selected stages of control (interphase, prophase, and telophase), PCC induced (early and middle PCC cells), and UV/caffeine treated cells (interphase and multilobulated cells) were first compared with regard to their chromatin patterns and then the localization of H3K4me3, RNA Pol II Ser 2P, and H3K9me3 as shown in **Figure 56+57** of section 4.3.1.2 was analyzed in detail.

The stages with highly condensed chromatin – of the control cells metaphase and anaphase, of the PCC induced cells middle, late I and late II PCC cells and of the UV/caffeine treated cells PALCCs – were not included, as they appeared not suitable for the evaluation: A mask of the nucleus is needed in order to define which pixels are to be evaluated. In these cell stages, this mask would have included only the condensed chromosomes. As these showed only little variation in DAPI intensity and chromatin density, a classification into density classes based on the DAPI intensities seemed inappropriate. Furthermore, potential signals at the surface of the condensed chromatin would have been located outside the mask and therefore would have been excluded from the analysis.

The comparison of the chromatin patterns of the different cell types is summarized in **Figure 59**. The images of the DAPI staining (**Figure 59 A+C**, upper rows) showed that chromatin in prophase of control cells and early PCC cells was as expected more condensed than in control interphase nuclei. To a lesser degree this was also the case in interphase PCC cells. In prophase of control cells the condensation of the chromosomes was accompanied by a widening of the interchromatin (IC) space keeping nuclear size comparable to control interphase cells. In contrast to that in PCC cells the IC widened only slightly – in interphase PCC cells even less than in early PCC cells – and consequently the nuclei appeared smaller. In telophase of control cells chromatin had decondensed again to almost the same level as in control interphase nuclei. In multilobulated cells as well as in interphase cells after UV/caffeine treatment chromatin density appeared very similar as in control interphase cells, however, these cells exhibited large IC lacunas or extended areas of very low DAPI intensity.

The corresponding segmented images (for details see sections 4.1.1 and 3.2.12.5) are shown in the lower rows of **Figure 59 A+C**, average segmentation profiles of multiple 3D acquisitions in **Figure 59 B+D**. Chromatin density increases from class 1 to class 7, i.e. from blue to white.

The profiles represented the observations made in the images: the distributions of normal prophase cells, as well as interphase and early PCC cells, were shifted towards higher chromatin classes compared to normal interphase, portraying the increased chromatin condensation in these cells. In addition, in normal prophase also class 2 was elevated, corresponding to the enlarged IC space observed in these cells. However, the shift was only moderate compared to the clear compaction in the images and in prophase cells actually an increase in class 1, rather than in class 2 was expected. This can be explained by the shortage of intermediate intensity values due to the condensed chromatin. As a consequence, the images of these cells appear – similar to those of granulocytes (see section 4.1.1) – also rather black-and-white and might therefore again cause the segmentation algorithm to create artificial subclasses (for details see section 4.1.1). Compared to normal interphase cells also the segmentation profile of normal telophase cells was shifted towards higher chromatin classes, indicating that these cells were not fully decondensed yet. In contrast, a shift towards lower chromatin classes was observed for the distributions of UC/caffeine treated multilobulated cells and to a limited extent also of interphase cells. Perhaps this reflects chromatin being present in a more open state in these cells, reflecting ongoing DNA repair process (see details in section 5.3.3 in the discussion).

Despite these differences in the chromatin pattern, on a global level functional nuclear architecture was consistent in all different conditions.

The localization of the “active” marks, H3K4me3 and RNA Pol II Ser 2P, in relation to chromatin was very similar: H3K4me3 (**Figure 60-63 A**) was mainly, RNA Pol II Ser 2P (**Figure 60+61 A**) almost exclusively located at the surface of the chromatin domain clusters (CDCs), showing basically no staining in the interior of the IC lacunas (characterized by no or extremely low DAPI signal). Certainly due to the progressing condensation of chromatin, a fraction of the H3K4me3 signals was also found on the condensed chromatin in prophase of control cells and early PCC cells. The “inactive” marker, H3K9me3, (**Figure 62+63 A**) showed a preferential localization in the interior of the more condensed CDCs. However, not all compacted chromatin was stained and H3K9me3 was also detected in regions of lower density. In prophase of control cells and early PCC cells, the amount of signal was reduced. Again the interior of the IC lacunas was basically free of staining.

The corresponding profiles of the marker signals mapped to the segmented DAPI intensity classes (**Figure 60-63 B** for H3K4me3, **Figure 60+61 B** for RNA Pol II Ser 2P, **Figure 62+63 B** for H3K9me3) confirmed the observations from the images: H3K4me3 typically showed an overrepresentation (relative signal enrichment) in the intermediate intensity classes (classes 3-5) and a corresponding underrepresentation (relative signal depletion) in the IC and the lowest density class (classes 1+2) as well as in the highest intensity classes (classes 6+7). RNA Pol II

Ser 2P was shifted towards lower chromatin classes compared to H3K4me3. Values were typically around 0 for the IC (class 1), an overrepresentation (relative signal enrichment) was observed for the decondensed chromatin regions (classes 2-4) and a corresponding underrepresentation (relative signal depletion) for the high-intensity classes of more compact chromatin (classes 5-7). In contrast to that H3K9me3 was shifted towards higher chromatin classes compared to H3K4me3. Very consistently H3K9me3 showed an overrepresentation (relative signal enrichment) in the high-intensity classes of more compact chromatin (classes 5-7) and a corresponding underrepresentation in the decondensed chromatin regions (classes 2-4) as well as the IC (class 1).

Figure 64 summarizes the observations described above by showing a comparison between all seven conditions – i.e. interphase, prophase, and telophase in control cells, interphase and early PCC cells, and UV/caffeine treated interphase and multilobulated cells – for each marker in both the classical profiles (left) and the over- and underrepresentations (relative signal enrichment and depletion) (right) of the segmentation profiles. For H3K4me3 all available data from both immunofluorescence stainings was combined. Although small variations were observed for H3K4me3 and RNA Pol II Ser 2P (for a detailed explanation see section 5.1.1 in the discussion), the functional nuclear architecture was consistent on a global level in all different conditions.

Figure 59: Comparison of the chromatin pattern in control, PCC induced and UV/caffeine treated V79 cells. (A, C) Upper row: DAPI stained DNA of PFA-fixed V79 cells, either without treatment (control cells) (left two images in (A), interphase and prophase; left image in (C), telophase), after PCC induction (right two images in (A), interphase and early PCC) or after UV/caffeine treatment (right two images in (C), interphase and multilobulated cell). Light optical mid-sections of whole 3D-SIM 3D acquisitions are shown. Lower row: corresponding segmented images. The segmentation algorithm converted the DAPI-intensities into seven classes with increasing density from class 1 to 7, i.e. from blue to white. Middle row: respective magnifications of the upper and lower row. (B, D) Profiles of the segmentations of whole 3D acquisitions exemplified by the images shown in (A) and (C). Average curves of multiple whole 3D acquisitions are shown. The distributions were not statistically significant different (for control interphase vs. prophase $p=0.575$, vs. telophase $p=0.073$, vs. interphase PCC cells $p=0.227$, vs. early PCC cells $p=0.170$, vs. UV/caffeine treated interphase $p=0.790$ and vs. multilobulated cells $p=0.279$). Only for interphase PCC and early PCC cells vs. multilobulated cells, and telophase vs. UV/caffeine treated interphase statistically significant ($p<0.05$) differences were found, for telophase vs. multilobulated cells very significant ($p<0.01$) differences. Note that the Wilcoxon rank-sum test used here can only check for differences in the mean value, not in the actual distribution. Error bars: standard deviation. Scale bars: 4 μm in images of whole nuclei, 1 μm in magnifications.

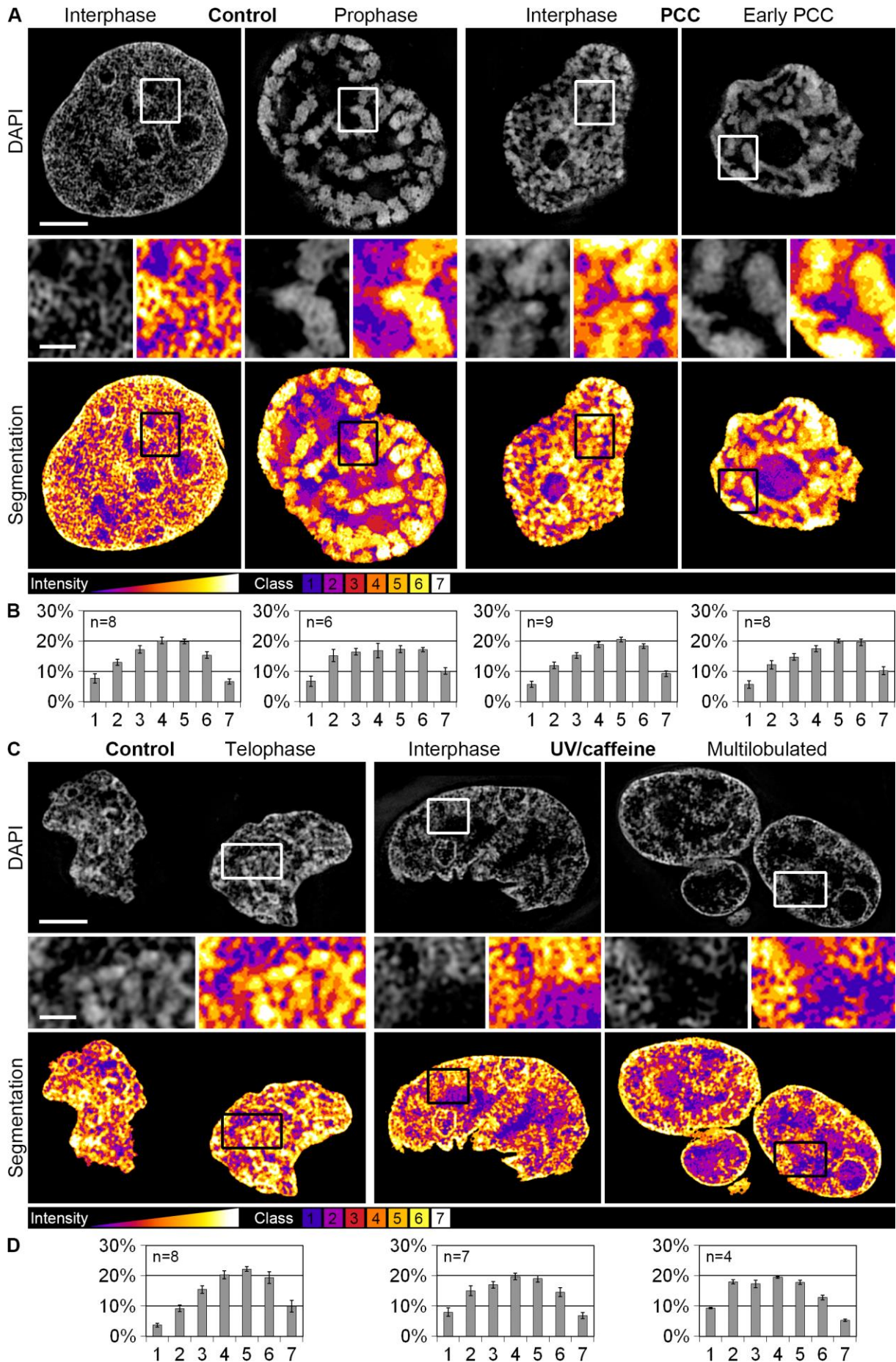


Figure 59: Comparison of the chromatin pattern in control and treated V79 cells (s. legend on previous page).

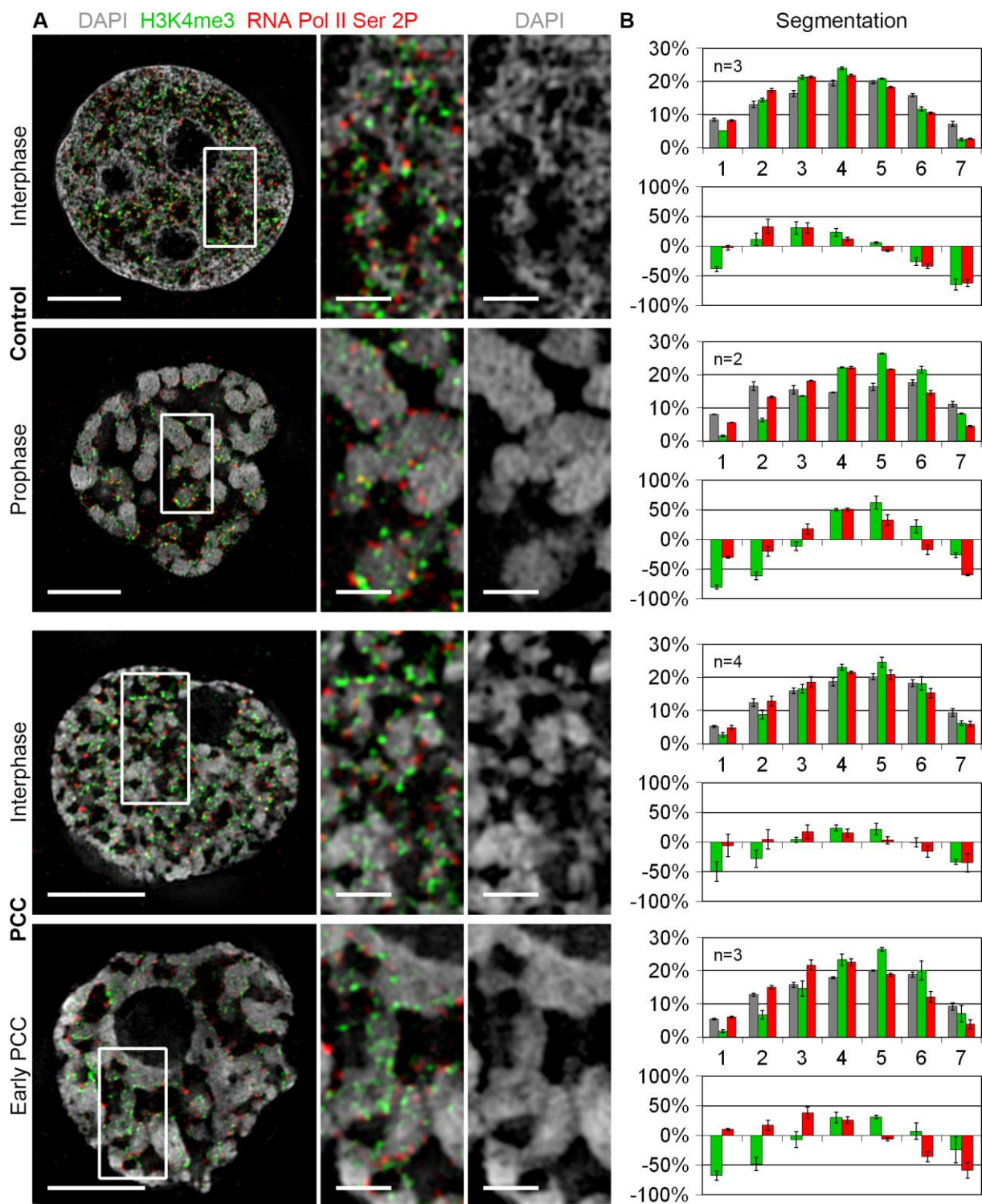


Figure 60: H3K4me3 and RNA Pol II Ser 2P in control and PCC induced V79 cells. (A) DAPI stained DNA (gray), Histone 3 tri-methylated on lysine 4 (H3K4me3) (green) and RNA Polymerase II phosphorylated on serine 2 (RNA Pol II Ser 2P) (red) of PFA-fixed V79 cells either without treatment (control cells) (upper two images, interphase and prophase) or after PCC induction (lower two images, interphase and early PCC). Immunofluorescence for the detection of H3K4me3 and RNA Pol II Ser 2P was performed using rabbit-anti-H3K4me3 and rat-anti-RNA Pol II Ser 2P antibodies, followed by goat-anti-rabbit-Alexa488 and donkey-anti-rat-Alexa594 antibodies, respectively. Light optical mid-sections of whole 3D-SIM 3D acquisitions are shown. Left column: whole nuclei. Middle column: magnifications of the images in the left column. Right column: magnifications of the DAPI staining alone; same area as in the middle column. **(B)** Profiles of the chromatin distributions (gray) of whole 3D acquisitions after the segmentation of the DAPI signals into seven classes with increasing density from class 1 to 7, together with H3K4me3 (green) and RNA Pol II Ser 2P (red) assigned to the respective chromatin classes. For each image shown in (A) both the classical profile (upper graph) as well as (*legend continued on next page*)

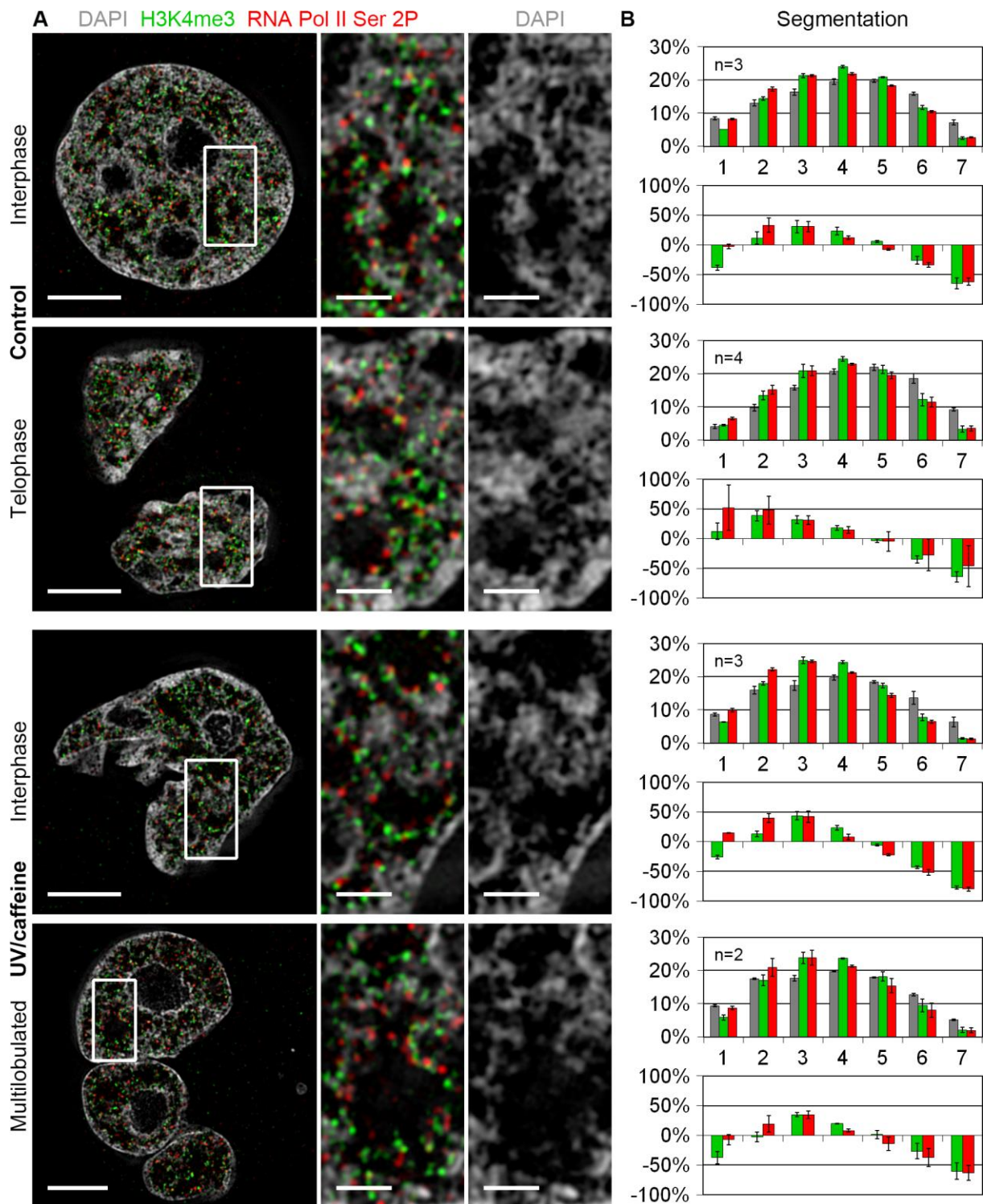


Figure 61: H3K4me3 and RNA Pol II Ser 2P in control and UV/caffeine treated V79 cells. Equivalent to **Figure 60**, therefore the legend is shortened here. **(A)** PFA-fixed V79 cells either without treatment (control cells) (upper two images, interphase, and telophase) or after UV/caffeine treatment (lower two images, interphase and multilobulated cell) are shown. The control interphase cell is repeated from **Figure 60** in order to facilitate the comparison with the other cell types. **(B)** Profiles of the chromatin distributions (gray) of whole 3D acquisitions with H3K4me3 (green) and RNA Pol II Ser 2P (red) assigned to the respective chromatin classes. For statistical evaluations please refer to **Figure 64**. Error bars: standard deviation. Scale bars: 4 μm in images of whole nuclei, 1 μm in magnifications.

Figure 60: (*legend continued from previous page*) the calculated over- and underrepresentation of H3K4me3 and RNA Pol II Ser 2P in comparison to DAPI (lower graph) is included. Average curves of multiple whole 3D acquisitions are shown. For statistical evaluations please refer to **Figure 64**. Error bars: standard deviation. Scale bars: 4 μm in images of whole nuclei, 1 μm in magnifications.

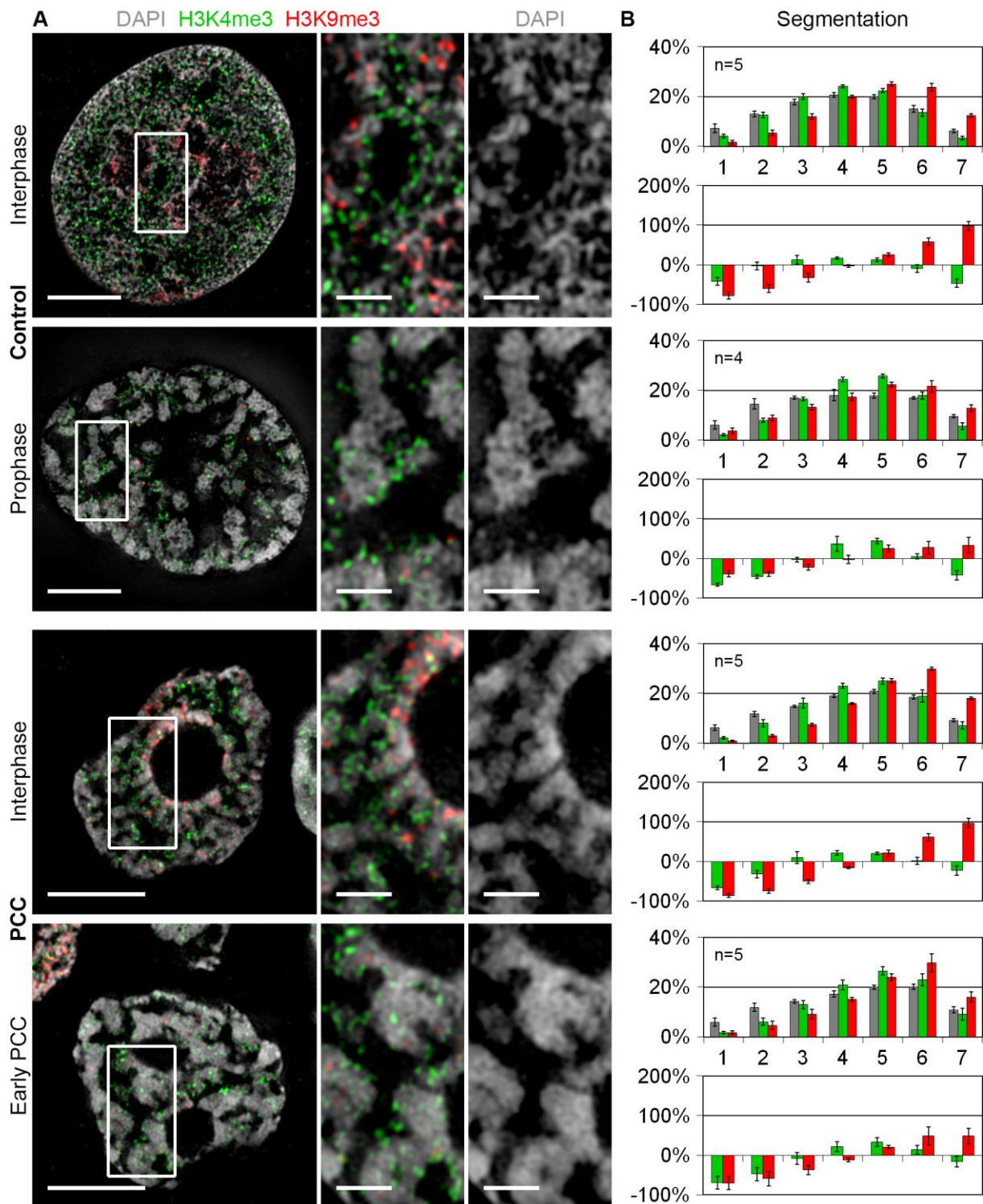


Figure 62: H3K4me3 and H3K9me3 in control and PCC induced V79 cells. Equivalent to **Figure 60**, therefore the legend is shortened here. **(A)** DAPI stained DNA (gray), Histone 3 tri-methylated on lysine 4 (H3K4me3) (green) and Histone 3 tri-methylated on lysine 9 (H3K9me3) (red) of PFA-fixed V79 cells either without treatment (control cells) (upper two images, interphase and prophase) or after PCC induction (lower two images, interphase and early PCC). Immunofluorescence for the detection of H3K4me3 and H3K9me3 was performed using rabbit-anti-H3K4me3 and mouse-anti-H3K9me3 antibodies, followed by goat-anti-rabbit-Alexa488 and goat-anti-mouse-Alexa594 antibodies, respectively. **(B)** Profiles of the chromatin distributions (gray) of whole 3D acquisitions with H3K4me3 (green) and H3K9me3 (red) assigned to the respective chromatin classes. For statistical evaluations please refer to **Figure 64**. Error bars: standard deviation. Scale bars: 4 μ m in images of whole nuclei, 1 μ m in magnifications.

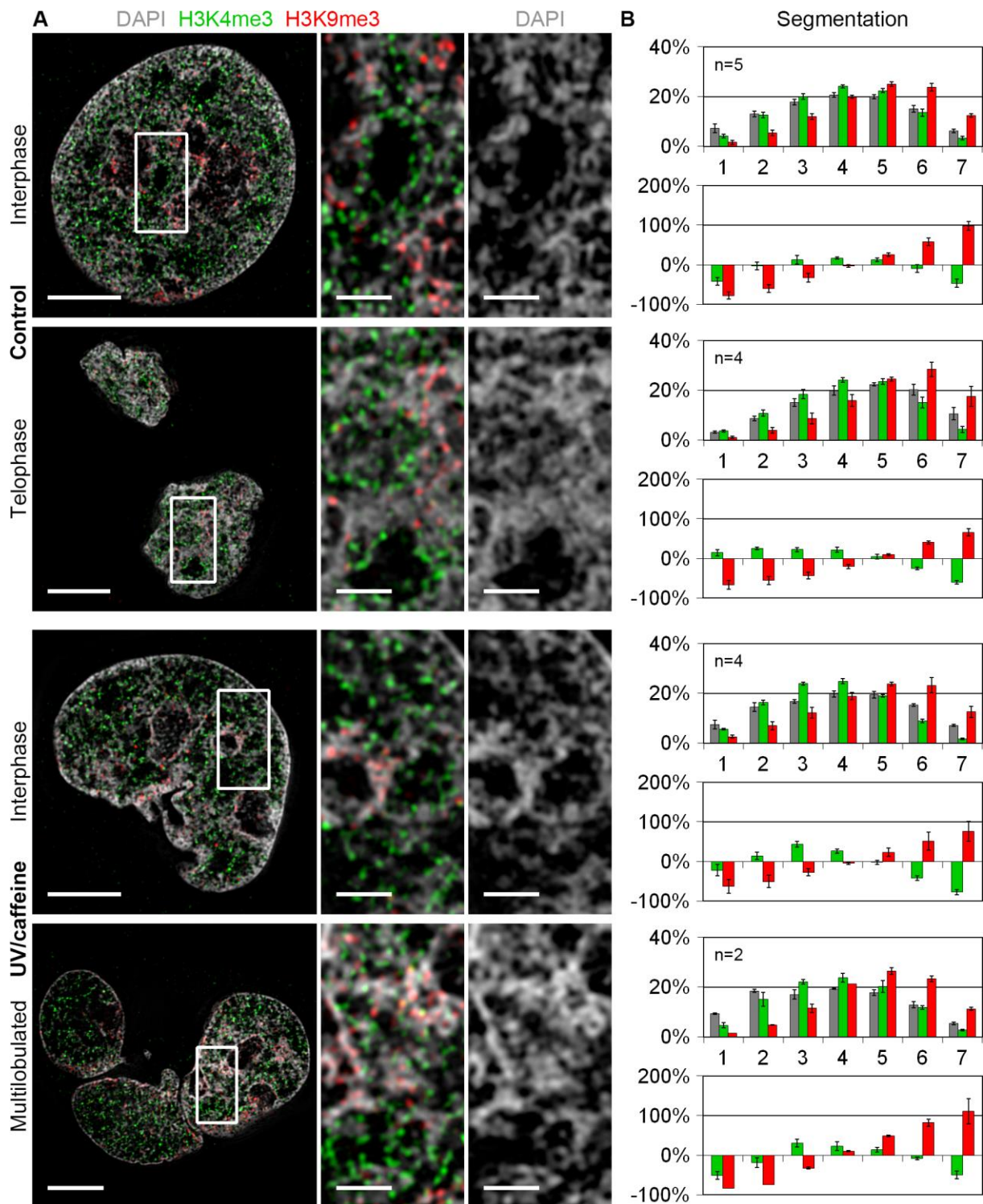


Figure 63: H3K4me3 and H3K9me3 in control and UV/caffeine treated V79 cells. Equivalent to **Figure 60**, therefore the legend is shortened here. **(A)** DAPI stained DNA (gray), Histone 3 tri-methylated on lysine 4 (H3K4me3) (green) and Histone 3 tri-methylated on lysine 9 (H3K9me3) (red) of PFA-fixed V79 cells either without treatment (control cells) (upper two images, interphase and telophase) or after UV/caffeine treatment (lower two images, interphase and multilobulated cell). The control interphase cell is repeated from **Figure 62** in order to facilitate the comparison with the other cell types. Immunofluorescence for the detection of H3K4me3 and H3K9me3 was performed using rabbit-anti-H3K4me3 and mouse-anti-H3K9me3 antibodies, followed by goat-anti-rabbit-Alexa488 and goat-anti-mouse-Alexa594 antibodies, respectively. **(B)** Profiles of the chromatin distributions (gray) of whole 3D acquisitions with H3K4me3 (green) and H3K9me3 (red) assigned to the respective chromatin classes. For statistical evaluations please refer to **Figure 64**. Error bars: standard deviation. Scale bars: 4 μ m in images of whole nuclei, 1 μ m in magnifications.

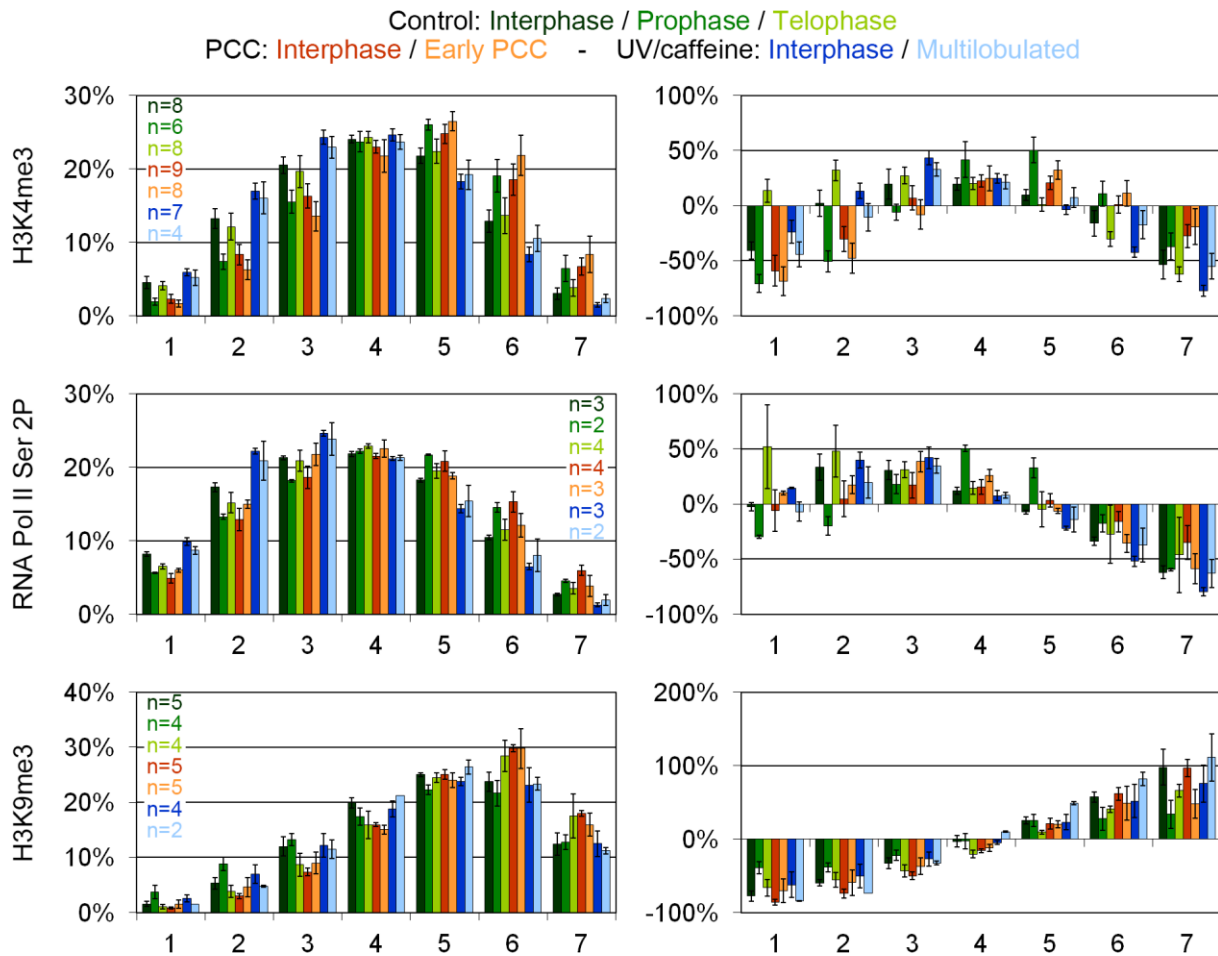


Figure 64: Comparison of markers in control, PCC induced and UV/caffeine treated V79 cells. Profiles of Histone 3 tri-methylated on lysine 4 (H3K4me3), RNA Polymerase II phosphorylated on serine 2 (RNA Pol II Ser 2P) and Histone 3 tri-methylated on lysine 9 (H3K9me3) (from top to bottom) after assigning them to the respective chromatin classes of the corresponding segmentations of the DAPI signals into seven classes with increasing intensity from 1 to 7. Average curves of multiple whole 3D acquisitions are depicted. For each marker both the classical profile (left) as well as the calculated over- and underrepresentation in comparison to DAPI (right) is shown. In each graph the curves for interphase, prophase, and telophase in control cells (dark green, green, light green, respectively), interphase and early PCC cells (red, orange, respectively), and UV/caffeine treated interphase and multilobulated cells (blue, light blue, respectively) are included. For H3K4me3 statistical differences were found between the profiles of control interphase vs. prophase (very significant, $p < 0.01$), vs. interphase PCC cells (significant, $p < 0.05$) and vs. early PCC cells (highly significant, $p < 0.001$), of prophase vs. both UV/caffeine treated interphase and multilobulated cells (highly significant, $p < 0.001$), of telophase vs. early PCC cells (very significant, $p < 0.01$), of interphase PCC cells vs. UV/caffeine treated interphase cells (highly significant, $p < 0.001$) and vs. multilobulated cells (very significant, $p < 0.01$) and of early PCC cells vs. both UV caffeine treated interphase and multilobulated cells (highly significant, $p < 0.001$). For RNA Pol II Ser 2P the distributions differed significantly ($p < 0.05$) for control interphase vs. interphase PCC cells, interphase PCC cells vs. UV/caffeine treated interphase and multilobulated cells, prophase vs. telophase and early PCC cells and very significantly ($p < 0.01$) for prophase vs. interphase PCC cells. For H3K9me3 statistical differences were found between the distributions of normal interphase vs. interphase PCC cells (significant, $p < 0.05$), of prophase vs. both UV/caffeine treated interphase and multilobulated cells (very significant, $p < 0.01$), of telophase vs. UV/caffeine treated interphase cells (significant, $p < 0.05$), of interphase PCC vs. UV/caffeine treated interphase (highly significant, $p < 0.001$) and multilobulated cells (very significant, $p < 0.01$) and of early PCC vs. UV/caffeine treated interphase cells (significant, $p < 0.05$). Between markers, statistical tests showed the following results: RNA Pol II Ser 2P and H3K4me3 differed in prophase (significant, $p < 0.05$), in early PCC cells (highly significant, $p < 0.001$) and in UV/caffeine treated interphase cells (very significant, $p < 0.01$). The distributions of both RNA Pol II Ser 2P and H3K4me3 differed from H3K9me3 highly significantly ($p < 0.001$) in all cases apart from H3K9me3 vs. RNA Pol II Ser 2P in prophase and H3K9me3 vs. H3K4me3 in early PCC cells were however still very significant ($p < 0.01$) respectively significant ($p < 0.05$) differences were found. Only for H3K9me3 vs. H3K4me3 (*legend continued on next page*)

Figure 64: (*legend continued from previous page*) in prophase no difference was detected ($p=0.411$). Note that the Wilcoxon rank-sum test used here can only check for differences in the mean value, not in the actual distribution. Error bars: standard deviation.

Summary of section 4.3

Characterization of nuclear phenotypes after UV irradiation and caffeine posttreatment (UV/caffeine treatment) or premature chromosome condensation (PCC) in V79 cells

After both UV/caffeine treatment and PCC induction similar nuclear phenotypes with shattered chromatin were observed after MAA fixation, termed GCS and S PCC, respectively. GCS was the fixation outcome of PALCCs, S PCCs of early and middle PCC stages.

Several markers (lamin B, H3S10p, centromeres, Ki67, α -tubulin, SMC2, H3K4me3, RNA Pol II Ser 2P, H3K9me3) and chromosome painting identified PALCCs as abnormal mitotic cells with a condensation failure. They did not divide correctly and as a consequence gave rise to abnormal multilobulated interphase cells. PALCCs and therefore also GCS did not represent cells in S phase. Also PCC induced cells corresponded to mitotic cells, however, they did not proceed to interphase. G1/G2 PCCs (deriving from middle-late and late PCC stages) were typically but not exclusively BrdU negative, while a significant part but not all S PCCs was BrdU positive. These observations characterize the processes occurring after UV/caffeine treatment and after PCC induction as two different although in both cases mitotic phenomena.

Despite the variable chromatin patterns in control, PCC induced and UV/caffeine treated cells, the functional nuclear architecture was consistent on a global level in all selected conditions analyzed here: H3K4me3 was mainly located at the surface of the chromatin domain clusters, RNA Pol II Ser 2P was found almost exclusively in this region and H3K9me3 was preferentially located on compacted chromatin.

4.4 Correlative microscopy – exemplified by studies of functional nuclear architecture in HeLa cells with hypercondensed chromatin (HCC)

As an alternative way to induce chromosome condensation, HeLa cells were subjected to high salt treatment which was shown previously to lead to the formation of hypercondensed chromatin (HCC) (see section 2.5.1 in the introduction). Again, the analysis of the functional nuclear architecture of these cells compared to control cells was the focus of interest (see section 4.4.2). In addition, these experiments served to establish a pathway of correlative microscopy including live cell imaging, multi-color fluorescence (super-resolution) microscopy and transmission electron microscopy (TEM). Correlative microscopy, i.e. the subsequent visualization of one and the same cell with different microscopic techniques, is a valuable tool in single-cell analyses as it allows the combination of information that could not be obtained with a single approach.

Some of the results in this chapter were published in Hübner et al. (2013). Therefore, a part of the text and the figures was adapted from there.

4.4.1 Two pathways of correlative microscopy

Two slightly different pathways of correlative microscopy were developed: pathway I which included live cell imaging (here spinning disk laser scanning microscopy (SDLSM)), confocal laser scanning microscopy (CLSM) and transmission electron microscopy (TEM), and pathway II where in addition also super-resolution fluorescence microscopy (here three-dimensional structured illumination microscopy (3D-SIM)) was applied. **Figure 11** in section 3.2.10.1 of the methods chapter illustrates the two pathways and also explains the technical differences.

An example of correlative microscopy according to pathway I is given in **Figure 65**. The stepwise induction of HCC was imaged with SDLSM by making use of the stably transfected H2B-mRFP (Histone 2B tagged with mRFP) construct expressed in the HeLa cells used here (**Figure 65 A**). With increasing osmolarity chromatin condensed more and more and accordingly the interchromatin (IC) lacunas widened. Immunofluorescence stainings performed after the fixation of the cells and imaged with CLSM (**Figure 65 B**) showed that splicing speckles detected by SC35 were located in the larger IC lacunas that were already present under normal conditions at the start of the live cell experiment (**Figure 65**, arrowheads). H3K4me3 was mainly found on the condensed chromatin, demonstrating that transcriptionally competent chromatin retracted together with chromatin in general. After

embedding the cells in resin and cutting of ultra-thin sections DAPI fluorescence could be imaged again with CLSM (**Figure 65 B**, lower right). The fluorescence of the immunofluorescence staining, however, was not maintained in the resin (for information on a different resin see section 3.2.10.2, page 146). Finally, chromatin in the physical sections was stained with osmium ammine and imaged with TEM (**Figure 65 D**). Here the distinct separation between the highly compacted chromatin domain clusters (CDCs) (circles) and the expanded IC (asterisks) after HCC induction became very apparent. A comparison of the TEM image (**Figure 65 D**, middle) with the corresponding areas acquired with SDLSM and CLSM – both with the optical sections of the 3D acquisitions and the image of the physical section – (**Figure 65 C**) demonstrates the increase in resolution from SDLSM to CLSM to TEM as well as from optical to physical sections. Accordingly, a successively sharper and more detailed image of the chromatin pattern could be obtained.

The corresponding experiment to **Figure 65** without the induction of HCC (**Figure 66**) confirmed the localization of the splicing speckles in the interior of the IC lacunas also under normal conditions (**Figure 66**, arrowheads), although they were typically associated more closely with chromatin as in HCC induced cells. As expected chromatin in these cells was much more homogeneously distributed, but also here areas of more condensed chromatin and IC lacunas largely free of DNA became apparent, especially in the TEM images (**Figure 66 D**). H3K4me3 was distributed rather uniformly across the nucleus, sparing basically only nucleoli, larger IC lacunas, and regions with very condensed DNA (**Figure 66 B**).

Figure 67+68 depict the corresponding experiments to **Figure 65+66** following pathway II of correlative microscopy, i.e. including also 3D-SIM in the analysis. The images of both conditions, of HCC induced cells (**Figure 67**) and of control cells (**Figure 68**), confirmed the observations made in **Figure 65+66** (see descriptions above). However, 3D-SIM provided much more details of the DAPI and H3K4me3 stainings and correspondingly a much better insight into the nuclear architecture of these cells. This correlative microscopy approach clearly demonstrates the immense advantage of super-resolution microscopy over conventional fluorescence microscopy. A twofold increase in resolution in each spatial direction (Schemmelleh et al. 2010) might sound little, but in 3D this represents an eightfold increase and the images leave no doubt about the impact of this improvement. For a detailed explanation of the localization of the marker signals see section 4.4.2 below. The 3D-SIM images furthermore revealed that – at least in the HeLa (H2B-mRFP) cells used for these experiments – nucleoli and IC lacunas can be distinguished by the lack of H3K4me3 staining at the inside of the former ones (**Figure 67+68**, arrows). Splicing speckles stained by SC35 were not imaged with 3D-SIM, but the comparison with the CLSM images allowed to draw conclusions about their localization.

Further examples for correlative microscopy according to pathway II are provided in **Figure 69+70**. In addition to H3K4me3 here RNA Pol II Ser 2P respectively H3K9me3 were detected after HCC induction. Also here the 3D-SIM acquisitions provided a much more detailed insight into the nuclear architecture of these cells (again, see section 4.4.2 below). Equivalent to H3K4me3 (compare also **Figure 67+68**), also RNA Pol II Ser 2P was found at the inside of IC lacunas, but not of nucleoli (**Figure 69**, arrows). For inactive chromatin marked by H3K9me3, the differences between 3D-SIM and CLSM were much less pronounced. Both microscopic techniques showed that this marker was mainly found in the interior of the more condensed CDCs (**Figure 70 B-C**). The stained regions already exhibited a high chromatin density at the start of the live cell experiment under normal conditions prior to HCC induction (**Figure 70 A**, arrowheads).

Figure 65: (*legend continued from next page*) on lysine 4 (H3K4me3) (red). The detection was performed using mouse-anti-SC35 and rabbit-anti-H3K4me3 antibodies followed by goat-anti-mouse-Cy5 and donkey-anti-rabbit-Alexa594 antibodies, respectively. DNA was stained with DAPI (gray). The merged image is shown in the upper right, the DAPI staining alone in the lower left. Corresponding xz-views are shown in the upper left. The lower right image was acquired from an ultrathin (100 nm) physical section obtained after resin embedding. The DAPI signals could still be visualized but not the fluorescence from the immunofluorescence staining. Note that some shrinkage of the nucleus occurred during the embedding process (compare the scale bars in the two lower images). **(C)** Magnifications of the live cell image acquired with SDLSM (highest level of HCC, i.e. 570 mOsm) (left), the CLSM image from the whole 3D acquisition (middle) and the CLSM image obtained from the physical section (right) depicted in (A) respectively (B). Chromatin stained by H2B-mRFP (live cell) respectively DAPI (CLSM) is shown. **(D)** TEM images of the same section shown in (B) with osmium ammine stained DNA. Physical section. Left: whole nucleus. Middle and right: magnification of the respective image on the left. The first magnification (middle) is equivalent to the magnifications shown in (C). Circles = compacted chromatin domain clusters (CDCs), asterisks = expanded IC. Only occasionally fiber-like bundles of less condensed chromatin (arrow) connecting HCC clusters were observed. However, these fibers could also represent HCC clusters that were cut very peripherally. The light optical sections in (A) and (B) were selected in such a way from the whole 3D acquisitions that they matched the CLSM and TEM images of the physical section (B lower right, C) in the best possible way. Selected IC lacunas are marked by arrowheads. Scale bars: 4 μm in images of whole nuclei, 1 μm in magnifications (except for the second magnification of the TEM image (D, right), here 0.25 μm). Figure adapted from Hübner et al. (2013).

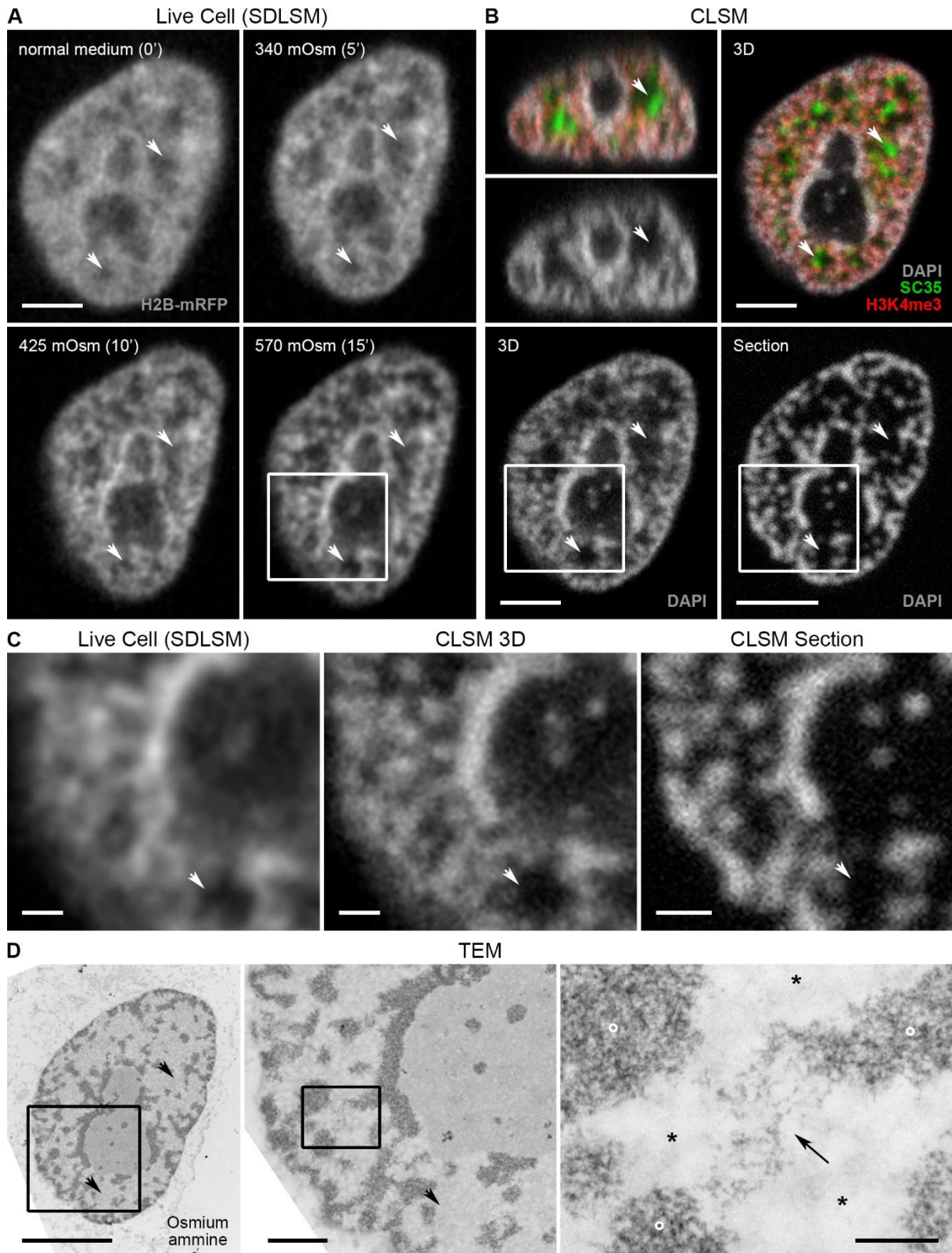


Figure 65: Correlative microscopy (pathway I) in HCC induced HeLa cells; SC35 and H3K4me3. For details regarding pathway I and II of correlative microscopy see **Figure 11**; the main difference is that in pathway I 3D-SIM is not included. **(A)** Chromatin (H2B-mRFP, gray) in living HeLa (H2B-mRFP) cells was imaged on a SDLISM during the stepwise induction of HCC, achieved by increasing the osmolarity of the medium from normal conditions (= 290 mOsm) (top left) over 340 mOsm (top right) and 425 mOsm (bottom left) to 570 mOsm (bottom right) in 5 min intervals. Light optical mid-sections of whole 3D acquisitions are shown. **(B)** Light optical mid-sections of whole CLSM 3D acquisitions of the same nucleus shown in (A) after fixation with PFA, bleaching of the H2B-mRFP signals and immunofluorescence staining for SC35 (green) and Histone 3 tri-methylated (*legend continued on previous page*)

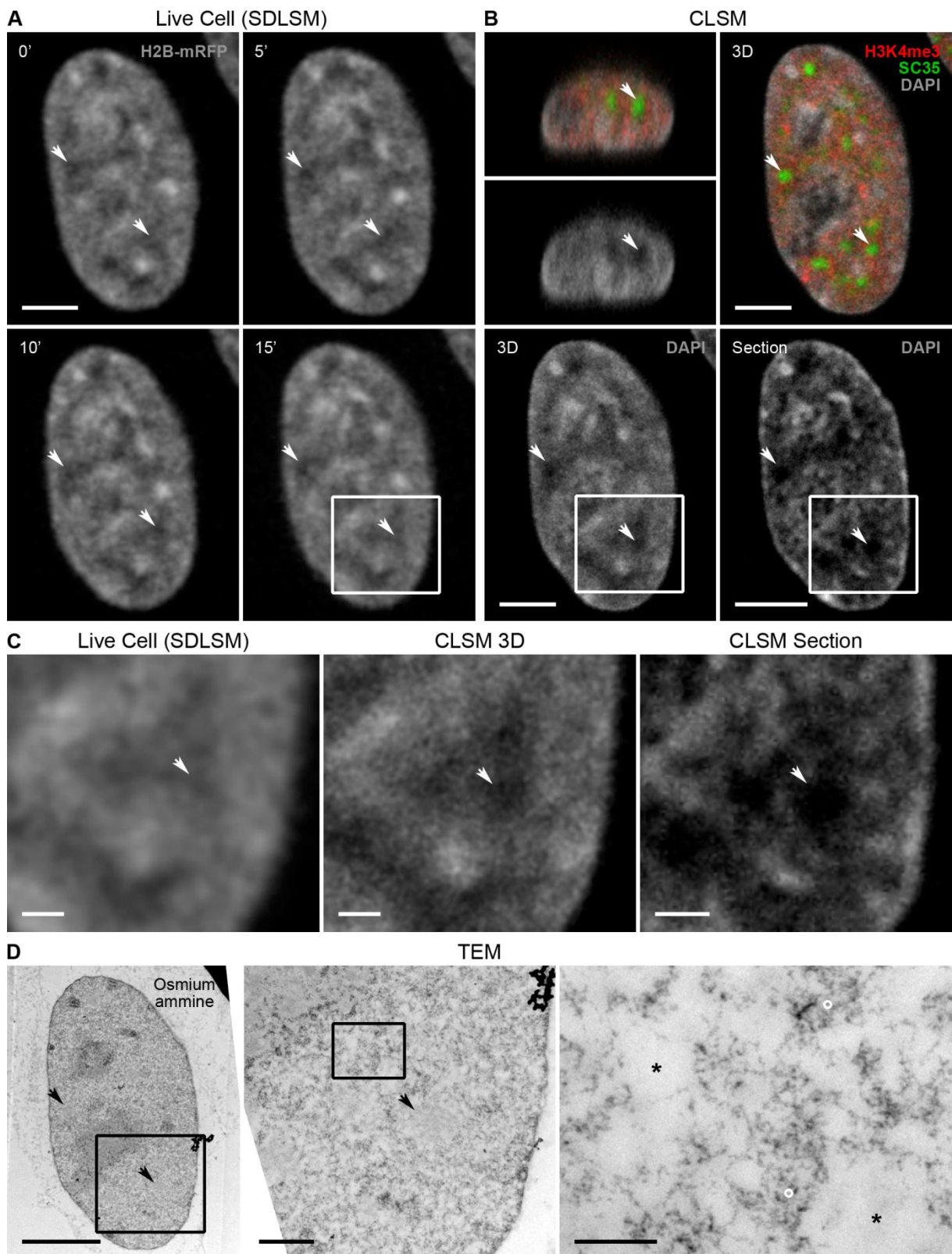


Figure 66: Correlative microscopy (pathway I) in control HeLa cells; SC35 and H3K4me3. Equivalent to **Figure 65**, therefore the legend is shortened here. Control cells without PCC induction. **(A)** Chromatin (H2B-mRFP, gray) in living HeLa (H2B-mRFP) cells was imaged on a SDLSM every 5 min over a total period of 15 min. **(B)** CLSM images after fixation and immunofluorescence staining. DAPI (gray), H3K4me3 (red), SC35 (green). **(C)** Magnifications of the live cell image acquired with SDLSM (last time point, i.e. 15 min) (left), the CLSM image from the whole 3D acquisition (middle) and the CLSM image obtained from the physical section (right) depicted in (A) respectively (B). **(D)** Circles = more condensed chromatin domain clusters (CDCs), asterisks = IC lacunas. Note that the staining quality was fine in the higher magnifications although the small magnification (*legend continued on page 253*)

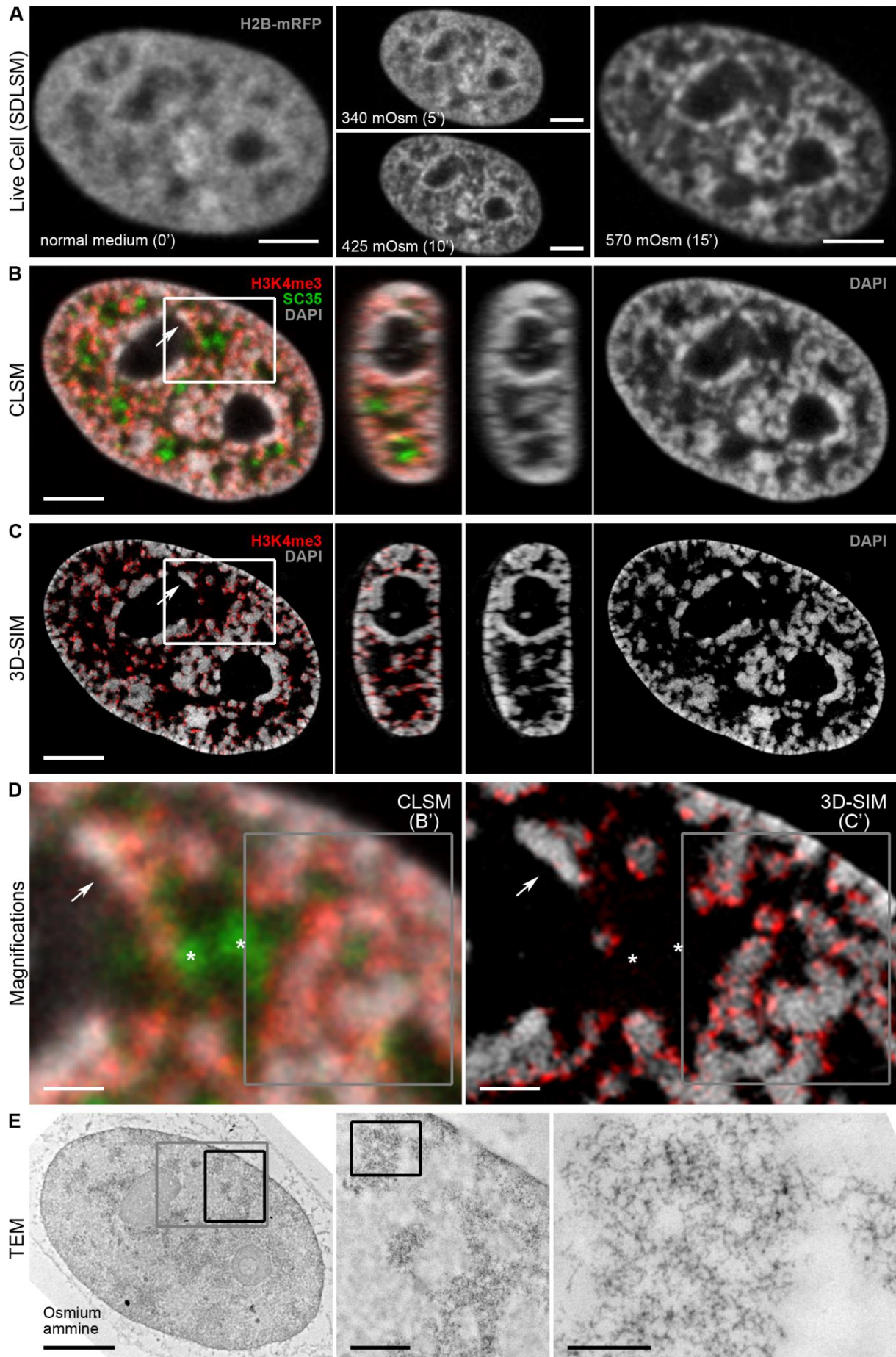


Figure 67: Correlative microscopy (pathway II) in HCC induced HeLa cells (see legend on page 253).

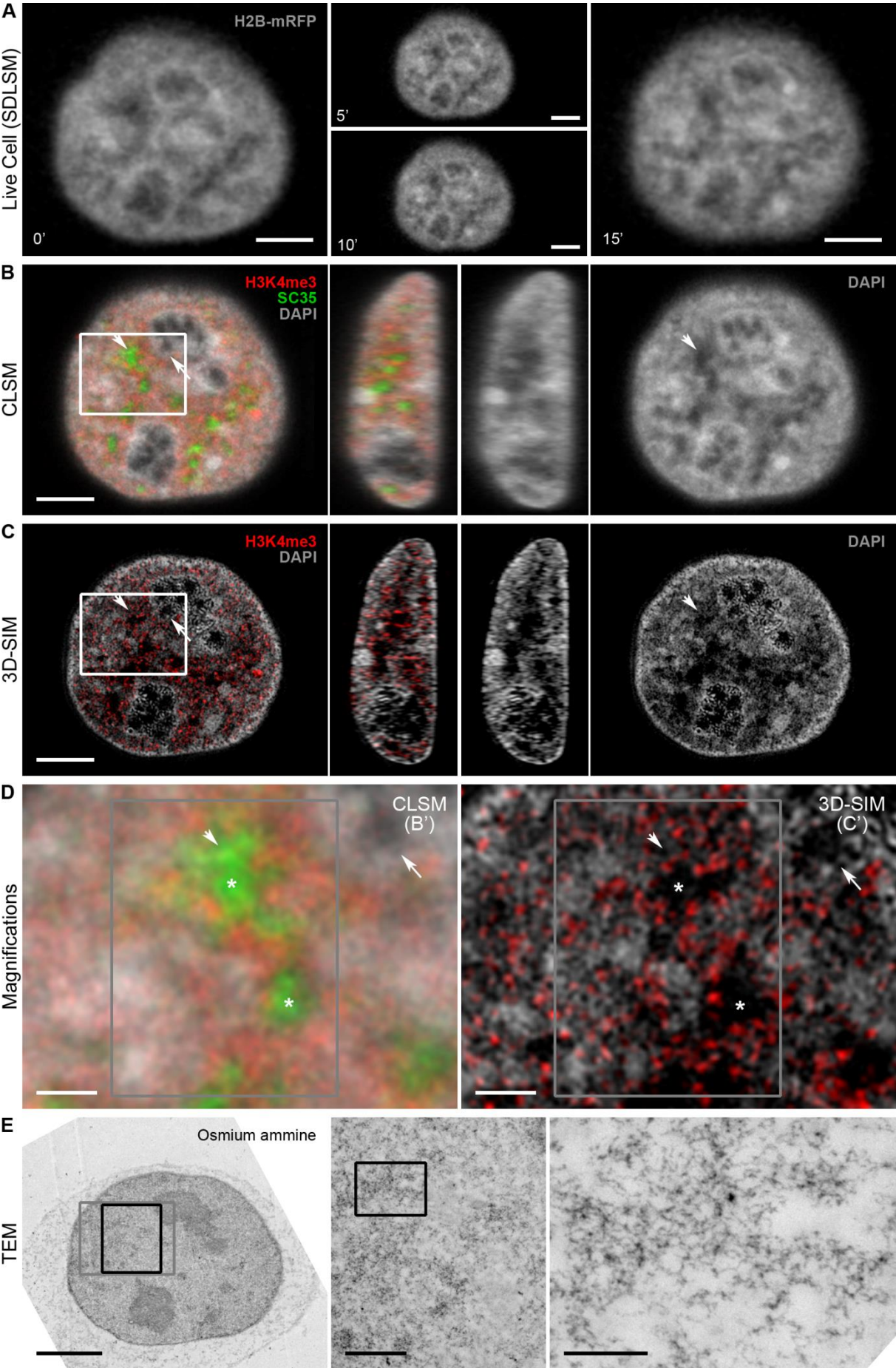


Figure 68: Correlative microscopy (pathway II) in control HeLa cells (see legend on next page).

Figure 66: (*legend continued from page 250*) of the whole cell (right) gave a rather poor impression. Scale bars: 4 μm in images of whole nuclei, 1 μm in magnifications (except for the second magnification of the TEM image (D, right), here 0.25 μm).

Figure 67: Correlative microscopy (pathway II) in HCC induced HeLa cells; SC35 and H3K4me3. For details regarding pathway I and II of correlative microscopy see **Figure 11**; the main difference is that in pathway II 3D-SIM is included. **(A)** Chromatin (H2B-mRFP, gray) in living HeLa (H2B-mRFP) cells was imaged on a SDLSM during the stepwise induction of HCC achieved by increasing the osmolarity of the medium from normal conditions (= 290 mOsm) (left) over 340 mOsm (middle, top) and 425 mOsm (middle, bottom) to 570 mOsm (right) in 5 min intervals. Light optical mid-sections of whole 3D acquisitions are shown. **(B, C, D)** Light optical mid-sections of whole CLSM (B) or 3D-SIM (C) 3D acquisitions of the same nucleus shown in (A) after fixation with PFA, bleaching of the H2B-mRFP signals and immunofluorescence staining for SC35 (green) and Histone 3 tri-methylated on lysine 4 (H3K4me3) (red). The detection was performed using mouse-anti-SC35 and rabbit-anti-H3K4me3 antibodies followed by goat-anti-mouse-Cy5 and donkey-anti-rabbit-Alexa594 antibodies, respectively. DNA was stained with DAPI (gray). The merged image is shown on the left, the DAPI-staining alone on the right. Corresponding yz-views are shown in the middle. Note that the splicing speckles could only be imaged with CLSM, not with 3D-SIM. Magnifications of the merged images depicted in (B) and (C) are shown in (D). The magnification of the CLSM image is shown on the left (B'), the one of the 3D-SIM image on the right (C'). Although splicing speckles were not imaged with 3D-SIM, their localization was obvious from the comparison with the CLSM image (asterisks). Arrows point at the inner borders of nucleoli. **(E)** TEM images with osmium ammine stained DNA corresponding to the images shown in (A-C) acquired from the physical section. Left: whole nucleus. Middle and right: magnification of the respective image on the left. The gray box in the left image marks the corresponding area to the magnifications shown in (D). The first magnification (middle) is equivalent to the boxed areas in (D). Note that the staining quality was fine in the higher magnifications although the small magnification of the whole cell (right) gave a rather poor impression. The light optical sections in (A) and (B) were selected in such a way from the whole 3D acquisitions that they matched the CLSM and TEM images of the physical section (B lower right, C) in the best possible way. Scale bars: 4 μm in images of whole nuclei, 1 μm in magnifications (except for the second magnification of the TEM image (E, right), here 0.25 μm). Figure adapted from Hübner et al. (2013).

Figure 68: Correlative microscopy (pathway II) in control HeLa cells; SC35 and H3K4me3. Equivalent to **Figure 67**, therefore the legend is shortened here. Control cells without PCC induction. **(A)** Chromatin (H2B-mRFP, gray) in living HeLa (H2B-mRFP) cells was imaged on a SDLSM every 5 min over a total period of 15 min. **(B, C, D)** CLSM (B) or 3D-SIM (C) images after fixation and immunofluorescence staining. Magnifications are shown in (D). DAPI (gray), H3K4me3 (red), SC35 (green). Note the splicing speckle marked by an arrowhead is also located in an IC lacuna, although the 3D-SIM image gives a different impression. This discrepancy can be explained by the increased resolution of 3D-SIM in comparison to CLSM (i.e. more out-of-focus signals of SC35 are included in the optical section of CLSM) and the not always perfect match between images obtained from different microscopes. Arrows point at the inner borders of nucleoli. **(E)** TEM images with osmium ammine stained DNA. Scale bars: 4 μm in images of whole nuclei, 1 μm in magnifications (except for the second magnification of the TEM image (D, right), here 0.25 μm).

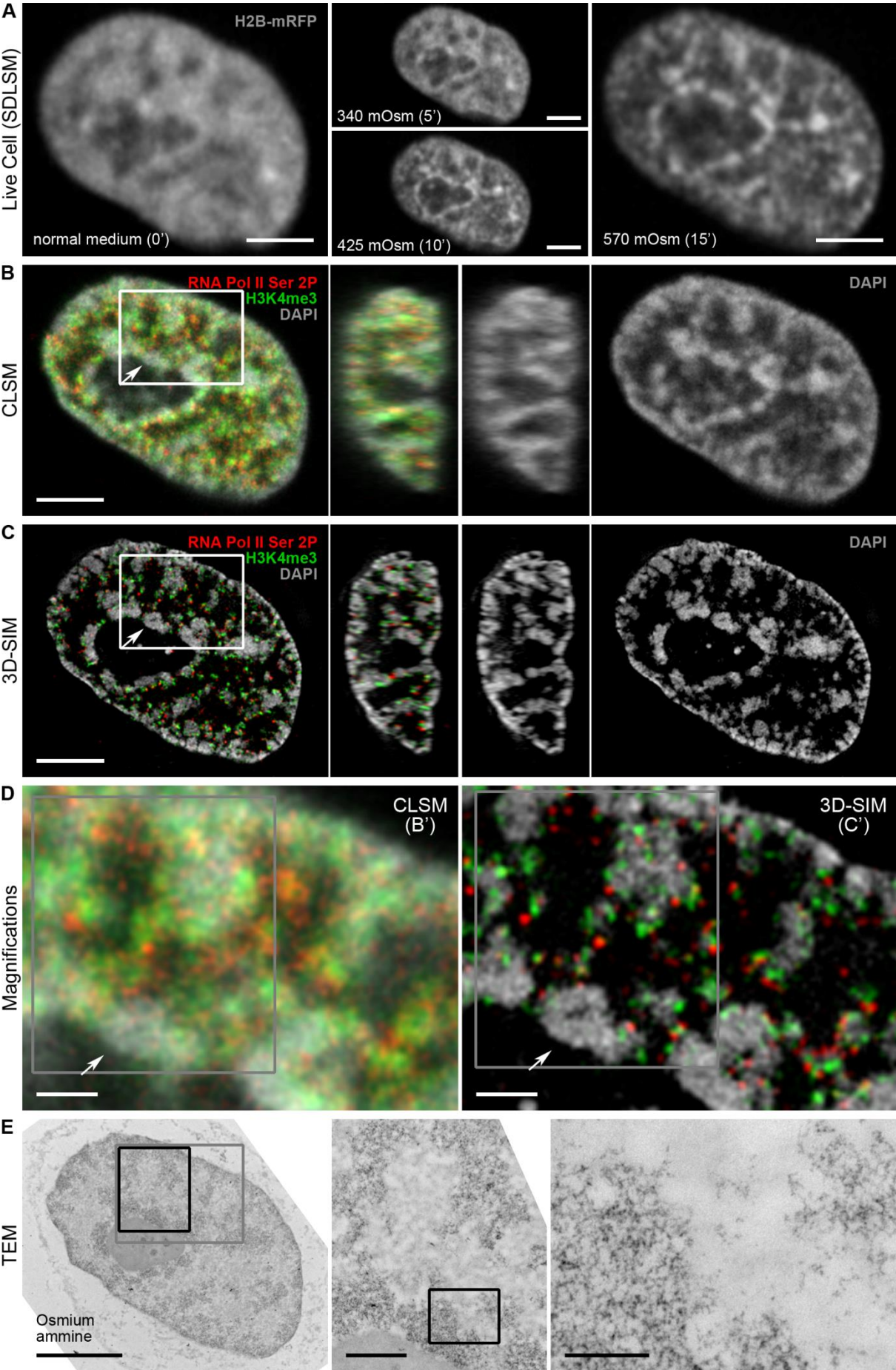


Figure 69: Correlative microscopy (pathway II) in HCC induced HeLa cells (see legend on page 256).

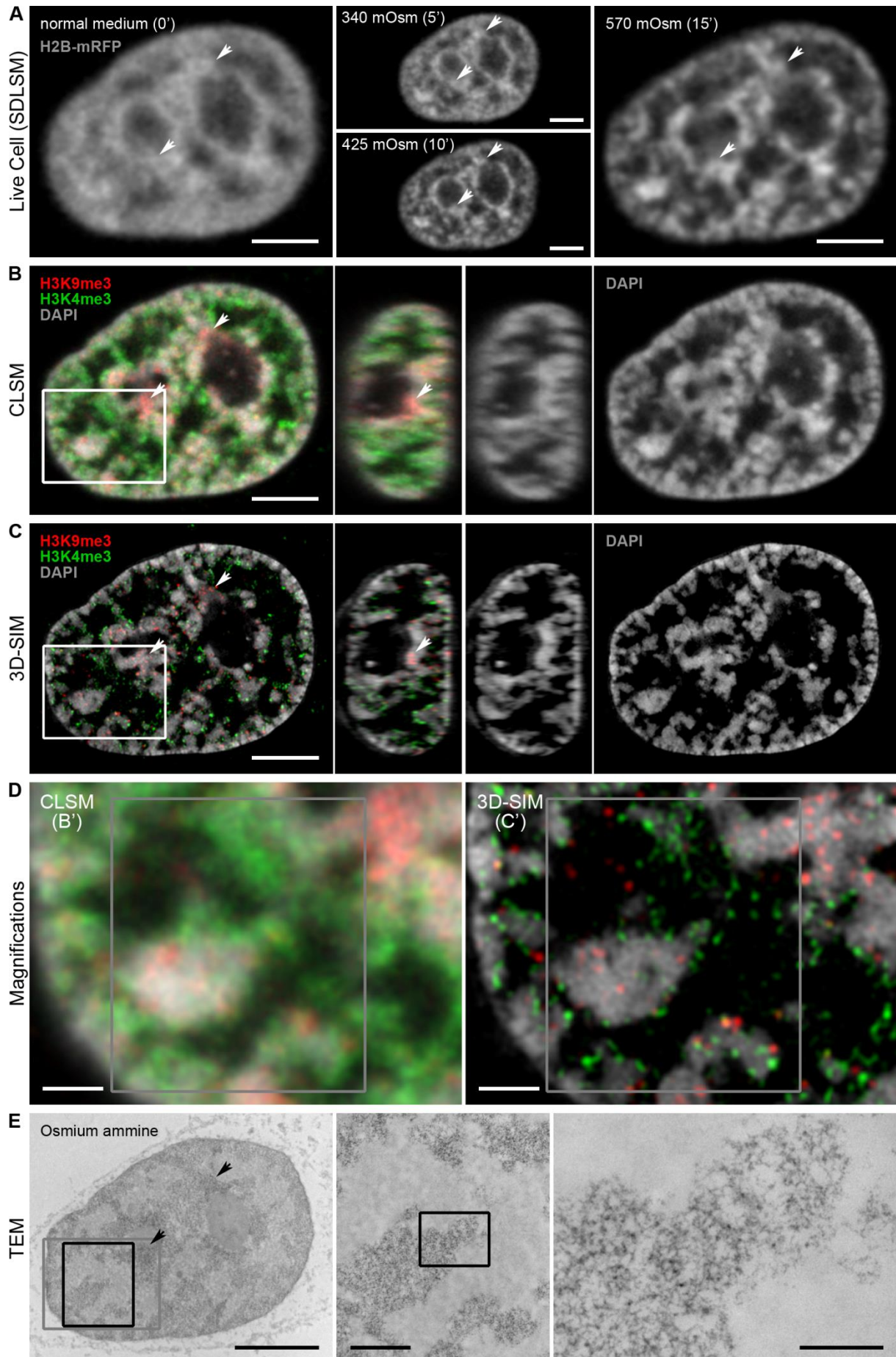


Figure 70: Correlative microscopy (pathway II) in HCC induced HeLa cells (see legend on next page).

Figure 69: Correlative microscopy (pathway II) in HCC induced HeLa cells; H3K4me3 and RNA Pol II Ser 2P. Equivalent to **Figure 67**, therefore the legend is shortened here. **(A)** Chromatin (H2B-mRFP, gray) in living HeLa (H2B-mRFP) cells was imaged with SDLSM during the stepwise induction of HCC. **(B, C, D)** CLSM (B) or 3D-SIM (C) images after fixation and immunofluorescence staining. Magnifications are shown in (D). Histone 3 tri-methylated on lysine 4 (H3K4me3) (green) and RNA Polymerase II phosphorylated on serine 2 (RNA Pol II Ser 2P) (red) were detected using rabbit-anti-H3K4me3 and rat-anti-RNA Pol II Ser 2P antibodies followed by donkey-anti-rabbit-DyLight488 and donkey-anti-rat-Alexa594 antibodies, respectively. DNA was stained with DAPI (gray). Arrows point at the inner border of nucleoli. For the evaluation of the localization of the markers see **Figure 72**. **(E)** TEM images with osmium ammine stained DNA. Scale bars: 4 μm in images of whole nuclei, 1 μm in magnifications (except for the second magnification of the TEM image (E, right), here 0.25 μm).

Figure 70: Correlative microscopy (pathway II) in HCC induced HeLa cells; H3K4me3 and H3K9me3. Equivalent to **Figure 67**, therefore the legend is shortened here. **(A)** Chromatin (H2B-mRFP, gray) in living HeLa (H2B-mRFP) cells was imaged with SDLSM during the stepwise induction of HCC. **(B, C, D)** CLSM (B) or 3D-SIM (C) images after fixation and immunofluorescence staining. Magnifications are shown in (D). Histone 3 tri-methylated on lysine 4 (H3K4me3) (green) and Histone 3 tri-methylated on lysine 9 (H3K9me3) (red) were detected using rabbit-anti-H3K4me3 and mouse-anti-H3K9me3 antibodies followed by goat-anti-rabbit-Alexa488 and goat-anti-mouse-Alexa594 antibodies, respectively. DNA was stained with DAPI (gray). Arrowheads point at chromatin domain clusters (CDCs) that exhibited a high chromatin density already in normal medium at the start of the live cell observation. For the evaluation of the localization of the markers see **Figure 73**. **(E)** TEM images with osmium ammine stained DNA. Scale bars: 4 μm in images of whole nuclei, 1 μm in magnifications (except for the second magnification of the TEM image (E, right), here 0.25 μm).

4.4.2 Consistent functional nuclear architecture in control and HCC induced cells

The chromatin patterns of control and HCC induced cells observed with both CLSM and 3D-SIM are shown in **Figure 71**: as already briefly mentioned in the previous section (section 4.4.1) the images of the DAPI staining (**Figure 71 A**, upper row) clearly demonstrate the condensed chromatin and the widened IC lacunas in HCC induced cells (right two images) in comparison to the control cells (left two images) as well as the increased resolution of 3D-SIM (second and last image) compared to CLSM (first and third image). The corresponding segmented images (for details see sections 4.1.1 and 3.2.12.5) are shown in the lower row of **Figure 71 A**, average segmentation profiles of multiple 3D acquisitions in **Figure 71 B**. Chromatin density increases from class 1 to class 7, i.e. from blue to white. With both microscopic approaches, CLSM and 3D-SIM, the fraction of signals in the lower chromatin classes was clearly elevated in HCC induced cells, representing the increased IC space of these cells. Surprisingly only a minor shift towards higher chromatin classes (for 3D-SIM) or even a reduction in the high chromatin classes (for CLSM) was observed in HCC cells compared to control cells. This might again be explained by the shortage of intermediate intensity values due to the condensed chromatin, the corresponding black-and-white appearance of the images of these cells and consequently the possibility of the segmentation algorithm creating artificial subclasses (for details see section 4.1.1).

To analyze functional nuclear architecture the images of the immunofluorescence stainings with H3K4me3 and RNA Pol II Ser 2P as well as H3K4me3 and H3K9me3 in HCC induced cells obtained in the correlative microscopy experiments described in section 4.4.1 (**Figure 69+70**) were compared with images acquired from untreated cells and the localization of the marker signals was evaluated in both conditions (**Figure 72+73**).

H3K4me3 and RNA Pol II Ser 2P, the “active” markers, showed a very similar localization in relation to chromatin: The 3D-SIM images revealed that in both, control and HCC induced cells, H3K4me3 (**Figure 72+73 A**, second and last row each) was mainly located at the surface of the CDCs and RNA Pol II Ser 2P (**Figure 72 A**, second and last row each) was found almost exclusively in this region. In both cases, the interior of the IC lacunas (characterized by no or extremely low DAPI signal) was basically free of staining. However, due to the condensed chromatin and the widened IC lacunas this preferential localization of the two markers was much clearer in HCC induced cells than in normal cells. In HCC induced cells a fraction of the H3K4me3 signals was also found on more condensed chromatin, certainly resulting from the increased condensation. In contrast to that the corresponding CLSM images (**Figure 72+73 A**, first and third row each) only very vaguely suggested this specific

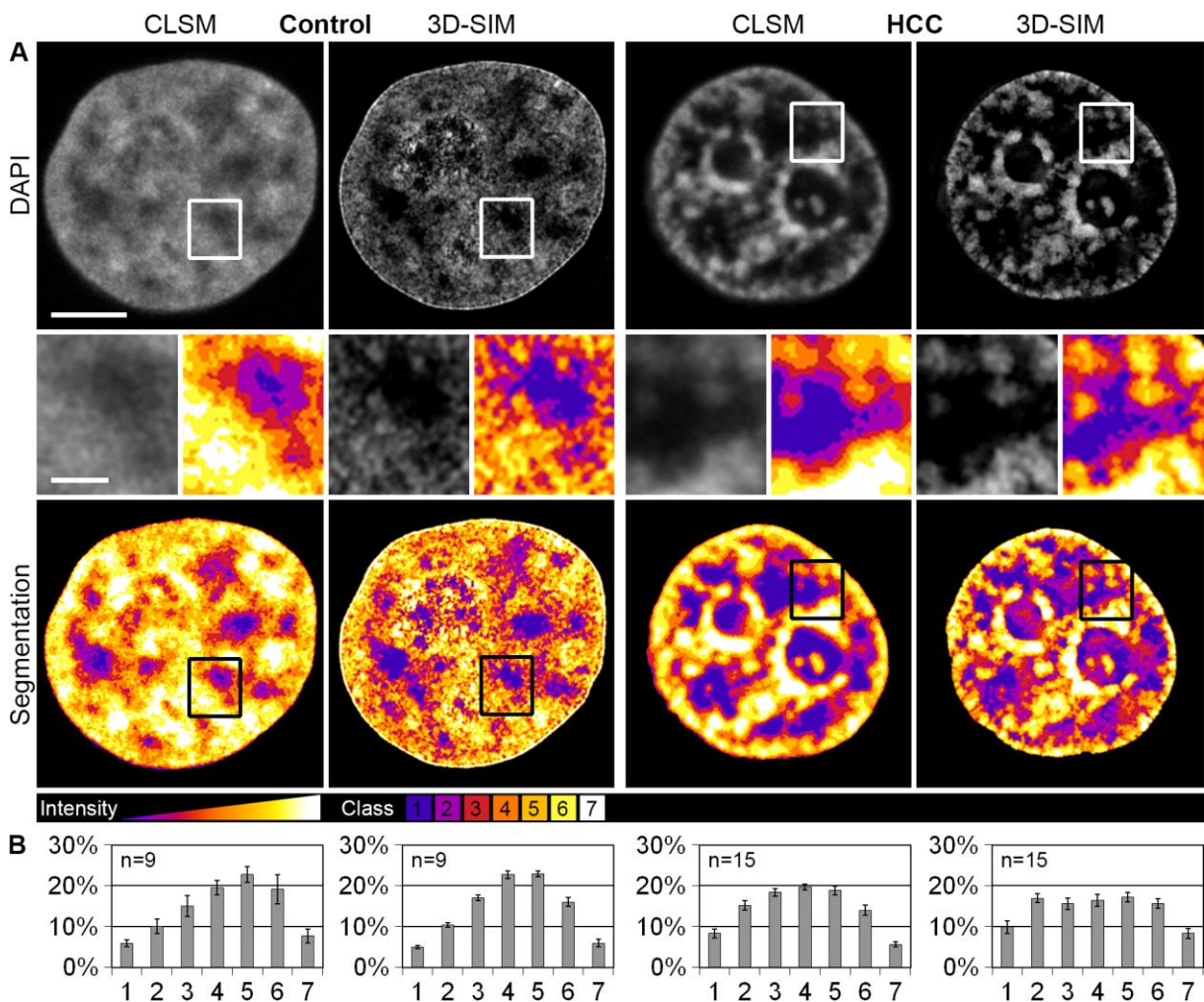
organization and instead gave the impression that the staining was rather uniformly distributed sparing basically only nucleoli, larger IC lacunas, and regions with very condensed chromatin. Only for RNA Pol II Ser 2P in HCC induced cells the CLSM images (**Figure 72 A**, third row) hinted at a preferential localization. For the “inactive” marker, H3K9me3, the differences between the CLSM images (**Figure 73 A**, first and third row) and the 3D-SIM images (**Figure 73 A**, second and last row) were much less pronounced than for the “active” markers described above. Both microscopic techniques showed that the staining was mainly found in the interior of the more condensed CDCs in both control as well as HCC induced cells. Not all compacted chromatin was stained. Again the interior of the IC lacunas was basically free of staining.

For H3K9me3 (**Figure 73 B**) the corresponding profiles of the marker signals mapped to the segmented DAPI intensity classes showed very consistent results for both conditions and both microscopic techniques: in all cases this marker was overrepresented (relative signal enrichment) in the high-intensity classes of more compact chromatin (classes 5-7) and correspondingly underrepresented (relative signal depletion) in the IC (class 1) as well as in the decondensed chromatin regions (classes 2-4). In contrast to that H3K4me3 (**Figure 72+73 B**) and RNA Pol II Ser 2P (**Figure 72 B**) exhibited variations in their localization. Consistent was an underrepresentation (relative signal depletion) of H3K4me3 in the lowest as well as the highest chromatin class (class 1 (the IC) and class 7) and of RNA Pol II Ser 2P in the two highest chromatin classes (classes 6+7). In the intermediate density classes around class 4, both markers were overrepresented (relative signal enrichment). This overrepresentation was clearly shifted towards lower density classes in the 3D-SIM images compared to the CLSM acquisitions as well as in control cells vs. HCC induced cells. Compared to H3K4me3 RNA Pol II Ser 2P was shifted towards lower chromatin classes.

Figure 74 summarizes the observations presented above by showing a comparison between all four conditions – i.e. control cells and HCC induced cells, each acquired with CLSM and 3D-SIM – for each marker in both the classical profiles (left) and the over- and underrepresentations (relative signal enrichment and depletion) (right) of the segmentation profiles. For H3K4me3 all available data from both immunofluorescence stainings were combined. Despite clear variations for H3K4me3 and RNA Pol II Ser 2P (for a detailed explanation see section 5.1.1, p. 267 in the discussion), the functional nuclear architecture was consistent on a global level in all different conditions.

The shift between the 3D-SIM data and the CLSM data is an indirect proof for the increased resolution of 3D-SIM. The acquisitions contain more details and therefore the specific

localization of signals can be resolved much better. For example, with the improved resolution small IC lacunas do not get covered up by out of focus signals, therefore the low-density areas are represented more realistically and as a consequence signals located in these chromatin classes also get assigned to them and not to higher classes as it is the case with the lower resolution of CLSM.



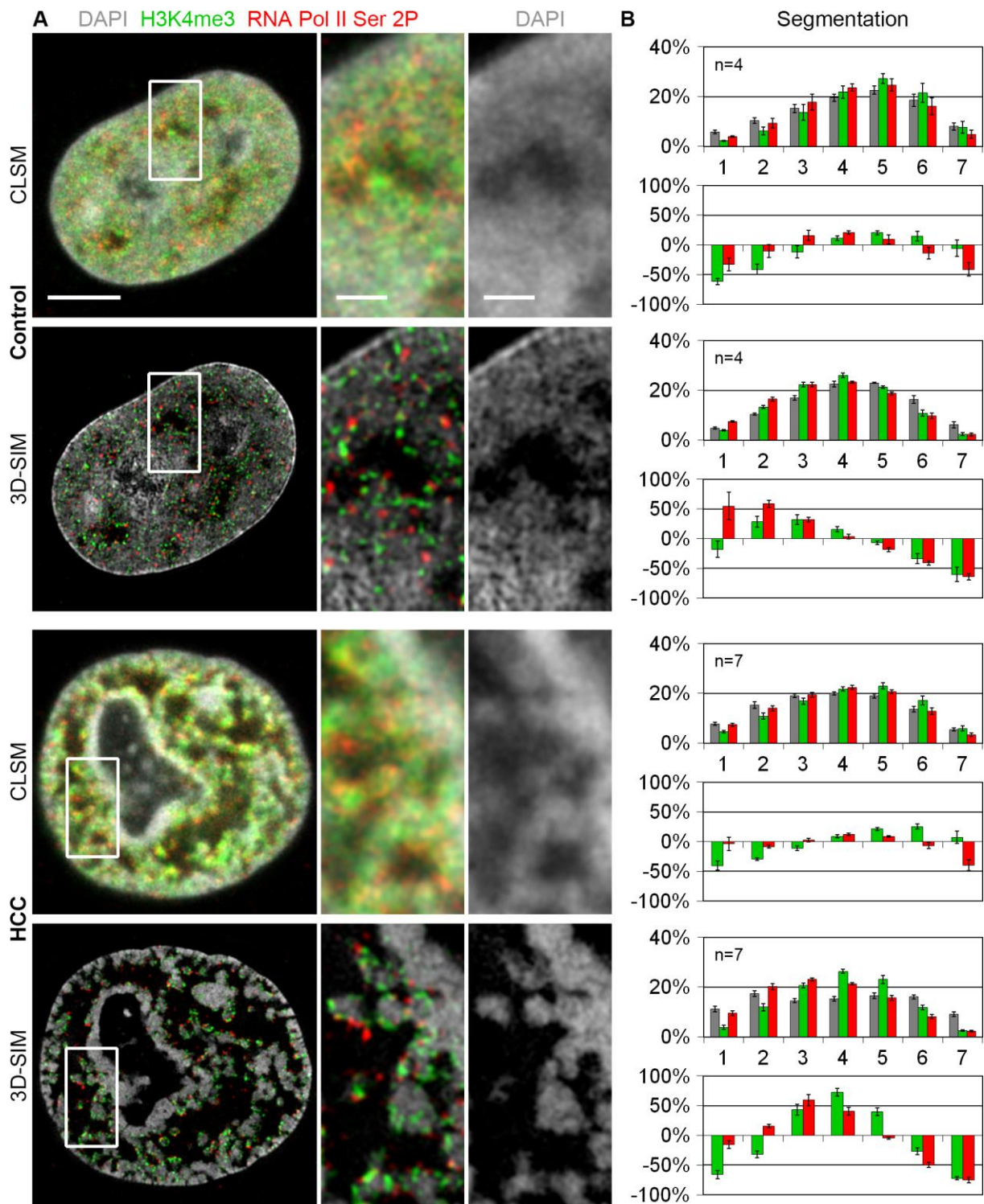


Figure 72: H3K4me3 and RNA Pol II Ser 2P in control and HCC induced HeLa cells. (A) DAPI stained DNA (gray), Histone 3 tri-methylated on lysine 4 (H3K4me3) (green) and RNA Polymerase II phosphorylated on serine 2 (RNA Pol II Ser 2P) (red) of PFA-fixed HeLa (H2B-mRFP) cells either without treatment (control cells) (upper two images) or after HCC induction (lower two images). Immunofluorescence for the detection of H3K4me3 and RNA Pol II Ser 2P was performed using rabbit-anti-H3K4me3 and rat-anti-RNA Pol II Ser 2P antibodies, followed by donkey-anti-rabbit-DyLight488 and donkey-anti-rat-Alexa594 antibodies, respectively. Light optical mid-sections of whole CLSM (first and third row) or the corresponding 3D-SIM (second and last row) 3D acquisitions are shown. Left column: whole nuclei. Middle column: magnifications of the images in the left column. Right column: magnifications of the DAPI staining alone; same area as in the middle column. **(B)** Profiles of the chromatin distributions (gray) of whole 3D acquisitions after the segmentation of the DAPI signals into seven classes with increasing density from class 1 to 7, together with H3K4me3 (green) and RNA Pol II Ser 2P (red) assigned to the respective chromatin classes. For each image (*legend continued on page 262*)

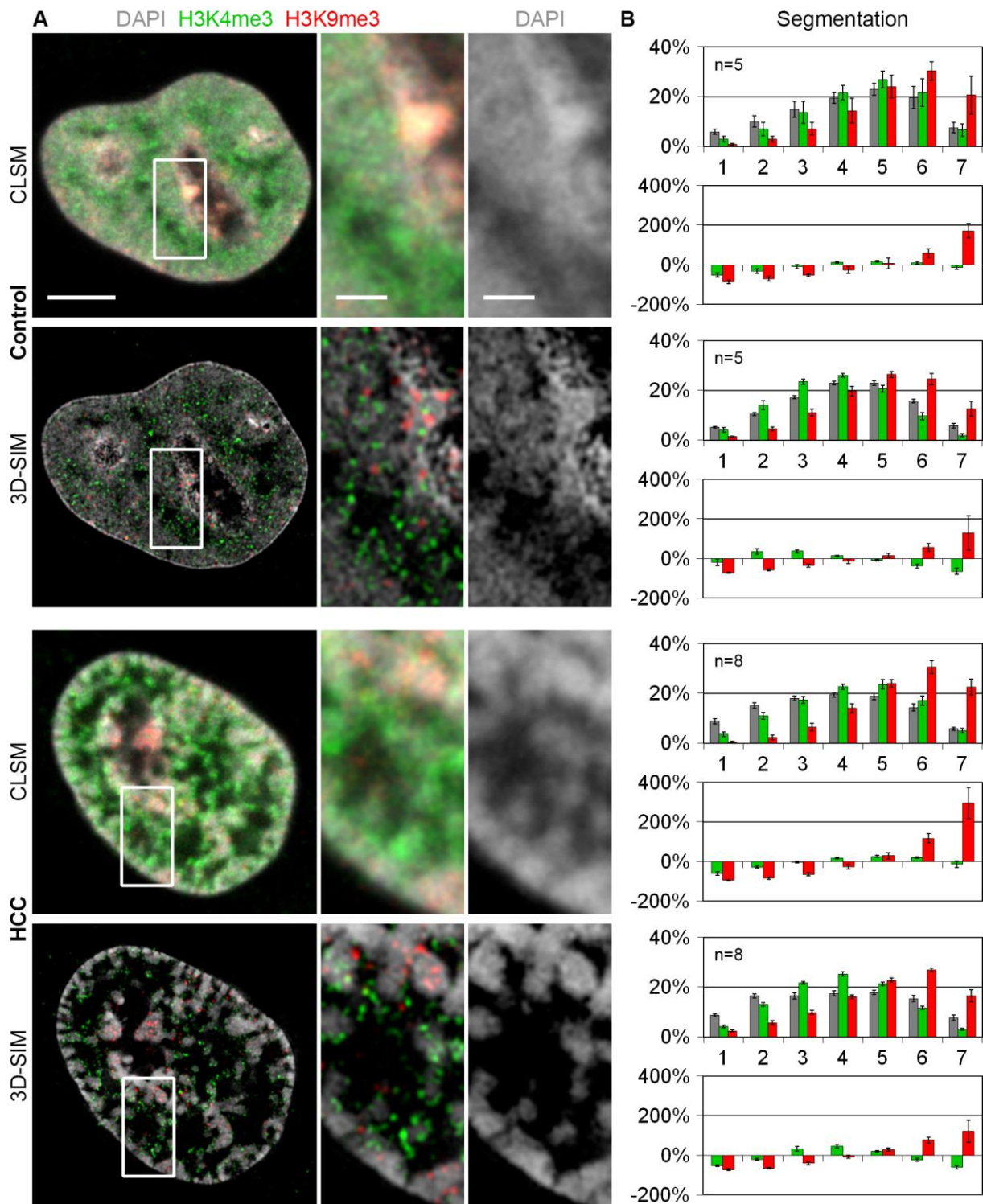


Figure 73: H3K4me3 and H3K9me3 in control and HCC induced HeLa cells. Equivalent to **Figure 72**, therefore the legend is shortened here. **(A)** DAPI stained DNA (gray), Histone 3 tri-methylated on lysine 4 (H3K4me3) (green) and Histone 3 tri-methylated on lysine 9 (H3K9me3) (red). Immunofluorescence for the detection of H3K4me3 and H3K9me3 was performed using rabbit-anti-H3K4me3 and mouse-anti-H3K9me3 antibodies followed by goat-anti-rabbit-Alexa488 and goat-anti-mouse-Alexa594 antibodies, respectively. **(B)** Profiles of the chromatin distributions (gray) of whole 3D acquisitions with H3K4me3 (green) and H3K9me3 (red) assigned to the respective chromatin classes. For statistical evaluations please refer to **Figure 74**. Error bars: standard deviation. Scale bars: 4 μm in images of whole nuclei, 1 μm in magnifications.

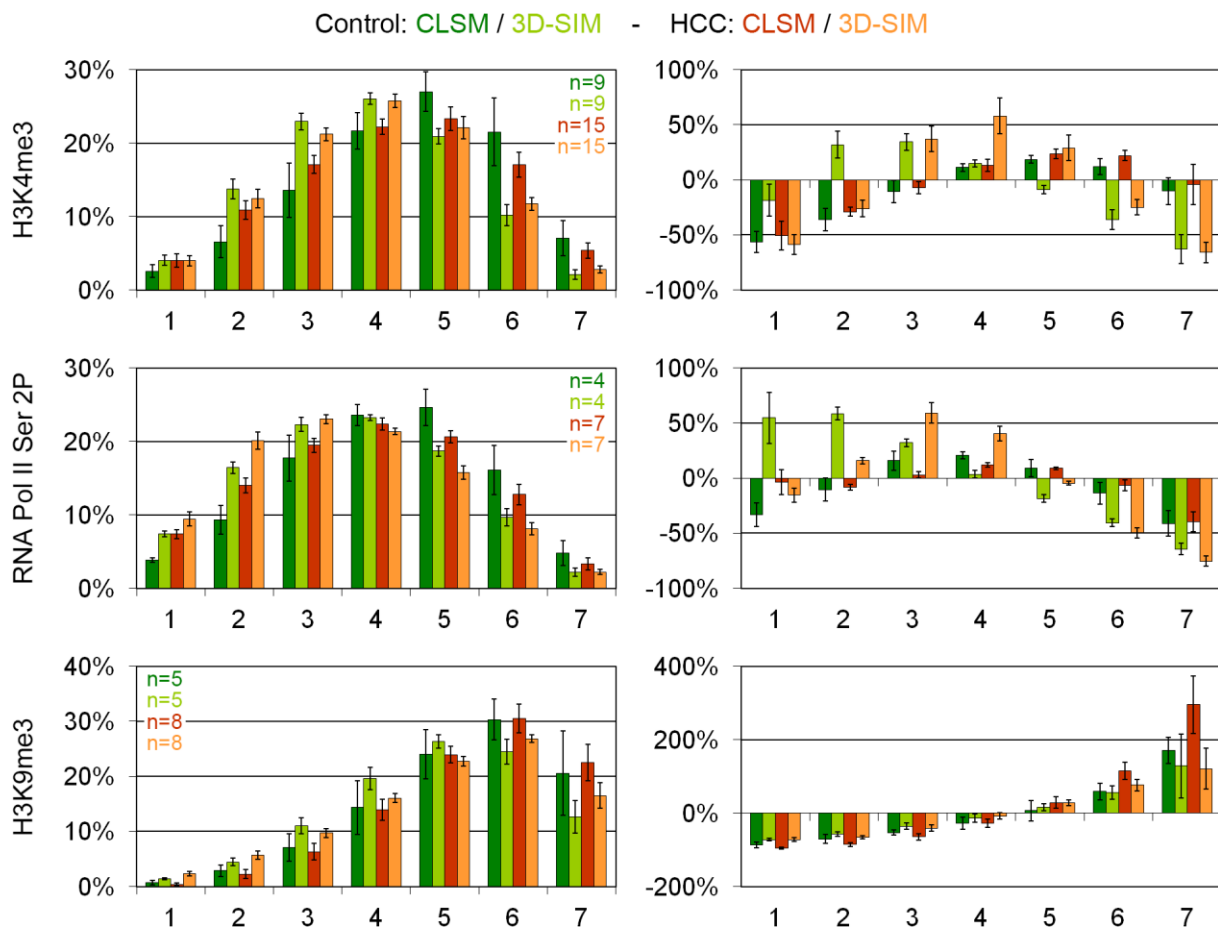


Figure 74: Comparison of markers in control and HCC induced HeLa cells. Profiles of Histone 3 tri-methylated on lysine 4 (H3K4me3), RNA Polymerase II phosphorylated on serine 2 (RNA Pol II Ser 2P) and Histone 3 tri-methylated on lysine 9 (H3K9me3) (from top to bottom) after assigning them to the respective chromatin classes of the corresponding segmentations of the DAPI signals into seven classes with increasing intensity from 1 to 7. Average curves of multiple whole 3D acquisitions are depicted. For each marker both the classical profile (left) as well as the calculated over- and underrepresentation in comparison to DAPI (right) is shown. In each graph the curves for the control cells imaged with CLSM or 3D-SIM (dark green, light green, respectively) and the HCC induced cells imaged with CLSM or 3D-SIM (red, orange, respectively) are included. Statistically significant differences between CLSM and 3D-SIM images were only found in control cells: H3K4me3 differed highly significantly ($p < 0.001$), RNA Pol II Ser 2P very significantly ($p < 0.01$) and H3K9me3 significantly ($p < 0.05$). Comparisons of the markers with each other revealed statistically significant differences between H3K4me3 and RNA Pol II Ser 2P only for HCC induced cells imaged with 3D-SIM ($p < 0.05$). For H3K9me3 vs. both H3K4me3 and RNA Pol II Ser 2P all distributions were statistically highly significant ($p < 0.001$). Note that the Wilcoxon rank-sum test used here can only check for differences in the mean value, not in the actual distribution. Error bars: standard deviation.

Figure 72: (legend continued from page 260) shown in (A) both the classical profile (upper graph) as well as the calculated over- and underrepresentation of H3K4me3 and RNA Pol II Ser 2P in comparison to DAPI (lower graph) is included. Average curves of multiple whole 3D acquisitions are shown. For statistical evaluations please refer to **Figure 74**. Error bars: standard deviation. Scale bars: 4 μm in images of whole nuclei, 1 μm in magnifications.

Summary of section 4.4

Correlative microscopy – exemplified by studies of functional nuclear architecture in HeLa cells with hypercondensed chromatin

Two pathways of correlative microscopy were established, exemplified by experiments including HCC induction and immunofluorescence staining of markers of functional nuclear architecture: pathway I which included live cell imaging (here SDLSM), CLSM and TEM, and pathway II were in addition also super-resolution fluorescence microscopy (here 3D-SIM) was applied.

Despite the different chromatin patterns in control and HCC treated cells the functional nuclear architecture was consistent on a global level under both conditions: H3K4me3 was mainly located at the surface of the chromatin domain clusters, RNA Pol II Ser 2P was found almost exclusively in this region and H3K9me3 was preferentially located on compacted chromatin.

Correlative images of CLSM and 3D-SIM and their evaluations demonstrated the great advantage of the improved resolution of 3D-SIM.

5. Discussion

5.1 Functional nuclear architecture

With the aim of gaining a better understanding of the functional architecture of the cell nucleus, this work stands in one row with Markaki et al. (2010), Markaki et al. (2012), Smeets et al. (2014) and Popken et al. (2014), using 3D-SIM and computational 3D analysis tools for gaining detailed insights into nuclear topography after DAPI staining and immunofluorescence. Through this combination of imaging with improved resolution and new evaluation techniques 3D-SIM opens up a whole field of new possibilities for the analysis of small subcellular structures and macromolecular complexes and so – together with the other super-resolution microscopy approaches (see section 2.6.3 in the introduction) – helped to reignite the interest in light microscopy.

The earlier studies investigated established mouse and human cell lines (mouse C127 cells in Markaki et al. 2010 and Markaki et al. 2012; human fibroblasts in Markaki et al. 2010; mouse C2C12 and ESCs and human RPE-1 cells in Smeets et al. 2014) or bovine embryos and fetal fibroblasts (Popken et al. 2014). Here the focus was the comparative analysis of a broad range of cell types: (A) Primary cell types during differentiation using human hematopoiesis as a model system (published in Hübner et al. 2015); (B) Established cell lines – Chinese hamster (V79) and HeLa cells – under normal conditions and (C) after the manipulation of the nuclear landscape using microinjection of small beads, UV-irradiation and caffeine posttreatment or the induction of PCC or HCC.

5.1.1 Functional nuclear architecture is consistent in normal cells and in cells with a manipulated nuclear landscape across all different nuclear phenotypes

The analysis of general nuclear morphological features revealed a high variability in the general nuclear morphology during hematopoiesis (**Figure 12**) and in the distinctly different chromatin patterns in the various cell types and conditions studied (**Figure 13-18, 59+71**; for summary see also **Figure 75**). But despite that, all cells – primary cells of all differentiation stages and established cell lines under normal conditions as well as after manipulation of the nuclear landscape – showed the same nuclear organization and functional nuclear architecture.

The nuclear landscape in all studied cell types was consistently built up from CDCs containing a compact core (segmented chromatin classes 5-7) and a peripheral layer of decondensed

chromatin (classes 2-4) segueing into the interchromatin compartment (IC) (class 1). Class 4 can be seen as a transitional or intermediate zone: while it shares the hallmarks of decondensed chromatin with an overrepresentation of H3K4me3 and RNA Pol II, the degree of this overrepresentation is reduced, especially in the case of RNA Pol II (**Figure 20-21, 23-25, 26-29, 60-63, 72-73**; for more details on the localization of the marker signals see below). Especially with TEM (**Figure 13-17 C, 18 A, 65+66 D, 67-70 E**) the IC was observed as a channel system connected to nuclear pores, expanding with finer and thicker branches and occasional large lacunas (harboring for example splicing speckles, here detected by SC35 (**Figure 23-25, 67-68**) throughout the entire nucleus and in between the CDCs. In monocytes and granulocytes (**Figure 16+17**) as well as in prophase cells, PCC and HCC induced cells (**Figure 59+71**) chromatin was much more compacted and formed (much) larger CDCs than in the other cell types. Accordingly, also the IC showed a different distribution in those cells: it was reduced or seemingly missing inside the clusters but expanded in between. However, like the regular CDCs also those extended clusters were lined with a layer of decondensed chromatin and thus also here nuclear organization followed the same principles as in the cells with more conventional chromatin patterns.

The same was also true for functional nuclear architecture as shown by the distribution of several different markers: in all analyzed cells transcriptionally competent chromatin marked by H3K4me3 (**Figure 20-21, 23, 26-29, 60-63, 72-73**; for summary see also **Figure 75**) was mainly located at the surface of the CDCs in the decondensed chromatin regions and in the IC. RNA Pol II Ser 2P (**Figure 20, 24, 60-61, 72**; for summary see also **Figure 75**) as well as RNA Pol II Ser 5P (**Figure 21+25**) were found almost exclusively in this region, shifted slightly towards lower chromatin density classes compared to H3K4me3.

In this work, the “mitotic” cell stages with highly condensed chromatin (metaphase and anaphase of control cells, middle and late PCC, PALCCs) were not subjected to the segmentation analysis due to problems in generating appropriate nuclear masks (see details in section 4.3.2). However, the images (**Figure 56-57**) suggest that also here H3K4me3 is localized in regions with comparatively lower chromatin density. Therefore, a segmentation analysis of these cell types would be interesting even if compromises have to be made on the mask. Studies investigating chromatin accessibility in mitosis using DNase I sensitivity (Hsiung et al. 2015) support this idea of a non-uniform chromatin organization in condensed mitotic chromosomes: they showed that some loci maintain a certain or even the same level of accessibility as in interphase. Consequently, differences in the level of chromatin condensation within mitotic chromosomes can be expected.

SC35 (**Figure 23-25**) was found almost exclusively in the interior of larger IC lacunas. H3K9me3 (**Figure 26-29, 62-63, 73**), in contrast, was mainly localized in more compact

chromatin. However, in hematopoietic cells, the over- and underrepresentation of the signals showed a high variability in between and even within cell types. In these cells a larger fraction of compacted chromatin was not stained compared to Chinese hamster and HeLa cells and H3K9me3 was also detected in regions of lower density. As already explained in section 4.1.2, one potential and obvious explanation for these results is provided by the similarity of the distributions of the DAPI and H3K9me3 signals which can easily lead to a change from an overrepresentation to an underrepresentation and vice versa. At the same time, this variability also demonstrates that this histone modification is not as strongly restricted to compacted chromatin as widely assumed. ChIP-seq (chromatin immunoprecipitation sequencing) data revealed that H3K9me3 is also found in coding regions of active genes (Vakoc et al. 2005, Brinkman et al. 2006) which indicates that it is not an exclusive marker for (extended) heterochromatin regions but can also operate on a smaller scale marking individual genes and might even have novel roles in transcriptional regulation. In addition, also stochastic cell-to-cell variability or functional differences between cells at different differentiation stages or during the cell cycle cannot be ruled out. Especially CD34⁺ cells represent a mixed population of various differentiation stages containing stem cells, multipotential progenitors as well as lineage-committed progenitors (see section 2.4 in the introduction). This stresses the importance of single-cell studies as only such approaches can detect differences between individual cells (compare also section 2.6 in the introduction).

Although – as described in the previous paragraph – the relative spatial localization of the marker signals in relation to chromatin was very similar in all cell types and conditions analyzed, the absolute localization of H3K4me3, RNA Pol II Ser 2P/5P, and SC35 in the density classes was shifted towards higher chromatin classes in the more condensed cell types and conditions. Especially in prophase of control cells, early PCC and HCC induced cells and to a lesser extent in interphase PCC cells and granulocytes. These variations are thought to arise primarily from the differences in the general condensation state of chromatin in the different conditions and cell types. In accordance with the DAPI signals also the marker signals got shifted towards higher classes: Upon contraction of the lower density classes, which harbor these signals in control interphase nuclei or cells with a conventional nuclear organization, the markers get automatically relocalized to higher chromatin classes. Telophase of control cells is an exception to this observation. In these cells the segmentation profile also suggested a slightly higher chromatin condensation, however, H3K4me3 and RNA Pol II Ser 2P were clearly shifted towards lower chromatin classes (**Figure 59, 61, 63, 64**). Maybe “active” chromatin decondenses first after mitosis, thus explaining the observed results.

Furthermore, the images of these cells with more condensed chromatin appearing rather black-and-white and therefore potentially causing the segmentation algorithm to create artificial

subclasses (for details see section 4.1.1) might contribute to a minor extent to the differences of the localization of these markers. It would be interesting to compare the results obtained here using seven chromatin density classes to segmentations applying a reduced number of classes, e.g. only five, in these phenotypes.

In addition, for all cell types also variations in the chosen threshold for the included pixels of the mapped markers as well as cell-to-cell variability of the staining efficiency have to be taken into account for contributing to differences observed within cell populations and between cell types. Especially small differences should therefore not be overinterpreted.

Overall, however, the quantitative assessment of the functional nuclear organization applied in this work showed consistent results and high reproducibility in all studied cell types, in particular in cells with similar chromatin patterns (for summary compare **Figure 30+64+74**). The frequently expressed concern that chromatin stained with DAPI might not be suitable as a reference structure for such evaluations due to the drug's preference for AT-rich sequences, consequently underrepresenting GC-rich chromatin, was addressed by comparing 3D-SIM acquisitions of DAPI stained chromatin with TEM data. For TEM imaging DNA was stained with osmium ammine B. Under the conditions used this compound acts as a Schiff-type reagent and stains DNA in a Feulgen-like reaction and is therefore not sequence-specific (see details in section 3.2.8.3). The comparative analysis of hematopoietic cells (**Figure 13-18**) demonstrated that the observed chromatin patterns of all five analyzed cell types were the same with both methods. Therefore – at the resolution level of 3D-SIM – there are no obvious objections to using DAPI for staining DNA.

In conclusion of this chapter, the principles of functional nuclear architecture observed here were the same in all cell types and conditions studied, including primary human hematopoietic cells of five differentiation stages, control, UV/caffeine treated and PCC induced Chinese hamster (V79) cells as well as normal and HCC induced HeLa cells.

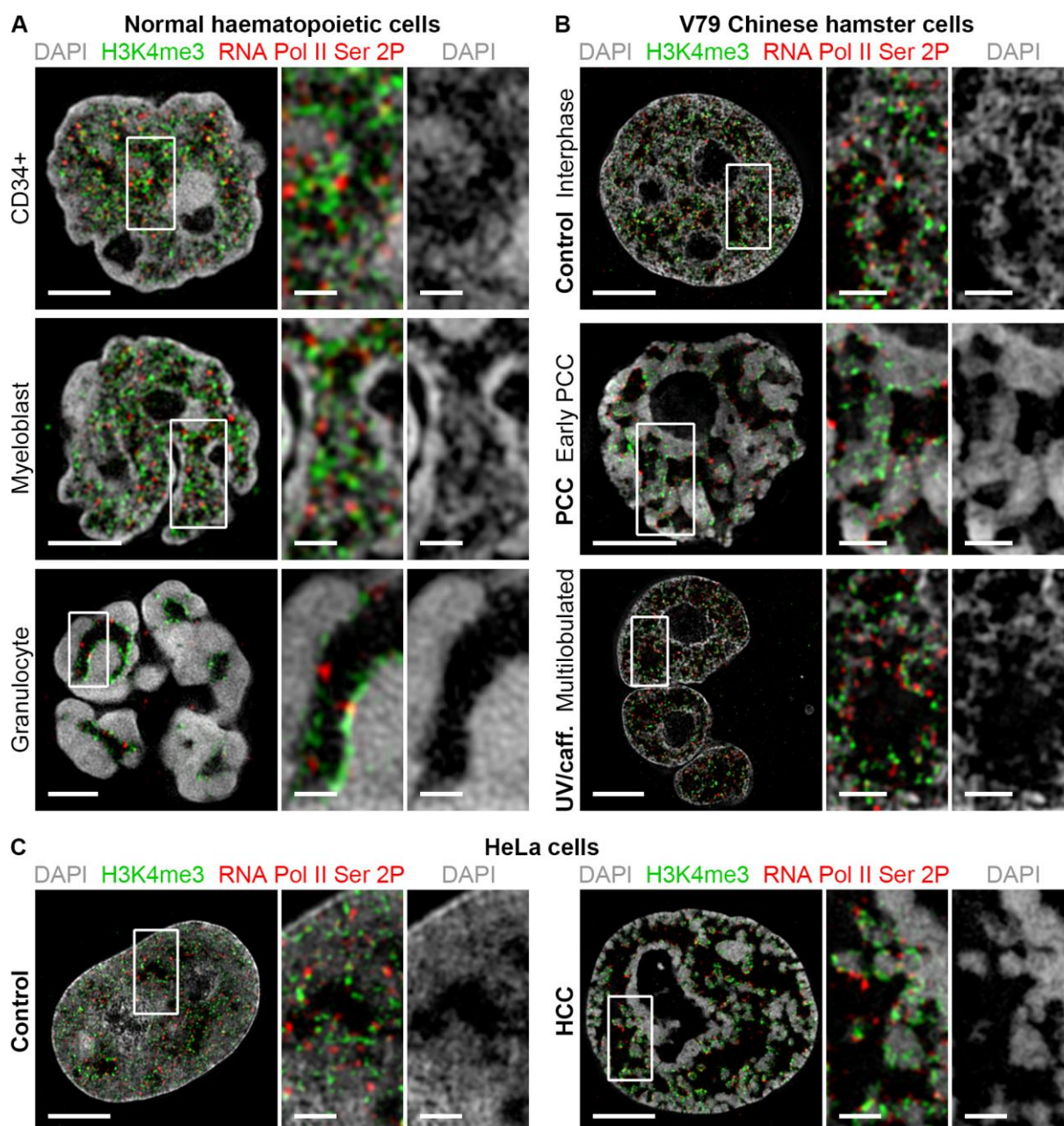


Figure 75: Summary – H3K4me3 and RNA Pol II Ser 2P in various selected cell types and conditions. DAPI stained DNA (gray), Histone 3 tri-methylated on lysine 4 (H3K4me3) (green) and RNA Polymerase II phosphorylated on serine 2 (RNA Pol II Ser 2P) (red) of PFA-fixed cells in light optical mid-sections of whole 3D-SIM 3D acquisitions. Left column: whole nuclei. Middle column: magnifications of the images in the left column. Right column: magnifications of the DAPI staining alone; same area as in the middle column. For details and/or further cell types/conditions refer to section 4.1.2 (A), 4.3.2 (B) and 4.4.2 (C), respectively. Scale bars: 2 μm in images of whole nuclei, 0.5 μm in magnifications.

5.1.2 Evidence for a chromatin organization free of entanglements

Beyond the functional architecture of the CDCs also the question about their structural organization is of high interest. The chromatin domains – whether on the level of entire TADs or on the level of smaller entities like subTADs also called contact domains (for review see Cubenas-Potts and Corces 2015) or otherwise defined fractions of TADs – are suggested to be organized into so-called fractal globules (Lieberman-Aiden et al. 2009, Mirny 2011; see section 2.2.5 in the introduction). In contrast to equilibrium globules, fractal globules are free of entanglements and allow an unproblematic unfolding of the polymer chain.

In order to shed light on higher-order chromatin organization at this scale, two types of experiments were performed: (1) live cell imaging of granulocytes subjected to repeated changes between normal and hypotonic medium and (2) observation of small microinjected beads in cells going through mitosis.

The live cell observations of granulocytes showed that both the decondensation of chromatin upon treatment with hypotonic medium as well as the (re)condensation after changing back to normal salt conditions are very rapid and reversible processes (**Figure 32**). The fact that these massive rearrangements took place in such a short time – 1 min was enough – strongly argues for a nuclear organization free of entanglements.

However, based on this experiment alone it cannot be excluded that knots and entanglements actually do occur, but are resolved by biochemical mechanisms like for example through the action of topoisomerases, especially type II topoisomerases which cut both DNA strands at the same time in an ATP dependent process (Alberts et al. 2015). Further studies are needed, e.g. testing for the ATP-dependency of the decondensation and condensation of chromatin. But given the large number of entanglements that is to be expected in a nucleus not organized into fractal globules and given the high amount of energy needed for their resolution, it seems more reasonable to assume that evolution instead found a possibility to avoid knots and entanglements in the first place.

Similar conclusions can be drawn from the microinjection experiments with HeLa cells: small fluorescent beads injected into the nucleus got expelled during the first cell division (**Figure 40+41**) and were found almost exclusively in the cytoplasm after the completion of mitosis (**Figure 42**). This demonstrated that small particles do not get trapped inside the chromosomes upon condensation, arguing for a chromatin organization that allows chromatin to condense in a smooth and ordered fashion. The fact that also after HCC induction the beads were found in lower density regions as in control cells (**Figure 33-36**), supports this finding.

However, also in control interphase nuclei, the beads were found in regions of low chromatin density (**Figure 33-36 A**). It therefore has to be considered that they might be located only in the wider IC channels and might not be situated within chromatin in the first place. Another parameter to be taken into account is the carboxylate-modified surface of the beads used in this work. Carboxyl groups can easily dissociate and release their protons, thus causing the surface of the beads to be negatively charged. Although the negative charge of the phosphate backbone of the DNA is thought to be neutralized by the net positive charge of the histone octamer (Alberts et al. 2015), it might still be possible that the negatively charged beads get repelled from chromatin. A comparison of the results obtained here using carboxylate-modified beads with the behavior of positively charged beads would be interesting to see.

Independent of these points and the question of higher-order chromatin organization, the resolute exclusion of the beads (**Figure 40-42**) as well as the co-injected dextran (**Figure 37+39**) from the daughter nuclei after mitosis complies with the well-established observation that the reassembly of the nuclear envelope in late anaphase occurs through membrane spreading at the surface of the densely packed chromosomes (for review see LaJoie and Ullman 2017), excluding all other molecules from the newly formed nuclei (Cooper 2000).

To summarize, both the live cell observations with granulocytes as well as the microinjection experiments support the idea of chromatin being organized into fractal globules, free of knots or entanglements.

5.1.3 The results of this work and the CT-IC / ANC-INC model of functional nuclear architecture

Together the results discussed in the preceding two sections 5.1.1 and 5.1.2 strongly endorse the CT-IC model of functional nuclear architecture with its suggested organization into globular chromatin domains with a functionally distinct substructure (compare section 2.2.1 in the introduction).

The arrangement of chromatin into globular domains per se is supported by the experiments on higher-order chromatin organization. They indicated the nucleus to be free of entanglements and thus support the idea of nuclear architecture being based on fractal globules with a domain substructure. Microscopic data of chromatin stainings alone like in this work / Hübner et al. (2015) the 3D-SIM acquisitions of DAPI stained DNA or TEM images after osmium ammine staining, or in other studies images acquired with 3D-SIM (Markaki et al.

2010, Smeets et al. 2014, Popken et al. 2014), STORM (Ricci et al. 2015, Szczurek et al. 2017) or TEM (Ou et al. 2017 (using ChromEMT, chromatin staining combined with electron tomography), Strickfaden et al. 2019 (using ESI, electron spectroscopic imaging)), however, do not show clearly recognizable domains. This indicates that the globular chromatin domains should not be seen as isolated spherical entities. Instead, it can be assumed that neighboring domains are often in close proximity to each other, that the more decondensed chromatin at their surfaces optically merges them together and/or that maybe even entire domains adopt a more stretched out configuration. Images obtained with STORM in combination with a new labeling approach of sequential rounds of oligopaint hybridizations (Nir et al. 2018) support these thoughts.

The results regarding functional nuclear architecture are in full accordance with the findings of the other preceding publications mentioned earlier (Markaki et al. 2010, Markaki et al. 2012, Smeets et al. 2014, Popken et al. 2014; for details see section 5.1): transcriptionally competent chromatin marked by H3K4me3 (here / Hübner et al. 2015, Markaki et al. 2010, Smeets et al. 2014, Popken et al. 2014) or H4K8ac (histone 4 acetylated on lysine 8) (Markaki et al. 2010) as well as RNA Pol II (here / Hübner et al. 2015, Markaki et al. 2010, Smeets et al. 2014, Popken et al. 2014) and also nascent RNA and DNA (Markaki et al. 2010, Markaki et al. 2012) were shown to be localized at the surface of chromatin domains (CDs) or chromatin domain clusters (CDCs) in the PR. This specific localization of RNA Pol II and nascent RNA demonstrates that transcription indeed takes place in a defined subcompartment of the nucleus and contradicts the assumption of transcription occurring in non-specialized sites distributed more or less randomly throughout the nuclear volume. The PR was in all cases lined by the IC, a basically DNA free channel system starting/ending at nuclear pores and pervading the chromatin compartment (CC) with finer and thicker branches and occasional larger lacunas carrying macromolecular aggregates such as nuclear bodies and splicing speckles marked by SC35 (here / Hübner et al. 2015, Markaki et al. 2010). The interior of the CDCs was characterized by inactive markers like H3K9me3 (here / Hübner et al. 2015, Popken et al. 2014) and H3K27me3 (histone 3 tri-methylated on lysine 27) (Smeets et al. 2014).

Also recent publications using STORM-based imaging are in line with this idea of functional nuclear architecture: Xu et al. (2018) confirmed active histone markers (H3K4me3, H3K9ac (histone 3 acetylated on lysine 9)) to be located in areas with less compact chromatin and inactive histone markers (H3K27me3) to be associated with more compact chromatin regions in MCF-10A human mammary epithelial cells; Kirmes et al. (2015) also observed an active histone marker – H3K14ac (histone 3 acetylated on lysine 14) – at the surface of chromatin domains; and Cattoni et al. (2017) demonstrated in *Drosophila* cells that inactive chromatin marked by H3K27me3 appeared as large(r) clusters, while active chromatin marked by

H3K4me3 was located as smaller spots at the surface of the large, inactive clusters. Furthermore, it was shown that DNase I hypersensitive sites (DHS[+]) representing transcriptionally active chromatin regions localized in more open chromatin at the surface of the CDs/CDCs, while sites not accessible to DNase I (DHS[-] sites) – i.e. inactive sequences – were preferentially found in more compact chromatin in the interior of the domains (Cremer et al. 2017). Similar results were also obtained by Boettiger et al. (2016), Szabo et al. (2018) and Nir et al. (2018) using FISH to label individual TADs or small domains. Although these studies investigated the DNA sequences in their entirety and did not analyze the localization of the markers within the domains they showed that chromatin associated with active markers (histone markers, RNA, DNase) has a tendency to adopt a more open chromatin conformation – i.e. to be characterized by a larger volume (Boettiger et al. 2016, Nir et al. 2018), bigger surface area (Nir et al. 2018), less round shape (Nir et al. 2018) and lower density (Szabo et al. 2018) – than chromatin associated with repressed or inactive markers (histone markers, Polycomb group (PcG) proteins).

Based on all this evidence the CT-IC model can be refined and replaced by the so-called ANC-INC network model (**Figure 76**) (for review and more details see Cremer et al. 2015, Cremer et al. 2018, Cremer and Cremer 2019, Cremer et al. 2020). It is based on the interpretation that functional nuclear architecture is determined by two co-aligned compartments, an active nuclear compartment (ANC) and an inactive nuclear compartment (INC). The ANC is suggested to include both the IC and the PR and with that represents the compartment where all active nuclear processes take place, while the INC forms the core regions of the CDCs. Chromatin accessibility is thought to differ between the two compartments, with the ANC containing decondensed chromatin of the segmentation classes 2-3 (corresponding to the PR; the IC is represented by class 1) and the INC comprising compact chromatin of the classes 5-7. Class 4 represents an intermediate zone and thus can be partially assigned to both and none of the compartments at the same time. However, the ANC should not exclusively be seen as open and accessible and the INC not exclusively as closed and inaccessible. Instead, the difference is gradual, with individual molecules still being able to enter the INC (although with a considerably lower diffusion rate) while aggregations of proteins and larger RNA/protein complexes are restricted to the ANC. Both compartments, the ANC and the INC, pervade the nucleus together as co-aligned 3D networks.

To further verify the ANC-INC network model on the level of microscopy-based methods as a continuation of the analyses performed in this work, it would be of particular interest to study the spatial distribution of proteins involved in the repair of DNA damage at selected time points after damage induction with the same methods applied here. Evidence suggests that the DNA

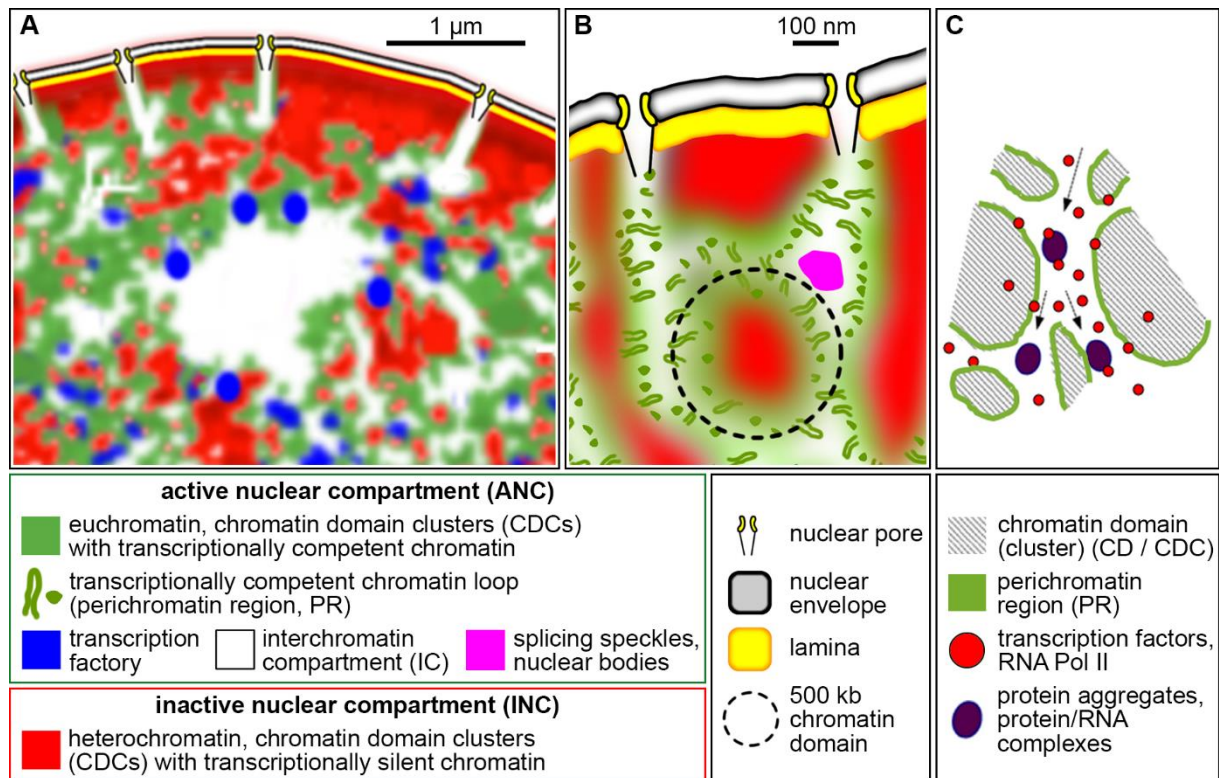


Figure 76: The ANC-INC network model of functional nuclear architecture. (A, B) The nucleus is pervaded by two co-aligned 3D networks: the ANC (green and white) comprising the IC and the PR and the INC (red). Shown are several CDCs associated with the nuclear envelope (gray). (C) Macromolecules are enriched in the IC. Individual molecules (red) can enter the INC (gray), however, there their diffusion is considerably more constrained than within the ANC (green and white). Aggregations of proteins and larger RNA/protein complexes (dark purple) are restricted to the ANC. Figure taken from Cremer et al. (2020). Reprinted in accordance with the Creative Commons Attribution NonCommercial License (Creative Commons NC 4.0).

repair processes occurring after DNA damage result in the rearrangement of chromatin due to damaged sites being relocated from the interior of compact CDCs onto their surface (Chiolo et al. 2011, Muller et al. 2013) in order to be accessible for the DNA repair machinery. First indications for proteins involved in the DNA damage response being preferentially located in the PR were provided by Solimando et al. (2009) and later this idea was supported by Rube et al. (2011) and Lorat et al. (2015). Note that the authors of the latter two studies argue that DNA repair factors are also found in heterochromatic regions of the nucleus – in my opinion, however, the provided images rather demonstrate that these proteins are consistently located at the surface of chromatin domains, i.e. in the PR. The data presented in these publications certainly provide valuable first insights, but detailed high-resolution studies and thorough analyses of the exact localization of DNA repair still seem to be missing.

Similarly, also more extended studies on the topography of DNA replication would be of interest. During S phase the entire genome has to be replicated, including the sequences forming the inactive cores of the CDCs. Temporary spatial rearrangements and/or changes in the structure of the domains, therefore seem to be inevitable during DNA replication. Indeed it was demonstrated that newly replicated chromatin exhibits a lower DNA density than adjacent

areas that were not yet replicated (Markaki et al. 2012) and that nascent DNA is initially found at the border of chromatin domains but localizes more internally within a time frame of several minutes (Jaunin et al. 2000, Markaki et al. 2012). However, these studies focused only on DNA replication in chromocenters of mouse cells (Markaki et al. 2012) or applied immunogold labeling of TEM sections which is known to provide only low signal frequencies (Jaunin et al. 2000). Therefore they leave the impression that more comprehensive analyses would be helpful.

And lastly, applying the methods used in this work to other cell types either (1) with an unusual nuclear organization, like for example rod photoreceptor cells of nocturnal animals exhibiting an inverted nuclear architecture (Solovei et al. 2009) or (2) coming from different species across a wide range of the eukaryotic tree, including remote species like ciliates (which carry a small diploid micronucleus as well as a large polyploid macronucleus), would be an appealing field of future research in order to further explore if the functional architecture described by the ANC-INC network model is a universal and evolutionary conserved principle of nuclear organization or not.

In conclusion, even if there are still many open questions and the folding and arrangement of chromatin on the small scale still requires further investigation, the combined evidence for a chromatin organization based on globular domains instead of extensive loops should be considered solid enough to update illustrations used in textbooks and other sources – the times in which the depiction of a “spaghetti organization” of chromatin was adequate or acceptable are over.

5.1.4 Side note: Correlation between general nuclear morphological features, transcriptional activity and differentiation stage in hematopoietic cell types

In hematopoietic cells also other general morphological features were studied apart from the chromatin patterns: the length of the IC surface, the size of the nucleoli and the number of nuclear pores. In addition, also the number of RNA Pol II signals was analyzed. Different from the principles of functional nuclear architecture which did not change during differentiation (see discussion in section 5.1.1) despite the dramatic changes in the chromatin patterns (compare **Figure 13-18**), these parameters and markers did change.

The length of the IC surface (**Figure 18 D**), the size of the nucleoli (**Figure 19**) and the number of RNA Pol II signals (**Figure 20-22**) correlated very closely with each other: for all three parameters the values were similar in CD34⁺ cells and monoblasts, decreased only slightly in

myeloblasts but clearly in monocytes and dropped to low numbers in granulocytes. A similar tendency was also seen in the number of nuclear pores (**Figure 12 C**) although for this parameter CD34⁺ cells and monoblasts showed reduced values compared to myeloblasts. Taken together these observations demonstrate a correlation between progressing differentiation on the one hand (progenitor cells / committed precursors (CD34⁺, monoblasts, myeloblasts) vs. differentiated cells (monocytes) vs. terminally differentiated cells (granulocytes)) and transcriptional activity on the other hand.

RNA Pol II, of course, represents a direct marker for (ongoing) transcription, especially when phosphorylated on serine 2 (RNA Pol II Ser 2P). As already mentioned in section 4.1.2, also other studies found lower amounts of RNA Pol II in more differentiated cells than in more undifferentiated cells (Faro-Trindade and Cook 2006, Brown et al. 2008, Eskiw and Fraser 2011). And also the other features are closely linked to transcriptional activity: As described in detail in section 5.1.3, active processes are supposed to occur in the PR, at the interface between the CDCs and the IC. The speculation that a higher transcriptional activity with more transcriptional sites involves more open chromatin and is therefore associated with a more extended PR, allows the length of the IC to be taken as an indicator for the transcriptional activity of the cells. Also nucleoli – being the center of ribosome biogenesis – are linked with the transcriptional and translational activity of the cell; they were furthermore reported to be decreased in size in differentiated cells (for review see Sirri et al. 2008). Nuclear pores represent the gateways between the nucleus and the cytoplasm with the entire traffic of macromolecules including mRNAs and proteins running through them. It is well established that their number doubles while the cell progresses from G1 to G2 phase, a time when also RNA and protein synthesis increase in preparation for mitosis and the formation of two fully functional daughter cells (Maul et al. 1972, Winey et al. 1997, Maeshima et al. 2006). The number of nuclear pores was furthermore shown to be reduced in quiescent cells (Maeshima et al. 2006) as well as in differentiated cells with lower transcriptional activity (Maul et al. 1980) and increased upon hormone stimulation of transcription (Oberleithner et al. 1994). A potential explanation for the results of the number of nuclear pores (**Figure 12 C**) not exactly fitting the distribution of the other features but instead being higher in monoblasts and myeloblasts than in CD34⁺ cells might lie in the replicative potential of these cells: myeloblasts and to a limited extent also monoblasts were observed to go into S phase and through cell division (Montanari et al. 2005 and own preliminary experiments (data not shown)). Thus the replicating cells with their increased numbers of nuclear pores (see above) might cause a shift to higher values for the number of nuclear pores in these cells compared to the heterogenous CD34⁺ cell population where the vast majority of cells is non-replicating (for review see Bethesda 2011, Rieger and Schroeder 2012).

At first glance also the amount of the IC (**Figure 18 D**) seems to fit into the scheme as it follows the same tendency as the number of nuclear pores. However, the central areas of the IC lacunas are often at a large distance from its surface, i.e. from the PR. Therefore it seems inappropriate to assume that the IC amount is linked to transcriptional activity. The fraction of a nucleus occupied by the IC more likely depends on other parameters. For example, it could serve as a storage compartment for proteins and other macromolecules or be important for the function of the cell, e.g. by providing enough flexibility for cell types that need to migrate into tissues such as monocytes and granulocytes (Henderson et al. 2003, Imhof and Aurrand-Lions 2004, Wantha et al. 2013) (see also below). Other studies (Rouquette et al. 2009, Popken et al. 2014) also found large differences in the IC amount between cell types, but detailed analyses and even more suggestions for the meaning and purpose of this variability still seem to be missing.

Detailed and comparable information on the global transcription levels of the cell types analyzed in this work still seems to be missing in the literature, although numerous studies are available analyzing differential gene expression in various (hematopoietic) cell types (e.g. Komor et al. 2005, Manfredini et al. 2005, Gemelli et al. 2006, Ferrari et al. 2007, Liu et al. 2007, Novershtern et al. 2011, Zhang et al. 2012a) (although, admittedly, the numerous approaches available to isolate and differentiate hematopoietic cells, the various markers used for cell identification and the sometimes confusing nomenclature all together make it difficult for the non-hematologist to identify corresponding cell types and thus relevant studies might have been overlooked here). But Yang et al. (2013) at least reported higher expression levels in erythroblasts (comparable in differentiation stage to monoblasts/myeloblasts) than in peripheral blood cells (presumably comparable to monocytes/granulocytes). However, the majority of isolated transcripts – everything that could not be mapped to the genome – was actually not included in the analysis. In combination with the observation of Efroni et al. (2008) that embryonic stem cells (ESCs) express a larger fraction of the genome than more differentiated neuronal progenitor cells including repetitive sequences and mobile elements, this limitation provides an explanation why Yang et al. (2013) found an even lower expression intensity in ESCs than in peripheral blood cells. The overall number of isolated transcripts, namely, with similar levels for ESCs and erythroblasts and reduced levels in peripheral blood cells, matches the results obtained in this work. Efroni et al. (2008) demonstrated that ESCs are transcriptionally even more active than neuronal progenitor cells. In conclusion one would expect CD34⁺ cells (progenitors) to be more active than monoblasts/myeloblasts (precursors). That this was not the case might be due to these cell types being too similar in differentiation stage or due to methodological differences (4 h pulse of radioactive labeling in Efroni et al. 2008 vs. immunofluorescence with RNA Pol II and indirect markers used here).

The increasing reduction of transcriptional activity with progressing differentiation probably reflects the cells being more and more restricted to a certain lineage and/or certain functions, and a smaller set of proteins being sufficient to maintain their cell state or fulfill their tasks. This thought is supported by reports of a decreased number of expressed and an increased number of silenced genes (Yang et al. 2013), as well as a smaller fraction of the genome being expressed (Efroni et al. 2008) in more differentiated cells. Consequently, the sequestration of the increasing number of genes that are not (or should not be) expressed anymore into more compact (hetero)chromatin with limited accessibility for the transcription machinery could explain the changes in the chromatin patterns observed here, i.e. the reduction of the length of the PR (measured by the IC surface) and the increase of the size of the CDCs. At the same time, genes that remain or become active during differentiation could be thought to receive a higher exposure to transcription factors and the transcription machinery, as the volume to be “scanned” reduces accordingly. Therefore, the changing chromatin patterns of hematopoietic cells during differentiation could serve as a good example of how the general 4D nuclear architecture can facilitate gene regulation (also discussed in a review by Woringer et al. 2014). In addition (or alternatively) it is also possible that the changes in the chromatin patterns correlate with the function of the cells and not (only) with their differentiation stage. Monocytes and granulocytes, for example, can migrate into tissues as a response to inflammations and infections (Henderson et al. 2003, Imhof and Aurrand-Lions 2004, Wantha et al. 2013). In order to pass through the tight collective of cells in tissues, a highly flexible nucleus is certainly of benefit, if not a prerequisite. A chromatin organization as observed here in these cell types might help with that: conceivably the few large CDCs can – in combination with the extensive and assumingly very flexible IC lacunas – more easily be shifted towards each other than the many small CDCs in nuclei with more conventional chromatin patterns.

In order to better understand if decreasing transcriptional activity is a general feature of progressing differentiation or whether it is rather characteristic for hematopoietic cells and especially in order to better understand if chromatin patterns indeed represent an (indirect) marker for transcriptional activity, more cell types, in particular also from other differentiation systems, need to be studied. Within the hematopoietic system macrophages (activated monocytes) or a pure population of HSCs would be interesting candidates for further analyses. Regarding other differentiation pathways neurogenesis comes to mind: Le Gros et al. (2016), for example, observed rearrangements in the chromatin patterns between multipotent stem cells and mature neurons in olfactory epithelium and the development of rod photoreceptor cells of nocturnal animals involves changes from the conventional to an inverted nuclear architecture (Solovei et al. 2009).

5.1.5 Conclusions on the analysis of functional nuclear architecture – the intertwined relationship of structure and function

The results and discussions presented in the preceding sections 5.1.1 to 5.1.4 strongly support the widely accepted thought (see for example Cremer et al. 2020) that structure and function inside the nucleus are inseparably linked to each other.

On the one hand, this includes nuclear structure on a larger scale, i.e. on the level of CDCs and chromatin patterns, and the functional role of the cell in the context of a multicellular organism, i.e. the specific task a certain cell type has to fulfill in the body. For a better explanation, comparisons of the nucleus with human settlements might help, where CDs and CDCs correspond to buildings and the PR and IC to the pavements, streets, and land in between (based on Cremer et al. 2020). In this analogy, structure in the sense of this first aspect of the structure-function relationship represents the overall layout and the predominant type of architecture of the town or village. Naturally, this strongly depends on the industry present or the purpose of the settlement, i.e. its function. Automobile industry, for example, requires large production halls but the space between buildings can be reduced to a minimum. (Traditional) agricultural areas, in contrast, typically involve smaller buildings and depend on wide stretches of land in between or around the premises. The example of agriculture also serves as a good model for how the surrounding conditions (i.e. environment) can play a role in structural organization: in flat territories individual farmsteads are typically larger and fields often have a rectangular shape, while in mountain areas buildings as well as land parcels are smaller and their outline can be much more variable.

On the other hand, the intertwining of structure and function also occurs on a smaller scale, i.e. how chromatin is structured on the level of individual domains or small CDCs in order to allow functional processes like transcription, replication and DNA repair to run in a smooth and efficient way. Using again the analogy to human settlements, this second aspect reflects where the majority of human interactions (i.e. active processes) takes place. Shops and restaurants are typically oriented towards the front of the buildings in order to be more accessible to potential clients walking along the pavements. Also the transport of smaller goods takes place along the sidewalks, while larger items or greater quantities of wares are moved and exchanged via streets and squares. Linking back to the first aspect of the structure-function relationship described above, the width of the pavements might vary from town to town. Cities with a bigger population and increased retail are typically characterized by more extended pavements than small villages with their limited number of inhabitants and shops. The organization itself, however, i.e. stores and restaurants being exposed to customers, remains the same throughout all types of settlements.

Exactly the same also applies to nuclear organization: some of the distinct cell types studied here showed significant differences in their chromatin patterns with partially great variations in the size of the CDCs and the width of the IC channels. As the example of the hematopoietic cell types revealed, general nuclear features are linked to transcriptional activity and to the differentiation stage and with that also to the function and/or the tissue environment of the cell. Despite these differences, however, the functional nuclear architecture was consistently the same in all cell types, whether their nuclei were examined under control conditions or after manipulation of the nuclear landscape. And not only in the cell types studied here but also in those analyzed in the preceding works of Markaki et al. (2010), Markaki et al. (2012), Smeets et al. (2014) and Popken et al. (2014) (for details see section 5.1). This allows the conclusion that the principles of nuclear organization are conserved across cell types and species – at least in mammalian cells – and consequently that these common structural arrangements represent the basic and essential building blocks for the proper function of the nucleus. The numerous studies demonstrating changes in nuclear structure being linked to cellular abnormalities and disease (for review see Chakraborty and Ay 2019, Spielmann et al. 2018) emphasize the importance of this structure-function relationship.

5.2 Microscopy

5.2.1 Microscopy vs. chromosome conformation capture (3C) – differences and similarities

Next to microscopic approaches also chromosome conformation capture (3C) -based methods, where chromatin contacts are crosslinked, isolated, amplified and sequenced (for review see Kong and Zhang 2019), aim at analyzing the structural organization of the nucleus. Representing top-down vs. bottom-up approaches, i.e. starting from the micrometer scale with the global structure of the nucleus vs. starting from the nanometer scale with macromolecular assemblies and interactions, and being primarily performed on the single-cell level vs. using mainly high throughput procedures, both methods, microscopy and 3C, are often regarded as completely opposing or even contradictory technologies. Not only because of the inherent differences in the methodologies but also due to the quantity and presentation format of the data obtained. However, contrary to this perception, the results collected with both technologies are actually very well in line with each other.

On the larger scale, 3C-based methods revealed a spatial separation of chromatin into two compartments, A and B (Lieberman-Aiden et al. 2009), which were recently also observed in

single cells (Nagano et al. 2017, Stevens et al. 2017, Tan et al. 2018). The A compartment was shown to be associated with transcriptionally competent chromatin marked by histone 3 tri-methylated on lysine 36 (H3K36me3) (Lieberman-Aiden et al. 2009) or increased CpG frequency (Tan et al. 2018), higher mRNA expression levels (Lieberman-Aiden et al. 2009, Stevens et al. 2017) and more accessible chromatin measured by increased DNase I sensitivity (Lieberman-Aiden et al. 2009) or higher decompaction of chromatin (Nagano et al. 2017). In their initial analysis using a resolution of 1 Mbp, Lieberman-Aiden et al. (2009) also found H3K27me3, a marker for inactive chromatin, to be enriched in the A compartment, which at first glance might seem contradictory to all the other characteristics described above. However, H3K27me3 shows a broader nuclear distribution than other markers for inactive chromatin, is typically associated with facultative heterochromatin and – in this context most importantly – is found in gene-rich regions (for review see Kimura 2013). Therefore a certain link to the A compartment is actually not surprising. But H3K27me3 is not a general hallmark of the A compartment, as a more detailed analysis of Lieberman-Aiden et al. (2009) showed: when using a higher resolution of 100 kbp the correlation between H3K27me3 and compartment A was clearly reduced while the other markers maintained a strong association. In contrast to the A compartment, the B compartment is consequently characterized by a lower CpG frequency, reduced mRNA expression levels and DNase I sensitivity (see references above) as well as a clear association with lamin associated domains (LADs) (Stevens et al. 2017) and more densely packed chromatin in general (Lieberman-Aiden et al. 2009, Nagano et al. 2017). Calculated 3D models of the 3C data sets of individual nuclei revealed that the B compartment is predominantly located at the nuclear periphery and around nucleoli while the A compartment occupies the nuclear interior (Stevens et al. 2017, Tan et al. 2018). This spatial distribution of the two compartments matches exactly the rough staining patterns of H3K4me3 and H3K9me3 observed in microscopic images (**Figure 26-29, 62-63, 73**, as well as numerous other examples available in the literature). H3K4me3 is located more internally in the nucleus, equivalent to the A compartment, and H3K9me3 is found in the same peripheral spaces as the B compartment. And not only that: since H3K4me3 is a marker for transcriptionally competent and therefore more open chromatin, while H3K9me3 is associated with inactive chromatin and is generally believed to label more compact chromatin, also the functional and topological features are in line between 3C-based methods and microscopic approaches. Using microscopy it was furthermore shown that chromosomes are organized into territories (Cremer et al. 1982b, Manuelidis 1985, Schardin et al. 1985; for review see Cremer and Cremer 2010) and that these CTs take up non-random radial positions inside the nucleus. Gene-rich chromosomes or chromosome segments are consistently found to be located more internally than gene-poor chromosomes (for review see Cremer and Cremer 2010, Cremer et al. 2018, Cremer et al. 2020). This matches the observation of Lieberman-Aiden et al. (2009) in the 3C-

based data sets that the more centrally located A compartment is associated with the presence of (a higher number of) genes. And also CTs in general were observed using both population (Lieberman-Aiden et al. 2009, Sexton et al. 2012, Zhang et al. 2012b) as well as single-cell (Nagano et al. 2013, Flyamer et al. 2017, Stevens et al. 2017, Tan et al. 2018) 3C-based methods.

Also on the smaller scale, the two technologies are in line with each other. As already mentioned in the introduction in section 2.2.1 and 2.2.5 both methods revealed that CTs and with that of course also the A and B compartment are built up from chromatin domains. In microscopic approaches these domains were initially observed as replication foci and were estimated to contain about 1 Mbp of DNA (Ma et al. 1998, Jackson and Pombo 1998; for review see Berezney et al. 2000, Cremer and Cremer 2001, Cremer and Cremer 2006). 3C-based methods later confirmed in population data sets that topologically associated domains (TADs), as they are called here, have a size of about 100 kbp to 3 Mbp (Dixon et al. 2012, Nora et al. 2012, Rao et al. 2014; for review see Cubenas-Potts and Corces 2015, Sexton and Cavalli 2015). Recently TADs of similar size were also observed in individual cells (Tan et al. 2018) (for details see below). Using a new labeling approach combined with STORM imaging Nir et al. (2018) could show that TADs indeed constitute physical entities inside the nucleus – at least in most cases (again: for details see below). Supported by Bintu et al. (2018) this study furthermore revealed a domain organization on an even smaller scale, in line with contact domains / subTADs detected with 3C-based methods (for review see Cubenas-Potts and Corces 2015) as well as the idea of fractal globules (Lieberman-Aiden et al. 2009, Mirny 2011; see section 2.2.5 in the introduction).

Beyond this organization into compartments, CTs, and domains per se, however, a more detailed look at the structural organization of the nucleus presented by microscopy and 3C-based approaches reveals the fundamental difference between the two methods. Super-resolution fluorescence microscopy and TEM imaging could clearly establish that the nucleus is pervaded by an IC with smaller channels and larger lacunas and that typically regions with higher chromatin compaction are found around the nuclear periphery as well as the nucleoli (see for example this work / Hübner et al. 2015, Markaki et al. 2010, Smeets et al. 2014, Popken et al. 2014, Ricci et al. 2015, Szczurek et al. 2017, Xu et al. 2018, Strickfaden et al. 2019). 3D visualizations of 3C-based data sets obtained from single cells (Stevens et al. 2017, Tan et al. 2018), however, give a totally different impression: they seem to almost completely lack IC space – especially the wider channels and lacunas – (compare also Cremer and Cremer 2019) and promote the picture of a very homogenous distribution of chromatin inside the nucleus.

In order to understand this discrepancy, it is important to keep in mind what 3C-based data actually are: individual contacts between isolated chromatin segments. The contact maps these approaches are known for are then generated in a second step by setting the obtained “dots” into context to each other based on reference genome sequences available in the databases. So, especially for 3D models derived from these data sets two factors play a decisive role: (1) the number of contacts obtained and (2) the accuracy of the assumptions required and parameters used for data processing and 3D modeling (for review see Pal et al. 2019, Kong and Zhang 2019; and see also the method sections of Stevens et al. 2017, Tan et al. 2018). The number of contacts determines the resolution and depends on the efficiency of genome digestion, recovery rate of the generated chromatin fragments, as well as sequencing depth. Since the first high throughput 3C study of Lieberman-Aiden et al. in 2009, a lot of progress was made for population data. However, these data sets represent an average of hundred thousands or even millions of cells and are therefore not suitable for the generation of 3D models. Single-cell data are essential, but in such approaches it is even more challenging to achieve a high contact frequency. Despite of advances being made in the last few years, Stevens et al. (2017) obtained in their best cell on average only one contact per 22 kbp, i.e. per 116 nucleosomes¹, and also the results of Tan et al. (2018) – although achieving further improvements in resolution – are limited to one imputed contact per 8 kbp in the best case and per 12 kbp in the cell shown in the publication, corresponding to one contact every 42 or 63 nucleosomes, respectively². Based on these numbers it should be obvious that the path of the DNA in the 3D visualizations shows neither the absolute position nor the detailed folding of the chromatin chain. Instead, it rather represents a backbone outlining the approximate course of the DNA at low resolution. As a consequence, 3C-based approaches (at least currently) cannot properly depict the IC and cannot contribute to the analysis of chromatin topology or chromatin compaction on the nanoscale as well as to the discussions about higher-order chromatin organization (10 nm vs 30 nm fibers, see section 2.1). For finding answers to these questions microscopic approaches are needed, like for example the ChromEMT method (chromatin staining combined with electron tomography) used by Ou et al. (2017). This study could confirm the by now widely accepted presumption (for review see Maeshima et al. 2014, Hansen et al. 2018) that chromatin inside the nucleus forms irregular, disordered chains with flexible diameters below 30 nm, instead of consistent higher-order 30 nm fibers.

While facing limitations in this area, 3C-based approaches have other advantages. First and foremost that the data is based on sequencing and that it is therefore always known which part

¹ Haploid mouse ES cells; haploid genome size of mouse: 2 689.66 Mbp (Pubmed genome database. *Mus musculus.*); final number of contacts: 122 475; average nucleosome repeat length assumed to be 190 bp.

² Diploid human GM12878 cells; haploid genome size of human: 2 988.7 Mbp (Pubmed genome database. *Homo sapiens.*); final number of imputed contacts: 743 628 / 499 581; average nucleosome repeat length assumed to be 190 bp.

of the genome is being looked at and which DNA sequences come together in 3D space. As a consequence the improved single-cell 3C-based approach of Tan et al. (2018) could not only clearly demonstrate that TADs also exist in single cells as already mentioned above, but could also confirm what the experiments of Flyamer et al. (2017) as well as the polymer folding simulations of Fudenberg et al. (2016) had indicated before – that TADs do not form static entities as it might have been expected from the population data, but instead exhibit a great variability from cell to cell regarding both, their borders as well as their size. This variability might provide an (additional) explanation (compare also section 5.1.3) why in the microscopic data sets of Nir et al. (2018) occasionally neighboring domains appear to be intertwined with each other: as the domains in this study were labeled based on the information obtained from 3C-based population data sets it is possible that parts of a domain assigned to a certain TAD actually belong to the neighboring TAD in this particular cell. In addition to the flexible borders also chromatin compaction at the domain level differs between cells, as calculations of the radius of gyration for each TAD in single-cell 3C-based data sets revealed (Stevens et al. 2017). Furthermore, the 3D models mentioned above help to visualize and underline what is actually long known from microscopic data: that the spatial chromatin configuration of one and the same DNA sequence differs between cells (Stevens et al. 2017, Tan et al. 2018) as well as between the two alleles within the same cell (Tan et al. 2018). Although the advanced labeling techniques of Bintu et al. (2018) and Nir et al. (2018) have recently pushed microscopic imaging and analyses to a whole new level and with that could confirm the observations of the single-cell 3C-based data sets for selected sequences, covering the entire genome in one experiment – like 3C-based approaches do – is still not feasible at the moment.

The variability of these parameters – TAD borders, chromatin compaction, and chromatin configuration – within what is usually considered a homogenous cell population (or even within one cell in the case of different alleles) shows two important points: First, it emphasizes the importance of single-cell analyses (see also section 2.6) and makes clear that they are highly needed and valuable even if they can only provide low throughput compared to other methods. And second, it allows the speculation that functional nuclear architecture is maybe “only” determined by certain cornerstones – whether these are architectural proteins like CTCF (CCCTC-binding factor) or histone modifications or interactions with cellular components such as the lamina or nucleoli or a combination of these and other factors still remains to be seen – that form a fundamental and solid framework of basic spatial and structural constraints, but do not determine the absolute configuration of the chromatin chain. Instead – within these basic but important limitations – the folding of the sequences might be highly flexible or even random at both the smaller scale of domains and subdomains / contact domains as well as on the larger scale of A and B compartments and CTs. This thought was also discussed in a recent

review (Ulianov et al. 2017) and goes in the direction of a liquid-like behavior of chromatin (for review see Maeshima et al. 2016). Potentially with such flexible arrangements of chromatin changes in the level of chromatin compaction and the spatial proximity of individual TADs / CDs and therefore the size and appearance of CDCs as well as the IC require only (comparatively) little effort. Thus distinct global chromatin patterns and different gene expression patterns could be established quite easily while the stable cornerstones of functional nuclear architecture would at the same time ensure the maintenance of the same principles of organization in all cell types and conditions, fully conform with the observations in this work.

In conclusion, this chapter should have made clear that every approach has certain advantages but also certain limitations. Thus, one method alone cannot provide answers to all questions and information obtained with different technologies has to be combined in order to make progress in deciphering the detailed functional and structural organization of chromatin and the nucleus as a whole (compare also Fudenberg and Imakaev 2017). An optimal use of different methods in an integrated approach can also help to avoid drawing (false) conclusions from artifacts when results can be confirmed with more than one technique. This is especially important since the current questions in the field of nuclear organization challenge microscopic and 3C-based technologies alike to push their boundaries to and across their current limits. Therefore the decisive question cannot be “Which approach is the best in general?”, but has to be “Which approach is the best for this particular aspect.” Here in this work, the focus was on the spatial organization of functional nuclear architecture on a more global level and not on the level of (macro)molecular interactions. Thus, the use of biophysical methods (microscopy) was better suitable than biochemical methods (3C-based approaches and/or others).

For future experiments the aim has to be to continue what the studies of Bintu et al. (2018), Nir et al. (2018), Stevens et al. (2017) and Tan et al. (2018) started – to try to close the gap between the biophysical top-down (e.g. Bintu et al. 2018, Nir et al. 2018) and the biochemical bottom-up approaches (e.g. Stevens et al. 2017, Tan et al. 2018). Performing first super-resolution imaging and then single-cell 3C in one and the same cell would be an amazing achievement as this should allow to create overlays of the global chromatin organization captured by microscopy with the exact sequence information obtained by 3C-based models. Such an approach could for example help to analyze the detailed spatial relationship between CTCF binding sites and “their” corresponding chromatin domain (for details on CTCF see reviews of Merckenschlager and Nora 2016 and Rowley and Corces 2018).

5.2.2 Thoughts on correlative microscopy

The experiments performed in section 4.4 of this work (**Figure 65, 66-70**) clearly demonstrate the benefits of correlative microscopy and make the importance of such approaches evident: live cell observations allow to follow dynamic processes, like here the condensation of chromatin upon hypertonic treatment, in space and time (4D). After fixation of the cells several substructures of the nucleus or the cell in general can be stained and 3D acquisitions of the multicolor experiments can be recorded with CLSM and/or 3D-SIM. Here H3K4me3, SC35, RNA Pol II Ser 2P, and H3K9me3 were detected in immunofluorescence stainings. After fluorescence imaging the cells can be embedded, prepared and stained for TEM, to make use of the dramatically increased resolution offering very detailed insights into cellular substructures. Here DNA specific osmium ammine staining was applied.

By combining the information collected with several microscopic approaches correlative microscopy can lead to findings that could not have been achieved with only one technique: here it could be shown that splicing speckles stained by SC35 (imaged by CLSM) located in the interior of IC lacunas that were free of DNA (demonstrated by TEM) and that already existed under normal conditions prior to HCC induction (shown by the live cell observation).

As already described in section 4.4, the direct comparison of CLSM and 3D-SIM in those experiments clearly demonstrated the advantage of the improved resolution of super-resolution fluorescence microscopy. As a consequence, CLSM imaging could be considered dispensable, although it certainly is not: with the setup used in this work, for example, 3D-SIM is currently limited to the detection of three colors, while CLSM allows the simultaneous staining and detection of five colors without any problems. Furthermore, not all samples seem to be (perfectly) suitable for 3D-SIM: (1) 3D-SIM has difficulties to handle larger uniformly or diffusely stained areas (compare also Liu and Wright 2014, Shao 2014). Image reconstructions of granulocytes with their large CDCs or mitotic cells with their condensed chromosomes were often characterized by severe artifacts and hematopoietic cells fixed under low salt conditions (resulting in a very uniform distribution of chromatin as shown by TEM (**Figure 31**)) could not at all be imaged with acceptable quality (data not shown). Apparently the standard reconstruction algorithms are optimized to find patterns and struggle when there are none. (2) Also thick samples provide a challenge for 3D-SIM imaging (compare also Liu and Wright 2014, Shao 2014). Again artifacts are frequent in such cells due to the increased volume and the correction of chromatic shift becomes very difficult, as chromatic aberration increases together with the distance from the coverslip. The combination of these two points is most probably the reason why only a small percentage of the mitotic cells imaged for this work reconstructed well enough to be included in the analysis.

One of the central challenges of correlative microscopy are the different and partially very specific requirements of each microscopic system (see also section 2.6.5). Having a close look at the data generated by the two different pathways of correlative microscopy indicates that 3D-SIM and TEM – at least with the protocols used here – seem to be not fully compatible. A comparison of the TEM images acquired according to pathway I (**Figure 65+66 D**) vs pathway II (**Figure 67-70 E**) revealed that the best possible TEM quality of osmium ammine stained DNA was only obtained with pathway I. In pathway II the structure of HCC appeared a bit more dispersed and the osmium ammine staining of the DNA slightly weaker. In control nuclei the difference was very small (**Figure 66+68**), but in HCC induced nuclei (**Figure 65+67+69+70**) it was not neglectable. Possibly the impaired image quality in pathway II results from the necessary mounting of the sample in Vectashield for imaging with 3D-SIM (compare also **Figure 11** in section 3.2.10.1) in combination with only mild fixation and post-fixation (2% and 4% PFA, respectively). In contrast to imaging with CLSM where the samples can be scanned in 1x PBS, the acquisition of images from samples not mounted in antifade is not possible with 3D-SIM due to the high light exposure during the scanning process. A stronger (post)fixation and/or modifications in the embedding protocol are promising approaches to achieve an improved staining quality of sections previously mounted in Vectashield (not tested in this thesis).

When performing correlative microscopy, typically the generation of overlay images of the data collected with the different microscopic systems is of high interest and importance in order to combine the collected information. Ideally one would like to view perfectly matched overlays. However, due to the differences in the z-resolution of the different microscopes, the movement of structural components in living cells prior to fixation, slightly different image planes in the optical and physical sections, shrinkage through the embedding of the cells in resin and deformations caused by the electron beam during TEM imaging (for details see Hübner et al. 2013), this is almost impossible to achieve with the raw images. However, through image processing that goes beyond the correction of rotation, mirroring and resolution differences by using for example also distortion and warping (compare section 3.2.11.3), a great part of the mismatches can be corrected and pretty good alignments can be achieved. However, as the corrections are done by hand the matches can never be perfect. Thus the resulting overlay images are not recommended for correlating small entities such as H3K4me3 signals for example. (Semi)automatic methods for image correlation have been and are constantly being developed and certainly would be worth to explore, although even with those approaches the correlation of subtle structures is expected to remain difficult. But for the correlation of larger structures or signals and/or the determination of their localization in images where the

acquisition of the same signals is not (easily) possible, the generation of overlay images – whether by hand or (semi)automated – is highly suitable and of great value.

In summary, despite certain difficulties, the power of correlative microscopy lies in the possibility to combine and sum up information from the different systems into a bigger picture than it could ever be achieved by one approach alone.

5.3 Addendum: Insights into the processes and mechanisms occurring upon UV/caffeine treatment and PCC

Starting from the similar shattered nuclear phenotypes observed after MAA, but not after PFA fixation (**Figure 43**; see also section 2.5.3 and 2.5.4 in the introduction), the processes involving these particular cells occurring after both UV/caffeine treatment and PCC induction were thoroughly investigated. The aim was to be able to understand what the respective phenotypes represent and to be able to judge potential differences compared to control cells.

5.3.1 UV/caffeine treated cells and PCC: two different phenomena but both representing mitotic events

Live cell observations combined with MAA fixation directly on the microscope (“correlative MAA fixation”) revealed that GCS, the shattered compliments occurring after UV/caffeine treatment of V79 cells, are the fixation outcome of PALCCs, abnormal mitotic cells with a parachute-like chromatin configuration (PALCC) consisting of a bulky chromatin mass and extended chromatin fibers on one side (**Figure 44**). Within about 1 h – the typical time frame for mitosis – PALCCs developed from morphologically inconspicuous prophase cells and proceeded to form multilobulated interphase cells (**Figure 45**). The occurrence of multilobulated cells after UV irradiation (UVA, wavelength: 365 nm) in the presence of caffeine posttreatment and psoralen was already reported previously (Cremer et al. 1981b) using the term micronucleated cells. PALCCs, however, were not mentioned in this study. Multilobulated cells were merely stated to be “[...] the result of an abnormal first postirradiation mitosis”. Immunofluorescence experiments demonstrated that multilobulated nuclei show all characteristics of control interphase nuclei (**Figure 52+54+56+57**). Only centromeres exhibited an unusual localization, being clustered together in one or two lobes instead of being distributed throughout the entire nuclear volume (**Figure 54**). This is probably a consequence of the abnormal spindle localization in PALCCs (see details below).

PCC cells, on the other hand, did not proceed to interphase after the removal of the inducing drug (**Figure 47**). Instead, they formed undefined chromatin clumps, a phenomenon that was also observed upon prolonged PCC induction (Yamashita et al. 1990). Note that Yamashita et al. (1990), as well as other authors cited in this and the following chapter, used Okadaic acid for PCC induction instead of Calyculin A applied here. But similar to Calyculin A, Okadaic acid is a potent inhibitor of phosphatase activity, especially of type 2A, but also of type 1 and to a lesser extent type 2B phosphatases (Bialojan and Takai 1988, Ishihara et al. 1989), and accordingly the two compounds induce PCC through the same mechanism (compare section 2.5.4 in the introduction). Thus it can be assumed that – although some differences in cell susceptibility seem to exist (Gotoh 2009) – Okadaic acid and Calyculin A can be used interchangeably and that the characteristics of PCC induced cells are the same for both drugs. In contrast to Yamashita et al. (1990) and the observations made in this work, Tosuji et al. (1992) observed in a part of their data set studying sea urchin eggs after PCC induction that cleavage occurs similarly as in normal fertilized eggs. This indicates that at least some steps towards interphase can take place upon PCC induction. However, sea urchin eggs might represent a special case, considering that eggs are anyways programmed for rapid cell divisions. Furthermore, in a later section of their article, the authors contradict themselves by mentioning that “Neither segregation nor decondensation of the chromosomes occurred [...]” and showing an additional set of images supporting this statement.

Figure 47+48 shows that PCC induction progressed with a fixed sequence of morphological changes with gradually increasing chromosome condensation and the nucleus seemingly opening up in the late stages. A similar observation was made by Tosuji et al. (1992) in sea urchin eggs after Calyculin A treatment, but apart from that only isolated snapshots of early PCC stages seem to be available in the literature. All of these images were obtained after PCC induction by cell fusion, but they are in line with the results presented here: Already 5 min after fusion chromatin appears more condensed than in normal interphase (Matsui et al. 1972), equivalent to very early PCC cells. 10 min (Matsui et al. 1972, Sperling and Rao 1974) or 20 min (Matsui et al. 1972) after fusion unsynchronized interphase cells show an early to middle PCC morphology. Also cells fused in S phase exhibit an early PCC morphology, while cells fused in G1 phase correspond to late I PCCs (Rattner and Wang 1992). However, despite the constant morphological progression of PCC induction, not all cells entered PCC at the same time and some also retained an interphase appearance throughout the entire period of PCC induction. Correlative MAA fixation (**Figure 49+50+51 C**) demonstrated a link between PCC stage and fixation outcome: early and middle PCCs resulted in the shattered S PCCs while late PCCs appeared as G1/G2 PCCs, similar to normal metaphase spreads. S PCCs were mainly BrdU positive, while G1/G2 PCCs were mainly BrdU negative (for a detailed assessment and discussion of these findings see section 5.3.2 below).

GCS cells after UV/caffeine posttreatment, in contrast, were always BrdU negative (**Figure 44 B**), despite their close morphological similarity to S PCCs, matching the observation of being the fixation outcome of (abnormal) mitotic cells.

But GCS and S PCCs, respectively PALCCs and PCC induced cells, exhibit also common features.

Most importantly, they share (almost) all major hallmarks of mitosis with each other and with normal mitotic control cells (for the explanation of the marker proteins see section 2.3 of the introduction): The lamina got degraded in the course of PCC induction (it was still present in the earlier PCC stages, but dissolved in late II PCC cells) and also PALCCs showed a dispersed Lamin B pattern (**Figure 52**). The breakdown of the nuclear lamina upon PCC induction was already indicated in earlier studies by (preliminary) immunofluorescence images (Yamashita et al. 1990) or electron micrographs (Matsui et al. 1972 (here after PCC induction by cell fusion), Ghosh et al. 1992). All PCC stages as well as PALCCs were intensely stained with H3S10p (**Figure 52**). For PCC cells this result confirms previous reports where phosphorylation of histone 3 or the increase of phosphorylated proteins in general was observed by indirect (western blots, flow cytometry) and/or direct methods (immunofluorescence) (Yamashita et al. 1990, Ajiro et al. 1996, Huang et al. 2006). Staining for centromeres indicated that kinetochores formed in both PCC cells (**Figure 53**) and PALCCs (**Figure 54**) as it was already demonstrated in earlier studies for PCC induced cells (Matsui et al. 1972, Rattner and Wang 1992; in these two articles after PCC induction by cell fusion), Ghosh et al. 1992). The localization of the centromeres, however, was (slightly) abnormal with being pulled out several μm from the bulky chromatin mass of PALCCs and being distributed throughout the nucleus in all PCC stages giving the impression that no proper metaphase plate was formed in these cells. A clumped localization as reported by Rattner and Wang (1992) after PCC induction by cell fusion, was not observed in this work. The analysis of the distribution of α -tubulin explained the abnormal localization of the centromeres: in PALCCs a normal spindle was present, however, shifted to one side of the chromatin mass (**Figure 54**). PCC cells, in contrast, lacked a proper spindle (**Figure 53**), in line with reports of several earlier studies (Rattner and Wang 1992 (here after PCC induction by cell fusion), Ghosh et al. 1992, Tosuji et al. 1992). Yamashita et al. (1990) on the other hand, although also not detecting proper mitotic spindles, observed the formation of mitotic asters after 1 h of PCC induction with 0.5 μM Okadaic Acid. Upon prolonged incubation, however, also in this study the asters were not detected anymore. Here, in this work, early PCC cells showed no cytoskeleton and/or spindle at all and in late II PCC cells only a very loose network of only a few microtubules was observed. In middle and late I PCC cells a rudimentary spindle was present, however, consisting of only one pole. This point underlines that PALCCs and PCC cells are different

phenomena. In addition, in PCC cells Ki67 (**Figure 53**) and SMC2 (**Figure 55**) relocated to the surface respectively the axis of the chromosomes during the condensation process, equivalent to what was observed in normal cells. Only in rare cases, only one broadened strand of SMC2 staining was observed instead of two chromatids (see also section 5.3.2 below). These SMC2 staining patterns were also described by Debatisse et al. (2006). Also RNA Pol II (**Figure 56**), H3K4me3 (**Figure 56+57**) and H3K9me3 (**Figure 57**) in PALCCs and PCC cells showed the same pattern as in control cells: the chromatin of PALCCs lacked RNA Pol II Ser 2P and H3K9me3 and also PCC cells showed a reduction of both markers with progressing PCC induction. H3K4me3, in contrast, was maintained in all cells, although in PALCCs it seemed to be more restricted to the surface of the chromatin domains.

Furthermore, GCS and S PCC observed after MAA fixation also have in common that evidence indicates that chromatin in these cells is actually not shattered or pulverized in the sense of broken or fragmented chromosomes despite the visual impression. GCS was negative for fragmentation detected by the TUNEL assay (data not shown, see Hübner et al. 2009) and in (late) S PCCs after PCC induction by cell fusion replication labeling was found in between chromosome fragments potentially coming from the same chromosome (Sperling and Rao 1974, Rohme 1975). This indicates that there are structural connections between the fragments as otherwise a much more random distribution of the pieces would have been expected. Scanning electron microscopy supports this idea, revealing that the chromosome pieces of S PCCs are in fact often interconnected by thin chromatin fibers (Hanks et al. 1983, Gollin et al. 1984). In addition, it can be assumed that the formation of multilobulated but otherwise typical interphase cells in the case of PALCCs or of properly condensed chromosomes in the later PCC stages (resulting in G1/G2 PCCs upon MAA fixation with a morphology equivalent to metaphase spreads of control cells) would not be possible if chromatin in these cells would indeed be characterized by such massive fragmentation as indicated by their morphology after MAA fixation.

Taken together the results discussed in this section show that despite their similar phenotype GCS and S PCCs are derived from very different, however, in both cases abnormal mitotic cells – GCS resulted from PALCCs, S PCCs occurred from early or middle PCC cells – and that the processes taking place after UV/caffeine treatment and PCC induction represent two different phenomena. Different nuclear phenotypes were observed and while PALCCs occurring after UV/caffeine irradiation represented indeed a mitotic event (although an abnormal one) as they gave rise to multilobulated interphase cells and were always negative for BrdU, PCC cells did not. The induction was not reversible, the cells did not proceed to interphase and depending on the stage of PCC induction at the point of fixation a significant fraction of PCC cells was positive for BrdU.

In closing, a brief thought of these two processes in the context of (delayed) cell death: As mentioned in section 2.5.3 in the introduction, besides the well-characterized pathways of apoptosis also other often only poorly defined, non-apoptotic endpoints have been described in the literature (for review see Blank and Shiloh 2007, Galluzzi et al. 2012). In cases where aberrant and/or fragmented mitotic figures are involved, the processes are typically classified as mitotic catastrophe and/or mitotic cell death, two terms which are often used interchangeably and which summarize a variety of phenomena (e.g. Ianzini and Mackey 1997, Castedo et al. 2004b, Nitta et al. 2004, Blank et al. 2006, Mansilla et al. 2006, Stevens et al. 2007, Zhang et al. 2011). Whether GCS/PALCCs and PCC can be considered as mitotic catastrophe / mitotic cell death depends on the definition of these expressions (compare also Castedo et al. 2004a, Eriksson and Stigbrand 2010, Caruso et al. 2011, Vitale et al. 2011, Galluzzi et al. 2012 for review): If these expressions are indeed considered to represent a form of cell death, then PALCCs do not fall into this category as they gave rise to cells with multilobulated nuclei but otherwise exhibited all characteristics of control interphase cells. If, however, mitotic catastrophe / mitotic cell death is seen as a catastrophic event that causes so much damage or such an aberrant situation that the cell dies later on, then PALCCs clearly characterize as such, as the cells were shown to go into apoptosis several hours after PALCC formation (data not shown; see Hübner et al. 2009). For PCC cells the situation is slightly different – they did not proceed to interphase but remained as undefined cell clumps, which can be considered as a form of cell death, although the cells appeared to proceed to apoptosis later on.

5.3.2 Revision of the definition of S phase PCCs

The classic categorization of MAA fixed PCC cells into G1, S or G2 PCCs is based on PCC induction by cell fusion using synchronized cells (e.g. Johnson and Rao 1970, Hanks et al. 1983). Judging from the morphology of the cells after MAA fixation these categories were later also transferred to PCC cells generated by other ways of PCC induction and/or to unsynchronized cells with unknown cell cycle phases (e.g. Gotoh et al. 1995, Bezrookove et al. 2003, Hatzi et al. 2006). The experiments performed in this work shed light on the correlation between cell morphology in the living cell state (i.e. PCC induction stage), morphology after MAA fixation (i.e. PCC category) and BrdU staining (i.e. evaluation whether the cells are in S phase or not). They suggest that the classic categorization of PCC cells into cell cycle phases purely based on their morphology after MAA fixation needs to be revised or expanded.

As already briefly mentioned above in section 5.3.1, after 1 h of PCC induction with Calyculin A S PCC cells were mainly BrdU positive (**Figure 49**), matching the general assumption of shattered PCC compliments representing S phase cells (see literature in the previous paragraph). However, a fraction of S PCC cells was also BrdU negative (**Figure 49**), as also observed previously by Gotoh et al. (1995). In a similar way, G1/G2 PCCs were mainly BrdU negative, but again not exclusively, and also positive G1/G2 PCCs were found (**Figure 50+51 C**) (reported also by Hanks and Rao 1980). Live cell observations (**Figure 47+48**) and correlative fixation (**Figure 49+50+51 C**) provide a solid explanation for this variation: PCC induction progressed with a fixed sequence of morphological changes and S PCCs emerged from early and middle PCC stages, while G1/G2 PCCs were the fixation outcome of late PCC stages. Thus, not the cell cycle phase at the point of fixation is the decisive criterion for the morphological outcome after MAA fixation, but the morphology of the living cell.

However, a certain link to the cell cycle cannot be denied and was revealed by applying various PCC incubation times (**Figure 51 A**): at all time points the fraction of BrdU positive cells was clearly higher in S PCCs (i.e. early or middle PCC cells in the living cell state) than in G1/G2 PCCs (i.e. middle-late or late PCC cells) cells, indicating that cells in S phase need more time to develop PCC than cells in G1/G2. With prolonged incubation, the cells have more time to develop into later PCC stages prior to fixation. As a consequence, the fraction of BrdU positive cells increased in S PCCs to (almost) 100% after 1 h 30 min and 2 h, as all BrdU negative cells had enough time to move on and leave the slower S phase cells behind. However, also S phase cells have a higher chance of reaching late PCC stages during the increased incubation period and therefore also among G1/G2 PCCs the fraction of positive cells increased. The assumption that a constant flow of cells enters PCC and develops into later stages explains that the relative amount of S PCCs was roughly the same at all incubation times (apart from 10 min and 30 min, see explanation below) and G1/G2 PCCs accumulated more and more. The drop in the fraction of PCC cells after 2 h probably results from the weaker attachment of the late stages to the surface of the coverslip and therefore from a loss of cells during fixation. The fact that there are no S PCCs detected after 10 min and that the main fraction of these cells was BrdU negative after 30 min indicates that PCC in general needs a certain time to develop – 10 min are apparently too short for any cells (even BrdU negative cells) to reach an early PCC stage and thus causing the S PCC phenotype after MAA fixation. 30 min are sufficient, but primarily only for the faster BrdU negative cells. Consequently one would expect that after 10 min also no G1/G2 PCCs can be found and only very few after 30 min. However, this was not the case. Most probably those cells were already in or just about to enter normal mitosis when PCC was induced. As such cells are already programmed for the condensation

of chromatin or even exhibited already condensed chromosomes, the PCC process in these cells can be assumed to be very fast so that even short incubation times are sufficient to result in a G1/G2 PCC phenotype after MAA fixation. This is supported by **Figure 51 B**, demonstrating that PCC cells either derived from mitotic cells or from cells late in the cell cycle. Evidence for this theory of S phase cells being less susceptible to PCC induction than cells in other phases of the cell cycle is also provided by Rattner and Wang (1992): after PCC induction by cell fusion S phase cells were shown to exhibit an early PCC morphology, while cells fused in G1 phase corresponded to late I PCCs. Assuming the cells were analyzed at the same time interval after fusion, this indicates that cells in G1/G2 proceed faster than cells in S phase.

The mechanistic background behind the delayed progression of S phase cells most probably lies in the fluctuating levels of cyclin B during the cell cycle. As described in detail in section 2.5.4 in the introduction, Calyculin A induces PCC by causing the activation of the cyclin B / Cdk1 complex, one of the key players in mitotic onset. Cyclin B starts to be expressed during S phase, reaches maximum levels in G2/M phase and gets rapidly degraded before the cells enter anaphase (Bai et al. 1994, Chang et al. 2003). Thus, cyclin B is basically absent in G1 phase and low in S phase, explaining the delayed onset of PCC in S phase cells. That cyclin B levels indeed have an influence on PCC induction was shown by Prasanna et al. (2000) where cyclin B / Cdk1 was added to the culture medium of the cells leading to an increase in the number of PCC cells. It can even be speculated that S phase first has to be completed before the cells can enter PCC: certainly, PCC induction is an artificial system where many of the normal processes in the cell could be deregulated. However, as Calyculin A basically only serves as an initiator for the normal processes of the cell, most probably the intrinsic control mechanisms and therefore also the G2-checkpoint, which prevents cells from entering mitosis without replication being finished (Alberts et al. 2015), are still intact.

As mentioned above, cyclin B is not present in G1 phase, making it even more difficult or unlikely to induce PCC in these cells than in S phase cells. The few G1 PCC cells that could be found (e.g. most likely the upper late II PCC cell in **Figure 53** and the lower late II PCC cell in **Figure 55**; compare also point 2 and 3 below) probably rather represent cells that were in late telophase at the point of PCC induction, as suggested by the evaluation of PCC morphologies before and after MAA fixation (**Figure 51 B**) and also mentioned by Gotoh and Durante (2006). This limitation of chemical PCC induction using Calyculin A or Okadaic acid was also noted in several publications (Bezrookove et al. 2003, Gotoh and Durante 2006, Gotoh 2009). Consequently, PCC cells resulting from those treatments mainly represent cells in G2 or maybe in late S phase, reaching G2 during PCC induction. Several experiments performed in this work provide evidence for this: (1) Apart from the cells that were already in mitosis at the time of PCC induction only cells that had not divided for minimum 16.5 h

(**Figure 51 B**) and had large or medium-sized nuclei (**Figure 48**) went into PCC. (2) Centromeres often appeared as doublet signals, representing one signal from each of the two sister chromatids (**Figure 53**), a finding that was also observed after PCC induction by cell fusion in G2 PCC cells (Rattner and Wang 1992). (3) The vast majority of PCC cells showed two strands of SMC2 staining in each chromosome, delineating the two sister chromatids (**Figure 55**).

To summarize, a shattered chromosome complement alone is not sufficient to assume that the cell was in S phase when PCC was induced. Evidence rather suggests that all PCC cells are in G2 phase, regardless of their morphology after MAA fixation. Nevertheless, the shattered S PCCs have a higher tendency to indeed represent cells that were in (late) S phase at the point of PCC induction as those cells seemed slower in developing PCC and thus within the 1 h incubation time reach only the early PCC stages which were shown to result in shattering upon MAA fixation. This suggests that the definition of S PCCs should be revised or expanded in such a way that at least a positive replication labeling is needed in order to classify S PCCs as true S phase cells.

5.3.3 The factor depletion model as a common background for shattered chromosome complements

Here in this work UV irradiation was performed by irradiating the entire nucleus of the cells (compare section 3.2.2.2) and so it was not surprising that the complete chromosome complement of PALCCs shattered upon MAA fixation (**Figure 44**). Earlier studies, however, showed that GCS also occurred after partial UV irradiation of nuclei (Cremer et al. 1981a, Cremer et al. 1981b, Cremer and Cremer 1986; for review see Cremer and Cremer 2006), suggesting that there are indirect effects of the irradiated chromatin on the undisturbed areas of the nucleus. To explain these unexpected findings the so-called factor depletion model was developed (Cremer et al. 1981a, Cremer et al. 1981b, Cremer and Cremer 1986; for review see Cremer and Cremer 2006). This model predicts that a limited pool of proteins exists in the cell which is directly involved in more than one function. For example in DNA repair and in an unknown process of chromatin maturation in G2 phase necessary for proper chromosome condensation during mitosis. If this pool of proteins gets exhausted, e.g. through UV irradiation, then the same factors might no longer be available to perform their other functions. Thus only the number of the damage sites in the nucleus is important and not their spatial distribution. And if the dose used for UV irradiation is high enough, also a partial irradiation can lead to the depletion of the protein pool resulting in GCS upon fixation.

As mentioned above, in this work only whole-cell irradiation was applied. But nevertheless, these experiments support the factor depletion model: As described in detail above in section 5.3.1 PALCCs were shown to represent abnormal mitotic cells. Comparing their chromosome complement with normal mitotic chromosomes reveals a condensation failure in these cells. Already looking at the chromatin staining alone (**Figure 43-45, 52+54, 56-57**) shows that they lack distinct mitotic chromosomes. The detection of individual chromosomes using FISH provided further evidence, as CTs in PALCCs appeared more like in interphase than in normal mitosis (**Figure 58**). Given the mode of action of caffeine, which allows the cells to proceed to S phase or mitosis despite of (massive) unrepaired DNA damage (compare section 2.5.3 in the introduction) this condensation failure indicates an exhaustion of a protein pool involved in both DNA repair on the one hand and chromosome condensation or an unknown process of chromatin maturation in G2 phase on the other hand.

Potential candidates for such a protein pool include factors involved in the alteration of chromatin structure. It is obvious that in mitosis the chromosomes first are massively condensed and then decondensed again in order to form the daughter nuclei and also in DNA repair changes in chromatin organization were shown to occur (for review see Xu and Price 2011, Nair et al. 2017). Topoisomerases are one example. Especially topoisomerase II was shown to be involved in both DNA repair and chromosome condensation in mitosis (for review see Bollimpelli et al. 2017, Piskadlo and Oliveira 2017).

The factor depletion model argues for the morphology after MAA fixation being not specific for the inducing agent, but rather representing a certain condition of the chromatin. This condition can potentially be the result of basically any severe stress situation, as shattered chromosome complements morphologically similar to or even identical with GCS were also found under other conditions than UV/caffeine treatment. For example after UV irradiation (Waldren and Johnson 1974) or γ -irradiation (Terzoudi et al. 2015) and subsequent cell fusion without caffeine treatment, after cell cycle inhibition during S phase by deprivation of amino acids (Freed and Schatz 1969), after treating mice (Yadav et al. 2014) or cells (Ochi et al. 2003) with genotoxic chemicals, or many other scenarios listed in Stevens et al. (2010). Also PCC induction represents a stress situation because the cells are forced into mitosis although other processes in the cell – potentially requiring the same set of proteins as chromosome condensation – might still be ongoing. In contrast to PALCCs, however, in early and middle PCCs resulting in the shattered S PCCs after MAA fixation (**Figure 49**), no problems with chromatin condensation were apparent. Maybe the lamina which was – different from PALCCs – still intact in these PCC stages (**Figure 52**) and/or other proteins or factors still retained in the closed nucleus offer enough structural support so that the fragile condition of the chromatin in these cells only

got revealed after MAA fixation.

In addition, this model might also explain why after UV/caffeine treatment interphase and multilobulated cells typically exhibited large IC lacunas or extended areas of very low DAPI intensity (**Figure 59**), reflecting chromatin being present in a more open state as than in control nuclei. Studies actually demonstrated that upon DNA damage chromatin only initially undergoes decondensation but then quickly compacts around the damage site (Burgess et al. 2014, Khurana et al. 2014). So, if the UV dose used for irradiation is high enough to cause excessive DNA damage – more than the available pool of DNA repair factors can handle – then chromatin might remain in a more open state instead of undergoing compaction. On the other hand, however, chromatin compaction upon DNA damage induction was shown to be ATM-dependent (Khurana et al. 2014). Thus it is also possible that caffeine alone is responsible for the more open chromatin structure if the steps leading to chromatin compaction cannot be initialized due to its presence. Either way, the effect of chromatin decompaction was not very prominent in interphase cells and cell numbers were low for multilobulated cells (n=4), so drawing final conclusions based on the results presented here is not appropriate. Further analyses would be needed, including for example time and dose-dependent studies.

6. References

4D Nucleome website. <https://commonfund.nih.gov/4Dnucleome>. 03/11/2019.

Abbe, E. (1873). Beiträge zur Theorie des Mikroskops und der mikroskopischen Wahrnehmung. Archiv für mikroskopische Anatomie, 9, 413-468.

Adams, S.R., Mackey, M.R., Ramachandra, R., Palida Lemieux, S.F., Steinbach, P., Bushong, E.A., Butko, M.T., Giepmans, B.N., Ellisman, M.H., and Tsien, R.Y. (2016). Multicolor Electron Microscopy for Simultaneous Visualization of Multiple Molecular Species. Cell Chem Biol, 23, 1417-1427.

Ajiro, K., Yoda, K., Utsumi, K., and Nishikawa, Y. (1996). Alteration of cell cycle-dependent histone phosphorylations by okadaic acid. Induction of mitosis-specific H3 phosphorylation and chromatin condensation in mammalian interphase cells. J Biol Chem, 271, 13197-13201.

Alberts, B., A., J., Lewis, J., Morgan, D., Raff, M., Roberts, K., Walter, P., Wilson, J., and Hunt, T. (2015). Molecular Biology of the cell, 6th edn. New York, Garland Science, Taylor & Francis Group.

Albiez, H., Cremer, M., Tiberi, C., Vecchio, L., Schermelleh, L., Dittrich, S., Kupper, K., Joffe, B., Thormeyer, T., von Hase, J., *et al.* (2006). Chromatin domains and the interchromatin compartment form structurally defined and functionally interacting nuclear networks. Chromosome Res, 14, 707-733.

Aragon, L., Martinez-Perez, E., and Merckenschlager, M. (2013). Condensin, cohesin and the control of chromatin states. Curr Opin Genet Dev, 23, 204-211.

Awasthi, P., Foiani, M., and Kumar, A. (2015). ATM and ATR signaling at a glance. J Cell Sci, 128, 4255-4262.

Bai, C., Richman, R., and Elledge, S.J. (1994). Human cyclin F. EMBO J, 13, 6087-6098.

Barcia, J.J. (2007). The Giemsa stain: its history and applications. Int J Surg Pathol, 15, 292-296.

Bassett, A., Cooper, S., Wu, C., and Travers, A. (2009). The folding and unfolding of eukaryotic chromatin. Curr Opin Genet Dev, 19, 159-165.

Baumeister, W. (2002). Electron tomography: towards visualizing the molecular organization of the cytoplasm. Curr Opin Struct Biol, 12, 679-684.

Beatty, B., and Scherer, S., eds. (2002). Human chromosome mapping of single copy genes. Oxford, United Kingdom, Oxford University Press.

Berezney, R., Dubey, D.D., and Huberman, J.A. (2000). Heterogeneity of eukaryotic replicons, replicon clusters, and replication foci. Chromosoma, 108, 471-484.

Berneburg, M., Lowe, J.E., Nardo, T., Araujo, S., Foustari, M.I., Green, M.H., Krutmann, J., Wood, R.D., Stefanini, M., and Lehmann, A.R. (2000). UV damage causes uncontrolled DNA breakage in cells from patients with combined features of XP-D and Cockayne syndrome. EMBO J, 19, 1157-1166.

Bethesda, M. (2011). Hematopoietic Stem Cells. <https://stemcells.nih.gov/info/2001report/chapter5.htm>. 25/10/2015.

Betzig, E., Patterson, G.H., Sougrat, R., Lindwasser, O.W., Olenych, S., Bonifacino, J.S., Davidson, M.W., Lippincott-Schwartz, J., and Hess, H.F. (2006). Imaging intracellular fluorescent proteins at nanometer resolution. Science, 313, 1642-1645.

- Bezrookove, V., Smits, R., Moeslein, G., Fodde, R., Tanke, H.J., Raap, A.K., and Darroudi, F. (2003). Premature chromosome condensation revisited: a novel chemical approach permits efficient cytogenetic analysis of cancers. *Genes Chromosomes Cancer*, 38, 177-186.
- Bialojan, C., and Takai, A. (1988). Inhibitory effect of a marine-sponge toxin, okadaic acid, on protein phosphatases. Specificity and kinetics. *Biochem J*, 256, 283-290.
- Bintu, B., Mateo, L.J., Su, J.H., Sinnott-Armstrong, N.A., Parker, M., Kinrot, S., Yamaya, K., Boettiger, A.N., and Zhuang, X. (2018). Super-resolution chromatin tracing reveals domains and cooperative interactions in single cells. *Science*, 362.
- Biocyclopedia (2012). Detection of Cell Cycle Stages in situ in Growing Cell Populations. http://biocyclopedia.com/index/cell_biology_methods/detection_of_cell_cycle_stages.php. 27/11/2019.
- Blank, M., Lerenthal, Y., Mittelman, L., and Shiloh, Y. (2006). Condensin I recruitment and uneven chromatin condensation precede mitotic cell death in response to DNA damage. *J Cell Biol*, 174, 195-206.
- Blank, M., and Shiloh, Y. (2007). Programs for cell death: apoptosis is only one way to go. *Cell Cycle*, 6, 686-695.
- Blasina, A., Price, B.D., Turenne, G.A., and McGowan, C.H. (1999). Caffeine inhibits the checkpoint kinase ATM. *Curr Biol*, 9, 1135-1138.
- Blom, H., and Widengren, J. (2014). STED microscopy - towards broadened use and scope of applications. *Curr Opin Chem Biol*, 20, 127-133.
- Bode, A.M., and Dong, Z. (2007). The enigmatic effects of caffeine in cell cycle and cancer. *Cancer Lett*, 247, 26-39.
- Boettiger, A.N., Bintu, B., Moffitt, J.R., Wang, S., Beliveau, B.J., Fudenberg, G., Imakaev, M., Mirny, L.A., Wu, C.T., and Zhuang, X. (2016). Super-resolution imaging reveals distinct chromatin folding for different epigenetic states. *Nature*, 529, 418-422.
- Bollen, M., Gerlich, D.W., and Lesage, B. (2009). Mitotic phosphatases: from entry guards to exit guides. *Trends Cell Biol*, 19, 531-541.
- Bollimpelli, V.S., Dholaniya, P.S., and Kondapi, A.K. (2017). Topoisomerase IIbeta and its role in different biological contexts. *Arch Biochem Biophys*, 633, 78-84.
- Bradley, M.O., Bhuyan, B., Francis, M.C., Langenbach, R., Peterson, A., and Huberman, E. (1981). Mutagenesis by chemical agents in V79 chinese hamster cells: a review and analysis of the literature. A report of the Gene-Tox Program. *Mutat Res*, 87, 81-142.
- Branco, M.R., and Pombo, A. (2006). Intermingling of chromosome territories in interphase suggests role in translocations and transcription-dependent associations. *PLoS Biol*, 4, e138.
- Brinkman, A.B., Roelofsen, T., Pennings, S.W., Martens, J.H., Jenuwein, T., and Stunnenberg, H.G. (2006). Histone modification patterns associated with the human X chromosome. *EMBO Rep*, 7, 628-634.
- Brown, J.M., Green, J., das Neves, R.P., Wallace, H.A., Smith, A.J., Hughes, J., Gray, N., Taylor, S., Wood, W.G., Higgs, D.R., *et al.* (2008). Association between active genes occurs at nuclear speckles and is modulated by chromatin environment. *J Cell Biol*, 182, 1083-1097.
- Brown, R. (1831/1833). Observations on the Organs and Mode of Fecundation in Orchideae and Asclepiadeae. *Transactions of the Linnean Society of London*, 16, 685-742.
- Burgess, R.C., Burman, B., Kruhlak, M.J., and Misteli, T. (2014). Activation of DNA damage response signaling by condensed chromatin. *Cell Rep*, 9, 1703-1717.

- Caruso, R., Fedele, F., Luciano, R., Branca, G., Parisi, C., Paparo, D., and Parisi, A. (2011). Mitotic catastrophe in malignant epithelial tumors: the pathologist's viewpoint. *Ultrastruct Pathol*, 35, 66-71.
- Castedo, M., Perfettini, J.L., Roumier, T., Andreau, K., Medema, R., and Kroemer, G. (2004a). Cell death by mitotic catastrophe: a molecular definition. *Oncogene*, 23, 2825-2837.
- Castedo, M., Perfettini, J.L., Roumier, T., Valent, A., Raslova, H., Yakushijin, K., Horne, D., Feunteun, J., Lenoir, G., Medema, R., *et al.* (2004b). Mitotic catastrophe constitutes a special case of apoptosis whose suppression entails aneuploidy. *Oncogene*, 23, 4362-4370.
- Cattoni, D.I., Cardozo Gizzi, A.M., Georgieva, M., Di Stefano, M., Valeri, A., Chamousset, D., Houbroun, C., Dejardin, S., Fiche, J.B., Gonzalez, I., *et al.* (2017). Single-cell absolute contact probability detection reveals chromosomes are organized by multiple low-frequency yet specific interactions. *Nat Commun*, 8, 1753.
- Chakraborty, A., and Ay, F. (2019). The role of 3D genome organization in disease: From compartments to single nucleotides. *Semin Cell Dev Biol*, 90, 104-113.
- Chang, D.C., Xu, N., and Luo, K.Q. (2003). Degradation of cyclin B is required for the onset of anaphase in Mammalian cells. *J Biol Chem*, 278, 37865-37873.
- Chang, W., Mi, L.J., and Boorstein, R.J. (1997). The p53 status of Chinese hamster V79 cells frequently used for studies on DNA damage and DNA repair. *Nucleic Acids Res*, 25, 992-994.
- Chen, B.C., Legant, W.R., Wang, K., Shao, L., Milkie, D.E., Davidson, M.W., Janetopoulos, C., Wu, X.S., Hammer, J.A., 3rd, Liu, Z., *et al.* (2014). Lattice light-sheet microscopy: imaging molecules to embryos at high spatiotemporal resolution. *Science*, 346, 1257998.
- Chieco, P., and Derenzini, M. (1999). The Feulgen reaction 75 years on. *Histochem Cell Biol*, 111, 345-358.
- Chiolo, I., Minoda, A., Colmenares, S.U., Polyzos, A., Costes, S.V., and Karpen, G.H. (2011). Double-strand breaks in heterochromatin move outside of a dynamic HP1a domain to complete recombinational repair. *Cell*, 144, 732-744.
- Chiolo, I., Tang, J., Georgescu, W., and Costes, S.V. (2013). Nuclear dynamics of radiation-induced foci in euchromatin and heterochromatin. *Mutat Res*, 750, 56-66.
- Chowdhury, I., Tharakan, B., and Bhat, G.K. (2006). Current concepts in apoptosis: the physiological suicide program revisited. *Cell Mol Biol Lett*, 11, 506-525.
- Chu, E.H. (1965). Effects of ultraviolet radiation on mammalian cells. I. Induction of chromosome aberrations. *Mutat Res*, 2, 75-94.
- Chubb, J.R., and Bickmore, W.A. (2003). Considering nuclear compartmentalization in the light of nuclear dynamics. *Cell*, 112, 403-406.
- Claxton, N., Fellers, T., and Davidson, M. (2005). Laser Scanning Confocal Microscopy. <https://www.ucc.ie/en/media/academic/anatomy/imagingcentre/imagegallery/confocalgallery/Laser-Scanning-Confocal-Microscopy-Introduction.pdf>. 27/11/2019.
- Cmarko, D., Verschure, P.J., Martin, T.E., Dahmus, M.E., Krause, S., Fu, X.D., van Driel, R., and Fakan, S. (1999). Ultrastructural analysis of transcription and splicing in the cell nucleus after bromo-UTP microinjection. *Mol Biol Cell*, 10, 211-223.
- Conchello, J.A., and Lichtman, J.W. (2005). Optical sectioning microscopy. *Nat Methods*, 2, 920-931.
- Cooper, G.M. (2000). *The cell: A molecular approach*, 2nd edn. Sunderland, Sinauer Associates.

- Cortez, D. (2003). Caffeine inhibits checkpoint responses without inhibiting the ataxia-telangiectasia-mutated (ATM) and ATM- and Rad3-related (ATR) protein kinases. *J Biol Chem*, 278, 37139-37145.
- Creative Commons 4.0. <https://creativecommons.org/licenses/by/4.0/>. 27/12/2020.
- Creative Commons NC 2.0. <https://creativecommons.org/licenses/by-nc/2.0/>. 27/12/2020.
- Creative Commons NC 4.0. <https://creativecommons.org/licenses/by-nc/4.0/>. 27/12/2020.
- Cremer, C., and Cremer, T. (1986). Induction of chromosome shattering by ultraviolet light and caffeine: the influence of different distributions of photolesions. *Mutat Res*, 163, 33-40.
- Cremer, C., Cremer, T., and Gray, J.W. (1982a). Induction of chromosome damage by ultraviolet light and caffeine: correlation of cytogenetic evaluation and flow karyotype. *Cytometry*, 2, 287-290.
- Cremer, C., Cremer, T., and Simickova, M. (1980). Induction of chromosome shattering and micronuclei by ultraviolet light and caffeine. I. Temporal relationship and antagonistic effects of the four deoxyribonucleosides. *Environ Mutagen*, 2, 339-351.
- Cremer, C., Cremer, T., Zorn, C., and Zimmer, J. (1981a). Induction of chromosome shattering by ultraviolet irradiation and caffeine: comparison of whole-cell and partial-cell irradiation. *Mutat Res*, 84, 331-348.
- Cremer, C., and Gray, J.W. (1982). DNA content of cells with generalized chromosome shattering induced by ultraviolet light plus caffeine. *Mutat Res*, 94, 133-142.
- Cremer, C., and Masters, B. (2013). Resolution enhancement techniques in microscopy. *Eur Phys J H*, 38, 281-344.
- Cremer, M., and Cremer, T. (2019). Nuclear compartmentalization, dynamics, and function of regulatory DNA sequences. *Genes Chromosomes Cancer*, 58, 427-436.
- Cremer, M., Grasser, F., Lanctot, C., Muller, S., Neusser, M., Zinner, R., Solovei, I., and Cremer, T. (2008). Multicolor 3D fluorescence in situ hybridization for imaging interphase chromosomes. *Methods Mol Biol*, 463, 205-239.
- Cremer, M., Muller, S., Kohler, D., Brero, A., and Solovei, I. (2007). Cell Preparation and Multicolor FISH in 3D Preserved Cultured Mammalian Cells. *CSH Protoc*, 2007, pdb prot4723.
- Cremer, M., Schmid, V.J., Kraus, F., Markaki, Y., Hellmann, I., Maiser, A., Leonhardt, H., John, S., Stamatoyannopoulos, J., and Cremer, T. (2017). Initial high-resolution microscopic mapping of active and inactive regulatory sequences proves non-random 3D arrangements in chromatin domain clusters. *Epigenetics Chromatin*, 10, 39.
- Cremer, T. (1985). *Von der Zellenlehre zur Chromosomentheorie*. Berlin, Germany, Springer-Verlag.
- Cremer, T., and Cremer, C. (2001). Chromosome territories, nuclear architecture and gene regulation in mammalian cells. *Nat Rev Genet*, 2, 292-301.
- Cremer, T., and Cremer, C. (2006). Rise, fall and resurrection of chromosome territories: a historical perspective. Part II. Fall and resurrection of chromosome territories during the 1950s to 1980s. Part III. Chromosome territories and the functional nuclear architecture: experiments and models from the 1990s to the present. *Eur J Histochem*, 50, 223-272.
- Cremer, T., Cremer, C., Baumann, H., Luedtke, E.K., Sperling, K., Teuber, V., and Zorn, C. (1982b). Rabl's model of the interphase chromosome arrangement tested in Chinese hamster cells by premature chromosome condensation and laser-UV-microbeam experiments. *Hum Genet*, 60, 46-56.
- Cremer, T., and Cremer, M. (2010). Chromosome territories. *Cold Spring Harb Perspect Biol*, 2, a003889.

- Cremer, T., Cremer, M., and Cremer, C. (2018). The 4D Nucleome: Genome Compartmentalization in an Evolutionary Context. *Biochemistry (Mosc)*, 83, 313-325.
- Cremer, T., Cremer, M., Hübner, B., Silahatoglu, A., Hendzel, M., Lanctôt, C., Strickfaden, H., and Cremer, C. (2020). The interchromatin compartment participates in the structural and functional organization of the cell nucleus. *Bioessays*, 42.
- Cremer, T., Cremer, M., Hübner, B., Strickfaden, H., Smeets, D., Popken, J., Sterr, M., Markaki, Y., Rippe, K., and Cremer, C. (2015). The 4D nucleome: Evidence for a dynamic nuclear landscape based on co-aligned active and inactive nuclear compartments. *FEBS Lett*, 589, 2931-2943.
- Cremer, T., Peterson, S.P., Cremer, C., and Berns, M.W. (1981b). Laser microirradiation of Chinese hamster cells at wavelength 365 nm: effects of psoralen and caffeine. *Radiat Res*, 85, 529-543.
- Cubenas-Potts, C., and Corces, V.G. (2015). Topologically Associating Domains: An invariant framework or a dynamic scaffold? *Nucleus*, 6, 430-434.
- Cuylen, S., Blaukopf, C., Politi, A.Z., Muller-Reichert, T., Neumann, B., Poser, I., Ellenberg, J., Hyman, A.A., and Gerlich, D.W. (2016). Ki-67 acts as a biological surfactant to disperse mitotic chromosomes. *Nature*, 535, 308-312.
- Dahm, R. (2005). Friedrich Miescher and the discovery of DNA. *Dev Biol*, 278, 274-288.
- De Paul, A., Mukdsi, J., Petiti, J., Gutiérrez, S., Quintar, A., Maldonado, C., and Torres, A. (2012). Immunelectron Microscopy: A reliable tool for the analysis of cellular processes. In *Applications of Immunocytochemistry*, H. Dehghani, ed. (InTech).
- Debatisse, M., El Achkar, E., and Dutrillaux, B. (2006). Common fragile sites nested at the interfaces of early and late-replicating chromosome bands: cis acting components of the G2/M checkpoint? *Cell Cycle*, 5, 578-581.
- Dechat, T., Adam, S.A., Taimen, P., Shimi, T., and Goldman, R.D. (2010). Nuclear lamins. *Cold Spring Harb Perspect Biol*, 2, a000547.
- Dehghani, H., Dellaire, G., and Bazett-Jones, D.P. (2005). Organization of chromatin in the interphase mammalian cell. *Micron*, 36, 95-108.
- Dekker lab website. <http://www.dekkerlab.org/>. 27/11/2019.
- Deng, W., Lee, J., Wang, H., Miller, J., Reik, A., Gregory, P.D., Dean, A., and Blobel, G.A. (2012). Controlling long-range genomic interactions at a native locus by targeted tethering of a looping factor. *Cell*, 149, 1233-1244.
- Deng, W., Tsao, S.W., Lucas, J.N., Leung, C.S., and Cheung, A.L. (2003). A new method for improving metaphase chromosome spreading. *Cytometry A*, 51, 46-51.
- Denk, W., and Horstmann, H. (2004). Serial block-face scanning electron microscopy to reconstruct three-dimensional tissue nanostructure. *PLoS Biol*, 2, e329.
- Derenzini, M., and Farabegoli, F. (1990). Selective staining of nucleic acids by osmium-ammine complex in thin sections from lowicryl-embedded samples. *J Histochem Cytochem*, 38, 1495-1501.
- Derouazi, M., Flaction, R., Girard, P., de Jesus, M., Jordan, M., and Wurm, F.M. (2006). Generation of recombinant Chinese hamster ovary cell lines by microinjection. *Biotechnol Lett*, 28, 373-382.
- Diaz, G., Isola, R., Falchi, A.M., and Diana, A. (1999). CO₂-enriched atmosphere on the microscope stage. *Biotechniques*, 27, 292-294.

- Dixon, J.R., Jung, I., Selvaraj, S., Shen, Y., Antosiewicz-Bourget, J.E., Lee, A.Y., Ye, Z., Kim, A., Rajagopal, N., Xie, W., *et al.* (2015). Chromatin architecture reorganization during stem cell differentiation. *Nature*, 518, 331-336.
- Dixon, J.R., Selvaraj, S., Yue, F., Kim, A., Li, Y., Shen, Y., Hu, M., Liu, J.S., and Ren, B. (2012). Topological domains in mammalian genomes identified by analysis of chromatin interactions. *Nature*, 485, 376-380.
- Djaldetti, M., Bergman, M., Salman, H., Cohen, A.M., and Bessler, H. (2004). Ultrastructural features of bone marrow cells from patients with acquired sideroblastic anemia. *Microsc Res Tech*, 63, 155-158.
- Donzelli, M., and Draetta, G.F. (2003). Regulating mammalian checkpoints through Cdc25 inactivation. *EMBO Rep*, 4, 671-677.
- Duan, Q., Chen, H., Costa, M., and Dai, W. (2008). Phosphorylation of H3S10 blocks the access of H3K9 by specific antibodies and histone methyltransferase. Implication in regulating chromatin dynamics and epigenetic inheritance during mitosis. *J Biol Chem*, 283, 33585-33590.
- Dubochet, J., and Sartori Blanc, N. (2001). The cell in absence of aggregation artifacts. *Micron*, 32, 91-99.
- EasySep. https://cdn.stemcell.com/media/files/pis/28510-PIS_3_2_2.pdf. 27/12/2020.
- Efroni, S., Duttagupta, R., Cheng, J., Dehghani, H., Hoepfner, D.J., Dash, C., Bazett-Jones, D.P., Le Grice, S., McKay, R.D., Buetow, K.H., *et al.* (2008). Global transcription in pluripotent embryonic stem cells. *Cell Stem Cell*, 2, 437-447.
- Ellisman, M.H., Deerinck, T.J., Shu, X., and Sosinsky, G.E. (2012). Picking faces out of a crowd: genetic labels for identification of proteins in correlated light and electron microscopy imaging. *Methods Cell Biol*, 111, 139-155.
- Endl, E., and Gerdes, J. (2000). The Ki-67 protein: fascinating forms and an unknown function. *Exp Cell Res*, 257, 231-237.
- Eriksson, D., and Stigbrand, T. (2010). Radiation-induced cell death mechanisms. *Tumour Biol*, 31, 363-372.
- Eskiw, C.H., and Fraser, P. (2011). Ultrastructural study of transcription factories in mouse erythroblasts. *J Cell Sci*, 124, 3676-3683.
- Esseling-Ozdoba, A. (2007). Getting there: Vesicles en route for plant cytokinesis. In *Laboratory of Plant Cell Biology* (Wageningen, Netherlands: Wageningen University).
- Fakan, S., and Bernhard, W. (1971). Localisation of rapidly and slowly labelled nuclear RNA as visualized by high resolution autoradiography. *Exp Cell Res*, 67, 129-141.
- Fakan, S., Leser, G., and Martin, T.E. (1984). Ultrastructural distribution of nuclear ribonucleoproteins as visualized by immunocytochemistry on thin sections. *J Cell Biol*, 98, 358-363.
- Fakan, S., and van Driel, R. (2007). The perichromatin region: a functional compartment in the nucleus that determines large-scale chromatin folding. *Semin Cell Dev Biol*, 18, 676-681.
- Faro-Trindade, I., and Cook, P.R. (2006). A conserved organization of transcription during embryonic stem cell differentiation and in cells with high C value. *Mol Biol Cell*, 17, 2910-2920.
- Featherstone, J.M., Speers, A.G., Lwaleed, B.A., Hayes, M.C., Cooper, A.J., and Birch, B.R. (2005). The nuclear membrane in multidrug resistance: microinjection of epirubicin into bladder cancer cell lines. *BJU Int*, 95, 1091-1098.

- Feng, Y.L., Xiang, J.F., Kong, N., Cai, X.J., and Xie, A.Y. (2016). Buried territories: heterochromatic response to DNA double-strand breaks. *Acta Biochim Biophys Sin (Shanghai)*, 48, 594-602.
- Ferrari, F., Bortoluzzi, S., Coppe, A., Basso, D., Bicciato, S., Zini, R., Gemelli, C., Danieli, G.A., and Ferrari, S. (2007). Genomic expression during human myelopoiesis. *BMC Genomics*, 8, 264.
- Fiolka, R., Shao, L., Rego, E.H., Davidson, M.W., and Gustafsson, M.G. (2012). Time-lapse two-color 3D imaging of live cells with doubled resolution using structured illumination. *Proc Natl Acad Sci U S A*, 109, 5311-5315.
- Fischle, W., Tseng, B.S., Dormann, H.L., Ueberheide, B.M., Garcia, B.A., Shabanowitz, J., Hunt, D.F., Funabiki, H., and Allis, C.D. (2005). Regulation of HP1-chromatin binding by histone H3 methylation and phosphorylation. *Nature*, 438, 1116-1122.
- Fisher, D., Krasinska, L., Coudreuse, D., and Novak, B. (2012). Phosphorylation network dynamics in the control of cell cycle transitions. *J Cell Sci*, 125, 4703-4711.
- Fitschen, M. (2009). Conventional cytogenetics for diagnostics and characterization of premature chromosome condensation (PCC), an alternative for obtaining chromosome spreads. In Department of Natural Sciences (Bonn-Rhein-Sieg, Germany: University of Applied Sciences).
- Flyamer, I.M., Gassler, J., Imakaev, M., Brandao, H.B., Ulianov, S.V., Abdennur, N., Razin, S.V., Mirny, L.A., and Tachibana-Konwalski, K. (2017). Single-nucleus Hi-C reveals unique chromatin reorganization at oocyte-to-zygote transition. *Nature*, 544, 110-114.
- Fraser, P., and Bickmore, W. (2007). Nuclear organization of the genome and the potential for gene regulation. *Nature*, 447, 413-417.
- Freed, J.J., and Schatz, S.A. (1969). Chromosome aberrations in cultured cells deprived of single essential amino acids. *Exp Cell Res*, 55, 393-409.
- Frei, M. (2011). Centrifugation. *Biofiles*, 6, 5. https://www.sigmaaldrich.com/content/dam/sigma-aldrich/docs/Sigma-Aldrich/Brochure/1/biofiles_v6_n5.pdf. 27/12/2020.
- Fudenberg, G., and Imakaev, M. (2017). FISH-ing for captured contacts: towards reconciling FISH and 3C. *Nat Methods*, 14, 673-678.
- Fudenberg, G., Imakaev, M., Lu, C., Goloborodko, A., Abdennur, N., and Mirny, L.A. (2016). Formation of Chromosomal Domains by Loop Extrusion. *Cell Rep*, 15, 2038-2049.
- Galluzzi, L., Vitale, I., Abrams, J.M., Alnemri, E.S., Baehrecke, E.H., Blagosklonny, M.V., Dawson, T.M., Dawson, V.L., El-Deiry, W.S., Fulda, S., *et al.* (2012). Molecular definitions of cell death subroutines: recommendations of the Nomenclature Committee on Cell Death 2012. *Cell Death Differ*, 19, 107-120.
- Gao, L., Shao, L., Higgins, C.D., Poulton, J.S., Peifer, M., Davidson, M.W., Wu, X., Goldstein, B., and Betzig, E. (2012). Noninvasive imaging beyond the diffraction limit of 3D dynamics in thickly fluorescent specimens. *Cell*, 151, 1370-1385.
- Gaspar-Maia, A., Alajem, A., Meshorer, E., and Ramalho-Santos, M. (2011). Open chromatin in pluripotency and reprogramming. *Nat Rev Mol Cell Biol*, 12, 36-47.
- Gemelli, C., Montanari, M., Tenedini, E., Zanocco Marani, T., Vignudelli, T., Siena, M., Zini, R., Salati, S., Tagliafico, E., Manfredini, R., *et al.* (2006). Virally mediated MafB transduction induces the monocyte commitment of human CD34+ hematopoietic stem/progenitor cells. *Cell Death Differ*, 13, 1686-1696.
- Gerlach, D. (2009). *Geschichte der Mikroskopie*. Frankfurt am Main, Germany, Verlag Harri Deutsch.

- Ghosh, S., Paweletz, N., and Schroeter, D. (1992). Failure of kinetochore development and mitotic spindle formation in okadaic acid-induced premature mitosis in HeLa cells. *Exp Cell Res*, 201, 535-540.
- Giebel, B., and Punzel, M. (2008). Lineage development of hematopoietic stem and progenitor cells. *Biol Chem*, 389, 813-824.
- Glaeser, R. (2008). Cryo-electron microscopy of biological nanostructures. *Physics Today*, 48-54.
- Glukhov, S.I., Rubtsov, M.A., Alexeyevsky, D.A., Alexeevski, A.V., Razin, S.V., and Iarovaia, O.V. (2013). The broken MLL gene is frequently located outside the inherent chromosome territory in human lymphoid cells treated with DNA topoisomerase II poison etoposide. *PLoS One*, 8, e75871.
- Gollin, S.M., Wray, W., Hanks, S.K., Hittelman, W.N., and Rao, P.N. (1984). The ultrastructural organization of prematurely condensed chromosomes. *J Cell Sci Suppl*, 1, 203-221.
- Gorisch, S.M., Richter, K., Scheuermann, M.O., Herrmann, H., and Lichter, P. (2003). Diffusion-limited compartmentalization of mammalian cell nuclei assessed by microinjected macromolecules. *Exp Cell Res*, 289, 282-294.
- Gotoh, E. (2009). Drug-induced premature chromosome condensation (PCC) protocols: cytogenetic approaches in mitotic chromosome and interphase chromatin. *Methods Mol Biol*, 523, 83-92.
- Gotoh, E., Asakawa, Y., and Kosaka, H. (1995). Inhibition of protein serine/threonine phosphatases directly induces premature chromosome condensation in mammalian somatic cells. *Biomedical Research*, 16, 63-68.
- Gotoh, E., and Durante, M. (2006). Chromosome condensation outside of mitosis: mechanisms and new tools. *J Cell Physiol*, 209, 297-304.
- Graf, R., Rietdorf, J., and Zimmermann, T. (2005). Live cell spinning disk microscopy. *Adv Biochem Eng Biotechnol*, 95, 57-75.
- Grigoryev, S.A., and Woodcock, C.L. (2012). Chromatin organization - the 30 nm fiber. *Exp Cell Res*, 318, 1448-1455.
- Gustafsson, M.G. (2000). Surpassing the lateral resolution limit by a factor of two using structured illumination microscopy. *J Microsc*, 198, 82-87.
- Gustafsson, M.G., Shao, L., Carlton, P.M., Wang, C.J., Golubovskaya, I.N., Cande, W.Z., Agard, D.A., and Sedat, J.W. (2008). Three-dimensional resolution doubling in wide-field fluorescence microscopy by structured illumination. *Biophys J*, 94, 4957-4970.
- Hajj, B., El Beheiry, M., Izeddin, I., Darzacq, X., and Dahan, M. (2014). Accessing the third dimension in localization-based super-resolution microscopy. *Phys Chem Chem Phys*, 16, 16340-16348.
- Hall-Jackson, C.A., Cross, D.A., Morrice, N., and Smythe, C. (1999). ATR is a caffeine-sensitive, DNA-activated protein kinase with a substrate specificity distinct from DNA-PK. *Oncogene*, 18, 6707-6713.
- Hanks, S.K., Brown, D.B., and Rao, P.N. (1982). Induction of premature chromosome condensation at high frequency following polyethylene glycol-mediated fusion of lectin-bound cells. *Exp Cell Res*, 138, 215-219.
- Hanks, S.K., Gollin, S.M., Rao, P.N., Wray, W., and Hittelman, W.N. (1983). Cell cycle-specific changes in the ultrastructural organization of prematurely condensed chromosomes. *Chromosoma*, 88, 333-342.
- Hanks, S.K., and Rao, P.N. (1980). Initiation of DNA synthesis in the prematurely condensed chromosomes of G1 cells. *J Cell Biol*, 87, 285-291.

- Hansen, J.C., Connolly, M., McDonald, C.J., Pan, A., Pryamkova, A., Ray, K., Seidel, E., Tamura, S., Rogge, R., and Maeshima, K. (2018). The 10-nm chromatin fiber and its relationship to interphase chromosome organization. *Biochem Soc Trans*, 46, 67-76.
- Hao, Q.L., Shah, A.J., Thiemann, F.T., Smogorzewska, E.M., and Crooks, G.M. (1995). A functional comparison of CD34 + CD38- cells in cord blood and bone marrow. *Blood*, 86, 3745-3753.
- Harnicarova Horakova, A., Bartova, E., and Kozubek, S. (2010). Chromatin structure with respect to histone signature changes during cell differentiation. *Cell Struct Funct*, 35, 31-44.
- Hartnell, L., Earl, L., Moran, A., and Subramaniam, S. (2016). Imaging Cellular Architecture with 3D SEM. *Encyclopedia of Cell Biology*, 2, 44-50.
- Hartwig, A. (1994). Role of DNA repair inhibition in lead- and cadmium-induced genotoxicity: a review. *Environ Health Perspect*, 102 Suppl 3, 45-50.
- Hatzi, V.I., Terzoudi, G.I., Paraskevopoulou, C., Makropoulos, V., Matthopoulos, D.P., and Pantelias, G.E. (2006). The use of premature chromosome condensation to study in interphase cells the influence of environmental factors on human genetic material. *ScientificWorldJournal*, 6, 1174-1190.
- Heidemann, M., Hintermair, C., Voss, K., and Eick, D. (2013). Dynamic phosphorylation patterns of RNA polymerase II CTD during transcription. *Biochim Biophys Acta*, 1829, 55-62.
- Heintzmann, R., and Cremer, C. (1999). Lateral modulated excitation microscopy: Improvement of resolution by using a diffraction grating. *Proc SPIE*, 3568, 185-196.
- Hell, S.W., and Wichmann, J. (1994). Breaking the diffraction resolution limit by stimulated emission: stimulated-emission-depletion fluorescence microscopy. *Opt Lett*, 19, 780-782.
- Helmholtz, H.v. (1874). Die theoretische Grenze für die Leistungsfähigkeit der Mikroskope. In Poggendorff's Annalen der Physik Jubelband. pp. 557-584.
- Henderson, R.B., Hobbs, J.A., Mathies, M., and Hogg, N. (2003). Rapid recruitment of inflammatory monocytes is independent of neutrophil migration. *Blood*, 102, 328-335.
- Hendzel, M.J., Wei, Y., Mancini, M.A., Van Hooser, A., Ranalli, T., Brinkley, B.R., Bazett-Jones, D.P., and Allis, C.D. (1997). Mitosis-specific phosphorylation of histone H3 initiates primarily within pericentromeric heterochromatin during G2 and spreads in an ordered fashion coincident with mitotic chromosome condensation. *Chromosoma*, 106, 348-360.
- Henegariu, O., Heerema, N.A., Lowe Wright, L., Bray-Ward, P., Ward, D.C., and Vance, G.H. (2001). Improvements in cytogenetic slide preparation: controlled chromosome spreading, chemical aging and gradual denaturing. *Cytometry*, 43, 101-109.
- Hess, S.T., Girirajan, T.P., and Mason, M.D. (2006). Ultra-high resolution imaging by fluorescence photoactivation localization microscopy. *Biophys J*, 91, 4258-4272.
- Heymann, J.A., Hayles, M., Gestmann, I., Giannuzzi, L.A., Lich, B., and Subramaniam, S. (2006). Site-specific 3D imaging of cells and tissues with a dual beam microscope. *J Struct Biol*, 155, 63-73.
- Houwen, B. (2000). Blood film preparation and staining procedures. *Laboratory Hematology*, 6, 1-7.
- Hsiung, C.C., Morrissey, C.S., Udugama, M., Frank, C.L., Keller, C.A., Baek, S., Giardine, B., Crawford, G.E., Sung, M.H., Hardison, R.C., *et al.* (2015). Genome accessibility is widely preserved and locally modulated during mitosis. *Genome Res*, 25, 213-225.
- Hu, B., Zhu, J., Zhou, H., and Hei, T.K. (2013). No significant level of inheritable interchromosomal aberrations in the progeny of bystander primary human fibroblast after alpha particle irradiation. *Adv Space Res*, 51, 450-457.

- Huang, B., Babcock, H., and Zhuang, X. (2010). Breaking the diffraction barrier: super-resolution imaging of cells. *Cell*, 143, 1047-1058.
- Huang, X., Kurose, A., Tanaka, T., Traganos, F., Dai, W., and Darzynkiewicz, Z. (2006). Sequential phosphorylation of Ser-10 on histone H3 and ser-139 on histone H2AX and ATM activation during premature chromosome condensation: relationship to cell-cycle phase and apoptosis. *Cytometry A*, 69, 222-229.
- Hübner, B. (2008). Charakterisierung Zelltyp-spezifischer Veränderungen der Kernstruktur als Antwort auf unterschiedliche DNA-Schädigungen. In Department Biology II (Munich, Germany: Ludwig-Maximilians Universität (LMU)).
- Hübner, B., Cremer, T., and Neumann, J. (2013). Correlative microscopy of individual cells: sequential application of microscopic systems with increasing resolution to study the nuclear landscape. *Methods Mol Biol*, 1042, 299-336.
- Hübner, B., Lomiento, M., Mammoli, F., Illner, D., Markaki, Y., Ferrari, S., Cremer, M., and Cremer, T. (2015). Remodeling of nuclear landscapes during human myelopoietic cell differentiation maintains co-aligned active and inactive nuclear compartments. *Epigenetics Chromatin*, 8, 47.
- Hübner, B., Strickfaden, H., Müller, S., Cremer, M., and Cremer, T. (2009). Chromosome shattering: a mitotic catastrophe due to chromosome condensation failure. *Eur Biophys J*, 38, 729-747.
- Hurley, P.J., and Bunz, F. (2007). ATM and ATR: components of an integrated circuit. *Cell Cycle*, 6, 414-417.
- Ianzini, F., and Mackey, M.A. (1997). Spontaneous premature chromosome condensation and mitotic catastrophe following irradiation of HeLa S3 cells. *Int J Radiat Biol*, 72, 409-421.
- Ihalainen, T.O., Niskanen, E.A., Jylhava, J., Paloheimo, O., Dross, N., Smolander, H., Langowski, J., Timonen, J., and Vihinen-Ranta, M. (2009). Parvovirus induced alterations in nuclear architecture and dynamics. *PLoS One*, 4, e5948.
- Illner, D. (2012). Untersuchungen von menschlichen Zellen mit ungewöhnlicher Chromatin-Anordnung und Zellkernform. In Department Biology II (Munich, Germany: Ludwig-Maximilians University (LMU)).
- Imhof, B.A., and Aurrand-Lions, M. (2004). Adhesion mechanisms regulating the migration of monocytes. *Nat Rev Immunol*, 4, 432-444.
- Ishihara, H., Martin, B.L., Brautigan, D.L., Karaki, H., Ozaki, H., Kato, Y., Fusetani, N., Watabe, S., Hashimoto, K., Uemura, D., *et al.* (1989). Calyculin A and okadaic acid: inhibitors of protein phosphatase activity. *Biochem Biophys Res Commun*, 159, 871-877.
- Izzo, A., and Schneider, R. (2010). Chatting histone modifications in mammals. *Brief Funct Genomics*, 9, 429-443.
- Jackson, D.A., and Pombo, A. (1998). Replicon clusters are stable units of chromosome structure: evidence that nuclear organization contributes to the efficient activation and propagation of S phase in human cells. *J Cell Biol*, 140, 1285-1295.
- Janke, C., and Bulinski, J.C. (2011). Post-translational regulation of the microtubule cytoskeleton: mechanisms and functions. *Nat Rev Mol Cell Biol*, 12, 773-786.
- Janmey, P.A., Winer, J.P., Murray, M.E., and Wen, Q. (2009). The hard life of soft cells. *Cell Motil Cytoskeleton*, 66, 597-605.
- Jaunin, F., Visser, A.E., Cmarko, D., Aten, J.A., and Fakan, S. (2000). Fine structural in situ analysis of nascent DNA movement following DNA replication. *Exp Cell Res*, 260, 313-323.
- Jeong, Y.S., Cho, S., Park, J.S., Ko, Y., and Kang, Y.K. (2010). Phosphorylation of serine-10 of histone H3 shields modified lysine-9 selectively during mitosis. *Genes Cells*, 15, 181-192.

- Joffe, B., Leonhardt, H., and Solovei, I. (2010). Differentiation and large scale spatial organization of the genome. *Curr Opin Genet Dev*, 20, 562-569.
- Johnson, R.T., and Rao, P.N. (1970). Mammalian cell fusion: induction of premature chromosome condensation in interphase nuclei. *Nature*, 226, 717-722.
- Jost, E., Herwartz, R., Hoss, M., Vankann, L., and Fuchs, R. (2015). Cup-like blasts in acute myeloid leukemia. *Am J Hematol*, 90, 847-848.
- Jurikova, M., Danihel, L., Polak, S., and Varga, I. (2016). Ki67, PCNA, and MCM proteins: Markers of proliferation in the diagnosis of breast cancer. *Acta Histochem*, 118, 544-552.
- Kanda, T., Sullivan, K.F., and Wahl, G.M. (1998). Histone-GFP fusion protein enables sensitive analysis of chromosome dynamics in living mammalian cells. *Curr Biol*, 8, 377-385.
- Kato, Y., Fusetani, N., Matsunaga, S., and Hashimoto, K. (1986). Calyculin A, a novel antitumor metabolite from the marine Sponge *Discodermia calyx*. *J Am Chem Soc*, 108, 2780-2781.
- Kaur, G., and Dufour, J.M. (2012). Cell lines: Valuable tools or useless artifacts. *Spermatogenesis*, 2, 1-5.
- Keohane, E., Smith, L., and Walenga, J. (2016). *Rodak's Hematology: Clinical principles and applications*, 5th edn. St. Louis, Missouri, USA, Elsevier Saunders.
- Khurana, S., Kruhlak, M.J., Kim, J., Tran, A.D., Liu, J., Nyswaner, K., Shi, L., Jailwala, P., Sung, M.H., Hakim, O., *et al.* (2014). A macrohistone variant links dynamic chromatin compaction to BRCA1-dependent genome maintenance. *Cell Rep*, 8, 1049-1062.
- Kill, I.R. (1996). Localisation of the Ki-67 antigen within the nucleolus. Evidence for a fibrillar-deficient region of the dense fibrillar component. *J Cell Sci*, 109 (Pt 6), 1253-1263.
- Kimura, H. (2013). Histone modifications for human epigenome analysis. *J Hum Genet*, 58, 439-445.
- Kiraz, Y., Adan, A., Kartal Yandim, M., and Baran, Y. (2016). Major apoptotic mechanisms and genes involved in apoptosis. *Tumour Biol*, 37, 8471-8486.
- Kirmes, I., Szczurek, A., Prakash, K., Charapitsa, I., Heiser, C., Musheev, M., Schock, F., Fornalczyk, K., Ma, D., Birk, U., *et al.* (2015). A transient ischemic environment induces reversible compaction of chromatin. *Genome Biol*, 16, 246.
- Klar, T.A., and Hell, S.W. (1999). Subdiffraction resolution in far-field fluorescence microscopy. *Opt Lett*, 24, 954-956.
- Klar, T.A., Jakobs, S., Dyba, M., Egnér, A., and Hell, S.W. (2000). Fluorescence microscopy with diffraction resolution barrier broken by stimulated emission. *Proc Natl Acad Sci U S A*, 97, 8206-8210.
- Kner, P., Chhun, B.B., Griffis, E.R., Winoto, L., and Gustafsson, M.G. (2009). Super-resolution video microscopy of live cells by structured illumination. *Nat Methods*, 6, 339-342.
- Knott, G., Marchman, H., Wall, D., and Lich, B. (2008). Serial section scanning electron microscopy of adult brain tissue using focused ion beam milling. *J Neurosci*, 28, 2959-2964.
- Komor, M., Guller, S., Baldus, C.D., de Vos, S., Hoelzer, D., Ottmann, O.G., and Hofmann, W.K. (2005). Transcriptional profiling of human hematopoiesis during in vitro lineage-specific differentiation. *Stem Cells*, 23, 1154-1169.
- Kong, S., and Zhang, Y. (2019). Deciphering Hi-C: from 3D genome to function. *Cell Biol Toxicol*, 35, 15-32.
- Kornberg, R.D. (1974). Chromatin structure: a repeating unit of histones and DNA. *Science*, 184, 868-871.

- Kornberg, R.D., and Thomas, J.O. (1974). Chromatin structure; oligomers of the histones. *Science*, 184, 865-868.
- Kosak, S.T., and Groudine, M. (2004). Form follows function: The genomic organization of cellular differentiation. *Genes Dev*, 18, 1371-1384.
- Kurukuti, S., Tiwari, V.K., Tavoosidana, G., Pugacheva, E., Murrell, A., Zhao, Z., Lobanenko, V., Reik, W., and Ohlsson, R. (2006). CTCF binding at the H19 imprinting control region mediates maternally inherited higher-order chromatin conformation to restrict enhancer access to *Igf2*. *Proc Natl Acad Sci U S A*, 103, 10684-10689.
- LaJoie, D., and Ullman, K.S. (2017). Coordinated events of nuclear assembly. *Curr Opin Cell Biol*, 46, 39-45.
- Lam, S.S., Martell, J.D., Kamer, K.J., Deerinck, T.J., Ellisman, M.H., Mootha, V.K., and Ting, A.Y. (2015). Directed evolution of APEX2 for electron microscopy and proximity labeling. *Nat Methods*, 12, 51-54.
- Lamadrid Boada, A.I., Romero Aguilera, I., Terzoudi, G.I., Gonzalez Mesa, J.E., Pantelias, G., and Garcia, O. (2013). Rapid assessment of high-dose radiation exposures through scoring of cell-fusion-induced premature chromosome condensation and ring chromosomes. *Mutat Res*, 757, 45-51.
- Lau, Y.F., Brown, R.L., and Arrighi, F.E. (1977). Induction of premature chromosome condensation in CHO cells fused with polyethylene glycol. *Exp Cell Res*, 110, 57-61.
- Le Gros, M.A., Clowney, E.J., Magklara, A., Yen, A., Markenscoff-Papadimitriou, E., Colquitt, B., Myllys, M., Kellis, M., Lomvardas, S., and Larabell, C.A. (2016). Soft X-Ray Tomography Reveals Gradual Chromatin Compaction and Reorganization during Neurogenesis In Vivo. *Cell Rep*, 17, 2125-2136.
- Leeuwenhoek, A.v. (1719-1730). *Opera Omnia, seu Arcana Naturae ope exactissimorum Microscopiorum detecta, experimentis variis comprobata, Epistolis ad varios illustres viros. In. Lugdunum Batavorum, J. Arnold et Delphis, A. Beman.*
- Leica (2013). EM Sample Preparation - Contrasting. https://webcdn.leica-microsystems.com/fileadmin/academy/Contrasting_final.pdf. 27/11/2019.
- Li, G., and Zhu, P. (2015). Structure and organization of chromatin fiber in the nucleus. *FEBS Lett*, 589, 2893-2904.
- Lieberman-Aiden, E., van Berkum, N.L., Williams, L., Imakaev, M., Ragoczy, T., Telling, A., Amit, I., Lajoie, B.R., Sabo, P.J., Dorschner, M.O., *et al.* (2009). Comprehensive mapping of long-range interactions reveals folding principles of the human genome. *Science*, 326, 289-293.
- Liu, D.F., el-Alfy, M., and Leblond, C.P. (1995). DNA changes involved in the formation of metaphase chromosomes, as observed in mouse duodenal crypt cells stained by osmium-ammine. II. Tracing nascent DNA by bromodeoxyuridine into structures arising during the S phase. *Anat Rec*, 242, 449-461.
- Liu, J., and Wright, G. (2014). OMX 3D structured illumination microscopy (3D-SIM) background. <https://www.a-star.edu.sg/imb/Tech-Platforms/AMP-Light-Microscopy/Microscopes/tid/148/DeltaVision-OMX-inverted>. 27/11/2019.
- Liu, X.L., Yuan, J.Y., Zhang, J.W., Zhang, X.H., and Wang, R.X. (2007). Differential gene expression in human hematopoietic stem cells specified toward erythroid, megakaryocytic, and granulocytic lineage. *J Leukoc Biol*, 82, 986-1002.
- Lorat, Y., Brunner, C.U., Schanz, S., Jakob, B., Taucher-Scholz, G., and Rube, C.E. (2015). Nanoscale analysis of clustered DNA damage after high-LET irradiation by quantitative electron microscopy--the heavy burden to repair. *DNA Repair (Amst)*, 28, 93-106.

- Lovelace, R. (1954). Chromosome Shattering by Ultraviolet Radiation (2650 Å). *Proc Natl Acad Sci U S A*, 40, 1129-1135.
- Lukasova, E., Koristek, Z., Falk, M., Kozubek, S., Grigoryev, S., Kozubek, M., Ondrej, V., and Kroupova, I. (2005). Methylation of histones in myeloid leukemias as a potential marker of granulocyte abnormalities. *J Leukoc Biol*, 77, 100-111.
- Lupianez, D.G., Kraft, K., Heinrich, V., Krawitz, P., Brancati, F., Klopocki, E., Horn, D., Kayserili, H., Opitz, J.M., Laxova, R., *et al.* (2015). Disruptions of topological chromatin domains cause pathogenic rewiring of gene-enhancer interactions. *Cell*, 161, 1012-1025.
- M'Kacher, R., El Maalouf, E., Terzoudi, G., Ricoul, M., Heidingsfelder, L., Karachristou, I., Laplagne, E., Hempel, W.M., Colicchio, B., Dieterlen, A., *et al.* (2015). Detection and automated scoring of dicentric chromosomes in nonstimulated lymphocyte prematurely condensed chromosomes after telomere and centromere staining. *Int J Radiat Oncol Biol Phys*, 91, 640-649.
- Ma, H., Samarabandu, J., Devdhar, R.S., Acharya, R., Cheng, P.C., Meng, C., and Berezney, R. (1998). Spatial and temporal dynamics of DNA replication sites in mammalian cells. *J Cell Biol*, 143, 1415-1425.
- MacKintosh, C., and MacKintosh, R.W. (1994). Inhibitors of protein kinases and phosphatases. *Trends Biochem Sci*, 19, 444-448.
- Maeshima, K., Ide, S., Hibino, K., and Sasai, M. (2016). Liquid-like behavior of chromatin. *Curr Opin Genet Dev*, 37, 36-45.
- Maeshima, K., Imai, R., Tamura, S., and Nozaki, T. (2014). Chromatin as dynamic 10-nm fibers. *Chromosoma*, 123, 225-237.
- Maeshima, K., Yahata, K., Sasaki, Y., Nakatomi, R., Tachibana, T., Hashikawa, T., Imamoto, F., and Imamoto, N. (2006). Cell-cycle-dependent dynamics of nuclear pores: pore-free islands and lamins. *J Cell Sci*, 119, 4442-4451.
- Majeti, R., Park, C.Y., and Weissman, I.L. (2007). Identification of a hierarchy of multipotent hematopoietic progenitors in human cord blood. *Cell Stem Cell*, 1, 635-645.
- Manfredini, R., Zini, R., Salati, S., Siena, M., Tenedini, E., Tagliafico, E., Montanari, M., Zanocco-Marani, T., Gemelli, C., Vignudelli, T., *et al.* (2005). The kinetic status of hematopoietic stem cell subpopulations underlies a differential expression of genes involved in self-renewal, commitment, and engraftment. *Stem Cells*, 23, 496-506.
- Mansilla, S., Priebe, W., and Portugal, J. (2006). Mitotic catastrophe results in cell death by caspase-dependent and caspase-independent mechanisms. *Cell Cycle*, 5, 53-60.
- Manuelidis, L. (1985). Individual interphase chromosome domains revealed by in situ hybridization. *Hum Genet*, 71, 288-293.
- Markaki, Y. (2008). Enzymatic complexes of the inner nuclear membrane that regulate genetic expression and differentiation of mouse embryonic stem cells (E14) - The role of histone H3 phosphorylation and haspin kinase. In Biology Department, School of Medicine and Biomedical Research Institute (FORTH-BRI) (Ioannina, Greece: University of Ioannina).
- Markaki, Y., Gunkel, M., Schermelleh, L., Beichmanis, S., Neumann, J., Heidemann, M., Leonhardt, H., Eick, D., Cremer, C., and Cremer, T. (2010). Functional nuclear organization of transcription and DNA replication: a topographical marriage between chromatin domains and the interchromatin compartment. *Cold Spring Harb Symp Quant Biol*, 75, 475-492.
- Markaki, Y., Smeets, D., Fiedler, S., Schmid, V.J., Schermelleh, L., Cremer, T., and Cremer, M. (2012). The potential of 3D-FISH and super-resolution structured illumination microscopy for studies of 3D nuclear architecture: 3D structured illumination microscopy of defined chromosomal structures visualized by 3D (immuno)-FISH opens new perspectives for studies of nuclear architecture. *Bioessays*, 34, 412-426.

- Marples, B., Lambin, P., Skov, K.A., and Joiner, M.C. (1997). Low dose hyper-radiosensitivity and increased radioresistance in mammalian cells. *Int J Radiat Biol*, 71, 721-735.
- Martell, J.D., Deerinck, T.J., Sancak, Y., Poulos, T.L., Mootha, V.K., Sosinsky, G.E., Ellisman, M.H., and Ting, A.Y. (2012). Engineered ascorbate peroxidase as a genetically encoded reporter for electron microscopy. *Nat Biotechnol*, 30, 1143-1148.
- Matsui, S.I., Yoshida, H., Weinfeld, H., and Sandberg, A.A. (1972). Induction of prophase in interphase nuclei by fusion with metaphase cells. *J Cell Biol*, 54, 120-132.
- Maul, G.G., Deaven, L.L., Freed, J.J., Campbell, G.L., and Becak, W. (1980). Investigation of the determinants of nuclear pore number. *Cytogenet Cell Genet*, 26, 175-190.
- Maul, G.G., Maul, H.M., Scogna, J.E., Lieberman, M.W., Stein, G.S., Hsu, B.Y., and Borun, T.W. (1972). Time sequence of nuclear pore formation in phytohemagglutinin-stimulated lymphocytes and in HeLa cells during the cell cycle. *J Cell Biol*, 55, 433-447.
- Mayani, H., and Lansdorp, P.M. (1998). Biology of human umbilical cord blood-derived hematopoietic stem/progenitor cells. *Stem Cells*, 16, 153-165.
- McManus, K.J., Biron, V.L., Heit, R., Underhill, D.A., and Hendzel, M.J. (2006). Dynamic changes in histone H3 lysine 9 methylations: identification of a mitosis-specific function for dynamic methylation in chromosome congression and segregation. *J Biol Chem*, 281, 8888-8897.
- Meister, P., Towbin, B.D., Pike, B.L., Ponti, A., and Gasser, S.M. (2010). The spatial dynamics of tissue-specific promoters during *C. elegans* development. *Genes Dev*, 24, 766-782.
- Mennella, V. (2016). Structured Illumination Microscopy. *Encyclopedia of Cell Biology*, 2, 86-98.
- Merkenschlager, M., and Nora, E.P. (2016). CTCF and Cohesin in Genome Folding and Transcriptional Gene Regulation. *Annu Rev Genomics Hum Genet*, 17, 17-43.
- Merz, J. (2008). Untersuchungen zur Zellkernarchitektur in humanen Granulozyten und promyeloischen Zellen. In Department Biology II (Munich, Germany: Ludwig-Maximilians Universität (LMU)).
- Meshorer, E., and Misteli, T. (2006). Chromatin in pluripotent embryonic stem cells and differentiation. *Nat Rev Mol Cell Biol*, 7, 540-546.
- Mirny, L.A. (2011). The fractal globule as a model of chromatin architecture in the cell. *Chromosome Res*, 19, 37-51.
- Misteli, T. (2011). The inner life of the genome. *Sci Am*, 304, 66-73.
- Molecular Probes (2010). Fluorescent tracers of cell morphology and fluid flow (Chapter 14). In *A guide to fluorescent probes and labeling technologies*.
- Montanari, M., Gemelli, C., Tenedini, E., Zanocco Marani, T., Vignudelli, T., Siena, M., Zini, R., Salati, S., Chiossi, G., Tagliafico, E., *et al.* (2005). Correlation between differentiation plasticity and mRNA expression profiling of CD34+-derived CD14- and CD14+ human normal myeloid precursors. *Cell Death Differ*, 12, 1588-1600.
- Morandell, S., and Yaffe, M.B. (2012). Exploiting synthetic lethal interactions between DNA damage signaling, checkpoint control, and p53 for targeted cancer therapy. *Prog Mol Biol Transl Sci*, 110, 289-314.
- Mortusewicz, O. (2004). Akkumulation und Dynamik von DNA-Replikationsproteinen nach Induktion von DNA-Schäden durch Laser-Mikrobestrahlung. In Department Biology II (Munich, Germany: Ludwig-Maximilians Universität (LMU)).

-
- Muller, I., Merk, B., Voss, K.O., Averbek, N., Jakob, B., Durante, M., and Taucher-Scholz, G. (2013). Species conserved DNA damage response at the inactive human X chromosome. *Mutat Res*, 756, 30-36.
- Nagano, T., Lubling, Y., Stevens, T.J., Schoenfelder, S., Yaffe, E., Dean, W., Laue, E.D., Tanay, A., and Fraser, P. (2013). Single-cell Hi-C reveals cell-to-cell variability in chromosome structure. *Nature*, 502, 59-64.
- Nagano, T., Lubling, Y., Varnai, C., Dudley, C., Leung, W., Baran, Y., Mendelson Cohen, N., Wingett, S., Fraser, P., and Tanay, A. (2017). Cell-cycle dynamics of chromosomal organization at single-cell resolution. *Nature*, 547, 61-67.
- Nagel, J., Gross, B., Meggendorfer, M., Preiss, C., Grez, M., Brack-Werner, R., and Dietzel, S. (2012). Stably integrated and expressed retroviral sequences can influence nuclear location and chromatin condensation of the integration locus. *Chromosoma*, 121, 353-367.
- Nair, N., Shoaib, M., and Sorensen, C.S. (2017). Chromatin Dynamics in Genome Stability: Roles in Suppressing Endogenous DNA Damage and Facilitating DNA Repair. *Int J Mol Sci*, 18.
- Nash, R.E., Puvion, E., and Bernhard, W. (1975). Perichromatin fibrils as components of rapidly labeled extranucleolar RNA. *J Ultrastruct Res*, 53, 395-405.
- Nelson, A.J., and Hess, S.T. (2014). Localization microscopy: mapping cellular dynamics with single molecules. *J Microsc*, 254, 1-8.
- Niedojadlo, J., Perret-Vivancos, C., Kalland, K.H., Cmarko, D., Cremer, T., van Driel, R., and Fakan, S. (2011). Transcribed DNA is preferentially located in the perichromatin region of mammalian cell nuclei. *Exp Cell Res*, 317, 433-444.
- Nir, G., Farabella, I., Perez Estrada, C., Ebeling, C.G., Beliveau, B.J., Sasaki, H.M., Lee, S.D., Nguyen, S.C., McCole, R.B., Chattoraj, S., *et al.* (2018). Walking along chromosomes with super-resolution imaging, contact maps, and integrative modeling. *PLoS Genet*, 14, e1007872.
- Nitta, M., Kobayashi, O., Honda, S., Hirota, T., Kuninaka, S., Marumoto, T., Ushio, Y., and Saya, H. (2004). Spindle checkpoint function is required for mitotic catastrophe induced by DNA-damaging agents. *Oncogene*, 23, 6548-6558.
- Nora, E.P., Lajoie, B.R., Schulz, E.G., Giorgetti, L., Okamoto, I., Servant, N., Piolot, T., van Berkum, N.L., Meisig, J., Sedat, J., *et al.* (2012). Spatial partitioning of the regulatory landscape of the X-inactivation centre. *Nature*, 485, 381-385.
- Novershtern, N., Subramanian, A., Lawton, L.N., Mak, R.H., Haining, W.N., McConkey, M.E., Habib, N., Yosef, N., Chang, C.Y., Shay, T., *et al.* (2011). Densely interconnected transcriptional circuits control cell states in human hematopoiesis. *Cell*, 144, 296-309.
- Oberleithner, H., Brinckmann, E., Schwab, A., and Krohne, G. (1994). Imaging nuclear pores of aldosterone-sensitive kidney cells by atomic force microscopy. *Proc Natl Acad Sci U S A*, 91, 9784-9788.
- Ochi, T., Suzuki, T., Isono, H., Schlagenhaufen, C., Goessler, W., and Tsutsui, T. (2003). Induction of structural and numerical changes of chromosome, centrosome abnormality, multipolar spindles and multipolar division in cultured Chinese hamster V79 cells by exposure to a trivalent dimethylarsenic compound. *Mutat Res*, 530, 59-71.
- Oesterle, A., and Sutter Instrument (2011). Pipette Cookbook. http://www.sutter.com/contact/faqs/pipette_cookbook.pdf. 20/06/2010.
- Ohwada, Y., and Eguchi, M. (1993). Ultrastructural investigation of DNA in megakaryoblastic leukemia by using osmium-ammine-B: comparison with several types of leukemia. *Med Oncol Tumor Pharmacother*, 10, 117-124.
-

- Olins, A.L., Moyer, B.A., Kim, S.H., and Allison, D.P. (1989). Synthesis of a more stable osmium ammine electron-dense DNA stain. *J Histochem Cytochem*, 37, 395-398.
- Olins, A.L., and Olins, D.E. (1974). Spheroid chromatin units (v bodies). *Science*, 183, 330-332.
- Olins, D.E., and Olins, A.L. (2003). Chromatin history: our view from the bridge. *Nat Rev Mol Cell Biol*, 4, 809-814.
- Olins, D.E., and Olins, A.L. (2005). Granulocyte heterochromatin: defining the epigenome. *BMC Cell Biol*, 6, 39.
- Ollion, J., Loll, F., Cochennec, J., Boudier, T., and Escude, C. (2015). Proliferation-dependent positioning of individual centromeres in the interphase nucleus of human lymphoblastoid cell lines. *Mol Biol Cell*, 26, 2550-2560.
- Orkin, S.H., and Zon, L.I. (2008). Hematopoiesis: an evolving paradigm for stem cell biology. *Cell*, 132, 631-644.
- Ou, H.D., Phan, S., Deerinck, T.J., Thor, A., Ellisman, M.H., and O'Shea, C.C. (2017). ChromEMT: Visualizing 3D chromatin structure and compaction in interphase and mitotic cells. *Science*, 357.
- Pal, K., Forcato, M., and Ferrari, F. (2019). Hi-C analysis: from data generation to integration. *Biophys Rev*, 11, 67-78.
- Pantelias, G.E., and Maillie, H.D. (1983). A simple method for premature chromosome condensation induction in primary human and rodent cells using polyethylene glycol. *Somatic Cell Genet*, 9, 533-547.
- Pau, G., Fuchs, F., Sklyar, O., Boutros, M., and Huber, W. (2010). EBImage--an R package for image processing with applications to cellular phenotypes. *Bioinformatics*, 26, 979-981.
- Pau, G., Oles, A., Smith, M., Sklyar, O., and Huber, w. EBImage: Image processing toolbox for R. <http://www.bioconductor.org/packages/release/bioc/html/EBImage.html>. 14/08/2015.
- Payne, K.J., and Crooks, G.M. (2002). Human hematopoietic lineage commitment. *Immunol Rev*, 187, 48-64.
- Pepperkok, R., Schneider, C., Philipson, L., and Ansorge, W. (1988). Single cell assay with an automated capillary microinjection system. *Exp Cell Res*, 178, 369-376.
- Peus, D., Meves, A., Pott, M., Beyerle, A., and Pittelkow, M.R. (2001). Vitamin E analog modulates UVB-induced signaling pathway activation and enhances cell survival. *Free Radic Biol Med*, 30, 425-432.
- Piskadlo, E., and Oliveira, R.A. (2017). A Topology-Centric View on Mitotic Chromosome Architecture. *Int J Mol Sci*, 18.
- Planchon, T.A., Gao, L., Milkie, D.E., Davidson, M.W., Galbraith, J.A., Galbraith, C.G., and Betzig, E. (2011). Rapid three-dimensional isotropic imaging of living cells using Bessel beam plane illumination. *Nat Methods*, 8, 417-423.
- Pombo, A., Jackson, D.A., Hollinshead, M., Wang, Z., Roeder, R.G., and Cook, P.R. (1999). Regional specialization in human nuclei: visualization of discrete sites of transcription by RNA polymerase III. *EMBO J*, 18, 2241-2253.
- Popken, J., Brero, A., Koehler, D., Schmid, V.J., Strauss, A., Wuensch, A., Guengoer, T., Graf, A., Krebs, S., Blum, H., *et al.* (2014). Reprogramming of fibroblast nuclei in cloned bovine embryos involves major structural remodeling with both striking similarities and differences to nuclear phenotypes of in vitro fertilized embryos. *Nucleus*, 5, 555-589.
- Prasanna, P.G., Escalada, N.D., and Blakely, W.F. (2000). Induction of premature chromosome condensation by a phosphatase inhibitor and a protein kinase in unstimulated

human peripheral blood lymphocytes: a simple and rapid technique to study chromosome aberrations using specific whole-chromosome DNA hybridization probes for biological dosimetry. *Mutat Res*, 466, 131-141.

Pubmed genome database. Homo sapiens. <https://www.ncbi.nlm.nih.gov/genome/51>. 03/11/2019.

Pubmed genome database. Mus musculus. <https://www.ncbi.nlm.nih.gov/genome/52>. 03/11/2019.

Puig, R., Barrios, L., Pujol, M., Caballin, M.R., and Barquinero, J.F. (2013). Suitability of scoring PCC rings and fragments for dose assessment after high-dose exposures to ionizing radiation. *Mutat Res*, 757, 1-7.

Puvion, E., Viron, A., Assens, C., Leduc, E.H., and Jeanteur, P. (1984). Immunocytochemical identification of nuclear structures containing snRNPs in isolated rat liver cells. *J Ultrastruct Res*, 87, 180-189.

R Core Team (2013). R: A language and environment for statistical computing. <http://www.R-project.org>. 14/08/2015.

Rao, S.S., Huntley, M.H., Durand, N.C., Stamenova, E.K., Bochkov, I.D., Robinson, J.T., Sanborn, A.L., Machol, I., Omer, A.D., Lander, E.S., *et al.* (2014). A 3D map of the human genome at kilobase resolution reveals principles of chromatin looping. *Cell*, 159, 1665-1680.

Rattner, J.B., and Wang, T. (1992). Kinetochore formation and behaviour following premature chromosome condensation. *J Cell Sci*, 103 (Pt 4), 1039-1045.

Rauch, J., Knoch, T.A., Solovei, I., Teller, K., Stein, S., Buiting, K., Horsthemke, B., Langowski, J., Cremer, T., Hausmann, M., *et al.* (2008). Light optical precision measurements of the active and inactive Prader-Willi syndrome imprinted regions in human cell nuclei. *Differentiation*, 76, 66-82.

Rebelo, S., Santos, M., Martins, F., da Cruz e Silva, E.F., and da Cruz e Silva, O.A. (2015). Protein phosphatase 1 is a key player in nuclear events. *Cell Signal*, 27, 2589-2598.

Ricci, M.A., Manzo, C., Garcia-Parajo, M.F., Lakadamyali, M., and Cosma, M.P. (2015). Chromatin fibers are formed by heterogeneous groups of nucleosomes in vivo. *Cell*, 160, 1145-1158.

Rieder, C.L., and Palazzo, R.E. (1992). Colcemid and the mitotic cycle. *J Cell Sci*, 102 (Pt 3), 387-392.

Rieger, M.A., and Schroeder, T. (2012). Hematopoiesis. *Cold Spring Harb Perspect Biol*, 4.

Rohme, D. (1975). Evidence suggesting chromosome continuity during the S phase of Indian muntjac cells. *Hereditas*, 80, 145-149.

Romero, I., Lamadrid, A.I., Gonzalez, J.E., Garcia, O., Voisin, P., and Roy, L. (2015). Shortening the culture time in cytogenetic dosimetry using PCC-R assay. *Radiat Prot Dosimetry*, 163, 424-429.

Rouquette, J., Cremer, C., Cremer, T., and Fakan, S. (2010). Functional nuclear architecture studied by microscopy: present and future. *Int Rev Cell Mol Biol*, 282, 1-90.

Rouquette, J., Genoud, C., Vazquez-Nin, G.H., Kraus, B., Cremer, T., and Fakan, S. (2009). Revealing the high-resolution three-dimensional network of chromatin and interchromatin space: a novel electron-microscopic approach to reconstructing nuclear architecture. *Chromosome Res*, 17, 801-810.

Rowley, M.J., and Corces, V.G. (2018). Organizational principles of 3D genome architecture. *Nat Rev Genet*, 19, 789-800.

- Ru, Y.X., Mi, Y.C., Liu, J.H., Wang, H.J., Zhao, S.X., Cui, W., Li, C.W., Li, Q.H., Zhu, X.F., Xiao, Z.J., *et al.* (2009). Significance of transmission electron microscopy in subtyping of monocytic leukemia. *Ultrastruct Pathol*, 33, 67-75.
- Rube, C.E., Lorat, Y., Schuler, N., Schanz, S., Wennemuth, G., and Rube, C. (2011). DNA repair in the context of chromatin: new molecular insights by the nanoscale detection of DNA repair complexes using transmission electron microscopy. *DNA Repair (Amst)*, 10, 427-437.
- Rust, M.J., Bates, M., and Zhuang, X. (2006). Sub-diffraction-limit imaging by stochastic optical reconstruction microscopy (STORM). *Nat Methods*, 3, 793-795.
- Saghaeian-Jazi, M., Mohammadi, S., and Sedighi, S. (2016). Culture and Differentiation of Monocyte Derived Macrophages Using Human Serum: An Optimized Method. *Zahedan J Res Med Sci*, 18.
- Sarkaria, J.N., Busby, E.C., Tibbetts, R.S., Roos, P., Taya, Y., Karnitz, L.M., and Abraham, R.T. (1999). Inhibition of ATM and ATR kinase activities by the radiosensitizing agent, caffeine. *Cancer Res*, 59, 4375-4382.
- Schaffer, M. (2018). Cryo-FIB: Overcoming the Hurdle of Sample Preparation for In Situ Cryo-Electron Tomography. *Microsc Microanal*, 24, 2326-2327.
- Schardin, M., Cremer, T., Hager, H.D., and Lang, M. (1985). Specific staining of human chromosomes in Chinese hamster x man hybrid cell lines demonstrates interphase chromosome territories. *Hum Genet*, 71, 281-287.
- Schermelleh, L., Carlton, P.M., Haase, S., Shao, L., Winoto, L., Kner, P., Burke, B., Cardoso, M.C., Agard, D.A., Gustafsson, M.G., *et al.* (2008). Subdiffraction multicolor imaging of the nuclear periphery with 3D structured illumination microscopy. *Science*, 320, 1332-1336.
- Schermelleh, L., Heintzmann, R., and Leonhardt, H. (2010). A guide to super-resolution fluorescence microscopy. *J Cell Biol*, 190, 165-175.
- Schindelin, J., Arganda-Carreras, I., Frise, E., Kaynig, V., Longair, M., Pietzsch, T., Preibisch, S., Rueden, C., Saalfeld, S., Schmid, B., *et al.* (2012). Fiji: an open-source platform for biological-image analysis. *Nat Methods*, 9, 676-682.
- Schmid, V. (2013). bioimagetools: Some tools for bioimaging. <http://volkerschmid.de>. 14/08/2015.
- Sengupta, P., Van Engelenburg, S., and Lippincott-Schwartz, J. (2012). Visualizing cell structure and function with point-localization superresolution imaging. *Dev Cell*, 23, 1092-1102.
- Sexton, T., and Cavalli, G. (2015). The role of chromosome domains in shaping the functional genome. *Cell*, 160, 1049-1059.
- Sexton, T., Yaffe, E., Kenigsberg, E., Bantignies, F., Leblanc, B., Hoichman, M., Parrinello, H., Tanay, A., and Cavalli, G. (2012). Three-dimensional folding and functional organization principles of the Drosophila genome. *Cell*, 148, 458-472.
- Shao, L. (2014). Structured-Illumination Microscopy: What types of samples are not suitable and why. <http://aicblog.janelia.org/?p=264>. 27/11/2019.
- Shao, L., Kner, P., Rego, E.H., and Gustafsson, M.G. (2011). Super-resolution 3D microscopy of live whole cells using structured illumination. *Nat Methods*, 8, 1044-1046.
- Shu, X., Lev-Ram, V., Deerinck, T.J., Qi, Y., Ramko, E.B., Davidson, M.W., Jin, Y., Ellisman, M.H., and Tsien, R.Y. (2011). A genetically encoded tag for correlated light and electron microscopy of intact cells, tissues, and organisms. *PLoS Biol*, 9, e1001041.
- Sirri, V., Urcuqui-Inchima, S., Roussel, P., and Hernandez-Verdun, D. (2008). Nucleolus: the fascinating nuclear body. *Histochem Cell Biol*, 129, 13-31.

- Smeets, D., Markaki, Y., Schmid, V.J., Kraus, F., Tattermusch, A., Cerase, A., Sterr, M., Fiedler, S., Demmerle, J., Popken, J., *et al.* (2014). Three-dimensional super-resolution microscopy of the inactive X chromosome territory reveals a collapse of its active nuclear compartment harboring distinct Xist RNA foci. *Epigenetics Chromatin*, 7, 8.
- Smith, O.K., and Aladjem, M.I. (2014). Chromatin structure and replication origins: determinants of chromosome replication and nuclear organization. *J Mol Biol*, 426, 3330-3341.
- Solimando, L., Luijsterburg, M.S., Vecchio, L., Vermeulen, W., van Driel, R., and Fakan, S. (2009). Spatial organization of nucleotide excision repair proteins after UV-induced DNA damage in the human cell nucleus. *J Cell Sci*, 122, 83-91.
- Solovei, I., Kreysing, M., Lanctot, C., Kosem, S., Peichl, L., Cremer, T., Guck, J., and Joffe, B. (2009). Nuclear architecture of rod photoreceptor cells adapts to vision in mammalian evolution. *Cell*, 137, 356-368.
- Spector, D.L., Fu, X.D., and Maniatis, T. (1991). Associations between distinct pre-mRNA splicing components and the cell nucleus. *EMBO J*, 10, 3467-3481.
- Spector, D.L., and Lamond, A.I. (2011). Nuclear speckles. *Cold Spring Harb Perspect Biol*, 3.
- Sperling, K., and Rao, P.N. (1974). The phenomenon of premature chromosome condensation: its relevance to basic and applied research. *Humangenetik*, 23, 235-258.
- Spielmann, M., Lupianez, D.G., and Mundlos, S. (2018). Structural variation in the 3D genome. *Nat Rev Genet*, 19, 453-467.
- Spierenburg, G.T., Oerlemans, F.T., van Laarhoven, J.P., and de Bruyn, C.H. (1984). Phototoxicity of N-2-hydroxyethylpiperazine-N'-2-ethanesulfonic acid-buffered culture media for human leukemic cell lines. *Cancer Res*, 44, 2253-2254.
- Stevens, J.B., Abdallah, B.Y., Regan, S.M., Liu, G., Bremer, S.W., Ye, C.J., and Heng, H.H. (2010). Comparison of mitotic cell death by chromosome fragmentation to premature chromosome condensation. *Mol Cytogenet*, 3, 20.
- Stevens, J.B., Liu, G., Bremer, S.W., Ye, K.J., Xu, W., Xu, J., Sun, Y., Wu, G.S., Savasan, S., Krawetz, S.A., *et al.* (2007). Mitotic cell death by chromosome fragmentation. *Cancer Res*, 67, 7686-7694.
- Stevens, T.J., Lando, D., Basu, S., Atkinson, L.P., Cao, Y., Lee, S.F., Leeb, M., Wohlfahrt, K.J., Boucher, W., O'Shaughnessy-Kirwan, A., *et al.* (2017). 3D structures of individual mammalian genomes studied by single-cell Hi-C. *Nature*, 544, 59-64.
- Strauss, M.P., Liew, A.T., Turnbull, L., Whitchurch, C.B., Monahan, L.G., and Harry, E.J. (2012). 3D-SIM super resolution microscopy reveals a bead-like arrangement for FtsZ and the division machinery: implications for triggering cytokinesis. *PLoS Biol*, 10, e1001389.
- Strickfaden, H. (2010). Nuclear architecture explored by live-cell fluorescence microscopy using laser and ion microbeam irradiation. In Department Biology II (Munich, Germany: Ludwig-Maximilians University (LMU)).
- Strickfaden, H., Sharma, A.K., and Hendzel, M. (2019). A charge-dependent phase transition determines interphase chromatin organization. *bioRxiv*.
- Subramaniam, S., Zhang, P., Lefman, J., Juliani, J., and Kessel, M. (2003). Electron tomography: a powerful tool for 3D cellular microscopy. *ASM News*, 69, 240-245.
- Sulli, G., Di Micco, R., and d'Adda di Fagagna, F. (2012). Crosstalk between chromatin state and DNA damage response in cellular senescence and cancer. *Nat Rev Cancer*, 12, 709-720.
- Szabo, Q., Jost, D., Chang, J.M., Cattoni, D.I., Papadopoulos, G.L., Bonev, B., Sexton, T., Gurgo, J., Jacquier, C., Nollmann, M., *et al.* (2018). TADs are 3D structural units of higher-order chromosome organization in *Drosophila*. *Sci Adv*, 4, eaar8082.

- Szczurek, A., Klewes, L., Xing, J., Gourram, A., Birk, U., Knecht, H., Dobrucki, J.W., Mai, S., and Cremer, C. (2017). Imaging chromatin nanostructure with binding-activated localization microscopy based on DNA structure fluctuations. *Nucleic Acids Res*, 45, e56.
- Tan, L., Xing, D., Chang, C.H., Li, H., and Xie, X.S. (2018). Three-dimensional genome structures of single diploid human cells. *Science*, 361, 924-928.
- Tanay, A., and Cavalli, G. (2013). Chromosomal domains: epigenetic contexts and functional implications of genomic compartmentalization. *Curr Opin Genet Dev*, 23, 197-203.
- Tang, J.Y., Hwang, B.J., Ford, J.M., Hanawalt, P.C., and Chu, G. (2000). Xeroderma pigmentosum p48 gene enhances global genomic repair and suppresses UV-induced mutagenesis. *Mol Cell*, 5, 737-744.
- Telenius, H., Carter, N.P., Bebb, C.E., Nordenskjold, M., Ponder, B.A., and Tunnacliffe, A. (1992). Degenerate oligonucleotide-primed PCR: general amplification of target DNA by a single degenerate primer. *Genomics*, 13, 718-725.
- Terasaki, M., Campagnola, P., Rolls, M.M., Stein, P.A., Ellenberg, J., Hinkle, B., and Slepchenko, B. (2001). A new model for nuclear envelope breakdown. *Mol Biol Cell*, 12, 503-510.
- Terzoudi, G.I., Karakosta, M., Pantelias, A., Hatzi, V.I., Karachristou, I., and Pantelias, G. (2015). Stress induced by premature chromatin condensation triggers chromosome shattering and chromothripsis at DNA sites still replicating in micronuclei or multinucleate cells when primary nuclei enter mitosis. *Mutat Res Genet Toxicol Environ Mutagen*, 793, 185-198.
- Testillano, P.S., Sanchez-Pina, M.A., Olmedilla, A., Ollacarizqueta, M.A., Tandler, C.J., and Risueno, M.C. (1991). A specific ultrastructural method to reveal DNA: the NAMA-Ur. *J Histochem Cytochem*, 39, 1427-1438.
- The GTK+ Team. <http://www.gtk.org>. 27/11/2019.
- The Royal Swedish Academy of Sciences (2014). Super-resolved fluorescence microscopy - Scientific Background on the Nobel Prize in Chemistry 2014. <https://www.nobelprize.org/uploads/2018/06/advanced-chemistryprize2014-1.pdf>. 27/11/2019.
- Theml, H., Diem, H., and Haferlach, T. (2004). *Color Atlas of Hematology - Practical microscopic and clinical diagnosis*, 2nd edn. Stuttgart, Germany, Georg Thieme.
- Tokuyasu, K.T. (1973). A technique for ultracryotomy of cell suspensions and tissues. *J Cell Biol*, 57, 551-565.
- Toomre, D., Langhorst, M., and Davidson, M. (2012). Digital Imaging Considerations. <http://zeiss-campus.magnet.fsu.edu/print/spinningdisk/introduction-print.html>. 27/11/2019.
- Tosuji, H., Mabuchi, I., Fusetani, N., and Nakazawa, T. (1992). Calyculin A induces contractile ring-like apparatus formation and condensation of chromosomes in unfertilized sea urchin eggs. *Proc Natl Acad Sci U S A*, 89, 10613-10617.
- Uhler, C., and Shivashankar, G.V. (2017). Regulation of genome organization and gene expression by nuclear mechanotransduction. *Nat Rev Mol Cell Biol*, 18, 717-727.
- Ulianov, S.V., Gavrilov, A.A., and Razin, S.V. (2015). Nuclear compartments, genome folding, and enhancer-promoter communication. *Int Rev Cell Mol Biol*, 315, 183-244.
- Ulianov, S.V., Tachibana-Konwalski, K., and Razin, S.V. (2017). Single-cell Hi-C bridges microscopy and genome-wide sequencing approaches to study 3D chromatin organization. *Bioessays*, 39.
- Vakoc, C.R., Mandat, S.A., Olenchock, B.A., and Blobel, G.A. (2005). Histone H3 lysine 9 methylation and HP1gamma are associated with transcription elongation through mammalian chromatin. *Mol Cell*, 19, 381-391.

- Vazquez-Nin, G.H., Biggiogera, M., and Echeverria, O.M. (1995). Activation of osmium ammine by SO₂-generating chemicals for EM Feulgen-type staining of DNA. *Eur J Histochem*, 39, 101-106.
- Vitale, I., Galluzzi, L., Castedo, M., and Kroemer, G. (2011). Mitotic catastrophe: a mechanism for avoiding genomic instability. *Nat Rev Mol Cell Biol*, 12, 385-392.
- Waldren, C.A., and Johnson, R.T. (1974). Analysis of interphase chromosome damage by means of premature chromosome condensation after X- and ultraviolet-irradiation. *Proc Natl Acad Sci U S A*, 71, 1137-1141.
- Wang, W., Sun, Y., Zhang, M., Anderson, R., Langille, L., and Chan, W. (2008). A system for high-speed microinjection of adherent cells. *Rev Sci Instrum*, 79, 104302.
- Wantha, S., Alard, J.E., Megens, R.T., van der Does, A.M., Doring, Y., Drechsler, M., Pham, C.T., Wang, M.W., Wang, J.M., Gallo, R.L., *et al.* (2013). Neutrophil-derived cathelicidin promotes adhesion of classical monocytes. *Circ Res*, 112, 792-801.
- Watanabe, A., Yamada, Y., and Yamanaka, S. (2013). Epigenetic regulation in pluripotent stem cells: a key to breaking the epigenetic barrier. *Philos Trans R Soc Lond B Biol Sci*, 368, 20120292.
- Webb, D.J., and Brown, C.M. (2013). Epi-fluorescence microscopy. *Methods Mol Biol*, 931, 29-59.
- Williams, R.R., Azuara, V., Perry, P., Sauer, S., Dvorkina, M., Jorgensen, H., Roix, J., McQueen, P., Misteli, T., Merckenschlager, M., *et al.* (2006). Neural induction promotes large-scale chromatin reorganisation of the Mash1 locus. *J Cell Sci*, 119, 132-140.
- Winey, M., Yarar, D., Giddings, T.H., Jr., and Mastronarde, D.N. (1997). Nuclear pore complex number and distribution throughout the *Saccharomyces cerevisiae* cell cycle by three-dimensional reconstruction from electron micrographs of nuclear envelopes. *Mol Biol Cell*, 8, 2119-2132.
- Wognum, A., and Szilvassy, S. (2015). Hematopoietic stem and progenitor cells. http://www.stemcell.com/~media/Technical%20Resources/F/B/7/E/9/MR019HematopoiesisOnline_29784WEB.pdf. 27/11/2019.
- Wolff, G., Hagen, C., Grunewald, K., and Kaufmann, R. (2016). Towards correlative super-resolution fluorescence and electron cryo-microscopy. *Biol Cell*, 108, 245-258.
- Woodcock, C.L., and Ghosh, R.P. (2010). Chromatin higher-order structure and dynamics. *Cold Spring Harb Perspect Biol*, 2, a000596.
- Woodcock, C.L., Safer, J.P., and Stanchfield, J.E. (1976). Structural repeating units in chromatin. I. Evidence for their general occurrence. *Exp Cell Res*, 97, 101-110.
- Woringer, M., Darzacq, X., and Izeddin, I. (2014). Geometry of the nucleus: a perspective on gene expression regulation. *Curr Opin Chem Biol*, 20, 112-119.
- Xu, J., Ma, H., Jin, J., Uttam, S., Fu, R., Huang, Y., and Liu, Y. (2018). Super-Resolution Imaging of Higher-Order Chromatin Structures at Different Epigenomic States in Single Mammalian Cells. *Cell Rep*, 24, 873-882.
- Xu, Y., and Price, B.D. (2011). Chromatin dynamics and the repair of DNA double strand breaks. *Cell Cycle*, 10, 261-267.
- Yadav, L., Khan, S., Shekh, K., and Jena, G.B. (2014). Influence of 3-aminobenzamide, an inhibitor of poly(ADP-ribose)polymerase, in the evaluation of the genotoxicity of doxorubicin, cyclophosphamide and zidovudine in female mice. *Mutat Res Genet Toxicol Environ Mutagen*, 770, 6-15.

- Yamaizumi, M., Sugano, T., Asahina, H., Okada, Y., and Uchida, T. (1986). Microinjection of partially purified protein factor restores DNA damage specifically in group A of xeroderma pigmentosum cells. *Proc Natl Acad Sci U S A*, 83, 1476-1479.
- Yamashita, K., Yasuda, H., Pines, J., Yasumoto, K., Nishitani, H., Ohtsubo, M., Hunter, T., Sugimura, T., and Nishimoto, T. (1990). Okadaic acid, a potent inhibitor of type 1 and type 2A protein phosphatases, activates cdc2/H1 kinase and transiently induces a premature mitosis-like state in BHK21 cells. *EMBO J*, 9, 4331-4338.
- Yang, Y., Wang, H., Chang, K.H., Qu, H., Zhang, Z., Xiong, Q., Qi, H., Cui, P., Lin, Q., Ruan, X., *et al.* (2013). Transcriptome dynamics during human erythroid differentiation and development. *Genomics*, 102, 431-441.
- Yu, H. (2007). Chk1: a double agent in cell cycle checkpoints. *Dev Cell*, 12, 167-168.
- Yuan, G.C., Cai, L., Elowitz, M., Enver, T., Fan, G., Guo, G., Irizarry, R., Kharchenko, P., Kim, J., Orkin, S., *et al.* (2017). Challenges and emerging directions in single-cell analysis. *Genome Biol*, 18, 84.
- Zankel, A., Kraus, B., Poelt, P., Schaffer, M., and Ingolic, E. (2009). Ultramicrotomy in the ESEM, a versatile method for materials and life sciences. *J Microsc*, 233, 140-148.
- Zhang, B., Huang, B., Guan, H., Zhang, S.M., Xu, Q.Z., He, X.P., Liu, X.D., Wang, Y., Shang, Z.F., and Zhou, P.K. (2011). Proteomic profiling revealed the functional networks associated with mitotic catastrophe of HepG2 hepatoma cells induced by 6-bromine-5-hydroxy-4-methoxybenzaldehyde. *Toxicol Appl Pharmacol*, 252, 307-317.
- Zhang, H., Jiao, W., Sun, L., Fan, J., Chen, M., Wang, H., Xu, X., Shen, A., Li, T., Niu, B., *et al.* (2013). Intrachromosomal looping is required for activation of endogenous pluripotency genes during reprogramming. *Cell Stem Cell*, 13, 30-35.
- Zhang, J.A., Mortazavi, A., Williams, B.A., Wold, B.J., and Rothenberg, E.V. (2012a). Dynamic transformations of genome-wide epigenetic marking and transcriptional control establish T cell identity. *Cell*, 149, 467-482.
- Zhang, Y. (2007). Microinjection Technique and Protocol to Single cells. *Nature protocols / Protocol exchange*.
- Zhang, Y., Brady, M., and Smith, S. (2001). Segmentation of brain MR images through a hidden Markov random field model and the expectation-maximization algorithm. *IEEE Trans Med Imaging*, 20, 45-57.
- Zhang, Y., McCord, R.P., Ho, Y.J., Lajoie, B.R., Hildebrand, D.G., Simon, A.C., Becker, M.S., Alt, F.W., and Dekker, J. (2012b). Spatial organization of the mouse genome and its role in recurrent chromosomal translocations. *Cell*, 148, 908-921.
- Zhou, B.B., Chaturvedi, P., Spring, K., Scott, S.P., Johanson, R.A., Mishra, R., Mattern, M.R., Winkler, J.D., and Khanna, K.K. (2000). Caffeine abolishes the mammalian G(2)/M DNA damage checkpoint by inhibiting ataxia-telangiectasia-mutated kinase activity. *J Biol Chem*, 275, 10342-10348.
- Zhou, V.W., Goren, A., and Bernstein, B.E. (2011). Charting histone modifications and the functional organization of mammalian genomes. *Nat Rev Genet*, 12, 7-18.
- Ziegler-Heitbrock, L., and Hofer, T.P. (2013). Toward a refined definition of monocyte subsets. *Front Immunol*, 4, 23.
- Zorn, C., Cremer, T., Cremer, C., and Zimmer, J. (1976). Laser UV microirradiation of interphase nuclei and post-treatment with caffeine. A new approach to establish the arrangement of interphase chromosomes. *Hum Genet*, 35, 83-89.

7. Appendix

7.1 Abbreviations

~1 Mbp CDs	Chromatin domains in the range of several hundred kbp up to 1 Mbp in size
2D	Two dimensional
3C	Chromosome conformation capture
3D	Three dimensional
3D-SIM	Three dimensional structured illumination microscopy
4D	Four dimensional (in space and time)
ANC	Active nuclear compartment
APEX(2)	Enhanced ascorbate peroxidase (2)
AT	Adenine / thymine
ATM	Ataxia telangiectasia mutated
ATR	Ataxia telangiectasia and Rad3-related
ATP	Adenosine triphosphate
bp	Base pairs
BrdU	Bromodeoxyuridine
BrUTP	5-Bromouridine-5'-triphosphate
BSA	Bovine serum albumin
CC	Chromatin compartment
CCD	Charge-coupled device
CD	Chromatin domain
CD14	Cluster of differentiation 14
CD34	Cluster of differentiation 34
CDC	Chromatin domain cluster
Cdc25(A/B/C)	Cell division cycle 25 (A/B/C)
Cdk(1/2)	Cyclin dependent kinase (1/2)
ChIP-seq	Chromatin immunoprecipitation sequencing
Chk1/2	Checkpoint kinase 1/2
ChromEMT	Chromatin staining combined with electron microscopy tomography
CLSM	Confocal laser scanning microscopy
CpG	Cytosine-guanine-dinucleotide
CT	Chromosome territory
CT-IC	Chromosome territory – interchromatin compartment
CTCF	CCCTC-binding factor
Cy3	Indocarbocyanine
Cy5	Indodicarbocyanine
DAB	Diaminobenzidine
DAPI	4'6-diamidino-2-phenylindole
DDB2	DNA damage binding protein 2
DHS[+]	DNase I hypersensitive sites
DHS[-]	Sites not accessible to DNase I
Dig	Digoxigenin
DMEM	Dulbecco's modified eagle medium
DMSO	Dimethyl sulfoxide
DNA	Deoxyribonucleic acid
DNP	Dinitrophenol
DOP-PCR	Degenerate oligonucleotide primed polymerase chain reaction
dUTP	Dexoyuridine triphosphate
EMCCD	Electron multiplying charge-coupled device
ERCB	Emilia Romagna Cord Blood Bank
ESC	Embryonic stem cell

ESI	Electron spectroscopic imaging
FACS	Fluorescence-activated cell sorting
FBS	Fetal bovine serum
FCD	Fetal calf serum
FIB	Focused ion beam
FISH	Fluorescence in situ hybridization
FITC	Fluorescein isothiocyanate
FIAsH	Fluorescein arsenical hairpin
FLT3-L	Fms-like tyrosine kinase 3 ligand
FPALM	Fluorescence photoactivation localization microscopy
FRAP	Fluorescence recovery after photobleaching
G1 PCC	G1 phase PCC
G1/G2 PCC	G1/G2 phase PCC
G2 PCC	G2 phase PCC
GC	Guanine / cytosin
GCS	Generalized chromosome shattering
GFP	Green fluorescent protein
H2B	Histone 2B
H2B-GFP	Histone 2B tagged with GFP
H2B-mRFP	Histone 2B tagged with mRFP
H3K4me3	Histone 3 tri-methylated on lysine 4
H3K9ac	Histone 3 acetylated on lysine 9
H3K9me2	Histone 3 di-methylated on lysine 9
H3K9me3	Histone 3 tri-methylated on lysine 9
H3K14ac	Histone 3 acetylated on lysine 14
H3K27me3	Histone 3 tri-methylated on lysine 27
H3K36me3	Histone 3 tri-methylated on lysine 36
H3S10p	Histone 3 phosphorylated on serine 10
H4K8ac	Histone 4 acetylated on lysine 8
HCC	Hypercondensed chromatin
HSC	Hematopoietic stem cell
IC	Interchromatin compartment
ICN	Interchromosomal network
INC	Inactive nuclear compartment
IdU	Iododeoxyuridine
IL-3/6	Interleukin 3/6
IMEM	Iscove's modified Dulbecco's media
kbp	Kilo base pairs
LAD	Lamin associated domain
LP	Low-pass
MAA	Methanol / acetic acid
Mbp	Mega base pairs
miniSOG	Mini singlet oxygen generator
MPF	Maturation/M-phase promoting factor
mRFP	Monomeric red fluorescent protein
mRNA	Messenger ribonucleic acid
NIH	National Institute of Health
OTF	Optical transfer function
PALCC	Parachute-like chromatin configuration
PALM	Photoactivated localization microscopy
PBS	Phosphate buffered saline
PCC	Premature chromosome condensation (induced cell)
PcG	Polycomb group
PCR	Polymerase chain reaction
PEG	Polyethylene glycol
PFA	Paraformaldehyde

PMT	Photomultiplier tube
POC-R	Perfusion open and closed - R
PP2A	Protein phosphatase 2A
PR	Perichromatin region
ReAsH	Resorufin arsenical hairpin
RNA	Ribonucleic acid
RNA Pol II (Ser 2/5P)	RNA polymerase II (phosphorylated on serine 2/5)
RNA Pol III	RNA polymerase III
ROI	Region of interest
RPMI	Roswell Park Memorial Institute medium
S - G1/G2 PCC	Intermediate form of S and G1/G2 PCC
S PCC	S phase PCC
SBF	Serial block face
SCF	Stem cell factor
SDLMS	Spinning disk laser scanning microscopy
SDS	Sodium dodecyl sulfate
SEM	Scanning electron microscopy
SIM	Structured illumination microscopy
SMC2	Structural maintenance of chromosomes 2
SSC	Saline sodium citrate
STED	Stimulated emission depletion
STORM	Stochastic optical reconstruction microscopy
TAC	Tetrameric antibody complex
TAD	Topologically associating domain
TEM	Transmission electron microscopy
TRITC	Tetramethylrhodamine-5-(and 6)-isothiocyanate
TUNEL	TdT-mediated dUTP-biotin nick end labeling
UV	Ultraviolet
UVA	Ultraviolet A
UV/caffeine	UV irradiation and caffeine post(treatment/treated)
WF	Wide field

7.2 List of figures and tables

7.2.1 List of figures

Figure 1: Models of functional nuclear architecture.	20
Figure 2: Evidence for a global organization of chromatin.	24
Figure 3: Hematopoietic differentiation pathways.	28
Figure 4: Morphology of generalized chromosome shattering (GCS).	31
Figure 5: Cell cycle control through ATM and ATR signaling and the influence of caffeine.	32
Figure 6: PCC induction using Calyculin A.	35
Figure 7: Schematic illustration of the working principle of the EasySep system.	68
Figure 8: Scheme of the Histopaque gradient.	72
Figure 9: Patterns of the gridded coverslips.	78

Figure 10: Illustration of the UV irradiation procedure.....	81
Figure 11: Flow chart for the setup of correlative microscopy.....	144
Figure 12: 3D characteristics of hematopoietic cell types.	172
Figure 13: Variability of the chromatin pattern in CD34 ⁺ cells.	173
Figure 14: Variability of the chromatin pattern in monoblasts.	174
Figure 15: Variability of the chromatin pattern in myeloblasts.....	175
Figure 16: Variability of the chromatin pattern in monocytes.	176
Figure 17: Variability of the chromatin pattern in granulocytes.	177
Figure 18: Chromatin pattern of hematopoietic cell types.....	179
Figure 19: Nucleoli in hematopoietic cell types.....	180
Figure 20: H3K4me3 and RNA Pol II Ser 2P in hematopoietic cell types.	185
Figure 21: H3K4me3 and RNA Pol II Ser 5P in hematopoietic cell types.....	186
Figure 22: Number of RNA Pol II signals in hematopoietic cell types.	187
Figure 23: SC35 and H3K4me3 in hematopoietic cell types.	188
Figure 24: SC35 and RNA Pol II Ser 2P in hematopoietic cell types.	189
Figure 25: SC35 and RNA Pol II Ser 5P in hematopoietic cell types.	190
Figure 26: H3K4me3 and H3K9me3 in CD34 ⁺ cells.	191
Figure 27: H3K4me3 and H3K9me3 in monoblasts.....	193
Figure 28: H3K4me3 and H3K9me3 in myeloblasts.	194
Figure 29: H3K4me3 and H3K9me3 in monocytes (mononuclear cells).....	195
Figure 30: Comparison of markers in hematopoietic cell types.....	196
Figure 31: Chromatin pattern of hematopoietic cell types after hypotonic treatment.	198
Figure 32: Changes between normal and hypotonic conditions in granulocytes.	199
Figure 33: Localization of beads in control and HCC induced HeLa cells.....	202
Figure 34: Localization of 20 nm beads in control and HCC induced HeLa cells.	203
Figure 35: Localization of 40 nm beads in control and HCC induced HeLa cells.	204
Figure 36: Summary of the localization of beads in control and HCC induced HeLa cells....	205
Figure 37: Live cell observation of HeLa cells after the microinjection of 40 nm beads.....	207
Figure 38: Duration of the cell cycle in HeLa control cells and cells microinjected with 40 nm beads.	208
Figure 39: Live cell observation of HeLa cells after the microinjection of 20 nm beads.....	208
Figure 40: Localization of 40 nm beads in HeLa cells before, during and after mitosis.	209
Figure 41: Localization of 20 nm beads in HeLa cells before and after mitosis.....	210
Figure 42: Evaluation of the localization of beads in HeLa cells before and after mitosis. .	211
Figure 43: Nuclear phenotypes in UV/caffeine treated and PCC induced V79 cells after fixation with MAA or PFA.....	214

Figure 44: Correlation of living and MAA fixed UV/caffeine treated V79 cells and subsequent BrdU staining.	217
Figure 45: Long-term live cell observation of UV/caffeine treated V79 cells.	218
Figure 46: Schematic representation of the processes occurring upon UV/caffeine treatment of V79 cells.....	219
Figure 47: Long-term live cell observation of PCC induction and subsequent release in V79 cells.	220
Figure 48: Long-term live cell observation with subsequent PCC induction in V79 cells....	221
Figure 49: Correlation of living and MAA fixed PCC induced V79 cells and subsequent BrdU staining of S PCCs.	222
Figure 50: Correlation of living and MAA fixed PCC induced V79 cells and subsequent BrdU staining of G1/G2 PCCs.	223
Figure 51: Evaluation of PCC induced V79 cells.	224
Figure 52: Lamin B and H3S10p in control and treated V79 cells.....	229
Figure 53: Centromeres, Ki67, and α -tubulin in control and PCC induced V79 cells.	230
Figure 54: Centromeres and α -tubulin in control and UV/caffeine treated V79 cells.	231
Figure 55: SMC2 in control and PCC induced HeLa cells.....	232
Figure 56: H3K4me3 and RNA Pol II Ser 2P in control, PCC induced and UV/caffeine treated V79 cells.	233
Figure 57: H3K4me3 and H3K9me3 in control, PCC induced and UV/caffeine treated V79 cells.	234
Figure 58: Chromosome painting (FISH) of whole chromosomes in V79 nuclei..	235
Figure 59: Comparison of the chromatin pattern in control and treated V79 cells.	239
Figure 60: H3K4me3 and RNA Pol II Ser 2P in control and PCC induced V79 cells.....	240
Figure 61: H3K4me3 and RNA Pol II Ser 2P in control and UV/caffeine treated V79 cells.	241
Figure 62: H3K4me3 and H3K9me3 in control and PCC induced V79 cells.	242
Figure 63: H3K4me3 and H3K9me3 in control and UV/caffeine treated V79 cells.	243
Figure 64: Comparison of markers in control, PCC induced and UV/caffeine treated V79 cells.....	244
Figure 65: Correlative microscopy (pathway I) in HCC induced HeLa cells; SC35 and H3K4me3.	249
Figure 66: Correlative microscopy (pathway I) in control HeLa cells; SC35 and H3K4me3.	250
Figure 67: Correlative microscopy (pathway II) in HCC induced HeLa cells	251
Figure 68: Correlative microscopy (pathway II) in control HeLa cells.....	252
Figure 69: Correlative microscopy (pathway II) in HCC induced HeLa cells.	254
Figure 70: Correlative microscopy (pathway II) in HCC induced HeLa cells.	255
Figure 71: Comparison of the chromatin pattern in control and HCC induced HeLa cells.	259
Figure 72: H3K4me3 and RNA Pol II Ser 2P in control and HCC induced HeLa cells.	260
Figure 73: H3K4me3 and H3K9me3 in control and HCC induced HeLa cells.....	261

Figure 74: Comparison of markers in control and HCC induced HeLa cells.	262
Figure 75: Summary – H3K4me3 and RNA Pol II Ser 2P in various selected cell types and conditions.	269
Figure 76: The ANC-INC network model of functional nuclear architecture.	274

7.2.2 List of tables

Table 1: Overview of cell lines and corresponding growth media.	65
Table 2: Overview of cultivation conditions and times of attachment for the hematopoietic cell types.	78
Table 3: Detection scheme for FISH.....	124

7.3 Contents of the enclosed DVD / ZIP archive

File S1: Rotatable PDF of the 3D reconstruction of the CD34 ⁺ cell shown in Figure 12 B.	
File S2: Rotatable PDF of the 3D reconstruction of the monoblast shown in Figure 12 B.	
File S3: Rotatable PDF of the 3D reconstruction of the myeloblast shown in Figure 12 B.	
File S4: Rotatable PDF of the 3D reconstruction of the monocyte shown in Figure 12 B.	
File S5: Rotatable PDF of the 3D reconstruction of the granulocyte shown in Figure 12 B.	
File S6: Complete movie of the live cell observation of HeLa cells after the microinjection of 40 nm beads shown in Figure 37. Dextran signals.	
File S7: Complete movie of the live cell observation of HeLa cells after the microinjection of 40 nm beads shown in Figure 37. Signals of the beads.	
File S8: Complete movie of the live cell observation of HeLa cells after the microinjection of 40 nm beads shown in Figure 37. Transmission light images.	
File S9: Complete movie of the live cell observation of HeLa cells after the microinjection of 40 nm beads shown in Figure 37. Merged images of dextran (gray) and beads (red).	
File S10: Complete movie of the live cell observation of HeLa cells after the microinjection of 20 nm beads shown in Figure 39. Dextran signals.	
File S11: Complete movie of the live cell observation of HeLa cells after the microinjection of 20 nm beads shown in Figure 39. Signals of the beads. Note that the filters available on the microscope were not optimal for the spectral separation of the dextran-TRITC and the green fluorescent beads.	
File S12: Complete movie of the live cell observation of HeLa cells after the microinjection of 20 nm beads shown in Figure 39. Transmission light images.	
File S13: Complete movie of the live cell observation of HeLa cells after the microinjection of 20 nm beads shown in Figure 39. Merged images of dextran (gray) and beads (red).	
File S14: Complete movie of example 1 of the long-term live cell observation of UV/caffeine treated V79 cells shown in Figure 45.	

- File S15: Complete movie of example 2 of the long-term live cell observation of UV/caffeine treated V79 cells shown in Figure 45.
- File S16: Complete movie of example 3 of the long-term live cell observation of UV/caffeine treated V79 cells shown in Figure 45.
- File S17: Movie of untreated V79 cells as a control for the data shown in Figure 45. This data set was acquired by Dr. Hilmar Strickfaden (University of Alberta, Edmonton, Canada) and Dr. Marion Cremer (LMU, Munich, Germany) in our lab. Cells imaged every 15 min for a total duration of 48 h divided normally throughout the entire observation period. The cells marked with an arrow, respectively their daughter cells, could be followed over two mitoses. Note that there was a shift in the sample after 30.5 h. Only towards the end of the movie (starting at ~41 h) occasionally apoptotic cells were found, most likely due to the very high cell density in the sample.
- File S18: Complete movie of the long-term live cell observation of PCC induction and subsequent release in V79 cells shown in Figure 47.
- File S19: Complete movie of an additional example of long-term live cell observation of PCC induction and subsequent release in V79 cells (equivalent to the data shown in Figure 47).
- File S20: Movie of untreated V79 cells as a control for the data shown in Figure 47. Cells imaged every 5 min for 1 h and then an additional 38.5 h every 15 min (total duration 39.5 h) divided normally throughout the whole observation period. The cells marked with an arrow, respectively their daughter cells, could be followed over two mitoses.
- File S21: Complete movie of the long-term live cell observation with subsequent PCC induction in V79 cells shown in Figure 48.

Acknowledgement / Danksagung

Zuerst und ganz besonders möchte ich mich bei Prof. Dr. Thomas Cremer bedanken: **Thomas**, danke, dass Du mir ermöglicht hast in Deiner Gruppe zu promovieren und dass Du mich so mit der Begeisterung für den Zellkern und die Mikroskopie angesteckt hast. Du hast mir stets viel Freiraum gelassen, um die Experimente und Projekte durchzuführen, an denen mir selbst viel gelegen hat, hast mir aber auch in zahlreichen Diskussionen und Gesprächen geholfen, mich auf die wesentlichen Dinge zu konzentrieren. Ich möchte Dir auch für die Möglichkeit danken, meinen Horizont auf verschiedenen nationalen und internationalen Konferenzen und Workshops erweitern zu können. Und ein besonderes Danke dafür, dass bei allem Fokus auf die Wissenschaft in Deiner Arbeitsgruppe immer die Menschlichkeit im Vordergrund gestanden hat.

Dann ein großer Dank an Dr. Marion Cremer: **Marion**, die langjährige Schreibtisch-nachbarschaft mit Dir habe ich sehr genossen – nicht nur weil Du stets für wissenschaftliche Diskussionen zu haben warst und immer ein offenes Ohr für meine Probleme aller Art im Hinblick auf Experimente, theoretische Fragen und unverständliche Verwaltungsangelegenheiten hattest, sondern auch weil so mancher Plausch das Arbeitsleben aufgelockert hat.

Vielen Dank an **Prof. Dr. Christof Osman** für die Übernahme der Zweitkorrektur und an **Prof. Dr. Andreas Klingl**, **Prof. Dr. Maria-Elena Torres-Padilla**, **Prof. Dr. Heinrich Leonhard** und **Prof. Dr. Martin Heß** für die Bereitschaft Teil meiner Prüfungskommission zu sein.

To **my collaborators in Modena/Italy**, especially to **Mariana** (without you this collaboration never would have started!), but also to **Fabiana** and **Claudio**: thanks a lot for the great time in Italy. I really enjoyed working with you! A big thank you also to **Prof. Dr. Sergio Ferrari** for taking me up in your group and so giving me the opportunity to do the hematopoiesis work, and also for the fruitful discussions. Thank you also to all the people I met over the years and who made working there a lot of fun! Grazie tante!

Vielen Dank auch an **Hilmar**: Du hast mir praktisch alles über Lebendzellmikroskopie beigebracht, was man wissen kann. Danke vor allem auch für die Hilfe und das Mitleiden beim Injizieren von Beads – nur jemand, der das selber mal gemacht hat, kann den Wahnsinn und die Unberechenbarkeit dieser Methode wirklich verstehen...

Yolanda, thanks for everything: you were not only an excellent advisor and teacher in all scientific questions ranging from immunofluorescence to OMX microscopy and beyond, but you also understand the hiccups that work in academia sometimes brings along and life inside and outside the lab was so much fun with you!

Thank you also to my TEM teachers, **Jacques** and **Martina**: you were brilliant in explaining! Martina, es beruhigt mich ungemein, dass es noch mehr Leute gibt, die Sections-Schneiden nicht als pure Qual betrachten... A big thank you also to **Prof. Dr. Stan Fakan** for providing all the equipment and therefore making this work possible in our lab. Thank you so much, **Prof. Dr. Ada Olins** and **Prof. Dr. Donald Olins**, for revealing some little tricks to me that make sample preparation for TEM a lot easier.

Volker, vielen Dank für die Entwicklung der Segmentierung und vor allem für Deine Geduld, mir die für einen Statistiker einfachsten Dinge wieder und wieder zu erklären.

Ein herzlicher Dank geht an **Nadine**, **Steffi P.**, **Mareike** und **Korbinian**: Mit Eurer Arbeit zu PCC habt Ihr den Grundstein für meine weitere Arbeit gelegt und/oder mit einigen Experimenten zum Projekt beigetragen. Es hat Spaß gemacht mit Euch!

Fritzi, danke für die Herstellung der Slides mit Lamin B und H3S10p in den V79 Zellen.

A big thank you to all the people involved in maintaining the microscopes: **Jürgen** und **Andreas** für das OMX; **Irina** and also **Olga** for the Confocal(s) – **Irina**, apart from that also thanks a lot for all the good times sharing one office and especially for all the discussions and

advice in so many aspects!; **Heidi, Martin** und **Otto** für das Morgagni; **Katrin** für das UltraView VoX – und zudem auch danke für das Entwickeln des OMX Makros: was hätte ich nur ohne das gemacht?; **Hilmar** und **Steffen** für das Axiovert 200 M – **Steffen**, außerdem danke, dass Du das Mikroskop noch so lange in unserer Obhut gelassen hast.

For a few weeks I “took over” the job from Irina, so I really know how much work taking care of a microscope is and I highly appreciate what you’re doing! Danke Euch allen!

Danke an **Prof. Dr. Heinrich Leonhardt** und **Prof. Dr. Roland Beckmann**, für den Zugang zum OMX bzw. zum Morgagni 268.

Heidi, Dir gebührt aller Dank und Respekt dafür, dass Du es über so lange Jahre mit uns allen ausgehalten hast ;-). Deine Ordnung im Labor war phänomenal und Deine kleineren und größeren Arbeiten für die Allgemeinheit rechne ich Dir noch immer sehr hoch an. Danke auch, dass Du mir stets zur Seite gestanden bist, wenn ich Rat und Hilfe bei den diversen Laborangelegenheiten gebraucht habe.

Vielen Dank an **Prof. Dr. Dirk Eick** für die Bereitstellung der RNA Polymerase II Antikörper und **Dr. Alexander Kaiser**, **Dr. Joachim Gündel** und **Dr. Horatiu Fantana** für die Hilfe bei der Entwicklung geeigneter Mikroinjektionsnadeln.

Auch an die **IT-Gruppe**, an das **Team aus der Spülküche** und an die **Werkstatt** geht mein Dank: für die Hilfe und Unterstützung bei den diversen größeren und kleineren Angelegenheiten.

Danke an **Prof. Dr. Wolfgang Enard**, dafür, dass wir unsere Zellkultur und den Abzug im Labor noch weiter nutzen durften und so trotz begrenzten Raumangebot unsere Arbeit noch in vollem Umfang aufrechterhalten konnten.

Ein ganz liebes Danke an **all die weiteren lang- und kurzzeitigen Weggefährten**: Sandro, Dani K., Nina, Charlotte, Claudi, Heppi, Florian, Micha, Stefan, Zuni, Isi, Jens N., Birgit, Alex, Dani W., Julia, Doris, Violet, Katrin, Yvonne, Vee, Kathi, Michi, Sabine Le., Christoph, Christina, Sabine La., Martin, Yana, Daniel, Steffi T., Martha, Xenia, Dagmar, Jens P., Boris, Gustavo, Federico, Pablo, Caroline, Fr. Zhao. Danke, dass Ihr alle da wart und die Arbeit so nicht nur Arbeit war, sondern auch wahnsinnig viel Spaß gemacht hat! Thanks for being there and making work not only work, but also a lot of fun!

Daneben auch ein herzlicher Dank **an die anderen Arbeitsgruppen** im 3. Stock im Biozentrum: an alle Doktoranden, Praktikanten, Mitarbeiter, etc. in der AG Böttger, AG Weiß, AG Classen und AG Grupe. Insbesondere an **Chris** und **Christina** für das langjährige Teilen der Qual mit dem Stickstofftank.

A big thank you also goes to everyone in Singapore. **Sara** and **Alex**, thanks for supporting me in every aspect and for giving me the environment to bring this to a good end. And thank you to **all the other people in our lab** for making the time at work so incredibly enjoyable!

Ein letzter, aber entscheidender Dank geht an meine **Familie** – Danke, dass Ihr immer da wart!

Curriculum Vitae

This information was omitted for the online submission of the dissertation.

Publications

Research Publications

Hübner B, Strickfaden H, Müller S, Cremer M, Cremer T, Chromosome shattering: a mitotic catastrophe due to chromosome condensation failure, Eur Biophys J, 38 (6): 729-47, 2009

Hübner B, Cremer T, Neumann J, Correlative microscopy of individual cells – sequential application of microscopic systems with increasing resolution to study the nuclear landscape, Methods Mol Biol, 1042: 299-336, 2013

Hübner B, Lomiento M, Mammoli F, Illner D, Markaki Y, Ferrari S, Cremer M, Cremer T, Remodeling of nuclear landscapes during human myelopoietic cell differentiation maintains co-aligned active and inactive nuclear compartments, Epigenetics & Chromatin, 8:47, 2015

Hübner B, von Otter E, Ashan B, Wee ML, Ludwig A, Sandin S, In situ ultrastructure of mammalian telomeres revealed by correlative light and electron microscopy (CLEM) and electron tomography, *in preparation*

Reviews

Cremer T, Markaki Y, **Hübner B**, Zunhammer A, Strickfaden H, Beichmanis S, Heß M, Schermelleh L, Cremer M, Cremer T, Chromosome Territory Organization within the nucleus, Meyers: Encyclopedia of Molecular Cell Biology and Molecular Medicine: Epigenetic Regulation and Epigenomics, Second Edition, Wiley-VCH Verlag GmbH & Co. KGaA, 2011

Cremer T, Cremer M, **Hübner B**, Strickfaden H, Smeets D, Popken J, Sterr M, Markaki Y, Rippe K, Cremer C, The 4D nucleome: Evidence for a dynamic nuclear landscape based on co-aligned active and inactive nuclear compartments, FEBS Lett, 589 (20 Pt A): 2931-43, 2015

Cremer T, Cremer M, **Hübner B**, Silahatoglu A, Hendzel M, Lanctôt C, Strickfaden H, Cremer C, The interchromatin compartment participates in the structural and functional organization of the cell nucleus, BioEssays, 42 (2): e1900132, 2020

Eidesstattliche Erklärung

Ich versichere hiermit an Eides statt, dass die vorgelegte Dissertation von mir selbstständig und ohne unerlaubte Hilfe angefertigt ist.

Tutzing, den ...24.3.2021...

.....

Barbara Hübner

Erklärung

Hiermit erkläre ich,

- dass die Dissertation nicht ganz oder in wesentlichen Teilen einer anderen Prüfungskommission vorgelegt worden ist.
- dass ich mich anderweitig einer Doktorprüfung ohne Erfolg **nicht** unterzogen habe.
- ~~dass ich mich mit Erfolg der Doktorprüfung im Hauptfach
und in den Nebenfächern
bei der Fakultät für der
unterzogen habe.~~
- ~~dass ich ohne Erfolg versucht habe, eine Dissertation einzureichen oder mich der
Doktorprüfung zu unterziehen.~~

Tutzing, den ...24.3.2021...

.....

Barbara Hübner

